UNIVERSITY OF CAMBRIDGE

The Molecular Anatomy of Mitochondrial Disease:

Identification and Characterisation of Novel Nuclear-Encoded Mitochondrial Disease Genes

Anabel Martinez Lyons

This Dissertation is Submitted for the Degree of Doctor of Philosophy

October 2019

Lucy Cavendish College

Declaration

This dissertation is the result of my own work, carried out under the supervision of Professor Massimo Zeviani at the Mitochondrial Biology Unit (MBU) and funded by the United Kingdom Research and Innovation Medical Research Council (UKRI MRC) between October 2015 and October 2019. It includes nothing that is the outcome of work done in collaboration with others except as declared in the text and further specified in the figure legends. Appropriate accreditation is given to all work cited from other sources, which are referenced accordingly. This thesis is not substantially the same as any that I have submitted, or is being concurrently submitted for a degree, diploma or any other qualification at the University of Cambridge or any other academic institution. I further state that no substantial part of my dissertation has already been submitted, or is being concurrently submitted for any such degree, diploma or other qualification at the University of Cambridge or any other academic institution. It does not exceed the prescribed word limit set by the University of Cambridge Degree Committee for Clinical and Veterinary Medicine upon successful approval of an extension of 20,000 words.

The results described in **Chapter 3** concerning the identification and characterisation of biallelic mutations in *COA7* in a mitochondrial disease patient led to a publication in the Journal of Medical Genetics: *COA7* (*C1orf163/RESA1*) mutations associated with mitochondrial leuko-encephalopathy and cytochrome *c* oxidase deficiency (Martinez Lyons *et al.*, *J Med Genet*, (12):846-849; doi: 10.1136/jmedgenet-2016-104194, Epub 28th Sept, 2016).

Anabel Martinez Lyons

October 2019

Abstract

The Molecular Anatomy of Mitochondrial Disease: Identification and Characterisation of Novel Nuclear-Encoded Mitochondrial Disease Genes

Anabel Martinez Lyons

Mitochondrial diseases are a group of clinically and genetically heterogeneous disorders typically associated with abnormal oxidative phosphorylation (OXPHOS). In recent years, next generation sequencing technologies have allowed for accurate genetic diagnoses of inherited mitochondrial diseases directly from patient DNA by facilitating the identification of potential candidate genetic defects in either nuclear or mitochondrial genomes. In such a manner, two compound heterozygous sequence variants in *COA7*, which encodes a putative cytochrome *c* oxidase (Complex IV, COX) assembly factor, and homozygous recessive sequence variants in *TMCO6*, which encodes an uncharacterised protein, were identified in patients presenting with classical clinical and biochemical hallmarks of mitochondrial disease. The aim of this work was to 1) assess the pathogenicity of the *COA7* and *TMCO6* mutant variants in causing mitochondrial disease, and 2) to investigate the association of the resulting proteins in the assembly pathways of complexes of the mitochondrial respiratory chain: Complex IV (CIV, COX) for COA7 and Complex I (CI) for TMCO6.

Compound heterozygous mutant variants in *COA7* (NM_023077.3:c.410A>G;c.287+1G>T) led to total disappearance of its gene product in patient skin fibroblasts, owing to two aberrant mRNA transcripts. Loss of COA7 steady-state level correlated with low abundance of certain COX subunits, intermediates, monomeric and supercomplex COX species, as well as isolated COX enzymatic deficiency. Stable expression of $COA7^{WT}$ in patient fibroblasts by lentivirus-mediated complementation rescued COX abundance, the quantities of its affected subunits, subassembly and supercomplex species, and its activity, to normal levels, confirming the pathogenicity of the compound heterozygous *COA7* mutant variants. A combination of super-resolution microscopy and subcellular fractionation and protease digestion studies confirmed the intracellular localisation of COA7 to be the mitochondrial intermembrane space.

Secondly, a novel homozygous recessive variant in *TMCO6* (NM_018502.5: c.271C>T) was identified in a paediatric proband presenting with severe developmental delay, generalised hypotonia and progressive cerebral and cerebellar atrophy. Biochemical measurement of a skeletal muscle biopsy revealed CI enzymatic deficiency, and patient-derived skin fibroblasts showed destabilisation of CI-containing supercomplexes. TMCO6 was found to co-localise with the CI holocomplex by 2D-BNGE, and this result was further corroborated by immunoprecipitation experiments. Additionally, cellular models for *TMCO6* gene silencing and overexpression were characterised, and an attempted generation of a knockout cellular model is described. Subcellular fractionation and protease treatment experiments determined TMCO6 to localise to the mitochondrial inner membrane. A *Tmco6*-knockout murine model was characterised, which exhibited several neurological, physiological and motor debilities, isolated CI deficiency in heart and skeletal muscle, and abnormal cardiac electrophysiology. Recombinant AAV-mediated expression of wildtype, human *TMCO6* rescued the CI deficiency and electrophysiological function of 3 month-old knockout mice hearts. In contrast, stable expression of the patient mutant protein variant failed to recover the isolated CI deficiency, and additionally resulted in severe cardiac fibrosis. Together, these findings causally link ablation of, or mutations in, *TMCO6* with mitochondrial dysfunction and disease.

Acknowledgements

I wish to thank Professor Massimo Zeviani for the opportunity to undertake this degree and for his continued support in the progression of this research. I am also very thankful to the UKRI MRC for funding my training and supporting this area of biomedical research. Special thanks to the MRC MBU Mitochondrial Medicine group, all members past and present. Specifically, I would like to thank Dr. Aurelio Reyes and Dr. Erika Fernandez-Vizarra for their expert day-to-day supervision, and continued guidance, teaching and encouragement throughout my time in the lab. I am also much indebted to Dr. Carlo Viscomi for his advice and skill concerning all mouse model upkeep and experiments.

Heartfelt thanks to the following individuals, who each contributed advice, assistance or training in their respective areas of expertise: Raffaele Cerutti (histology), Dr. Cristiane Beninca (super resolution microscopy), Stephen Moore (echocardiography), Dr. Alan Robinson (bioinformatics), and Dr. Mark Johnson (CRISPR/Cas9). Primary patient fibroblasts were provided by Dr. Daniele Ghezzi from the Unit of Molecular Neurogenetics, Foundation IRCCS Besta Institute of Neurology (Milan, Italy), and Dr. Caterina Garone, previously of the MRC MBU (Cambridge, UK), kindly supplied the clinical history and associated information regarding the *TMCO6* patient.

Thank you very much to the MRC MBU's IT and administrative teams, all of whom were extremely generous with their time and support. Thanks also to the Phenomics Facility animal care technicians and staff who kept all *in vivo* work running smoothly.

Lastly, and importantly, thank you to my wonderful parents, siblings and better half, David, for the unconditional 'at home' support, without which this PhD would not have been possible.

Abbreviations

AAV	adeno-associated virus
ADP	adenosine diphosphate
ATP	adenosine triphosphate
BNGE/BN-PAGE	blue native polyacrylamide gel electrophoresis
bp	base pairs
BSA	bovine serum albumin
CD68	cluster of differentiation 68
CDS	coding sequence
CI	complex I
CII	complex II
CIII	complex III
CIV	complex IV
CLAMS	comprehensive laboratory animal monitoring system
CNPase	2', 3'-cyclic nucleotide 3'-phosphodiesterase
CNS	central nervous system
COX	cytochrome *c* oxidase
CRISPR	clustered regularly interspaced short palindromic repeats
CS	citrate synthase
CV	complex V
Cyt c	cytochrome c
DAB	3, 3' diaminobenzidine
DDM	n-dodecyl-β-D-maltoside
DMEM	Dulbecco's modified Eagle's medium
DNA	deoxyribonucleic acid
DOX	doxycycline
DPX	dibutylphthalate polystyrene xylene
ER	endoplasmic reticulum
ETC	electron transport chain
EV	empty vector
FAD	flavin adenine dinucleotide
FBS	foetal bovine serum
Fe-S	iron-sulphur
FMN	flavin mononucleotide
FS	FLAG/Streptavidin
GATK	genome analysis toolkit

gDNA	genomic DNA
GFAP	glial fibrillary acidic protein
HA	hemagglutinin
H&E	hematoxylin and eosin
HEK	human embryonic kidney
HS	heavy strand
ICC	immunocytochemistry
IHC	immunohistochemistry
IMAGE	integrated molecular analysis of genomes and their expression
IMM	inner mitochondrial membrane
IMS	intermembrane space
KO	knockout
LS	light strand
MEFs	mouse embryo fibroblasts
MELAS	mitochondrial encephalopathy, lactic acidosis and stroke-like episodes
MIA	mitochondrial intermembrane space assembly machinery
MITRAC	mitochondrial translation regulation assembly intermediate of COX
mMPT	mitochondrial membrane permeability transition
MRS	magnetic resonance spectrometry
mtDNA	mitochondrial DNA
MTS	mitochondrial targeting signal
MW	molecular weight
NAD	nicotinamide adenine dinucleotide
NBF	neutral buffered saline
NBT	nitro blue tetrazolium
nDNA	nuclear DNA
NGS	next generation sequencing
OMM	outer mitochondrial membrane
OXPHOS	oxidative phosphorylation
PBS	phosphate buffered saline
PCR	polymerase chain reaction
PDH	pyruvate dehydrogenase
Pi	inorganic phosphate
Δp	protonmotive force
Q, CoQ	ubiquinone, coenzyme Q
RET	reverse electron transfer
RNA	ribonucleic acid

SAM	sorting and assembly machinery
SDH	succinate dehydrogenase
SDS-PAGE	sodium dodecyl sulphate polyacrylamide gel electrophoresis
shRNA	short hairpin RNA
SOD	sodium dismutase
TCA	tricarboxylic acid
T_m	melting temperature
TIM(M)	translocase of the inner membrane
TOM(M)	translocase of the outer membrane
tRNA	transfer RNA
VDAC	voltage-dependent anion channel
WB	Western blot
WES	whole exome sequencing
WT	wild type

Table of Contents

Chapter 1

Introduction

1.1 General Introduction to Mitochondria

1.1.1 Origin of Mitochondria

Mitochondria are subcellular organelles that have been crucial to the development and existence of eukaryotic life. The phylogenetic origin of mitochondria is an α-proteobacterium (Yang *et al.*, 1985; Andersson *et al.*, 1998), which formed an endosymbiotic relationship with an archaeal host cell between 1.5 and 2 billion years ago (Sicheritz-Pontén, Kurland, and Andersson 1998; Martin 2010). The most likely cause for their union and the mechanism of incorporation of the former has been much debated. The endosymbiotic theory (Sagan 1967), many versions of which were proposed throughout the 1970s to the 1990s, posits that an anaerobic, nucleate and amitochondriate early eukaryotic cell (Cavalier-Smith, 1987) engulfed an oxygen (O_2)-utilising α-proteobacterium by phagocytosis (Ford Doolittle, 1998), which evaded digestion and formed a mutually beneficial relationship with the host in an increasingly O_2-rich atmosphere (Lane and Martin, 2010). However, recent comparative genomic and geochemical evidence instead suggest that the driving force for eukaryogenesis was in fact the beneficial exchange of hydrogen (H_2) from an α-proteobacterial facultative anaerobe, which synthesised H_2 by fermentation, but could also respire aerobically in the presence of O_2, to a H_2-dependent archaeal (prokaryotic) host cell (Martin and Müller 1998; Koonin 2010). Furthermore, the host and endosymbiont were brought together through syntrophy, where one species consumes the end product(s) of metabolism of the other, and not by phagocytosis (Martin *et al.*, 2016), with the compartmentalisation of a nucleus occurring afterwards (Mans *et al.*, 2004). This hydrogen hypothesis (Martin and Müller 1998), as it is termed, explains important factors that the canonical endosymbiotic theory does not, including the discovery that mitochondria share the majority of their genes with hydrogenosomes (Embley and Martin, 2006), mitochondria-like organelles that generate H_2 as an end product of adenosine triphosphate (ATP) synthesis in several species of anaerobic eukaryote (Lindmark and Müller, 1973), and the revelation that the Proterozoic ocean was predominantly anoxic at the time when eukaryotes arose (Mentel and Martin, 2008). In either case, the endosymbiont conferred to the host a set of novel and beneficial metabolic processes that ultimately allowed for the adaptation of the host to new environmental niches, and the host, in turn, protected and provided ample substrates to the mitochondrial ancestor.

Over time, the majority of the genetic material from the mitochondrial ancestor governing its functions and biogenesis was transferred to the genome of the host (Ku *et al.*, 2015), consolidating their symbiotic relationship and eliminating organellar autonomy of the mitochondrion. Mitochondrial gene transfer resulted in expansion of the nuclear genome, a

key factor in the development of more functionally complex organisms (Lane and Martin, 2010). However, by retaining a small genome of essential genes for ATP production and protein synthesis, mitochondria can quickly respond to changes in cellular metabolic demand, effectively acting as an “ATP sensor”, and can do so proportionately to the relative influx of nuclear-encoded proteins (Amiott and Jaehning, 2006; Richter-Dennerlein *et al.*, 2016). Mitochondria have been decisively essential to the evolutionary transition from prokaryotes to eukaryotes, directly enabling the vast biodiversity we observe today.

1.1.2 Mitochondrial Discovery, Structure and Dynamics

In 1890, Richard Altmann recognised the ubiquitous presence of mitochondria in eukaryotic cells, terming them “bioblasts”, and concluded that they were self-replicating "elementary organisms" within cells that carried out vital cellular functions (Altmann 1890). The name “mitochondrion” was introduced in 1898 by Carl Benda, derived from “mitos” (μίτος, “thread”) and “chondros” (χονδρίον, “granule”), referring to the appearance of these structures by light microscopy as “threads dotted with grains” (Benda 1898; Ernster and Schatz 1981). In 1912, Benjamin Freeman Kingsbury described mitochondria as "a structural expression of the reducing substances concerned in cellular respiration", linking the unique shape of these organelles with their role in cellular energy metabolism (Kingsbury 1912; Ernster and Schatz 1981). The first high-resolution images of the internal mitochondrial structure were published in the 1950s owing to the development of electron microscopy (Palade, 1953; Sjöstrand, 1953). Since then, the understanding of mitochondrial morphology, dynamics, bioenergetics and other characteristic features and functions has increased substantially. This understanding has cemented mitochondria as essential mediators of normal cellular physiology, as well as of disease pathology, the latter of which is a role still requiring much elucidation (Pagliarini and Rutter, 2013).

Mitochondria consist of two phospholipid bilayers, the outer mitochondrial membrane (OMM) and the inner mitochondrial membrane (IMM); between the OMM and IMM lies the intermembrane space (IMS), and the IMM encloses a central compartment, the mitochondrial matrix (MM) (Palade, 1953; Sjöstrand, 1953; Perkins *et al.*, 1997) (**Fig. 1.1**). The lipid compositions, protein densities and relative permeabilities of the OMM and IMM differ considerably. The OMM has a phospholipid composition similar to that of the plasma membrane with an approximately 1:1 protein to phospholipid ratio (Parsons and Yano 1967; Ernster and Schatz 1981). The OMM acts as the interface between the mitochondrion and the cytosol, and so, protects the cell from mitochondrial factors that lead to oxidative stress (Pernas and Scorrano, 2016), inflammation (West, Shadel and Ghosh, 2011) and cell death

(Danial and Korsmeyer, 2004). Additionally, the OMM mediates physical interaction of a mitochondrion with other mitochondria and other organelles, principally the endoplasmic reticulum (ER) (Marchi, Patergnani and Pinton, 2014). The OMM is selectively permeable to small hydrophilic molecules due to numerous mitochondrial porins, the voltage-dependent anion channels (VDAC) (Benz, 1985), which allow selective passage of molecules less than 6.8 kDa in size (Shoshan-Barmatz *et al.*, 2010). In addition, nuclear-encoded proteins are imported into the mitochondria by the translocase of the outer mitochondrial membrane (TOM) complex, a multimeric channel that imports unfolded preproteins into the IMS, and from there they are translocated to the correct mitochondrial compartment by other translocases and assembly machineries (Wiedemann, Frazier, and Pfanner 2004). One such example is the sorting and assembly machinery (SAM) complex, which inserts proteins into the OMM (Wiedemann *et al.*, 2003).

The second of the mitochondrial membranes, the IMM, is densely packed with protein, with a roughly 3:1 protein to phospholipid ratio (Parsons and Yano 1967; Ernster and Schatz 1981), and is rich in cardiolipin, similarly to prokaryotic cell membranes (Paradies *et al.*, 2014). The IMM contains its own protein import machinery, the translocase of the inner membrane (TIM) complexes TIM22 and TIM23, for embedment of proteins into the IMM or import into the MM, respectively (Wiedemann, Frazier, and Pfanner 2004). The IMM invaginates into the MM to form cristae (folds), which drastically increase its surface area (Mannella, 2006). Cristae are structurally organised in part by the mitochondrial contact-site and cristae organising system (MICOS) complex (Kozjak-Pavlovic, 2017), which interacts with the SAM complex of the OMM to form the mitochondrial intermembrane space bridging (MIB) complex (Huynen *et al.*, 2016). Importantly, cristae are the site of mitochondrial aerobic respiration, and subsequent ATP synthesis, altogether termed oxidative phosphorylation (OXPHOS), as will be discussed in detail in the next section. The IMM is relatively impermeable compared to the OMM, and so has developed a sophisticated set of mitochondrial protein carriers for the import, export or exchange of specific substrates and reaction products (Kunji, 2004). The tight control of the permeability of the IMM allows for the generation and maintenance of an electrochemical proton gradient (of H^+ ions) during respiration, that is essential for ATP synthesis (Nicholls, 1974), and for calcium (Ca^{2+}) uptake through the mitochondrial calcium uniporter (Stefani *et al.*, 2014).

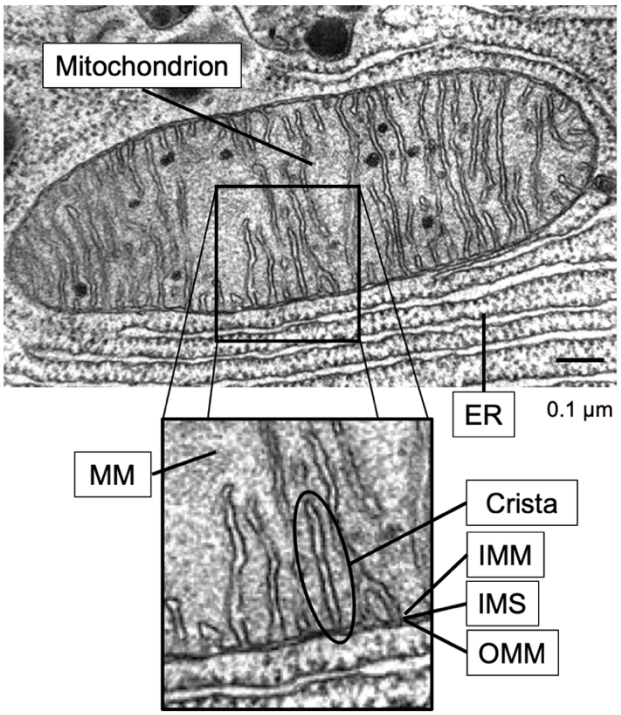

Figure 1.1. Classical mitochondrial structure.

Figure shows a transmission electron micrograph of a single mitochondrion from a pancreatic acinar cell of the little brown bat, *Myotis lucifugus*, sliced longitudinally across its midplane, and the surrounding cytoplasm, including the endoplasmic reticulum (ER). A magnified inset of a portion of the mitochondrion highlights the outer mitochondrial membrane (OMM) and inner mitochondrial membrane (IMM), which lie either side of the intermembrane space (IMS). The IMM invaginates into the central mitochondrial compartment, the mitochondrial matrix (MM), to form distinctive folds termed cristae (singular: crista), which greatly increase its surface area. The cristae are variable in length and shape, and house the proteins necessary for mitochondrial energy production (by the coupled processes of the electron transport chain and ATP synthesis). This figure was compiled by the author using an electron micrograph courtesy of Keith R. Porter (2011) CIL:11397, *Myotis lucifugus*. CIL Dataset. Available from: https://doi.org/doi:10.7295/W9CIL11397.

The IMS, an approximately 20 nm wide space between the OMM and IMM, has protein and metabolite concentrations similar to that of the cytoplasm (Kühlbrandt, 2015). The IMS houses the majority of cellular cytochrome *c* (cyt *c*), which, along with its role in electron transfer during OXPHOS, can initiate the death pathway of the cell, apoptosis, upon release into the cytosol (Ding and Yin, 2012). The IMS also contains the mitochondrial intermembrane space assembly (MIA) complex, which mediates disulphide bond creation in cysteine-rich proteins that localise to the IMS, and also the translocation of oxidative proteins that ultimately localise to the IMM following transport through the IMS (Stojanovski, Bragoszewski and Chacinska, 2012). Additionally, the IMS is a site of mitochondrial lipid synthesis (Horvath and Daum, 2013), detoxification of the reactive oxygen species superoxide by the action of Cu/Zn

superoxide dismutase (SOD1) (Fischer *et al.*, 2011), and metal ion exchange between the matrix and cytosol (Wiedemann, Frazier, and Pfanner 2004). In contrast to the IMS, the MM is extremely protein-rich, with a protein concentration of ~ 500 mg/ml (Kühlbrandt, 2015), and serves many mitochondrial anabolic and catabolic reactions, including the tricarboxylic acid cycle (TCA) cycle (also named the 'citric acid cycle') (Akram, 2014), the biosynthesis of haem moieties and iron-sulphur (Fe-S) clusters (Lill *et al.*, 2012), and the synthesis and degradation of amino acids (Guda, Guda, and Subramaniam 2007). Importantly, the MM houses the mitochondrial DNA (mtDNA) and the ribosomes necessary for mitochondrial protein synthesis (Clay Montier, Deng and Bai, 2009). Additionally, the respiratory chain protein complexes each protrude into the MM, whereby proton pumping by Complexes I, III and IV results in an elevated pH of ~7.2 compared to that of the IMS or cytoplasm (Porcelli *et al.*, 2005).

Mitochondria were originally believed to exist as individual, rod-shaped entities owing to their presentation in early electron micrographs (Palade, 1953; Sjöstrand, 1953), but are nowadays recognised to form extensive and dynamic networks, with variations in average number, size and motility within cells differing between various tissue types (McCarron *et al.*, 2013). For example, in skeletal muscle, mitochondria are confined to rows that lie parallel to the contractile fibrils (Vendelin *et al.*, 2005), but in neurons, mitochondria often translocate along the cytoskeleton from the dendrites to the synapses and vice versa in response to fluctuations in energy demands relative to nerve transmission (Barnhart, 2016). Mitochondrial shape, size and number per cell are further dictated by the competing processes of fusion, the combination of two organelles into one, and fission, division of one organelle into two (Koshiba *et al.*, 2004). Eukaryotic cells have no means of *de novo* mitochondrial synthesis, and so, proliferation can only occur from pre-existing mitochondria by fission. The morphology of mitochondria will also vary depending on their physiological state (Kuznetsov and Margreiter, 2009); fusion allows for the equilibration of mtDNA, proteins and/or metabolites when resources are low, and fission makes it possible to isolate damaged mitochondria from the network and target them for degradation through selective autophagy, called mitophagy (Pickles, Vigié and Youle, 2018). It is not only the external mitochondrial structure that responds to the physiological state of the cell and of the organelle. The abundance, width, length and alignment of the cristae of the IMM can fluctuate in response to substrate availability, metabolic demand and as a consequence of the release of apoptotic signals (Heath-Engel and Shore, 2006). The dynamic morphology of mitochondria ultimately allows cells to balance metabolic demand with nutrient supply in a flexible manner.

1.1.3 ATP Production via OXPHOS

Arguably, the most essential function of mammalian mitochondria is ATP production via OXPHOS (**Fig. 1.2**). Firstly, a series of redox reactions is carried out by four multimeric protein complexes, each embedded within the IMM. These are Complex I (CI), NADH:ubiquinone oxidoreductase; Complex II (CII), succinate:ubiquinone oxidoreductase; Complex III (CIII), ubiquinone:cytochrome *c* oxidoreductase; and Complex IV (CIV or COX), cytochrome *c* oxidase) (Hatefi, 1985). Electrons are transferred from protein or molecular donors to acceptors from CI or CII to CIII, and then from CIII to CIV (Sazanov, 2015). In the case of CI, CIII and CIV, the free energy liberated as electrons travel down the redox potential gradient is used to pump protons (H^+ cations) across the IMM from the MM to the IMS: 4 H^+ ions for CI and CIII and 2 H^+ ions for CIV (Schultz and Chan, 2001). Two mobile electron carriers, the lipophilic molecule coenzyme Q_{10}/ubiquinone (CoQ/Q) (Turunen, Olsson and Dallner, 2004) and the hydrophilic protein cyt *c* (Hüttemann *et al.*, 2011), transfer electrons from CI and CII to CIII, and from CIII to CIV, respectively. These processes together are known as the electron transport chain (ETC), or mitochondrial respiratory chain. Reduced forms of nicotinamide adenine dinucleotide (NADH) and flavin adenine dinucleotide ($FADH_2$), products of the catabolism of carbohydrates, fatty acids and/or amino acids, are key electron donors in the ETC, providing electrons at the CI and CII points of entry, respectively (Akram, 2014; Martínez-Reyes *et al.*, 2016). A protonmotive force (Δp) is generated from the resulting higher concentration of protons present in the IMS than in the MM (ΔpH), as well as an asymmetrical distribution of electrical charges across the IMM, termed the mitochondrial membrane potential ($\Delta\psi_M$) (Mitchell and Moyle, 1969; Dzbek and Korzeniewski, 2008). This protonmotive force drives transfer of protons back through the IMM from the IMS to the MM by a fifth protein complex, F_oF_1-ATP synthase (CV) (Elston, Wang and Oster, 1998). OXPHOS is the coupled actions of the ETC (CI-CIV) and chemiosmosis (Mitchell, 1961), ultimately leading to the production of ATP, the 'energy currency' of mammalian cells, from condensation of adenosine diphosphate (ADP) and inorganic phosphate (Pi) molecules, catalysed by the F_1 catalytic domain of ATP synthase (Mitchell, 1961; Walker, 2013). The newly synthesised ATP produced in the MM is exchanged for ADP by the ADP/ATP carrier (Kunji *et al.*, 2016), which is located in the IMM along with the OXPHOS complexes. Once in the IMS, ATP can pass freely through the OMM via VDAC (Bonora *et al.*, 2012). The dephosphorylation of ATP to ADP is a crucial means of providing the free energy necessary for a myriad of essential reactions within eukaryotic cells, and allows these reactions to be thermodynamically favourable.

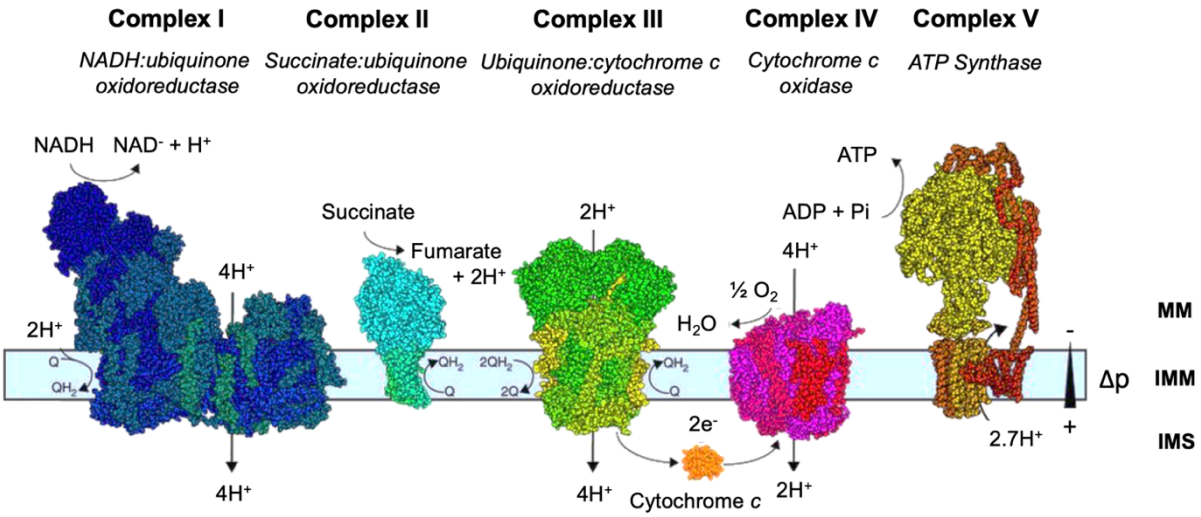

Figure 1.2. The composite structures and reactions involved in mammalian OXPHOS.

Figure depicts the atomic spherical structures and individual reactions of each of the complexes of the mammalian mitochondrial OXPHOS system; CI is ovine (PDB ID: 5LNK), CII is porcine (PDB ID: 1ZOY), and CIII (PDB ID: 1NTM), CIV (PDB ID: 5B1A) and CV (PDB ID: 5ARA) are bovine. Cytochrome c is equine (PDB ID: 5IY5), and ubiquinone is denoted by 'Q', which is its reduced form (QH_2) is termed ubiquinol. MM = mitochondrial matrix, IMM = inner mitochondrial membrane, and IMS = intermembrane space. CI-CIV comprise the electron transport chain (ETC) or 'mitochondrial respiratory chain', and ATP synthase is responsible for the production of ATP from condensation of adenosine diphosphate (ADP) and inorganic phosphate (Pi) molecules. A protonmotive force (Δp) is generated by movement of H^+ cations from the MM to the IMS. Adapted from Figure 1, Letts and Sazanov 2017.

In normal physiological conditions, OXPHOS is incompletely coupled, whereby protons in the IMS can return to the MM independently of ATP synthase in a process known as proton leak, which generates heat instead of ATP (Jastroch *et al.*, 2010). Thermogenesis occurs naturally through the actions of uncoupler proteins (UCPs), which uncouple ATP synthesis from electron transport, dissipating Δp and increasing production of heat (Cannon and Nedergaard, 2011). UCP1 is one such protein primarily found in brown adipose tissue (Cannon and Nedergaard, 2004), and is responsible for adaptive non-shivering thermogenesis typically observed in newborn or hibernating mammals (Nedergaard *et al.*, 2001). The ionophore carbonyl cyanide m-trifluoromethoxyphenylhydrazone (CCCP) is capable of chemically inducing uncoupling of the ETC by disrupting the integrity of the IMM, causing proton leak, and prompting the ETC to run at its maximal rate (Benz and McLaughlin 1983). Chemically inducible uncoupling is useful for the study of the maximal respiratory rate of isolated mitochondria *in vitro* (Plitzko and Loesgen, 2018).

1.1.4 Additional Mitochondrial Functions

In addition to OXPHOS, mitochondria are involved in a number of other crucial metabolic and homeostatic processes that will be briefly addressed here. Mitochondria mediate iron homeostasis, both its storage and utilisation, in eukaryotic cells, and are also directly involved in the biosynthesis of haem moieties and iron-sulphur (Fe-S) clusters (Stehling and Lill, 2013), which are metal prosthetic groups found in each of CI, CII and CIII of the mitochondrial ETC. Mitochondrial Fe-S cluster synthesis depends on the Fe-S cluster assembly machinery and occurs in the MM (Paul *et al.*, 2017). Secondly, all of the 20 amino acids that compose proteins have metabolic pathways concerning mitochondria; both catabolic and anabolic reactions are associated with the non-essential residues and strictly catabolic reactions are associated for the essential ones (Guda, Guda, and Subramaniam 2007). In addition, some steps of the synthesis and degradation of nucleotides, particularly as a part of the salvage synthetic pathway, occur within mitochondria (Wang 2016). Other metabolic pathways include cardiolipin synthesis (Schlame, 2008), essential for the unique composition of the IMM membrane, and biosynthesis of quinones (Stefely and Pagliarini, 2017), such as CoQ, and steroid hormones (Miller, 2013).

Along with the ER, mitochondria are pivotal organelles in the uptake and regulation of intracellular calcium (Carafoli and Lehninger, 1971). Calcium cations (Ca^{2+}) are transported through the IMM by the mitochondrial calcium uniporter (MCU), which is activated according to free calcium concentration (Chem *et al.*, 2015). Calcium also activates three dehydrogenases of the TCA cycle that produce NADH and $FADH_2$: pyruvate dehydrogenase, NAD^+-dependent isocitrate dehydrogenase, and 2-oxoglutarate dehydrogenase (Traaseth *et al.*, 2004). This, in turn, increases the rate of ATP synthesis given the increase of electron donors, and shows the tight coordination and feedback mechanism of cellular calcium signalling (Tarasov, Griffiths and Rutter, 2012). Calcium, which is essential for processes such as muscle contraction (Yamada and Huzel 1988; Brandes and Bers 1997), for example, is also a signal molecule for activating a metabolic process that produces the ATP needed to sustain further muscle contractions. Calcium overload in mitochondria has been linked to activation of cell death by apoptosis (Prudent and McBride, 2017) and as a control of reactive oxygen species (ROS) signalling (Hempel and Trebak, 2017).

Electron leak during the ETC is the major source of ROS production in mammalian cells (Muller, 2000), and naturally contributes to cellular and organismal senescence (Starkov, 2008), but if not regulated effectively, this oxidative stress, as it is termed, can lead to mitochondrial dysfunction and subsequent pathologies (Dröge, 2002). However, it is now

established that ROS also act as signalling molecules in normal biological and physiological processes (Murphy, 2009). For example, there is substantial evidence that some ROS are essential secondary messengers in innate and adaptive immune cells (West, Shadel and Ghosh, 2011; Schieber and Chandel, 2014). Superoxide ($O_2^{\bullet -}$) is the most prominent free radical that is generated by electron leak to diatomic oxygen at certain sites of CI, CII and CIII (Martínez-Cayuela, 1995). Superoxide is damaging to Fe-S cluster-containing apoproteins in particular, and can lead to the formation of additional reactive species that can damage biological molecules including DNA, lipids and proteins (Halliwell and Cross, 1994). Generation of ROS from CIV is prevented due to the rapid kinetics of the reduction of O_2 to two water molecules (Bourens *et al.*, 2013). In normal conditions, superoxide is rapidly converted to hydrogen peroxide (H_2O_2), either spontaneously or enzymatically by SOD1, resident in the cytosol and IMS, or superoxide dismutase 2 (SOD2/MnSOD), found only in the MM (Murphy, 2009). H_2O_2 can be further reduced to water by the thioredoxin and mitochondrial glutathione peroxidases (Ren *et al.*, 2017). However, superoxide is able to react with nitric oxide ($NO^{\bullet}$), which can diffuse into mitochondria and generate peroxynitrite ($ONOO^-$), a highly reactive and damaging radical (Murphy, 2009). Lastly, H_2O_2 can be reduced by different mechanisms to form hydroxyl radicals ($OH^{\bullet}$), which indiscriminately oxidise lipids, proteins and DNA, often leading to genome instability (Dizdaroglu *et al.*, 2002). In humans, the balance between superoxide production and dismutation by the SOD family of proteins is key for overall health.

Lastly, but importantly, mitochondria are mediators of cell fate, and can effect cell death via apoptosis (Ding and Yin, 2012) or via necrosis (Baines, 2010). Apoptosis is “programmed” cell death arising from irreparable DNA damage, growth factor inhibition and oxidative stressors (such as the ROS described above) (Kanduc *et al.*, 2002; Davis *et al.*, 2010), to name a few factors, and is characterised by permeabilization of the OMM that leads to a release of several pro-apoptotic proteins from the IMS, namely cyt *c* (Liu *et al.*, 1996). This activates a cascade of caspases that cleave cytosolic proteins and eventually cause lysis of the plasma membrane (Kawai *et al.*, 2007). Necrosis is activated by more severe cellular stressors, such as cytosolic Ca^{2+} overload, and prompts the permeabilization of the IMM in a process called mitochondrial membrane permeability transition (mMPT) (Kim, He and Lemasters, 2003; Tsujimoto and Shimizu, 2007), and leads to the dissipation of the membrane potential of the IMM (Baines, 2010). Ion deregulation, mitochondrial and cellular swelling, and activation of degradative enzymes follow (Manjo and Joris, 1995), the latter of which leads to plasma membrane lysis.

This overview highlights just how integral mitochondria are for survival. Dysregulation of any of these functions has the potential to cause disease; however, perturbations to the subunits,

assembly factors and co-factors necessary for formation, function or regulation of the OXPHOS protein complexes, in particular, are responsible for the majority of clinical cases of mitochondrial diseases (Manfredim and Beal, 2006; Wang *et al.*, 2014).

1.1.5 Bigenomic Regulation of Mitochondria

As mentioned previously, during eukaryogenesis, the majority of the genetic material from the mitochondrial ancestor governing its functions and biogenesis was transferred to the genome of the host cell (Ku *et al.*, 2015), consolidating their symbiotic relationship and eliminating organellar autonomy of the mitochondrion. In this way, mitochondria exist under bigenomic regulation from genes resident in both mitochondrial DNA (mtDNA) and nuclear DNA (nDNA) (Sinha *et al.*, 2010). Although nuclear mitochondrial genes are the focus of this work, it is important to appreciate the contribution made by mtDNA to mitochondrial physiology. In humans, mtDNA is a circular, double-stranded DNA loop of 16.6 kilobases (kb), composed of a guanine-rich "heavy" strand (HS) and the cytosine-rich "light" strand (LS) (**Fig. 1.3**) (Andrews *et al.*, 1999). The number of mtDNA copies per mitochondrion differs and so too does the overall mtDNA copy number per cell depending on its energy demands (Chinnery and Hudson, 2013). The genes present within the mtDNA are contiguous, separated by one or two non-coding base pairs between genes and containing no introns (Andrews *et al.*, 1999); the mtDNA also has a small, non-coding region termed the displacement loop (D-loop) (Sharma *et al.*, 2005). In humans, the D-loop houses the origin of replication site of the HS and the transcriptional promoters for both the HS and LS. The genetic code of the mtDNA differs slightly from the nDNA, and uses 2 stop codons that are not comparable to any of the 3 of the nDNA (Temperley *et al.*, 2010). Human mtDNA encodes 37 genes: 22 of them encode transfer ribonucleic acids (tRNAs), 2 encode ribosomal RNAs (rRNAs) and 13 encode structural subunits of CI, CIII, CIV or CV of the OXPHOS system (Chinnery and Hudson, 2013). CII is the only respiratory protein complex to be completely encoded by genes in the nDNA (Bezawork-Geleta *et al.*, 2017). The mtDNA is often anchored to the IMM on the MM-facing side in nucleoprotein particles termed nucleoids (Bogenhagen, 2012). All other mitochondrial proteins required for normal mitochondrial physiology, estimated to be ~ 1,200 in total (Rhee *et al.*, 2013), are encoded by the nDNA. The coordination of both genomes is essential for the biogenesis, and subsequently the correct functioning, of the OXPHOS system.

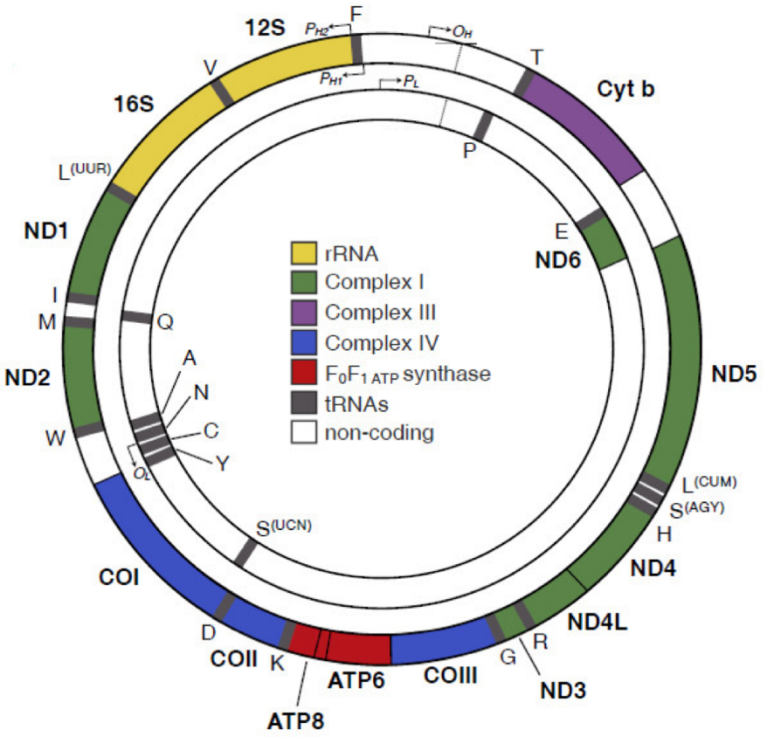

Figure 1.3 The human mitochondrial genome (mtDNA).

The human mtDNA is a circular, double-stranded DNA molecule of ~ 16.6 kb, composed of a guanine-rich "heavy" strand (outer) and the cytosine-rich "light" strand (inner). Genes encoding core OXPHOS structural subunits of CI, CIII, CIV and CV are as follows: CI subunits ND1, ND2, ND3, ND4, ND4L, ND5, and ND6, CIII subunit Cyt *b*, CIV subunits MT-CO1, MT-CO2, and MT-CO3, and CV subunits ATP6 and ATP8. rRNA genes 16S and 12S are located on the HS, and tRNA genes are located both on the HS and the LS. OH and OL indicate the origins of replication of the HS and LS, respectively, and P_{H1}, P_{H2} and P_L indicate the three transcriptional promoters (H = heavy and L = light). Non-coding regions are in white; the D-loop is situated in the top right. Image extracted from Figure 1, Amorim, Fernandes, and Taveira 2019.

1.2 Catalysis and Biogenesis of Complexes I and IV

The structural biogenesis and functional proficiency of the five multimeric protein complexes of the OXPHOS system require the concerted efforts of a large number of proteins, including core and supernumerary structural subunits, and crucially, complex-specific 'assembly factors', which assist the maturation and assembly of nascent complexes but do not form a part of the final structures (Ghezzi and Zeviani 2018). These assembly factors facilitate a range of functions, including the synthesis and/or incorporation of haem (Kim et al. 2012), Fe-S cluster (Ye and Rouault, 2010) and copper ion (Cu^{++}) (Marmocchi *et al.*, 1975) prosthetic groups, as well as chaperoning, stabilising and inserting the structural subunits or subassembly intermediates in the correct order per complex (Fernández-Vizarra, Tiranti and Zeviani, 2009; Nouws *et al.*, 2012). The mechanisms of assembly for each of CI, CII, CIII, CIV and CV have been mostly elucidated (Signes and Fernandez-Vizarra 2018); however, some assembly factors remain undiscovered, and the roles of several that have been identified remain uncharacterised. Due to the focus of this work, only the assembly pathways of CI and CIV will be detailed here.

1.2.1 Complex I

CI is an essential point of entry for electrons into the mitochondrial ETC, and it functions to oxidize NADH, reduce ubiquinone (Q), and transport protons across the IMM (Sharma, Lu, and Bai 2009; Hirst 2013), the latter of which contributes to the protonmotive force necessary for ATP synthesis by CV (Walker, 2013). CI is an L-shaped multimeric protein complex that, in mammals, is composed of 45 individual subunits (comprised of 44 different subunits) (Carroll *et al.*, 2006), and is the largest individual integral structure of the OXPHOS system with a molecular weight of ~ 970 kDa (Hirst, 2010; Guerrero-Castillo *et al.*, 2017). It contains two domain arms: a hydrophilic arm and a hydrophobic arm (Hirst *et al.*, 2003; Berrisford and Sazanov, 2009). The hydrophilic arm protrudes into the MM and is a site of NADH oxidation by a FMN mononucleotide (Wirth *et al.*, 2016), whereby the resulting electron is transferred along a chain or Fe-S clusters to reach a Q-binding site at the interface of both arms (Tocilescu *et al.*, 2007), followed by the hydrophobic arm, which is embedded within the IMM and mediates proton pumping (Hirst, 2013). Upon receival of an electron pair, Q shuttles these electrons to the CIII dimer, $CIII_2$ (Ernster and Dallner, 1995). The catalytic core of CI consists of 7 mtDNA-encoded subunits (ND1, ND2, ND3, ND4, ND4L, ND5, and ND6), all located within the hydrophobic membrane-embedded arm and involved in proton translocation across the IMM, and 7 nDNA-encoded subunits (NDUFV1, NDUFV2, NDUFS1, NDUFS2, NDUFS3, NDUFS7, and NDUFS8), all located within the hydrophilic arm, and are responsible for

electron transfer via 1 FMN (via NDUFV1) and 7 Fe-S clusters (via all 7 subunits, including NDUFV1) (Hirst *et al.*, 2003; Carroll *et al.*, 2006). The remaining 31 subunits of CI, termed 'supernumerary' subunits, are not directly involved in catalysis (Hirst, 2011). The biogenesis of CI is a multifaceted and sophisticated process, requiring coordination of an as-yet undefined number of assembly factors to mediate holocomplex formation (Guerrero-Castillo *et al.*, 2017). **Fig. 1.4** shows the currently known pathway of CI biosynthesis, which is accepted to be modular (Ugalde *et al.*, 2004; Saada *et al.*, 2009; Guerrero-Castillo *et al.*, 2017), containing three separate functional components: the N-module (NADH binding and oxidation), the Q-module (transfer of electrons to ubiquinone), and the P-module (proton-pumping), as described:

1.2.1.1 N-module

The N-module (~ 160 kDa in size) is located at the distal end of the hydrophilic arm, and results from the assembly of NDUFV1, NDUFV2, NDUFS1 and NDUFA2, to which NDUFA6, NDUFA7, NDUFA12, NDUFS4, NDUFS6 and NDUFV3 are later added (Stroud *et al.*, 2016; Guerrero-Castillo *et al.*, 2017). It is the last module to be incorporated (Lazarou *et al.*, 2007), and contains both an integral FMN site as a part of NDUFV1 (Bénit *et al.*, 2001), and also begins the chain of Fe-S clusters necessary for electron translocation along the hydrophilic arm (Tocilescu *et al.*, 2007). The assembly factors necessary for integration of these subunits to form the N-module are not known.

1.2.1.2 Q-module

The Q-module, sandwiched between the N-module and P-module at the interface of both domain arms (Vinothkumar, Zhu, and Hirst 2014), forms by interaction of NDUFA5, NDUFS2 and NDUFS3, to create a 88.9 kDa structure, whereby NDUFS7 and NDUFS8 are then added to form a structure of ~ 129 kDa (Guerrero-Castillo *et al.*, 2017; Signes and Fernandez-Vizarra, 2018). The chaperones NDUFAF3 and NDUFAF4 remain bound to this module until the final steps of assembly (Saada *et al.*, 2009). NDUFAF6 also seems to participate in the assembly of the Q-module but its exact role is not known (Pagliarini *et al.*, 2008). NDUFAF5 hydroxylates an arginine residue of NDUFS7 (Arg 73) (Rhein *et al.*, 2016) and NDUFAF7 demethylates NDUFS2 also at an arginine residue (Arg 85) (Rhein *et al.*, 2013; Zurita Rendón *et al.*, 2014). Additionally, NUBPL has been shown to deliver Fe-S clusters specifically to N- and Q-module subunits, which ultimately make up the Fe-S cluster chain (Sheftel *et al.*, 2009). In the later stages of CI assembly, NDUFA9 is added to this module (Guerrero-Castillo *et al.*, 2017), but the assembly factor involved in this step is not known.

1.2.1.3 P-module

The proton-pumping part of the P-module (termed the P_P-module) is embedded within the IMM and is comprised of two distinct submodules (termed here as P_P-a and P_P-b, but are also termed ND1 and ND2, respectively, in the literature) (Stroud *et al.*, 2016; Guerrero-Castillo *et al.*, 2017; Signes and Fernandez-Vizarra, 2018). Biogenesis of the P_P module begins around the Q-module by the action of the assembly factor TIMMDC1 (Liu et al. 2018), which remains bound to CI subassemblies until the last steps of CI biogenesis (Stroud *et al.*, 2016). Firstly, MT-ND1 is added beneath the N-module, followed by NDUFA3, NDUFA8 and NDUFA13 in quick succession to create a 283 kDa complex, the P_P-a module (Guerrero-Castillo et al. 2017). Separately, MT-ND2, NDUFC1 and NDUFC2 are combined by the actions of a number of assembly factors: NDUFAF1, ECSIT, ACAD9 and COA1 (Stroud *et al.*, 2016; Guerrero-Castillo *et al.*, 2017), the latter of which is also a COX assembly factor (Mick *et al.*, 2012). Then, the MT-ND3 structural subunit is added together with TMEM126B (Heide *et al.*, 2012) and TMEM186 (Guerrero-Castillo *et al.*, 2017), to which subunits MT-ND6 and MT-ND4L then bind (Signes and Fernandez-Vizarra, 2018). The last assembly stage for the P-module involves the incorporation of subunits NDUFA1, NDUFA10 and NDUFS5 by unknown steps of assembly (Stroud *et al.*, 2016; Guerrero-Castillo *et al.*, 2017), to create the P_P-b structure.

The distal part of the P-module (the P_D-module) forms within the IMM and is also comprised of two distinct submodules (P_D-a and P_D-b, as termed here), starting with the incorporation of NDUFB1, NDUFB5, NDUFB6, NDUFB10, NDUFB11 and MT-ND4 into the membrane by the assembly factors FOXRED1 (Fassone *et al.*, 2010), ATP5SL (Andrews *et al.*, 2013) and TMEM70 (Čížková *et al.*, 2008; Jonckheere *et al.*, 2011). The addition of NDUFB4 by an unknown assembly factor step completes the P_D-a module, which then forms a ~ 680 kDa subassembly complex with the P_P-b module (Guerrero-Castillo *et al.*, 2017). The P_D-b module is formed separately by the structural subunits MT-ND5, NDUFB2, NDUFB3, NDUFB7, NDUFB8, NDUFB9 and NDUFAB1 (Guerrero-Castillo *et al.*, 2017). TMEM261 is implicated in the assembly and subsequent stability of the P_D-b module (Stroud *et al.*, 2016; Horlbeck *et al.*, 2018), but no other mediators of the assembly of this submodule are known.

1.2.1.4 Final Steps of CI Assembly

The final intermediate of CI biogenesis contains the Q-module, complete P_P and P_D modules and only lacks the N-module; it is stabilised by NDUFAF2 as well as the already bound assembly factors mentioned above (Ogilvie, Kennaway, and Shoubridge 2005; Vinothkumar, Zhu, and Hirst 2014). In the last steps of CI biogenesis, the N-module attaches along with various subunits that bind to the outside of the complex including NDUFV3, NDUFS4,

NDUFA12 and NDUFS6 (N-module), and NDUFAB1, NDUFA6 and NDUFA7 (Q-module). At this stage, all assembly factors are then released (Guerrero-Castillo *et al.*, 2017).

Fig. 1.4. Mammalian Complex I Biogenesis.

Cartoon representation of the proposed assembly pathway of CI within the mitochondria. For simplicity, the subunits are labelled by omitting the 'NDUF-' portion of the subunit names. N-module = orange, Q-module = yellow, P_P module = green and P_D-module = blue. Assembly factors are purple. The molecular weights in kilodaltons (kDa) of the various subunits, subcomplexes and the holocomplex are included beneath each in black text. Image extracted from Figure 7, Guerrero-Castillo *et al.* 2017.

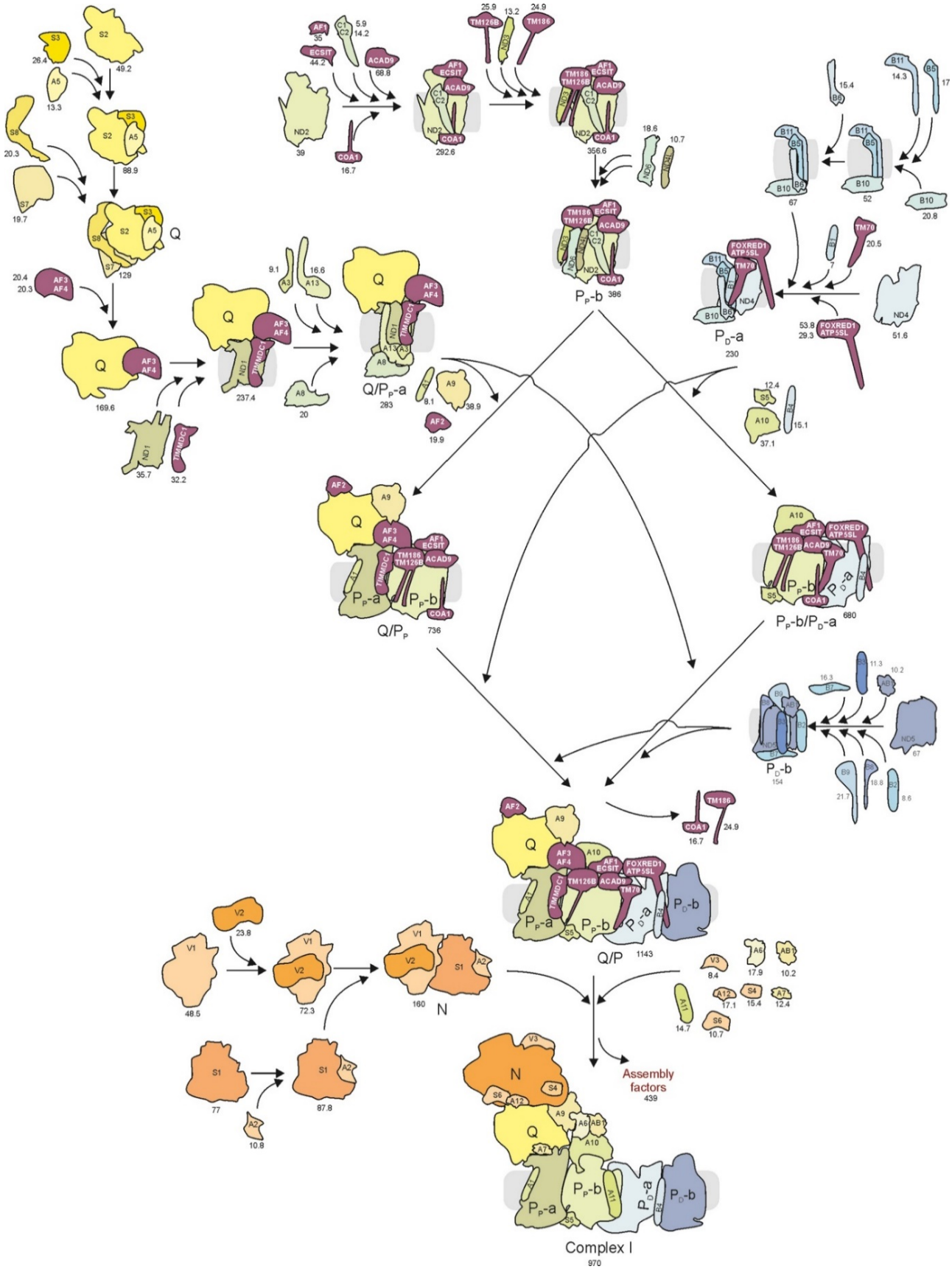

Figure 1.4 . Mammalian Complex I Biogenesis.

1.2.2 Complex IV/COX

Complex IV (cytochrome *c* oxidase; COX) is the terminal enzymatic complex of the ETC that acts in oxidising cyt *c* and then reducing diatomic oxygen to two molecules of water (Wikström, Krab and Sharma, 2018). Like CI, these redox reactions are coupled to proton pumping across the IMM (Michel, 1998; Soto *et al.*, 2012). Mammalian COX was first crystallised from bovine heart and was found to contain 13 subunits (Tsukihara *et al.*, 1996; Yoshikawa, Shinzawa-Itoh and Tsukihara, 1998); however, it has since been demonstrated that COX contains a fourteenth subunit, NDUFA4 (COXFA4), which was previously thought to be a structural subunit of CI, as indicated by its name (Balsa *et al.*, 2012).

The core of the enzyme is formed by three mtDNA-encoded proteins: MT-CO1, MT-CO2 and MT-CO3 (Signes and Fernandez-Vizarra, 2018), but only MT-CO1 and MT-CO2 are involved in catalysis (Michel, 1998). Buried within the IMM, MT-CO1 contains a haem *a* group and a binuclear haem a_3-Cu_B centre and MT-CO2 contains a Cu_A centre facing towards the IMS (Pacheu-Grau *et al.*, 2015; Signes and Fernandez-Vizarra, 2018). MT-CO3 has no prosthetic groups, but is believed to be integral to the stability of the holocomplex (Wikström, Krab and Sharma, 2018). The eleven remaining structural subunits, COX4, COX5A, COX5B, COX6A, COX6B, COX6C, COX7A, COX7B, COX7C, COX8 and NDUFA4, are each encoded by the nDNA and are necessary for the stabilisation of the catalytic core of COX and regulation of its activity (Fornuskova *et al.*, 2010; Timón-Gómez *et al.*, 2017). All these subunits contain hydrophobic transmembrane regions except COX5A, COX5B, (both MM-facing) and COX6B (IMS-facing) (Fontanesi, Soto, and Barrientos 2008). Electrons from reduced cyt *c* are transferred to the Cu_A centre of MT-CO2, then to the haem *a* group of MT-CO1 and finally to the haem a_3-Cu_B binuclear centre of MT-CO1 (Signes and Fernandez-Vizarra, 2018). In the last step of catalysis, O_2 that is bound to the haem a_3 centre of MT-CO1 is reduced to two molecules of water (Michel, 1998). These redox reactions are coupled to proton pumping across the IMM, with 4 net H^+ ions pumped per electron that enters the complex (Banting and Glerum, 2006; Sharma *et al.*, 2017). Currently, the proton exit pathway through COX to the IMS is not well defined (Siletsky and Konstantinov, 2012).

COX assembly has been mainly elucidated by studying mutant strains of the yeast *S. cerevisiae*, which has highlighted many of the evolutionarily conserved assembly factors involved in COX biogenesis (Tzagoloff and Dieckmann 1990; Banting and Glerum 2006; Fontanesi, Soto, and Barrientos 2008). However, it has become apparent that there are some differences in the assembly factors present amongst different species, particularly between lower order and higher order eukaryotes (Mootha *et al.*, 2003; Vidoni *et al.*, 2017). Study of

mouse disease models and patient-derived cell lines have become crucial genetic, molecular and experimental bases for the identification and characterisation of higher taxonomic order assembly factors that are not known to have yeast orthologues. Like CI biogenesis, the assembly pathway of COX is modular (Vidoni *et al.*, 2017; Signes and Fernandez-Vizarra, 2018), starting with an initial subassembly and followed by generation of three assembly modules containing one of each of the mtDNA-encoded subunits (MT-CO1, MT-CO2 and MT-CO3), as shown in **Fig. 1.5**.

1.2.2.1 Initial COX Subassembly

The initial COX subassembly consists of two nDNA-encoded structural subunits, COX4I1 and COX5A (Vidoni *et al.*, 2017), and HIGD1A, a human homologue of yeast Rcf1 (Hayashi *et al.*, 2015; Kadenbach, 2017) that is not a structural subunit, but a positive regulator of COX which preserves its function under hypoxic conditions (Hayashi *et al.*, 2015).

1.2.2.2 MT-CO1 Module

Together, the chaperones and assembly factors involved in the maturation and stabilisation of the MT-CO1 subunit form the mitochondrial translation regulation assembly intermediate of cytochrome *c* oxidase (MITRAC) complex (Mick *et al.*, 2012). Firstly, the transmembrane assembly factors COX14 and COA3 bind nascent MT-CO1 and aid its insertion into the IMM (Mick *et al.*, 2010; Soto *et al.*, 2012). Next, the metallochaperone CMC1 binds copper (Cu) and participates in Cu-trafficking to MT-CO1 (Horn, Al-Ali and Barrientos, 2008; Horn *et al.*, 2010; Bourens and Barrientos, 2017). Haem *a* biosynthesis is carried out by both COX10 (Antonicka, Leary, *et al.*, 2003) and COX15 (Antonicka, Mattman, *et al.*, 2003). The exact molecular functions of SURF1 (Zhu *et al.*, 1998) and PET117 (Taylor *et al.*, 2017) remain unconfirmed, but they have been proposed to be involved in haem *a* delivery and integration after the synthesis of this prosthetic group by COX10 and COX15 (Timón-Gómez *et al.*, 2017; Signes and Fernandez-Vizarra, 2018). Cu_B assembly requires another metallochaperone, COX11 (Hiser *et al.*, 2000), and copper ion donation by COX17 (Glerum, Shtanko and Tzagoloff, 1996). COX11 is stabilised by COX19 until Cu-transfer (Bode *et al.*, 2015). CMC1 is released prior to the addition of the factors COA1, SURF1, and MITRAC7 (Pierrel *et al.*, 2007; Signes and Fernandez-Vizarra, 2018). Other proteins involved in COX biogenesis upstream of the assembly of the MT-CO1 module are the multifunctional protein LRPPRC (Ruzzenente *et al.*, 2012), which plays a crucial role in translation and maturation of newly synthesised mtDNA subunits, and TACO1, a translational activator of MT-CO1 (Richman *et al.*, 2016).

1.2.2.3 MT-CO2 Module

The MT-CO2 module is synthesised by its own set of assembly factors before it combines with the MT-CO1 module (Signes and Fernandez-Vizarra, 2018). As well as the MT-CO2 structural subunit, this module consists of nDNA-encoded structural subunits COX5B, COX6C, COX7C, COX8A, and COX7B (Nijtmans *et al.*, 1998); although, the latter is debated in the literature (Signes and Fernandez-Vizarra, 2018). Firstly, COX18 is required for membrane insertion of MT-CO2 (Bourens and Barrientos 2017), and then COX20 stabilises MT-CO2 prior to metalation (Bourens *et al.*, 2014). The assembly of Cu_A precedes the merging of the MT-CO2 module with the MT-CO1 module since once they are combined, MT-CO1 and MT-CO2 are tightly and strongly associated, barring access to the Cu_A site by assembly factors (Fontanesi, Soto and Barrientos, 2008; Soto *et al.*, 2012). The biosynthesis of the Cu_A centre of MT-CO2 occurs in the IMS, where COX17 transfers Cu ions to SCO1 and SCO2 (Glerum, Shtanko and Tzagoloff, 1996; Leary *et al.*, 2004; Horn and Barrientos, 2008), which are each bound to the IMM but contain IMS-exposed regions for copper binding (Bourens *et al.*, 2014). SCO1 and SCO2 then interact with COA6 to form a metallochaperone module that binds to the COX20/MT-CO2 intermediate and coordinates insertion of the mature Cu_A centre (Pacheu-Grau *et al.*, 2015; Stroud *et al.*, 2015; Ghosh *et al.*, 2016). COX18 is released prior to binding of SCO2 and COA6 but it is not known whether it is still bound at the time of SCO1 interaction. At this stage, TMEM177 stabilises the MT-CO2 subunit (Lorenzi *et al.*, 2018) and COX16 binds the MT-CO2/COX20/SCO1/SCO2 subassembly (Aich *et al.*, 2018; Cerqua *et al.*, 2018). Once COX5B, COX5C, COX7B, COX7C and COX8A are bound (Vidoni *et al.*, 2017; Signes and Fernandez-Vizarra, 2018), COX16 is proposed to aid joining of the MT-CO1 and MT-CO2 modules (Aich *et al.* 2018).

The assembly factors MR-1S (Ghezzi *et al.*, 2009; Vidoni *et al.*, 2017), PET100 (Church *et al.*, 2005; Oláhová *et al.*, 2015), and PET 117 (Renkema *et al.*, 2017) bind at the point of MT-CO1/MT-CO2 module joining; however their functions have not been fully explicated (Signes and Fernandez-Vizarra, 2018).

1.2.2.4 MT-CO3 Module & Final COX Composition

The MT-CO3 module consists of MT-CO3 and nDNA-encoded structural subunits COX6A, COX6B and COX7A2 (Fontanesi, Soto and Barrientos, 2008; Signes and Fernandez-Vizarra, 2018). No specific assembly factors for this module are known. Following their integration into the COX complex, NDUFA4 is added (Pitceathly and Taanman 2018; Balsa *et al.* 2012; Pitceathly *et al.* 2013) to produce the final COX holocomplex structure (Zong *et al.*, 2018).

Other supposed COX factors have been identified, principally from being causal proteins in COX deficiency as detected in mitochondrial disease patients (Alston *et al.*, 2017). Some of these are FASTKD2 (Ghezzi *et al.*, 2008), CEP89 (van Bon *et al.*, 2013), OXA1L (Thompson *et al.*, 2018), and APOPT1/COA8 (Signes *et al.*, 2019); however, the mechanistic roles of each within COX biogenesis remain either unknown or unconfirmed; therefore, they have not been included here.

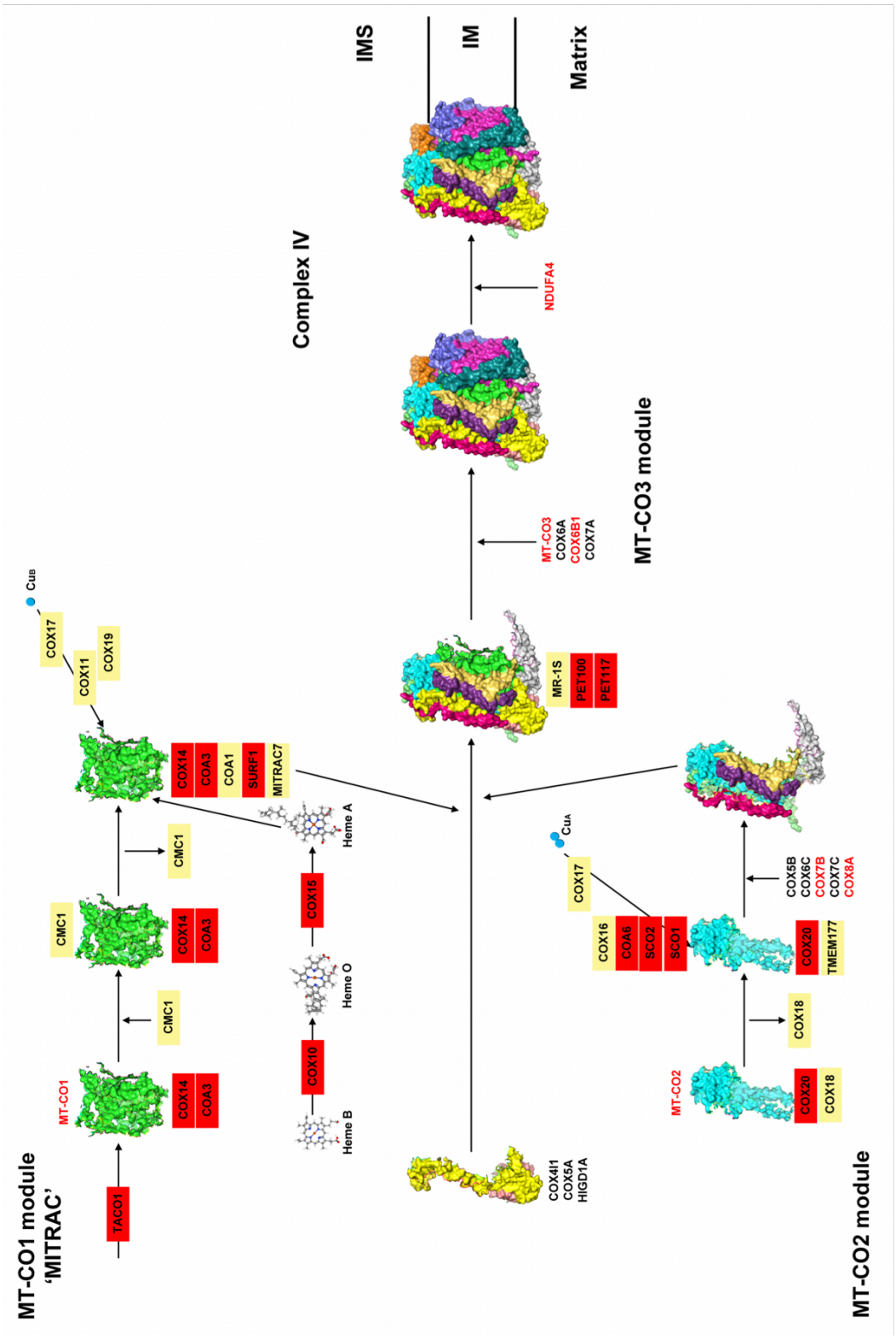

Figure 1.5. Model of mammalian COX assembly.

Figure shows COX modular assembly based on the bovine crystal structure (PDB ID: 2OCC) (Yoshikawa, Shinzawa-Itoh and Tsukihara, 1998), and the assembly pathway proposed in references (Vidoni *et al.*, 2017) and (Signes and Fernandez-Vizarra 2018). Red = proteins or assembly factors found to have pathological mutations in human patients, and yellow = known assembly factors. Image extracted from Figure 4, Signes and Fernandez-Vizarra, 2018.

1.3 Supercomplexes and the Mystery of Their Assembly

The development of blue native polyacrylamide gel electrophoresis (BN-PAGE or BNGE) in the late 1990s revolutionised the way in which scientists could study the assembly and naturally occurring configurations of the native complexes of the mitochondrial OXPHOS system (Schägger and von Jagow, 1991; Nijtmans, Henderson and Holt, 2002). This technique allows for the separation and detection of 1) individual OXPHOS complexes in non-denaturing conditions, and following solubilisation with the mild anionic detergent digitonin, the presence of 2) several supercomplex assemblies, which are distinct combinations of CI, $CIII_2$ and CIV (Hirst, 2018) (**Fig 1.6**). The main stoichiometries of these supercomplexes are III_2IV_1, I_1III_2, $I_1III_2IV_1$, also termed the "respirasome" given its ability to undergo electron transfer and proton pumping independently of the other OXPHOS complexes (Wu *et al.*, 2016), and $I_2III_2IV_1$, also termed the "megacomplex" (Guo *et al.*, 2017). In recent years, the existence of these supercomplexes has been validated by structural homology methods (Dudkina *et al.*, 2005; Davies, Blum and Kühlbrandt, 2018) and by cryo-electron microscopy (Mourier *et al.* 2014; Wu *et al.* 2016). In fact, the structure of the human megacomplex has been determined in this way (Guo *et al.*, 2017). Additionally to the supercomplexes mentioned above, CIV and CV have been found to form dimers or oligomers (Wittig and Schägger, 2008; Mourier *et al.*, 2014), which may be related to stabilisation of cristae morphology (Letts and Sazanov, 2017). The reasons for the existence of the supercomplexes have been heavily debated. One possibility is that they are necessary for substrate channelling, in which enclosed pools of free ubiquinone and cyt *c* lead to an increased electron transfer efficiency (Alvarez-Paggi *et al.*, 2017). In addition, the "plasticity model" proposes that the mature complexes associate and disassociate in a flexible way to adapt to cellular energy demands (Acín-Pérez *et al.*, 2008). However, substrate channelling is not supported by kinetic data (Blaza *et al.*, 2014; Guo *et al.*, 2018) and, in opposition to the latter, there is evidence that subunits from different complexes co-assemble during assembly of the separate complexes (Fernández-Vizarra, Tiranti, and Zeviani 2009). For example, $CIII_2$ and CIV have been proposed to bind to an incomplete CI scaffold with assembly of CI continuing after this step (Moreno-Lastres *et al.*, 2012). In addition, a recent assembly kinetic study using mass spectrometry-based complexomic profiling following BN-PAGE found COA1, an established COX assembly factor, to associate with CI assembly intermediates (Guerrero-Castillo *et al.*, 2017), suggesting co-assembly of at least CI and CIV.

Another hypothesis that has been proposed to explain the existence of the supercomplexes is that they minimise production of ROS, evidenced by disruption of the I_1III_2 supercomplex in

bovine heart resulting in increased levels of superoxide (Maranzana *et al.*, 2013). In support of this, studies in neurons and astrocytes showed a correlation between the intracellular levels of ROS and the amount of CI resident within supercomplexes (Lopez-Fabuel *et al.* 2016), suggesting a ROS-regulated supercomplex assembly system. The supernumerary subunits have been proposed to be necessary for the protection of the catalytic core of these enzymes from undergoing ROS-mediated damage (Milenkovic *et al.*, 2017). More studies are needed to understand the physiological role, regulation and assembly of supercomplexes.

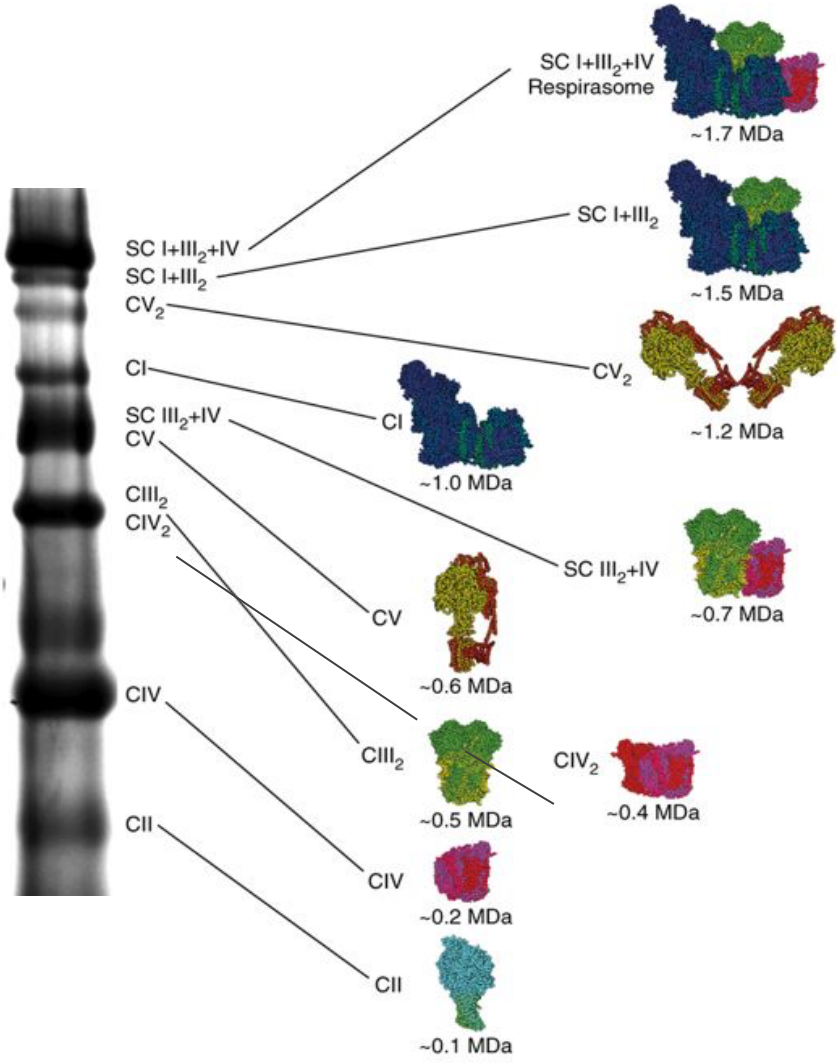

Figure 1.6. BNGE analysis aids assessment of OXPHOS complex assemblies.

BN-PAGE and Western blot analysis of digitonin-solubilised mitoplasts from ovine heart are separated with labels of the relative positions of the individual OXPHOS complexes and supercomplexes (SCs). The different SCs with the respective approximate molecular weights and molecular structures are indicated on the right. The CI structure is ovine (PDB ID: 5LNK), CII is porcine (PDB ID: 1ZOY), and CIII (PDB ID: 1NTM), CIV (PDB ID: 5B1A) and CV (PDB ID: 5ARA) are bovine. Imaged adapted from Figure 2, Letts and Sazanov 2017.

The yeast proteins Rcf1, Rcf2 and Rcf3 were the first to be suspected of mediating supercomplex assembly (Strogolova *et al.*, 2012; Lundin *et al.*, 2016). However, they are also known to be necessary for the individual assembly of COX (Vukotic *et al.*, 2012), and gene silencing experiments led to isolated COX deficiency (Lundin *et al.*, 2016), suggesting that their effect on supercomplex assembly may be indirectly due to a primary effect on COX. HIGD1A and HIGD2A are the mammalian orthologs of Rcf1 (Denko *et al.*, 2000). HIGD1A has been found to interact with early assembly intermediates of COX (Vidoni *et al.*, 2017), and gene silencing experiments did not affect supercomplex formation (Hayashi *et al.* 2015). However, HIGD2A knock-down by gene silencing led to depletion of III_2IV_1, suggesting a role in supercomplex stabilisation (Chen *et al.*, 2012). Recent work has shown that this is not the case, and that HIGD2A in fact functions in the stabilisation of newly translated MT-CO3, and its loss leads to turnover of partner subunits found within the MT-CO3 module (see **Fig. 1.5**) (Hock *et al.*, 2019). Whilst this led to a decrease in the abundance of a COX-containing supercomplex, it was proven that this supercomplex harboured only misassembled COX lacking MT-CO3; therefore, HIGD2A is a classical assembly factor involved in COX assembly, and is decidedly not a supercomplex assembly factor (Hock *et al.*, 2019). Another protein of considerable debate is COX7A2L, which was proposed to be crucial for insertion of CIV into supercomplex structures (Lapuente-Brun *et al.*, 2013), but has since been shown to act as a checkpoint for the assembly of $CIII_2$ (Lobo-Jarne *et al.*, 2018). It is worth noting that supercomplexes have never been found to contain any of these proteins (Mourier *et al.* 2014; Wu *et al.* 2016). This is to be expected given that the methods used seek to isolate and purify mature multimeric complexes, of which assembly factors are not found.

In summary, supercomplexes are composite protein structures capable of aerobic respiration that are readily found in eukaryotes (Lapuente-Brun *et al.*, 2013; Sousa *et al.*, 2016); however, at present, their pathway(s) of assembly remain elusive.

1.4 Mitochondrial Diseases

1.4.1 Definition and Prevalence of Mitochondrial Diseases

Mitochondrial diseases are a group of rare and phenotypically heterogeneous disorders, commonly arising from defects in some part of the assembly or function of the OXPHOS system (Zeviani and Di Donato, 2004; Gorman *et al.*, 2016). Recent epidemiological studies have estimated that the prevalence of mitochondrial diseases owing to mutations in mtDNA-encoded genes is 1 in 5,000 live births (Thorburn *et al.*, 2004), and in the general adult population nDNA-encoded mutations are responsible for cases of mitochondrial diseases in 2.9 per 100,000 adults (Gorman *et al.*, 2015). Despite impressive development in the mitochondrial medicine field in recent years, the genetic bases and pathophysiology of mitochondrial diseases remain a mystery for many patients, their families, and their clinical teams. In most cases, mitochondrial diseases are progressive and debilitating, with no cure.

1.4.2 Mitochondrial Disease Inheritance

Mitochondrial disorders can arise from inherited or *de novo* mutations in either the mtDNA or the nDNA (Zeviani, Spinazzola and Carelli, 2003; Gorman *et al.*, 2015). Mammalian somatic cells typically harbour between 10^3 and 10^4 mtDNA copies (Stewart *et al.* 2008), and a single mtDNA mutant variant can exist in all mtDNA copies of a mitochondrion (homoplasmy) or in a proportion of these (heteroplasmy) (Cree, Samuels and Chinnery, 2009). If the mutant mtDNA load exceeds a threshold in which a cell cannot sustain normal respiratory or mitochondrial function, mitochondrial disease phenotypes can occur; this is termed the 'threshold effect' (Stewart and Chinnery 2015). The combination of a decrease in total mtDNA copy number as well as asymmetrical segregation of mutant and wildtype mtDNA into a mother's primordial cells during gametogenesis is referred to as the 'bottleneck effect', resulting in a variable distribution of an mtDNA mutation in newly generated oocytes (Lang, Gray and Burger, 1999).

Together, the threshold and bottleneck effects explain why families with identical mtDNA mutations may present with a wide range of clinical presentations and severity of symptoms, as well as tissue-specific phenotypes (McFarland, Taylor and Turnbull, 2010; Gorman *et al.*, 2016). Currently, more than 250 pathogenic mtDNA mutations have been identified (Mito-MAP database, www.mitomap.org) and can be classified as either 1) large-scale rearrangements (i.e. partial deletions or duplications), that are usually sporadic, or 2) point mutations, that are usually maternally inherited (Viscomi and Zeviani, 2017; Ghezzi and Zeviani, 2018). The mode of inheritance of mitochondrial diseases arising from mutations in the nDNA can be Mendelian,

either autosomal or sex-linked, or non-Mendelian (i.e. through the maternal lineage) (Ghezzi and Zeviani, 2018), which complicates molecular diagnosis.

1.4.3 Clinical Presentation

Mitochondrial diseases arising from either nuclear or mitochondrial genomes have the potential to affect any tissue that has mitochondria; typically these are the central nervous system (with associated pathologies termed encephalopathies), the skeletal muscle (myopathies), a combination of the two (encephalomyopathies), the heart (cardiomyopathies) or the liver (hepatopathies) (Duchen, 2004; Zeviani and Di Donato, 2004; Ghezzi and Zeviani, 2018), although other organs and systems have been found to be affected. Mitochondrial dysfunction has been linked to metabolic disorders that are not classified as canonical 'mitochondrial diseases', including diabetes mellitus (Kelley *et al.*, 2002) and various cancers (Gammage and Frezza, 2019). Herein, we define "mitochondrial disease" as any disorder arising from inherited mutations in OXPHOS structural subunits, co-factors, assembly factors, factors controlling the lipid composition of mitochondrial membranes or the quality control of mitochondrial proteostasis, and of course, factors regulating mtDNA maintenance and expression, encoded by either the mtDNA or nDNA. Patients with adult-onset mitochondrial disease usually display myopathies caused by CNS abnormalities (Gorman *et al.*, 2016), whilst infantile or childhood presentations are typically more severe and impact development, including cognitive impairment, muscular tone and coordination, and can be further characterised by spino-cerebellar ataxia, dystonia, seizures, and respiratory abnormalities (Gorman *et al.*, 2016).

1.4.4 Complex I Deficiency

CI deficiency is the most frequently occurring OXPHOS complex defect found in children and adults, making up approximately a third of all clinical cases (Janssen *et al.*, 2006). Presentations correlating with CI deficiency are extremely heterogeneous (Ghezzi and Zeviani 2018); however, most infantile or paediatric cases fall into one of six phenotypic groups, which are 1) Leigh syndrome, 2) fatal infantile lactic acidosis, 3) neonatal cardiomyopathy, 4) leukoencephalopathy, 5) pure myopathy, and 6) combined hepatopathy and tubulopathy (Loeffen *et al.*, 2000; Ghezzi and Zeviani, 2012). Cases that do not fall into one of these are generally classed as "mitochondrial encephalomyopathies with CI deficiency" (Ghezzi and Zeviani 2018). Most CI defects remain undefined at the genetic and molecular levels with an average successful molecular diagnostic rate of 20 – 40 % of cases (Fernández-Vizarra, Tiranti, and Zeviani 2009). Reasons for this include variability in the stringency of the biochemical screening and clinical investigation of patients (Challa *et al.*, 2004), and whether

the mutant variant(s) are able to be reliably detected by WES or other sequencing strategies (Stenton and Prokisch 2018). **Table 1.1** lists the assembly factors of CI that have been found associated with mitochondrial diseases (Legati *et al.* 2016; Ghezzi and Zeviani 2018), along with their predicted or known functions, and a brief description of the associated clinical phenotypes.

Table 1.1 Assembly factors of CI with the proposed role and clinical presentations of each.

Protein	*OMIM ID*	*Role*	*Associated phenotypes*
NDUFAF1	606934	CI chaperone; transient interaction with the P_P-b module	Cardiomyoencephalopathy, lactic acidosis; leukodystrophy, neuropathy
NDUFAF2	609653	Stabilizer of late intermediate; binds to the N-module	Leukoencephalopathy with vanishing white matter, Leigh syndrome
NDUFAF3	612911	Interacts with Q-module subunits and with NDUFAF4	Variable phenotypes: macrocephaly, severe muscle weakness, myoclonic seizures, brain leukomalacia; Leigh syndrome
NDUFAF4	611776	Interacts with Q-module subunits and with NDUFAF3	Encephalopathy, antenatal cardiomyopathy, Leigh syndrome
NDUFAF5	612360	Methyltransferase of NDUFS7	Leigh syndrome, progressive spasticity
NDUFAF6	612392	Assembly/stability of the Q module	Leigh syndrome
NDUFAF7	615898	Methyltransferase of NDUFS2; stabilizer of early intermediate(s)	Pathologic myopia
ACAD9	611103	Interacts with NDUFAF1, ECSIT and TMEM126B in P_P-b module	Cardiomyopathy, encephalopathy, lactic acidosis, exercise intolerance
FOXRED1	613622	Involved in P_D-a assembly; forms a complex with ATP5SL	Leigh syndrome; microcephaly and cardiomyopathy
TIMMDC1	615534	Assembly of multiple subunits of P_D-a module	Variable neurological phenotypes: Leigh syndrome; seizures, hypotonia, deafness, peripheral neuropathy, nystagmus
TMEM126B	615533	Assembly of late-stage P_D-b module	Exercise intolerance; cardiomyopathy and renal tubular acidosis
NUBPL	613621	Facilitates the assembly of Fe–S cofactors and subunits in CI	Leukodystrophy, myopathy, ataxia (CI deficiency)

1.4.5 COX Deficiency

Mutations in the mtDNA-encoded subunits MT-CO1 (Herrero-Martín *et al.*, 2008), MT-CO2 (Kytövuori *et al.*, 2017), and MT-CO3 (Mkaouar-Rebai *et al.*, 2011) are associated with more than 20 distinct pathological phenotypes owing to COX deficiency, the most common of which are myopathy, anaemia, amyotrophic lateral sclerosis-like syndrome, and mitochondrial encephalomyopathy, lactic acidosis, and stroke-like episodes (MELAS) (Rak *et al.*, 2016). Mutations in the nDNA-encoded COX subunits are uncommon and until the first mutation was discovered in *COX6B1* relatively recently (Massa *et al.*, 2008), they were thought to be embryonic lethal. Pathological mutations in *COX4I2* (Shteyer *et al.*, 2009), *COX6A1* (Tamiy *et al.*, 2014), *COX6B1* (Massa *et al.* 2008), *COX7B* (Indrieri *et al.*, 2012), *COX8A* (Hallmann *et al.*, 2016) and *NDUFA4* (Pitceathly *et al.* 2013) have since been identified. The majority of isolated COX deficiencies to date are caused by mutations in genes encoding COX assembly factors and co-factors responsible for the biosynthesis, coordination and integration of metal prosthetic groups (Ghezzi and Zeviani, 2018). **Table 1.2** summarises the COX assembly factors known to cause mitochondrial diseases.

Table 1.2 Assembly factors of CIV with the proposed role and clinical presentations of each.

Protein	*OMIM*	*Role*	*Associated phenotypes*
SURF1	185620	Formation of the early MTCO1 subcomplexes	Leigh syndrome
COA3	614775	Interaction with early COX intermediates and assembly factors	Exercise intolerance and neuropathy
COA5	613920	Involved in a very early step of the COX assembly	Fatal neonatal cardiomyopathy
COX14	614478	Coupling synthesis of MTCO1 with assembly into COX holoenzyme	Respiratory and neurologic distress, metabolic acidosis and neonatal death
COX20	614698	Involved in early steps of the COX assembly; interaction with MTCO2	Ataxia and muscle hypotonia, dystonia-ataxia
PET100	614770	Involved in intermediate stage of COX assembly	Psychomotor delay, seizures, hypotonia, and Leigh syndrome
PET117	614771	Coupling Heme *a* synthase activity to COX assembly. Interaction with PET100	Neurodevelopmental regression
APOPT1	616003	Unknown	Leukoencephalopathy
COA6	614772	Copper homeostasis and transport to CIV	Fatal infantile cardioencephalomyopathy
SCO1	603644	Incorporation of copper atoms in the catalytic sites of the nascent CIV	Infantile encephalopathy, neonatal hepatopathy, ketoacidotic comas
SCO2	604272	Incorporation of copper atoms in the catalytic sites of the nascent CIV	Infantile cardioencephalomyopathy, myopia, CMT
COX10	602125	Heme A synthesis (conversion of heme *b* into heme *o*)	Leigh syndrome, proximal renal tubulopathy, hypertrophic cardiomyopathy, sensorineural deafness, metabolic acidosis
COX15	603646	Heme A synthesis (conversion of heme *o* into heme *a*)	Infantile cardiomyopathy, Leigh syndrome

1.4.6 Clinical, Biochemical and Histological Diagnoses

Mitochondrial diseases present a diagnostic challenge for both clinicians and scientists due to their phenotypic and genetic heterogeneity. However, several imaging, biochemical and histological methods are routinely used to aid in their diagnosis. Magnetic resonance imaging (MRI) and proton MR-spectroscopy (MRS) are important tools for the detection of structural or biochemical abnormalities in mitochondrial disease patients (Saneto, Friedman and Shaw, 2008). Biochemical deficiencies in one or more OXPHOS complexes are commonly found in mitochondrial disease patients (Ghezzi and Zeviani 2018). These enzymatic deficiencies can be detected biochemically using tissue homogenates or purified mitochondria from muscle or cutaneous biopsies, or by using patient-derived cultured cells (Rodenburg 2011), or lastly, by histopathological analyses using fixed tissue sections (Challa *et al.*, 2004). Another useful biochemical disease marker is increased lactate levels in the blood and/or cerebrospinal fluid, caused by a reduction of pyruvate to lactate, utilising the reduced NADH formed during glycolysis (Finsterer and Zarrouk-Mahjoub, 2018). Experimentally, molecular analyses, such as SDS-PAGE and BN-PAGE, and subsequent immunodetection of proteins by Western blotting, help to determine changes in the abundance and assembly of each of the OXPHOS complexes, their subunits, subassemblies and various supercomplexes, as has been demonstrated widely throughout the literature.

1.4.7 Genetic Diagnosis

Genetic diagnosis of mitochondrial diseases is notoriously difficult due to the bigenomic regulation of mitochondria, as previously described, with a pathogenic gene variant potentially being found in either mitochondrial or nuclear genomes (Gorman *et al.*, 2016). Recently, whole exome sequencing (WES) and bioinformatic filtering steps have allowed for the detection of mitochondrial disease genes not previously known to localise to the mitochondria or have mitochondrial functions (Stenton and Prokisch, 2018). The stalwart techniques of homozygosity mapping (Seelow *et al.*, 2009), used for identifying recessive traits in consanguineous families, and Sanger sequencing of single genes or panels of suspected candidate genes (Wortmann *et al.*, 2017), are both effective strategies still used today, but they are comparatively laborious and time-consuming methods that rely on a narrowing down of potential genetic candidates, either from selecting genes based on a characteristic clinical phenotype or from knowing the aetiology of a disease within a family (Stenton and Prokisch, 2018). In contrast, WES allows for the unbiased sequencing of all exonic regions of the human genome, in which ~85 % of known monogenic disease-causing mutations are found (Botstein and Risch, 2003), and along with downstream bioinformatic filtering, it has been integral to the rapid rate of discovery of new mitochondrial disease genes in recent years.

1.5 Identifying & Characterising New Mitochondrial Disease Genes

More than 300 individual human genes have been implicated in causing mitochondrial diseases (Stenton and Prokisch, 2018). More recently, the advent of WES has allowed the detection of nDNA-encoded assembly factors only found in Metazoan species, including APOPT1 (recently renamed COA8) (Signes *et al.*, 2019), LRPPRC (Cui *et al.*, 2019), and TMEM126B (Alston *et al.*, 2016). Much of what is currently known regarding human OXPHOS protein complex assembly, for instance that of CIII and CIV, has been possible due to genetic manipulation and study of orthologues in model organisms such as baker's yeast, *Saccharomyces cerevisiae* (McEwen *et al.*, 1993; Stoldt *et al.*, 2018). Importantly, CI is not present in *S. cerevisiae*, and most of the investigation of its biogenesis has been carried out in other model organisms, e.g. the fruit fly, *Drosophila melanogaster* (Garcia *et al.*, 2017) or by genetic characterisation of CI-deficient patients (Zeviani and Di Donato, 2004). This is because, in order to identify and characterise OXPHOS assembly factors and associated proteins that have evolved only in organisms of higher taxonomic orders, suitable genetic models must be used, including patient-derived cultured cell lines and *in vivo* animal models, particularly recombinant mice (Fernández-Vizarra, Tiranti, and Zeviani 2009).

In this work, two probands that had been preliminarily diagnosed with mitochondrial diseases by means of clinical, biochemical and/or histopathological findings (as will be detailed in **Chapters 3** and **4**) were selected for enrolment in this study following the failure of mtDNA Sanger sequencing and deep sequencing of a panel of > 250 pre-selected OXPHOS-related nuclear genes to yield any potential genetic candidates. WES was undertaken to examine the entire exome of these individuals; this strategy successfully identified mutant variants in two genes that are only found to be present in metazoans, and also, that had never before been associated with mitochondrial disease, or in fact, any human disease pathology. These two genes, *COA7* and *TMCO6*, were found to be associated with severe CIV and CI deficiencies, respectively.

1.5.1 Cytochrome *c* Oxidase Assembly Factor 7 (COA7)

Cytochrome *c* oxidase assembly factor 7 (COA7; C1orf163, SELRC1 or RESA1), was first identified in a proteomics screen of proteins whose steady-state levels were significantly reduced after knockdown of cristae-forming proteins SAM50 and mitofilin (Kozjak-Pavlovic *et al.*, 2014). COA7 is a member of the HCP β-lactamase protein family, and has known homologues in chordates, arthropods, nematodes, cnidarians and echinoderms (HomoloGene: 11317). The *COA7* gene, located at genetic locus Chr 1 p32.3 (NC_000001.11:

52,684,449 - 52,698,347), produces a single 1,581 bp mRNA transcript (NM_023077.3) from 3 coding exons (**Fig. 1.7 A.**). The resulting protein (NP_075565.2) consists of 231 amino acids and is cysteine-rich in its native form, containing 13 individual cysteines. Although the tertiary structure of human COA7 is unknown, homology modelling has predicted the presence of five Sel1-like repeats (Interpro ID: IPR006597), which are short α-helical domains involved in protein-protein interactions. The human primary COA7 protein sequence, with labeled Sel1-like repeats and highlighted cysteine residues is displayed in **Fig 1.7 B**.

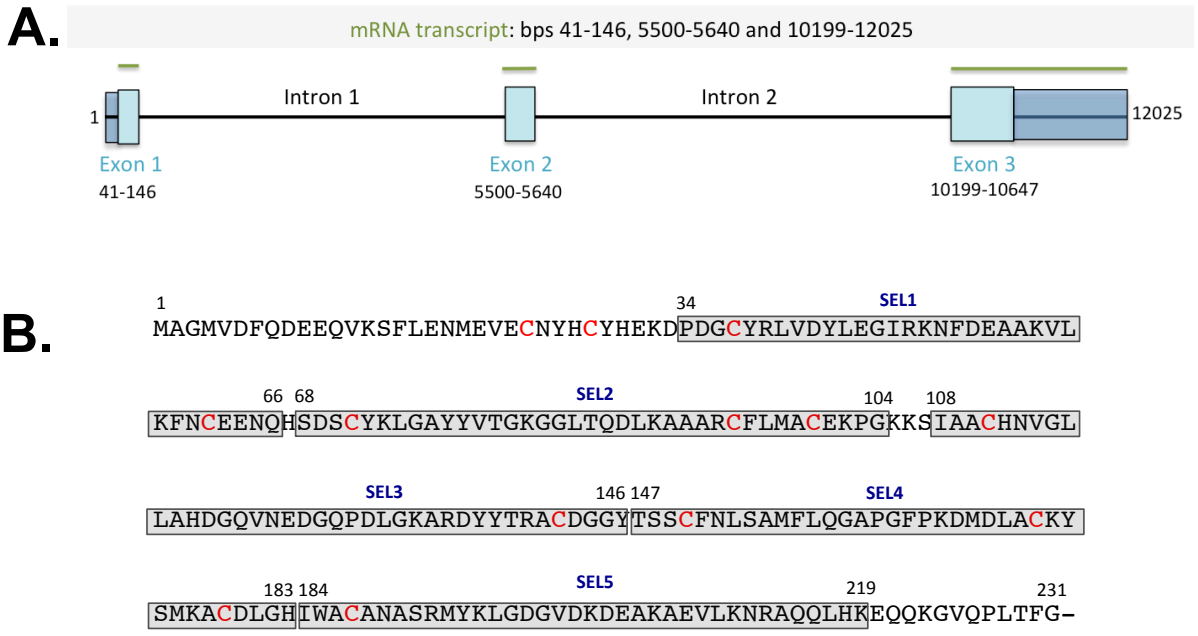

Figure 1.7. *COA7* gene composition and annotated COA7 primary protein sequence.

(**A.**) The *COA7* gene (NC_000001.11: 52,684,449 - 52,698,347) is composed of 3 coding exons and 2 intronic regions, and yields a single mRNA of 1,581 bps (NM_023077.3). (**B.**) The COA7 protein (NP_075565.2) is predicted to contain 5 SEL1-like tetratricopeptide repeat domains as labelled (grey boxes) (Interpro ID: IPR006597), and 13 cysteines (red text).

Kozjak-Pavlovic *et al*. performed preliminary analyses of COA7 localisation and function via knockout and knockdown studies in HeLa cells, which suggested a putative role for it in COX assembly (Kozjak-Pavlovic *et al.*, 2014). Cellular subfractionation and membrane swelling experiments revealed that COA7 is a soluble protein localising to the mitochondria, specifically the IMS, but this result was somewhat unclear given the lack of a suitable experimental control. Gene silencing in HeLa cells significantly reduced the steady-state levels of several COX subunits, and 1D-BNGE showed reduction in the amount of fully assembled COX. There were weaker reductive effects on subunits of CI and CIII, and no discernable effects on the quantities of CII or CV subunits or holocomplexes. Furthermore, in-gel activity measurements

of COA7-knockout HeLa cells indicated reduced COX activity by approximately 66 % relative to controls. Following doxycycline (DOX)-induced gene silencing for 7 days, isolation of mitochondria and incubation with radioactively labeled CI, CIII, COX and CV subunits, it was determined that total COX assembly was reduced by ~50 % and progressed slower than biogenesis of CI, CII, CIII and CV. It is worth noting that COA7 knockdown had no effect on mitochondrial morphology, membrane potential or protein import (Kozjak-Pavlovic *et al.*, 2014). At the time of this research, no other information existed regarding the structure, function, intracellular localisation, protein interactors, mitochondrial protein import or role in human disease pathology of COA7.

1.5.2 Transmembrane Coil-Coiled Domain 6 (TMCO6)

Transmembrane and coiled-coil domains 6 (TMCO6, other aliases: PRO1580, HQ1580 and FLJ39769.1) is a nuclear-encoded protein found only in vertebrates, including mammals, birds, reptiles, amphibians, and bony and cartilaginous fishes (Homologene ID: 12431). The *TMCO6* gene (NC_000005.10: 140,596,529 – 140,647,411) is situated at genetic locus Chr 5 q31.3, and contains 12 exons that are predicted to encode two main protein isoforms of 493 (NP_060972.3) and 499 (NP_001287909.1) amino acids (aas). The discovery of the two *TMCO6* coding sequences (NM_018502.5 and NM_001300980.1, respectively) came from its cDNA sequences, sequenced as a part of genome-wide mRNA screening studies of human and murine transcriptomes (Strausberg *et al.*, 2002; Ota *et al.*, 2004). TMCO6 has since been found to be expressed in all human tissues (https://www.proteinatlas.org/ENSG00000113119-TMCO6/tissue). However, presently, no seminal literature or research has been published regarding TMCO6, including its structure, intracellular localisation or its role in normal cellular physiology or human disease pathology. Consolidation and evaluations of all available information regarding TMCO6 is described in detail in **Chapter 4**.

1.6 Research Aims

The genetic aetiology of mitochondrial diseases remains a mystery in approximately two thirds of clinical cases (Ghezzi and Zeviani, 2018). This could be due, in part, to the existence of unique OXPHOS assembly factors in humans that are not present in lower taxonomic order eukaryotes, which have served as the primary genetic and experimental bases for understanding OXPHOS complex assembly to date (Schägger, 2002; Banting and Glerum, 2006). The advent of WES and other next generation sequencing technologies has made it possible to identify as-yet undiscovered mitochondrial disease genes present only in higher order eukaryotes.

The three main aims of this work are: 1) to determine the pathogenicity of compound heterozygous mutant variants in *COA7* (NM_023077.3:c.410A>G;c.287+1G>T) and a singular homozygous recessive mutation in *TMCO6* (NM_018502.5: c.271C>T) relating to COX or CI deficiency, respectively, in two unrelated mitochondrial disease patients, 2) to assess whether COA7 and TMCO6 are novel mitochondrial disease proteins, and 3) to characterise the potential roles of each of these proteins in COX or CI biogenesis.

In **Chapter 3**, I describe the identification and characterisation of the first pathogenic mutations in *COA7,* a putative COX assembly factor (Kozjak-Pavlovic *et al.*, 2014). Additionally, super-resolution microscopy and submitochondrial fractionation and protease digestion experiments were carried out to confirm the intramitochondrial localisation of COA7, which is the IMS.

In **Chapter 4**, I introduce *TMCO6*, a gene identified through WES to be mutated in a paediatric, male proband with severe CI deficiency. Firstly, I discuss what is currently known regarding the gene structure, evolutionary conservation, protein isoforms and key structural features of TMCO6. I then describe the patient's clinical history and characterise alterations to CI biogenesis and formation of CI-containing supercomplexes in primary and immortalised patient cells, despite presence of TMCO6 in these cells and no discernible CI deficiency or impairment of aerobic respiration in these cells. Lastly, TMCO6 was found to co-migrate with CI by 2D-BNGE using mitochondrial protein extracts from immortalised patient cells.

In **Chapter 5**, I detail the generation of overexpression and knockdown cellular models to assess the role of TMCO6 in normal mammalian physiology. Furthermore, I confirm that TMCO6 localises only to the mitochondria, and specifically to the IMM. I also verify the co-migration of endogenous TMCO6 with CI observed by 2D-BNGE in these cells, and

corroborate this result with immunoprecipitation experiments, which showed physical interaction between TMCO6 and CI N-module subunit NDUFS6. Lastly, attempted generation of knockout and patient mutant knockin HAP1 cell lines is described.

Chapter 6 describes the phenotypic characterisation of a *Tmco6*-knockout murine model, which emulated the symptoms of the human patient and revealed tissue-specific cardiac and muscular CI deficiencies, not observed in any other tissue that was tested, as well as severe histopathological abnormalities in the brain, and a significant reduction in body weight, size and fitness.

Lastly, the work of **Chapter 7** concerns the successful functional complementation of *Tmco6*-KO mice with the human wildtype gene, *TMCO6*. No such recovery was observed for mice stably expressing the patient mutant protein variant (NP_060972.3: p.Arg91Cys). This, along with exacerbation of cardiac dysfunction and a novel phenotype of cardiac fibrosis, confirms that the human patient variant is indeed pathogenic *in vivo*.

Chapter 2

Materials and Methodology

2.1 Biological Materials

2.1.1 Human Subjects

Patients that had been diagnosed with mitochondrial diseases by means of clinical, biochemical and morphological investigations were enrolled in the present study (NGSP001-NGSP125) following referral to the Neurological Institute Carlo Besta (Milan, Italy). Histological analyses and measurements of respiratory chain and pyruvate dehydrogenase (PDH) enzymatic activities were performed in-house according to standard procedures. Based on the resulting biochemical profiles, as well as mtDNA characterisation, obtained using fibroblasts, skeletal muscle, or both, patients were divided into one of the following groups: Complex I deficiency, Complex II deficiency, Complex III deficiency, Complex IV deficiency, Complex V deficiency, multiple complex deficiencies, Coenzyme Q10 deficiency, mtDNA multiple deletions and/or depletion, and PDH deficiency. All patients were screened for mtDNA mutations by Sanger sequencing, and were additionally screened for a set of ~ 250 nuclear genes associated with the specific biochemical or molecular (mtDNA) defect and/or clinical presentation. In no case were mutations found that suggested a pathogenic role. Two patients, one with Complex IV deficiency and another with Complex I deficiency, were selected for further investigation. A custom panel of genomic regions corresponding to the transcribed sequences of 132 nuclear-encoded genes (including exons and UTR regions) that had previously been associated with mitochondrial disorders or to be candidate genes that took part in the defective molecular pathways were additionally sequenced, yielding no genetic candidates. Informed consent for further genetic investigation at the MRC Mitochondrial Biology Unit (Cambridge, UK) was obtained from the parents of both human subjects in agreement with the Declaration of Helsinki.

2.1.2 Cell Lines

2.1.2.1 Skin Fibroblasts

Primary skin fibroblasts from two mitochondrial disease patients (see **section 2.1.1**) were kindly provided by Daniele Ghezzi from the Neurological Institute "Carlo Besta" (Milan, Italy). WES (as detailed in **section 2.2.2**) revealed compound heterozygous mutant variants in *COA7*: a paternally inherited nucleotide transition variant (NM_023077.3: c.410A>G), resulting in a tyrosine to cystine amino acid substitution (NP_075565.2:p.Tyr137Cys), and a maternally inherited G>T transversion affecting the first intronic nucleotide of the exon 2/intron 2 splice junction (NM_023077.3:c.287+1G>T, p.(?)). Primary skin fibroblasts from a second patient harboured homozygous recessive mutations in *TMCO6* (NM_018502: c. 271C>T), resulting in an arginine to cysteine amino acid substitution (p.Arg91Cys). Four control human skin fibroblast cell lines were used in this work; two alongside the mutant *COA7* patient cells (termed here as Controls 1 and 2), provided by Dr. Erika Fernandez-Vizarra, and an additional two alongside the mutant *TMCO6* patient cells (termed here as Controls A and B, for clarity), provided by Dr. Aurelio Reyes.

2.1.2.2 Embryonic Cell Lines

Human embryonic kidney 293T (HEK 293T) cells (Sigma-Aldrich®) were used for the production of lentiviruses (**section 2.3.2**), sub-mitochondrial localisation studies (**section 2.6.7**), and immunoprecipitation (**section 2.6.8**.). Flp-In™ HEK-293 cells (Invitrogen™), derived from HEK 293T cells, were used for shRNA-mediated knockdown of endogenous *TMCO6* (**section 2.3.4**) and inducible overexpression of the TMCO6 protein, C-terminally tagged with either HA or FLAG/STREP (**section 2.3.5**).

2.1.2.3 Cancer Cell Lines

HeLa epithelioid cervical cancer cells (Sigma-Aldrich®) and 143B human osteosarcoma cells (Thermo Fisher Scientific Inc., UK) were used for confocal microscopy (**section 2.4.2**). HeLa cells constitutively overexpressing HA-tagged COA7 protein were kindly generated and provided by Dr. Cristiane Beninca and used exclusively for super-resolution microscopy experiments (**section 2.4.3)**.

2.1.2.4 Haploid Cell Line

HAP1 cells (Horizon Discovery Group plc., UK), a near-haploid human cell line derived from the male chronic myelogenous leukaemia (CML) KBM-7 cell line (Kotecki, Reddy and Cochran, 1999), were used for CRISPR/Cas9 experiments (**section 2.2.15**).

2.1.2.5 Murine Cell Lines

Primary MEFs were derived as per **section 2.5.3** and spontaneous immortalisation of primary MEFs occurred after several passages, as previously described (Amand *et al.* 2016).

2.1.3 *Tmco6*-Knockout Mouse Model

A transgenic *Tmco6*-knockout mouse model, B6N(Cg)-*Tmco6*$^{tm1.1(KOMP)Vlcg}$/J, was obtained for use in this work from the Knockout Mouse Phenotyping Project (KOMP^2) repository (Stock No. 028602, The Jackson Laboratory, USA) (Koscielny *et al.*, 2014), and chosen in order to study the effects of TMCO6 ablation on development, physiology, neuromuscular control and mitochondrial metabolism at the tissue and organism levels. The ZEN-Ub1 Velocigene cassette, a *lacZ* reporter construct derived from *Escherichia coli (E. coli)* that contains a neomycin resistance (*neo*^{R}) selection cassette, was inserted via homologous recombination between positions 36,894,829 and 36,901,908 of Chromosome 18 (Genome Build37) in embryonic murine stem cells of the C57BL/6NJ genetic background (see **Fig. 2.1**). Cre-mediated excision of the *neo*^{R} selection cassette was achieved by selective crossing with a mouse line that constitutively expressed Cre recombinase, B6N.Cg-*Edil3*$^{Tg(Sox2-cre)1Amc}$/J (Stock No. 014094, The Jackson Laboratory). This process yielded a 7,080 bp deletion within *Tmco6* (NC_000084.6: 36,735,019 – 36,742,400), disrupting all coding exons and intervening sequences, and led to complete loss of endogenous protein expression.

All experiments and procedures were conducted according to the Animals (Scientific Procedures) Act 1986 under UK Home Office licenses PPL 70/7538 and P6C97520A, and approved by local ethical review. Mice were housed in a temperature- and humidity-controlled animal care facility (Phenomics Laboratory, Forvie Site, Cambridge Biomedical Campus, Cambridge, CB2 0PY), under a 12 h light/dark cycle with access to water and standard chow *ad libitum*. Mice were monitored weekly to examine changes to body condition and general health. Metabolic, neurological and motor phenotypes resulting from Tmco6 protein ablation were evaluated using a set of tests detailed in **sections 2.5.3** to **2.5.8**.

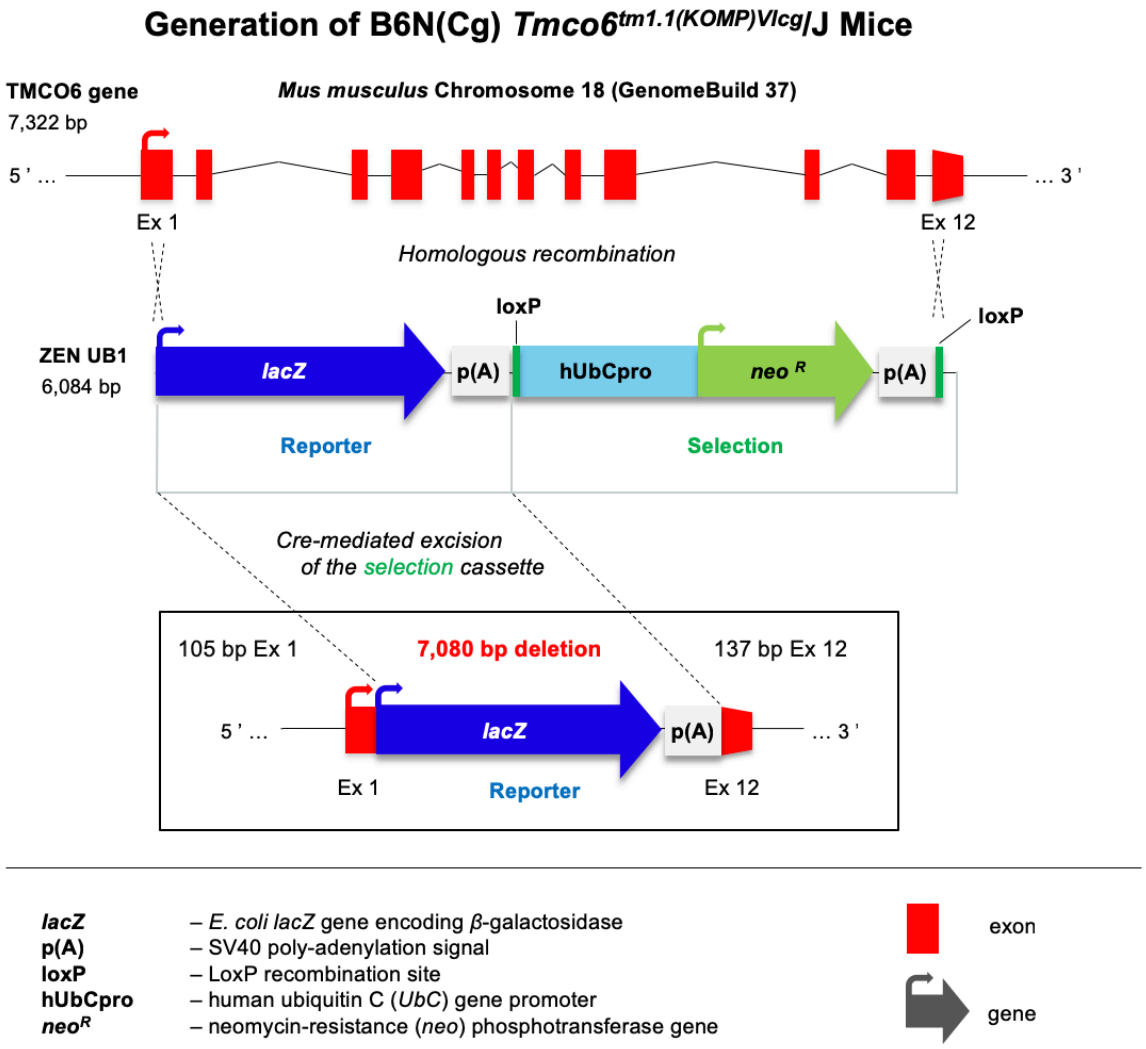

Figure 2.1. Generation of a *Tmco6*-knockout transgenic mouse line.

Transgenic *Tmco6*-knockout mice (B6N(Cg)-*Tmco6*$^{tm1.1(KOMP)Vlcg}$/J) were generated as schematically depicted above by The Jackson Laboratory, as a part of the KOMP^2 initiative. Homologous recombination replaced 7,080 bp of *Tmco6* (NC_000084.6: 36,735,019 – 36,742,400) with a ZEN-UB1 *lacZ* reporter cassette and *neo*^{R} selection cassette. Removal of the selection cassette was achieved by selective crossing with a mouse line that expressed *Cre* recombinase, B6N.Cg-*Edil3*$^{Tg(Sox2-cre)1Amc/J}$ (Stock No. 014094, The Jackson Laboratory). This process yielded a final genetic construct with the initial 105 bp of *Tmco6* exon 1, followed by the *E. coli lacZ* gene and a poly-adenylation signal, and the last 137 bp of *Tmco6* exon 12, yielding total loss of codons 2-11 and subsequently the loss of endogenous Tmco6 protein levels.

2.2 Genetic Manipulation and Microbiological Techniques

2.2.1 gDNA Extraction from Cultured Cells

In all cases, gDNA was extracted and purified using the Wizard® Genomic DNA Purification Kit and protocol (Catalogue Number: A1120, Promega). Briefly, plasma membranes and nuclei were lysed, and RNA digested by RNAse treatment. Protein was removed by salt precipitation, and gDNA was concentrated and desalted by means of isopropanol precipitation. All gDNA was eluted in 50 µl Buffer elution buffer (EB) (10 mM Tris-Cl, pH = 8.5) and DNA concentrations estimated by NanoDrop™ 8000 Spectrophotometer (Thermo Scientific™, Thermo Fisher Scientific, UK) at λ = 260/280.

2.2.2 Whole Exome Sequencing (WES)

DNA library preparation was carried out entirely by Dr. Aurelio Reyes using an initial 50 ng of template gDNA obtained from cultured human patient skin fibroblasts for the construction of pair-ended DNA libraries, as previously described (Legati *et al.*, 2016), using the Nextera Rapid Exome Capture kit (Illumina) and following manufacturer's instructions. Downstream bioinformatic analysis of perspective variants was performed by Dr. Alan Robinson and the MRC MBU Bioinformatics Group. For WES, an Illumina MiSeq platform was used with 12 pM template DNA libraries and 1 % 12.5 pM PhiX control libraries. Libraries were run several times until 12-15 gigabytes of data per template sample were obtained. Resulting sequences (in the form of FASTAQ files) were aligned to the human genome (hg19) sequence using the Burrows-Wheeler Aligner (BWA) software (version 0.7.5) in the "mem" mode for long paired-end reads. The MarkDuplicates program from Picard tools was used to identify duplicate sequences in the resulting SAM files. Base quality scores were determined using the BaseRecalibrator from the Broad Institute's genome analysis toolkit (GATK): https://www.broadinstitute.org/gatk/.

Sequences surrounding previously confirmed or potential indels were identified and realigned further using the IndelRealigner feature, also from the Broad Institute's GATK. Potentially pathogenic variants were identified by using the HaplotypeCaller feature of the GATK. Indels and single nucleotide polymorphisms were evaluated and scored separately by using the Variant Quality Score Recalibration (VQSR) feature of the GATK using an in-house database of patient exomes, and a "ts_filter" of 90.0 %. Heterozygous and homozygous variants were separated. If a variant had a Phred-based genotype score (PL) of less than 30, then it was assigned as both heterozygous and homozygous. Heterozygous variants were phased using HAPCUT software (version 0.5). All variants were filtered and annotated using Annovar software. Variants with an allelic frequency of greater than 2 % were discarded, as were variants in intronic and intergenic

regions, or those within protein-coding regions that were synonymous. The following annotations were added per variant: RefSeq ID, gene name and description, the predicted presence or absence of a mitochondrial targeting presequence (MTS) (using Mitoprot, TargetP and IPSort prediction tools), descriptions of the patient phenotypes and any available clinical information (using ClinVar and OMIM databases), the predicted pathogenicity scores (using PolyPhen, SIFT and MutationTester tools), and the relative allelic frequency (ESP, 1000 Genomes, CG69, dbSNP138, and ExAC databases). The most likely causal genetic variant(s) per patient exome identified by WES were amplified by PCR (**section 2.2.3**) from patient skin fibroblasts and validated by Sanger sequencing (**section 2.2.7**).

2.2.3 PCR

2.2.3.1 Design and Synthesis of Oligonucleotide Primers for PCR

SnapGene® software (GSL Biotech LLC, Chicago, Illinois, USA) was used to visualise a plasmid sequence or genomic region of interest. Oligonucleotide primers were designed manually, considering the following parameters:

- Primer Length – designed to be around 20 bp to enable a compromise between high sequence fidelity and low likelihood of mispriming.
- Total GC Content – the proportion of guanine (G) and cytosine (C) nucleotide bases per primer was selected to be 60 % or higher; G and C bases are bound by 3 hydrogen bonds as opposed to 2 connecting adenosine (A) and thymine (T) bases, leading to stronger bonding (Boland and Ratner, 1995).
- GC Clamp – 1 or 2 G's or C's were selected to terminate the 3' end of each primer in order to strengthen the intermolecular binding at this point and create an anchor from which the *Taq* polymerase could replicate the sequence/gene region of interest.
- Melting temperature (T_M) – defined as the temperature at which one half of the double-stranded DNA dissociates to single strands was determined approximately by the following equation:

$$T_M = 4(n_G + n_C) + 2(n_A + n_T)$$

where n = number of nucleotide bases. Primer T_Ms were selected to fall within a range of 55 to 65 °C, with F and R primer pairs not differing by more than 1.5 °C. The annealing temperature per reaction was typically 2 °C lower that the lesser T_M of the primer pair.

- Secondary structures – intramolecular or intermolecular interactions within primers or between primers can lead to little or no product yield. Secondary structures include hairpins, self-dimerization, and cross dimerization with the paired primer. Secondary structure formation potential was determined using the OligoEvaluator™ sequence calculator (Sigma-Aldrich®).

- Cross homology – primers must not nonspecifically amplify off-targets. To ensure this, primer sequence homology to other genomic regions was determined using the NCBI Basic Local Alignment Search Tool (BLAST): https://blast.ncbi.nlm.nih.gov/Blast.cgi.

2.2.3.2 Thermocycling Conditions and PCR

All PCR reactions were performed using a Biometra TRIO Thermocycler (Thistle Scientific, Germany) with thermostable *Taq* polymerase to enzymatically amplify a specific DNA sequence of interest by three temperature-mediated steps: 1) **denaturation** of the double-stranded template DNA, 2) **annealing** of specific forward (F) and reverse (R) oligonucleotide primers to the region of interest on both denatured strands and 3) **extension** of replicate DNA sequences by the *Taq* polymerase (Saiki *et al.*, 1985). Primer sequences, the specific *Taq* polymerase used, and the thermocycling conditions per experiment are stated in tables within the relevant subsections of **Chapter 2**. Primers were synthesised by Merck, Sigma-Aldrich® and delivered dry and desalted. Denaturation occurred at either 94 or 95 °C, annealing between 55 and 65 °C (determined by primer T_M, as per **section 2.2.2.1**), and extension was carried out at 72 °C in all cases.

2.2.3.3 Purification of PCR Products

Following PCR, DNA fragments between 100 bp and 10,000 bp in size were purified from other reaction mixture components using the QIAquick PCR Purification kit (Qiagen), and corresponding protocol. Briefly, a bind-wash-elute procedure was followed, in which a high-salt binding buffer was added to the PCR sample to facilitate binding of DNA to the QIAquick spin column, a silica-based membrane; impurities were eliminated over several ethanol-based washing steps. Pure DNA was then eluted using a low-salt elution buffer or dH_20.

2.2.4 PCR Amplification of Patient Mutations

Purified gDNA from patient primary skin fibroblasts (see **section 2.1.2.1**) was used as a template for PCR amplification (see **section 2.2.3.2**) of the two heterozygous mutations of *COA7*, at the exon 2/intron 2 junction (primer set 1) and within exon 3 (primer set 2), and the single homozygous recessive transition mutation of *TMCO6* within exon 3 (primer set 3). PCR

was performed for 50 µl reactions containing gDNA (50-100 ng/reaction) or dH_20 (negative control), 1mM dNTP mix (0.2mM each dNTP), 1.25 units (U) GoTaq® polymerase (5 U/µl final concentration), 1X Green GoTaq® Reaction Buffer and 1 µM of each primer (listed in **Table 2.1**) as per the corresponding GoTaq® PCR protocol (Promega, USA) under conditions detailed in **Table 2.2**.

Table 2.1 Primers for PCR amplification of patient mutations

Primer	***Sequence (5' → 3')***
COA7 Exon 2/Intron 2 F	CAA GTC CCC ACT GCG AGC AG
COA7 Exon 2/Intron 2 R	TGC CTG CGA GAC CCT TCT GC
COA7 Exon 3 F	GAG ACA TTT AGG TTG TGC CC
COA7 Exon 3 R	GTA CAG AAC ACC CAG ATA AAG
TMCO6 Exon 3 F	GAT TCT CTG TCC ACT CCA CTG C
TMCO6 Exon 3 R	CAC TCT CCA CGA TCA GGT TAC C

Table 2.2 Thermocycling conditions for PCR amplification of patient mutations

Step	***Temperature***	***Duration***	
Hot Start	95°C	3 min	
Denaturation	95°C	30 sec	X 35 cycles
Annealing	56°C	30 sec	
Extension	72°C	1 min	
Final Extension	72°C	5 min	
Hold	12°C	∞	

2.2.5 Agarose Gel Electrophoresis

Agarose gel electrophoresis was used for the separation of DNA fragments by size: 0.8 % for plasmids, 1.0 % for all general applications and 1.5 % for small fragments, < 300 bp in size. Gels were cast with the appropriate weight per volume (w/v) of agarose (Invitrogen™), dissolved in 75 ml Tris/Borate/EDTA (TBE) buffer (89 mM Tris-borate, 100 mM boric acid, 2 mM ethylenediaminetetraacetic acid (EDTA)) and 7.5 µl 10,000 X SYBR Safe dye (Invitrogen™). PCR products containing GoGreen® master mix were loaded directly; all other PCR products and DNA samples were first mixed with 5 X GelPilot® DNA loading buffer (Qiagen) or 6X DNA gel loading dye (Invitrogen™). A 1kb Plus DNA ladder (Invitrogen™) was used for fragment size determination, and samples were electrophoresed at 90 V (EM100, Mini Gel Unit, Engineering & Design Plastics, UK) for approximately 40-50 min with 1X TBE

as the running buffer. An ultraviolet (UV) light transilluminator (Gel Doc™ Imaging System, Bio-Rad, UK) was used to visualize the electrophoresed DNA in all cases.

2.2.6 Agarose Gel Extraction and Purification of DNA

PCR products were extracted from 0.8 - 1.5 % w/v agarose-TBE gel slices using the QIAquick Gel Extraction Kit (Qiagen), and corresponding protocol. Slices were weighed, dissolved by heating at 50 °C for 10 min in QG buffer (5.5 M guanidine thiocyanate and 20 mM Tris-HCl (pH = 6.6)) with a pH indicator. DNA fragments were then purified identically as per **section 2.2.3.3** by silica membrane binding of DNA in high-salt conditions and elution with low-salt buffer or water. The purification procedure removes primers, nucleotides, proteins, oils, salts, agarose, and other contaminants from the DNA by several ethanol-based washes.

2.2.7 DNA Sequencing and Analysis

Sequencing of PCR products and cloned plasmids was carried out using the dideoxy-chain termination method (Sanger, Nicklen and Coulson, 1977) by a commercial service (Source Bioscience Ltd, Cambridge, UK). Resulting query sequences were aligned with a desired template sequence using SnapGene® software or the BLAST sequence alignment tool, Blast® nucleotide suite: https://blast.ncbi.nlm.nih.gov/Blast.cgi.

2.2.8 RNA Extraction and cDNA Retrotranscription

Total RNA from cultured cells or frozen murine tissues was extracted using the TRIzol™ Plus RNA Purification Kit and the PureLink™ RNA Mini Kit (both from Invitrogen™), as per manufacturer's instructions. Briefly, TRIzol, a monophasic solution of phenol and guanidinium isothiocyanate, solubilises all membranes whilst also denaturing proteins. The addition of chloroform to the mixture separates total RNA into the aqueous phase. The RNA is then purified by column purification and eluted in RNAse-free water. Treatment with 1 µl TURBO™ DNase (Ambion®, Life Technologies™) for 30 min at 37 °C removes any trace DNA. Retrotranscription was performed using the Omniscript Reverse Transcription (RT) Kit and protocol (Qiagen), components of which are detailed in **Table 2.3**.

Table 2.3. Omniscript Reverse Transcription Reaction Solution

Reagents from the Omniscript RT kit are in *italics*; all reagents from other sources are cited accordingly.

Reagent	***Stock Concentration***	***Working Concentration***	***Volume (µl)***
Buffer RT	10X	1X	2
dNTPs	5 mM	0.5 mM each	2
Oligo dT primer (Sigma-Aldrich®)	10 µM	1 µM	2
Omniscript Reverse Transcriptase	1 U/µl	0.2 U/µl	1
Random Hexamer (Invitrogen™)	50 µM	10 µM	0.2
RNA template	(variable)	0.1 µg/µl	5
RNAsin® RNase inhibitor (Promega)	40 U/µl	10 U/µl	0.25
RNase-free H_20	-	-	7.55
			TOTAL: 20 µl

RT reactions, containing 2 µg template RNA in each case, were incubated for 1 h at 37 ºC, and further incubated for 5 min at 95 ºC. The resulting cDNA mixtures were diluted to 50 µl with dH_20 and amplified by PCR with PFU TurboTaq® polymerase (Agilent Technologies, UK). Primers, reagents and thermocycling conditions used for cDNA retrotranscription are detailed in **Tables 2.4 – 2.6**, respectively.

Table 2.4. PCR primers for cRNA amplification

Primer	*Sequence (5' → 3')*
COA7-cDNA-F	AGA ACA TGG AGG TGG AGT GC
COA7-cDNA-R	CCT TGG CCT CAT CCT TAT CA
TMCO6-cDNA-F	TGC AAC CAG GCC CGA AG
TMCO6-cDNA-R	TAA AGG GTG ATA TTT GAG CAG C

Table 2.5. PCR reagents for cDNA Amplification

Reagent	*Stock Concentration*	*Working Concentration*	*Volume (µl)*
10X PFU Buffer	10X	1X	5
1mM dNTPs	10 µM each	250 µM	1
F primer	10 µM	1 µM	1
R primer	10 µM	1 µM	1
PFU TurboTaq	2.5 U / µl	0.05 U/ µl	1
dH_20	-	-	40
			TOTAL: 50 µl

Table 2.6. PCR thermocycling conditions for cDNA amplification

Step	*Temperature*	*Duration*	
Hot Start	95ºC	2 min	
Denaturation	95ºC	30 sec	X 31 cycles
Annealing	55ºC	30 sec	
Extension	72ºC	3 min	
Final Extension	72ºC	10 min	
Hold	4ºC	∞	

2.2.9 Ligation of cDNA Sequences into Cloning Plasmids

Wildtype full coding sequence (CDS) *COA7* cDNA was obtained commercially from the Integrated Molecular Analysis of Genomes and their Expression (IMAGE) cDNA library (IMAGE ID: 4430419/IRATp970-0D0921D, Source Bioscience Ltd). Approximately 200 ng of cDNA was used as a template for PCR amplification with the BIOTAQ™ DNA Polymerase (Bioline Reagents Ltd, London, UK), which possesses 5' → 3' exonuclease activity and leaves an 'A' overhang such that the PCR product is suitable for effective integration into TA cloning vectors. PCR reactions were set up as detailed in **Table 2.7** and thermocycling conditions were optimized for two specific reactions (**Table 2.9**). F and R primers (**Table 2.8**) were designed to insert *Pme* I and *Bgl* II restriction sites at the start and end of the WT-*COA7* cDNA sequence, respectively; a second PCR reaction was performed using a different reverse primer encoding a downstream hemagglutinin (HA) epitope tag: 5' TAC CCA TAC GAC GTC CCA GAC TAC GCT 3' (peptide sequence: YPYDVPDYA).

Table 2.7. PCR reagents for introducing flanking restriction sites to cDNA sequences

Reagents included in the BIOTAQ™ DNA Polymerase kit are in *italics*; all reagents from other sources are cited accordingly.

Reagent	***Volume (µl)***	***Final concentration***
BIOTAQ™ Reaction Buffer (10X)	5	1X
$MgCl_2$ (50 mM)	2.5	2.5 mM
dNTP Mix (10 mM each) *(Catalogue number: 10297018, Invitrogen™)*	1	0.2 mM each
Forward primer (10 µM) (Merck, Sigma-Aldrich®)	2	0.4 µM
Reverse primer (10 µM) (Merck, Sigma-Aldrich®)	2	0.4 µM
Template cDNA (Bioline Reagents Ltd)	4	1 ng/µl
BIOTAQ™ DNA polymerase (5 U/µl)	0.25	1.25 U
Nuclease-Free Water (Ambion®)	Up to 50 total	

Table 2.8. PCR primers for restriction site sequence amplification

Primer	***Sequence (5' → 3')***
COA7-PmeI-F	GTT TAA ACG AAC CAT GGC CGG CAT GG
COA7-BglII-R	AGA TCT CAA GCA CTT TGT TGC CTG G
COA7-HA-BglII-R	AGA TCT CAA GCG TAA TCT GGA ACA TCG TAT GGG TAC CCA AAT GTT AAG GGT TGG

Table 2.9. PCR thermocycling conditions for restriction site sequence amplification

Step	***Temperature***	***Duration***	
Hot Start	95ºC	3 min	
Denaturation	95ºC	30 sec	X 30 cycles
Annealing	58ºC	30 sec	
Extension	72ºC	3 min	
Final Extension	72ºC	10 min	
Hold	4ºC	∞	

Amplified WT-*COA7* and WT-*COA7-HA* PCR products, both with flanking *Pme* I and *Bgl* II-compatible restriction sites, were resolved by agarose gel electrophoresis (**section 2.2.5**) (1 % w/v agarose) and the desired DNA fragments excised and purified (see **section 2.2.6**). Either WT-*COA7* or WT-*COA7-HA* (~670bp) sequences were ligated into the linearized pCR™2.1-TOPO® cloning vector (**Fig 2.2**) via a 5 min reaction at RT with 1 µl purified PCR

product, 1 µl NaCl salt solution, 1 µl pCR™2.1-TOPO® vector and 3 µl dH_20 (as per the TOPO® TA Cloning® Kit, Thermo Fisher Scientific). The pCR™2.1-TOPO® cloning vector contains 3´ 'T' overhangs that allow for rapid ligation with the 'A' overhangs added by the BIOTAQ™ polymerase.

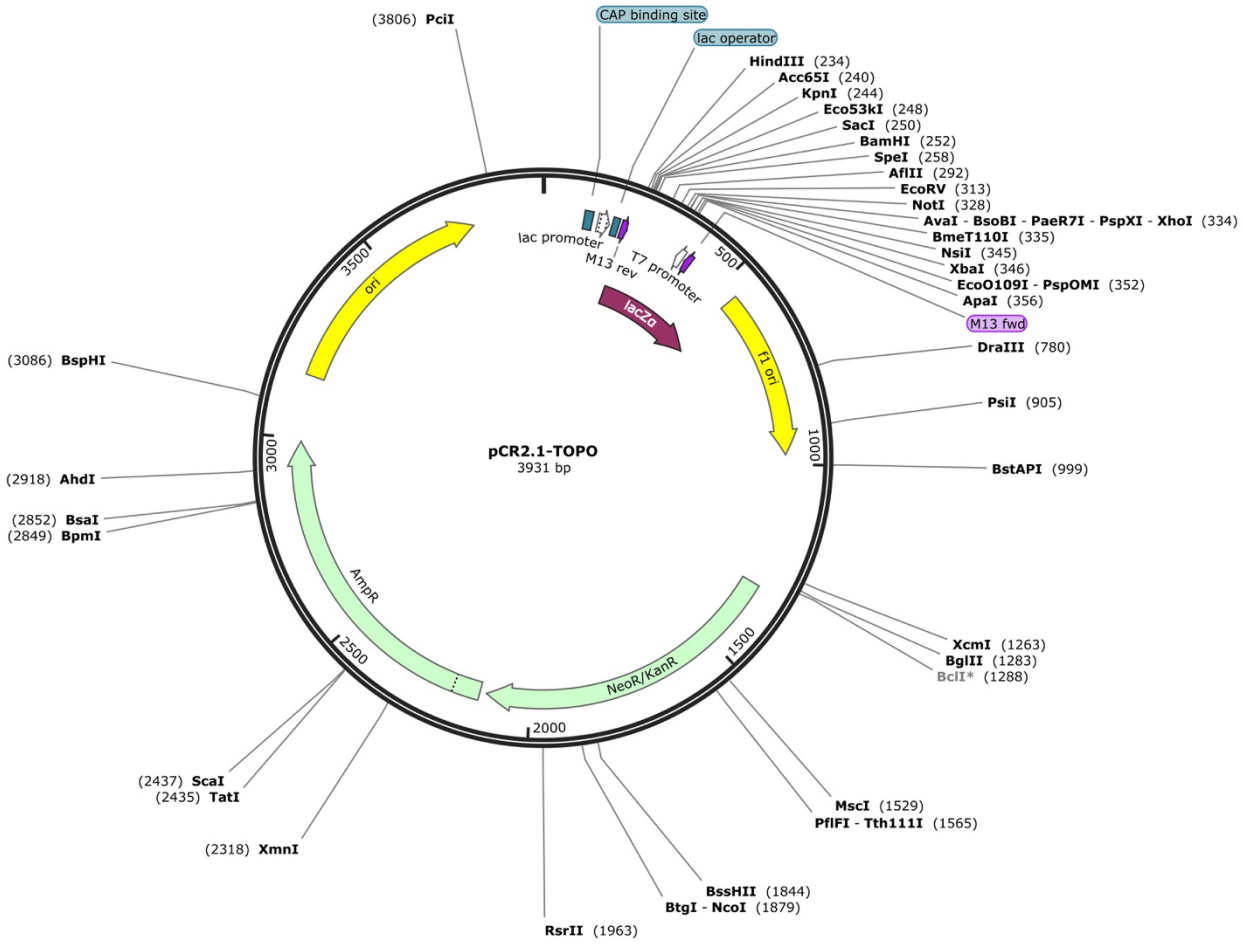

Figure 2.2 Cloning vector for *Taq*-amplified PCR products.

The pCR2.1-TOPO cloning plasmid contains 3' T-overhangs for direct ligation of a Taq-amplified PCR product, a T7 promoter, M13 forward and reverse primer sites for sequencing, *Eco*R I restrictions sites on either side of the PCR insert site, kanamycin and ampicillin resistance genes, and the lacZ gene α-subunit for X-gal screening.

2.2.10 Competent *E. coli* Transformation and Plasmid Mini-Preparation

Two separate 50 µl aliquots of Subcloning Efficiency DH5α™ competent *E. coli* cells (Thermo Fisher Scientific) were transformed with 2 µl of WT-*COA7*-pCR™2.1-TOPO® or WT-*COA7*-HA-pCR™2.1-TOPO® plasmids. This was done by an initial incubation on ice for 30 min, heat shock at 42 °C in a water bath for 45 sec, and further incubation on ice for 5 min. Addition of

200 µl super optimal broth with catabolic repressor (SOC) (2 % tryptone, 0.5 % yeast extract, 10 mM NaCl, 2.5 mM KCl, 10 mM $MgCl_2$, 10 mM $MgSO_4$, and 20 mM glucose) to the transformed bacteria, and subsequent growth for 1 h at 37 °C with shaking at 225 rpm allowed production of ampicillin (Amp) resistance. Separately, agar plates made with lysogeny broth (LB) (1 % tryptone, 0.5 % yeast extract, and 10 mM NaCl), containing 100 µg/ml ampicillin, were covered topically with 40 µl X-gal (5-bromo-4-chloro-3-indolyl β-D-galactopyranoside) stain (Catalogue Number: R0404, Thermo Scientific™), which indicates correct reporter gene expression by staining false positive colonies dark blue. After the surface of these plates had dried completely, 100 µl of the transformed bacterial solutions were spread onto each plate and incubated O/N at 37 °C. Positive (white) colonies (*n* = 5 for each plasmid) were then picked with a sterile loop and cultured in 5 ml LB, containing 100 µg/ml amp, in a shaking incubator (225 rpm) at 37 °C O/N.

2.2.11 Restriction Enzyme Digestion

WT-COA7-pCR™2.1-TOPO® and *WT-COA7-HA*-pCR™2.1-TOPO® plasmids were isolated and purified from bacterial suspensions (see **section 2.2.10**) using the QIAgen® plasmid miniprep kit (Qiagen). 10 µg of each were digested with *Pme* I and *Bgl* II restriction enzymes (1 U/µl) (New England Biosciences®, New England Biolabs Ltd, UK) at 37 °C for 3 h in sequential reactions since they required separate buffers: 1X CutSmart® buffer for *Pme* I and NEBuffer 3.1 for *Bgl* II (both from New England Biosciences®). *Bgl* II was used in this step since the preferred enzyme, *Bam*H I, recognized a restriction site within the *COA7* and *COA7-HA* sequences. *Pme* I-digested *WT-COA7* and *WT-COA7-HA* DNA products were purified with the QIAspin® DNA Purification Kit, as per **section 2.2.3.3**. *Bgl* II digestion followed, and the purified and linearised DNA was resolved on a 1.0 % w/v agarose-TBE gel via electrophoresis (see **section 2.2.5**) to confirm presence of the insert. Gel extraction and purification of the interest followed (see **section 2.2.6**). In two separate reactions, pWPXLd lentiviral plasmids (gift from the Trono lab, Salmon *et al.* 2000) in which the GFP sequence was substituted with a puromycin or hygromycin B resistance cassette (pWPXLd-IRES-Puro^R or pWPXLd-IRES-Hygro^R, respectively; **Fig. 2.3 A.** and **B.**) was dually digested with *Pme* I and *Bam*H I in NEB 4 Buffer (New England Biosciences®) for 3 h at 37 °C, and purified as per **section 2.2.3.3**.

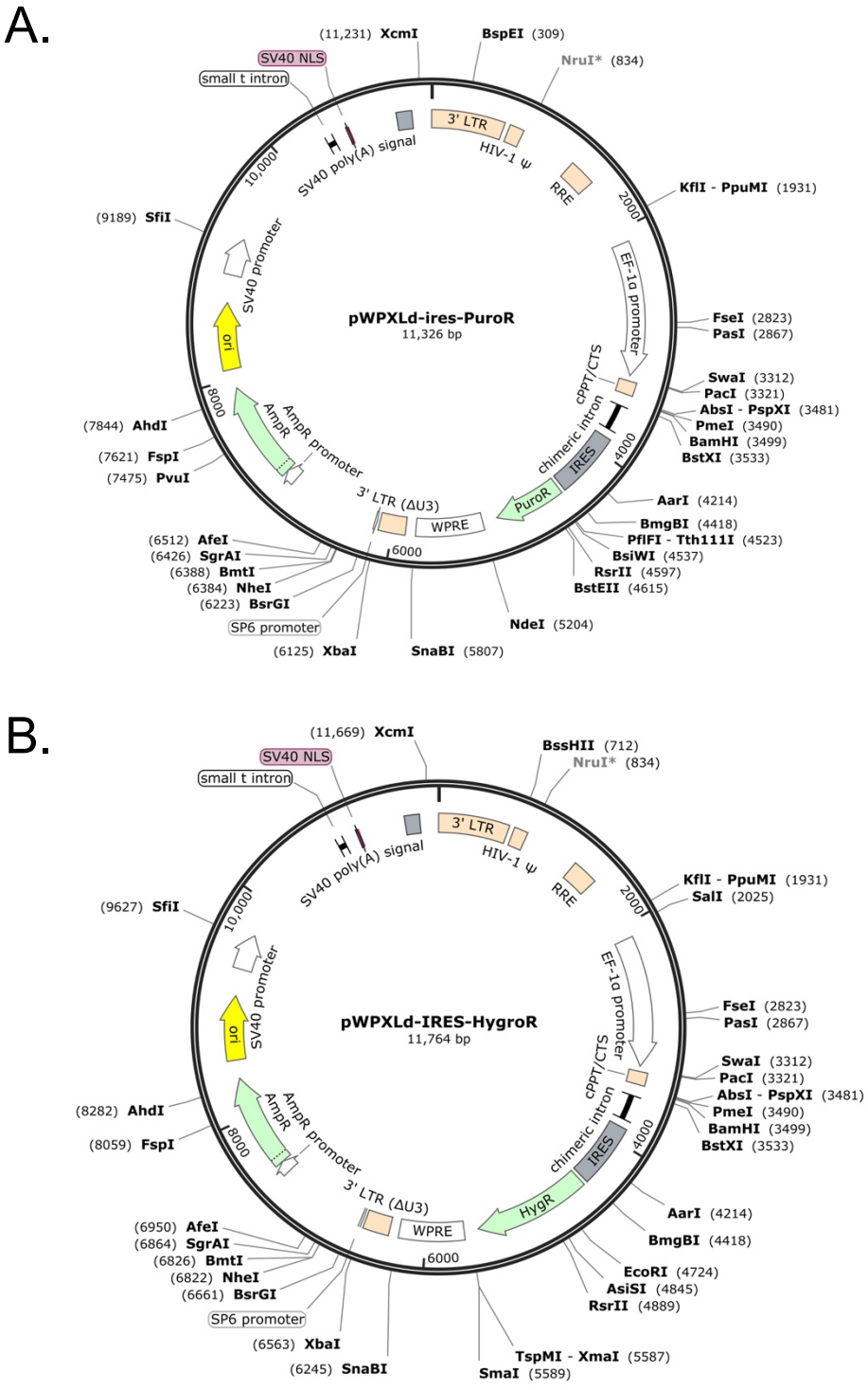

Figure 2.3 pWPXld transfer vectors for generating *COA7*-overexpressing cell lines.

(**A**) pWPXLd-IRES-Puro^R and (**B**) pWPXLd-IRES-Hygro^R plasmids encode Puro^R or Hygr^R genes for selection in mammalian systems and Amp^R for selection in bacterial systems. A desired insert of interest (not shown but cloned between *Pme* I- and *Bam*H I sites) is flanked by LTR sequences to facilitate construct integration into the host genome, an RRE site allowing lentiviral replication, and an internal ribosome entry site (IRES) for transcription of several genes to one mRNA transcript. Eukaryotic EF-1α and bacterial SV40 promoters, and a Woodchuck hepatitis virus post-transcriptional enhancer (WPRE) element enable transcription at one origin or replication.

2.2.12 Ligation of DNA into Lentiviral Transfer Plasmids

*Bam*H I and *Bgl* II restriction enzymes generate compatible 5' overhang ends (Cost and Cozzarelli, 2007); therefore, 37.5 ng *Pme* I- and *Bg*l II-digested *WT-COA7* and *WT-COA7-HA* PCR products were ligated into 50 ng *Pme* I- and *Bam*H I- linearised pWPXLd-IRES-Puro^R or pWPXLd-IRES-Hygro^R in 20 µl reactions using T4 DNA ligase (New England Biosciences), as per manufacturer's instructions. Ligation (at 16 ^{o}C O/N) in 1X T4 reaction buffer with 6 U/µl T4 ligase was achieved using a 1:3 vector to insert ratio and resulted in two distinct lentiviral plasmid constructs: *COA7^{WT}*-pWPXLd-*Ires-Puro^R* and *COA7^{WT}-HA*-pWPXLd-*Ires-Hygro^R*.

2.2.13 Long-Term Storage of Transformed *E. coli*

Microbank™ vials (Pro-Lab Diagnostics), porous beads in cryo-preservation fluid, were used for the long-term storage of transformed *E. coli*. A young colony (between 18-24 h after plating) was picked and used to inoculate the beads and fluid, which were stored long-term at - 80 °C.

2.2.14 Quantitative Reverse Transcription PCR (RT-qPCR)

TMCO6 gene expression was assessed by RT-qPCR for Flp-In™-293T cells that had undergone shRNA-mediated gene silencing (see **section 2.3.4**) and for validating total loss of endogenous *Tmco6* gene expression in 3 month-old *Tmco6* KO mice (see **section 2.1.3**).

TaqMan® gene expression assays were used, which utilise the 5' exonuclease activity of *Taq* polymerase to cleave a dual-labelled hybridisation probe during the extension phase of traditional PCR (Kim, 2001). TaqMan® hybridisation probes consist of a complimentary primer sequence for a given cDNA target sequence, flanked by a 5' reporter fluorophore, 6-carboxyfluorescein (FAM), and a 3' quencher molecule, 6-carboxy-tetramethylrhodamine (TAMRA). Upon binding its target sequence, *Taq* polymerase extends the primer sequence to synthesize a nascent strand. Dually, its 5' to 3' exonuclease activity degrades the hybridisation probe and TAMRA quencher molecule, in turn liberating the FAM reporter fluorophore. Fluorescence detected at 518 nm resulting from the cleaved reporter is directly proportional to the amount of cDNA template present in the reaction (Nolan, Hands and Bustin, 2006).

A commercially available human-targeted TaqMan® Gene Expression Assay (Hs00382836_m1, Thermo Fisher Scientific) was used to quantify relative abundance of *TMCO6* mRNA transcripts in four shRNA knockdown cell lines (shRNA 1-4), and in empty vector (EV) and non-mammalian negative (-) controls. Total RNA was extracted and retrotranscribed to cDNA (as per **section 2.2.8**). The relative abundances of each of these were normalised against levels of human glyceraldehyde 3-phosphate dehydrogenase

(*GAPDH*) (TaqMan® Gene Assay ID: Hs02758991_g1), a stably and constitutively expressed house-keeping enzyme essential for glycolysis. For verifying total loss of *Tmco6* expression in knockout mice, total RNA was extracted from brain tissue and retrotranscribed to cDNA (as per **section 2.2.8**). A mouse-specific gene expression assay targeted for *Tmco6* (TaqMan® Gene Assay ID: Mm00511056_m1) was used, and gene expression levels for WT (*n* = 2), HET (*n* = 1) and KO (*n* = 3) mice were normalised against expression levels of myosin heavy chain 10 (*Myh10*) (TaqMan® Gene Assay ID: Mm00805131_m1), a non-muscle myosin stably expressed in the brain. Reactions were set up as per manufacturer's guidelines, in volumes of 20 µl containing 1X TaqMan® Gene Expression Assay (see **Table 2.10**), 1X TaqMan® Gene Expression Master Mix, 100 ng cDNA template, and adjusted with RNase-free water.

Table 2.10. Gene Expression Assays for RT-qPCR

Gene	*TaqMan Gene Assay ID*	*Amplicon Sequence (5' → 3')*
Human GAPDH	**Hs02758991_g1**	CAG TCC ATG CCA TCA CTG CCA CCC AGA AGA CTG TGG ATG GCC CCT CCG GGA AAC TGT GGC GTG ATG GCC GCG GGG CTC TCC AGA ACA TCA TCC
Human TMCO6	**Hs00382836_m1**	GGT GCA GCA GTT CCT GCG GCA AGC CCA GCC GGG GAC AGA GGA AAA GGA GAG AGA G
Murine Tmco6	**Mm00511056_m1**	GTC CAG CAG TTC CTT CGG CTC GCC CAA CGC GGG ACA GAT GAA AAG GAG AGG GAG AAG GCT CTG GTC AGC CTT CGT CGA GGC TTG CAG C
Murine Myh10	**Mm00805131_m1**	GAG AAG GCT AAT GCC AGG ATG AAG CAG CTT AAA CGA CAG TTG GAA GAG GCT GAG GAA GAG G

Each 20 µl reaction mixture was transferred to individual wells of a 96-well plate, which was sealed and loaded into a 7900HT RT-QPCR System (Applied Biosystems, Thermo Fisher Scientific, USA). Three technical replicates were performed per gene concurrently for both the gene of interest and respective loading control. Thermocycling conditions were 95°C for 10 min (initial denaturation), followed by 40 cycles of 95 °C for 15 s (denaturation) and 60 °C for 1 min (annealing and extension). The extension cycle at which fluorescence becomes detectable is termed the cycle of threshold (C_t) (**Figure 2.4**). The C_t value was then used to calculate relative gene expression using Double Delta C_t analysis, as previously described (Livak and Schmittgen, 2001).

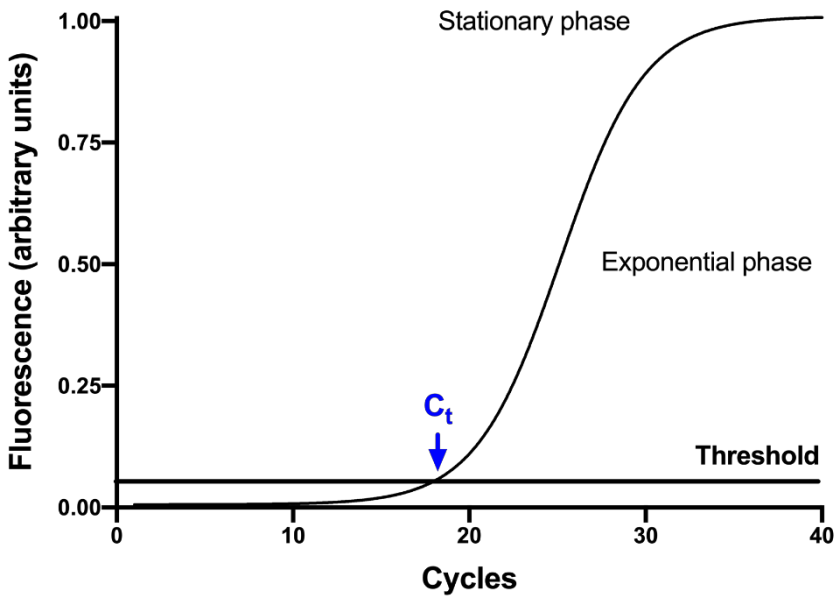

Figure 2.4 RT-qPCR florescence intensity progression.

The point at which fluorescence exceeds the signal threshold is called "C_t" (cycle of threshold) and correlates to the initial DNA template amount. The lower the C_t value, the more initial template cDNA present.

2.2.15 CRISPR/Cas9 Genome Editing

In this work, CRISPR/Cas9 technology was used to edit the genome of HAP1 cells (see **section 2.1.2.4**) by both nonhomologous end joining (NHEJ) in order to generate a *TMCO6* knockout cellular model, as well as homology-directed repair (HDR) in order to generate a knock-in for the human patient mutation (NM_018502: c.271C>T, NP_060972.3:p.Arg91Cys) with the aid of a specific single-stranded donor oligonucleotide (ssODN). A specific sgRNA was designed using the CHOPCHOP software (http://chopchop.cbu.uib.no/) (Montague *et al.*, 2014; Labun *et al.*, 2019) to target a region of exon 3 within the human *TMCO6* gene (GenBank ID: 55374): sgRNA1 (5' GGT GCT GCA AGC CTC GAC GAA GG 3'). Oligonucleotide primers were designed (as per **section 2.2.2.1**) to contain the forward and anti-parallel sequence for sgRNA1, with specialised flanking sequences (in green) as described by Ran *et al.* (Ran *et al*. 2013) (**Table 2.11**). 2 µM per oligonucleotide were combined with 5 µl (10X) T4 DNA ligase, diluted to 50 µl with nuclease-free dH_20, and annealed by heating to 95 ^oC for 5 min, followed by gradual cooling at a rate of 0.1 ^oC sec^{-1} to a final temperature of 25 ^oC.

Table 2.11. PCR primers for annealing sgRNAs

Primer	Sequence (5' → 3')
TMCO6 sgRNA top	CAC CGG GTG CTG CAA GCC TCG ACG AAG G
TMCO6 sgRNA bottom	AAA CCC TTC GTC GAG GCT TGC AGC ACC C

Annealed oligonucleotides were ligated into the pSpCas9(BB)-EGFP plasmid (Addgene ID: 48138, a gift from Feng Zhang; **Fig 2.5**) that had been digested with 1 U/µl *Bbs* I (Catalogue number: R0539S, New England Biosciences®) in 1X NEBuffer® 2.1 buffer for 1 h at 37 ºC. Ligated plasmids were transformed into DH5α™ competent *E. coli* cells and purified from resultant colonies as per **section 2.2.10.** Correct integration of the desired sequences was confirmed by Sanger sequencing (**section 2.2.7**) using the U6 forward primer (sequence: 5' ACT ATC ATA TGC TTA CCG TAA C 3').

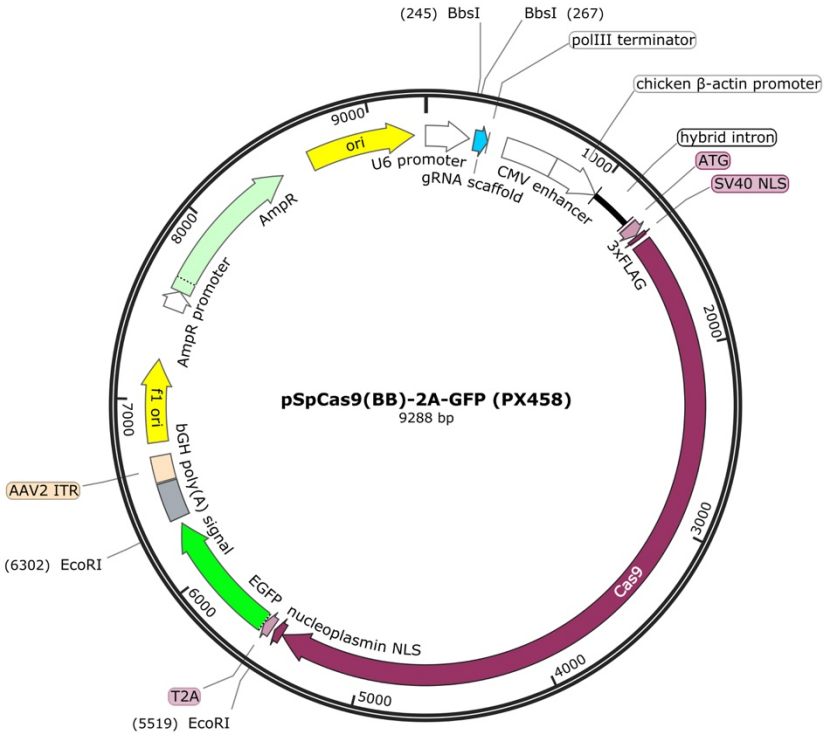

Figure 2.5 CRISPR expression vector.

The pSpCas9(BB)-2A GFP (PX458) plasmid (Addgene ID: 48138) encodes *S. pyogenes* Cas9 nuclease, with an N-terminal 3X FLAG tag, a C-terminal EGFP tag, and a 3' polyA tail from bGH. The Cas9 gene is followed downstream by an AAV2-derived ITR, and is under the control of a hybrid CMV promoter. A *Bbs* I/*Bbs* I sgRNA cloning site is encoded upstream of this, with a sgRNA scaffold, under control of a U6 promoter. The Amp^R gene allows for selection following transformation in bacterial systems.

HAP1 gDNA was extracted as per **section 2.2.1** and ~500 bp surrounding the target region within exon 3 was amplified in a 50 µl reaction by PCR with the primers, reagents and thermocycling conditions detailed in **Tables 2.12 - 2.14**, respectively.

Table 2.12 PCR primers for amplifying HAP1 *TMCO6* exon 3

Primer	*Sequence (5' → 3')*
TMCO6 ScPr F	CTC CAC TGC AAG GTA GAT GCT TAT TAG T
TMCO6 ScPr R	GCT CAT GCA GGC ACC GAG

Table 2.13 Reagents for PCR amplification of HAP1 *TMCO6* exon 3

Reagent	***Volume (µl)***	***Final concentration***
LA PCR Buffer (Mg^{2+} free) (10X)	5	1X
$MgCl_2$ (50 mM)	4	4 mM
dNTP Mix (2.5 mM each)	8	0.4 mM
TMCO6 ScPr F (10 µM)	4	0.8 µM
TMCO6 ScPr R (10 µM)	4	0.8 µM
gDNA (200 ng/µl)	1	4 ng/µl
Takara LA Taq (5 U/µl)	0.5	2.5 U
Nuclease-Free Water (Ambion®)	23.5	-

Table 2.14 PCR thermocycling conditions amplifying HAP1 *TMCO6* exon 3

Step	***Temperature***	***Duration***	
Hot Start	95ºC	3 min	
Denaturation	95ºC	30 sec	X 35 cycles
Annealing	60ºC	45 sec	
Extension	72ºC	1 min	
Final Extension	72ºC	5 min	
Hold	4ºC	∞	

The Guide-it™ Complete sgRNA Screening System (Catalogue number: 632636, Takara Bio Europe) was followed as per manufacturer's instructions to screen the efficiency of sgRNA1 to cut its desired gDNA sequence *in vitro*. 5 µl Guide-It™ scaffold template was combined with 1 µM sgRNA1 F primer (**Table 2.15**) and diluted to a final volume of 25 µl with nuclease-free dH_20. This solution was added to a commercial aliquot of High Yield PCR EcoDry premix and amplified as per **Table 2.16**. 5 µl of the PCR product mixture was resolved by agarose gel electrophoresis (see **section 2.2.5**) (1.8 % w/v agarose) and the resulting ~140 bp band,

containing the sgRNA1 sequence in a template DNA backbone, were purified with the included NucleoSpin Gel and PCR Clean-Up kit. *In vitro* transcription of the sgRNA-encoding template followed, as per **Table 2.17**. Each 20 µl mixture was incubated at 42 °C for 1 h.

Table 2.15 PCR primers for amplification of sgRNA-encoding scaffold template

69 bp primer for integrating sgRNA1 into a DNA template backbone, including a T7 promoter sequence (blue), sgRNA sequence of interest (red) and specific scaffold template DNA sequence (green).

Primer	*Sequence (5' → 3')*
TMCO6 sgRNA1	GCG GCC TCT AAT ACG ACT CAC TAT AGG GGG TGC TGC AAG CCT CGA CGA GTT TTA GAG CTA GAA ATA GCA

Table 2.16 PCR conditions for amplification of a sgRNA-encoding scaffold template

Step	***Temperature***	***Duration***	
Hot Start	95°C	1 min	
Denaturation	95°C	30 sec	X 33 cycles
Annealing and Extension	68°C	1 min	
Final Extension	68°C	1 min	

Table 2.17 PCR conditions for amplification of a sgRNA-encoding scaffold template

Reagent	***Volume (µl)***	***Final concentration***
Purified PCR fragment	1	5 ng/µl
Guide-It™ Transcription Buffer	7	1X
Guide-It™ T7 Polymerase Mix	3	1X
RNase-free dH$_2$0	9	0.8 µM

Following transcription, 1 µl TURBO™ DNase (Ambion®, Life Technologies™) was added to the mixture and incubated for 30 min at 37 °C to remove template DNA. RNase-free water was added to a volume of 100 µl, and an equal volume of phenol:chloroform:isoamyl alcohol in a 25:24:1 ratio, equilibrated in 10 mM Tris (pH = 8.0) + 1 mM EDTA, was then added. The reaction was mixed by vortex and centrifuged at 12,000 rpm for 2 min at RT. The supernatant, containing the sgRNA, was collected into a fresh, sterile 1.5 ml Eppendorf tube and 100 µl of chloroform added. The mixture was centrifuged again as above, and the supernatant collected again. 10 µl 3M sodium acetate and 100 µl pure isopropanol were then added and incubated for 5 min at RT. Purified sgRNA was pelleted at 15,000 rpm for 5 at RT, washed with 80 %

ethanol, centrifuged again as above, and air-dried for ~15 min. Pellets were resuspended in 20 µl RNAse-free dH_20, and the concentration of sgRNA1 was estimated by NanoDrop™ 8000 spectrophotometer (λ = 260). Cleavage reactions were then immediately set up as per **Table 2.18** with 100 ng of the amplified and purified HAP1 *TMCO6* exon 3 region (generated as per **Tables 2.12 - 2.14)** and 20 ng purified sgRNA1. An identical reaction was run concurrently using a 2 kbp control DNA fragment and control sgRNA. Experimental and control reactions were incubated for 1 h at 37 °C. Cleavage was halted immediately following this by incubation at 70 °C for 10 min. Entire reaction volumes were loaded into individual wells of a 1 % w/v TBE-agarose gel, with uncleaved DNA fragments loaded alongside as negative controls.

Table 2.18 sgRNA *in vitro* cleavage reaction conditions

Reagent	***Volume (µl)***
HAP1 gDNA PCR-amplified DNA template	Equivalent to 100 ng
Purified sgRNA	Equivalent to 20 ng
Guide-It™ Recombinant Cas9 Nuclease	1
10X Cas9 Reaction Buffer	1
10X BSA	1
RNase-free PCR-grade dH_20	Up to 10

Following successful *in vitro* cleavage by sgRNA1 of the template gDNA region as determined by agarose gel electrophoresis, 1.5 x 10^5 HAP1 cells were seeded per well of a 6-well culturing plate and allowed to adhere completely at 37 °C for 24 h. For generating a knockout by NHEJ, 100 ng of purified sgRNA1/pSpCas9(BB)-2A GFP (PX458) plasmid was diluted into 250 µl Opti-MEM™ (Catalogue number: 51985034, Gibco™). A ratio of 3:1 TurboFectin 8.0 reagent (Catlogue number: TF81001, Origene) was added to the mixture, mixed by inversion, and incubated for 15 min at RT. The mixture was the pipetted dropwise per well. The plate was then rocked laterally in all directions for 30 secs manually, and incubated at 37 °C for 24 h. For generating a knock-in of the patient mutation by HDR, the same process was followed but an additional 10 µM of ssODN (**Table 2.19**) was added to the 250 µl sgRNA1/pSpCas9(BB)-2A GFP (PX458) + Opti-MEM™ mixture prior to the addition of TurboFectin 8.0

Table 2.19 ssODN encoding the patient mutation (c.271C>T) and a *Sac* I restriction enzyme site within human *TMCO6* exon 3

Primer	*Sequence (5' → 3')*
ssODN1	CCC TGC CCT GAA CTC CAG GTG CAG CAG TTC CTG CGG CAA GCC CAG CGG GGG ACA GAG GAA AAG GAG AGA GAG GGG GCT CTG GTC AGC CTT TGT CGA GGC TTG CAG CAC CCT GAA ACA CAG CAA ACC TTC ATC CGG TCA GTG TGG ATG GTG TGG TGG AGG GAG GAG TTG GAG CTC TGA GGG ATG

Cells were trypsinised, cell density determined by the Countess II™ FL cell counter (Life Technologies) and solutions diluted to a final concentration of 1 x 10^6 cells/ml with fresh HAP1 culturing media (see **section 2.3.1**). 10 µg/ml 7-aminoactinomycin D (7-AAD) (Catalogue number: A1310, Invitrogen™) nucleic acid stain was added to the solutions and incubated for 15 min at 37 °C. 7-AAD is a membrane impermeant fluorescent dye excluded by viable cells, but able to enter semi-permeable apoptotic or dead cells. Cells that had been correctly transfected with the sgRNA1/pSpCas9(BB)-2A GFP (PX458) plasmid expressed GFP. Following 7-AAD staining, the HAP1 cells were sorted by fluorescence-activated cell sorting (FACS), gating for GFP-positive and 7-AAD-negative cell populations for sgRNA1 and sgRNA1 + ssODN1 subtypes. Approximately 500 GFP-positive, live cells were distributed into individual wells of a 96-well plate (Corning, Costar), containing pre-warmed IMDM media supplemented with 20 % FBS. Cells were cultured for approximately 2 week, undisturbed until detection of a cell colony in any well, wherein cells were trypsinised and seeded into 24-well and then 6-well culturing plates. Cells were labelled by their 96-well plate column and row designation (Ex.: A1 for column 'A', row '1'), and KO or MUT for the knockout or patient mutant knock-in subtypes, respectively.

Screening of *TMCO6*-KO HAP1 cells was performed by SDS-PAGE (**section 2.6.2**) and immunodetection by Western blotting (**section 2.6.4**) for the endogenous TMCO6 protein, using the antibody and conditions specified in **Table 2.29**. Clones with observed decreases in native *TMCO6* expression were cultured further, and their gDNA extracted (see **section 2.2.1**). PCR amplification of the target region followed using the primers, reagents and thermocycling conditions as per **Tables 2.12 – 2.14**, and Sanger sequencing (**section 2.2.7**) was performed using the TMCO6 ScPr F primer (**Table 2.12**).

Screening of *TMCO6* knock-in cells was performed by gDNA extraction (see **section 2.2.1**), PCR amplification of the target region using the primers, reagents and thermocycling conditions as per **Tables 2.12 – 2.14**, and then restriction digestion with 1 U/µl *Sac* I (Catalogue number: R0156S, New England Biosciences®) in 1X NEBuffer® 1.1 buffer for 3 h

at 37 ^{o}C. A non-synonymous mutation was introduced into the ssODN to create an artificial *Sac* I restriction site, which did not alter the reading frame or order of the resulting amino acid sequence, in order to streamline the process of screening. *Sac* I-digested fragments were loaded onto 1 % w/v TBE-agarose gels and resolved via electrophoresis (see **section 2.2.5**). Any candidate clones resulting from this screening were then sent for Sanger sequencing (**section 2.2.7**), to verify correct insertion of the knock-in sequence.

2.3 Cell Culture and Associated Procedures

2.3.1 Culturing Conditions

All cells were cultured at 37 °C in a humidified incubator under 5 % CO_2, and harvested or split with 10 % Trypsin/EDTA (TE) (Gibco™) at confluence. Fresh media was added every 3 to 4 days to cells yet to reach confluence.

Human primary and immortalised skin fibroblast cell lines (**section 2.1.2.1**), HEK 293T cells (**section 2.1.2.2**), HeLa cells (**section 2.1.2.3**), 143B cells (**section 2.1.2.3**) and MEFs (**section 2.1.2.5**) were cultured in 'standard culturing medium': 4.5 g/L D-glucose and 1 mM sodium pyruvate-enriched 1X Dulbecco's Modified Eagle Medium (DMEM), supplemented with 2 mM GlutaMAX™, 10 % foetal bovine serum (FBS), 100 units/ml penicillin and 100 µg/ml streptomycin (P/S) (all from Gibco™, Thermo Fisher Scientific, UK). COA7 patient fibroblasts, as well as their counterpart controls, were additionally given 50 µg/ml uridine (Sigma-Aldrich®, Merck, UK) since cells with COX deficiency are known to suffer impaired activity of dihydroorotate dehydrogenase, a mitochondrial enzyme that catalyses an essential step of *de novo* pyrimidine biosynthesis and whose activity is coupled to the MRC (Evans and Guy, 2004). Uridine supplementation is speculated to bypass this rate-limiting step, allowing cells to undergo DNA replication normally (Desler, Lykke and Rasmussen, 2010). The pWPXLd-IRES-Puro^R and pWPXLd-IRES-Hygro^R vectors (see **Fig. 2.7**) used for lentiviral transduction (see **section 2.3.5**) conferred puromycin or hygromycin B resistance, respectively; therefore, cell lines transduced with either of these vectors were selected for by addition of puromycin (1 µg/ml) or hygromycin B (100 µg/ml) (both from Gibco™) to the normal culturing media. HEK 293T cells with inducible overexpressing forms of wildtype or patient *TMCO6* (see **section 2.3.6**) were cultured with 10 % dialysed, tetracycline-free FBS (Biochrom, Berlin, Germany), and selected for by 1 µg/ml blasticidin S (Gibco™) and 100 µg/ml hygromycin. shRNA-knockdown TMCO6 HEK 293T cell lines (see **section 2.3.4**) were selected for by puromycin (1 µg/ml) added to standard culturing media. HAP1 cells (**section 2.1.2.4**) were exclusively grown in Iscove's Modified Dulbecco's Media (IMDM) (Gibco™) supplemented with 10 % FBS and 5 % PBS. Lastly, MEFs (**section 2.1.2.5**) were cultured in standard culturing media with 25 µg/ml of the antifungal drug, amphotericin B (Gibco™).

2.3.2 Lentiviral Particle Production

Lentiviral particles were produced by cotransfection of HEK 293T cells with the following plasmids: packaging plasmid psPAX2 (Addgene ID: 12260, **Fig. 2.6 A.**), envelope plasmid pMD2.G (Addgene ID: 12259, **Fig. 2.6 B.**), and a pWPXLd-based transfer plasmid. Four different transfer plasmids were used for constitutive protein overexpression: COA7-pWPXLd-

IRES-Puro^R, COA7-HA-pWPXLd-IRES-Hygro^R, and counterpart pWPXLd-IRES-Puro^R and pWPXLd-IRES-Hygro^R empty vector (EV) controls (generated as detailed in **sections 2.2.9** - **2.2.12**).

Producer HEK 293T cells were seeded at a concentration of 2 x 10^6 cells per 100 mm petri dish and allowed to adhere completely. Following this, the packaging, envelope and a desired transfer plasmid were mixed with FuGENE® HD transfection reagent (Promega, Southampton, UK) and 1X DMEM as per **Table 2.20**. This mixture was incubated at RT for 30 min and subsequently added to the media of producer HEK 293T cells after incubation with 25 ug/ml chloroquine for 1h. After 8 h incubation at 37 ^oC, the transfection media was replaced with standard culturing media (see **section 2.3.1**). Cells were incubated at 37 ^oC in a humidified 5 % CO_2 atmosphere for 48 h. After this time, the media, now containing newly synthesised lentiviral particles encapsulating the desired expression construct, was collected, cell debris pelleted by centrifugation (3,000 rpm for 5 min at RT), and the resulting supernatant filtered for contaminants through a 0.45 µm PVDF syringe filter (Elkay Laboratory Products (UK) Ltd, Basingstoke, UK). A second collection and purification of lentivirus was performed as above by centrifugation (3,000 rpm x 5 min, RT) and filtering through a 0.45 µm PVDF syringe filter after another 24 h incubation with standard culturing medium. Lentiviruses from either the first or second collections were used directly to transduce human skin fibroblast cells (see **section 2.1.2.1**), or frozen at -80 ^oC until future use.

Table 2.20. Reagents for transfection of 293T HEK cells with lentiviral components

Reagent	***Volume***
Transfer plasmid	Corresponding to 10 µg
Packaging plasmid (psPAX2)	Corresponding to 6.55 µg
Envelope plasmid (pMD2.G)	Corresponding to 3.5 µg
FuGENE	FUGENE: plasmid DNA ratio of 3:1 (60 µl)
1X DMEM	Adjusted to 1 ml

A.

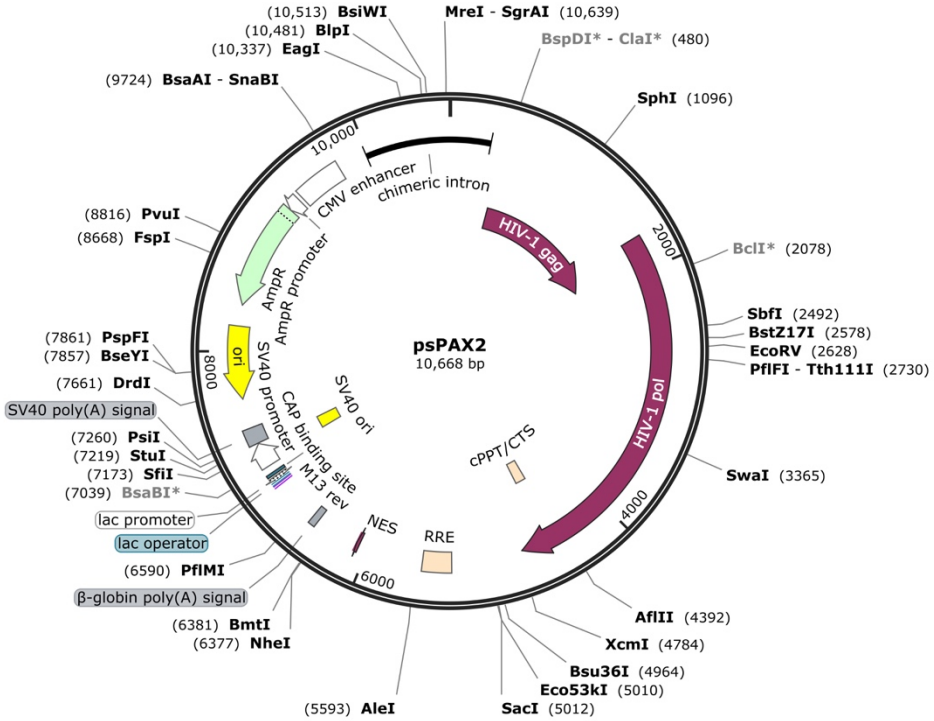

B.

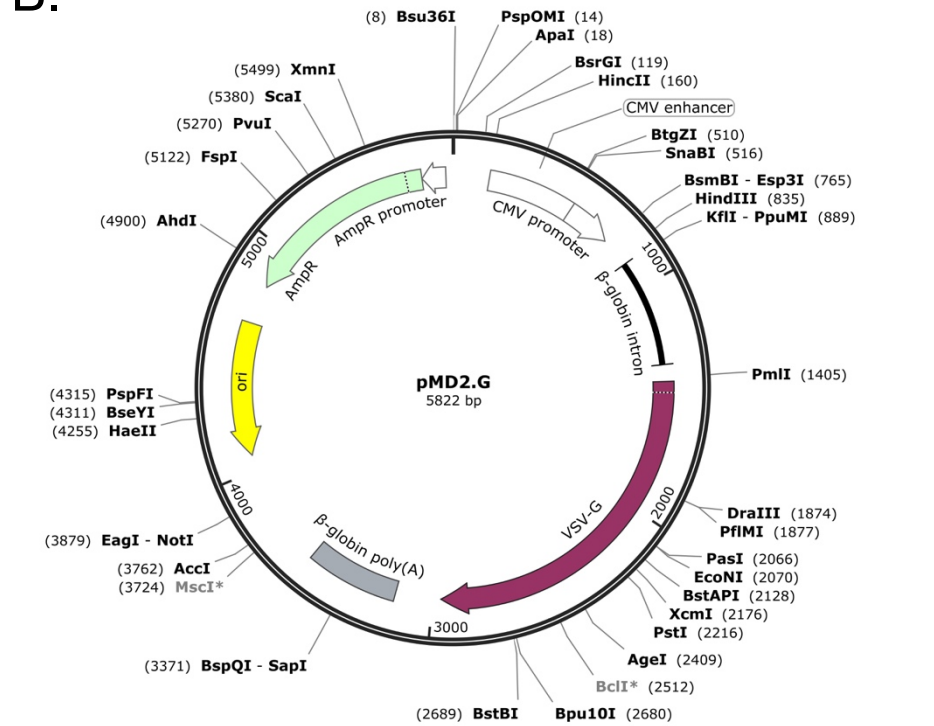

Figure 2.6 Packaging and envelope plasmids used for the second-generation lentiviral expression system.

(**A**) psPAX2 (Addgene ID: 12260) packaging plasmid encodes the polymerases/proteins necessary for synthesising pseudoviral capsids. (**B**) pMD2.G (Addgene ID: 12259) envelope plasmid encodes vesicular stomatitis virus GP (VSV-G) glycoproteins, allowing for effective transduction of a wide range of target cell types.

2.3.3 Cell Immortalisation

Primary cells have a finite replicative capability (Hayflick and Moorhead, 1961; Howard, 1996); therefore, patient and control human skin fibroblasts were immortalised by lentiviral transduction with the pLOX-*Ttag-iresTK* plasmid, obtained from Didier Trono (Tronolab; Addgene plasmid No: 12246), and performed as previously described (Salmon *et al.*, 2000). This retroviral construct allows for immortalisation of primary cells by expression of the replicative large T antigen (TAg) from Simian virus 40 (SV40) (Sompayrac and Danna, 1991; Cavender *et al.*, 1995), which induces malignant transformation of cells. Following transduction, cells underwent at least five passages to allow immortalised cells to overtake residual primary culture.

2.3.4 shRNA Knockdown

Gene silencing for *TMCO6* was achieved through short hairpin RNA (shRNA)-mediated RNA interference (RNAi), a means of targeted mRNA-degradation utilising the cell's RNA-induced silencing complex (RISC), followed by endogenous nuclease activation, as previously described (Moore *et al.*, 2010). In this work, four different short hairpin RNA (shRNA) variants specific for *TMCO6* mRNA, already cloned into the pLKO.1-Puro vector (Addgene ID: 8453, **Fig 2.7**), were purchased from the MISSION® TRC1 library (MISSION® shRNA Library, Sigma-Aldrich®). Plasmid vectors were delivered as bacterial glycerol stocks (*E. coli* in 1X Terrific Broth (TB) containing 100 μg/ml carbenicillin and 15 % glycerol) and vectors were purified using the QIAprep Spin Miniprep Kit (Catalogue number: 27104, Qiagen Ltd, Manchester, UK), as per manufacturer's instructions. Two relevant controls were used alongside these: 1) an empty vector (EV) control, the MISSION® pLKO.1-puro control vector (Catalogue Number: SHC001), encoding no shRNA sequence, and 2) a non-mammalian negative (-) control, the MISSION TurboGFP shRNA Control Vector (Catalogue Number SHC004), which encodes an shRNA sequence for Turbo green florescent protein (GFP), derived from crustacean *Pontellina plumata*.

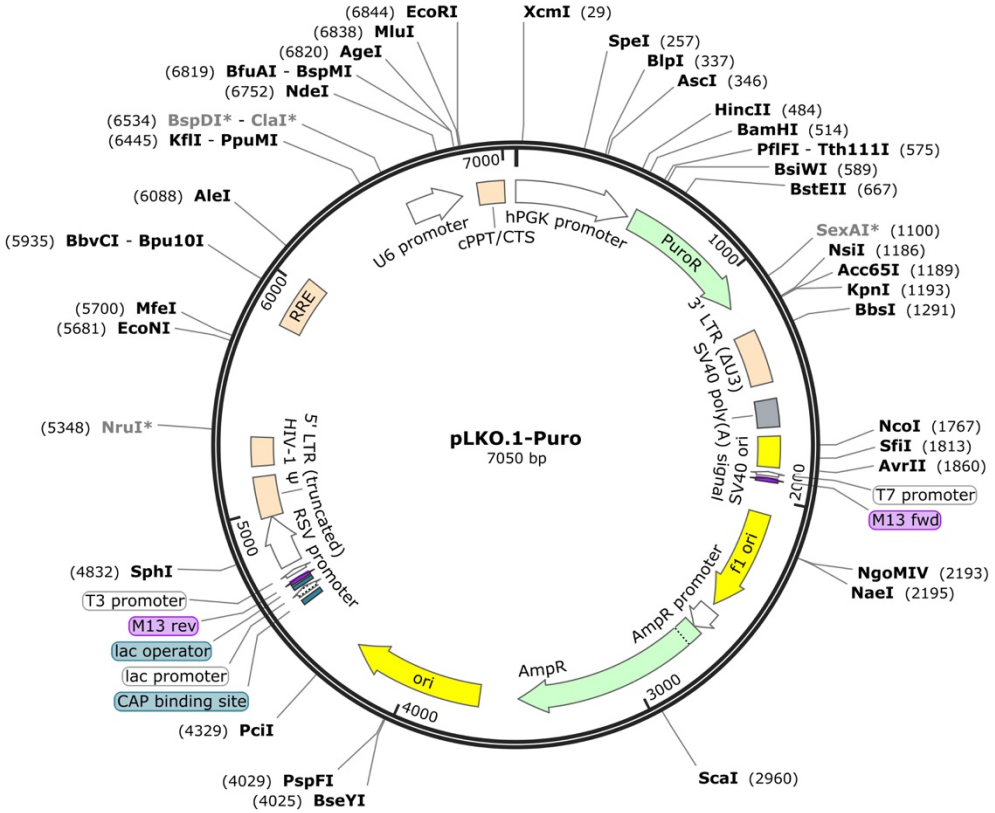

Figure 2.7 Vector for generation of shRNA-knockdown cell lines.

The pLKO.1-Puro 3rd generation lentiviral vector (Addgene ID: 8453) encodes Puro-resistance and ampicillin (Amp)-resistance genes, for selection in mammalian or bacterial systems, respectively, and encodes U6 and human phosphoglycerate kinase (hPGK) promoters, a central polypurine tract (cPPT) motif for increased transduction of non-dividing cells, and Psi RNA packaging signal. The vector includes a 3' self inactivating (SIN) long terminal repeat (LTR), 5' LTR, Rev response element (RRE) for lentiviral replication and three origins of replication.

Lentiviral particles were produced by lentiviral production (as per **section 2.3.2**) by co-transfection of 2 x 10^6 producer HEK 293T cells with psPAX2 packaging (**Fig. 2.6 A.**) and pMD2.G envelope (**Fig. 2.6 B.**) plasmids, but this time with a pLOX.1-Puro-based transfer vector (**Fig 2.7**) encoding one of the four TMCO6-specific or two control shRNA sequences (**Table 2.21**). Lentiviral transduction of HEK 293T cells using filtered lentivirus was performed as per **section 2.3.5,** and cells that had successfully taken up the lentiviral vectors were selected for by addition of 1 µg/ml puro to the standard culturing media for 24 h and continually thereafter.

Table 2.21. MISSION® shRNA sequences encoded within plasmid vector pLKO.1-Puro

Name	*Catalogue Number*	*Target*	*shRNA Sequence (5' → 3')*
EV	SHC001	-	-
-	SHC004	TurboGFP	CCG GCG TGA TCT TCA CCG ACA AGA TCT CGA GAT CTT GTC GGT GAA GAT CAC GTT TTT
shRNA-1	TRCN0000138674	Human TMCO6 Ex 10	CCG GGT ATC TAA CGT GGT GAG CGT ACT CGA GTA CGC TCA CCA CGT TAG ATA CTT TTT TG
shRNA-2	TRCN0000138522	Human TMCO6 Ex 9	CCG GCC TCA ACA ACC TCA CTG CAA ACT CGA GTT TGC AGT GAG GTT GTT GAG GTT TTT TG
shRNA-3	TRCN0000138363	Human TMCO6 3' UTR- Ex 12	CCG GCA CAC CTA AGC CAA GAC CTT TCT CGA GAA AGG TCT TGG CTT AGG TGT GTT TTT TG
shRNA-4	TRCN0000134999	Human TMCO6 Ex 10	CCG GCA AAC AGT CCT AGT TTC TGT ACT CGA GTA CAG AAA CTA GGA CTG TTT GTT TTT TG

2.3.5 Lentiviral Transduction for Constitutive Protein Overexpression

Constitutive protein overexpression in cultured cells was achieved by a second-generation lentiviral expression system for the COA7 patient and Control 1 immortalised skin fibroblasts. Cells were seeded at a density of 2 x 10^6 cells per 10 cm^3 petri dish and allowed to adhere for at least 24 h. Filtered lentiviral supernatant (see **section 2.3.2**) was mixed with 8 µg/µl polybrene (Sigma-Aldrich®), to increase the efficiency of transduction, and added to the target cell media for 24 h. Cells that had successfully taken up the lentiviral vectors were selected for by addition of 1 µg/ml puromycin or 100 µg/ml hygromycin B antibiotics to standard culturing medium (see **section 2.3.1**) for another 24 h, and continuously thereafter.

The cell lines generated in this manner are listed in **Table 2.22**.

Table 2.22. Constitutive protein-overexpressing cell lines

Cell Line Name	*Parental Cell Type*	*Overexpression Transfer Vector*
P1i-COA7^{WT}	Immortalised skin fibroblast	COA7^{WT}-pWPXLd-IRES-Puro^{R}
P1i-COA7^{HA}	Immortalised skin fibroblast	COA7^{HA}-HA-pWPXLd-IRES-Hygro^{R}
P1i-EV	Immortalised skin fibroblast	pWPXLd-IRES-Puro^{R}
P1i-EV^{Hygro}	Immortalised skin fibroblast	pWPXLd-IRES-Hygro^{R}
C1i-COA7^{WT}	Immortalised skin fibroblast	COA7^{WT}-pWPXLd-IRES-Puro^{R}
C1i-COA7^{HA}	Immortalised skin fibroblast	COA7^{HA}-pWPXLd-IRES-Hygro^{R}
C1i-EV	Immortalised skin fibroblast	pWPXLd-IRES-Puro^{R}
C1i-EV^{Hygro}	Immortalised skin fibroblast	pWPXLd-IRES-Hygro^{R}

2.3.6 Inducible Protein Overexpression

Tetracycline (Tet)-inducible overexpression of human *TMCO6* was accomplished using the Flp-In™ T-Rex™ Core Kit (Invitrogen™), which is a conditional recombination system that relies on the *Saccharomyses cerevisiae*-derived recombinase Flp (O'Gorman, Fox and Wahl, 1991). Flp-In™-293 cells (Invitrogen™) contain an integrated Flp recombination target (FRT) site that allows for locus-specific integration of a DNA sequence by Flp-mediated homologous recombination. Flp-In-293™ cells were co-transfected with pcDNA5/FRT/TO© genomic expression vectors (plasmid template shown in **Fig. 2.8 A.**), in which eight variants of *TMCO6* were cloned, and the non-integrating Flp-encoding plasmid, pOG44 (**Fig. 2.8 B.**).

TMCO6 has two predominant mRNA transcript isoforms that yield protein products, termed here as *TMCO6.1* (Ensembl Transcript ID: ENST00000394671.7, 493 aa product) and *TMCO6.2* (Ensembl Transcript ID: ENST00000252100.6, 499 aa product). It is unknown if one of these is expressed in a greater abundance, and whether there is tissue-specificity or separate functional roles for either translated isoform, so both were considered when overexpressing *TMCO6*. In addition to the two wildtype *TMCO6.1* and *TMCO6.2* isoforms, the human patient mutation, c.C271T, was introduced into either of these. These four *TMCO6* variants (*TMCO6.1-WT, TMCO6.1-R91C, TMCO6.2-WT* and *TMCO6.2-R91C*) were each C-terminally tagged with HA (see **section 2.2.9** for sequence) or separately, FLAG/STREP (FS) (peptide sequence: DYKDDDDK/WSHPQFEK), to generate 8 different *TMCO6* transgenes: *TMCO6.1-WT^{HA}, TMCO6.2-WT^{HA}, TMCO6.1-R91C^{HA}, TMCO6.2-R91C^{HA}, TMCO6.1-WT^{FS}, TMCO6.2-WT^{FS}, TMCO6.1-R91C^{FS},* and *TMCO6.2-R91C^{FS}*.

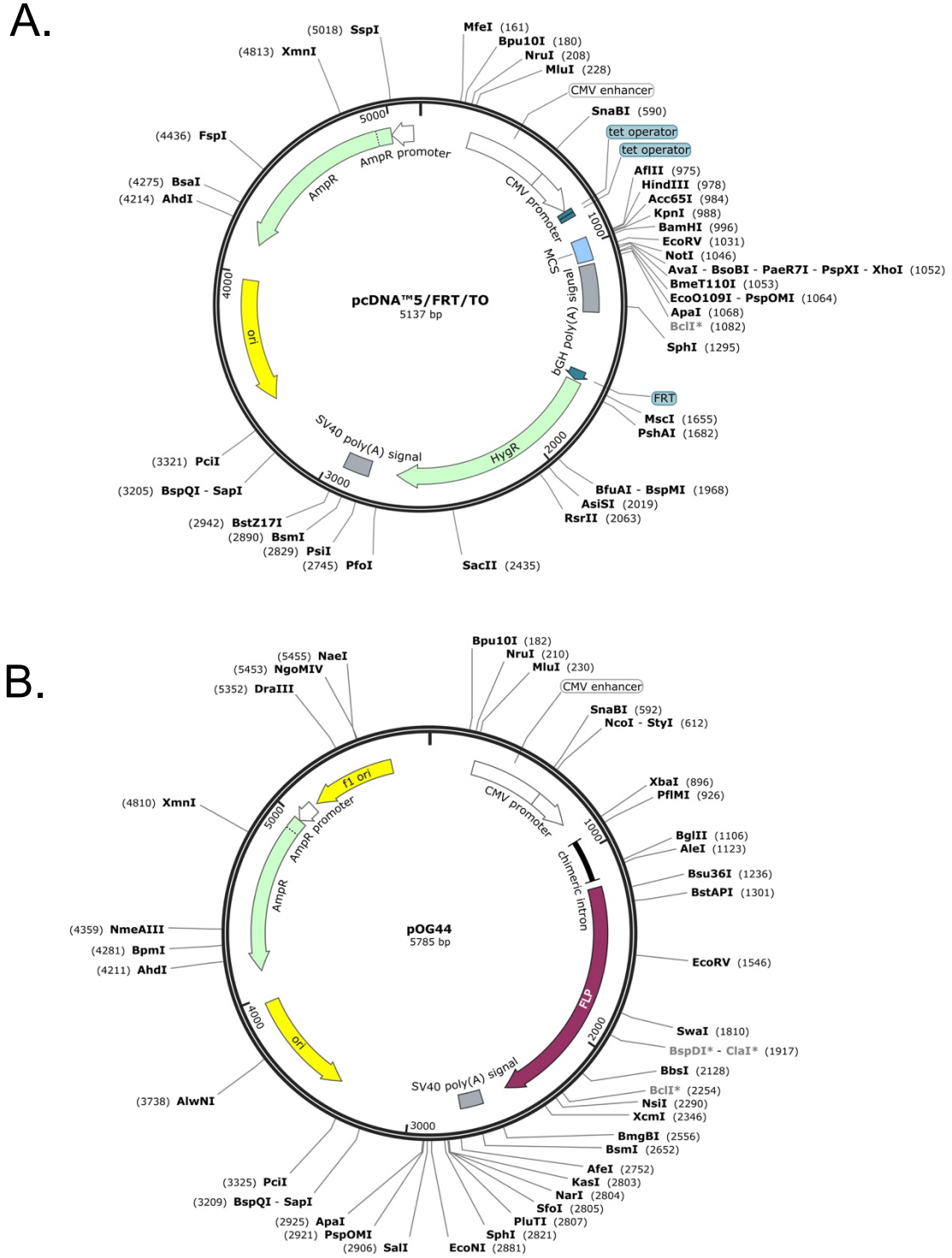

Figure 2.8 Genomic integration vector and Flp-encoding vector for Tet-inducible expression of proteins in mammalian cells.

(**A.**) pcDNA™5/FRT/TO® (Catalogue Number: V652020, Invitrogen™) contains a hybrid CMV/TetO2 inducible promoter, a multiple cloning site (MCS) with restriction sites for cloning a range of transgenic sequences of interest, a bGH polyA sequence, an FRT site for Flp-mediated integration into a Flp-In™ T-REx™ host cell line, an SV40 polyA sequence and finally, Amp^R and Hyg^R genes for antibiotic selection. (**B.**) pOG44 (Catalogue Number: V600520, Invitrogen™) encodes yeast-derived Flp recombinase, under control of a CMV promotor, with an SV40 polyA tail, and encodes the Amp^R gene.

These were ligated into HindIII and BamHI-digested pcDNA5/FRT/TO© vectors, using the T4 DNA ligase (New England Biosciences), as per manufacturer's instructions. Ligation (at 16 ºC O/N) in 1X T4 reaction buffer with 6 U/µl T4 ligase was achieved using a 1:3 (vector:insert) ratio, as directed, and was performed by Dr. Aurelio Reyes. The resulting plasmids were used to co-transfect 2 x 10^6 Flp-In™-293 cells using Lipofectamine 3000 reagent® (Life Technologies™, Thermo Fisher Scientific, UK), as per manufacturer's instructions. Each transgene was under the control of a Tet-inducible hybrid CMV promoter, so that transcription is only initiated in the presence of Tet or its derivative effector compound doxycycline (DOX), as previously described (Gossen *et al.*, 1995). Flp recombinase, expressed transiently by the pOG44 plasmid prior to antibiotic selection, mediates the insertion of the expression constructs above into the nuclear genome at the FRT site by homologous recombination. This insertion also interrupts the parental Flp-In™-293 cell's zeocin-resistance cassette and instead introduces hygro- and blasticidin (blast)-resistance genes. Cells correctly transfected were selected for with addition of 100 ug/ml hygromycin B and 1 µg/ml blasticidin S to the standard culturing media for 24 h and continuously thereafter.

2.4 Cellular Imaging

2.4.1 Live Cell Growth Assay

Cell growth was assessed by phase contrast light microscopy using an IncuCyte HD instrument (Essen Bioscience, UK). Cell density was determined by Countess II™ FL Cell counter (Life Technologies) and 2 x 10^4 cells per cell line were seeded in duplicate in a 6-well culturing plate (Corning® Costar®). Images were captured at 16 locations per well every 4 hours for 7 days, with duplicates averaged per time point. Growth curves were graphed using Prism 7.0 software.

2.4.2 Immunocytochemistry (ICC)

ICC analysis was used to demonstrate the presence and subcellular localisation of endogenous TMCO6. HeLa or 143B cells were counted as per **section 2.4.1** and approximately 2.5 x 10^4 cells seeded onto glass coverslips in separate wells of a 6-well culturing plate. Cells were incubated at 37 °C in 5 % humidified CO_2 for 24 h prior to cell fixation. Cells were given a preliminary wash with 2ml 1X DMEM. For visualisation of the mitochondrial network, MitoTracker™ Red CMXRos (Invitrogen™) was added to the culturing media at a final concentration of 80 nM and incubated for 20 min at 37 ºC. Cells were washed with 2 ml DMEM, and fixed with 1 ml 4 % weight/vol (w/v) paraformaldehyde (PFA) for 15 min at RT on a shaking platform, washed 3X with 2 ml PBS at RT for 5 min per wash, and permeabilised for 5 min at RT with permeabilization buffer (1X PBS with 0.3 % vol/vol Triton X-100 (Fisher Bioreagents, Fisher Scientific, Louborough, UK) and 5 % FBS). Coverslips were then washed 6X with 1 ml PBS over a 5 min period, followed by incubation with 1 ml primary Anti-TMCO6 (Catalogue Number: 20117-1-AP, Proteintech Group Inc, Rosemont, Illinois, USA) rabbit polyclonal antibody (1:500 dilution), diluted in 1X PBSS (1X PBS + 5 % FBS) for 2 h at RT. Coverslips were washed 6X with 2 ml PBSS for 5 min per wash, and then incubated with Alexa Fluor 647 goat anti-rabbit IgG secondary antibody (Catalogue Number: A21245, Invitrogen™) (1:200 dilution) for 1 h at 37 °C. Coverslips were washed 3X with 2 ml PBSS for 5 min per wash and then with 1X PBS for 5 min once at RT. Coverslips were mounted with 20 µl ProLong™ Diamond antifade mountant with 4',6-diamidino-2-phenylindole dihydrochloride (DAPI) (Invitrogen™) nuclear stain, and left to dry O/N at RT under an opaque cover. Images were acquired using the A1/A1R Confocal Microscope System (Nikon UK Ltd, Kingston upon Thames, UK) with a 63x 1.40 numerical aperture oil immersion objective by Dr. Aurelio Reyes. Images were post-processed using Fiji Image J software (Schindelin *et al.*, 2012).

2.4.3 Super-Resolution Microscopy

In order to determine COA7 intramitochondrial localisation, 5 x 10^4 HeLa cells constitutively overexpressing COA7-HA were seeded onto glass coverslips placed into individual wells of a 12-well culturing plate (Corning® Costar®) the day prior to fixation and sample preparation. Cells were fixed with 4 % w/v PFA in standard culturing media (see **section 2.3.1**) for 30 min at 37 ºC, washed 3X with 1 ml 1X PBS at RT and permeabilised with 1 ml permeabilization buffer (see **section 2.4.2**) for 5 min at RT. Permeabilised cells were washed again 3X with 1 ml PBS at RT, and subsequently immunostained with anti-TOM20, anti-Aconitase, anti-CO1 and anti-COA7 antibodies (see **section 2.6.4**), all at a dilution of 1:300 for 1 h at RT under an opaque cover. Respective secondary antibodies, Alexa Fluor 647 goat anti-rabbit IgG (Catalogue Number: A21245, Invitrogen™) or Alexa Fluor 488 goat anti-mouse IgG (Catalogue Number: A11029, Invitrogen™), were incubated also at a dilution of 1:300 for 1 h at RT. Coverslips were mounted with ProLong™ Diamond antifade mountant (Catalogue Number: P36965, Invitrogen™). Acquisition of 3D Z-stacks was performed using a Nikon N-SIM microscope with SR Apo TIRF 100x 1.49 N.A. objective. Images were acquired and then processed using Imaris 9.0 XT software by Dr. Cristiane Beninca (Microscope Facility Manager, MRC MBU, University of Cambridge, Cambridge, UK).

2.5 Animal Model and Associated Procedures

2.5.1 Genotyping of B6N(Cg)-Tmco6$^{tm1.1(KOMP)Vlcg}$/J Mice

Ear biopsies were routinely collected at the time of weaning for the dual purposes of individual identification and genotyping. Genomic DNA (gDNA) was extracted per biopsy using the Maxwell® 16 Tissue DNA Purification Kit and Maxwell® 16 (AS1000) instrument (Promega, UK), with the associated protocol for DNA purification from tissues. For knockout (*Tmco6*$^{-/-}$, KO) and heterozygous (*Tmco6*$^{+/-}$, HET) mice, the latter 441 base pairs (bp) of the ZEN-UB1 cassette (section **2.1.3**) and 55 bp of murine *TMCO6* exon 12 (in the 3' UTR region) were amplified by polymerase chain reaction (PCR) (see **section 2.2.3**) to produce a 496 base pair (bp) DNA fragment. For HET and wildtype (*Tmco6*$^{+/+}$, WT) mice, the entirety of *TMCO6* exons 3 and 4, as well as the interceding intronic sequence, were amplified to yield a 384 bp DNA fragment. Primers, conditions and reagents used are specified in **Tables 2.23-2.25**. PCR products were resolved by agarose gel electrophoresis (see **section 2.2.5**) for approximately 50 min at 90 volts (V), and the respective genotypes assigned to each animal.

Table 2.23. Primers for genotyping B6N(Cg)-*Tmco6*$^{tm1.1(KOMP)Vlcg}$/J mice

Primer	***Sequence 5' → 3'***
Wildtype F	CCT GTT CTG GGA TCC AGG T
Wildtype R	AGG TGA GGA GGT AGG AAG TCG
Mutant F	CGG TCG CTA CCA TTA CCA GT
Mutant R	CAA GTT GCT GAA GAG CAT GAA C

Table 2.24. Thermocycling conditions for genotyping B6N(Cg)-*Tmco6*$^{tm1.1(KOMP)Vlcg}$/J mice

Step	*Temp (°C)*	*Time*	
1	94	2 min	
2	94	20 sec	
3	65	15 sec	**Steps 2-4 X 10 cycles**
4	68	10 sec	
5	94	15 sec	
6	60	15 sec	**Steps 5-7 X 28 cycles**
7	72	10 sec	
8	72	2 min	
9	10	∞	

Table 2.25. Reagents for genotyping B6N(Cg)-*Tmco6*$^{tm1.1(KOMP)Vlcg}$/J mice

Reagent	*Volume (µl)*
GoGreen® Master Mix (5 x)	5
25 mM dNTPs (10 x)	2.5
DMSO (100 %)	1.25
F WT Primer (20 µM)	2
R WT Primer (20 µM)	2
DNA template (25 ng/µL)	2
dH_20	10
*GoTaq® DNA polymerase (5 u/µL)**	0.25
TOTAL:	**25**

2.5.2 Derivation of Mouse Embryonic Fibroblasts (MEFs)

MEFs were derived from females 11.5 to 12.5 days following detection of a post-copulation plug. The pregnant female was culled by cervical dislocation, the abdominal wall and uterus dissected, and whole embryonic sacs retrieved and placed into 4 ^{o}C phosphate buffered saline (PBS), lacking both Ca^{2+} and Mg^{2+} (Gibco®, Thermo Fisher Scientific Inc., UK).

All procedures from this point onwards were performed in a tissue culture hood using sterilized surgical tools and reagents. Individual embryos were removed from the surrounding yolk sac, transferred to separate wells of a 6-well culturing plate (Costar®, Corning®, USA) and submerged in 1 ml 4 ^{o}C PBS. Under 4X magnification (Nikon SMZ1000 light microscope, Nikon UK Ltd, UK), all viscera, limbs and tail were removed per embryo. Heads were isolated for gDNA extraction and genotyping (as per **section 2.5.1**). Remaining soft tissues were

minced into 1 - 2 mm pieces with scissors, transferred to a 15 ml Falcon tube (Sarstedt, Germany) containing 5ml sterile 4 ºC PBS, and pelleted for 5 min (300 x g) at room temperature (RT). A second wash was performed as above with 5ml sterile 4 ºC PBS (5 min, 300 x g, RT). The resulting pellet was resuspended in 1 ml digestion solution: 2 mg/ml collagenase type IV (Gibco®) in standard culturing medium (see **section 2.3.1**), supplemented with 25 µg/ml amphotericin B (Gibco®). Solutions were incubated in a 37 °C water bath (Grant Instruments, UK) for 60-90 min, until individual tissue pieces were no longer visible. Solutions were regularly mixed with a P1000 micropipette every 15-20 minutes. Cells were then washed with 5 ml 37 ºC PBS, pelleted for 5 min (300 x g at RT), diluted into a final volume of 15 ml MEF culturing medium (as per **section 2.3.1**). MEFs were transferred to individual 15 cm^3 Petri dishes (Corning®) and cultured at 37 ºC in a humidified atmosphere with 5 % CO_2.

2.5.3 Metabolic Monitoring via CLAMS

The Oxymax Comprehensive Lab Animal Monitoring System (CLAMS) (Columbus Instruments, Ohio, USA) allows for non-invasive and automated measurement of numerous metabolic and behavioural parameters including VO_2 (total volume of oxygen consumed, ml/Kg/hr), VCO_2 (total volume of carbon dioxide produced, ml/Kg/hr), locomotor activity in the *x*-, *y*- and *z*-planes (measured by infrared beam, with each break in the beam defined as a 'count') and total consumption of food and water (measured as accumulated change in mass (g) and volume (ml), respectively) over time. *Tmco6* KO mice and control littermates were placed into individual cages of the CLAMS with access to food and water *ad libitum*. Mice were monitored over a 36 h period composed of two 12 h night cycles and one 12 day cycle. Data per parameter were collected automatically every 10 min, averaged per animal and normalised to body weight, and analysed separately for day and night 12 h cycles.

2.5.4 Treadmill Exhaustion Trials

The LE8710 series treadmill (Panlab, Harvard Apparatus, Barcelona, Spain) was used to evaluate exercise capability and endurance (Castro and Kuang, 2017). Mice underwent acclimatisation for two consecutive days prior to testing. Each mouse was placed into individual, closed chambers on top of a treadmill conveyor belt, fixed at a 10 ° inclination angle, and forced to maintain a walking speed of 11 meters per minute (m/min) for 10 min. A motivational 'air puff' (LE8711 Air Puff Control, Panlab, Harvard Apparatus, Barcelona, Spain) was activated when mice made contact with a metal grid at the base of the treadmill belt, encouraging continuation of the task. For the test, mice were run at an initial speed of 11 m/min for 3 min, followed by continuous increase of 0.3 m/min to a maximum speed of 75 m/min or until exhaustion was reached. Exhaustion was defined as 10 'falls' onto the metal

grid within 1 minute, or continuous triggering of the air puff for more than 5 s (indicating failure to continue the task). Speed increase was controlled automatically by the accompanying SeDaCom 2.0 software. The distance in meters reached at exhaustion was recorded manually per animal. Upon test completion, mice were returned to their home cages for a minimum of 24 h before any further experiments were conducted.

2.5.5 Rotarod Test

A well-established motor performance test using a rotarod apparatus (Model 46700, Ugo Basile®, Varese, Italy) was performed to assess neuromuscular coordination and balance (Ingram and Reynolds, 1986). Acclimatisation was performed for two consecutive days prior to testing. Mice were placed into individual segments on a suspended, cylindrical treadmill rod for 5 min statically, and then forced to maintain a walking speed of 10 rpm/min for 5 min. If a mouse fell from the rod, or faced oppositely to the intended direction of travel, they were orientated correctly to continue the adaptation until completion. For the test, three separate trials were run per animal with gradual acceleration in speed from 2 to 40 rpm over 5 min. The latency to fall (s) was recorded manually per animal for each of the three trials, and an average of these was used in subsequent analyses. Mice were returned to their home cage between trials for 30 min minimum, with unrestricted access to food and water. Upon test completion, mice were returned to their home cages for at least 24 h before any further experiments were conducted.

2.5.6 Hindlimb Clasping Evaluation

Hindlimb clasping is commonly observed in murine models of neurodegenerative disease (Guyenet *et al.*, 2010) and can be used to mark neurological symptom progression with age. Mice were suspended in the air by the base of the tail facing downwards for 10 s with the ventral side of the animal visible to the observer. A normal response was classified as hindlimbs remaining outstretched and away from the abdomen, and a positive pathological response was defined as both hindlimbs retracting fully towards the abdomen for a continuous period of 5 s or longer.

2.5.7 Pole Test

The pole test assesses motor agility and bradykinesia (Rial *et al.*, 2014), the impaired ability to move the body or limbs in a coordinated manner on command. Mice were placed head-upward on the top of a vertical rough-surfaced pole (diameter: 10 mm; height: 50 cm). The

base of the pole was positioned within the home cage, and mice were tasked to orientate themselves downwards and descended the pole completely. Three acclimatisation trials were conducted the day prior to testing by placing the mouse head-downward at the top of the pole. The total time (in seconds) taken to orientate downward and descend the pole was recorded for three separate tests per animal, and an average of these was used in subsequent analyses. Videos were taken per animal and are available upon request.

2.5.8 Micro-Echocardiography

Cardiovascular function and physiology were evaluated by echocardiography using the Vevo 770® High Resolution Imaging System (VisualSonics, Inc., Toronto, Canada) and a 30 MHz RMV 707B transducer scanhead. Mice were anaesthetised non-invasively in an induction chamber with 5 % vol isoflurane gas mixed in 100 % O_2, and then secured in a supine position with limbs outstretched on a heated VEVO mouse handling platform under constant 2 % vol isoflurane gas. A temperature probe was inserted rectally to monitor body temperature. Heart rate (HR) was recorded continuously by electrocardiogram (ECG) contact pads connected to each paw (see **Fig. 2.9 D.** for a representative trace). The chest hair of each mouse was removed with an electrical razor followed by depilatory cream, and ultrasound gel was then applied. A standardized protocol was followed by Stephen Moore (Research Assistant, Nick Morrell Laboratory, University of Cambridge, UK) to systematically image and measure various parameters from parasternal short axis (**Fig 2.9 A.**) and long axis (**Fig 2.9 B.)** views, and an apical four-chamber view (**Fig 2.9 C.**) in the pulsed-wave (PW) doppler or motion (M) modes, as previously described (Gao *et al.*, 2011). Mice were then cleaned of any gel or residual tape, woken up with exposure to ambient air in a recovery cage, and returned to their home cages. Aortic ejection time (AET) (ms), left ventricle (LV) myocardial performance index (MPI), mitral valve (MV) atrial (A) and early (E) peak wave flows (mm/s), MV E/A peak ratio, right ventricular outflow tract (RVOT) mean velocity (VTI) (mm/s), RVOT pressure gradient (mmHg), cardiac output (CO) (ml/min), ejection fraction (EF) (%), fraction shortening (FS) (%), HR (bpm), stroke volume (SV) (µl), and volumes expelled in diastole and systole (V;d, V;s) (µl) were calculated by the Vevo LAB and Auto LV Analysis software packages (VisualSonics). The formulas used to calculate each of the above parameters are accessible from: https://mbi-ctac.sites.medinfo.ufl.edu/files/2017/02/Vevo-770-Protocol-Based-Measurements-and-Calculations-Rev-2-0.pdf).

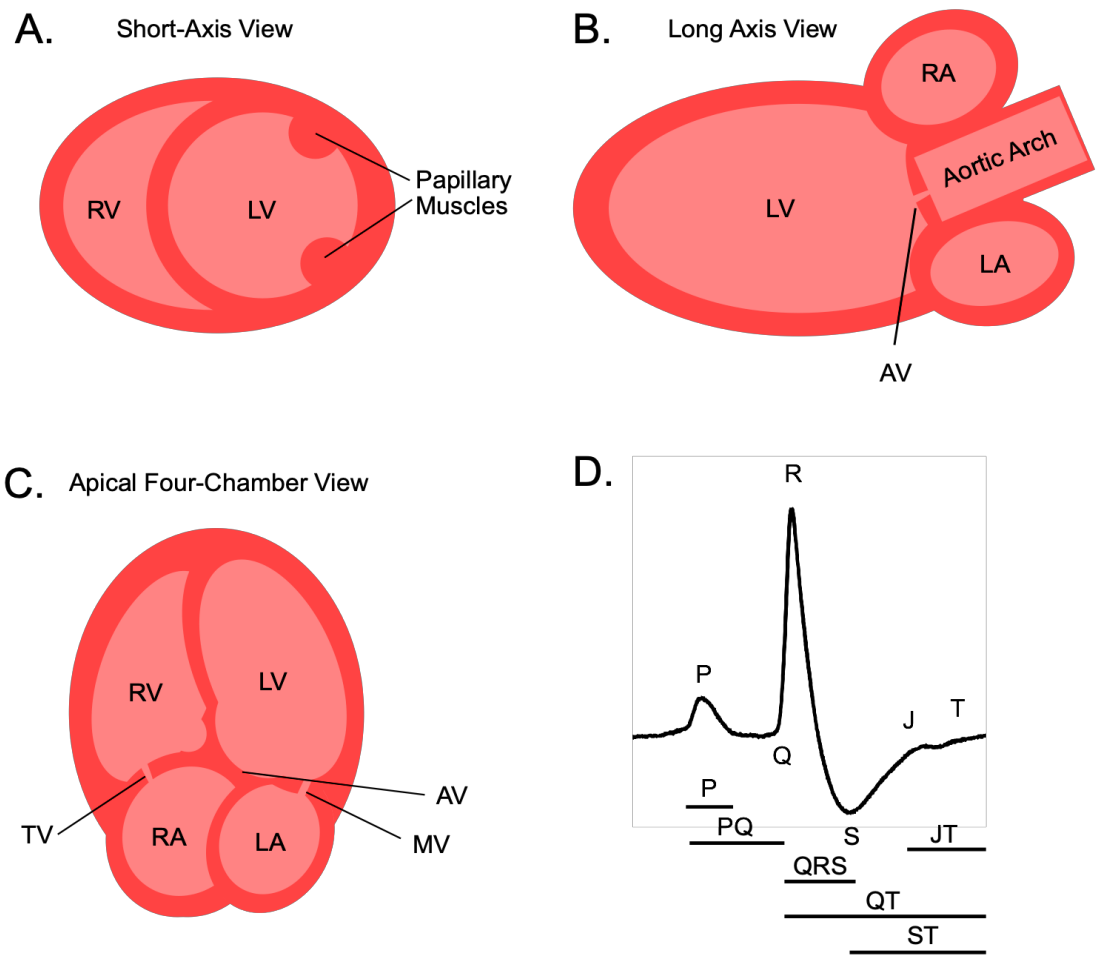

Figure 2.9. Views used for micro-echocardiography and a representative ECG trace.

Echocardiography was performed using the Vevo 770® High Resolution Imaging System (VisualSonics, Inc., Toronto, Canada) and a 30 MHz RMV 707B transducer scanhead. Imaging was performed on 3- to 12-month old mice, as previously described (Gao *et al.*, 2011), to obtain parasternal (**A.**) short axis and (**B.**) long axis views, as well as an (**C.**) apical four-chamber view, per animal. AV = aortic valve, LA = left atrium, LV = left ventricle, MV = mitral valve, RA = right atrium, RV = right ventricle, and TV = tricuspid valve. (**D.**) A representative wildtype murine ECG trace for the C57Bl/6J strain shows each discrete segment of a heart beat starting with the P wave, indicating atrial depolarization and contraction, followed by the QRS complex, correlating with depolarisation of the ventricles and ventricular contraction, the J-point at which ventricular depolarisation finishes, and finally, the T wave, which marks ventricular repolarisation. The time intervals between any of these events is denoted by the corresponding letters, as specified below the trace; abnormal interval values are readily used as an indicator of pathology.

2.5.9 Preparation of Murine Tissues for Histological & Histochemical Analyses

Preparation of tissues and subsequent anatomical, histological and histochemical analyses were performed primarily by Raffaele Cerutti, with assistance by Dr. Aurelio Reyes.

2.5.9.1 Tissue Preparation and Processing for Skeletal Muscle

All histological and histochemical studies for skeletal muscle samples were performed on murine gastrocnemius muscles, snap-frozen by immersion in isopentane that had been cooled with liquid nitrogen. Samples were stored at -80 ^{o}C until use. For preparation of sections, each sample was mounted onto a specimen disk with optimal cutting temperature compound, and sectioned at to 8 µm thickness with a cryostat at -20 ^{o}C. Sections were then subjected to one of four histological methods, as detailed below.

2.5.9.1.1 Haematoxylin and Eosin (H&E)

H&E staining is the most common histological method that shows overall structure of a tissue in relation to its composite fibres, the intracellular distribution of nuclei, and the presence of fibrous and adipose cells, inflammatory cells and vacuoles, or vascular and neural components. Nuclei are stained blue, muscle fibres pink and the connective tissues a lighter pink. Sections were placed in Mayer's haematoxylin for 5 min, rinsed with tap water for 3 min, and then placed in 1 % eosin-Y solution for 15 secs. Sections were briefly washed with tap water, and then dehydrated with a series of ascending alcohol concentrations (70 – 100 %). Finally, stained sections were cleared in xylene and mounted with dibutylphthalate polystyrene xylene (DPX), a synthetic non-aqueous mountant.

2.5.9.1.2 Nicotinamide Adenine Dinucleotide-Tetrazolium Reductase (NADH-TR)

For the study of NADH reductase activity in sectioned skeletal muscle samples, nitroblue tetrazolium (NBT) was used as an electron acceptor, which produces a deep blue final colour at the site of enzymatic activity. The intensity of the signal produced by the NBT histochemical reaction is a reflection of the number of NADH-metabolising mitochondria within a fibre. This produces a characteristic checkboard pattern of fibre types. It is important to note that the sarcoplasmic reticulum is also stained during this process. Sections were incubated in a damp atmosphere for 1 h at 37 ^{o}C in 10 ml of NADH-TR incubation medium (1 mg/ml NADH and 1 mg/ml NBT in 200 mM Tris-HCl buffer (pH = 7.4)). Sections were then briefly rinsed in tap water, dehydrated with a series of ascending alcohol concentrations, and finally, cleared with xylene and mounted with DPX.

2.5.9.1.3 Succinate Dehydrogenase (SDH)

SDH histochemistry was also performed with NBT as an electron acceptor. Sections were incubated in a damp atmosphere for 30 min at 37 ºC in 5 ml of SDH incubation medium (35.2 mg/ml succinate, 1.22 mg/ml NBT, 61 µg/ml PMS and 65 µg/ml sodium azide in 100 mM sodium phosphate buffer (pH = 7.0)). Sections were briefly rinsed in tap water, dehydrated with a series of ascending alcohol concentrations, and finally, cleared with xylene and mounted with DPX.

2.5.9.1.4 Cytochrome c Oxidase (COX)

For the histochemical evaluation of COX activity, diaminobenzidine (DAB) was used as an electron acceptor to produce a brown end product for visualisation. The COX histochemical reaction reveals differences in mitochondrial number and their relative distribution in different fibre types as well as demonstrates whether certain fibres are devoid of COX activity. Sections were incubated in a damp atmosphere for 40 min at 37 ºC in COX incubation medium (5 µM DAB and 100 µM cytochrome *c* in 100 mM sodium phosphate buffer (pH = 7.4)). Sections were rinsed in tap water, dehydrated with a series of ascending alcohol concentrations, cleared with xylene and mounted with DPX.

2.5.9.2 Tissue Preparation and Processing for Brain, Heart, Liver, and Kidney

Formaldehyde, in the form of 10 % neutral buffered formalin (NBF), is the most common fixative for the majority of histopathological analyses. Formalin stabilizes cell structures by introducing covalent crosslinks between proteins. In this work, mice were anesthetised by intraperitoneal injection of Euthasol® (390 mg/ml pentobarbital and 50 mg/ml sodium phenytoin) (Esteve, Barcelona, Spain). Perfusion was performed through the circulatory system. Each mouse was first exsanguinated with phosphate-buffered saline (PBS) and then perfused with NBF. The tissues were then dissected and further fixed in NBF for at least 48 hours. Hearts from non-perfused mice were excised and fixed by long-term immersion in NBF.

Tissues were processed with a Leica ASP300S Tissue Processor using either the “Small” (**Table 2.26**) or “Biopsy” (**Table 2.27**) protocols and infiltrated with Tissue Infiltration Medium paraffin (Leica). All sections were cut on a Leica RM2245 semi-automated rotary microtome to a thickness of 4 µm. After drying, the sections were stained with H&E, picrosirus red or Pathogreen, or were subjected to immunohistochemistry as detailed below.

Table 2.26. Small Protocol for the Leica ASP300S Tissue Processor

Station	*Solution*	*Duration*	*Temperature*	*Pressure/vacuum*
1	70 % ethanol	30 min	RT	yes
2	80 % ethanol	30 min	RT	yes
3	95 % ethanol	30 min	RT	yes
4	95 % ethanol	30 min	RT	yes
5	100 % ethanol	30 min	RT	yes
6	100 % ethanol	30 min	RT	yes
7	100 % ethanol	30 min	RT	yes
8	Xylene	30 min	RT	yes
9	Xylene	1 h	RT	yes
10	Paraffin	30 min	60 °C	yes
11	Paraffin	30 min	60 °C	yes
12	Paraffin	1 h	60 °C	yes

Table 2.27. Biopsy Protocol for the Leica ASP300S Tissue Processor

Station	*Solution*	*Duration*	*Temperature*	*Pressure/Vacuum*
1	70 % ethanol	10 min	RT	no
2	80 % ethanol	15 min	RT	no
2	95 % ethanol	15 min	RT	no
4	95 % ethanol	15 min	RT	no
5	100 % ethanol	15 min	RT	no
6	100 % ethanol	15 min	RT	no
7	Xylene	10 min	RT	no
8	Xylene	10 min	RT	no
9	Xylene	10 min	RT	no
10	Paraffin	15 min	60 °C	yes
11	Paraffin	15 min	60 °C	yes
12	Paraffin	15 min	60 °C	yes

2.5.9.2.1 Haematoxylin and Eosin (H&E) Staining

Sections were deparaffinized, hydrated, placed in Mayer's haematoxylin for 15 min, rinsed with tap water for 3 min, and then placed in 1 % eosin-Y solution for 35 s. Sections were briefly washed with tap water, dehydrated with a series of ascending alcohol concentrations, cleared in xylene and mounted with DPX.

2.5.9.2.2 Picrosirius Red Staining

Sirius red F3B (C.I. 35780) is a strong anionic dye that stains collagen by reacting with basic groups present in the collagen molecule (Junqueira, Bignolas and Brentani, 1979). A solution in picric acid provides red staining of collagen and a yellow background. Sections were incubated with 0.1 % Sirius red F3B in a saturated solution of picric acid for 1 h at room temperature. Sections were then washed with 0.5 % acetic acid, dehydrated, cleared and mounted with DPX.

2.5.9.2.3 Pathogreen Staining

Pathogreen stain™ (Catalogue Number: 80027, Biotium) is an anionic green histofluorescent dye that stains degenerating neurons by an unknown mechanism similarly to Fluoro-Jade® (Schmued and Hopkins, 2000). Paraffin sections were de-waxed and hydrated. Slides were incubated in a 0.06 % potassium permanganate solution for 10 min, rinsed twice with distilled water and further incubated in distilled water for 2 min. Slides were then incubated for 10 min in 1X Pathogreen™ staining solution (1:1000 stock in 0.1 % acetic acid), rinsed three times for 1 min each with distilled water and then air-dried on a slide warmer at 50-60 ^{o}C for at least 5 min. Finally, sections were cleared in xylene and mounted with DPX.

2.5.9.2.4 Immunohistochemistry (IHC)

IHC is an antibody-based method that allows for visualisation of the specific distribution and localization of biomarkers and differentially expressed proteins in different parts of a tissue section. There are numerous IHC techniques that can be used to localize and demonstrate tissue antigens. The polymer chain two-step indirect method was employed here (Novolink™ Polymer Detection System, Leica Biosystems) for unconjugated primary antibodies against GFAP (Sigma-Aldrich 1:1000), ubiquitin (Abcam 1:5000), CD68 (Abcam 1:100), CNPase (Sigma-Aldrich 1:1000), cleaved caspase 3 (Cell Signaling 1:200), and Ki-67 (Cell Signaling 1:400).

2.5.10 Adeno-Associated Virus (AAV) Transduction

Systemic delivery of recombinant AAV serotype 9 (AAV9) vectors in adult mice was achieved by tail-vein intravenous injection to produce robust, long-term expression of either 1) the human wild-type *TMCO6* cDNA sequence (NM_018502) (AAV WT), or 2) the human patient homozygous recessive variant (NM_018502: c.271C>T) (AAV MUT), both with a downstream HA epitope tag (see **section 2.2.9** for the peptide sequence). Two vectors, AAV2-HSA-TMCO6-cDNA-HA and AAV2-HSA-TMCO6_MUT-cDNA-HA (**Fig. 10**), were kindly generated and provided by Dr. Aurelio Reyes (Senior Investigator Scientist, Mitochondrial Medicine Laboratory, MRC MBU, University of Cambridge, UK). AAV9 particles were synthesized by the AAV Vector Core of the Telethon Institute of Genetics and Medicine (TIGEM, Naples, Italy) and suspended in storage buffer (1X PBS with 350 mM NaCl + 5 % *D*-Sorbitol (both from Sigma-Aldrich®, UK)) until use. A titre of 4.5 x 10^{11} genome copies was administered by tail-vein intravenous injection by Dr. Carlo Viscomi (Senior Investigator Scientist, Mitochondrial Medicine Laboratory, MRC MBU, University of Cambridge, UK) to weaned KO or WT mice at 5-8 weeks of age. Mice were immobilised, and blanching of the tail-vein was used to verify successful injection. This process led to the creation of 4 distinct transgenic groups: $Tmco6^{-/-\,(AAV\ WT)}$, $Tmco6^{-/-\,(AAV\ MUT)}$, $Tmco6^{+/+\,(AAV\ WT)}$, and $Tmco6^{+/+\,(AAV\ MUT)}$. Mice were culled and tissues collected as per **section 2.5.9** at 3 months of age.

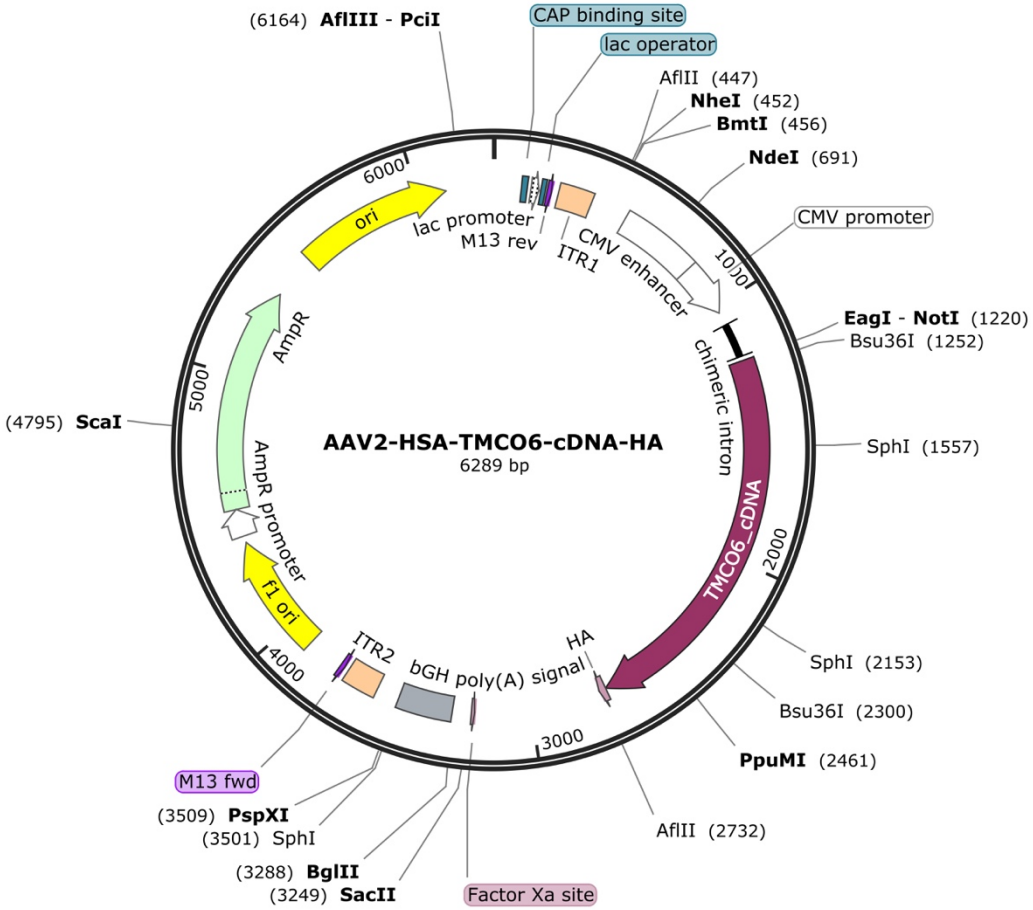

Figure 2.10 Plasmid used for recombinant AAV9 injection in adult mice.

pAAV-HSA-TMCO6-cDNA-HA (AAV WT) or a mutant variant form, pAAV2-HSA-TMCO6pat-cDNA-HA (AAV MUT), were used for systemic delivery of 4.5 x 10^{11} genome copies of either recombinant AAV9 variant to weaned KO (TMCO6$^{-/-}$, *n* = 4 per group) and WT (TMCO6$^{+/+}$, *n* = 3 per group) mice, aged 5-8 weeks. Each plasmid contains a 3' poly-adenosine (poly A) tail from bovine growth hormone (bGH), flanked by AAV2-derived inverted terminal repeats (ITRs), and is under the control of a hybrid cytomegalovirus (CMV) and *lac z* promoter.

2.6 Protein-Based Techniques

2.6.1 Determining Protein Concentration

Protein concentrations for whole cell lysates were estimated by NanoDrop™ 8000 Spectrophotometer (λ = 280 nm) and for those derived from murine tissues, a modified version of the Lowry protein assay, the DC™ Protein Assay (Bio-Rad), was used. The absorbance of the protein samples with unknown concentration and of seven BSA standards in a concentration range from 0 to 2 mg/ml were measured at λ= 750 nm with a SpectraMax Plus384 plate reader (Molecular Devices, Sunnyvale, CA, USA). The absorbances were plotted against the concentrations of the known standards, and the resulting calibration curve used to extrapolate the unknown protein concentrations by use of their absorbance values.

2.6.2 Sodium Dodecyl Sulfate Polyacrylamide Gel Electrophoresis (SDS-PAGE)

2.6.2.1 Sample Preparation: Whole Cell Lysates from Cultured Cells

Cultured cells (≥ 2 x 10^6 cells) were harvested by trypsinisation (Trypsin-0.5 % EDTA) in a sterile culture hood, washed twice with PBS and pelleted by centrifugation at RT (300 g x 5 min). Cell pellets were lysed with 2 % n-dodecyl-β-D-maltoside (DDM) in 4 ºC PBS containing 1X cOmplete™ mini EDTA-free Protease Inhibitor Cocktail (Roche, UK). Lysates were mixed by continuous rotation at 4 ºC for 15 min using an PTR-35 orbital shaker (Grant Bio™, UK) and then centrifuged (20,000 x g for 20 min at 4 ºC). Supernatants, containing solubilised cellular proteins, were transferred to sterile 1.5 ml Eppendorf tubes and protein concentration determined (see **section 2.6.1**). Samples were stored at -20 ºC until use.

2.6.2.2 Sample Preparation: Homogenates from Frozen Murine Tissues

Frozen murine tissues were weighed and ~50 mg pieces cut finely with a scalpel. Tissue pieces were suspended in 10 volumes cold organ lysis buffer (pH = 7.4, **Table 2.28**) and homogenised by the gentleMACS™ Dissociator (Miltenyi Biotec, Bergisch Gladbach, Germany) with the recommended setting per tissue type. Following this, a 'soft spin' at (500 g for 5 min at 4 ºC) was performed to remove extracellular fibrous debris. Supernatants were transferred to sterile 1.5 ml Eppendorf tubes and protein concentration determined (see **section 2.6.1**). Samples were stored at -80 ºC until use.

Table 2.28. Organ lysis buffer for murine tissue homogenate preparation

Reagent	Final concentration
0.5 M HEPES, pH = 7.4	50 mM
10 % Triton X-100	1 %
100 mM sodium orthovanadate ($Na_3VO_4 \cdot 2H_2O$)	10 mM
1M sodium fluoride (NaF)	100 mM
0.5 M EDTA	10 mM
20 % SDS	0.1 %
5M sodium chloride (NaCl)	50 mM
200 mM PMSF	2m M
1 tablet PhosSTOP™ phosphatase inhibitor (Roche)	1X

2.6.2.3 Running SDS-PAGE

Cell-derived protein lysates (10 – 40 µg) were mixed with an equal volume of 2X Laemmli Loading Dye (100 mM Tris-HCl (pH = 6.8), 2 % w/v SDS, 20 % w/v glycerol, 10 % w/v β-mercaptoethanol, and 100 µg/ml bromophenol blue (all from Sigma-Aldrich®)), and incubated for 5 min at RT. Tissue-derived homogenates (5 – 10 µg) were mixed with 10 X NuPAGE™ sample reducing agent and 4X NuPAGE™ LDS sample buffer (Invitrogen™), and incubated for 10 min at 70 °C. Both cell- and tissue- derived protein samples were separated under denaturing conditions by SDS-PAGE using either 12 % or 4-12 % gradient precast polyacrylamide NuPAGE® Bis-Tris gels (Invitrogen™). NuPAGE® MOPS SDS Running Buffer (1X: 50 mM MOPS, 50 mM Tris Base, 0.1 % SDS, 1 mM EDTA, pH 7.7) was used for separation of proteins >20 kDa in size; NuPAGE® MES SDS Running Buffer (1X: 50 mM MES, 50 mM Tris Base, 0.1 % SDS, 1 mM EDTA, pH 7.3) was used for the separation of proteins ≤ 20 kDa in size (both from Invitrogen™). In all cases, gels were run at 120V for 1-2 h at RT, with 10 µl Precision Plus Protein™ All Blue Standard (Bio-Rad, UK) for size comparison.

2.6.3 Blue Native Gel Electrophoresis (BN-PAGE)

BNGE uses a mild non-ionic detergent to solubilise proteins and intact protein complexes embedded within biological membranes (Wittig, Braun and Schägger, 2006). In this work, mitochondrial respiratory complexes were analysed from mitoplasts from freshly harvested cultured cells or snap-frozen murine tissues.

2.6.3.1 Sample Preparation: Mitoplasts from Cultured Cells

Plasma membranes of cultured cells were permeabilised with 8 mg/ml digitonin (DIG) for 10 minutes at 4 °C. Cytosolic proteins were removed by two cycles of 1 ml PBS washes and

centrifugation (10,000 x g for 5 min at 4ºC). Proteins embedded within the mitochondrial IM were suspended in 50 mM Bis-Tris-HCl (pH = 7.0) and 1.5 M aminocaproic acid, and solubilised with 1 % DIG or 2 % DDM in PBS, as previously described (Calvaruso, Smeitink and Nijtmans, 2008). Finally, membrane fragments and non-soluble material were pelleted by centrifugation (18,000 x g for 30 min at 4ºC) and discarded. Supernatants were either prepared immediately or stored at -80 ºC.

2.6.3.2 Sample Preparation: Mitoplasts from Frozen Murine Tissues

Frozen murine tissue (~ 50 mg) were homogenised in 10 volumes of Medium A (320 mM sucrose, 1mM EDTA, 10mM Tris-Hcl, pH 7.4) in a 5 ml Dounce-type glass homogeniser using a manually-driven glass or Teflon pestle, 5-15 strokes depending on the tissue type. The homogenates were centrifuged (800 x g for 5 minutes at 4 ºC) to remove nuclei and extracellular debris. The supernatant was collected and centrifuged at higher speed (9,000 x g for 10 min at 4 ºC) to obtain mitochondria-enriched pellets, which were resuspended in equivalent volumes of Medium A. Protein concentration was determined per sample (see **section 2.6.1**) and mitochondria were pelleted again (9,000 x g for 5 minutes at 4 ºC.), followed by resuspension in volumes of 1.5 M aminocaproic acid and 50 mM Bis-Tris/HCl (pH = 7) to obtain a final protein concentration of 10 mg/ml. Samples were solubilised with 1.6 mg of DDM or 4 mg of DIG per mg of protein, incubated on ice for 5 mis, and centrifuged (18,000 x g for 30 min at 4 ºC). Supernatants were either prepared immediately or stored at -80 ºC.

2.6.3.3 First (1D) and Second (2D) Dimension BN-PAGE

Supernatants from solubilised mitoplasts were mixed with sample buffer (750 mM aminocaproic acid, 50 mM Bis-Tris, 0.5 mM EDTA, and 5 % Coomassie® G 250 (Serva, UK)) to generate BN-PAGE samples. These samples were resolved by 3-12 % gradient Novex® NativePAGE gels (Invitrogen™), run for 1 h at 150 V in Cathode Buffer A (50 mM tricine, 15 mM Bis-Tris (pH = 7.0), and 0.02 % Coomassie® G 250), and further run for 1-2 h at 200 V (~8mA) in Cathode Buffer B (50 mM Tricine, 15 mM Bis-Tris (pH = 7.0), and 0.002 % Coomassie® G 250). In the case of 1D BN-PAGE, after the run, samples were electro-transferred to methanol-activated PVDF membranes and immunoblotted (as described in **sections 2.6.4** and **2.6.5**). For 2D BN-PAGE, individual lanes were cut using a scalpel and incubated with denaturing solution (1 % β-mercaptoethanol and 1 % SDS) for 1 h at RT. Treated lanes were inserted into individual 1.0 mm x 1D wells of 4-12 % gradient NuPage® gels (Invitrogen™) and resolved in the second dimension by SDS-PAGE (see **section 2.6.2.3)**.

2.6.4 Western Blotting

Proteins separated by SDS-PAGE, 1D-BNGE and 2D-BNGE were electroblotted to methanol-activated polyvinyl difluoride (PVDF) membranes via wet electrotransfer: 100 V for 1 h at 4 ^{o}C. Electrotransfer of SDS-PAGE gels (pre-cast and from the NuPAGE range (Invitrogen™)), including 2D-BNGE gels, was performed using 1X Tris-Glycine Transfer Buffer (50 ml 20X Tris-Glycine stock buffer (30.3 g Tris, 114.2 g Glycine), 200 ml Methanol, 1.25 ml 20 % SDS and filled to 1 L with dH20) and the Mini-PROTEAN® Tetra Cell system (Mini Trans-Blot® Module, Bio-Rad, UK). 1D BNGE gels (pre-cast and from the NativePAGE range (Invitrogen™)) were electro-transferred using 1X bicarbonate transfer buffer (10 mM $NaHCO_3$ and 3 mM $NaCO_3$).

2.6.5 Immunodetection

Membranes were blocked with 5 % milk in PBS-0.1 % Tween® 20 (NBS Biologicals, UK) (PBST) for 1 h, washed three times with PBST (for 10 min, 5 min and 5 min intervals, respectively) and immobilised proteins were immunodetected by primary antibodies (full list in **Table 2.29**). Each antibody was diluted in 3 % BSA, and incubated O/N at 4 ^{o}C. Membranes were washed as above and secondary antibody detection of the primary antibody was performed using anti-mouse (Catalogue Number: W4021, Promega), anti-rabbit (Catalogue Number: W4011, Promega) or anti-rat antisera (Catalogue number SC-2006, Santa Cruz Biotechnology Inc., Dallas, Texas, USA), as appropriate, with each conjugated to the enzyme horseradish peroxidase (HRP) and diluted 1:2,000 in 0.1 % milk. Membranes were washed three times with PBST (for 10 min, 5 min and 5 min intervals, respectively) and Amersham ECL Western Blotting Detection Reagents (GE Healthcare Life Sciences, UK) were used to detect the HRP signal by chemiluminescence, as per manufacturer's instructions. Bands per protein signal were visualised using X-ray film (Fujifilm, Tokyo, Japan) for different lengths of exposure and developed using an automated film processor (ECOMAX, Protec, Germany), or imaged digitally with the Amersham Imager 680 blot and gel imager (GE Healthcare, Bio-Sciences, Pittsburgh, Pennsylvania, USA).

Table 2.29. Antibodies used for immunodetection

Antigen	*Type*	*Dilution*	*Company*	*Catalogue Number*
ACAD9	Mouse polyclonal	1:1,000	Abcam	ab72655
ACO2	Mouse monoclonal	1:10,000	Abcam	6F12BD9
AIF	Mouse monoclonal	1:10,000	Santa Cruz	sc-13116
ATP5A	Mouse monoclonal	1:1,000	Abcam	ab110273
β-ACTIN	Mouse monoclonal	1:5,000	Abcam	ab8224
β-TUBULIN	Rabbit polyclonal	1:10,000	ProteinTech	100094-1-AP
COA7	Rabbit polyclonal	1:1,000	Atlas Antibodies	HPA028154
COX4	Mouse monoclonal	1:3,000	Abcam	ab14744
COX5A	Mouse monoclonal	1:1,000	Abcam	ab110262
COX5B	Mouse monoclonal	1:1,000	Abcam	ab110263
CS	Rabbit polyclonal	1:1,000	Abcam	ab96600
CYT C	Mouse monoclonal	1:1,000	ProteinTech	66264-1-Ig
ETFB	Rabbit polyclonal	1:1,000	Abcam	ab232815
ECSIT	Rabbit polyclonal	1:1,000	Abcam	ab21288
FLAG	Rabbit polyclonal	1:1,000	Sigma Aldrich	F7425
FOXRED1	Rabbit polyclonal	1:1,000	Invitrogen	PA5-61178
GAPDH	Mouse monoclonal	1:5,000	Abcam	ab8245
GRP75	Mouse monoclonal	1:1,000	Abcam	ab2799
HA	Rat monoclonal	1:1,000	Roche	11 867 431 001
LRPPRC	Rabbit polyclonal	1:1,000	Abcam	ab97505
MT-CO1	Mouse monoclonal	1:1,000	Abcam	ab14705
MT-CO2	Mouse monoclonal	1:1,000	Abcam	ab110258
NDUFA2	Rabbit polyclonal	1:1,000	Atlas antibodies	HPA035933
NDUFA3	Rabbit polyclonal	1:200	Invitrogen	PA5-61390
NDUFA9	Mouse monoclonal	1:1,000	Invitrogen	20C11B11B11
NDUFA9	Mouse monoclonal	1:1,000	Abcam	ab14713
NDUFA10	Rabbit polyclonal	1:1,000	Invitrogen	PA5-22348
NDUFA11	Rabbit polyclonal	1:1,000	Novus biologicals	NBP2-58831
NDUFA12	Rabbit polyclonal	1:1,000	Sigma	SAB2701046
NDUFAB1	Rabbit monoclonal	1:1,000	Invitrogen	PA5-30099
NDUFB3	Rabbit monoclonal	1:1,000	Abcam	ab202585
NDUFB8	Mouse monoclonal	1:1,000	Abcam	ab110242
NDUFB11	Rabbit monoclonal	1:1,000	Abcam	ab183716
NDUFAF1	Rabbit polyclonal	1:1,000	Abcam	Ab198186
NDUFAF2	Rabbit polyclonal	1:1,000	Invitrogen	PA5-63019
NDUFAF3	Rabbit polyclonal	1:1,000	Invitrogen	PA5-72636
NDUFS1	Rabbit polyclonal	1:1,000	Abcam	ab102552
NDUFS2	Mouse monoclonal	1:1,000	Abcam	ab110249
NDUFS3	Mouse monoclonal	1:1,000	Abcam	ab110246
NDUFS6	Rabbit Polyclonal	1:1,000	Abcam	ab230464
NDUFS8	Mouse monoclonal	1:1,000	Santa Cruz	Sc-515527

NDUFV1	Rabbit polyclonal	1:1,000	Abcam	ab203208
POLG	Rabbit monoclonal	1:1,000	Abcam	ab128899
SDHA	Mouse monoclonal	1:1,000	Abcam	ab14715
SDHB	Mouse monoclonal	1:10,000	Abcam	ab14714
SF2	Rabbit polyclonal	1:1,000	Abcam	ab38017
SOD2	Mouse monoclonal	1:2,000	Abcam	ab16956
TIMM23	Goat polyclonal	1:1,000	Santa Cruz	Sc-14046
TMCO6	Rabbit polyclonal	1:1,000	ProteinTech	20117-1-AP
TMCO6	Rabbit Polyclonal	1:1,000	Novus Biologicals	NBP1-57660
TOMM20	Rabbit monoclonal	1:10,000	Abcam	ab186734
TOMM70	Mouse polyclonal	1:1,000	Abcam	ab89624
TUBB	Mouse monoclonal	1:1,000	Sigma-Aldrich	WH020
UQCRC1	Rabbit polyclonal	1:1,000	Abcam	ab96333
UQCRC2	Mouse monoclonal	1:2,000	Abcam	ab14745
VINICULIN	Rabbit monoclonal	1:5,000	Abcam	ab129002

2.6.6 Mitochondrial Isolation

2.6.6.1 Sample Preparation from Cultured Cells

About 4 x 10^8 cultured cells were harvested by trypsinisation (Trypsin-0.5 % EDTA) and washed with 5 ml of 4 ºC PBS twice (300 x g for 5 min at RT). The resulting pellet was resuspended in an equivalent volume of hypotonic buffer (IB 0.1X: 3.5 mM Tris-HCl, pH 7.8, 2.5 mM NaCl, 0.5 mM $MgCl_2$) so that 1 g cells = 1ml hypotonic buffer. Cells were homogenised with a motor-driven Teflon pestle (~1000 rpm for 10-15 strokes) at 4 ºC. Immediately following this, 1/10^{th} of the initial volume of cells of hypertonic buffer (IB 10X: 350 mM Tris–HCl, pH 7.8, 0.25 M NaCl, 50 mM $MgCl_2$) was added to make the solution isotonic. Homogenates were transferred to a 15 ml Falcon tube and centrifuged (1,000 x g for 5 min at 4 °C) in order to pellet unbroken cells, extracellular debris and nuclei. The supernatant, containing intact mitochondria, was transferred to a clean 15 ml Falcon tube and the remaining pellet was homogenised again, as above. Supernatants from both homogenisations were pooled and centrifuged once more to remove remaining extracellular debris and nuclei (1,000 x g for 5 min at 4 °C). Supernatants were transferred to four 1.5 ml Eppendorf tubes and mitochondria were then pelleted by centrifugation in a refrigerated microfuge (13,000 rpm, 2 min at 4 °C). The supernatant obtained after this spin contained cytosolic proteins and was kept for posterior analysis for both sub-mitochondrial localisation studies (**section 2.6.7**) and immunocapture (**section 2.6.8**). Pellets were washed 4-5 times with 1 ml cold PBS (13,000 rpm for 2 min at 4 °C), and mitochondria resuspended in filtered 4 ºC Medium A (0.32 M sucrose, 1 mM EDTA, and 10 mM Tris-HCl, pH 7.4) for sub-mitochondrial localisation studies, and in sterile 1X sterile PBS for immunocapture.

2.6.6.2 Sample Preparation from Frozen Murine Tissues

Cut pieces of frozen mouse organs (~ 50 mg) were weighed, and minced finely with sterilised surgical scissors on a platform cooled to 4 ºC on top of ice. Tissue pieces were suspended in 10 volumes of Medium A (see **section 2.6.6.1**). A glass Elvehjem potter, cooled in ice, and a Teflon pestle was used to homogenate liver and brain samples; a glass pestle was used instead for heart and skeletal muscle. Homogenisation was performed manually until no tissue pieces remained per tissue type (6-15 strokes depending on the tissue softness), performed on ice. Homogenates were transferred to a 15 ml Falcon tube and centrifuged (1,000 x g for 5 min at 4 °C) to remove unbroken cells, extracellular debris and nuclei. The supernatant, containing intact mitochondria, was transferred to a clean 15 ml Falcon tube and the remaining pellet was homogenised again, as above. Supernatants from both homogenisations were pooled and centrifuged once more to remove remaining extracellular debris and nuclei (1,000

x g for 5 min at 4 °C). Supernatants were transferred to eight 1.5 ml Eppendorf tubes and mitochondria were then isolated by centrifugation in a refrigerated microfuge (13,000 rpm for 2 min at 4 °C). The supernatants were discarded and pellets washed twice with 1 ml cold PBS (13,000 rpm, 2 min at 4 °C).

2.6.7 Sub-Mitochondrial Localisation Studies

Mitochondria from cultured HEK 293T cells were isolated as described in **section 2.6.6.1**, and the mitochondrial preparations were portioned into multiple 200 µg aliquots suspended to a final volume of 200 µl with Medium A (see **section 2.6.6.1**). Two identical aliquots were treated with increasing concentrations of DIG (0, 75, 150, 300, 600 and 1200 µg/ml) for 10 min at 4 °C. Proteins in the IMS or IMM facing the IMS become more accessible to proteolysis with the increasing concentrations of DIG; IMM proteins facing the matrix and matrix-localising proteins would be spared in these treatments. One aliquot of each pair was immediately centrifuged (9,000 x g for 10 min at 4 ºC) following DIG incubation, and supernatants were collected while the pellets were washed twice with 200 µl Medium A. The second aliquot was further incubated with 150 µg/ml of trypsin for 30 min at RT, to degrade all unprotected, solubilised proteins. Proteolysis was halted by addition of a protease inhibitor cocktail (cOmplete™ Protease Inhibitor Cocktail, Roche) and samples were centrifuged (13,000 x g for 2 min at 4 ºC) and washed twice with 1X PBS. All pellets were finally solubilised in 1 % SDS and the presence or absence of proteins of interest in each of the treated samples was analysed by SDS-PAGE (**section 2.6.2**), Western blotting (**section 2.6.4**) and immunodetection (**section 2.6.5**).

2.6.8 Immunoprecipitation

Mitochondrial isolation from cultured cells was performed as per **section 2.6.6**. 'Whole cell lysates' (WC) and a 'cytosolic fraction' (C) were collected for each cell line per experiment. Mitochondrial pellets were resuspended in 500 µl 1X PBS, and protein quantification performed using the DC assay (see **section 2.6.1**). Mitochondria were pelleted (12,500 x g for 2 min at 4 ºC) and resuspended with a relative volume of cold PBS to achieve a final protein concentration of 5.5 mg/ml. An equivalent amount for 0.5 mg protein was removed and designated the 'mitochondrial fraction' (M). A 50X protease inhibitor cocktail (cOmplete™ Protease Inhibitor Cocktail, Roche) was added per suspension, and for every 180 µl of solution, 20 µl 10 % DDM was added. Solutions were incubated on ice for 30 min to solubilise membrane-embedded proteins and centrifuged at high speed (20,000 x g for 30 min at 4 ºC) in a tabletop microfuge. Supernatants, containing all mitochondrial-localising proteins, were incubated O/N at 4 ºC on a rotator with ~100 µl of a 1:2 antibody-bead slurry using one of the following: 1) the Complex I Immunocapture Kit (Abcam ID: ab109711C, Abcam, Cambridge, UK), 2) anti-TMCO6 polyclonal rabbit antibody (Proteintech ID: ID: 20117-1-AP, Proteintech),

or 3) anti-HA Pierce™ magnetic beads (Catalogue Number: 88836, Thermo Scientific™). The anti-TMCO6 antibody was crosslinked to magnetic beads at least 24 h prior to use by means of the Pierce Crosslink Magnetic IP/Co-IP kit (Catalogue Number: 88805, Thermo Scientific™), as per manufacturer's instructions.

For mitochondrial suspensions incubated with the Complex I immunocapture kit, beads were incubated with solubilised mitochondrial protein for at least 18 h and then pelleted (500 x g for 1 min at 4 ^{o}C). An aliquot of the bead 'supernatant' (S) was collected, as was a portion of the 'beads' (B). Beads were washed with 1 ml wash buffer (X PBS + 0.5 % DDM) and pelleted (500 x g for 1 min at 4 ^{o}C). This process was repeated 4 to 5 times and wash fractions collected and labelled sequentially (W1-W[X]). Bound proteins were then suspended in elution buffer (1X PBS + 1 % SDS), mixed for 10 min at RT with constant agitation using a vortex, and beads were pelleted by centrifugation (500 x g for 1 min at 4 ^{o}C). Eluted protein within the supernatant was collected and labelled elution 1 (E1). A second elution was performed as above and the supernatant labelled elution 2 (E2). Protein concentrations for all collected fractions were determined by DC assay (see **section 2.6.1**).

For anti-TMCO6 antibodies crosslinked to Pierce™ magnetic beads, beads were incubated with solubilised mitochondrial protein for at least 18 h and then pelleted (500 x g for 1 min at 4 ^{o}C). An aliquot of the B and S fractions were collected. Washes were then performed by adding 1 ml wash buffer (same as for the CI immunocapture kit), and placing tubes into a magnetic tube rack for 1 min at RT. Supernatants were collected and labelled W1-W[X] for up to five washes. In order to avoid denaturing conditions, low-pH glycine was used for elution; this limited the pull down of unspecific IgG's in the eluates and limited the likelihood of removing the crosslinked 'bait' antibodies by agitation. Tubes were incubated on ice for 20 min without mixing using 200 µl 0.1M glycine (pH = 2). A second elution was performed as above and the supernatant labelled elution 2 (E2). Protein concentrations for all collected fractions were determined by DC assay (see **section 2.6.1**).

For the anti-HA Pierce™ crosslinked magnetic beads, an aliquot of the B and S fractions were collected after at least 18 h incubation on a rotator at 4 ^{o}C. A magnetic tube rack was used for all washes, as detailed above. Elution was performed using 15 µl of anti-HA competing peptide (100 µg mixture, Catalogue ID: AB3254, Milipore, Merck), amino acid sequence: YPYDVPDYA, incubated for 20 min on ice, with the resulting eluate labelled 'E1'. A second elution (E2) was performed with 100 µl 0.1 M glycine (pH = 2) (20 min on ice) to ensure that all bound proteins were removed.

The presence or absence of proteins in the eluates was analysed by SDS-PAGE (**section 2.6.2**), Western blotting (**section 2.6.4**) and immunodetection (**section 2.6.5**) in all cases.

2.7 Mitochondrial Respiratory Chain Functional Assays

2.7.1 Mitochondrial Respiratory Chain Enzymatic Activity Assays

Specific activities (μM of substrate consumed per minute) of the mitochondrial respiratory chain complexes CI-CIV, and that of matrix-localising enzyme citrate synthase (CS), was measured spectrophotometrically for DIG-treated cells and homogenised frozen murine tissue samples. Protein concentration and path length per each 200 μl reaction was also determined spectrophotometrically; these values, the known extinction coefficient (ε) of each reaction, and the determined absorbances (λ) per reaction were used to calculate the specific biochemical activities of each sample using the Beer-Lambert law:

$$\frac{\Delta Abs \times total\ reaction\ volume\ (ml)}{\epsilon \times sample\ volume\ (ml) \times [prot](mgml^{-1}) \times pathlength(cm)}$$

The specific activities of CI-CIV were each normalised against the relative activity of CS. Technical replicates (n ≥ 3) were performed per sample under the same temperature and using the same reaction buffer.

2.7.1.1 Sample Preparation from Cultured Cells

Harvested cells were solubilised in 400 μl Buffer A (20mM MOPS, 250mM sucrose, pH 7.4) and an equal volume of 0.2 mg/ml DIG. Homogenates were kept on ice for 5 min and centrifuged (5,000 x g for 3 min at 4°C). The supernatant was discarded and the mitochondria-enriched pellet was resuspended in 600 μl Buffer B (Buffer A + 1mM EDTA), incubated on ice for 5 min and centrifuged (10,000 x g for 3 min at 4 °C) to generate mitoplasts. The pellet was stored at −80 °C until use. Once thawed on ice, pellets were resuspended in 200 μl 10 mM potassium phosphate (PK) buffer (pH = 7.4) and snap frozen in liquid nitrogen and then thawed in a 37°C water bath three times successively to disrupt the mitochondrial membranes. Protein concentration was determined by DC assay, as described in **section 2.6.1**. Samples were loaded into individual wells of a 96-well plate and placed on ice.

2.7.1.2 Sample Preparation from Frozen Murine Tissues

Frozen murine tissues (~50 mg) were minced into small pieces with sterilised surgical scissors and then homogenised in 15 volumes of Medium A in a glass Dounce-type homogeniser using a manually-driven glass pestle (~15 strokes). Homogenates were centrifuged (800 x g for 5 min at 4 °C) and supernatants were snap frozen immediately in liquid nitrogen. For the experiment, pellets were thawed on ice initially and then snap frozen and quickly thawed between liquid nitrogen and a 37°C water bath for three consecutive freeze-thaw cycles.

Protein concentration was determined as described in **section 2.6.1**, and samples were loaded into individual wells of a 96-well plate and placed on ice.

2.7.1.3 Measuring Mitochondrial Protein Complex Activities by Spectrophotometry

Kinetic spectrophotometric measurement of CI was performed at 30 °C (λ = 340 nm) to follow NADH oxidation over 2 min. Oxidised NADH (NAD^+) is not detectable at this wavelength so the 'disappearance' of NADH following the addition of CoQ was measured. Cell-derived samples were incubated in CI buffer (**Table 2.30**) for 2 min and tissue homogenates in the same buffer for 10 min prior to measurement. The CI-inhibitor rotenone was then added and incubated for at least 1 min, and a second measurement under the same conditions was taken as a baseline for all non-CI linked NADH oxidation. The difference between these values was calculated relative to the extinction coefficient of the reaction ($\varepsilon_{NADH340nm}$ = 6.81 ($mlnmol^{-1}cm$), volume and concentration of the sample, and path length through each well per measurement to account for any inconsistencies in pipetting.

Table 2.30 CI enzymatic activity reaction buffer

Reagent	*Reagent Manufacturer | CN*	*Final Concentration*
PK buffer (pH = 8.0)	-	20 mM
NADH (in dH_20)	Roche | 10107735	0.2 mM
Sodium azide (NaN_3) (in dH_20)	Sigma-Aldrich® | S8032	1 mM
BSA (in dH_20 + EDTA 10 mM pH 7.4)	Sigma-Aldrich® | A6003	1 mg/ml
CoQ (in 10 % EtOH)	Sigma-Aldrich® | C7956	50 µM
Rotenone (in 25 % EtOH)	Sigma-Aldrich® | R8875	5 µM

Kinetic spectrophotometric measurement of CII was performed using the mixture detailed in **Table 2.31.** Measurement was performed at 30 °C by following the reduction rate of DCPIP (an electron acceptor); λ= 600 nm for 2 min. $\varepsilon_{DCPIP600nm}$ = 19 $mlnmol^{-1}cm$. Addition of CoQ followed to measure MRC-linked CII activity in particular.

Table 2.31 CII enzymatic activity reaction buffer

Reagent	*Reagent Manufacturer | CN*	*Final Concentration*
PK buffer (pH = 7)	-	50 mM
Potassium cyanide (KCN) (in dH_20)	Sigma-Aldrich® | 31252	1.5 mM
2,6-Dichlorophenolindophenol (DCPIP)	Sigma-Aldrich® | D1878	0.1 mM
Sodium succinate (in dH_20)	Sigma-Aldrich® | S2378	16 µM
CoQ (in 10 % EtOH)	Sigma-Aldrich® | C7956	50 µM

Kinetic spectrophotometric measurement of CIII was performed using the mixture detailed in **Table 2.32** in 96-well plates at 30 °C by following the reduction of cytochrome *c* (electron acceptor); λ= 550 nm for 2 min. $\varepsilon_{NADH340nm}$ = 21 mlnmol^{-1}cm.

Table 2.32 CIII enzymatic reaction buffer

Reagent	***Reagent Manufacturer | CN***	***Final Concentration***
PK buffer (pH = 7.4)	-	50 mM
NaN_3 (in dH_20)	Sigma-Aldrich® | S8032	1.5 mM
BSA (in dH_20 + EDTA 10 mM pH 7.4)	Sigma-Aldrich® | A6003	0.1 mM
Cytochrome c (in dH_20)	Sigma-Aldrich® | C7752	16 µM
Reduced decylubiquinone (DBH_2)	Sigma-Aldrich® | D7911	50 µM

Kinetic spectrophotometric measurement of CIV was performed using the mixture detailed in **Table 2.33** in 96-well plates at 37 °C by following oxidation of cytochrome *c* (electron donor); λ= 550 nm for 2 min. $\varepsilon_{Cytc550nm}$ = 18.5 mlnmol^{-1}cm.

Table 2.33 CIV enzymatic reaction buffer

Reagent	***Reagent Manufacturer | CN***	***Final Concentration***
90-95 % reduced cytochrome c (1.3 mg/ml) (in 50 mM KP buffer (pH = 7))	Sigma-Aldrich® | C7752	50 mM

Kinetic spectrophotometric measurement of CS was performed using the mixture detailed in **Table 2.34** in 96-well plates at 30 °C. The absorbance of thionitrobenzoic acid (TNB), the main reaction product of CoA and 5-dithio-bis-(2)-nitrobenzoic acid (DTNB) is proportional to the amount of liberated CoA and indicates the relative activity of CS; λ= 412 nm for 2 min. $\varepsilon_{TNB412nm}$ = 13.8 mlnmol^{-1}cm.

Table 2.34 CS enzymatic reaction buffer

Reagent	***Reagent Manufacturer | CN***	***Final Concentration***
Tris-HCl buffer (pH = 8)	-	75 mM
DTNB (in 187.5 mM Tris-HCl (pH = 8))	Sigma-Aldrich® | D8130	0.1 mM
Triton X-100	Roche | 11332481001	0.1 %
Acetyl-CoA	Sigma-Aldrich® | A2181	0.4 mM
Oxalacetic acid	Sigma-Aldrich® | O4126	0.5 mM

2.7.2 In-Gel Activity

In-gel activity assays were utilised to visually indicate differences in mitochondrial complex activities for cultured cells or murine tissues, following principles first described by Zerbetto *et al.* (Zerbetto, Vergani and Dabbeni-Sala, 1997). 1D-BNGE was performed as per section **section 2.6.3**, and gels were then directly submerged in 10 ml of either CI detection solution (0.1 M Tris-HCl pH 7.4, 0.14 mM NADH, and 1 mg/ml nitro blue tetrazolium (NBT, Sigma-Aldrich), or CIV detection solution (50 mM PK buffer pH 7.4, 1 mg/ml 3,3′-diaminobenzidine (DAB) (Sigma-Aldrich®), 24 U/ml catalase (Sigmal-Aldrich®), 1 mg/ml cytochrome c (Sigma-Aldrich®), 75 mg/ml sucrose (Acros Organics)), and incubated for 2 h at RT. Gels were digitally scanned at the desired band intensity.

2.7.3 Oroboros

Mitochondrial O_2 consumption rate was measured for live cultured cells and fresh murine brains using an Oxygraph-2k respirometer (Catalogue number: 10023-02, Oroboros Instruments, Innsbruck, Austria), which contains two chambers in which dissolved O_2 is measured in real-time by an amperometric oxygen electrode.

For cultured immortalised skin fibroblasts, cells were trypsinised, counted by Countess II™ FL Cell counter (Life Technologies) and 2.5 x 10^6 cells were suspended in 2.5 ml warmed standard culturing medium (**section 2.3.1**) to yield a final cell density of 1 x 10^6 cells/ml. Both chambers of the apparatus were calibrated for ~1 h at 37 °C with 2.0 ml standard culturing medium immediately prior to measurement. Cell suspensions were then added to the separate chambers, which were closed and any residual media aspirated. Basal respiration was recorded for 2 min at 37 °C with 775 rpm stirring, followed by addition of 5 µl 1 mM oligomycin (Catalogue number: O4876, Sigma-Aldrich®) diluted in H_20 with a Hamilton syringe, in order to inhibit ATP synthase and determine oxygen consumption solely due to OXPHOS. Addition of 10 µl 250 µM carbonyl cyanide m-chlorophenylhydrazone (CCCP) (Catalogue number: C2759, Sigma-Aldrich®) (diluted in EtOH) followed via Hamilton syringe three times successively, and once with 5 µl CCCP, to uncouple the respiratory chain and induce maximal respiration. Combined addition of 2 µl 1 mM rotenone (in EtOH) (Catalogue number: R8875, Sigma-Aldrich®) and 2.5 µl 2.5 mM Antimycin A (in EtOH) (Catalogue number: A8674, Sigma-Aldrich®) then inhibited Complexes I and III, respectively, to effectively halt the respiratory chain activity. A representative trace of this experiment is available in **Fig. 2.11 A**.

For murine tissues, whole brains were excised quickly and suspended in 4 °C filtered Medium A (see **section 2.6.6.1**) until sample preparation. Brains were then transferred to Medium A + 0.2 % fatty-acid free BSA, added immediately prior to homogenisation so that 1 g tissue = 5

ml buffer, and homogenised manually using a Teflon-glass Elvenhiem potter (~6 strokes). All homogenisations occurred on ice and were followed by mitochondrial isolation as per **section 2.6.6.2**. Protein concentrations were determined by DC assay (**section 2.6.1**). 0.25 mg/ml of isolated mitochondria was used for measurements. Chambers were calibrated with 2 ml of MiR05 buffer (**Table 2.35**) at 37 ^{o}C with a stirring rate of 775 rpm for ~1 h immediately prior to measurement.

Table 2.35 MiR05 respiration buffer

Reagent	***Reagent Manufacturer | CN***	***Final Concentration***
EGTA	Sigma-Aldrich® | E4378	0.5 mM
$MgCl_2 \cdot 6\ H_2O$	Sigma-Aldrich® | M9272	3 mM
Lactobionic acid	Sigma-Aldrich® | L2398	60 mM
Taurine	Sigma-Aldrich® | T0625	20 mM
Potassium phosphate monobasic	Sigma-Aldrich® | P5655	10 mM
HEPES	Sigma-Aldrich® | H7523	20 mM
Sucrose	Sigma-Aldrich® | 84097	110 mM
Fatty acid-free BSA	Sigma-Aldrich® | A6003	1 mg/ml

Basal respiration was measured until O_2 flux remained constant, followed directly by addition of 5 µl 2 M pyruvate, 4 µl 50 mM malate and 10 µl 2 M glutamate via Hamilton syringes. Baseline respiration was recorded until a linear O_2 consumption rate was reached. To determine CI-linked respiration, 5 µl 1 mM ADP was added to the Oxygraph-2k chambers until a linear flux was reached (~5 min), followed by addition of 1 µl 1 mM rotenone to inhibit CI activity. 20 µl of 1 M succinate was then added to determine CII-linked respiration. Two successive addition of 5 µl 250 µM CCCP followed to induce maximal respiration via uncoupling. ATP activity was then inhibited by the addition of 5 µl 1 mM oligomycin. Lastly, 1 µl 2.5 mM antimycin A was added to inhibit CIII and halt respiration. A representative trace of this experiment is available in **Fig. 2.11 B.** Duplicates were performed per homogenate using both of the two Oxygraph-2k chambers to eliminate the variability of the different electrodes used, and values were averaged per each substrate or inhibitor added. Posterior analysis was performed using the accompanying DatLab software (Oroboros).

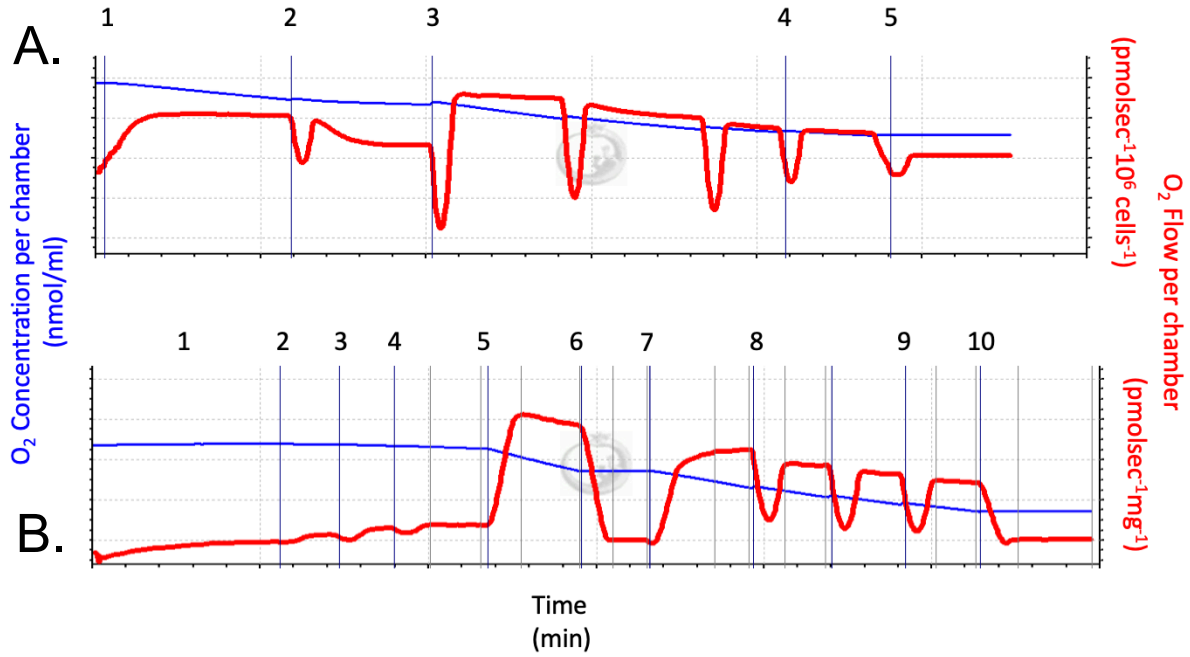

Figure 2.11 Representative traces for measuring mitochondrial O_2 consumption rates.

An Oxygraph-2k respirometer was used to (**A.**) measure O_2 flow for cultured cells suspended in standard culturing media at 37 °C, as follows: 1) basal respiration was recorded for ~2 min until a constant O_2 flux was reached, 2) ATP synthase activity was inhibited after 5 µl addition of 1 mM oligomycin, 3) total uncoupling of the respiratory chain followed by three additions of 10 µl 250 µM CCCP, 4) and one further addition of 5 µl CCCP to confirm no further change in O_2 flux, and finally, 5) inhibition of CI and CIII was achieved by addition of 2 µl 1 mM rotenone and 2.5 µl 2.5 mM antimycin A, respectively. (**B.**) Equivalent measurements for isolated mitochondrial from murine tissues, suspended in MiR05 buffer (**Table 2.33**) at 37 °C, were performed as follows: 1) basal respiration was recorded ~10 min until O_2 flux remained constant, followed by addition of 2) 5 µl 2 M pyruvate, 3) 4 µl 50 mM malate and 4) 10 µl 2 M glutamate and baseline respiration was recorded. To determine CI-linked respiration, 5) 5 µl 1 mM ADP was added, followed by 6) addition of 1 µl 1 mM rotenone to inhibit C I activity. 7) 20 µl of 1M succinate was then added to determine CII-linked respiration. 8) Two successive addition of 5 µl 250 µM CCCP followed to induce maximal respiration via uncoupling. 9) ATP activity was then inhibited by the addition of 5 µl 1 mM oligomycin. Lastly, 10) 1 µl 2.5 mM antimycin A was added to inhibit CIII and halt respiration.

2.8 Statistics

Graphical visualisation of data and all statistical analyses were performed with GraphPad Prism software (versions 7.0 and 8.0). All numerical data for $n = 3$ or greater is expressed as mean ± standard error (SEM) or mean ± standard deviation (SD), as labelled in each figure legend. The numbers of biological replicates per sample per figure are also included in the figure legends. Results were analysed by unpaired Student *t*-tests for 2 experimental groups with error bars representing range of values, and by one-way or two-way analysis of variance (ANOVA) as appropriate for greater than 2 experimental groups. For one-way ANOVA, Tukey's multiple comparison *post-hoc* test was routinely applied, and for two-way ANOVA, Sidak's multiple comparison *post-hoc* test was routinely applied. The statistical procedure used for each set of results will be mentioned either in-text and/or in the corresponding figure legends. In all cases, *p*-values < 0.05 were considered statistically significant, with the following system used for denoting statistical significance:

$p < 0.05$ = *, $p < 0.01$ = **, $p < 0.005$ = *** and $p < 0.001$ = ****.

Chapter 3

Compound Heterozygous Mutations in *COA7* are Associated with COX Deficiency and Mitochondrial Leukoencephalopathy

3.1 Introduction

COA7 (NC_000001.11: 52,684,449 - 52,698,347) encodes a soluble protein (NP_075565.2) that is present only in Metazoans, which is translated from 3 coding exons of one known mRNA transcript (NM_023077.3). The COA7 protein is predicted to contain 5 SEL1-like tetratricopeptide repeats (Interpro ID: IPR006597), which are likely to mediate interactions with partner proteins. The distribution of these domains is shown in **Fig. 1.7 B.**. COA7 was first characterized following its detection in a screen for proteins that bound the cristae-forming MIB components SAM50 and Mitofilin, with subsequent shRNA-mediated *COA7* gene silencing in HeLa cells yielding a decrease in fully assembled COX abundance and its enzymatic activity by approximately 66 % (Kozjak-Pavlovic *et al.*, 2014). Cellular fractionation and membrane swelling experiments revealed that COA7 was a soluble protein localising only to the mitochondria, specifically to the IMS; however, this finding, although indicative, was not confirmative given the lack of a suitable experimental control. At the time this research was conducted, no other published literature existed concerning the structure, function, mechanism of action, binding partners, intracellular transport nor involvement in human disease pathology of COA7. Herein, I describe the compound heterozygous mutant variants in *COA7* (NM_023077.3:c.410A>G;c.287+1G>T) detected in a mitochondrial disease patient presenting with mitochondrial leukoencephalopathy and COX deficiency, and I also verify its intracellular localisation.

3.2 Patient Clinical History and Genetic Investigation

An Italian female proband (b.1996) was born at term after a normal pregnancy, the only child of healthy, unrelated parents. The perinatal period was uneventful and her early physiological development was considered to be normal. At 12 months of age, psychomotor delay became evident, and she did not start walking autonomously until 22 months of age, with poor balance and frequent falls. At 3 years of age, she developed a demyelinating sensorimotor peripheral neuropathy, and a brain MRI disclosed supratentorial leukodystrophy (white matter degeneration). At 10 years of age, her walking difficulties worsened, and limb weakness and tremor ensued. Neurological evaluation revealed dysarthria (unclear speech), dysmetria (uncoordinated limb movement), hyporeflexia of the four limbs, with muscle wasting. She was able to walk only for a few steps with an ataxic gait, supported by orthopaedic ankle-foot aids. Mild cognitive impairment was also documented (IQ 75, WISC-R scale). The clinical evolution was slowly progressive. At her last follow-up examination at 19 years of age, she had developed a marked dorsal-lumbar scoliosis. Additionally, neurophysiological evaluation confirmed worsening of her mixed axonal demyelinating peripheral neuropathy. MRI scans of the brain and spinal cord at 19 years of age showed extensive cavitation in the cerebral white matter, with no effects to the cerebellum and brainstem (**Fig. 3.1 A. i-ii**). The spinal cord was atrophied but had no obvious focal lesions (**Fig. 3.1 A. iii**). Cerebrospinal fluid lactate was found elevated to 2.995 mM (n.v. 0.8 – 2.1 mM) and histological analysis of a skeletal muscle biopsy showed hypotrophy of type IIA muscle fibres. Finally, biochemical activity measurements of patient muscle and cutaneous biopsies by spectrophotometry revealed isolated COX deficiencies of 64 % and 66 % relative to the control values, respectively.

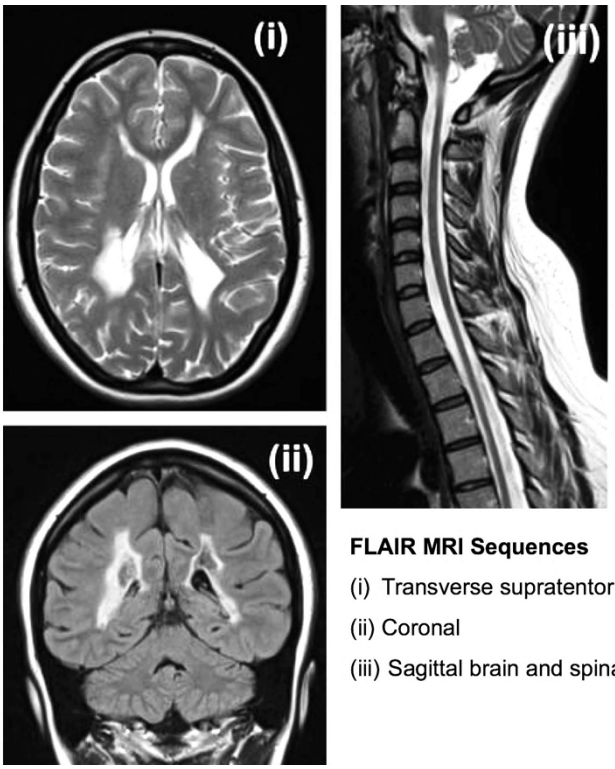

Figure 3.1 T2- FLAIR MRI sequences of the brain and spinal cord.

An Italian female proband (b. 1996) underwent T2-FLAIR MRI brain and spinal cord scans at 19 years of age that revealed (i) cavitation of the cerebral white matter, (ii) no obvious defect to the midbrain including the cerebellum and brainstem, and (iii) atrophy of the spinal cord. Sequences acquired by clinicians at the Neurological Institute "Carlo Besta" (Milan, Italy).

Taken together, the clinical progression and biochemical findings suggested a mitochondrial disease origin. After initial Sanger sequencing of the mtDNA at the "C. Besta" Neurological Institute (Milan, Italy), which revealed no plausible gene candidates, the patient's genomic DNA was subjected to whole exome sequencing (WES) at the MRC Mitochondrial Biology Unit (Cambridge, UK). This process identified 13 nDNA-encoded genes with either homozygous recessive or two compound heterozygous recessive variants. *COA7* was determined to be the only gene of these that encoded a protein localising to mitochondria. The following compound heterozygous mutations were detected in *COA7*: an A>G transition in exon 3 (NM_023077.3:c.410A>G), predicted to result in a missense tyrosine to cysteine amino acid substitution (p.Tyr137Cys), and a G>T transversion affecting the first intronic nucleotide of the exon 2/intron 2 boundary (NM_023077.3:c.287+1G>T), affecting an essential nucleotide of the splice site consensus sequence (**Fig. 3.2 B.**). These variants had not previously been reported in the ExAc or Clinvar databases. Genetic interrogation of the parents' genomic DNA followed in order to confirm the parental origin of the two mutant alleles. Sanger sequencing of the two regions of interest within *COA7* (at the exon2/intron2 boundary, and within exon 3) was carried out for both parents; the c.410A>G mutant variant was inherited from the father and the c.287+1G>T mutant variant from the mother (**Fig. 3.2 A.**).

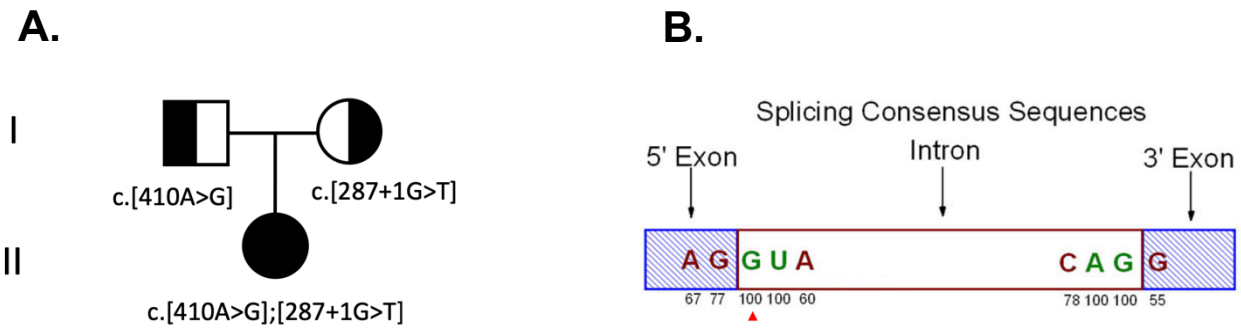

Figure 3.2 Compound heterozygous mutations in *COA7*.

(**A.**) A family pedigree of an Italian female proband (b. 1996) who inherited a c.410A>G transition mutation within exon 3 of *COA7* (NC_000001.11: 52,684,449 - 52,698,347) from her father, resulting in a tyrosine to cysteine amino acid substitution, p.Tyr137Cys, and a c.287+1G>T transversion affecting the first intronic nucleotide of the exon 2/intron 2 boundary from her mother. (**B.**) The latter was predicted to disrupt splice site consensus recognition sequence at the exon 2/exon 3 splice junction. The position of the affected nucleotide is indicated by a red arrowhead. The percentage frequency for the occurrence of the nucleotide at each position is labelled underneath.

3.3 Results

3.3.1 Confirming Biallelic Mutant Variants in *COA7* in Patient Skin Fibroblasts

We first verified that both of the *COA7* gene mutations were present in cultured patient-derived skin fibroblasts. Purified genomic DNA was obtained from patient (P1) or control (C1) cells, and used as templates to generate two PCR fragments: 1) a 296 bp fragment from position 5,419 to position 5,714 of the *COA7* gene (NC_000001.11: 52,684,449 - 52,698,347), which spanned exon 2 and the exon 2/intron 2 boundary, and 2) a 723 bp fragment from position 10,121 to position 10,843, spanning part of the coding region of exon 3 (**Fig. 3.3 A.** and **B.**). Sanger sequencing of these two different PCR fragments confirmed the presence of a heterozygous G → T transversion mutation at nucleotide 247 + 1, and a heterozygous A → G transition mutation at position 410, for P1 compared with the control human cDNA *COA7* sequence (NM_023077.3), shown by C1 (**Fig. 3.3 C.**).

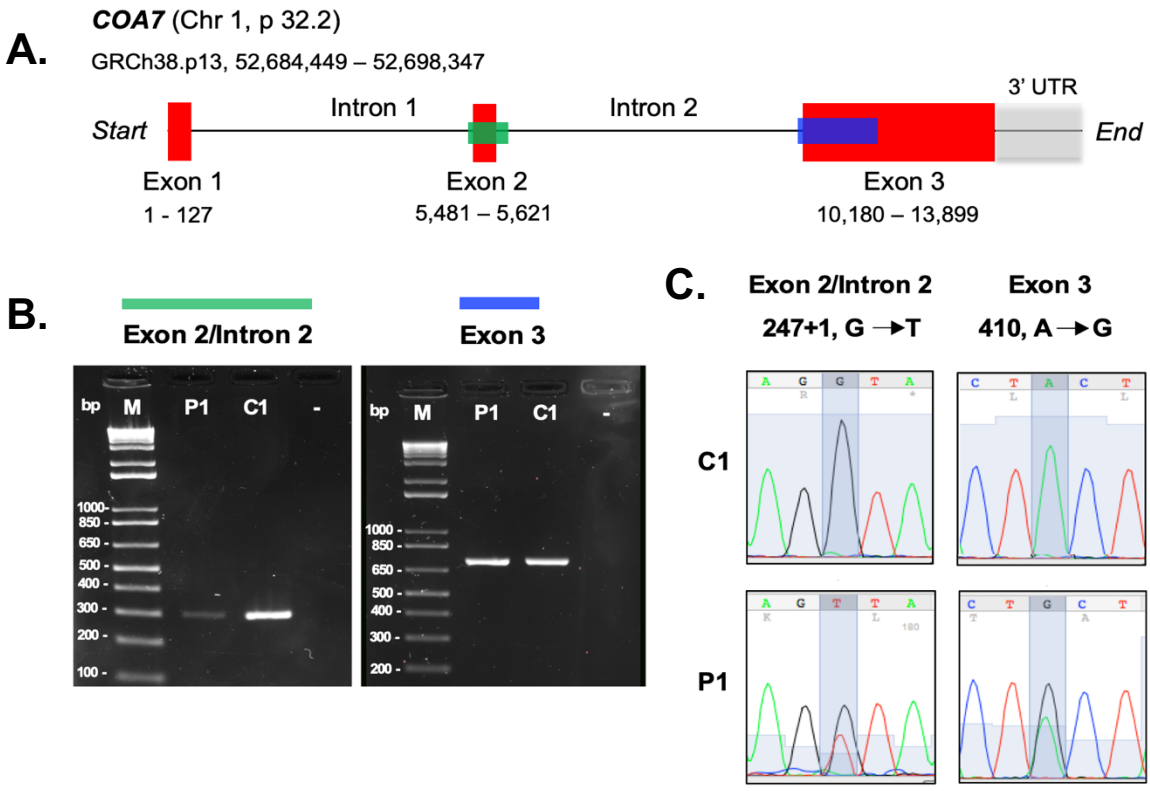

Figure 3.3. Verifying compound heterozygous mutations in *COA7*.

(**A.**) Map of the genomic structure of human *COA7* (NC_000001.11: 52,684,449 - 52,698,347, genetic locus: Chr 1, p 32.2), marking the positions of the PCR-amplified regions for the exon 2/intron 2 boundary (highlighted in green) and within exon 3 (highlighted in blue). (**B.**) PCR products were amplified from P1 and C1 skin fibroblast gDNA and a blank control reaction (-). Fragments were separated by agarose gel electrophoresis, and run alongside a 1 kilobase (Kb) DNA marker (M) (Invitrogen™, UK) for size comparison (as labelled). Gels were digitally visualized via UV transilluminator. (**C.**) Sections of chromatograms produced by Sanger sequencing (Source Bioscience, UK) confirm the presence of the compound heterozygous *COA7* mutations in P1 that had been originally identified by WES.

3.3.2 Aberrant *COA7* mRNA Transcripts Present in Immortalised Patient Cells

In order to assess the consequences of the genomic mutations at the *COA7* transcript level, total mRNA was extracted from immortalised patient (P1i) and control (C1i) skin fibroblast cells, retrotranscribed, and the resulting *COA7* cDNA sequence(s) were amplified by PCR using primers that should produce a single amplification product of 567 bp. PCR products were resolved by agarose gel electrophoresis, and revealed two bands for P1i of approximately ~550 and ~450 bp, compared to a single ~550 bp band for the control, C1i (**Fig. 3.4**).

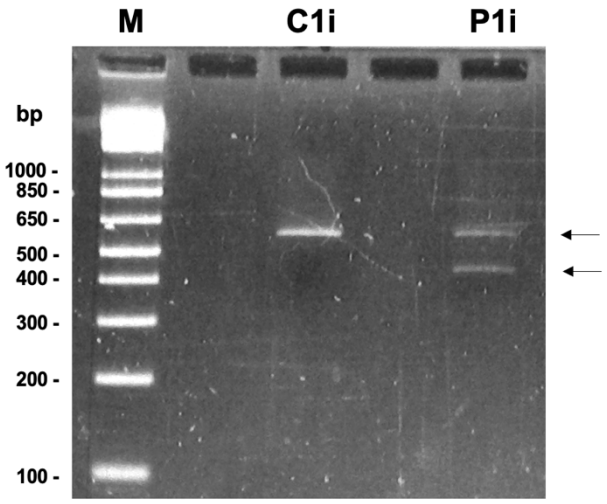

Figure 3.4. *COA7* cDNA amplification by PCR reveals two mRNA transcript isoforms in immortalised patient skin fibroblasts.

Control (C1i) and patient (P1i) *COA7* cDNA was retrotranscribed from purified mRNA and amplified by PCR. PCR products for both C1i and P1i were separated by size by agarose gel electrophoresis with a 1 Kb Ladder (Invitrogen™, UK) run alongside for size comparison. Gels were visualized by UV transilluminator. Arrows indicate two distinct bands present for P1i.

Next, the single band for the control (C1i) and the two individual bands for the patient (P1i) were excised, the cDNA purified, and then each of the three were subjected to Sanger sequencing using the same primers that had been used for amplification. As shown in **Fig. 3.5 A.**, the paternally inherited variant (NM_023077.3:c.410A>G) was verified in the larger of the two bands of P1i, compared to the counterpart sequence for C1i. It caused an in-frame TAC → TGC codon change, coding for a missense tyrosine to cysteine amino acid substitution (NP_075565.2:p.Tyr137Cys). Secondly, as shown in **Fig. 3.5 B.**, the maternally inherited nucleotide substitution at the exon 2/intron 2 splice junction (NM_023077.3:c.247+1G>T) led to an aberrant mRNA transcript with an in-frame 141-bp deletion of the entirety of exon 2. Its translation product is only 184 amino acids in length, with a deletion of 47 residues from positions 37 to 84 of the wildtype protein sequence (NP_075565.2:p.Cys37_Gly84del), which is 231 amino acids in length.

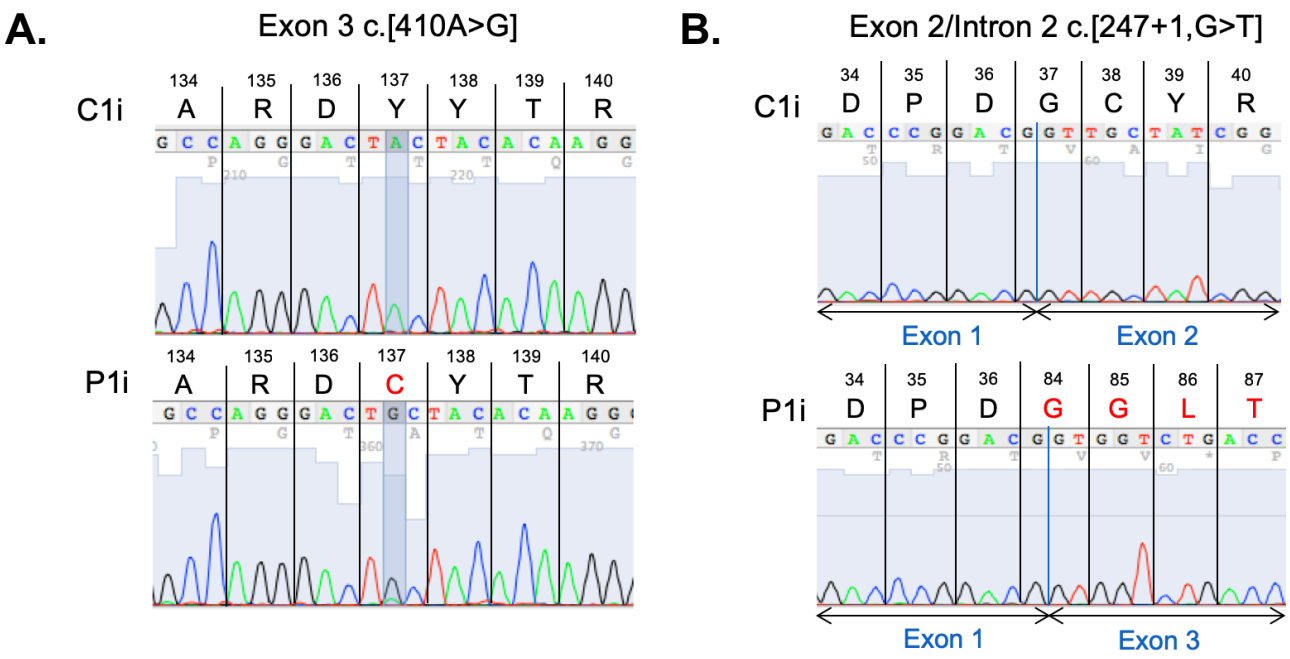

Figure 3.5. Consequences of *COA7* compound heterozygous mutations on mRNA transcript and primary protein sequences.

Purified *COA7* cDNA retrotranscribed from control, C1i, and patient, P1i, total RNA was subjected to Sanger sequencing (Source Bioscience, UK). Compared to the wildtype mRNA transcript, the two patient *COA7* mutations resulted in (**A.**) a TAC→TGC codon change in the paternally inherited mRNA variant, resulting in a p.Tyr137Cys missense mutation at the protein sequence level, and (**B.**) a 141 bp deletion at the mRNA level in the maternally inherited variant, leading to skipping of the entirety of exon 2 (p.Cys37_Gly84del). The latter resulted in a 47 aa-long deletion between positions 37 and 84 of the wildtype protein sequence. Mutant effects are labelled in red; and wildtype sequences/positions in black.

3.3.3 Both *COA7* Mutant Variants are Predicted to be Pathogenic

Fig. 3.6 A. shows a Clustal Omega (version 1.2.1) multiple sequence alignment for the C1i wildtype primary protein sequence compared to both maternal and paternal P1i mutant alleles. Notably, the maternal mutant variant with the 47-amino acid long deletion is missing the majority of the first and part of the second predicted SEL1 domains (Interpro ID: IPR006597, **Fig 1.7 B.**). Additionally, Tyr137 resides within the third SEL1 domain and is conserved amongst vertebrates, including mammals, reptiles, birds and amphibians, as well as in some species of annelids (HomoloGene ID: 11317) (**Fig. 3.6 B.**). There is no known conservation of *COA7* in invertebrate animals, bacteria, fungi nor plants. A tyrosine to cysteine substitution is likely to have a considerable destabilizing effect given that *COA7* is already cysteine-rich in its native form (13 cysteines within 231 residues); ultimately, the addition of an extra thiol group could drastically interfere with its intrinsic disulphide bridge secondary structure, as will be discussed further in **Chapter 8**.

A.

```
CLUSTAL O(1.2.1) multiple sequence alignment

                                                                SEL 1
Mat-COA7        MAGMVDFQDEEQVKSFLENMEVECNYHCYHEKDPDG----------------------  36
WT-COA7         MAGMVDFQDEEQVKSFLENMEVECNYHCYHEKDPDGCYRLVDYLEGIRKNFDEAAKVLKF  60
Pat-COA7        MAGMVDFQDEEQVKSFLENMEVECNYHCYHEKDPDGCYRLVDYLEGIRKNFDEAAKVLKF  60
                ********************************** 
                                        SEL 2
Mat-COA7        ----------------------GLTQDLKAAARCFLMACEKPGKKSIAACHNVGLLAHD  73
WT-COA7         NCEENQHSDSCYKLGAYYVTGKGGLTQDLKAAARCFLMACEKPGKKSIAACHNVGLLAHD  120
Pat-COA7        NCEENQHSDSCYKLGAYYVTGKGGLTQDLKAAARCFLMACEKPGKKSIAACHNVGLLAHD  120
                                      ************************************
                        SEL 3                                SEL 4
Mat-COA7        GQVNEDGQPDLGKARDYYTRACDGGYTSSCFNLSAMFLQGAPGFPKDMDLACKYSMKACD  133
WT-COA7         GQVNEDGQPDLGKARDYYTRACDGGYTSSCFNLSAMFLQGAPGFPKDMDLACKYSMKACD  180
Pat-COA7        GQVNEDGQPDLGKARDCYTRACDGGYTSSCFNLSAMFLQGAPGFPKDMDLACKYSMKACD  180
                *************** ******************************************
                          SEL 5
Mat-COA7        LGHIWACANASRMYKLGDGVDKDEAKAEVLKNRAQQLHKEQQKGVQPLTFG        184
WT-COA7         LGHIWACANASRMYKLGDGVDKDEAKAEVLKNRAQQLHKEQQKGVQPLTFG        231
Pat-COA7        LGHIWACANASRMYKLGDGVDKDEAKAEVLKNRAQQLHKEQQKGVQPLTFG        231
                ************************************************
```

B.

```
UniProt ID|GENE_Species (Common Name)                    Y137C
Q23450|COA7_C. elegans (Roundwork)          116  LVHWNGEK--DRKADSEKAERYMRRACELEDGEACWLLSTWYMGNKEK  171
Q9W5N0|COA7_D.melanogaster (Fruit Fly)      123  LLLVSKSMPREIDWNVPKGLEFLTKSCDLNNATACFYLSGMHISGVQK  172
Q96BR5|COA7_H.sapiens (Human)               116  LLAHDGQVNEDGQPDLGKARDYYTRACDGGYTSSCFNLSAMFLQGAPG  163
Q921H9|COA7_M.musculus (Mouse)              116  LLAHDGQVNEDGQPDLGKARDYYSRACDGGYAASCFNLSAMFLQGAPG  163
Q66KY0|COA7_X.laevis (African Clawed Frog)  116  LLAHDGRVNDE-KADAVTARDYYNKACDGNFAASCFNLSATYLQGAPG  162
G1NFC4|COA7_M.gallopavo (Turkey)            116  LLAHDGRVNDD-KPDPVVARDYYTKACDGSFAPSCFNLSVMYLQGAAG  162
A0A151M4E6|COA7_A.mississippiensis          115  LLAHDGRINDD-KPDLDVARDYYDKACNGSFAPSCFNLSAIYLQGAPG  161
          (American Alligator)
```

Figure 3.6. Multiple sequence alignment of mutant *COA7* primary protein sequences and evolutionary conservation of tyrosine residue 137.

(**A.**) Clustal O (version 1.2.1) multiple sequence alignment shows the primary protein sequence of wildtype COA7 (WT-COA7) compared with the maternal and paternal patient mutant isoforms, Mat-COA7 and Pat-COA7. The maternally inherited 47 aa-long deletion is highlighted in red, the paternally inherited Y→C missense mutation in blue, and each of the 5 SEL1 domains is labelled above. (**B.**) Multiple sequence alignment with various orthologues reveals that Tyr137 (Y137) is evolutionarily conserved amongst mammals (human and mouse), amphibians (African clawed frog), birds (turkey) and reptiles (American alligator), and some species of the order Annelida, including the roundworm. Each residue in the alignment is assigned a colour corresponding to its respective biochemical properties: blue = negatively charged, magenta = positively charged, red = hydrophobic, and green = hydrophilic or polar.

3.3.4 Patient Cells Lack COA7 & Show Reduced Levels of Some COX Subunits

In order to assess the molecular consequences of the two mutations on COA7 protein steady-state level and stability (see **Section 3.3.3**), we extracted total protein lysates from P1, C1 and C2 (another control primary skin fibroblast cell line). As shown in **Fig. 3.7 A.**, SDS-PAGE and subsequent immunodetection after Western blotting resulted in no detection of COA7 in P1 cells relative to both controls in three biological replicates. Additionally, densitometric quantification (**Fig. 3.7 B.**) determined a statistically significant reduction in the abundance of CIV (COX) subunits COX5B and MT-CO2, with all averaged values normalised to the relative abundance of the loading control GAPDH per cell line. Interestingly, there was a small but reproducible increase observed in the abundance of NDUFB8 in P1 cells, an accessory subunit of CI not involved in its catalysis but found essential for the oligomerisation of CI with CIII and CIV (Wu *et al.*, 2016), although this difference was not significant by statistical analysis (n = 3). There were no qualitative or quantitative differences observed in levels of CI subunit NDUFS3, CII subunit SDHA, or CIII subunits UQCRC1 and UQCRC2 (n = 2 for each). The relative abundance of LRPPRC, a multifunctional protein with an essential role in the translation and stability of mtDNA-encoded COX subunits (Xu *et al.*, 2004; Cui *et al.*, 2019) was also unaffected in one biological replicate.

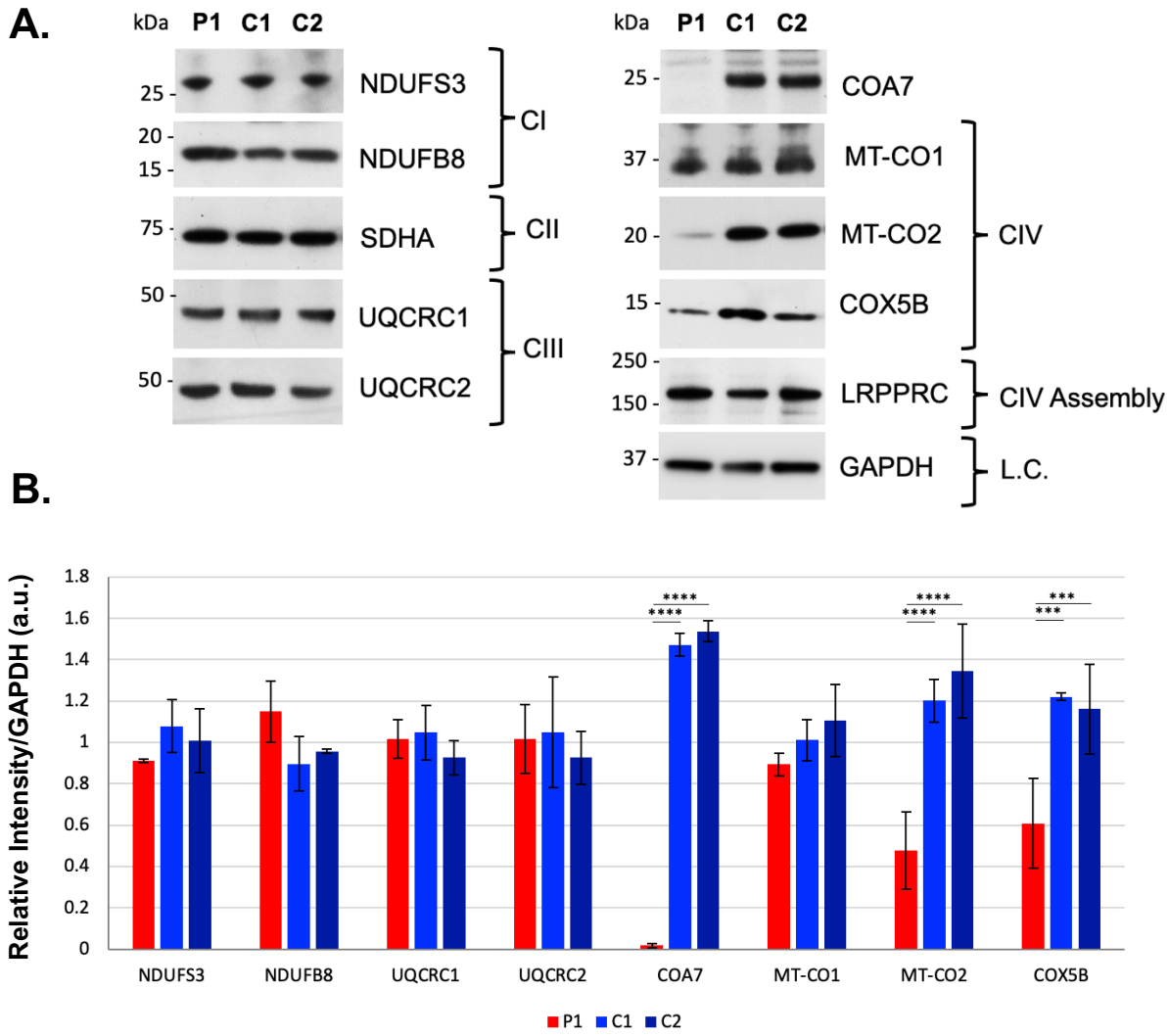

Figure 3.7. Loss of COA7 correlates with decresed steady state levels of COX subunits.

(**A.**) SDS-PAGE was used to resolve 15 µg of whole cell protein lysates from primary patient skin fibroblasts (P1), and two control cell lines (C1 and C2) under denaturing conditions. WB analysis followed for CI subunits NDUFS3, NDUFB6 and NDUFB8, CII subunit SDHA, CIII subunits UQCRC1 and UQCRC2, CIV subunits MT-CO1, MT-CO2, and COX5B, COX assembly factor, LRPPRC, cytosolic loading control (L.C.) GAPDH, and COA7, using the primary antibodies, concentrations and conditions detailed in **Table 2.29**. (**B.**) Densitometric quantification was performed using the Fiji ImageJ software Gel Analysis feature. Data are presented for NDUFS3, UQCRC1, UQCRC2, MT-CO1 and COX5B (all $n = 2$) as mean ± range and NDUFB8, COA7 and MT-CO1 (all $n = 3$) as mean ± SD. Statistical analysis: two-way ANOVA with the *post-hoc* Tukey multiple comparison test applied. Legend: $p < 0.005$ = *** and $p < 0.001$ = ****.

3.3.5 Reduced COX Holocomplex Levels Apparent in Patient Cells

In order to avoid cellular senescence and facilitate an increase in the rate of proliferation of the cell lines, primary fibroblasts were subjected to immortalisation (see **section 2.3.3**). Following the observation that depleted COA7 steady-state level was found in primary patient cells that also displayed reduced quantities of COX subunits, SDS-PAGE was performed as before and the same differences were observed (data not shown). 1D-BNGE was performed in order to determine whether the same trend was true for the abundance of the COX holocomplex and the other protein complexes of the respiratory chain. Mitochondrial protein extracts from both primary (**Fig. 3.8 A.**) and immortalised (**Fig. 3.8 B.**) cell lines were analysed to confirm that the mutant phenotype was not lost or diminished during the immortalisation process. Mitochondrial protein extracts solubilised with 1 % DDM from the primary and immortalised patient cell lines, P1 and P1i, showed considerable reduction in the abundance of monomeric COX (CIV) (immunodetected by MT-CO1) and the $CIII_2$+CIV supercomplex (immunodetected by MT-CO1 for both and also UQCRC2 in the case of the immortalised samples) compared to the respective control. As shown by the relative abundances of CII (immunodetected by SDHB), the loading of both sets of samples was equal. Immortalised samples revealed that there are no observable decreases in abundance of any of the other complexes of the mitochondrial respiratory chain: CI, CII or $CIII_2$. In fact, the quantity of $CIII_2$ appears increased, as has been observed in other COX deficient patients (Baertling *et al.*, 2015).

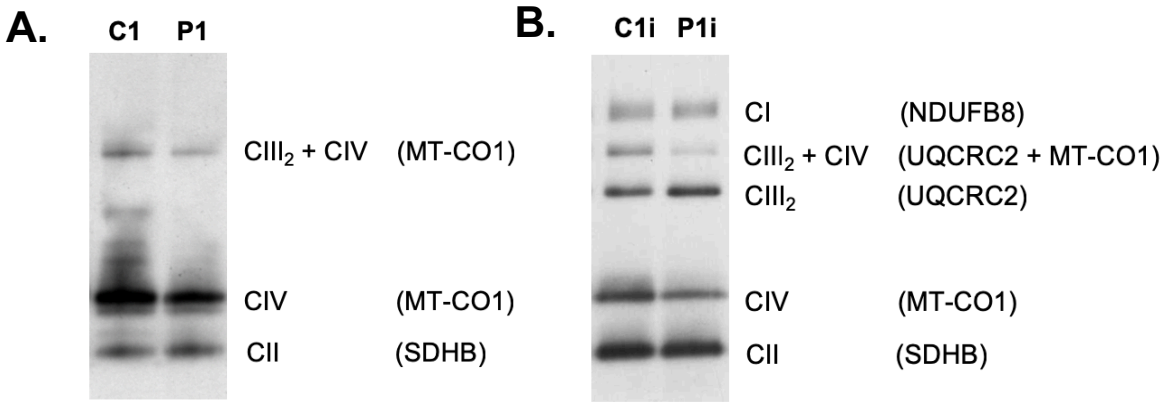

Figure 3.8. Total Abundance of COX and COX-Containing Supercomplexes Are Decreased Following Reduced COA7 Steady-State Levels.

(**A.**) 1D-BNGE was performed with approximately 100 µg of mitochondrial protein from primary patient (P) and control (C) mitoplasts, solubilised with 1 % DDM. Samples were resolved under non-denaturing conditions on a 3 – 12 % gradient Novex® NativePAGE gel. Immunodetection followed for detection of CIV and CII holocomplexes with antibodies indicated in parentheses. (**B.**) The same process was followed for immortalised patient (P1i) and control (C1i) cell lines with subsequent 1D-BNGE and WB analysis using primary antibodies against NDUFB8 (CI), UQCRC2 (CIII), MT-CO1 (CIV) and SDHB (CII) (for antibody details, see **Table 2.29**).

2D-BNGE was then performed to determine whether the decrease in COX amount was due to stalled assembly or destabilisation of COX before the point of complete assembly. Protein samples from immortalised patient (P1i) and control (C1i) skin fibroblasts were solubilised from the IMM of mitoplasts with 1 % DDM. Samples were then resolved in the first dimension as in **Fig. 3.8,** and then subjected to further separation of the individual members of each complex in the second dimension under denaturing conditions by SDS-PAGE. Immunodetection of the mtDNA-encoded COX subunits MT-CO1 and MT-CO2 and nDNA-encoded subunit COX5A followed, with CII subunit SDHB acting as a loading control. As shown in **Fig. 3.9**, total abundance of COX intermediates and subassemblies, monomeric COX, and two COX-containing supercomplex species, $CIII_2$ + CIV and CI + $CIII_2$ + CIV, were all reduced in the patient compared to the control. Importantly, there is no accumulation or abnormal segregation of COX intermediates in the patient. Rather, we observed a 'global' reduction in the abundances of COX intermediate species, the holocomplex and COX-containing supercomplexes. Additionally, COA7 could not easily be detected in 2D-BNGE due to nonspecific protein recognition of the polyclonal endogenous antibody, so it was not possible to determine whether COA7 co-migrated with fully assembled COX at this time.

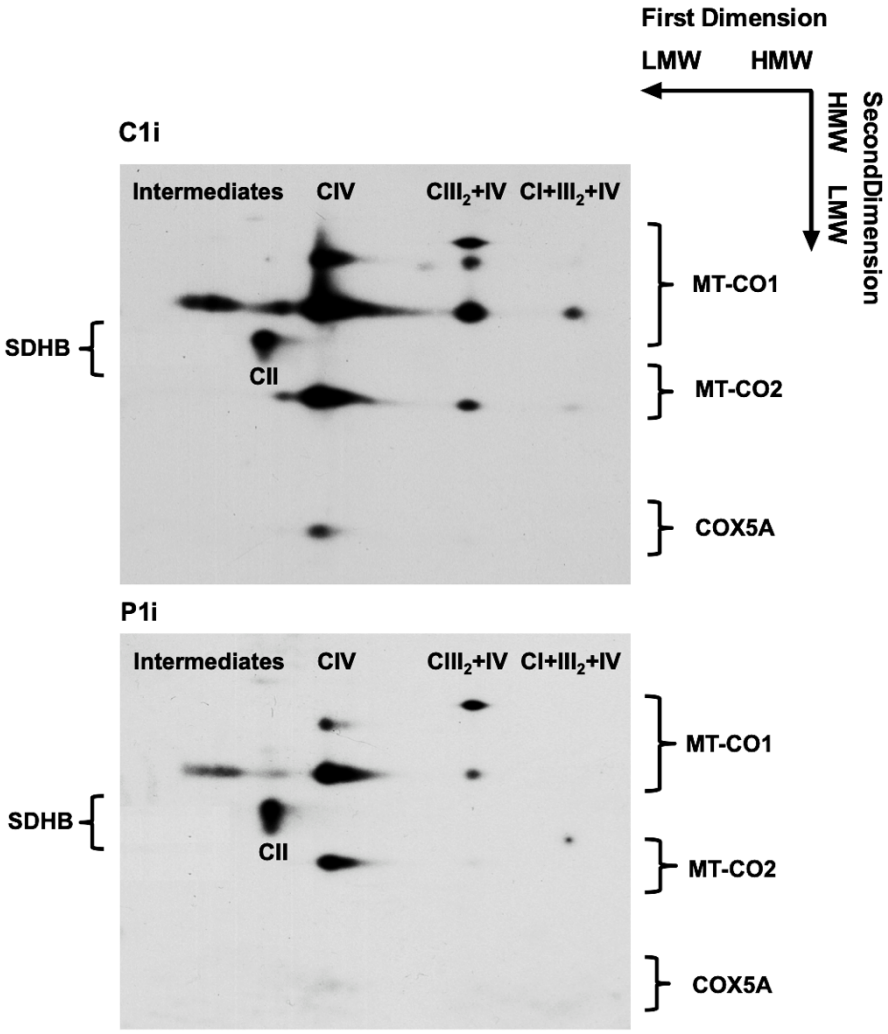

Figure 3.9. 2D-BNGE shows global reduction of COX intermediates, COX holocomplex and COX-containing supercomplexes in immortalised patient cells

2D-BNGE was performed with approximately 200 µg of 1 % DDM-solubilised mitochondrial protein from immortalised patient (P1i) and control (C1i) skin fibroblast mitoplasts. Samples were run in the first dimension on NativePage 3-12 % gradient gels (as per **section 2.6.3**), and in the second dimension under denaturing conditions by SDS-PAGE (see **section 2.6.2**), with 1X MOPS running buffer. MT-CO1, MT-CO2, COX5A and SDHB primary antibodies were used for immunodetection (see **Table 2.29** for antibody manufacturer details, and concentrations and conditions used for each)**.** LMW = Low Molecular Weight, and HMW = High Molecular Weight.

3.3.6 Immortalised Patient Skin Fibroblasts Have Isolated COX Deficiency

As part of the mitochondrial disease diagnostic pipeline, respiratory chain enzymatic activities relative to that of citrate synthase (CS) were measured in both cutaneous and skeletal muscle biopsies. COX showed 33 % and 36 % residual activities with respect to the control reference levels, in skin fibroblasts and skeletal muscle respectively; whereas the activities of the remainder of the mitochondrial respiratory chain complexes were within the normal ranges. Following immortalisation we confirmed the conservation of the COX deficiency in the patient cell line (P1i). As shown in **Fig. 3.10**, P1i COX/CS activity was significantly decreased compared to both C1i (p = 0.0045) and C2i (p = 0.0093) controls, with approximately 37 % residual activity.

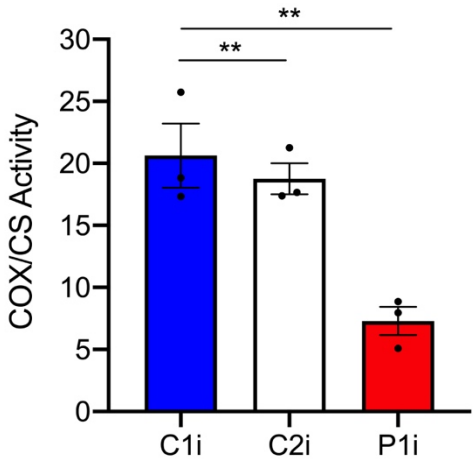

Figure 3.10. COX deficiency was validated in P1i skin fibroblasts.

COX activity was determined spectrophotometrically for immortalised patient skin fibroblasts (P1i) compared with two control cell lines (C1i and C2i), as described in **section 2.7.1**, and normalised against the activity of citrate synthase (CS) per cell line. Data is presented as mean ± SEM for n = 3 replicates. One-way ANOVA with the *post hoc* Tukey multiple-comparison test confirmed statistically significant reduction in P1 COX/CS activity compared to both C1i (p = 0.0045) and C2i (p = 0.0093) controls, with approximately 37 % residual activity.

3.3.7 Stable Expression of *COA7^{WT}* Rescues COX Abundance and Enzymatic Activity

In order to determine whether the loss-of-function mutations in *COA7* were indeed the cause of the observed isolated COX deficiency in the patient cells, a functional complementation assay was performed using the wildtype (*COA7^{WT}*) cDNA sequence. For this, patient-derived (P1i) and control (C1i) immortalised skin fibroblasts were transduced with lentiviral particles containing an expression vector encoding the wild-type *COA7* cDNA sequence (COA7^{WT}-pWPXLd-*Ires-Puro^{R}*). As a negative control, the pWPXLd-*Ires-Puro^{R}* empty vector (EV) was used to discard any possible effects caused merely by the transduction and selection processes. The COA7^{WT}-pWPXLd-*Ires-Puro^{R}* plasmid was generated as per **sections 2.2.9 – 2.2.12** and the correct insertion of the COA7^{WT} cDNA sequence was confirmed by Sanger sequencing prior to lentiviral particle generation. Lentiviral particles were produced in HEK 293T cells, by co-transfection of the pWPXLd-based expression vectors with the lentiviral second generation pSPAX2 packaging and pMD2.G envelope plasmid vectors (Salmon *et al.*, 2000). Subsequent transduction and antibiotic selection with 1 µg/ml puromycin yielded 4 cell lines: C1i-COA7^{WT}, C1i-EV, P1i-COA7^{WT}, and P1i-EV.

SDS-PAGE, Western Blot and immunodetection were performed to determine the steady-state protein levels of COA7 relative to various subunits of the other OXPHOS complexes (CI, CII, CIII and CV) for immortalised fibroblast patient, P1i, and control, C1i, cell lines transduced with either the *COA7^{WT}* cDNA sequence or the empty vector (EV) negative control (**Fig. 3.11**). Firstly, overexpression of COA7 in C1i-COA7^{WT} and P1i-COA7^{WT} cell lines was successful, and yielded a similar protein abundance in both. Secondly, the levels of MT-CO2 were clearly increased in P1i-COA7^{WT} to within normal levels compared to C1i and C2i control cell lines. There is no such complementation in the P1i-EV negative control. This indicates that the absence of COA7 in the patient cells is directly related to the observed low levels of MT-CO2. The steady-state levels of COX subunits MT-CO1 and COX5A are not as severely affected as those of MT-CO2, suggesting that this subunit is a major target of COA7. Lastly, there were no observable effects of COA7 absence or complementation on relative abundances of individual subunits belonging to the other OXPHOS complexes: NDUFS3 (CI), SDHA (CII), UQCRC2 (CIII) or ATP5A (CV), all relative to the loading control GAPDH.

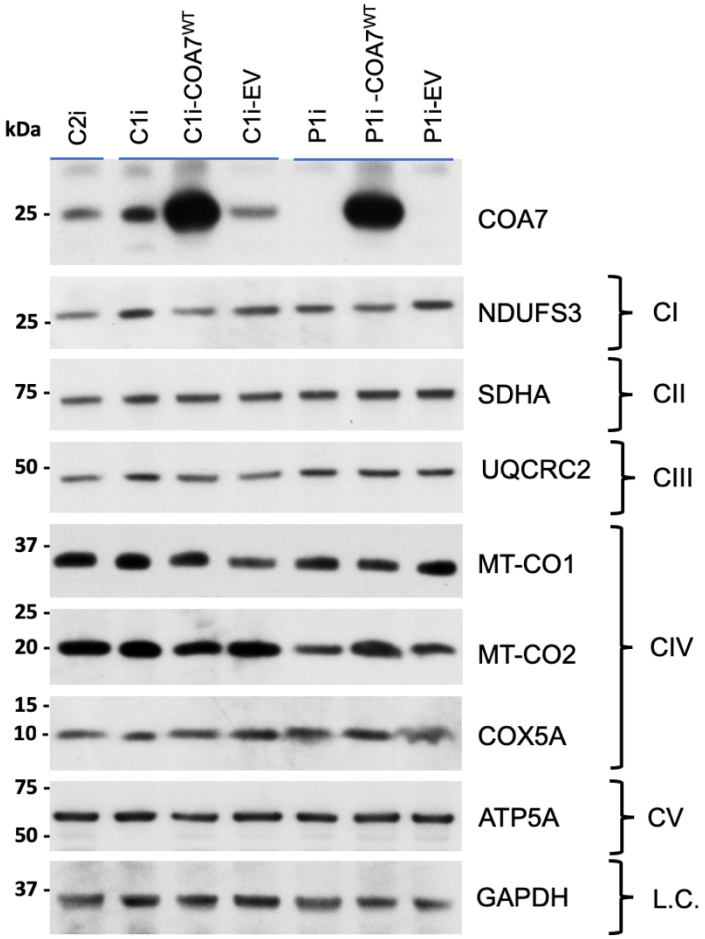

Figure 3.11. Complementation of immortalised patient fibroblasts with *COA7^{WT}* successfully restores MT-CO2 steady-state levels.

10 µg of whole cell protein lysates from C1i and C2i controls, C1i-COA7^{WT}, C1i-EV, P1i, P1i-COA7^{WT} and P1i-EV cell lines were separated by size under denaturing conditions by SDS-PAGE. WB analysis followed to detect the relative abundances of COA7, CI subunit NDUFS3, CII subunit SDHA, CIII subunit UQCRC2, CIV subunits MT-CO1, MT-CO2, and COX5A, CV subunit ATP5A and a GAPDH loading control (L.C.) (see **Table 2.29** for primary antibody details, and concentrations and conditions used) (*n* = 1 for each).

3.3.8 *COA7*^{WT} Complementation Rescues COX Assembly in Immortalised Patient Cells

1D-BNGE and Western blot analysis was used to observe changes in the relative abundances of fully assembled COX in the *COA7*^{WT}-complementated immortalised skin fibroblast cell lines. As is evident in **Fig. 3.12**, P1i-COA7^{WT} cells have an increased amount of COX relative to the P1i cells, within the range of both C1i and C2i controls. Interestingly, overexpressing *COA7*^{WT} in a control cell line, C1i-COA7^{WT}, produced a reduction in the abundance of the COX holocomplex, suggesting that the COA7 steady-state level must exist in a physiological range with too little or too much COA7 affecting COX assembly or stability. Anti-SDHB immunodetection of CII was used as a loading control.

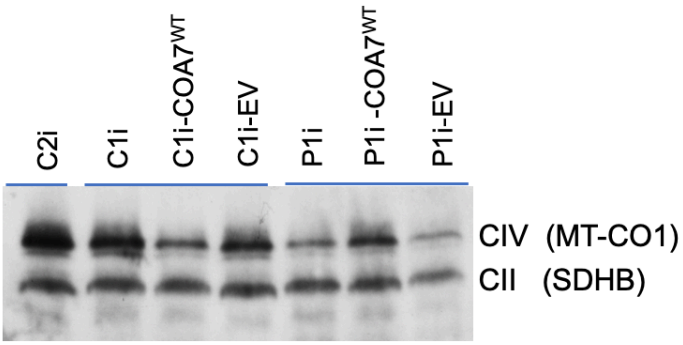

Figure 3.12. COA7^{WT} Rescues COX Abundance in Immortalised Patient Fibroblasts.

1D-BNGE was performed with approximately 100 µg of mitochondrial protein from C1i, C2i, C1i-COA7^{WT}, C1i-EV, P1i, P1i-COA7^{WT} and P1i-EV immortalised skin fibroblast cell lines, solubilised with 1 % DDM. Samples were resolved as per **section 2.6.3**. Immunodetection of COX and CII complexes was performed by WB analysis with primary antibodies against MT-CO1 (CIV) and SDHB (CII) (see **Table 2.29** for primary antibodys and concentrations used).

Furthermore, 2D-BNGE analysis (**Fig. 3.13**) revealed an overall increase in levels of monomeric COX and in the $CIII_2$ + COX supercomplex, through immunodetection of MT-CO1 and MT-CO2 subunits, for P1i-COA7^{WT} cells compared to the negative control cell line, P1i-EV. There also seems to be more intermediate species as immunodetected by MT-CO1, with a pattern comparable to the control C1i cell line (**Fig. 3.9**). Separately, immunodetection with an anti-HA primary antibody for patient and control cells overexpressing COA7^{HA} revealed that COA7 does not co-migrate with any of the mature respiratory chain protein complexes, including COX (**Fig. 3.14**). Instead it was only immunodetected as a single spot focalising to the low molecular weight portion of the gel. It was reproducibly not found to co-localise with any high molecular weight COX intermediates or subassemblies.

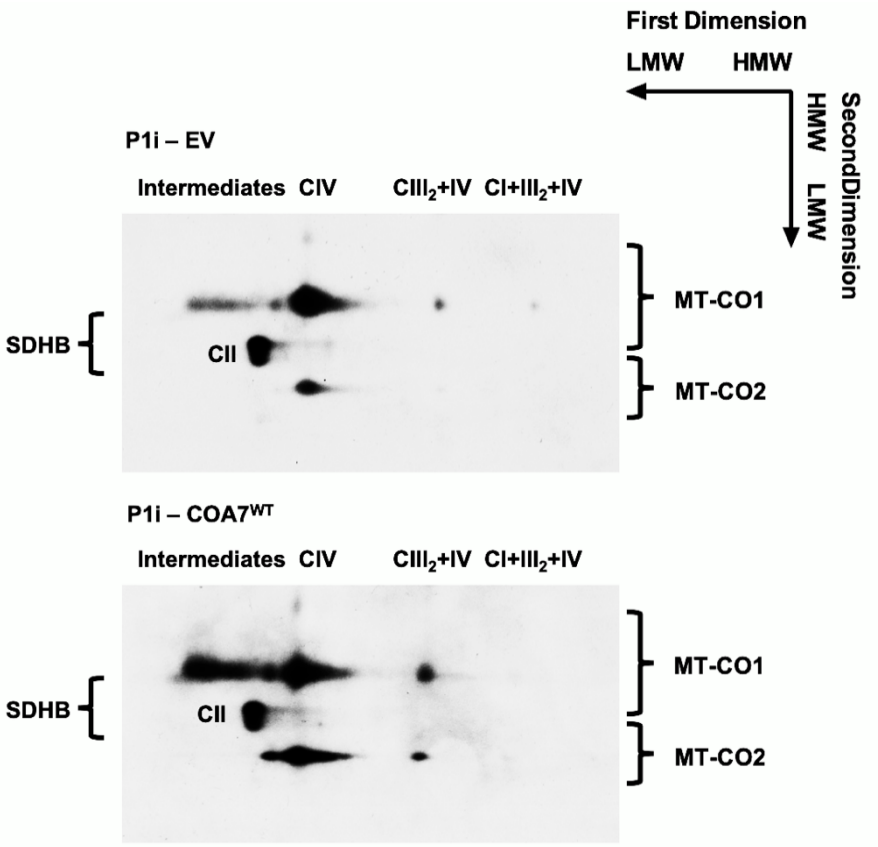

Figure 3.13. 2D-BNGE shows recovery of the levels of COX intermediates, COX and COX-containing supercomplexes in patient cells stably overexpressing *COA7^{WT}*.

2D-BNGE was performed with approximately 200 µg of DDM-solubilized mitochondrial protein prepared from immortalised skin fibroblast patient cells transduced with an empty vector (P1i-EV) and patient cells stably overexpressing *COA7^{WT}* (P1i-COA7^{WT}). Samples were resolved in the first dimension using NativePage 3-12 % gradient gels as per **section 2.6.3**, and in the second dimension under denaturing conditions by SDS-PAGE (see **section 2.6.2**), with 1X MOPS running buffer. MT-CO1, MT-CO2, and SDHB primary antibodies were used for immunodetection (see **Table 2.29** for antibody manufacturer details, and concentrations and conditions used for each)**.** LMW = Low Molecular Weight, and HMW = High Molecular Weight.

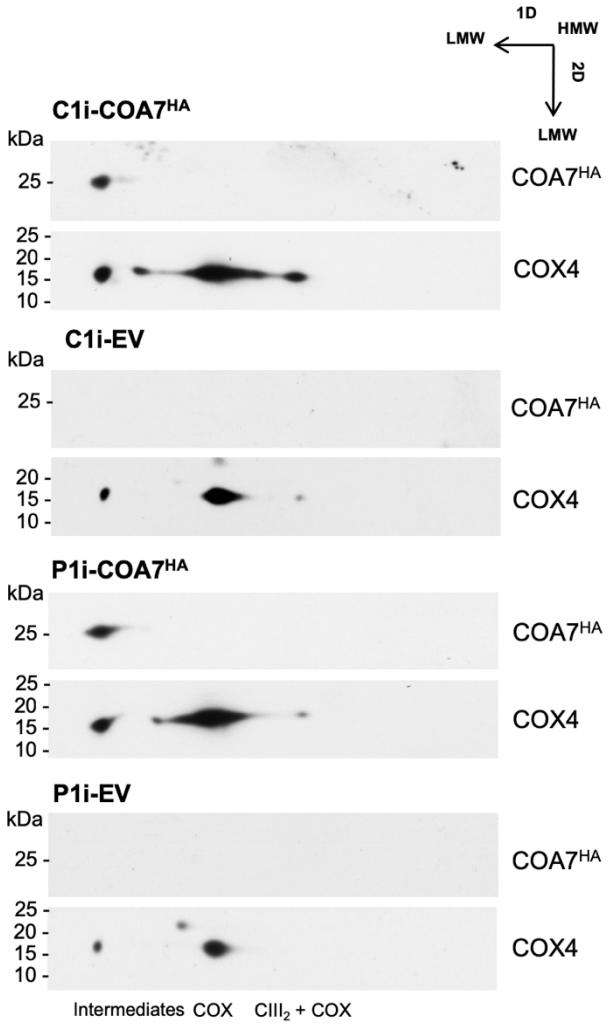

Figure 3.14. 2D-BNGE shows no co-migration of COA7 with COX and a COX-containing supercomplex in patient cells stably overexpressing *COA7^{HA}*.

2D-BNGE was performed with approximately 200 µg of DDM-solubilized mitochondrial protein prepared from immortalised skin fibroblast patient or control cells stably overexpressing *COA7^{HA}* (P1i-COA7^{HA} or C1i-COA7^{HA}) or empty vector control cell lines for each (P1i-EV and COA7-EV). Samples were resolved in the first dimension using NativePage 3-12 % gradient gels as per **section 2.6.3**, and in the second dimension under denaturing conditions by SDS-PAGE (see **section 2.6.2**), with 1X MOPS running buffer. Anti-HA and anti-COX4 primary antibodies were used for immunodetection (see **Table 2.29** for antibody manufacturer details and concentrations used for each)**.** LMW = Low Molecular Weight, and HMW = High Molecular Weight.

3.3.9 *COA7^{WT}* Complementation Rescues COX Enzymatic Activity

Following on from the observed rescue of COX subunit levels (**Fig 3.11**), COX abundance (**Fig 3.12**), and the quantity of COX intermediate assembly species and supercomplexes (**Fig 3.13**), COX/CS specific activity was measured spectrophotometrically for C1i, C1i-COA7^{WT}, C1i-EV, P1i, P1i-COA7^{WT} and P1i-EV immortalised skin fibroblast cell lines (**Fig 3.15**).

COX/CS activity in patient cells stably overexpressing *COA7*^{WT} (P1i-COA7^{WT}) was significantly increased, relative to patient cells transduced with an empty vector control (P1i-EV), which remained as low in quantity as for the non-transduced patient cells, P1i. Ultimately, the stable expression of *COA7*^{WT} in patient-derived cells is able to restore COX activity to nearly normal levels, proving that the compound heterozygous mutations found in *COA7* (NM_023077.3: c.410A>G;287+1G>T) are indeed responsible for the observed COX deficiency in the patient.

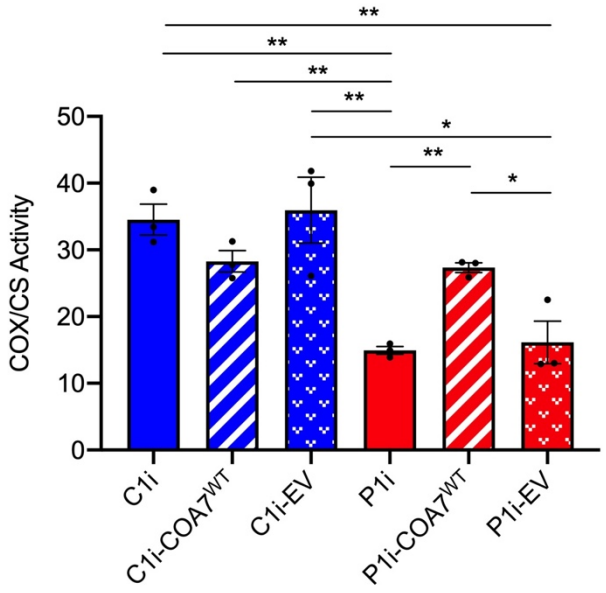

Figure 3.15. COX activity is rescued in patient cells after complementation with *COA7*^{WT}.

COX activity was determined spectrophotometrically (see **section 2.7.1**) for C1i, C1i-COA7^{WT}, C1i-EV, P1i, P1i-COA7^{WT} and P1i-EV immortalised skin fibroblast cell lines. COX specific activities were normalised against the relative activity of citrate synthase (CS). Data are presented as mean ± SEM for n = 3 replicates per cell line. * $p < 0.05$, ** $p < 0.01$, determined by one-way ANOVA with the *post hoc* Tukey multiple-comparison test applied.

3.3.10 Endogenous COA7 Localises Specifically to the IMS

Following the discovery of the first pathogenic mutations in *COA7*, we sought to confirm the protein's submitochondrial localisation. As a first approach, we used trypsin digestion of mitoplast fractions generated with two different concentrations of digitonin. After protease digestion, the samples were separated by SDS-PAGE and analysed by Western blotting and immunodetection (**Fig. 2 F.**, Martinez Lyons *et al*. 2016). In our analyses, COA7 was completely protected from trypsin digestion in all mitoplast fractions, similarly to the MM marker CS, whereas the IMS marker cytochrome *c* was clearly reduced. This led us to conclude localisation to the MM, rather than the IMS as originally proposed by Kozjac-Pavlovic *et al.* However, recent evidence that COA7 is an interactor of CHCHD4/MIA40, the principal component of the disulphide-relay system responsible for the import and targeting of IMS

proteins (Mohanraj, *et al.* 2019), led us to reconsider this finding and attempt to resolve this contradiction. Mitochondrial sub-fractionation by hypotonic shock and protease digestion assays proved not to be trivial. COA7 was found to be fairly protease-insensitive and so often appeared unaffected in all fractions regardless of treatment. Secondly, finding a suitable hypotonic/digitonisation condition which would entirely disrupt the OMM whilst leaving the IMM intact was a challenge. Therefore, we opted for two biochemical approaches, one using protease digestion and the other only using OMM solubilisation by digitonin. In addition, we used super-resolution microscopy of HA-tagged COA7 in a $COA7^{HA}$ overexpressing HeLa cell line relative to markers for each of mitochondrial compartments to resolutely confirm the intramitochondrial localisation of COA7.

For the first of the biochemical experiments, a range of digitonin (DIG) concentrations were used to gradually open the OMM of isolated mitochondria from HEK 293T cells, performed by 10-minute incubations on ice in each case, and both the pellet and supernatant fractions were collected after ultracentrifugation (**Fig. 3.16 A.**). COA7 is detectable in the supernatant fractions from 150 µg/ml DIG onwards, with associated decrease in the pellet fractions. This is similar to the behaviour of OMM protein translocase of the outer mitochondrial membrane 20 (TOMM20) and IMS proteins apoptotic-inducing factor (AIF) and cytochrome c (CYT *C*). Importantly, the COX proteins MT-CO2 and COX4, resident in the IMM, and the soluble MM protein superoxide dismutase 2 (SOD2), were not released into the supernatant with any amount of digitonin. Secondly, when the same procedure was followed but with the subsequent addition of 150 µg/ml trypsin to each fraction for 30 min at RT (**Fig. 3.16 B**.), TOMM20 was quickly digested, even without the addition of DIG, and the IMS proteins AIF and CYT *C,* IMM protein COX4 and MM protein SOD2 were degraded from 75 or 150 µg/ml DIG onwards. COA7 followed this pattern. Taken together, these two parallel experiments strongly indicate that COA7 is an IMS protein. Due to its protease resistance, small amounts of the protein are still detectable even after incubation with 1.2 mg/ml DIG + 150 µg/ml trypsin and after addition of 1 % Triton + 150 µg/ml trypsin. However, a smaller band is detectable in the fractions incubated with > 600 µg/ml DIG and in the 1 % Triton + trypsin control, indicating partial digestion of the protein. These results explain the lack of protease digestion in our original experiment, given that only 20 and 50 µg/ml DIG concentrations were used as standard practice and no control for complete membrane solubilisation (1 % Triton) was used on that occasion. In is also worth mentioning that COA7 was ever only found in the mitochondria, and never detected in the cytoplasmic protein fractions.

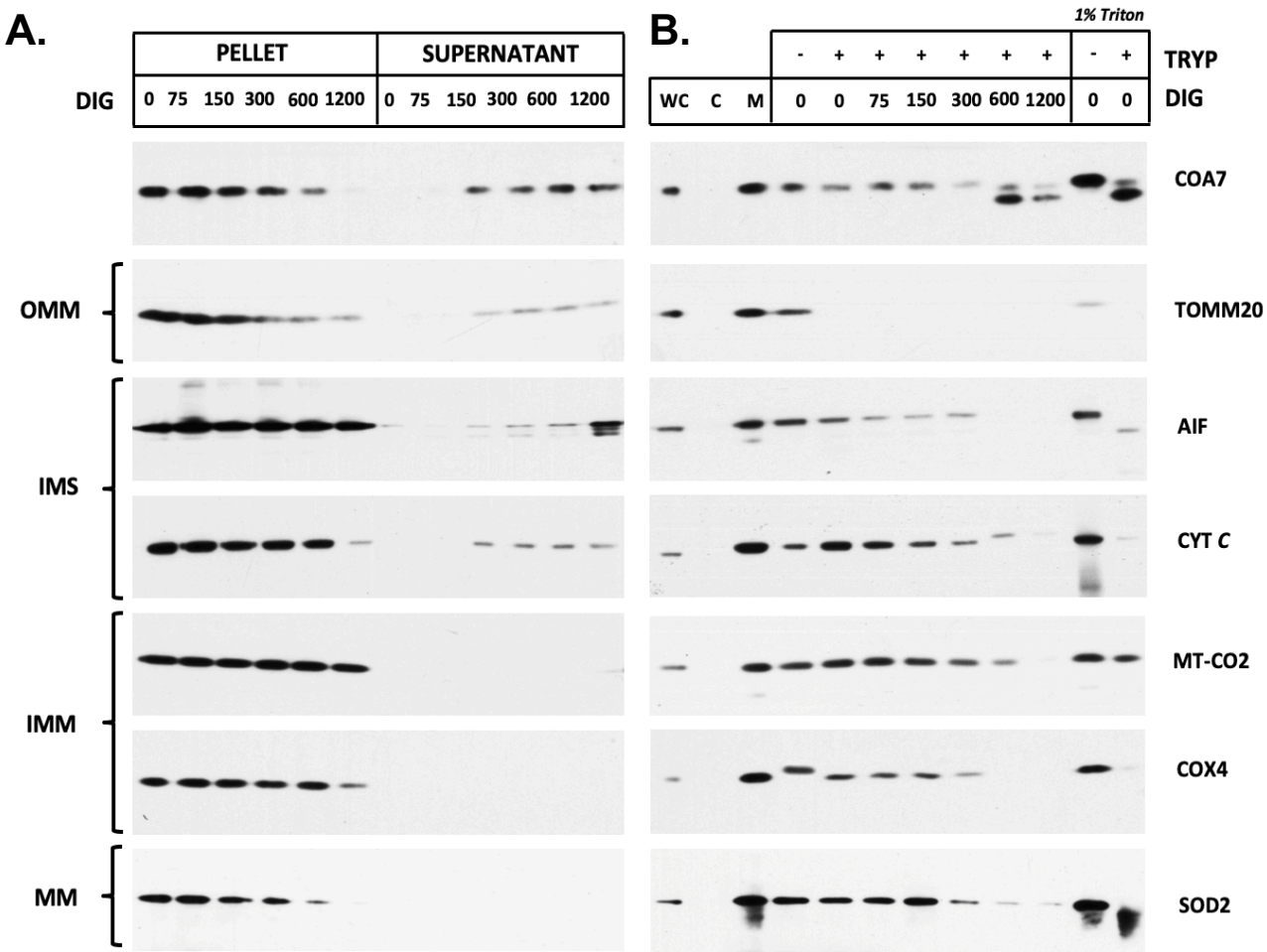

Figure 3.16. HEK293 Mitochondrial sub-fractionation and protease protection assays.

Mitochondria were isolated from HEK 293T cells as previously described (Fernández-Vizarra *et al.*, 2010) and the mitochondrial preparation was divided into multiple aliquots of 200 µg of mitochondrial protein each. (**A.**) Western blot and immunodetection analysis of the pellet and supernatant samples from isolated mitochondria solubilised with increasing concentrations of DIG: 0, 75, 150, 300, 600 and 1,200 µg/ml. (**B.**) Western blot and immunodetection analysis from mitochondria solubilised with increasing amounts of DIG (as in **A.**) or with 1 % Triton X-100, and further treated with 150 µg/ml of trypsin for 30 min at RT, as indicated. WC: Whole cell protein lysate, C: cytoplasmic fraction (post-mitochondrial supernatant), M: mitochondrial fraction.

Super-resolution fluorescence microscopy was employed to independently determine the submitochondrial localisation of COA7. All cell preparation, imaging and subsequent analyses were performed by Dr. Cristiane Benincá. As shown in **Fig. 3.17**, HA-tagged COA7 co-localises with the IMS marker SMAC (see insets), a part of the SMAC/DIABLO dimer involved in caspase activation in the apoptotic pathway (Du *et al.*, 2000). The signal corresponding to $COA7^{HA}$ was clearly distinct from that of the OMM marker TOMM20, the IMM marker COX8A, and a MM-localising photoactivatable GFP construct, mtPAGFP, which all displayed significantly lower colocalisation coefficients than SMAC (**Fig. 2 D.**, Mohanraj *et al*. 2019).

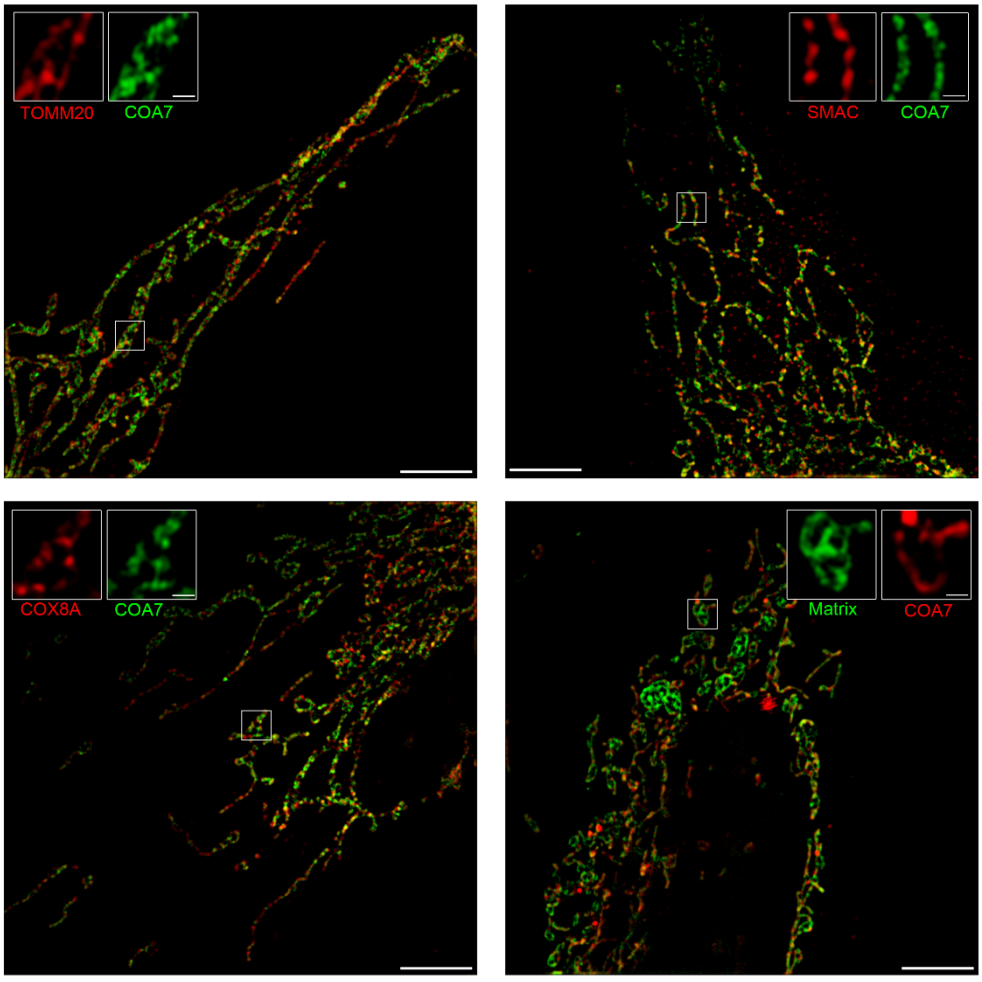

Figure 3.17. HeLa cells show COA7 co-localisation with an IMS marker.

Immunofluorescence and super-resolution microscopy was performed as described (Mohanraj *et al.*, 2019). N-SIM super-resolution micrographs show 0.6 µm Maximum Intensity Projection (0.15 µm per Z-stack) of HeLa cells expressing COA7-HA, immunostained for the OMM marker TOMM20-DsRed, IMS marker SMAC/DIABLO, IMM marker COX8A-DsRed, or transfected with a matrix targeted photoactivatable GFP construct (mtPAGFP) (MM). Scale bars: 5 µm and 0.5 µm in inset images. Images acquired and post-processed entirely by Dr. Cristiane Benincá.

3.4 Conclusions

This work: 1) confirmed the pathogenicity of two novel *COA7* mutations, 2) established a role for COA7 in maintaining normal COX stability and activity, and 3) unequivocally determined the subcellular and intramitochondrial localisation of COA7 to the IMS.

Compound heterozygous mutations in *COA7* (NM_023077.3:c.410A>G;c.287+1G>T) were detected by WES and downstream bioinformatic filtering in a proband presenting with progressive leukoencephalopathy and isolated COX deficiency. Sanger sequencing analysis of the *COA7* gene of the proband and her parents confirmed the presence of the biallelic mutations and allowed assignment of parental origin to each. These were a paternally-inherited A>G transition mutation in exon 3 (NM_023077.3:c.410A>G;), coding for a tyrosine to cysteine amino acid substitution (NP_075565.2:p.Tyr137Cys) and a maternally-inherited G>T transversion at the exon 2/intron 2 splice site junction (NM_023077.3:c.287+1G>T) with unknown consequence on the resulting mRNA transcript(s) and protein primary sequence(s). Two different aberrant mRNA transcripts were determined to be expressed in the patient following RNA extraction and retrotranscription to cDNA; one lacked the entirety of exon 2, arising from the maternal allelic variant, and resulted in an in-frame deletion of 47 amino acids from position 37 of the primary protein sequence (NP_075565.2:p.Cys37_Gly84del), and the paternally inherited transcript variant encoded a TAC → TGC codon change, leading to a tyrosine to cysteine amino acid substitution (NP_075565.2:p.Tyr137Cys). Both variants are predicted to be strongly pathogenic by computational analyses. The maternal variant disrupted the majority of the first and part of the second predicted SEL1 domains. The paternal mRNA transcript variant encoded a change to a highly conserved tyrosine residue within the third SEL1 domain.

Indeed, primary and immortalised patient skin fibroblasts revealed total absence of COA7 steady-state level by SDS-PAGE. The abundance of COX subunits MT-CO2, COX5B, and to a lesser extent, MT-CO1, were decreased. Subunits from the other respiratory chain complexes and the COX assembly factor LRPPRC revealed no alterations. 1D-BNGE showed a clear reduction in the abundance of free COX and a COX-containing supercomplex species ($CIII_2$ + CIV). No accumulation of COX intermediates or subassemblies were detectable by 2D-BNGE, and COA7 was not found to co-migrate with the mature COX holocomplex, but the same global reduction in COX subunit quantities observed by SDS-PAGE was evident. Biochemical evaluation of cultured immortalised patient fibroblasts confirmed the significant COX deficiency of approximately 66 %, in line with that observed in isolated mitochondria from patient cutaneous and skeletal muscle biopsies.

Lentiviral complementation with *COA7*^{WT} successfully rescued COX abundance and its enzymatic activity to normal levels. *COA7*^{WT} overexpression in a wildtype fibroblast control cell line resulted in reduced COX abundance and some reduction in enzymatic activity, suggesting that overexpression as well as depletion of COA7 is deleterious. Patient fibroblasts complemented with COA7^{WT} showed no difference in the abundances of MT-CO1 and COX5A COX subunits, involved in early stage COX biogenesis, but revealed a marked increase in the abundance of MT-CO2 to control levels, suggesting that the main target of COA7 is MT-CO2 and/or the MT-CO2 module, inserted in the intermediate stages of COX assembly (**Fig. 1.5**).

Lastly, a combination of super-resolution microscopy and cellular fractionation and protease digestion experiments confirmed that the intracellular localisation of COA7 is the IMS.

The publication of this research (Martinez Lyons *et al.* 2016) led to the subsequent identification and diagnosis of other mitochondrial disease patients whose symptoms were a result of pathogenic mutations in *COA7*, all of whom exhibited COX deficiency, leukodystrophy and spinal cord atrophy (Higuchi *et al.*, 2018). It also prompted the characterisation of the mitochondrial import of the COA7 protein, which does not contain a conventional mitochondrial targeting sequence, into the IMS, as well as research into the detrimental effects of the mutated variants in the import process (Mohanraj *et al.*, 2019). These findings and their interpretations will be discussed in **Chapter 8**.

Chapter 4

Introducing *TMCO6*, a Gene Found Mutated in a Mitochondrial Disease Patient with Severe Complex I Deficiency

4.1 Introduction

The work described in this chapter concerns TMCO6 (Transmembrane and Coiled-Coil Domains 6; NC_000005.10: 40,596,529–140,647,411), an uncharacterised, nuclear-encoded protein found only in vertebrates, including mammals, birds, reptiles, amphibians, and bony and cartilaginous fishes (Homologene ID: 12431). The *TMCO6* cDNA sequence was initially discovered through genome-wide mRNA screening of human and mouse transcriptomes (Strausberg *et al.*, 2002; Ota *et al.*, 2004). It has since been found to be expressed in all human tissues (https://www.proteinatlas.org/ENSG00000113119-TMCO6/tissue). However, to date, no seminal literature or research has been published regarding TMCO6, its role in normal cellular physiology or human disease pathology. The first aim of this work was to perform an *in silico* investigation into *TMCO6* to compile the available information regarding its gene structure, conservation, different protein isoforms and key structural features. The second aim was to assess the molecular and metabolic consequences of a novel point mutant variant identified in *TMCO6* (NM_018502: c.271C>T) by WES in a Bangladeshi male adolescent proband using patient-derived skin fibroblasts as the bases for all experiments.

4.2 Results

4.2.1 An Introduction to *TMCO6*

The human *TMCO6* gene (Locus: Chr 5, q31.2; NC_000005.10: 140,596,529 – 140,647,411) contains 12 coding exons and gives rise to two mRNA isoforms, termed here as *TMCO6.1* (NM_018502.5, 493 aa product) and *TMCO6.2* (NM_001300980.1, 499 aa product). These isoforms originate from alternative splicing at the exon 6/exon 7 slice junction (**Fig. 4.1**) with gene products TMCO6.1 and TMCO6.2 differing by six in-frame amino acids (PASASS) from position 230 of the primary protein sequence. The human TMCO6 protein has been found to be ubiquitously expressed in all tissues (https://www.proteinatlas.org/ENSG00000113119-TMCO6/tissue); however, it is not known whether there is tissue-specificity, difference in levels of expression, or separate functional roles for either isoform.

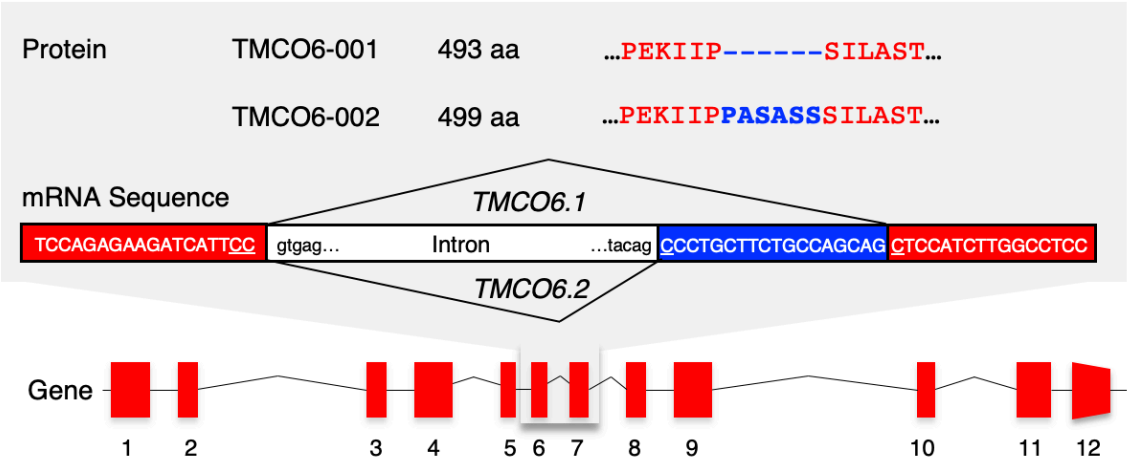

Figure 4.1 *TMCO6* encodes two protein isoforms by alternative splicing.

The *TMCO6* gene (Locus: Chr 5, q31.2; NC_000005.10: 140,596,529 – 140,647,411) contains 12 exons, which produce two mRNA isoforms, *TMCO6.1* (NM_018502.5, 493 aa product) and *TMCO6.2* (NM_001300980.1, 499 aa product) by alternative splicing at the exon 6/exon 7 slice junction.

At the protein level, TMCO6 is predicted to contain several structural features (as annotated in **Fig 4.2**). An arginine-rich region spans the first 110 amino acids of the protein, with a fifth of these (21 in total) in both TMCO6.1 and TMCO6.2 being arginine residues. Mitochondrial targeting signal (MTS) prediction programs did not predict the presence of an N-terminal MTS. Instead, the first 52 amino acids are annotated to make up an importin-β binding (IBB) domain (Interpro ID: IPR002652), typically found in members of the α-importin protein family, all known members of which localise to the nucleus. These proteins are known to form a heterodimer

complex with β-importin. Whilst β-importin mediates interaction with the nuclear pore complex, α-importin binds the nuclear localisation signal (NLS) of their cargo allowing for import into the nucleus from the cytosol (Lott and Cingolani, 2011). In addition to the IBB sequence predicted in TMCO6, a related structural motif, the armadillo (ARM) domain, is also present in this protein. Within both isoforms, there are up to 5 predicted ARM repeats (InterPro ID: IPR000225), a ~42 amino acid motif that does not show amino acid conservation, but characteristically folds into two or three separate α-helices (Huber, Nelson and Weis, 1997). Multiple tandem ARM repeats typically form a superhelical solenoid structure (ARM-type fold, Interpro: IPR016024), and can mediate a wide range of intracellular functions that require protein-protein interaction (Choi and Weis, 2005). Although the tertiary structure of TMCO6 is unknown, and structural homology modelling programs such as SWISS-MODEL did not return any significant matches from input of either TMCO6.1 or TMCO6.2 query sequences, the PSIPRED 2.0 (Jones, 1999) secondary structure prediction tool confidently predicted the presence of 34 α-helices, 27 of which were assigned the highest possible confidence score (indicated by the blue bars above the corresponding amino acids in **Fig. 4.2**). A further 6 α-helices were predicted with less confidence, and are not included. Overall, this secondary structure fits well with the secondary structure described in proteins from the α-importin family.

TMCO6 was initially described as a transmembrane protein, giving it its name. In support of this, the online tool Protter (Omasits *et al.*, 2014) predicted the presence and distribution of two transmembrane regions (positions 338–358 and 386–406) towards the C-terminus of the protein. Another prediction tool, SACS MEMSAT2, only predicts one transmembrane domain in a different region (positions 274-290). However, others, including the Human Protein Atlas Transmembrane prediction tool, predict no transmembrane regions. It is worth noting that none of the α-importin proteins described to date are known to be membrane-embedded or membrane-associated proteins. Only experimental evidence will be able to provide an answer to this apparent incongruity (described in **Chapter 5**). In summary, TMCO6 is found in humans in two main isoforms, TMCO6.1 and TMCO6.2, which are both predicted to contain a large number of α-helices. The majority of these α-helices are likely to make up several ARM repeats, in turn leading to a solenoid-like tertiary structure. What is still unknown is whether TMCO6 does indeed localise to the nucleus, or if it localises to one or more other cellular compartments. Additionally, it is unclear whether TMCO6 contains at least one transmembrane region or if it is soluble, as are all known members of the α-importin protein family.

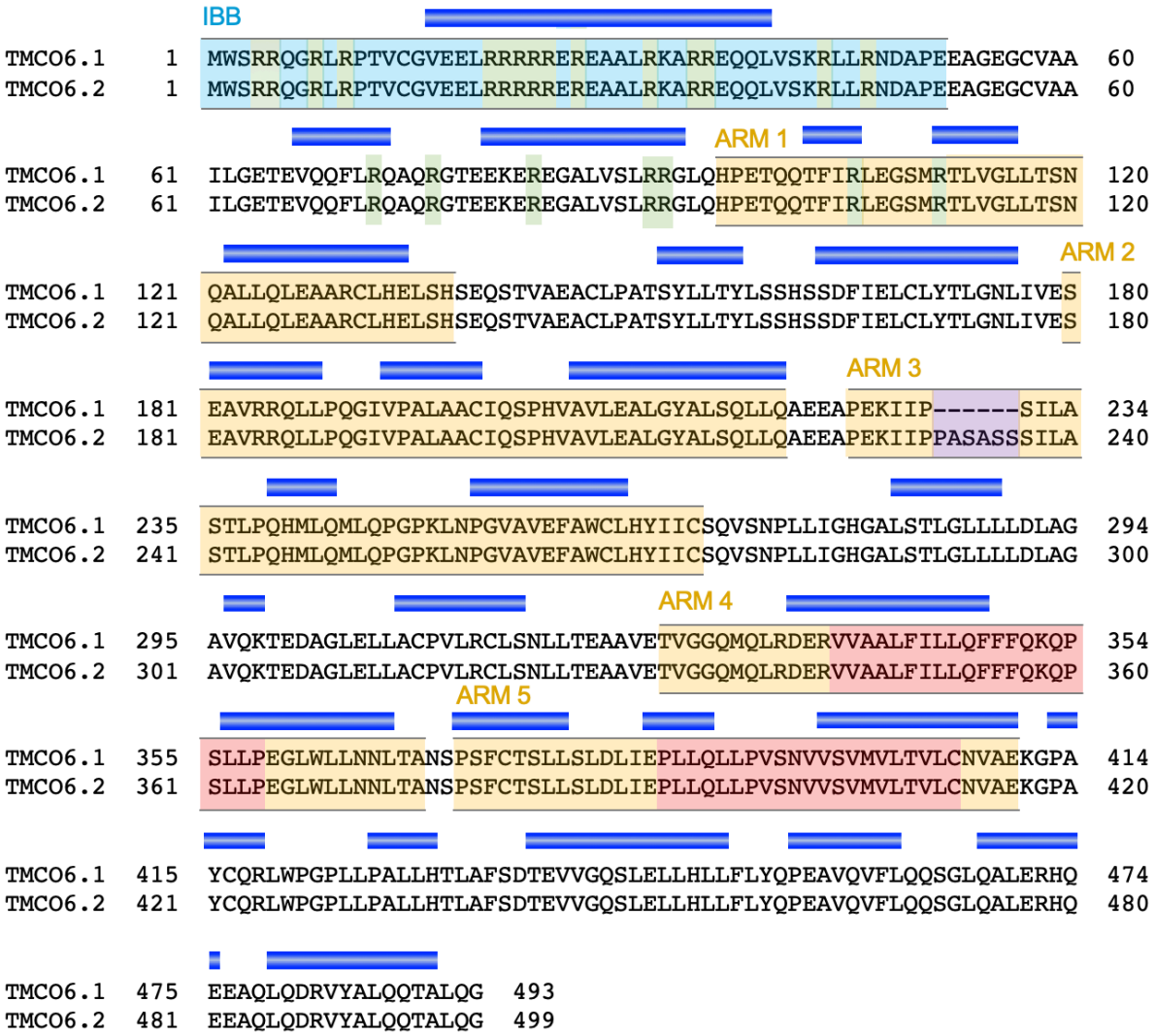

Figure 4.2 Annotation of predicted structural features of TMCO6.

The primary protein sequences encoded by mRNA transcripts *TMCO6.1* (NM_018502.5 493 aa product) and *TMCO6.2* (NM_001300980.1, 499 aa product) are aligned above, with the six differing in-frame amino acids highlighted in purple. An arginine-rich region (each individual arginine highlighted in green) is present in the first 110 amino acids. A predicted importin-β binding domain (IBB) (blue) is annotated to occur in the first 52 amino acids. There are 5 armadillo (ARM) helices (yellow) predicted by the InterPro database from residues 96 – 137, 180 – 220, 225 – 268, 326 – 369 and 371 – 410. PSIPRED 2.0 secondary structure prediction was used to predict the abundance and distribution of secondary structural features, yielding only α-helices (the positions of which are denoted by the blue bars); only amino acids with the highest confidence scores for involvement in an α-helix are shown, yielding 27 distinct helices (an additional 6 predicted with less confidence are not shown). Lastly, topology prediction with Protter (Omasits *et al.*, 2014) predicts the presence of two transmembrane regions (each highlighted in red) from residues 338 – 358 and 386 – 406.

4.2.2 Patient Clinical History and Genetic Investigation

A male paediatric proband of Bangladeshi descent was born at term to consanguineous parents. He presented in infancy with nystagmus (involuntary eye movement), generalised hypotonia, hyporeflexia and severe developmental delay. At 7 months of age, magnetic resonance imaging (MRI) disclosed extensive cortical and subcortical hypomyelination. At 12 months of age, he developed epilepsy, dystonia (uncontrolled muscle spasms), spasticity (involuntary muscle contraction), and axial hypotonia (abnormally low muscle tone), with no acquisition of language or motor milestones. An MRI scan at 16 months of age (**Fig. 4.3 A.**) showed progression of the hypomyelination and cerebral atrophy. Magnetic resonance spectroscopy (MRS) (**Fig. 4.4)** performed at the same time revealed an increase in intraventricular lactate (22 mg/dl, n.v. 9-19 mg/dl) and a reduction of N-acetyl aspartate (NAA), the most prominent MRS signal abnormalities observed in mitochondrial disorders (Lunsing *et al.*, 2017). Visual evoked potentials demonstrated a defect in nerve conduction with latency delay and low voltage. Cardiac ultrasound excluded the presence of cardiomyopathy at that time, but no echocardiographic or electrocardiographic scans were performed. At his last follow-up appointment at 7 year of age, neurophysiological evaluation showed worsening of the dystonia and spasticity and another MRI scan (**Fig. 4.3 B.**) revealed progression of the cerebral atrophy with involvement of subtentorial areas. Biochemical activity measurement of a skeletal muscle biopsy determined Complex I (CI) deficiency (5.58 nmol/min/mg, n.v. 13 - 24) and reduced citrate synthase (CS) activity (37 nmol/min/mg, n.v. 80-120).

In combination, the clinical presentation, MRS spectra and biochemical data strongly suggested mitochondrial involvement in the disease. After initial Sanger sequencing of the patient's mtDNA at the Neurological Institute "Carlo Besta" (Milan, Italy) and further sequencing of a panel of 132 nuclear-encoded genes associated with mitochondrial disease, particularly OXPHOS deficiency, no plausible genetic candidates were found. The patient's DNA was subjected to WES and subsequent bioinformatic analyses at the Medical Research Council Mitochondrial Biology Unit (MRC-MBU, Cambridge, UK). A total of 1,366 individual SNPs were identified, 179 of which were nonsynonymous or stop-gain mutations and a further 27 of these had gene products of strongly predicted or known mitochondrial localisation. *TMCO6* was determined to be the most likely causal gene candidate of these, with a homozygous recessive missense mutation in exon 3 (NM_018502.5:c.271C>T) leading to an arginine to cysteine amino acid substitution (NP_060972.3:p.Arg91Cys) (**Fig. 4.5**). This variant has not been previously reported in the ExAc or Clinvar databases. Single heterozygous mutations were confirmed in both parents and an older sister by Sanger sequencing.

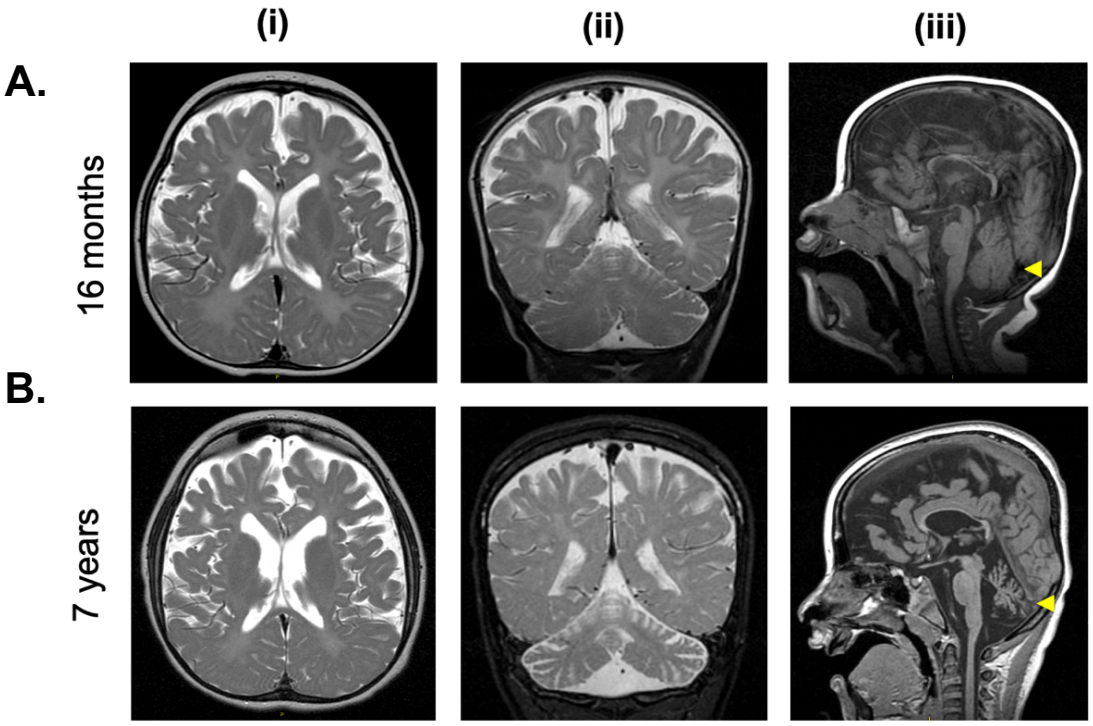

Figure 4.3 Patient T2- FLAIR MRI sequences reveal hypomyelination and cerebral and cerebellar atrophy.

T2-FLAIR MRI (i) transverse supratentorial, (ii) coronal and (iii) sagittal sequences were imaged at (**A.**) 16 months and (**B.**) 7 years of age. Cortical and subcortical hypomyelination, and progressive cerebral and cerebellar atrophy (the latter is indicated by yellow arrowheads) were evident. The brain stem and spinal cord were spared. Sequences acquired and compiled by clinicians at the Neurological Institute “Carlo Besta” (Milan, Italy).

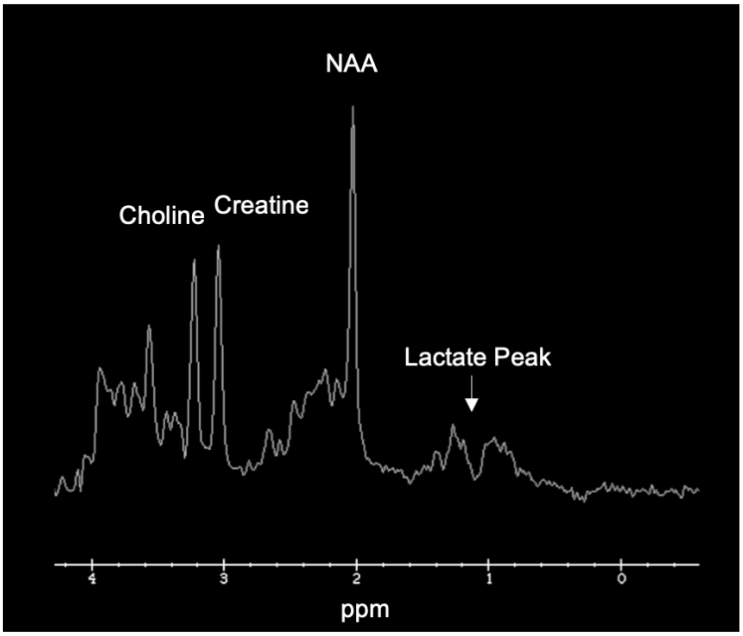

Figure 4.4 Patient magnetic resonance spectrometry (MRS) intraventricular spectra.

MRS was carried out at 16 months of age on the lateral ventricles of the brain to determine the metabolic status of this region, and to compliment the results of counterpart MRI imaging (see **Fig 4.1**). An N-acetyl aspartate (NAA) peak, occurring at 2.00 to 2.05 parts per million (ppm), was decreased signifying a reduction in overall neuronal density since it is an amino acid abundant in the brain and primarily localising to neuronal tissues. Additionally, a lactate peak was detected at 1.3 ppm, signifying increased anaerobic respiration. A choline peak detected at 3.20 ppm serves as a marker of cell membrane integrity and cellularity, and was normal. Lastly, a creatine peak (3.03 ppm), which is a marker of intracellular energy state and routinely used as a reference standard for characterising other peaks, was also normal. Analysis was performed as previously described (Verma *et al.*, 2016).

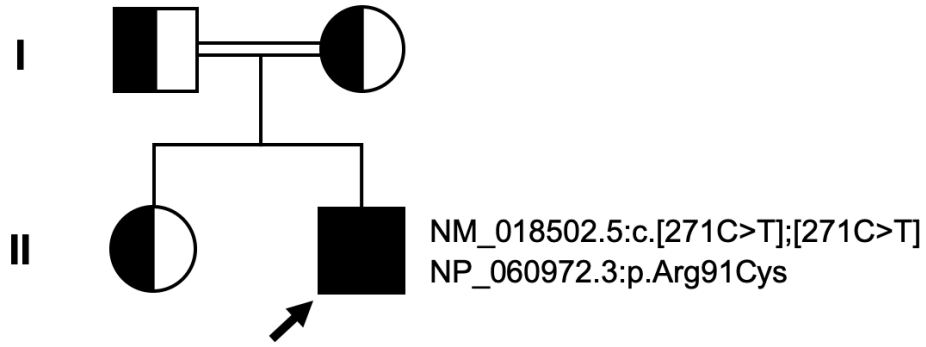

Figure 4.5 Family pedigree for a mitochondrial disease patient with a homozygous recessive missense mutation in *TMCO6.*

Figure shows a family pedigree for an adolescent male proband of Bangladeshi descent (b. 2008) that exhibited CI deficiency in skeletal muscle, infantile-onset epilepsy, nystagmus, dystonia, spasticity, generalised hypotonia and severe developmental delay. WES analysis found a homozygous recessive mutation in exon 3 of *TMCO6* (NM_018502.5: c.271C>T) in the patient, encoding a missense arginine to cysteine amino acid substitution at position 91 of the primary protein sequence (NP_060972.3: p.Arg91Cys). The probands' parents are consanguineous as denoted by the double line, and have the mutation in heterozygosity. The proband has an older sister who is heterozygous for the mutation.

4.2.3 Homozygous Recessive *TMCO6* Mutant Variant is Predicted by Computational Analyses to be Strongly Pathogenic

In order to confirm the presence of the homozygous recessive mutation found by WES in patient-derived primary skin fibroblasts supplied for use in this work, genomic DNA was purified from these cells and used as genetic templates for PCR-based amplification of the mutant region within exon 3 of *TMCO6*. Sanger sequencing confirmed the presence of a single C>T nucleotide transition in homozygosity (**Fig. 4.6 A.**), encoding an in-frame CGT>TGT codon change from an arginine to a cysteine residue affecting the 91st amino acid of the TMCO6 primary protein sequence (NP_060972.3: p.Arg91Cys). This change is predicted to be strongly pathogenic by bioinformatic analyses, yielding a Polymorphism Phenotyping v 2 (PolyPhen-2) score of 0.997 (max. score = 1.000) (**Fig. 4.6 B.**) (Adzhubei *et al.*, 2010), and a Functional Analysis through Hidden Markov Models (FATHMM)-MKL score of 0.923 (max score = 1.000) (**Fig. 4.6 C.**) (Shihab *et al.*, 2015).

A.

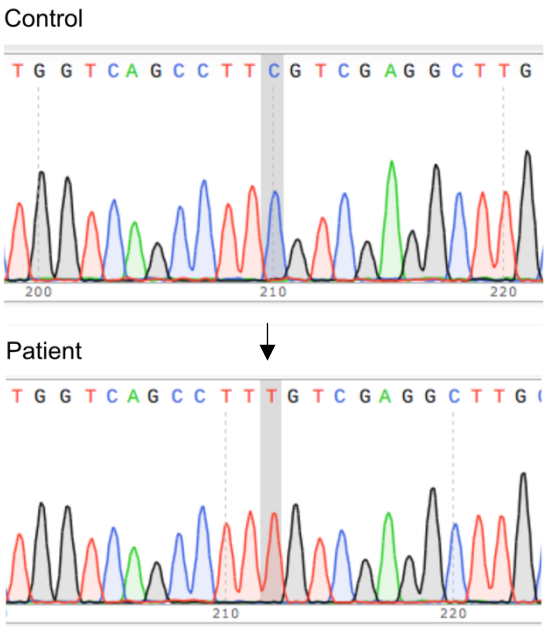

B.

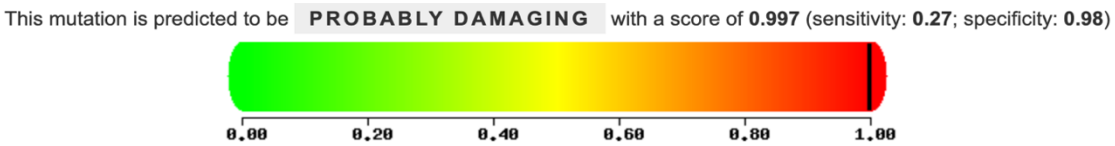

C.

Chromosome	Position	Variant	Non-Coding Score	Non-Coding Groups	Coding Score
5	140021322	C/T	0.93531	ALL	0.92339

Figure 4.6 The *TMCO6* point mutation was verified in cultured primary patient fibroblasts and is predicted to be highly pathogenic by bioinformatic analyses.

(**A.**) Sections of chromatograms generated by Sanger sequencing of exon 3 of *TMCO6* amplified from genomic DNA purified from patient and control primary skin fibroblasts confirmed the C>T nonsynonymous point mutation originally identified by WES. (**B.**) The PolyPhen-2 online tool (available from: http://genetics.bwh.harvard.edu/pph2/) predicts whether an amino acid substitution will have an effect on the structure and function of a human protein. Variants with scores of 0 - 0.15 are predicted to be 'benign', scores of 0.15 - 0.85 are 'possibly deleterious' and scores > 0.85 are predicted to be 'probably damaging' (Adzhubei *et al.*, 2010). The score for the patient mutation is 0.997. (**C.**) FATHMM-MKL is a predictive tool for pathogenicity (available from: http://fathmm.biocompute.org.uk) based on a machine learning approach that scores the functional consequences of non-coding and coding DNA variants based on 10 selected elements from the Encyclopaedia of DNA Elements (ENCODE) database. Scores < 0.5 are classed as 'neutral', scores ≥ 0.5 as 'potentially deleterious' and scores ≥ 0.7 are classed as 'pathogenic' (Shihab *et al.*, 2015). The score for the patient mutation (see 'coding score') is 0.923.

Following on from this, the CLUSTAL Omega (version 1.2.4) multiple sequence alignment tool (available from: https://www.genome.jp/tools-bin/clustalw) was used to compare the affected region of the wildtype TMCO6 human primary sequence (NP_060972.3) with the sequences of nine orthologs chosen to represent mammals, birds, reptiles, amphibians, and fish (**Fig. 4.7**). Arg91 of the human primary protein sequence (indicated by the red arrowhead) is ubiquitously conserved amongst the sampled species. TMCO6 is not known to be present in invertebrate animals, plants, bacteria nor fungi, and no UNIPROT entries for these were found. Additionally, the affected arginine falls within a predicted α-helix. Repeating the PSIPRED 2.0 secondary structure prediction with the mutated primary protein sequence did not suggest a change in the presence, position or length of this helix.

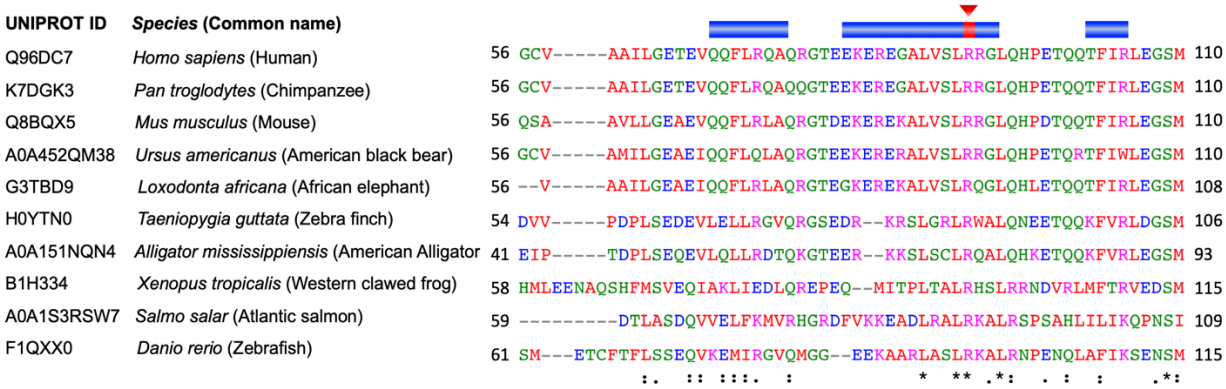

Figure 4.7. Multiple sequence alignment of mammalian TMCO6 shows conservation of Arg91.

A multiple sequence alignment for amino acids 56 – 110 of the human TMCO6.1 primary sequence (NP_060972.3) compared to 9 vertebrate orthologs representing a range of taxonomic classes was created using the CLUSTAL Omega (version 1.2.4) online tool. The position of the patient p.Arg91C mutant amino acid substitution is indicated by a red arrow. An asterisk (*) denotes conservation of an amino acid amongst all query species, a colon (:) denotes conservation of amino acids with similar biochemical properties, a period (.) denotes amino acids with weakly similar biochemical properties, and no symbol indicates no predicted conservation of residues at that position. Each residue in the alignment is assigned a colour corresponding to its respective biochemical properties: blue = negatively charged, magenta = positively charged, red = hydrophobic, and green = hydrophilic or polar. Secondary structure prediction for the human TMCO6 protein was carried out using the PSIPRED 2.0 online tool (available from: http://bioinf.cs.ucl.ac.uk/psipred/) (Jones, 1999). The residues with the highest possible confidence score for the prediction of involvement in an α-helix are annotated by the blue bar above the sequence. The affected arginine falls within an α-helix. Repeating the PSIPRED 2.0 secondary structure prediction with the mutated primary protein sequence did not predict alterations to the overall presence or length of this helix.

4.2.4 Characterising Patient Fibroblasts by SDS-PAGE and Western Blot Analysis

Since this is, to our knowledge, the first time *TMCO6* had been linked to mitochondrial disease or human disease pathology of any kind, a preliminary molecular assessment of the patient cells was carried out.

Firstly, whole cell lysates were extracted from patient-derived skin fibroblasts (P) and two control primary fibroblast cell lines (Controls A and B). Equivalent quantities of protein were separated by size under denaturing conditions by SDS-PAGE. Western blotting and immunodetection was performed in order to determine the steady-state levels of TMCO6, CI subunits from each of the modules, CI assembly factors, as well as various subunits of the other OXPHOS complexes (CII-CV).

As evident in **Fig 4.8,** the steady-state level of endogenous TMCO6 normalised to the cytosolic loading control GAPDH is decreased by approximately a third in patient cells. Additionally, quantities of the CI subunits NDUFS3 (Q-module), and NDUFA11 (P_P-module) were also reduced to varying extents. NDUFV1 (N-module), NDUFA9 (N-module/Q-module border) and NDUFB8 (P_D-module) showed no observable differences in quantity. The relative abundances of CI assembly factors ACAD9 and NDUFAF3, involved in intermediate to late-stage CI biogenesis, were also decreased by ~ 55 and ~ 35 %, respectively. Reduction in protein levels for subunits of other respiratory chain complexes, namely SDHA and SDHB (CII), UQCRC1 and UQCRC2 (CIII), and MT-CO1, MT-CO2 and COX4 (CIV), were observed, which led us to question whether mitochondrial mass was affected. Indeed, mitochondrial loading control TOMM20 was decreased but the abundances of CS and HSP60 were unaffected compared to counterpart controls. From this initial experiment, it is not possible to determine whether the mutant form of TMCO6 is directly impacting the steady-state levels of these subunits or whether the reductions seen are an indirect consequence of decreased mitochondrial mass.

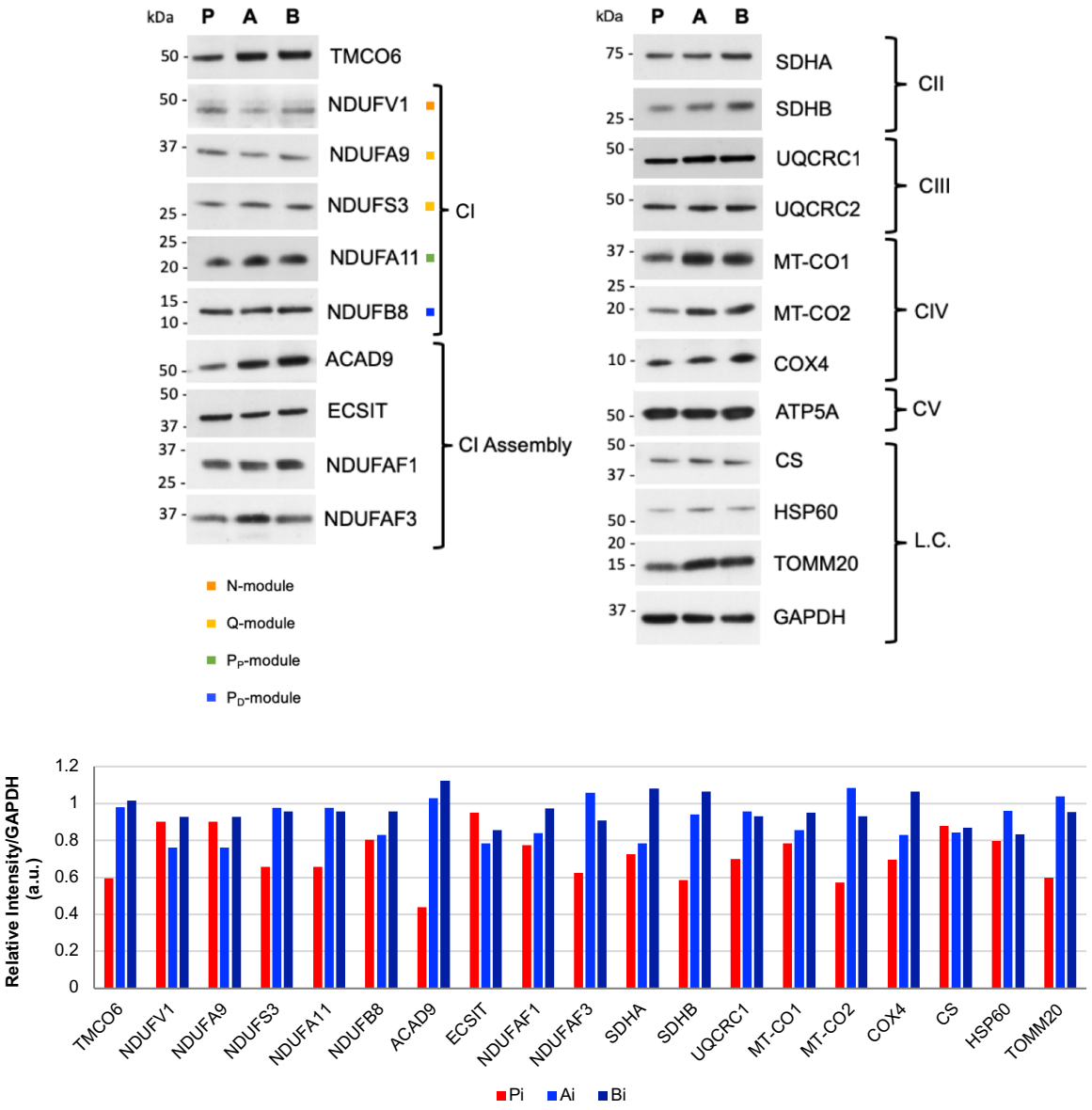

Figure 4.8. Decrease in TMCO6 protein steady-state level found alongside a reduction in CI, CII, CIII, and CIV subunits, CI assembly factors and mitochondrial mass markers in patient primary fibroblasts.

SDS-PAGE was performed as per **section 2.6.2** with 10 µg of protein from whole cell lysates obtained from patient-derived skin fibroblasts (P), and two control skin fibroblast cell lines (A and B). WB analysis followed for immunodetection of TMCO6, CI subunits NDUFA9, NDUFA11, NDUFB8, NDUFS3, and NDUFV1, CI assembly factors ACAD9, ECSIT, NDUFAF1 and NDUFAF3, CII subunits SDHA and SDHB, CIII subunits UQCRC1 and UQCRC2, CIV subunits MT-CO1, MT-CO2, and COX4, CV subunit ATP5A, mitochondrial loading controls (L.C.) CS, HSP60 and TOMM20, and cytosolic L.C. GAPDH using the primary antibodies and concentrations detailed in **Table 2.29**. At least three biological replicates have been analysed; one representative image for each protein is shown here. The corresponding module of each CI subunit is indicated by a coloured square, see legend. Densitometric quantification of the band intensities relative to the signal for GAPDH were calculated with the Gel Analysis function of Fiji Image J software (Schindelin *et al.*, 2012)) (*n* = 1 each).

Patient and control primary fibroblasts were subjected to immortalisation in order to avoid cellular senescence and also to increase the rate of proliferation (see **section 2.3.3**). No differences in cellular morphology or growth rate were observed compared to control cell lines. SDS-PAGE analysis was performed as before, with more CI subunits and assembly factors immunodetected (**Fig 4.9)**. Again, reduction in the steady-state level of TMCO6 was observed in patient cells normalised to the signal of the cytosolic loading control, GAPDH. Densitometric quantification showed reductions in CI subunits NDUFS1 (N-module), NDUFA9, NDUFS2, and NDUFS3 (Q-module), NDUFA10 and NDUFA11 (P_P-module), the CI assembly factors ACAD9, NDUFAF1, NDUFAF2, and NDUFAF3. The levels of the subunits of the P_D module, NDUFB3, NDUFB8 and NDUFB11, were only slightly reduced compared to controls. Various subunits of the other respiratory complexes and all chosen markers for mitochondrial mass, HSP60, CS and TOMM20, showed decreases. We concluded from this that mitochondrial mass was very likely decreased in patient cells. Importantly, primary and immortalised patient fibroblasts showed comparable differences indicating that the immortalisation process had not led to a loss of the mutant phenotype. It was unclear at this stage whether mitochondrial mass was affected as a direct consequence of the patient mutant variant.

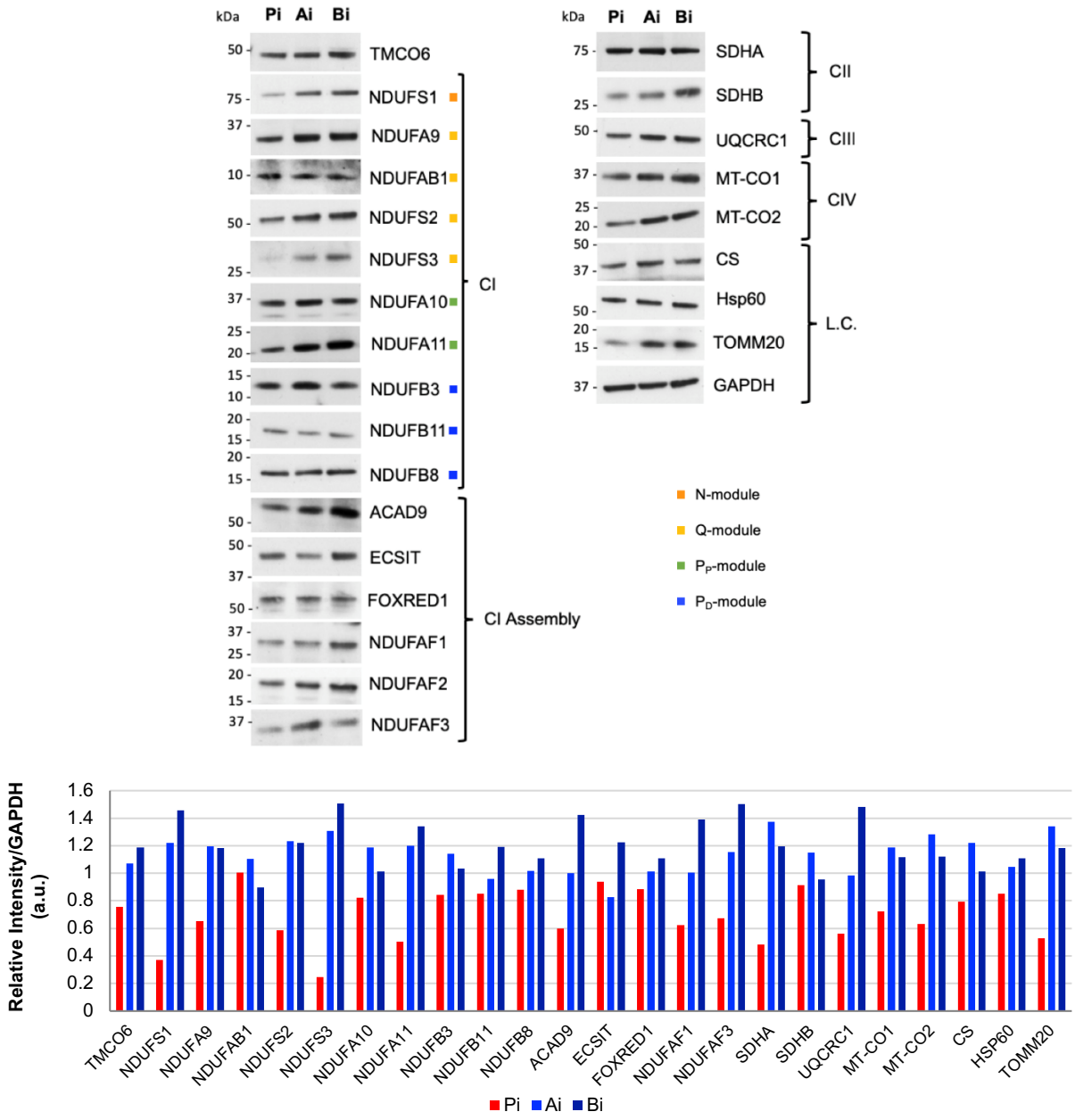

Figure 4.9. A reduction in the quantities of additional subunits of Complex I and CI assembly factors was observed in patient immortalised fibroblasts.

SDS-PAGE was performed as per **section 2.6.2** with 15 µg of protein from whole cell lysates obtained from immortalised patient (Pi), and control (Ai and Bi) skin fibroblast cell lines. WB analysis followed for detecting TMCO6, CI subunits NDUFA9, NDUFA10, NDUFA11, NDUFAB1, NDUFB3, NDUFB8, NDUFB11, NDUFS1, NDUFS2, and NDUFS3, CI assembly factors ACAD9, ECSIT, FOXRED1, NDUFAF1, NDUFAF2 and NDUFAF3, CII subunits SDHA and SDHB, CIII subunit UQCRC1, CIV subunits MT-CO1 and MT-CO2 and mitochondrial loading controls (L.C.) CS, HSP60 and TOMM20, and cytosolic L.C. GAPDH using the primary antibodies and concentrations detailed in **Table 2.29**. At least three biological replicates have been analysed; one representative image for each protein is shown here. The corresponding module of each CI subunit is indicated by a coloured square, see legend (bottom right). Densitometric quantification of the band intensities relative to the signal for GAPDH were calculated with the Gel Analysis function of Fiji Image J software (Schindelin *et al.*, 2012).

4.2.5 Abundances of CI Supercomplex and Subcomplex Species Altered in Immortalised Patient Fibroblasts

Next, we sought to investigate the effect of the observed reduction in steady-state levels of OXPHOS subunits (**Figs. 4.8** and **4.9**) on relative levels of the respiratory chain complexes, and their respective subcomplexes or supercomplexes for both primary and immortalised patient cell lines. The endogenous anti-TMCO6 antibody did not recognise the native protein, so it was not possible to detect a signal for native TMCO6 or study its co-localisation with any of the mature respiratory chain complexes by 1D-BNGE. 1D-BNGE, Western blotting and immunodetection with an anti-NDUFB8 primary antibody revealed little difference in the amount of CI holocomplex between primary or immortalised patient-derived cells (P, Pi) compared to two control (A, Ai and B, Bi) fibroblast cell lines, for mitoplasts solubilised with 1 % DDM (**Fig. 4.10 A.**), with the signal of CI normalised against that of CII (immunodetected by SDHB). Since quantity of mitochondrial protein was routinely used to normalise the loading of samples, and not quantity of cells, it is possible that this process masked any reduction in levels of all the respiratory chain complexes owing to reduced mitochondrial mass. This result did show that there is a 1:1 ratio for each of CI, CII, $CIII_2$ and CIV between the patient cells and the two controls for both primary and immortalised cell lines. Long exposure of immunodetection of NDUFB8 (P_D-module) in DDM-treated mitoplasts revealed no change in the amount of the CI holocomplex, but it did show a relative increase in the quantity of a subassembly product of ~680 kDa (denoted by the red arrowhead) in the patient versus both controls (**Fig. 4.10 B.**). This fits with the expected size of the NDUFB8-containing P_P-b/P_D-a/P_D-b subassembly complex (**Fig. 1.4**). Immunodetection of NDUFS3 (Q-module) also revealed no change in the amount of the CI holocomplex in primary and immortalised patient cells (**Fig. 4.10 C.**). A ~900 kDa subcomplex (indicated by the green arrowhead), corresponding to the size of CI lacking the N-module but with assembly factors still bound, was decreased, and the quantity of a~740 kDa subcomplex (indicated by the blue arrowhead), corresponding to the expected size of the Q/P_P module, showed no changes in quantity for patient cells relative to controls. The amount of a ~400 kDa subcomplex (indicated by the orange arrowhead), corresponding to the size of the Q/P_P-a module, is slightly elevated in patient cells. Together, these results suggest a role for TMCO6 in the assembly or the maintenance of stability of CI assembly intermediates.

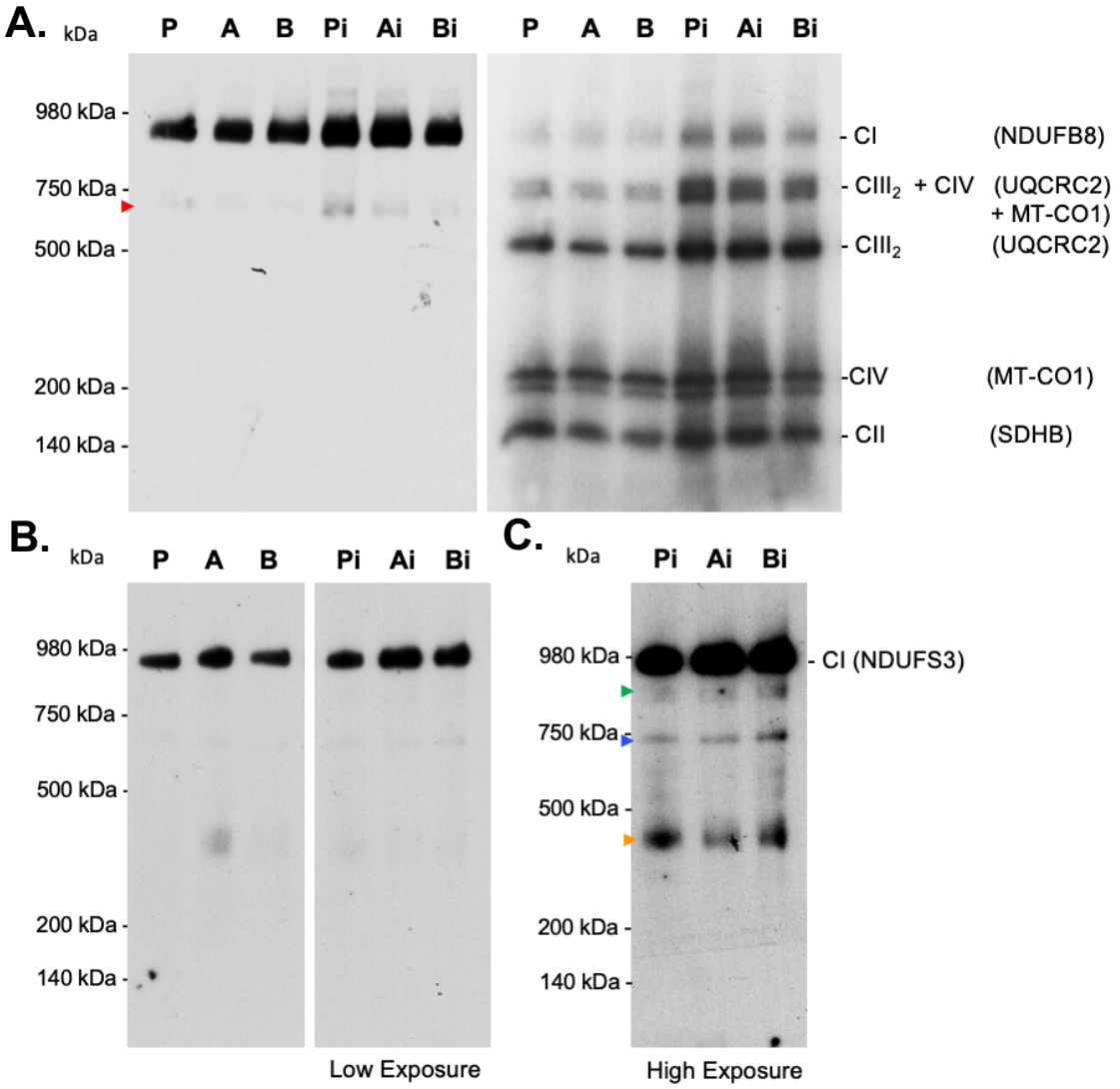

Figure 4.10. Primary and immortalised patient cells show no change in monomeric CI abundance, but exhibit an increase in a NDUFB8-containing subcomplex.

(**A.**) 1D-BNGE was performed with approximately 120 µg of mitochondrial protein treated with 1 % DDM from primary or immortalised patient (P, Pi) and control (A, Ai and B, Bi) skin fibroblast cell lines. Samples were resolved using 3 – 12 % gradient Novex® NativePAGE gels as per **section 2.6.3**. Immunodetection of native CI, CII, $CIII_2$, CIV and the $CIII_2$ + CIV supercomplex was performed by WB analysis by successive incubations with primary antibodies against NDUFB8, SDHB, UQCRC2, and MT-CO1, respectively (for antibody manufacturer details and concentrations used for each, see **Table 2.29**). Long exposure of immunodetection of NDUFB8 (right) revealed a ~680 kDa protein subcomplex species (red) elevated in patient cells, but no differences to the relative abundance of the CI holocomplex between patient and control cell lines for both primary and immortalised cells. (**C.**) Immunodetection of NDUFS3 in primary and immortalised cells were also showed no change in amount of the CI holocomplex, and an overexposed image of the immortalised samples shows decrease of the ~900 kDa band (green), no change in quantity of a ~740 kDa subassembly band (blue), and increase in a ~400 kDa band (orange).

Given that the primary and immortalised patient cells showed equivalent molecular phenotypes, immortalised cells were used for all additional investigation into alterations to CI stability and assembly by 1D-BNGE analyses. Immunodetection of NDUFS1 (N-module) in mitochondrial protein extracts from immortalised cell lines solubilised with DDM showed a reduction in the amount of fully assembled CI (**Fig. 4.11**), relative to the loading control, CII. CIV and the $CIII_2$ + CIV complexes also showed slight reductions.

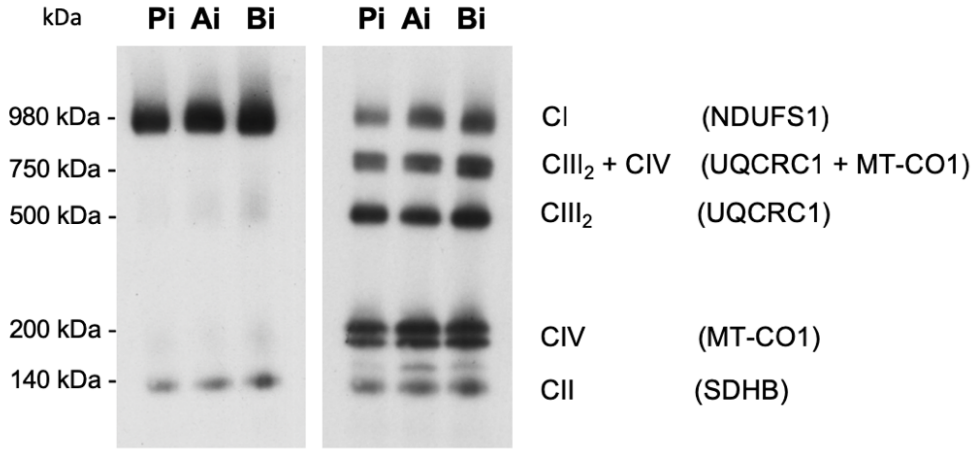

Figure 4.11. Immortalised patient cells show reduction in CI holocomplex abundance following immunodetection of NDUFS1.

1D-BNGE was performed with approximately 120 µg of mitochondrial protein treated with 1 % DDM from immortalised patient (Pi) and control (Ai and Bi) skin fibroblast cell lines. Samples were resolved using 3 – 12 % gradient Novex® NativePAGE gels as per **section 2.6.3**. Immunodetection of native CI, CII, $CIII_2$, CIV and the $CIII_2$ + CIV supercomplex was performed by WB analysis by successive incubations with primary antibodies against NDUFS1, SDHB, UQCRC1, and MT-CO1, respectively (for antibody manufacturer details and concentrations used for each, see **Table 2.29**). CI holocomplex abundance, and to a lesser extent that of CIV and the $CIII_2$ + CIV supercomplex, showed reductions in the patient sample relative to controls.

Mitochondrial protein extracts from immortalised patient and control cells treated with a milder non-ionic detergent, digitonin (DIG), again showed no reduction in the amount of the fully assembled CI following immunodetection of NDUFB8 (**Fig. 4.12 A.**). However, preparation with DIG revealed a significant decrease in the quantities of several CI-containing supercomplexes. The presence of a subcomplex species of ~400 kDa was also detectable in the patient sample signifying destabilisation or stalled assembly of CI or a CI-containing supercomplex species containing NDUFB8. Abundances of monomeric CII, dimeric $CIII_2$ and monomeric CIV were equivalent between patient and control cell lines. Immunodetection of NDUFS3 (**Fig. 4.12 B.**) also showed a reduction in the abundance of CI-containing supercomplex species to a lesser extent, and the absence of detection of a ~900 kDa subassembly product in patient cells

(indicated by the green arrowhead), likely to be CI lacking the N-module with assembly factors attached (**Fig. 1.4**). There was no accumulation of other bands, suggesting that the 400 kDa band detected with NDUFB8 contains a subset of the P_P-b/P_D-a/P_D-b subcomplex, in line with the results reported above (**Fig. 4.10**). The abundances of $CIII_2$ and the $CIII_2$ + CIV supercomplex were unaffected. Together, these results suggest disruption of assembly or association of CI with the other respiratory chain complexes, and potential destabilisation or stalled assembly of the fully assembled complex.

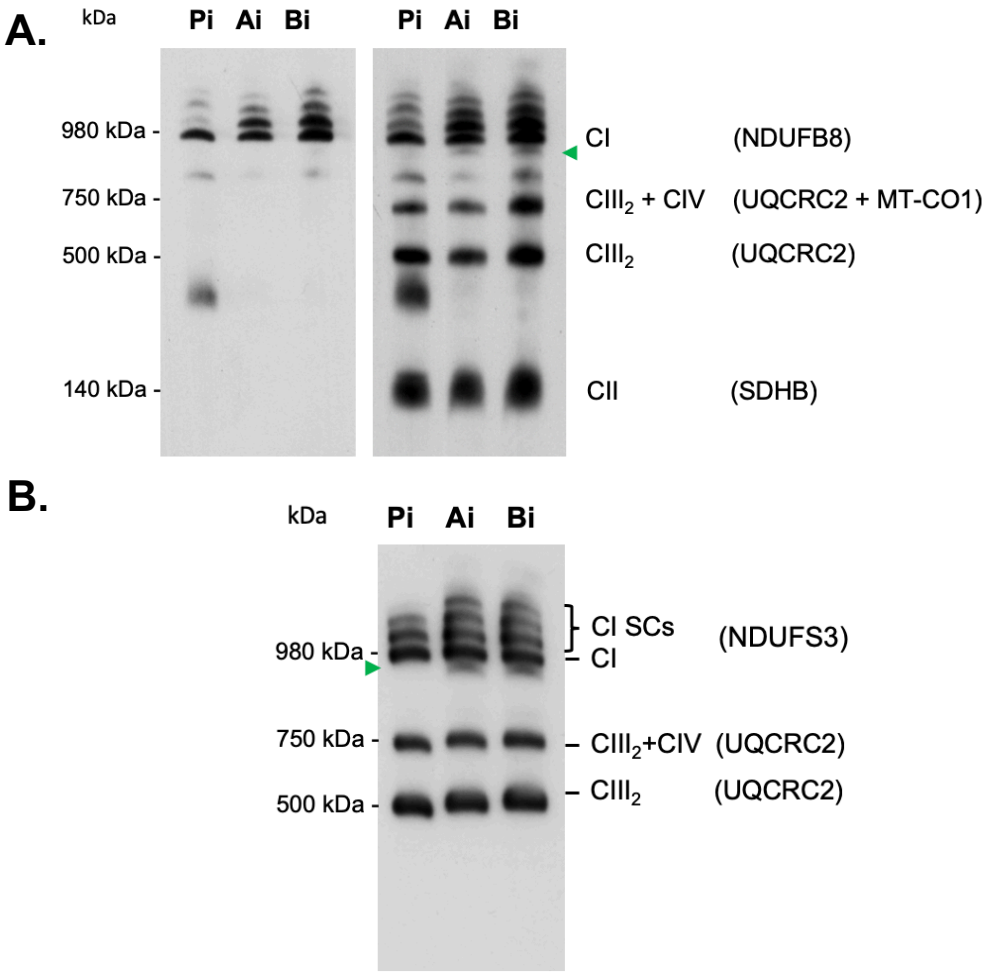

Figure 4.12. CI-containing supercomplexes reduced in immortalised patient fibroblasts.

1D-BNGE was performed with approximately 120 µg of mitochondrial mitoplasts treated with 1 % DIG from immortalised patient (Pi) and control (Ai and Bi) skin fibroblast cell lines. Samples were resolved using 3 – 12 % gradient Novex® NativePAGE gels as per **section 2.6.3**. Immunodetection of native CI, CII, $CIII_2$, CIV and the $CIII_2$ + CIV supercomplex was performed by WB analysis with primary antibodies against NDUFB8 (**A**.), NDUFS3 (**B**.), SDHB, UQCRC2, and MT-CO1 (for antibody manufacturer details and concentration and conditions used for each, see **Table 2.29**). A reduction in CI-containing supercomplex species were observed for both antibodies, as was the absence of a ~900 kDa band (indicated by the green arrowheads).

4.2.6 TMCO6 Co-Migrates with CI by 2D-BNGE

2D-BNGE, Western blotting and immunodetection was then performed to assess whether TMCO6 co-localises with any of the mitochondrial protein complexes or their subcomplexes. Importantly, this analysis revealed co-migration of endogenous TMCO6 specifically with the CI holocomplex (**Fig. 4.13**) (indicated by the blue arrows), which was detected by an anti-NDUFS3 primary antibody in both primary patient and control samples solubilised with 1 % DDM, and not with any of the other respiratory chain complexes. Patient cells displayed more unassociated or 'free' TMCO6 (indicated by the green arrows) in the low molecular weight region than the control. Densitometric quantification determined that whilst 71 % of the TMCO6 signal was co-migrating with NDUFS3 in the control cells, only 25 % was found co-migrating in the patient cells. This result suggests that the NP_060972.3:p.Arg91Cys mutation may impair or destabilize TMCO6, affecting its ability to associate with the CI holocomplex. Furthermore, a ~900 kDa subcomplex product (indicated by the red arrow), again likely to be CI lacking the N-module with assembly factors attached, is also detected when immunodetecting with NDUFS3 in the patient but not in the control. The membranes were successively immunoblotted with anti-UQCRC1 (recognising CIII), anti-MT-CO1 (CIV) and anti-SDHB (CII) antibodies, with no significant changes to the quantities or assembly of CII, CIV, $CIII_2$ and the $CIII_2$ + CIV supercomplex (*) observed between the patient and the control. SDHB was used as a loading control.

The same process was performed again as for **Fig. 4.13**, with the sample samples, but membranes were immunodetected for a greater number of proteins. CI subunit NDUFB8 (P_D-module) was immunodetected as well as NDUFS3 (Q-module), and in addition to this, CII subunit SDHA, CIII subunit UQCRC1 and CIV subunits MT-CO1 and MT-CO2 were immunodetected to show the distribution the mature respiratory chain complexes CI, CI, $CIII_2$, CIV and the $CIII_2$ + CIV supercomplex (**Fig. 4.14**). The relative distribution of all subunits for the patient were comparable to the control, with slight differences observed in the relative amounts of several of the subunits, namely a decrease in the amount of NDUFB8 (P_D module, CI) and SDHA (CII), and an increase in the amounts of UQCRC1 ($CIII_2$, and $CIII_2$ + CIV), and MT-CO1 (CIV, CIII2 + CIV), and no observable difference in the amount of NDUFS3 (Q-module, CI). However, 2D-BNGE is not strictly a quantitative method so any differences In abundances must be interpreted with cautious, lest they be a result of using less antibody or from longer primary antibody incubation time for one membrane compared to another, etc. What can be concluded is that there seems to be no loss of any of the mature complexes owing to complete destabilisation of the holocomplexes or entirely stalled assembly.

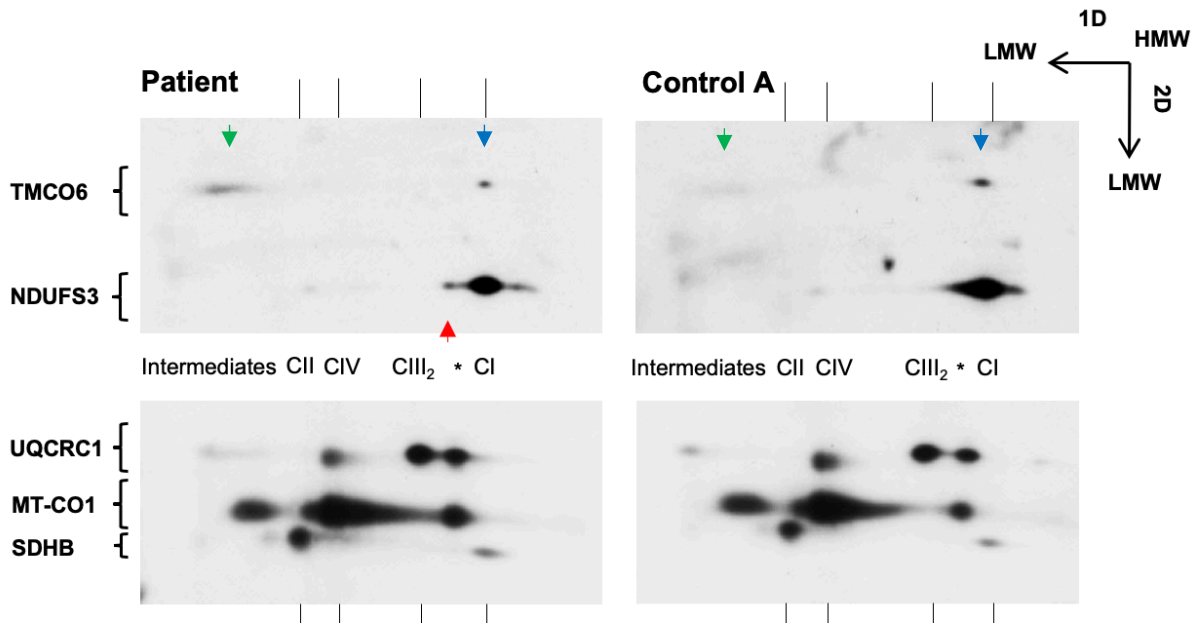

Figure 4.13. TMCO6 co-migrates with the mature CI holocomplex.

2D-BNGE was performed with approximately 250 µg of mitochondrial protein (+ 1 % DDM) prepared from patient and control A primary skin fibroblasts. Samples were run in the first dimension using NativePAGE 3-12 % gradient gels as per **section 2.6.3**, and then resolved under denaturing conditions by SDS-PAGE (with 1X MOPS running buffer). Membranes were sequentially immunodetected with TMCO6, SDHB (CII), NDUFS3 (CI), UQCRC1 ($CIII_2$), and MT-CO1 (CIV) primary antibodies (details in **Table 2.29**). The asterisks (*) denote supercomplex $CIII_2$ + CIV.

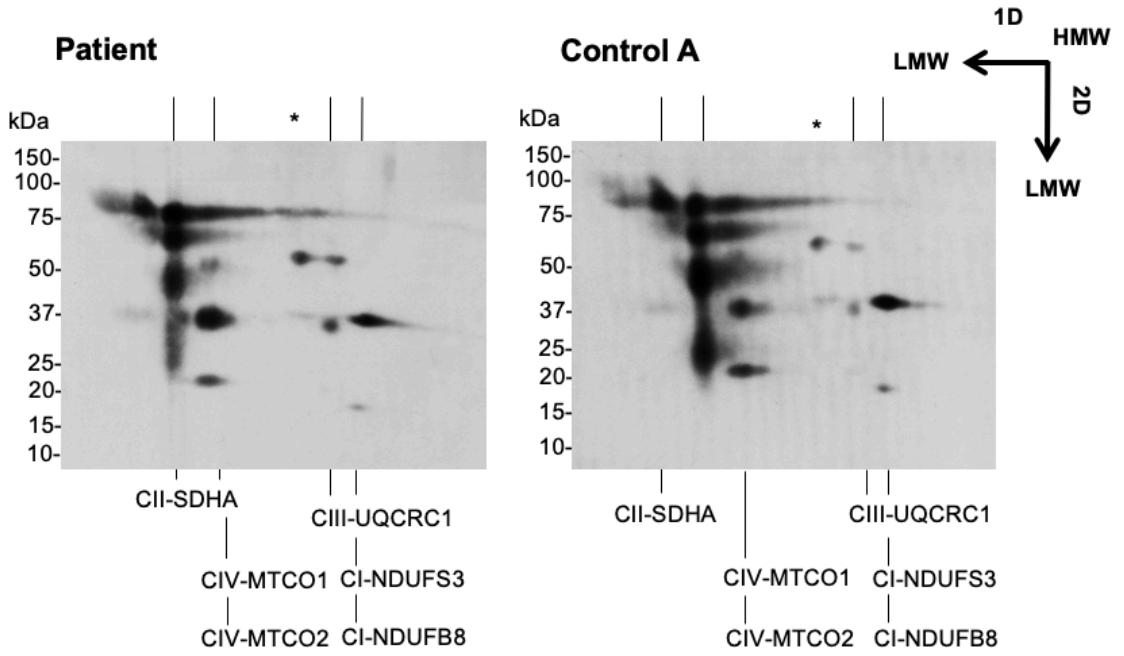

Figure 4.14. 2D-BNGE shows similar migration of OXPHOS subunits and for patient and control skin fibroblasts.

2D-BNGE was performed with approximately 250 µg of mitochondrial protein (+ 1 % DDM) prepared from patient and control A primary skin fibroblasts. Samples were run in the first dimension using NativePAGE 3-12 % gradient gels as per **section 2.6.3**, and then resolved under denaturing conditions by SDS-PAGE (with 1X MOPS running buffer). Membranes were sequentially immunodetected with SDHA (CII), NDUFS3 and NDUFB8 (CI), UQCRC1 ($CIII_2$), and MT-CO1 and MT-CO2 (CIV) primary antibodies (details in **Table 2.29**)**.** The asterisks (*) denote supercomplex $CIII_2$ + CIV.

4.2.7 CI Enzymatic Activity and O_2 Consumption Is Unaffected in Patient Fibroblasts

The next aim of this initial investigation was to conclude whether there were differences in specific CI enzymatic activity and mitochondrial oxygen (O_2) consumption for the patient immortalised fibroblasts. 1D-BNGE analysis of mitochondrial protein extracts solubilised with 1 % DDM was performed in duplicate, with one gel subjected to Western blotting and immunodetection and the other incubated in NADH/NBT CI detection solution (**Fig. 4.15 A.**). This qualitative analysis revealed no differences in CI specific activity, corresponding with no changes in overall CI abundance, relative to CII as a loading control. Specific biochemical activity for CI, CII and CIV were then determined quantitatively by spectrophotometry for two biological replicates (**Fig. 4.15 B.**). CIII values were not sufficient for analysis. Again, no significant differences were observed in the specific activity of CI, as determined by two-way ANOVA with Sidak's *post hoc* test applied. Importantly, these values were normalised to CS. It is possible that these cells have less overall CI activity due to a reduction in mitochondrial mass, and indeed raw values indicated this was the case compared to both controls before normalisation to CS; however, if mitochondrial mass is normalised by taking into account CS activity, the proportional CI/CS value is equivalent for Pi, Ai and Bi cell lines. The specific activities measured for CII and CIV in Pi cells were also considered to be non-significant compared to both Ai and Bi controls.

Following this, mitochondrial aerobic respiration was measured by Oroboros (**Fig. 4.15 C.**). No differences in basal or maximal (uncoupled) O_2 consumption was detected in three biological replicates using comparable quantities of suspended cultured cells. These data together conclude no CI-specific or other mitochondrial respiratory defect in this cell type, perhaps owing to the relatively low energy demands of fibroblasts. In support of this, the CI deficiency detected in the patient was only determined in skeletal muscle, and not in any other tissue, including a cutaneous biopsy. Further models for the study of this protein and its potential involvement in CI assembly, stability and/or function were necessary, including knockdown, overexpression and knockout cellular models (**Chapter 5**), and a recombinant murine knockout model (**Chapter 6**).

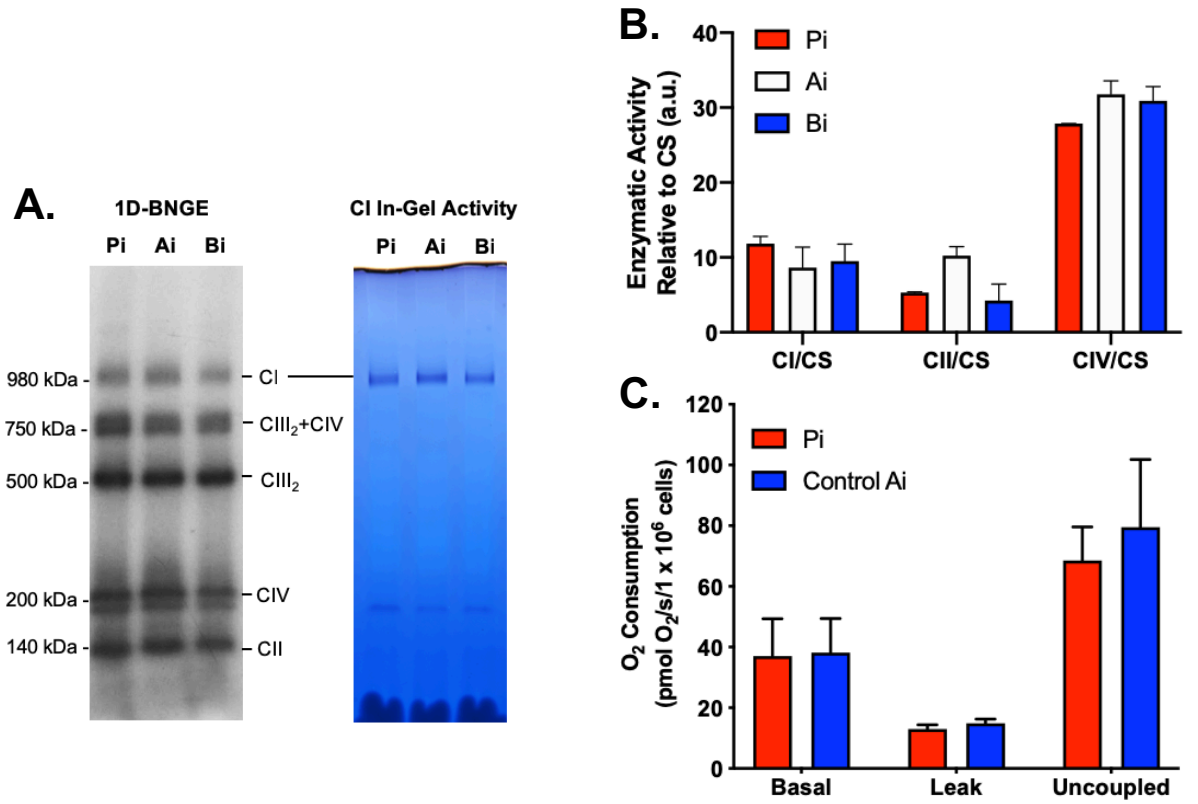

Figure 4.15. OXPHOS activity and oxygen consumption unaltered in patient fibroblasts.

(A.) 1D-BNGE was performed in duplicate with approximately 120 µg of mitochondrial protein extracts treated with 1 % DDM from patient (Pi) and control (Ai and Bi) immortalised skin fibroblast cell lines. For one gel, each of the respiratory chain protein complexes were immunodetected successively by Western blotting using antibodies raised against the subunits in brackets: CI (NDUFB8), $CIII_2$ (UQCRC1), MT-CO1 (CIV) and SDHB (CII) (antibody details in **Table 2.29**). The second gel was submerged in NADH/NBT stain (see **section 2.7.2**) to visually assess specific CI activity. No difference in activity was observed by this qualitative method. (**B.**) Specific enzymatic activity for CI, CII and CIV, each normalised to the activity of citrate synthase (CS), was measured for Pi, Ai and Bi cell lines as per **section 2.7.1**. Data are presented as mean ± range (*n* = 2). One-way ANOVA with Tukey's multiple comparisons test revealed no significant differences. (**C.**) Mitochondrial O_2 consumption rate was measured for live cultured patient (Pi) and control (Ai) immortalised skin fibroblasts using an Oxygraph-2k respirometer (Oroboros Instruments, Innsbruck, Austria) as per **section 2.7.3**. Basal = mitochondrial O_2 consumption rate at body temperature, Leak = ATP-independent O_2 consumption, and Uncoupled = maximal respiration after addition of the uncoupler carbonyl cyanide m-chlorophenylhydrazone (CCCP) (C2759, Sigma-Aldrich®). Data are presented as mean ± SEM (*n* = 3). No differences in basal or maximal respiration were detected for the patient cells relative to the control.

4.3 Conclusions

This work: 1) presents what is currently known regarding the conservation, gene structure, expression and structural features of the uncharacterised protein TMCO6, and 2) investigates the molecular and metabolic consequences of a homozygous recessive mutation in *TMCO6* in patient-derived skin fibroblasts.

At the time of this work, TMCO6 is a completely uncharacterised, nuclear-encoded protein found in Metazoans. It is ubiquitously expressed amongst all human tissues as two main isoforms, *TMCO6.1* and *TMCO6.2,* which produce gene products that differ by 6 in-frame amino acids from position 230 of the primary protein sequence. TMCO6 is expected to form up to 5 armadillo (ARM) repeats that likely produce a superhelical ARM-type fold tertiary structure. Transmembrane predictions are contradictory, suggesting occurrence of two, one or no transmembrane regions situated towards its C-terminus. Its intracellular localisation is unknown, requiring experimental confirmation (see **Chapter 5**).

A novel mutant variant in *TMCO6* (NM_018502.5: c.271C>T,p.Arg91Cys) was identified by WES as the most likely causal genetic candidate in a paediatric proband presenting with severe psychomotor delay, nystagmus, epilepsy, and progressive hypomyelination of cortical and subcortical brain regions. Biochemical activity measurements of a skeletal muscle biopsy determined CI deficiency (5.58 nmol/min/mg, n.v. 13 - 24) and reduced CS activity (37 nmol/min/mg, n.v. 80-120), suggesting a mitochondrial disease origin. Sanger sequencing confirmed the presence of a recessive point mutation in *TMCO6* in homozygosity in the patient and in heterozygosity in both parents. Additionally, the mutation was predicted by *in silico* analyses to be highly pathogenic. A multiple sequence alignment for human TMCO6 and nine vertebrate orthologs showed strong conservation of the affected arginine residue (Arg91).

TMCO6 steady-state level was found to be partially decreased in patient cells, but still present. Subunits from all respiratory chain complexes showed a decrease in their relative abundances to varying extents, suggesting a reduction in overall mitochondrial mass. This was supported by a reduction in mitochondrial mass markers HSP60, CS and TOMM20. 1D-BNGE showed no change in the abundance of the CI holocomplex following immunodetection of NDUFB8 (P_D module) or NDUFS3 (Q-module) in DDM-solubilised mitoplast samples. However, immunodetection with NDUFS1 (N-module) showed some reduction in fully assembled CI abundance and immunodetection with NDUFB8 revealed accumulation of a CI subcomplex in the patient. Digitonin-solubilised samples revealed a clear reduction in the abundance of CI-containing supercomplexes. We also observed loss of a ~950 kDa species and the presence of an additional NDUFB8-containing subassembly/degradation product in the patient sample.

2D-BNGE analysis demonstrated co-migration of TMCO6 with CI. The distribution of subunits of CI, CII, CIII and CIV were similar between patient and control cells. Free/unassociated TMCO6 was detected in the low molecular weight portion of the membrane in both samples, but the relative quantity was increased in the patient. This result suggests that the NP_060972.3:p.Arg91Cys mutant variant may impair or destabilize TMCO6, affecting its ability to associate with the CI holocomplex.

In-gel activity (qualitative) and biochemical evaluation by spectrophotometry (quantitative) determined no specific CI enzymatic activity deficiency in this tissue type. Additionally, no differences in CII or CIV specific activities were determined. Oxygen consumption was unchanged in both basal conditions and following uncoupling of the respiratory chain.

Although computational analyses predicted a high likelihood of pathogenicity for the *TMCO6* mutant variant, patient fibroblasts revealed only mild molecular and biochemical phenotypes. The severe CI deficiency observed in the patient was only determined in skeletal muscle, and no other tissues from the patient were analysed. This suggests that, as also described for other mitochondrial diseases, the effects of the mutant form are only observable in tissues with higher demands in aerobic respiration than skin fibroblasts. Importantly, this preliminary investigation revealed possible physical interaction between TMCO6 and CI *in vivo*. To provide further support to this result, immunoprecipitation experiments for endogenous TMCO6 and for the native CI complex were performed (**Chapter 5**). Additionally, several other cellular models (**Chapter 5**) and a *Tmco6*-knockout mouse model (**Chapter 6**) were studied to elucidate the consequences of alterations in TMCO6 abundance on mitochondrial physiology and function, as described in the following chapters.

Chapter 5

Cell-Based Strategies and Cellular Models for Characterizing Human TMCO6

5.1 Introduction

The work presented in this chapter concerns cell-based strategies and cellular models for the study of the TMCO6 protein. Our first aim was to determine the specific intracellular localisation of TMCO6 through a combination of immunocytochemistry, performed using HeLa and 143B cell lines, and subcellular fractionation, protease digestion and salt gradient experiments, using HeLa and HEK 293T cells. Proving mitochondrial localisation of TMCO6 was crucial for allowing it to be considered a contender as the causal protein responsible for the severe CI deficiency detected in a human mitochondrial disease patient with a homozygous recessive mutation in *TMCO6* (described in **Chapter 4**). Secondly, I describe the generation and subsequent characterisation of shRNA knockdown and doxycycline-inducible overexpression cellular models, and the attempted generation of a CRISPR/Cas9 knockout model, all used to further investigate the association of TMCO6 with Complex I (CI). In particular, we sought to interrogate the consequences of alterations to *TMCO6* expression on CI stability, the abundance of the CI monomer, its subunits, subassembly intermediates and supercomplex species, and its specific enzymatic activity. Lastly, immunoprecipitation for endogenous TMCO6 and the native CI holocomplex were used in tandem to assess whether there is in fact physical interaction between the two, as originally suggested by 2D-BNGE in patient primary skin fibroblasts (**Fig. 4.12**). This strategy was also used to identify potential protein interactors between TMCO6 and CI.

5.2 Results

5.2.1 TMCO6 Localises Specifically to the IMM

In order to establish the specific intracellular localisation of TMCO6, two independent methods were undertaken. Firstly, immunocytochemistry (ICC) of fixed HeLa and 143B cancer cell lines was performed to compare the signal of a primary antibody that recognises endogenous TMCO6 with nuclear (DAPI) and mitochondrial (MitoTracker) markers. As shown in **Fig 5.1**, the signal for endogenous TMCO6 co-localises faithfully with MitoTracker, but not with DAPI in both cell lines. Independently, subcellular fractionation of HeLa and HEK 293T cells was performed by hypotonic shock and differential centrifugation to separate mitochondrial, cytoplasmic and nuclear fractions from whole cell protein lysates. As shown in **Fig. 5.2**, SDS-PAGE and Western blot analysis showed TMCO6 to be present only in the whole cell protein lysates and mitochondrial fractions, similarly to the known nuclear-encoded mitochondria-localising protein SDHA, and not in either nuclear or cytoplasmic fractions, unlike SF2 or TUBB, respectively. Both of these results strongly indicate that endogenous TMCO6 localises specifically to the mitochondria in cultured human cells. Despite the annotated IBB domain predicted at the N-terminal of the protein (**Fig. 4.2**), TMCO6 was not found to localise to the nucleus or cytoplasm.

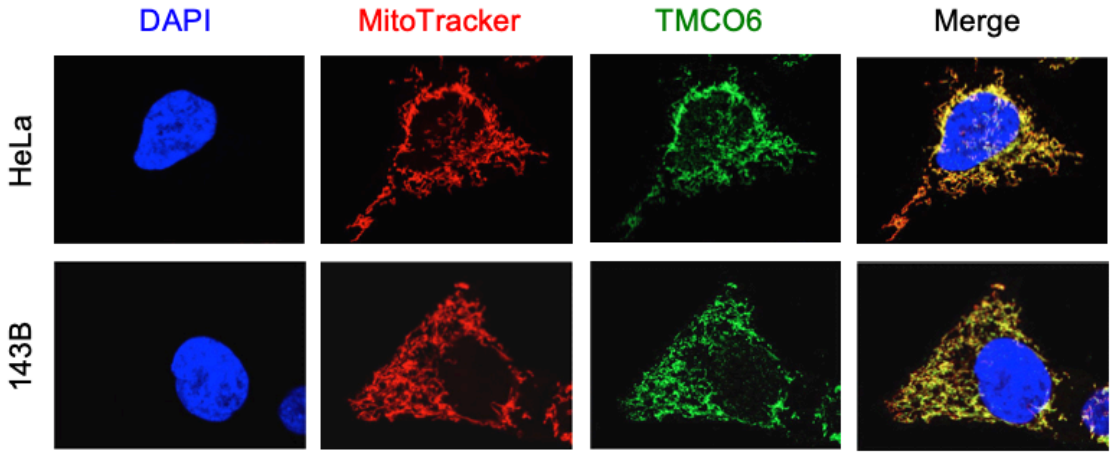

Figure 5.1 TMCO6 localises to the mitochondria in HeLa and 143B cells by ICC.

ICC was performed as per **section 2.4.2** to visualise the subcellular localisation of endogenous TMCO6 in HeLa or 143B cells relative to the mitochondrial network, as stained by MitoTracker™ Red CMXRos and nuclei, as stained by DAPI (both from Invitrogen™). Images were acquired using the A1/A1R Confocal Microscope System (Nikon UK Ltd, Kingston upon Thames, UK) with a 63x 1.40 numerical aperture oil immersion objective. Images were post-processed and compiled using Fiji Image J software (Schindelin *et al.* 2012). Experiment performed and figure compiled by Dr. Aurelio Reyes.

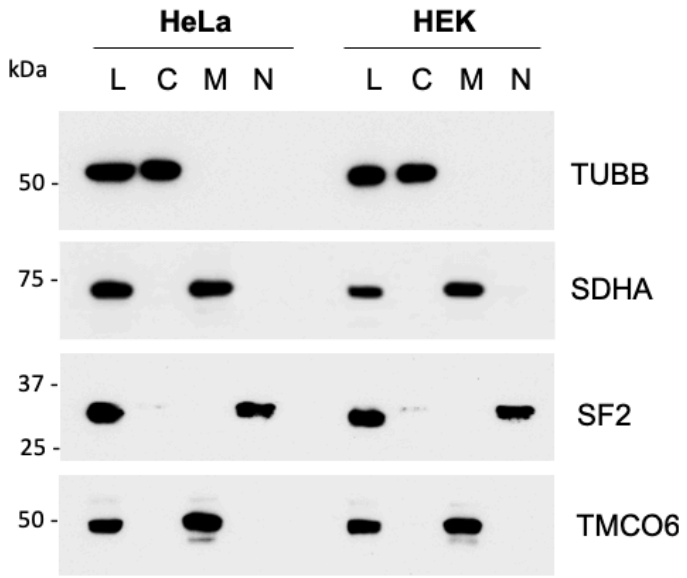

Figure 5.2 TMCO6 localises to the mitochondria in HeLa and HEK 293T cells.

Subcellular fractionation by differential centrifugation was performed as per **section 2.6.7** in order to separate whole cells from both HeLa and HEK 293T, here shown as protein lysates (L), into mitochondrial (M), cytosolic (C), and nuclear (N) fractions. SDS-PAGE was performed as per **section 2.6.2**, followed by Western blotting (**section 2.6.4**) and immunodetection (**section 2.6.5**) with anti-TUBB, anti-SDHA, anti-SF2, and anti-TMCO6 primary antibodies (see **Table 2.29** for manufacturer details and concentrations used).

Next, we sought to determine the specific intramitochondrial localisation of TMCO6, again by a two-part method. Firstly, isolated mitochondria from HEK 293T cells were subjected to hypotonic shock or membrane solubilisation with two concentrations of digitonin, 20 or 50 µg/ml. Trypsin digestion of each sample was performed as indicated in **Fig. 5.3**. The OMM protein TOMM70 is degraded in all cases of trypsin treatment, regardless of membrane swelling or solubilisation of the OMM. TIM23, part of the TIM23 translocase complex of the IMM that protrudes into the IMS, is degraded partially in all conditions of trypsin treatment, and more so after membrane swelling of the OMM by hypotonic shock or solubilisation of the OMM by digitonin treatment. SDHB, known to localise to the IMM, and ETFB, known to localise to the MM, are protected in all conditions of protease treatment or membrane rupture/solubilisation. TMCO6 is protected in all cases of trypsin treatment or OMM membrane disruption similarly to these markers. This result indicates TMCO6 either localises to the mitochondrial IMM or the MM.

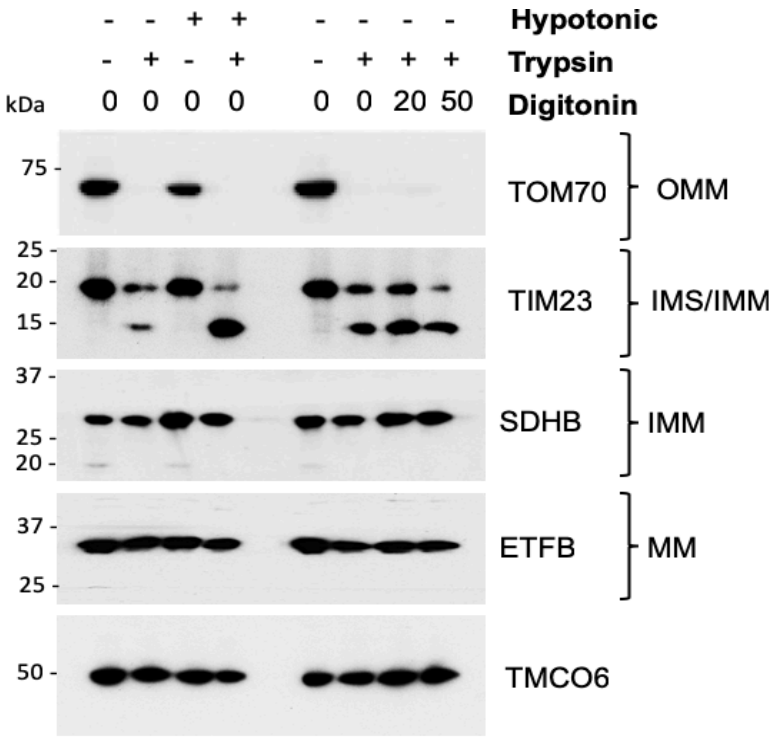

Figure 5.3 TMCO6 is protected from trypsin digestion following OMM swelling and solubilisation with digitonin.

Subcellular fractionation by differential centrifugation was performed as per **section 2.6.7** in order to isolate mitochondria from HEK 293T cells. Mitochondria were separated into aliquots of equal protein amount and subjected to hypotonic shock or digitonin solubilisation (with 20 or 50 µg/ml digitonin, as indicated), and either collected immediately or further incubated with 25 µg/ml trypsin. SDS-PAGE was performed as per **section 2.6.2**, followed by Western blotting (**section 2.6.4**) and immunodetection (**section 2.6.5**) with anti-TOM70, anti-TIM23, anti-SDHB, anti-ETFB, and anti-TMCO6 primary antibodies (see **Table 2.29** for manufacturer details and concentrations used).

Following on from this, intact mitochondria isolated from HEK 293T cells were subjected to digitonin treatment to create mitoplasts, containing only the IMM and MM. Mitoplasts were sonicated to disrupt the IMM, and centrifuged to result in a pellet, containing all membrane-embedded or membrane-tethered IMM proteins, and a supernatant fraction, containing all soluble MM proteins. Pellets and supernatants were then incubated in low-salt (150 mM) or high-salt (500 mM) conditions, to gradually dissociate proteins from their resident membrane, or 2 % SDS, to confirm disruption of the IMM since all proteins would then be accessible for denaturation by SDS. All fractions were analysed by SDS-PAGE and Western blotting, as shown in **Fig 5.4**.

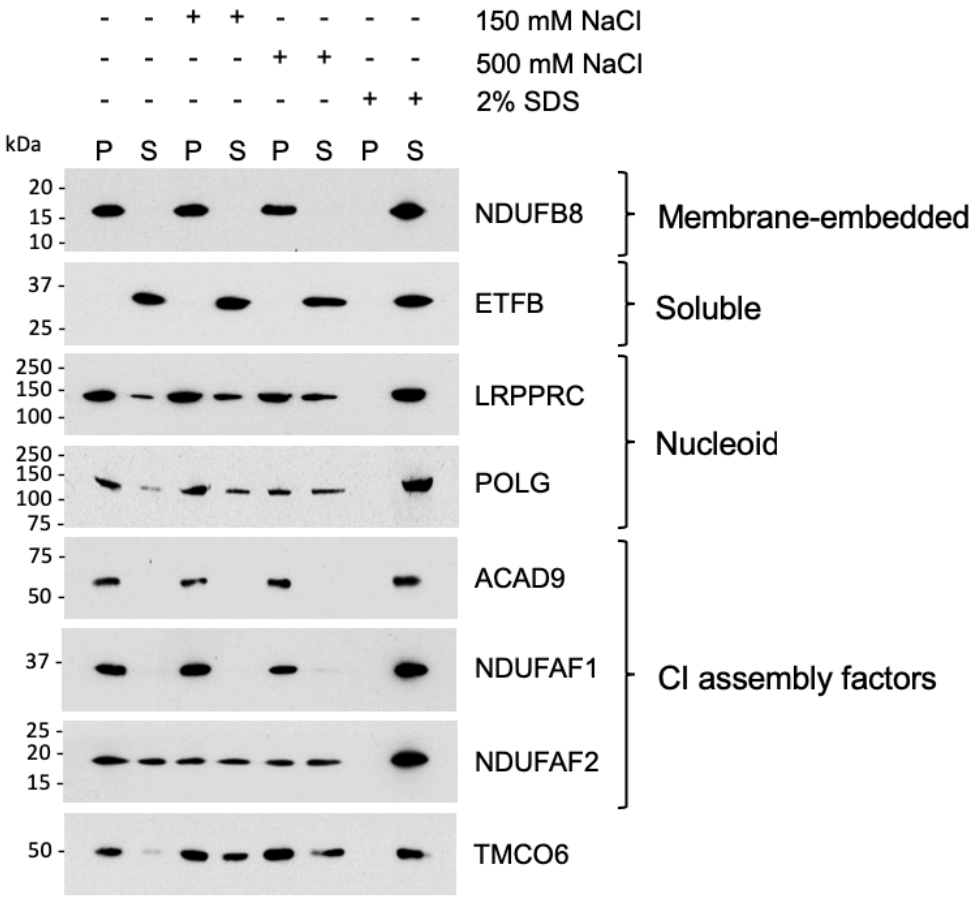

Figure 5.4 TMCO6 is a membrane-bound protein which can be dissociated from the membrane with the addition of salt.

Subcellular fractionation by differential centrifugation was performed as per **section 2.6.7** in order to isolate mitochondria from HEK 293T cells. Intact mitochondria were sonicated and then separated into aliquots of equal protein amount and incubated with nothing, one of two different concentrations of salt (150 mM or 500mM) or 2 % SDS, as indicated. Aliquots were then centrifuged once more and resulting pellet (P) and supernatant (s) fractions were collected. SDS-PAGE was performed as per **section 2.6.2**, followed by Western blotting (**section 2.6.4**) and immunodetection (**section 2.6.5**) with anti-NDUFB8, anti-ETFB, anti-LRPPRC, anti-POLG1, anti-ACAD9, anti-NDUFAF1, anti-NDUFAF2 and anti-TMCO6 primary antibodies (see **Table 2.29** for manufacturer details and concentrations used).

As shown in **Fig 5.4**, TMCO6 is primarily found in the membrane fraction of untreated mitoplasts. With increasing salt gradient, TMCO6 can be dissociated from the membrane into the soluble fraction, similarly to the CI assembly factor NDUFAF2 and the nucleoid proteins LRPPRC and POLG1, and in clear contrast to other CI assembly factors like ACAD9 and NDUFAF1. In combination, these experiments suggest that TMCO6 is a mitochondrial protein, localising to the IMM, which is tethered to the membrane and not embedded given its susceptibility to dissociation.

5.2.2 Investigating the Effects of *TMCO6* Gene Silencing

To begin to investigate the role of TMCO6 in CI assembly and stability, RNA interference (RNAi) was performed by lentiviral transduction of HEK 293T cells with four different short hairpin RNAs (shRNAs) specific for human *TMCO6* (shRNA1 – 4, see **Table 2.21** for details). Two control vectors were used alongside these: an empty vector (EV) control, encoding no shRNA sequence, and a non-mammalian negative (-) control, encoding an shRNA sequence for a synthetic version of *GFP* derived from the crustacean *Pontellina plumata*. Following selection of successfully transduced cells by puromycin treatment, we first sought to quantify the extent of *TMCO6* gene silencing. Total RNA was extracted from each of the six cell lines, retrotranscribed to cDNA and then subjected to RT-qPCR (procedure and components detailed in **section 2.2.14**) in technical triplicates to quantify the relative abundance of *TMCO6* mRNA transcripts normalised to the relative abundance of *GAPDH* mRNA transcripts. Quantification was performed using the $\Delta\Delta C_t$ method (**Fig 5.5**) and revealed that shRNA-1 was the least effective of the four shRNAs, producing only a ~35 % reduction in *TMCO6* gene expression, whereas the other three shRNAs (shRNA-2, shRNA-3 and shRNA 4) produced reductions of between 80 – 95 %.

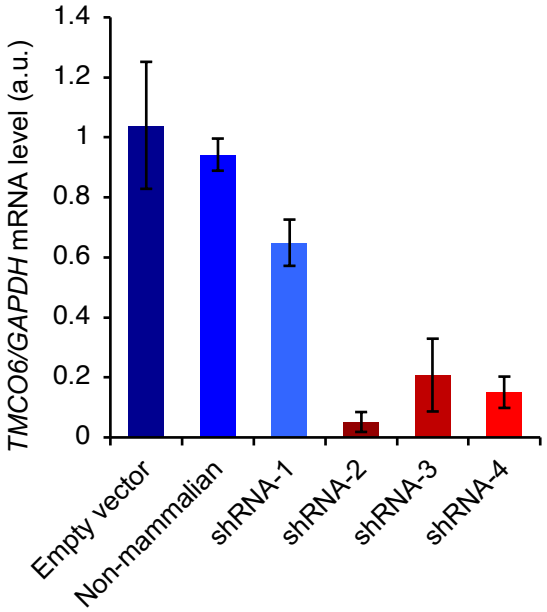

Figure 5.5 *TMCO6* mRNA transcript abundances after *TMCO6* shRNA knockdown.

RT-qPCR was performed as per **section 2.2.14** to quantify *TMCO6* mRNA transcript abundance in four shRNA knockdown cell lines for *TMCO6* and two control cell lines, and empty vector (EV) control and a non-mammalian-targeted shRNA control, relative to mRNA transcript abundances for *GAPDH*. shRNA-1 is the least effective of the four, producing only ~ 35 % reduction. shRNA-2, shRNA-3 and shRNA-4 each produced reductions in *TMCO6* gene expression of approximately 80 – 95 %. Data are presented as mean ± range (n = 2).

Next, the protein levels for TMCO6 and the loading control GAPDH were determined by immunodetection following SDS-PAGE and Western blotting using whole cell protein lysates obtained from each of the four shRNA-knockdown cell lines and both controls. As shown in **Fig 5.6**, densitometric quantification revealed approximately 70 % residual abundance of TMCO6 in shRNA-1, 20 % for shRNA-2, 40 % for shRNA-3 and 30 % for shRNA-4. All knockout cell lines were found to recover *TMCO6* expression to normal levels compared to the two control cell lines relatively quickly; therefore, all experiments performed with these knockdown cell lines were carried out within the first few weeks following transduction.

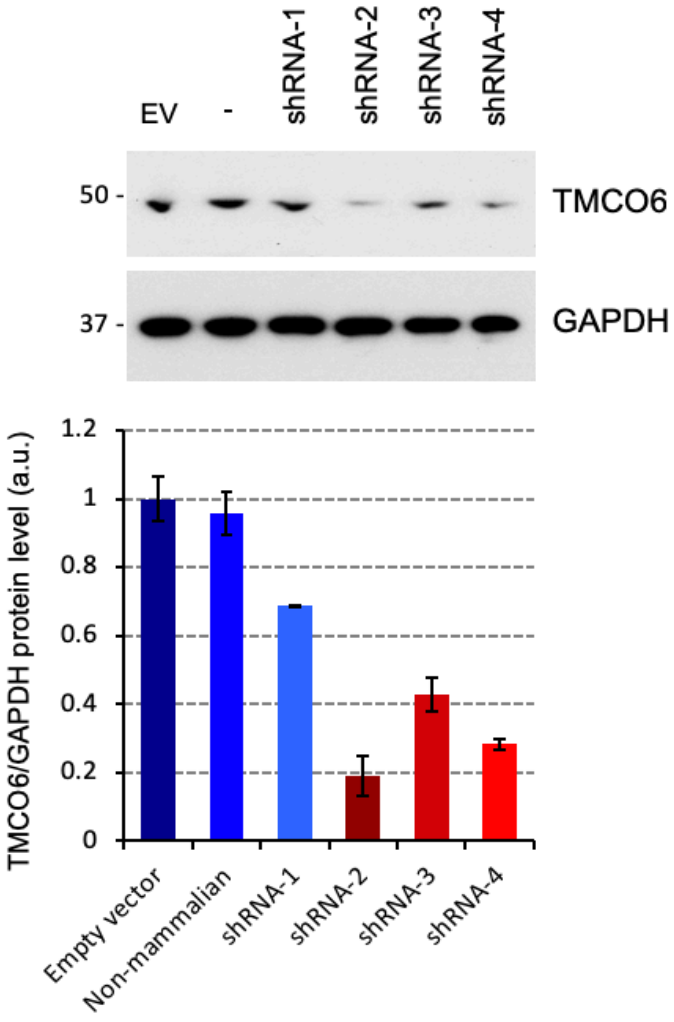

Figure 5.6 TMCO6 protein abundances after *TMCO6* shRNA knockdown.

SDS-PAGE, Western blot analysis and immunodetection using anti-TMCO6 and anti-GAPDH primary antibodies (see **Table 2.29** for antibody details) for whole cell protein lysates from four HEK 293T *TMCO6*-knockdown cell lines (shRNA1-4), and empty vector (EV) and non-mammalian negative (-) controls. Shown underneath is densitometric quantification of the TMCO6 signal normalised to the GAPDH signal for each cell line, calculated with the Fiji Image J software (Schindelin *et al.*, 2012) using the Gel Analysis integrated function. Data are presented as mean ± SEM (n = 3).

We also observed a slower growth rate for shRNA-2 and shRNA-3 cell lines cultured in glucose-rich media, compared to the empty vector and non-mammalian controls, and the shRNA-1 cell line, following *TMCO6* gene silencing (**Fig. 5.7.**). shRNA-1 grew comparably to both experimental controls, most probably given that it had only a mild reduction in TMCO6 abundance. shRNA-4 was also tested but the results varied greatly, so was discounted from analysis. These differences in growth speeds for shRNA-2 and shRNA-3 cell lines compared to the others was determined to be statistically significant.

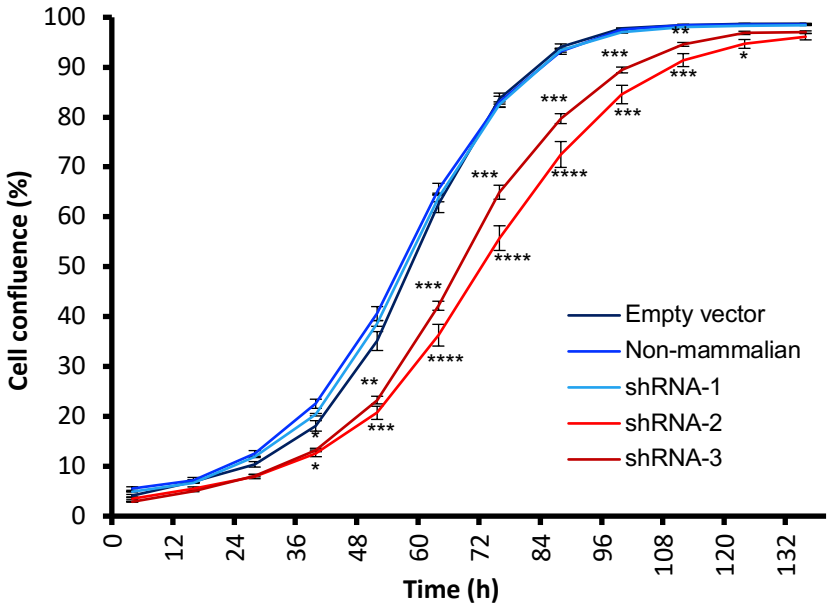

Figure 5.7 Growth curves for shRNA-knockdown cell lines vs. controls in glucose-rich culturing media.

Growth rate for empty vector, non-mammalian control, shRNA-1, shRNA-2 and shRNA-3 cell lines cultured in glucose-rich media was assessed by phase contrast light microscopy using an IncuCyte HD instrument (Essen Bioscience, UK) in technical triplicates, as per **section 2.4.1**. Statistical analysis: * $p < 0.05$, ** $p < 0.01$, *** $p < 0.005$, **** $p < 0.001$, calculated by one-way ANOVA with the Tukey *post hoc* test applied, performed as per **section 2.7**.

Next, 1D-BNGE was performed to assess differences in the abundance and distribution of the mitochondrial respiratory chain protein complexes by size. As shown in **Fig 5.8 A.**, native CI abundance is partially decreased for shRNA-2, shRNA-3 and shRNA-4 cell lines compared to the non-mammalian and empty vector controls, and the ineffective knockdown cell line, shRNA-1. However, the largest observable difference was in the abundance of CI-containing supercomplexes. The $CIII_2$ + CIV supercomplex band is also reduced to some extent, whereas both $CIII_2$ and CIV quantities are comparable to the abundances of the two controls. CI in-gel activity of an identical 1D-BNGE gel shows clear reduction in shRNA-2, shRNA-3 and shRNA-

3 samples. This qualitative result was corroborated quantitatively by spectrophotometric analyses (**Fig 5.8 B.**). *TMCO6* gene silencing resulted in an isolated CI deficiency of ~ 40 % in shRNA-2, shRNA-3 and shRNA-4 cell lines in two biological replicates. Specific activities for CII, CIII and CIV were within normal values for all knockdown cell lines.

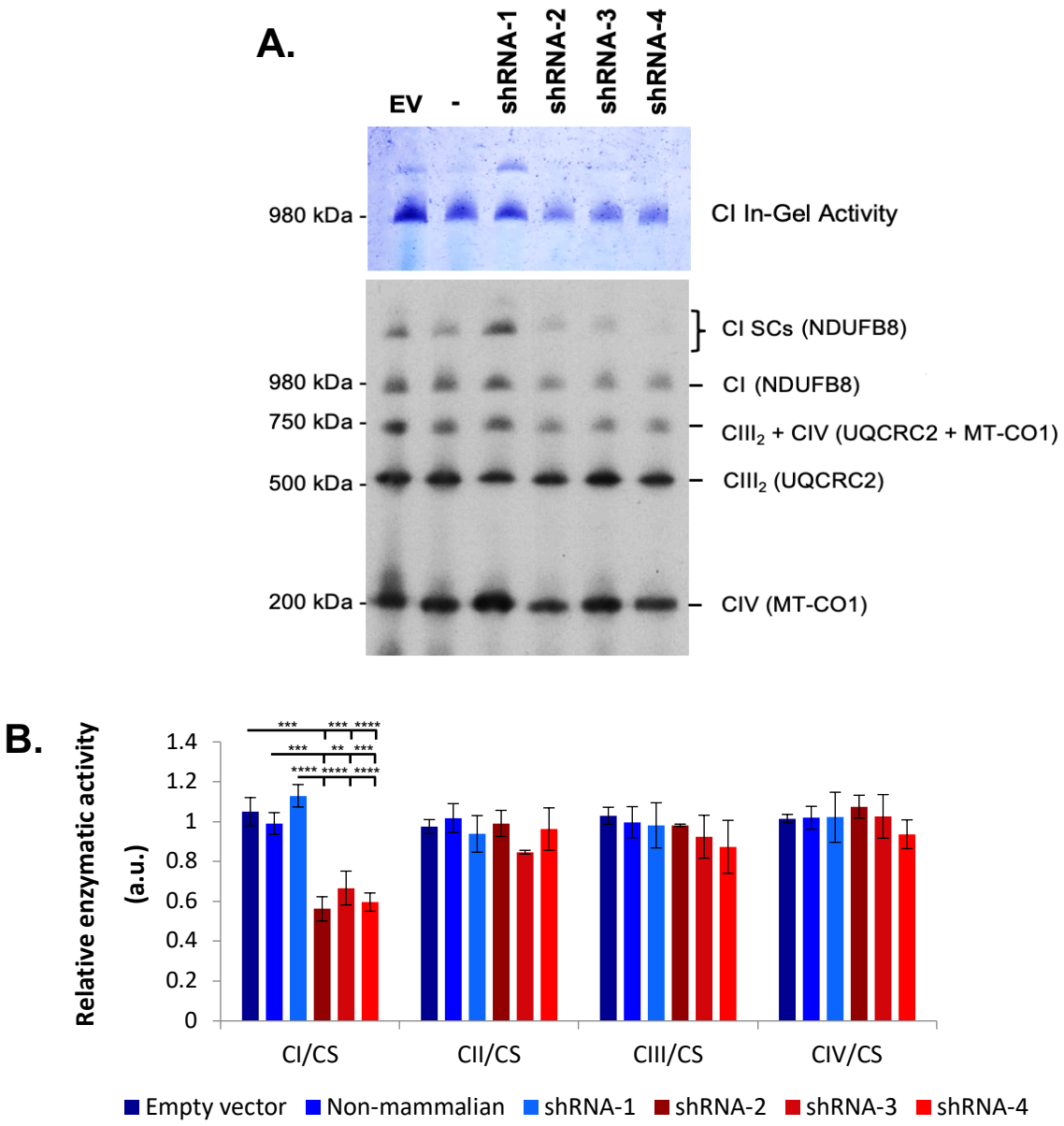

Figure 5.8 Abundance of native CI and CI-containing supercomplexes was reduced in three shRNA-knockdown cell lines, as was specific CI enzymatic activity.

(**A.**) 1D-BNGE, Western blot analysis and immunodetection using anti-NDUFB8 (recognising CI), anti-UQCRC2 (recognising CIII), and anti-CO1 (recognising CIV) (see **Table 2.29** for antibody details) for mitochondrial protein extracts treated with 1 % DDM from four HEK 293T TMCO6-knockdown cell lines (shRNA1-4), and empty vector (EV) and non-mammalian negative (-) controls. CI in-gel activity (above) was performed as per **section 2.7.2** on an identical gel. (**B.**) Specific enzymatic activities for CI, CII, CIII and CIV were measured as per **section 2.7.1** for EV, -, shRNA-1, shRNA-2 shRNA-3 and shRNA-4 cell lines and normalised to the specific activity of citrate synthase (CS) per cell line. Data are presented as mean ± range (n = 2 biological replicates). Statistical analysis: ** $p < 0.01$, *** $p < 0.005$, calculated by two-way ANOVA with Sidak's multiple comparisons *post hoc* test applied.

Since we had observed an increased presence of some CI subcomplexes, and also, TMCO6 dissociation from fully assembled CI in patient fibroblasts, we wanted to investigate these aspects in gene silenced cells. A fraction of TMCO6 co-localises with native CI by 2D-BNGE in the control and knockdown cell lines (**Fig. 5.9**). This finding corroborates the co-localisation seen for control and patient-derived primary skin fibroblasts (**Fig 4.12**). However, the proportion of TMCO6 co-migrating with fully assembled CI is higher in empty vector and non-mammalian HEK 293T control cell lines than in shRNA-3 and shRNA-4 TMCO6-knockdown cell lines, calculated by quantifying the relative amounts of S1, S2 and CI for each cell line out of 100 %. As shown in **Fig. 5.9**, the amount of TMCO6 colocalising with CI in knockdown cell lines is reduced between 20 – 30 % by densitometric quantification compared to both controls, and there is an equivalent increase in the relative quantity of the smaller of two sub-assembly intermediates. This result suggests TMCO6 dissociation from fully assembled CI in this cell model, perhaps owing to stalled assembly of the CI holocomplex.

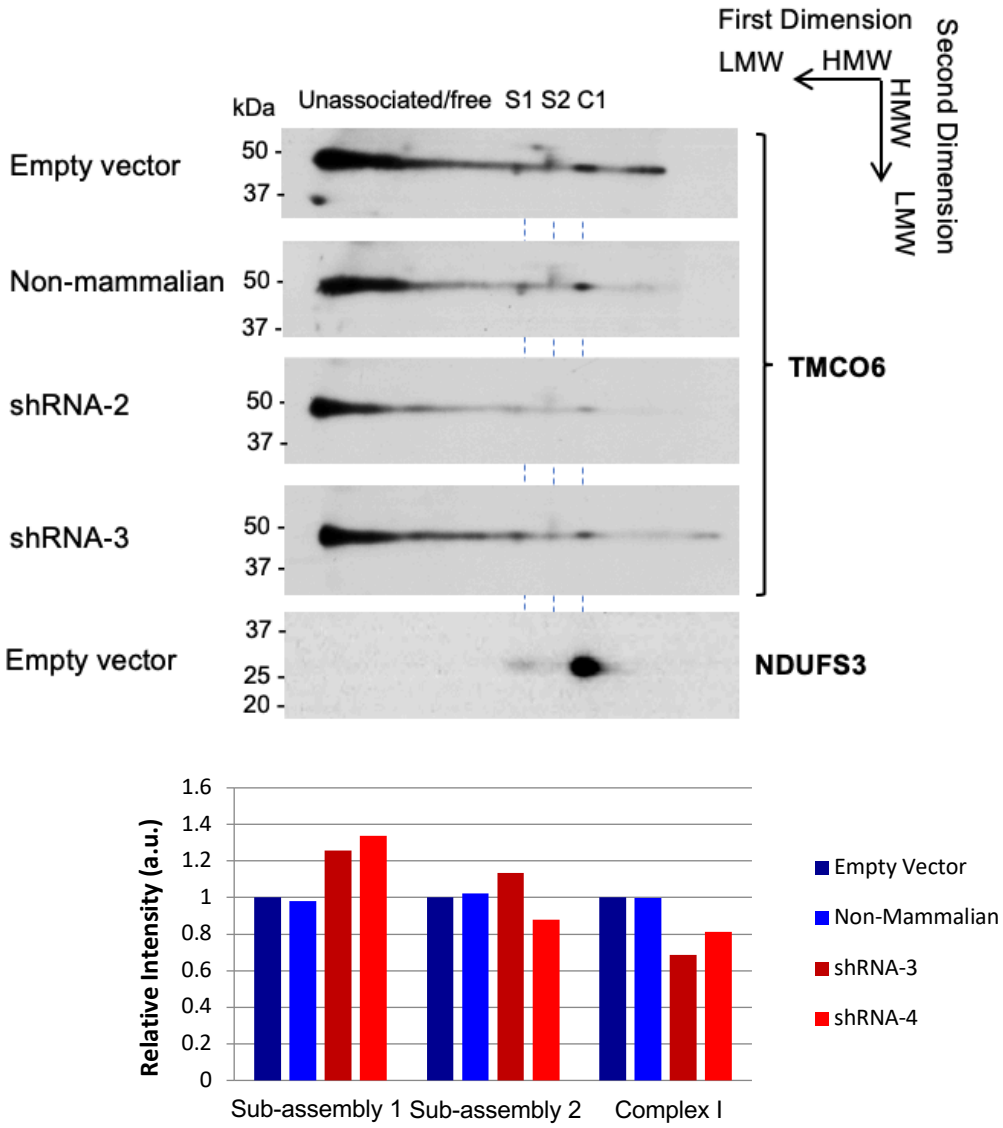

Figure 5.9 Reduced fully assembled CI and subassembly accumulation in TMCO6-knockdown HEK 293T cell lines

(**A.**) 2D-BNGE, Western blot analysis and immunodetection of mitochondrial protein extracts treated with 1 % DDM from empty vector and non-mammalian 293T control and two shRNA-knockdown cell lines using anti-TMCO6 and anti-NDUFS3 (recognising CI) primary antibodies (see **Table 2.29** for antibody details). (**B.**) Densitometric quantification of the TMCO6 signals for subassembly 1 (S1), subassembly 2 (S2) and Complex I (CI) for each of the four cell lines, calculated with Gel Analysis tool of Fiji Image J software (Schindelin *et al.* 2012).

5.2.3 Investigating the Effects of *TMCO6* Gene Overexpression

A doxycycline-inducible overexpression system for human *TMCO6* was generated in Flp-In™ HEK 293T cells in order to investigate the function of TMCO6. For this, we studied both major isoforms, TMCO6.1 (NM_018502.5, 493 aa product) and TMCO6.2 (NM_001300980.1, 499 aa product), as well as the addition of the human patient mutation (NM_018502.5: c.271C>T), into both of these in order to determine whether the mutant protein affected CI stability or enzymatic activity. These four *TMCO6* variants (*TMCO6.1-WT, TMCO6.1-R91C, TMCO6.2-WT* and *TMCO6.2-R91C*) were each C-terminally tagged with HA (peptide sequence: YPYDVPDYA), or FLAG/STREP (FS) (peptide sequence: DYKDDDDK/WSHPQFEK), to generate 8 distinct inducible *TMCO6* transgenes: *TMCO6.1-WT^{HA}, TMCO6.2-WT^{HA}, TMCO6.1-MUT^{HA}, TMCO6.2-MUT^{HA}, TMCO6.1-WT^{FS}, TMCO6.2-WT^{FS}, TMCO6.1-MUT^{FS},* and *TMCO6.2-MUT^{FS}*.

SDS-PAGE and WB analysis (**Fig 5.10 A.**) shows the outcome of 48-hour incubations of four HEK 293T cell lines either expressing FLAG-tagged wildtype (WT) or mutant (R91C) *TMCO6*, TMCO6.1-WT^{FLAG}, TMCO6.1-R91C^{FLAG}, TMCO6.2-WT^{FLAG}, and TMCO6.2-R91C^{FLAG}, with three different concentrations of doxycycline (DOX). The signal for FLAG-tagged TMCO6 was detectable only in induced cell lines, and non-induced (0 ng/ml DOX, - DOX) controls showed no ‘leakage’ of the FLAG-tagged TMCO6 gene products by SDS-PAGE. 2.5 ng/µl DOX was selected for subsequent experiments given its reproducible effectiveness and lack of effect on growth rate of the cell lines.

Samples resolved under non-denaturing conditions by 1D-BNGE (**Fig 5.10 B.**) revealed that the majority of FLAG-tagged TMCO6 was detectable in the low molecular weight region of the gel, with far more detected for isoform TMCO6.1 than for TMCO6.2; however, some of the FLAG-tagged TMCO6 signal co-migrated into at least two discrete high molecular weight bands (indicated by the red arrowheads). These bands are most probably caused by nonspecific binding of the anti-FLAG primary antibody, since the signal was also found to varying extents in the non-induced controls. Given the intensity of these unspecific bands, it was not possible to discern co-migration of the TMCO6-FLAG signal with that of CI subunits NDUFB8 and NDUFS3, or any CI subassembly intermediates by 1D-BNGE or 2D-BNGE analyses (data not shown). Next, we sought to determine the effect of overexpression of wildtype and mutant TMCO6 on the relative abundances of CI subunits and assembly factors, and on subunits of the other protein complexes of the mitochondrial respiratory chain.

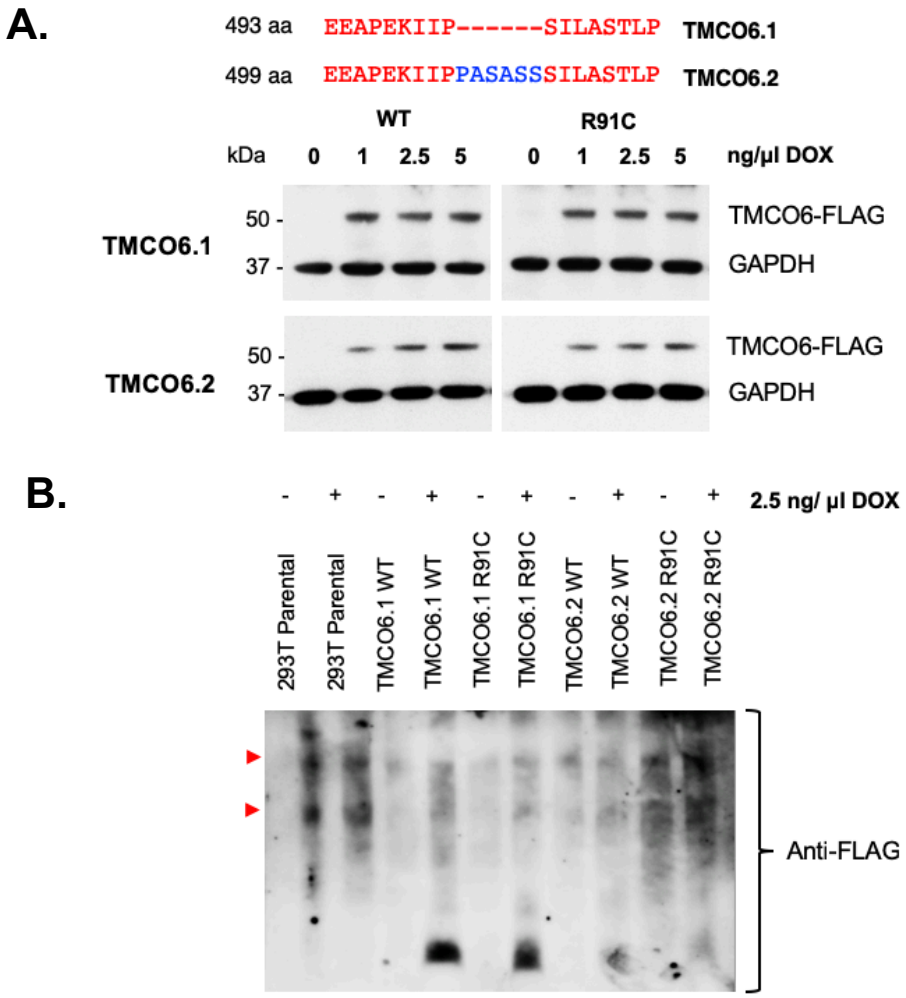

Figure 5.10 Overexpressing wildtype or mutant TMCO6.1 and TMCO6.2 in HEK 293T cells.

(**A.**) SDS-PAGE, Western blot analysis and immunodetection was performed for 10 µg of whole cell protein extracts from HEK 293T cell lines with inducible *TMCO6* transgenes for *TMCO6.1* or *TMCO6.2,* each with either wildtype (WT) or patient mutant (R91C) sequences. Anti-FLAG and anti-GAPDH primary antibodies were successively immunoblotted on the same membranes (see **Table 2.29** for antibody details). (**B.**) 1D-BNGE, Western blot analysis and immunodetection followed using an anti-FLAG (recognising TMCO6.1-WT^{FS}, TMCO6.1-MUT^{FS}, TMCO6.2-WT^{FS}, and TMCO6.2-MUT^{FS}) primary antibody (see **Table 2.29** for antibody details). Mitochondrial protein from four HEK 293T overexpression cell lines, TMCO6.1 WT, TMCO6.1 R91C, TMCO6.2 WT and TMCO6.2 R91C, following incubation with 2.5 ng/µl DOX for 48 h or equivalent cell lines that were non-induced (- DOX) were solubilised with 1 % DDM and approximately 150 µg loaded per lane (*n* = 1 each).

SDS-PAGE, Western blot analysis and immunodetection was performed using 10 µg of whole cell protein extracts from transduced HEK 293T cell lines following inducible expression of *TMCO6.1* or *TMCO6.2* transgenes, each with either the wildtype (WT) (NM_018502.5/ NM_001300980.1) or the patient mutant (c.271C>T) cDNA sequences. As shown in **Fig. 5.11 A.**, FLAG-tagged WT and Arg91Cys (R91C) forms of TMCO6 were only present in the DOX-treated cell lines showing that the inducible expression system had been successful, as immunodetected by use the endogenous anti-TMCO6 antibody. Unexpectedly, the overexpression of epitope-tagged TMCO6 had a respective increase in the abundance of endogenous TMCO6 levels (**Fig. 5.11 A.**) (as indicated by the red arrowheads) in DOX-treated TMCO6.1 WT, TMCO6.1 R91C, TMCO6.2 WT and TMCO6.2 R91C cell lines treated with DOX. This trend was not seen for the parental HEK 293T + DOX negative control (blue arrowhead). This finding is supported by densitometric quantification for intensity of TMCO6 or TMCO6-FLAG bands relative to the cytosolic loading control, GAPDH (**Fig. 5.11 B.**). In addition, this densitometric quantification revealed that the expression of TMCO6.1 (either WT or R91C variants) was between two- and three-fold higher than for both variants of TMCO6.2, despite treatment with the same concentration of DOX for an equivalent length of time. All induced cell lines showed a clear increase in TOMM20 (**Fig. 5.11 A.**), supported by densitometric quantification (**Fig. 5.11 B.**), suggesting an increase in overall mitochondrial mass. However, this trend was also observed for the parental HEK 293T + DOX control, and so it is not possible to credit this change to *TMCO6* expression. Instead, the increase in mitochondrial mass could be merely an effect of DOX treatment, which has previously been shown to alter mitochondrial proteostasis and function (Luger *et al.*, 2018). The abundances per cell line of NDUFA9 (Q module) followed the expression pattern for TMCO6 faithfully, more so than for any of the other CI subunits, assembly factors or subunits of the other respiratory chain complexes. The other subunits that showed variable differences in abundance were NDUFB8, and to a lesser extent NDUFB11 (both P_D module). However, amounts of NDUFB8 and NDUFB11 with or without DOX treatment are similar for all cell lines, ie. there is no increase or decrease observed following the addition of DOX for any of the cell lines. No striking differences in abundance were observed in any of the CI assembly factors or subunits of CII, CIII, CIV or CV.

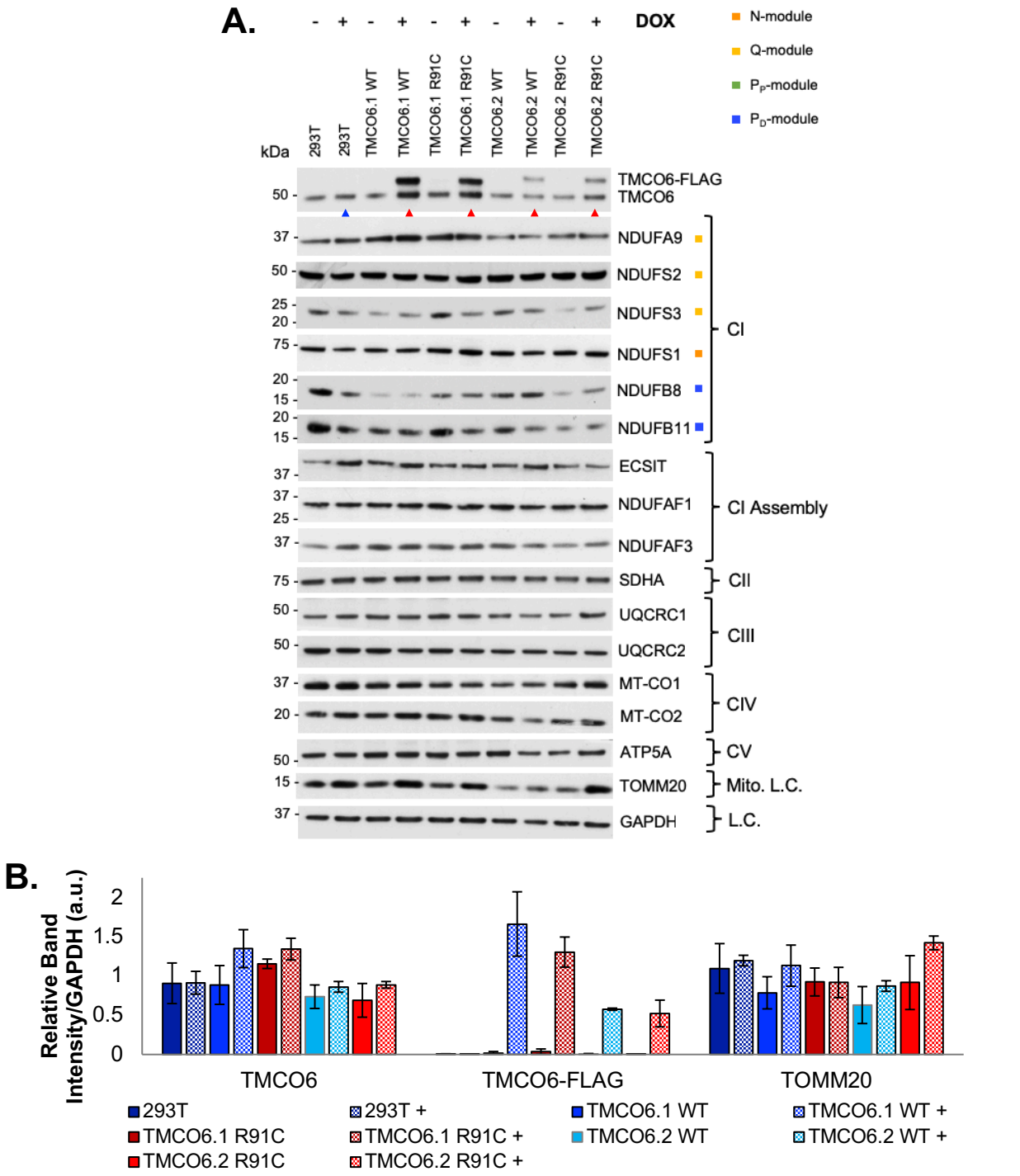

Figure 5.11 Characterising inducible expression of wildtype or mutant TMCO6.1 and TMCO6.2 in Flp-In™ HEK 293T cells by SDS-PAGE and WB analysis

(**A.**) SDS-PAGE (4-12 % NuPAGE Bis-Tris, Thermo Fisher Scientific), Western blot analysis and immunodetection of 10 µg of whole cell protein lysates from parental HEK 293T cells or four HEK 293T overexpression cell lines, TMCO6.1 WT, TMCO6.1 R91C, TMCO6.2 WT and TMCO6.2 R91C, following incubation with 2.5 ng/µl DOX for 48 h or equivalent cell lines that were non-induced (- DOX). (**B.**) Densitometric quantification was carried out for TMCO6, FLAG-tagged TMCO6 and TOMM20 signals were normalised to the signal for GAPDH per cell line. Bars corresponding to non-induced cell lines are solid colours, and those corresponding to induced cell lines are shaded. Data are presented as mean ± range (*n* = 2).

No differences in CI activity was detected by in-gel activity for any of the inducible *TMCO6* overexpression cell lines compared to the parental HEK 293T negative controls following 2.5 ng/µl DOX treatment for 48 h (**Fig 5.12 A.**). 1D-BNGE was performed again for separate samples prepared with equivalent cell quantities (8 x 10^6 cells per cell line) (**Fig 5.12 B.**). This showed increased overall mitochondrial mass for the induced cell lines as all complexes were upregulated when induced with DOX. Following this, 1D-BNGE and Western blot analysis was used again to determine the abundance of CI, immunodetected by NDUFA9, normalised to the signal for CII, immunodetected by SDHB, for three biological replicates of samples loading accorded to equal quantity of mitochondrial protein (150 ug per cell line) (**Fig 5.12 C.**). Densitometric analysis showed no significant differences in CI levels normalised to CII levels by 1D-BNGE. CI was immunodetected by NDUFA9 (Q-module boundary) in particular to see whether the trend in protein level seen by SDS-PAGE (**Fig. 5.11**) would correlate with differences in overall CI abundance, but this proved not to be the case.

In summary, this inducible overexpression model did not yield many clues about the function or involvement of TMCO6 in CI stability or activity. The unspecific binding of the anti-FLAG antibody made specific recognition of high molecular weight complexes by BNGE difficult, and DOX treatment was affecting overall mitochondrial mass, perhaps masking any reduction in mitochondrial mass in the cell lines overexpressing the mutant TMCO6.1 or TMCO6.2 isoforms. What we could conclude is 1) that TMCO6.1 is the predominantly overexpressed isoform in this cell type, abundant at two- to three-fold higher levels than TMCO6.2, and 2) the FLAG-tagged patient mutant variant of both TMCO6 isoforms is stably expressed at detectable levels, but at a slightly lower abundance than the wildtype variant, which is identical to what we had seen in the patient skin fibroblasts by recognition of the endogenous protein (**Fig. 4.8** and **Fig. 4.9**).

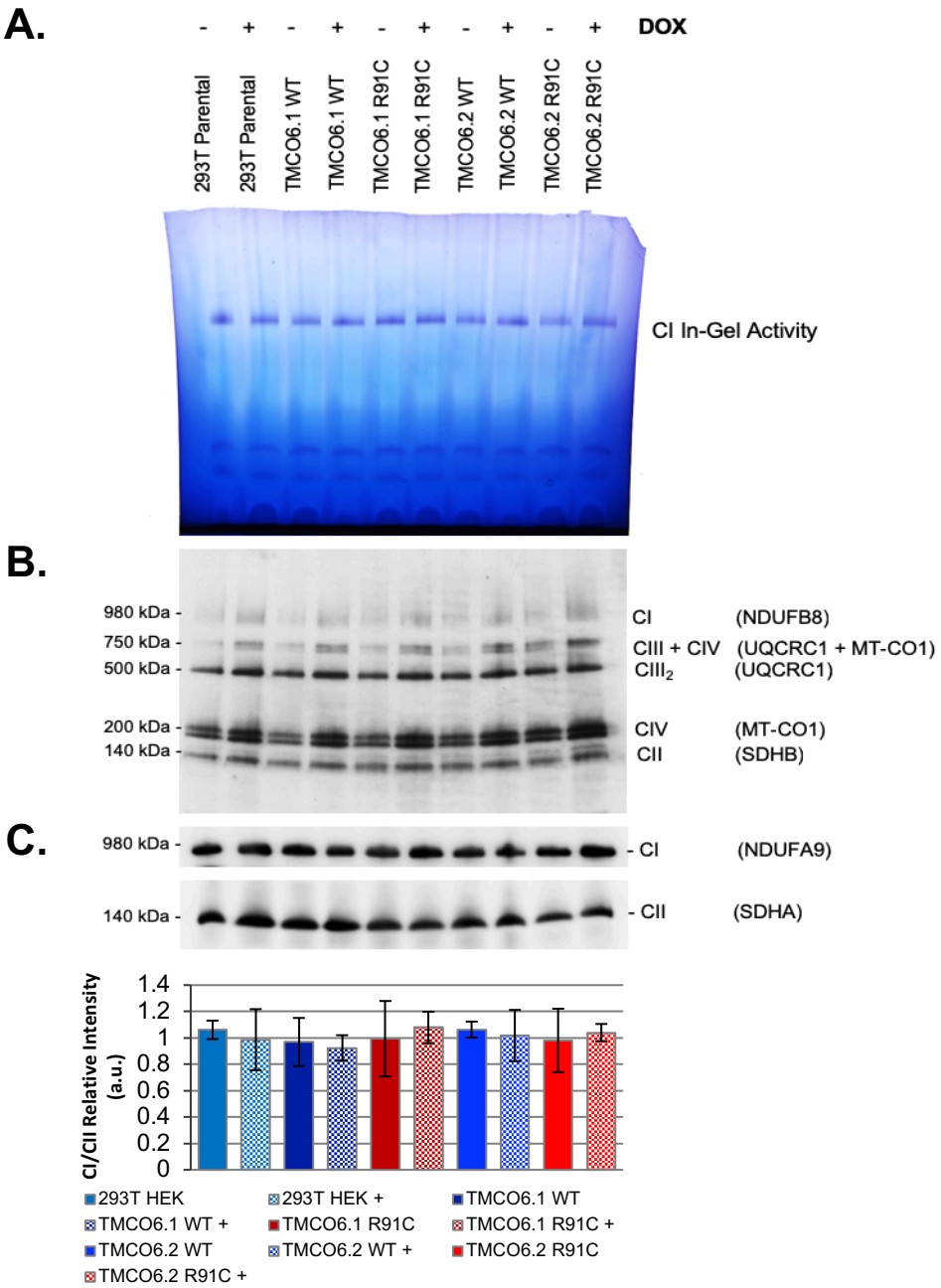

Figure 5.12 Overexpressing wildtype or mutant *TMCO6* isoforms does not affect CI amount or activity when normalised to mitochondrial mass.

(**A.**) 1D-BNGE and Complex I in-gel activity were carried out as per **sections 2.6.3** and **2.7.2** for equivalent protein quantities of DDM-treated mitochondrial proteins from HEK 293T cells and inducible *TMCO6*-overexpressing HEK 293T cell lines expressing wildtype (WT) or mutant (R91C) versions of the TMCO6.1 and TMCO6.2 isoforms. (**B.**) 1D-BNGE was performed as before with samples prepared from equal quantities of cells (8 x 10^6 in total), and WB analysis followed using anti-NDUFB8 (CI), anti-UQCRC1 (CIII), anti-CO1 (CIV) and anti-SDHB (CII) primary antibodies (see **Table 2.29** for antibody details). (**C.**) 1D-BNGE was performed again as for **B.**, and densitometric quantification was carried out for the band intensities of NDUFA9 (recognising CI) per cell line relative to SDHA (recognising CII). Bars corresponding to non-induced cell lines are solid colours, and those corresponding to induced (DOX-treated) cell lines are shaded. Data are presented as mean ± SD (*n* = 3).

5.2.4 TMCO6 Physically Interacts with the CI Holocomplex by Immunoprecipitation

Given the result that endogenous TMCO6 co-localised with fully assembly CI by 2D-BNGE in patient fibroblasts (**Fig. 4.13**), the same process was carried out with HEK 293T cells in order to assess whether co-localisation was found in other types of human cells (**Fig. 5.13**). Indeed this was the case, as shown for CI immunodetected by NDUFS1 (N-module), NDUFS3 (Q-module) and NDUFB8 (P_D module). Given this finding and their replicative speed/ease to harvest, HEK 293T cells were chosen for use in *in vitro* immunoprecipitation experiments.

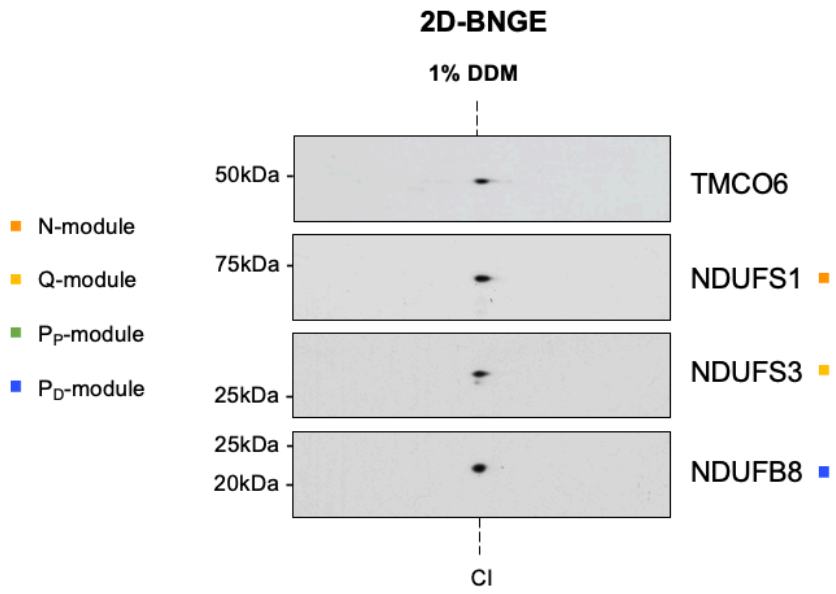

Figure 5.13. 2D-BNGE shows co-migration of TMCO6 and CI subunits in HEK 293T cells.

2D-BNGE was performed with approximately 200 µg of mitochondrial protein (+ 1 % DDM), prepared from commercial HEK 293T cells. Samples were run in the first dimension using NativePAGE 3-12 % gradient gels as per **section 2.6.3**, and then resolved under denaturing conditions by SDS-PAGE (with 1X MOPS running buffer). Membranes were sequentially immunodetected for TMCO6, NDUFS1 (N-module), NDUFS3 (Q-module), and NDUFB8 (P_D module) primary antibodies (details in **Table 2.29**).

Mitochondrial proteins isolated from HEK 293T cells were subjected to immunoprecipitation by three different methods: using 1) the Complex I Immunocapture Kit (Abcam ID: ab109711C, Abcam, Cambridge, UK), pre-bound to silica beads, 2) the anti-TMCO6 polyclonal rabbit antibody (Proteintech ID: ID: 20117-1-AP, Proteintech), recognising endogenous TMCO6 and crosslinked to Pierce™ magnetic beads and 3) anti-HA antibody (Catalogue Number: 88836, Thermo Scientific™) for detecting TMCO6.1^{HA} in Flp-In™ HEK 293T cells following inducible expression with DOX treatment (as described in **section 5.2.3** for a FLAG-tagged variant), crosslinked to Pierce™ magnetic beads. HA-tagged TMCO6.1 was used instead of FLAG-tagged TMCO6 since the antibody for anti-HA is more specific in its recognition.

As shown in **Fig. 5.14**, TMCO6 was found in the eluted fraction following immunoprecipitation with a commercial CI immunocapture kit (one representative image of three biological replicates is shown). As expected, the presence of subunits from all CI modules were also found in the eluted fraction to a greater extent than for TMCO6. These include NDUFS1 (N-module), NDUFA3 (Q-module). NDUFS8 (P_P module) and NDUFB8 (P_D module). Subunits of CII (SDHA), CIII (UQCRC1) and CIV MT-CO1) were not detected in the eluted fraction in any experiment. CI structural subunits are enriched in the eluted fraction compared to the mitochondrial fraction (M) and the supernatant (S). By contrast, most of the TMCO6 protein is retained in the S fraction and a small but significant proportion associates to CI. These results verify the observation that part of the TMCO6 pool is associated with CI as seen by 2D-BNGE, and strongly supports that TMCO6 does in fact physically interact with CI *in vivo*. Two IgG bands of ~28 kDa and ~54 kDa size were readily detected in all eluted fractions, due to the method of elution using the protein denaturant SDS, making visualisation of proteins of these sizes not possible. I repeated visualisation of equivalent samples using a goat anti-rabbit secondary antibody that should not have recognised the two IgG bands, but unfortunately this was not the case. In addition, the unspecific band at ~54 kDa (marked with an asterisk in **Fig. 5.14**) was present regardless of the elution strategy used, including incubation with 1 % SDS (as used in **Fig. 5.14**), incubation with glycine (pH = 2.0) or 3 M urea (data not shown).

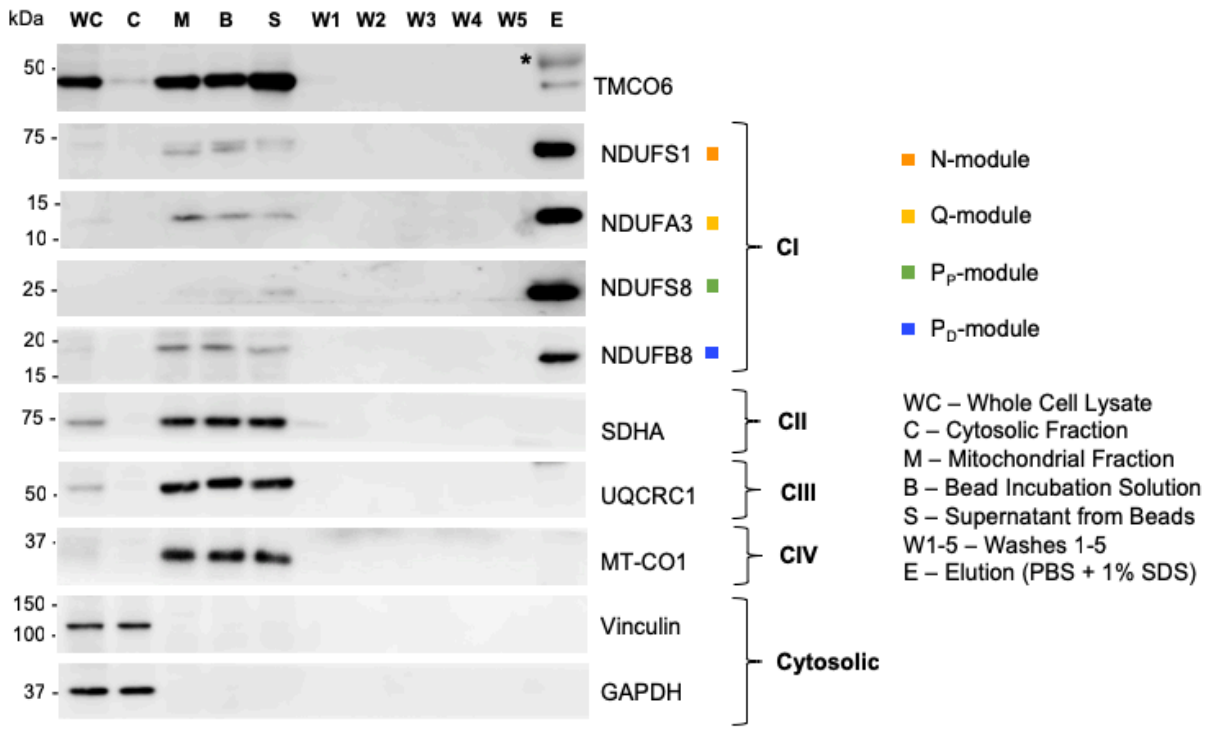

Figure 5.14. TMCO6 is immunocaptured by the CI holocomplex.

Mitochondria were isolated from HEK 293T cells, as previously described (Fernández-Vizarra *et al.*, 2010), and 0.5 mg mitochondrial protein incubated with Complex I Immunocapture beads (Abcam ID: ab109711C, Abcam, Cambridge, UK), as per **section 2.6.8**. Fractions from whole cell lysates (WC), cytosolic proteins (C), mitochondrial proteins (M), DIG-solubilised mitochondrial protein incubated with CI immunocapture beads (B), the supernatant of this incubation containing all non-bound protein (S), five washes (W1-5) and the eluted fraction (E), prepared with incubation with 1 % SDS. For abbreviations, see legend. The ~54 kDa IgG band detected by the secondary antibody is marked with and asterisk (*).

Following on from this, we sought to determine which CI subunits in particular interreacted with TMCO6. As a first attempt, immunoprecipitation was performed with the endogenous anti-TMCO6 antibody bound to magnetic beads, incubated with HEK 293T mitochondrial protein extract and eluted with pH = 3.0 glycine or 1 % SDS. However, the expression of native TMCO6 is naturally very low, making it difficult to detect even TMCO6 in the eluted fractions regardless of the method of elution or starting amount of mitochondrial protein used.

Therefore, another immunoprecipitation strategy was devised, utilising a finding we observed in Flp-In™ HEK 293T cells overexpressing FLAG-tagged TMCO6 (**section 5.2.3**) that overexpression of epitope-tagged TMCO6 also increased the steady-state level of the endogenous protein. Therefore, expression of HA-tagged TMCO6.1, was induced by DOX treatment for 48 h prior to extracting total mitochondrial protein and incubating these mitochondrial protein extracts with anti-HA-crosslinked magnetic beads. This second strategy

had another advantage in that a synthetic HA-competitor peptide could be used to elute the HA-bound proteins, and this elution strategy yielded no IgG unspecific bands by SDS-PAGE and Western blot analysis, making specific recognition of $TMCO6^{HA}$ clearer than for the endogenous protein (given that the epitope-tagged TMCO6 proteins were ~ 55 kDa in size, similarly in size to the larger of the IgG bands). As shown in **Fig. 5.15**, $TMCO6^{HA}$ only partly localises to the mitochondria, with the majority detected in the cytosolic fraction. This could be due to impaired mitochondrial import of the protein with the epitope tag. Regardless, $TMCO6^{HA}$ was detectable in the eluted fraction following incubation of mitochondrial proteins with anti HA-beads. When the anti-TMCO6 antibody was used for immunodetection, most of the signal was mitochondrial but no TMCO6 band was found in the eluted fraction, perhaps due to the amount present being under the detection limit. However, a slightly bigger band corresponding to $TMCO6^{HA}$ could easily be detected by Western blot analysis, suggesting that more HA-tagged TMCO6 species were bound to CI in these cells than endogenous TMCO6. In addition, several CI antibodies were immunodetected by Western blotting following SDS-PAGE and none of these were detectable in the eluted fractions, achieved by two different elution strategies (E1 = HA competitor peptide, and E2 = 1 % SDS).

The antibodies that recognise native CI in the CI immunocapture kit cocktail are not reported by the manufacturer (Abcam), which made it difficult to pinpoint which CI subunit(s) or interactors were found to immunoprecipitate endogenous TMCO6 by CI immunocapture (**Fig. 5.14**). Upon contacting the manufacturer, one of the antibodies they believe to be involved in the cocktail, but are not certain, is NDUFS6 (N-module). As shown in **Fig. 5.16**, NDUFS6 was detectable in both E1 and E2 fractions following long exposure. We concluded from this that TMCO6 does interact with NDUFS6, but it is possible it also interacts with other CI subunits or with known CI assembly factors. This line of inquiry requires more rigorous proteomic investigation, as discussed in **Chapter 8**.

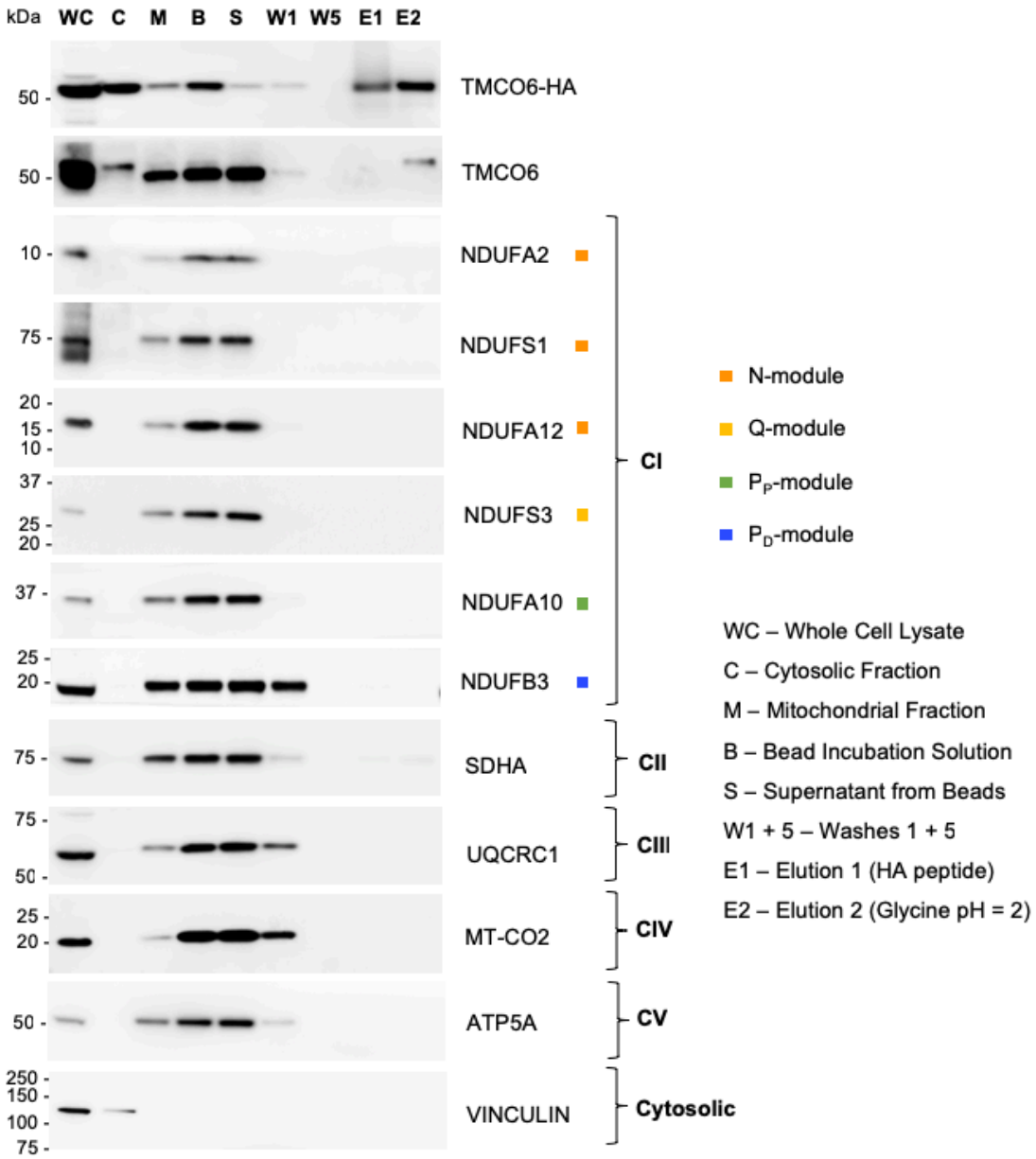

Figure 5.15. TMCO6^{HA} was initially not found to bind CI subunits by SDS-PAGE

Mitochondria were isolated from Flp-In™ HEK 293T cells, as previously described (Fernández-Vizarra *et al.*, 2010), after overexpression of HA-tagged *TMCO6.1* as per **section 2.3.6**. Following this, 0.5 mg mitochondrial protein was incubated with anti-HA Pierce™ magnetic beads overnight at 4 °C, and bound proteins washed and eluted the following day as per **section 2.6.8**. Equivalent amount of proteins from whole cell protein lysates (WC), cytosolic fractions (C), mitochondrial fractions (M), DIG-solubilised mitochondrial protein extracts incubated with CI immunocapture beads (B), the supernatant of this incubation containing all non-bound protein (S), five washes of immunocaptured proteins (W1-5) and the eluted protein fractions E1, prepared with incubation with a competing HA peptide (Catalogue ID: AB3254, Milipore, Merck), and E2, prepared with incubation in low-pH glycine (pH = 2.0) were separated by SDS-PAGE (**section 2.6.2**) and proteins immunodetected by Western blotting (**section 2.6.4**) (for antibody details and concentrations used, see **Table 2.29**).

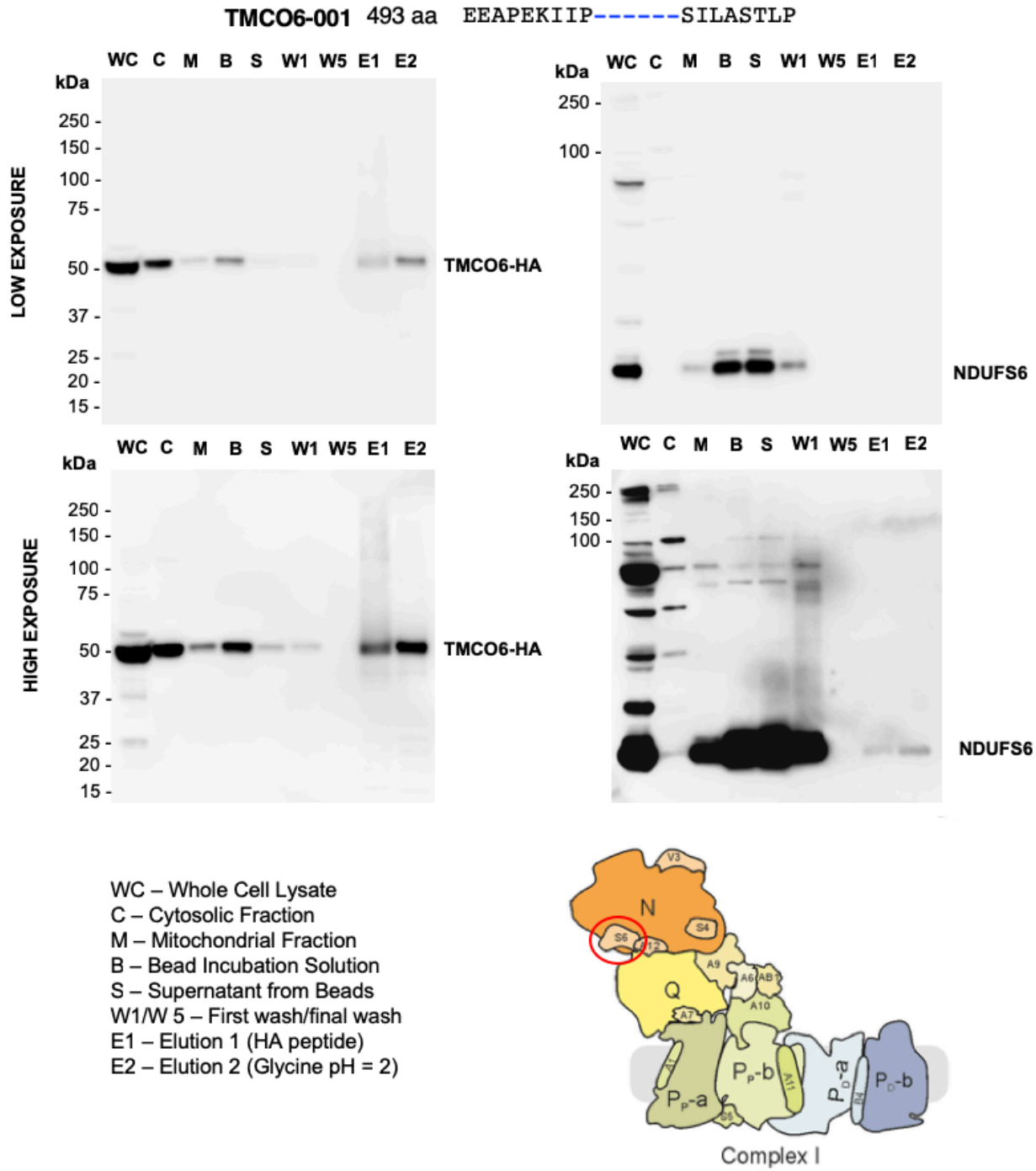

Figure 5.16. NDUFS6 is immunocaptured by HA-tagged TMCO6.

Mitochondria were isolated from Flp-In™ HEK 293T cells, as previously described (Fernández-Vizarra *et al.*, 2010), after overexpression of HA-tagged *TMCO6.1* as per **section 2.3.6**. Following this, 0.5 mg mitochondrial protein was incubated with anti-HA Pierce™ magnetic beads overnight at 4 °C, and bound proteins washed and eluted the following day as per **section 2.6.8**. Identical samples as in **Fig 5.15** were separated by size by SDS-PAGE (**section 2.6.2**) and subjected to immunodetection by Western blotting with anti-HA or anti-NDUFS6 antibodies (see **Table 2.29**). The location of NDUFS6 at the N-module/Q-module perimeter is shown in the cartoon beneath (image replicated from apart of **Fig. 7**, Guerrero-Castillo *et al.* 2017).

5.2.5 Attempting Generation of *TMCO6* Knockout and Knockin Cellular Models

CRISPR/Cas9 technology was used in this work to attempt to generate *TMCO6* knockout and knockin cell lines using HAP1 cells, a near-haploid human cell line derived from the male chronic myelogenous leukaemia (CML) KBM-7 cell line (Kotecki, Reddy and Cochran, 1999). HAP1 cells were chosen since they contain only one allelic target, making gene editing simpler than for diploid cells. Briefly, the RNA-guided nuclease Cas9, from the *Streptococcus pyogenes* clustered regularly interspaced short palindromic repeats (CRISPR) adaptive immune system, is directed by a single-stranded guide RNA (sgRNA), composed of a scaffold and a spacer sequence, to a complimentary ~20 bp target sequence within a genome, which is followed by a 3 bp protospacer adjacent motif (PAM) sequence (5' [N]GG 3'). Upon successful sequence recognition and binding by the Cas9/sgRNA complex, the Cas9 enzyme undergoes a conformational change and creates a double stranded break ~3 bp upstream of the PAM site, sequence: [N]GG (Jinek *et al.*, 2012), which is then repaired by one of two mechanisms: 1) nonhomologous end joining (NHEJ), which commonly introduces indel mutations into the site of repair that impact the open reading frame, or 2) homology-directed repair (HDR), which with the aid of a specific single-stranded donor oligonucleotide (ssODN), mediates precise genetic editing at the site of interest. Both mechanisms were employed here in order to attempt to generate a *TMCO6* knockout HAP1 cellular model, as well as a knock-in HAP1 cell line for the human patient mutation (NM_018502.5: c.271C>T) (**Fig. 5.17**).

An sgRNA sequence, sgRNA1 (sequence: 5' GGT GCT GCA AGC CTC GAC GAA GG 3'), targeted to exon 3 of the human *TMCO6* gene (GenBank ID: 55374), was designed using the CHOPCHOP online tool (http://chopchop.cbu.uib.no/) (Montague *et al.*, 2014; Labun *et al.*, 2019). Despite not having the highest quality score, determined by factors such as its fidelity to the target sequence and presence of a downstream PAM sequence, sgRNA1 allowed for convenience in generating both a knockout and, with the addition of a specific ssODN, a knock-in for the human patient mutation at the same genetic locus. Firstly, I ligated separate forward and reverse primers containing reserve complement sgRNA1 sequences, containing both the 20 bp spacer sequence targeting *TMCO6* exon 3 and the prerequisite scaffold sequences for Cas9 binding, as per the protocol devised by Ran *et al.* (Ran *et al.* 2013). Next, these ligated sequences were amplified by PCR and cloned into a commercial plasmid vector encoding the *S. pyogenes* Cas9 enzyme, pSpCas9(BB)-EGFP (Addgene ID: 48138, a gift from Feng Zhang; **Fig. 2.5**).

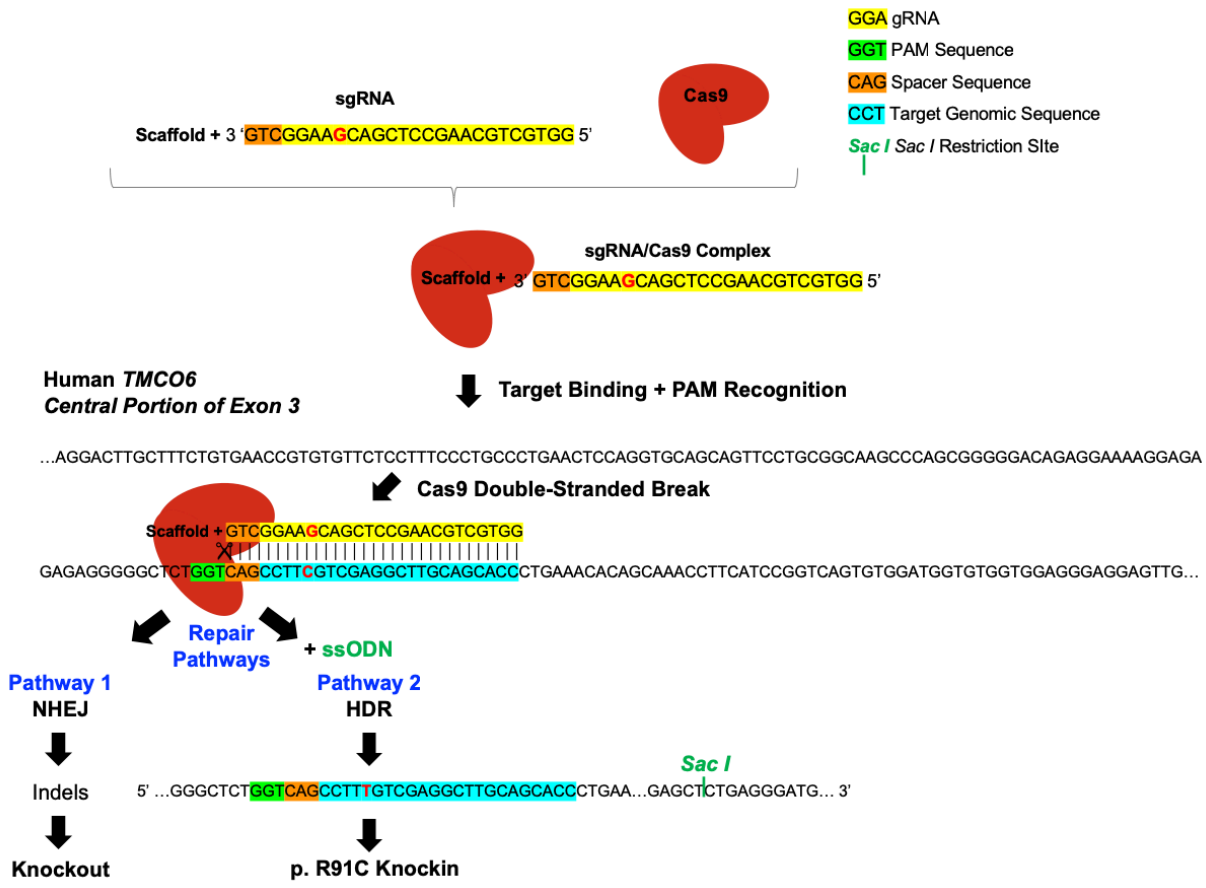

Figure 5.17 Schematic representation of CRISPR/Cas9 technology for targeting Exon 3 of human *TMCO6*.

Cas9 binds to the scaffold sequence of an sgRNA to form a Cas9:sgRNA ribonucleoprotein complex. Then, the spacer sequence of the sgRNA (yellow) guides the complex to the target genomic sequence (light blue), whereby Cas9 cleaves the double-stranded DNA after recognition of an upstream protospacer adjacent motif (PAM) (green) 3 bp before the start of the spacer sequence (orange). As shown above, this process was employed for cleavage of a site within exon 3 of *TMCO6* in HAP1 cells. After a Cas9-mediate double-stranded break of the genomic DNA at this local, two repair pathways (dark blue) could be followed. For generation of a *TMCO6* knockout, the non-homologous end joining (NHEJ) pathway commonly introduces insertion/deletion (indel) mutations into the site of repair that may impact the open reading frame. For generation of a knock-in for the patient mutation (p.Arg91Cys), homology-directed repair (HDR), which with the aid of a specific single-stranded donor oligonucleotide (ssODN), mediates precise genetic editing at the site of interest. Here, a 183 bp ssODN was used to span the middle of exon 3, where the mutated base pair was located centrally, and towards the 3' end it encodes an artificial, synonymous *Sac I* restriction site, not naturally present in this region. This restriction site was used to streamline screening of clones for successful integration of the knockin mutation (C → T, highlighted in red text).

Following verification that the cloning of sgRNA1 into pSpCas9(BB)-EGFP had been successful by restriction digestion and agarose electrophoresis (data not shown), the Guide-it™ Complete sgRNA Screening System (Catalogue number: 632636, Takara Bio Europe) was then used to screen the efficiency of sgRNA1 to cut its desired genomic site *in vitro*. Genomic DNA was extracted from HAP1 cells and purified before being subjected to PCR-based amplification of the region of interest spanning *TMCO6* exon 3, with a resulting fragment of ~500 bp (see **section 2.2.15** for thermocycling conditions, primers and reaction details). *In vitro* transcription of the pSpCas9(BB)-EGFP-sgRNA1 plasmid followed, and the resulting sgRNA1 transcript purified. Cleavage reactions were set up including the HAP1 purified genomic DNA fragment, purified sgRNA1 and Cas9 enzyme. This reaction was run alongside a positive control, the Whitescript™ (Takara Bio Europe) 2 kb control vector, with the addition of a corresponding control sgRNA. As shown in **Fig. 5.18**, sgRNA1 was able to cut the HAP1 genomic sequence at the desired locus. Similarly to the positive control, the cleavage was imperfect since a portion of the full ~500 bp fragment was still detectable, suggesting it is as effective as the positive control provided in the Guide-it™ kit.

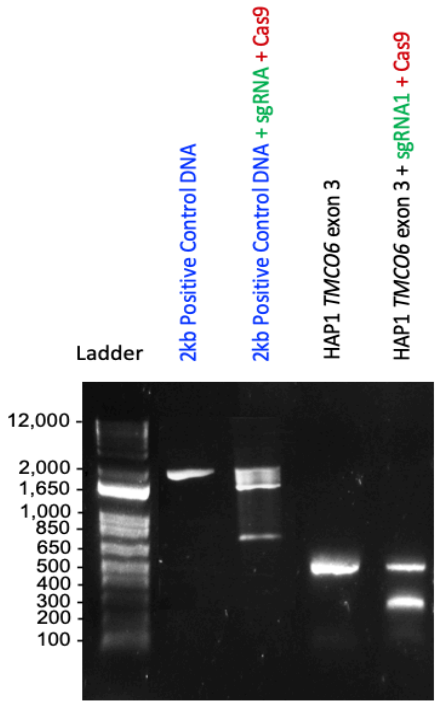

Figure 5.18 *In vitro* cleavage by sgRNA1/Cas9 of its target genomic site was successful.

The Guide-it™ Complete sgRNA Screening System (Catalogue number: 632636, Takara Bio Europe) was used to assess the efficiency of sgRNA1 to cut its desired genomic site *in vitro*. Agarose gel electrophoresis confirms partial *in vitro* cleavage of HAP1 genomic DNA within exon 3 of *TMCO6*, similarly to a 2 kb positive DNA control and corresponding sgRNA. A 1 kb DNA ladder (L) (Invitrogen™, UK) was used for size comparison (as labelled). Gels were digitally visualized via UV transilluminator.

For generating a knockout by the NHEJ pathway, 100 ng of purified pSpCas9(BB)-EGFP-sgRNA1 plasmid was transfected into HAP1 cells by means of the TurboFectin 8.0 reagent (Catlogue number: TF81001, Origene) and corresponding protocol. For generating a knock-in of the patient mutation by HDR, the same process was followed but with the addition of 10 μM of a specific ssODN (**Table 2.19**), encoding the patient C→T transition mutation and a downstream synthetic, synonymous *Sac I* restriction site. Cells that had been transfected with the pSpCas9(BB)-EGFP-sgRNA1 plasmid expressed GFP, which could can be used for cell sorting. Additionally, cells were stained with 7-AAD, a membrane impermeant fluorescent dye taken up only by apoptotic or dead cells. The transfected and 7-AAD stained cells were sorted by fluorescence-activated cell sorting (FACS) (**Fig. 5.19**), performed entirely by the Cambridge Institute for Medical Research's Flow Cytometry Core Facility, gating for GFP-positive and 7-AAD-negative cell populations for sgRNA1 and sgRNA1 + ssODN1 subtypes. For each, approximately 500 GFP-positive/7-AAD negative live cells were distributed into individual wells of a 96-well plate and cultured undisturbed for 1-2 weeks until detection of cell colonies.

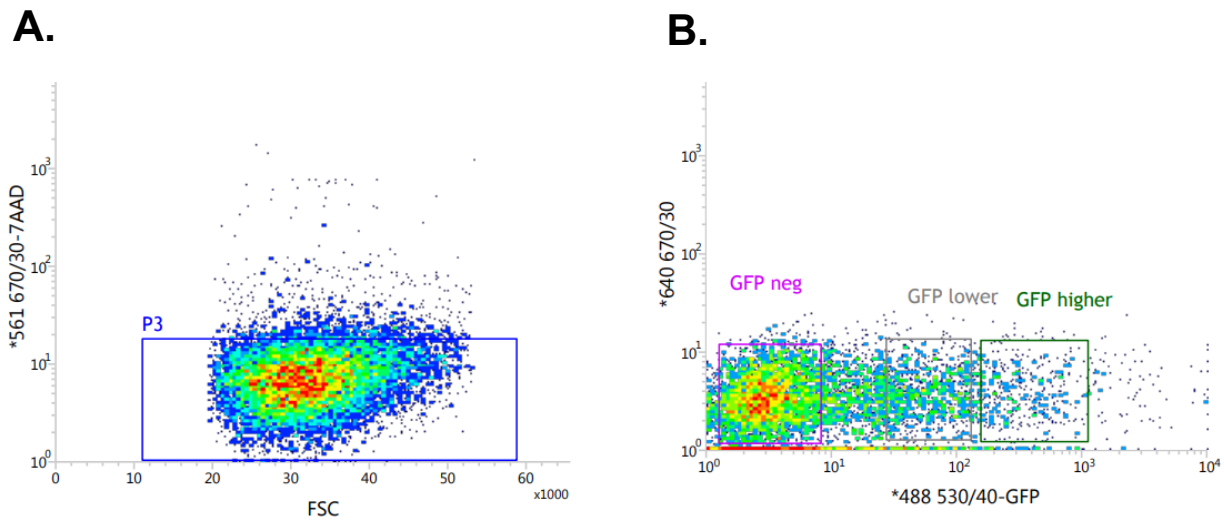

Figure 5.19 FACS gating for HAP1 cells transfected with pSpCas9(BB)-EGFP-sgRNA1 and stained with 7-AAD.

For selection of live HAP1 cells successfully transfected with the pSpCas9(BB)-EGFP-sgRNA1 plasmid, FACS was performed at the Cambridge Institute of Medical Research's Flow Cytometry Core Facility. (**A**.) Cells were firstly gated for 7-AAD-negative populations, so that only live cells were selected. In addition (**B.**), two groups of GFP-positive populations were chosen to segregate GFP-high (green square) and GFP-low (grey square) cell populations. GFP-negative cells (pink square) were routinely discarded. This process was performed for both knockout and knockin strategies.

Screening of *TMCO6*-KO cells was performed by SDS-PAGE using whole cell protein extracts and immunodetection of the endogenous TMCO6 protein**. Fig. 5.20** shows screening of 50 colonies showing ubiquitous presence of the TMCO6 protein signal. In total, 98 colonies were screened in this way, and 30 of the colonies that showed the greatest decreases in TMCO6 abundance relative to GAPDH were subjected to gDNA extraction, amplification of the *TMCO6* exon 3 region by PCR and Sanger sequencing (using the same primers that were used for amplification of the HAP1 *TMCO6* exon 3 fragment shown in **Fig. 5.18**). Unfortunately, there were no observed changes to the wildtype gene sequences for any of these, indicating that cleavage by sgRNA1/Cas9 had been unsuccessful. Since successful uptake of the plasmid had been proven by the GFP-positive gating during FACS, it is most likely that sgRNA1 could not find or bind its target sequence within the native genomic DNA as it had done *in vitro*. However, we cannot rule out at this stage the possibility that *TMCO6* knockout cells were not viable, resulting in the absence of *TMCO6*-knockout clones.

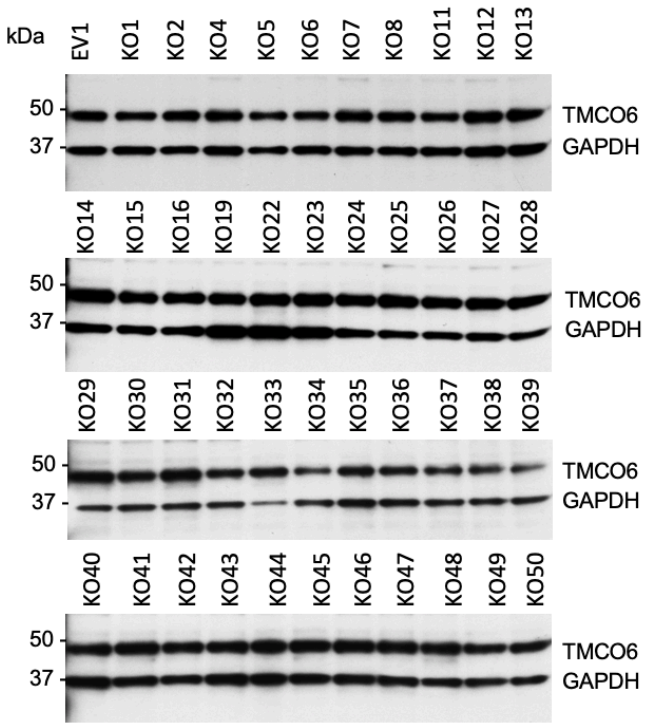

Figure 5.20 SDS-PAGE revealed unsuccessful *TMCO6*-knockout in HAP1 cells.

SDS-PAGE (4-12 % NuPAGE gels, Invitrogen™), Western blot analysis and immunodetection using anti-TMCO6 and anti-GAPDH primary antibodies (see **Table 2.29** for antibody details) was performed for 15 ug of whole cell protein lysates from one empty vector (EV) control (only transfected with pSpCas9(BB)-EGFP plasmid) and 98 HAP1 knockout (KO) cell lines that had been transfected with pSpCas9(BB)-EGFP-sgRNA1 (a representative 50 are shown). TMCO6 was detected in all cell lines relative to GAPDH indicating failure of target binding or PAM recognition or double-stranded cleavage by sgRNA1/Cas9.

Screening of *TMCO6* knock-in cells was performed by gDNA extraction, PCR amplification of the target region using the primers, reagents and thermocycling conditions as per **Tables 2.12 – 2.14**, and then restriction digestion with 1 U/µl *Sac* I (Catalogue number: R0156S, New England Biosciences®). **Fig. 5.21** shows *Sac I*-digested genomic DNA fragments for 15 of the total 78 colonies screened by this method, with no successful digestion shown. It is likely that if the cleavage by the sgRNA1/Cas9 ribonucleoprotein complex was unsuccessful, as inferred from the knockout process, then the ssODN could not successfully bind to its target site allowing for replication of the intended patient mutant variant (C→T).

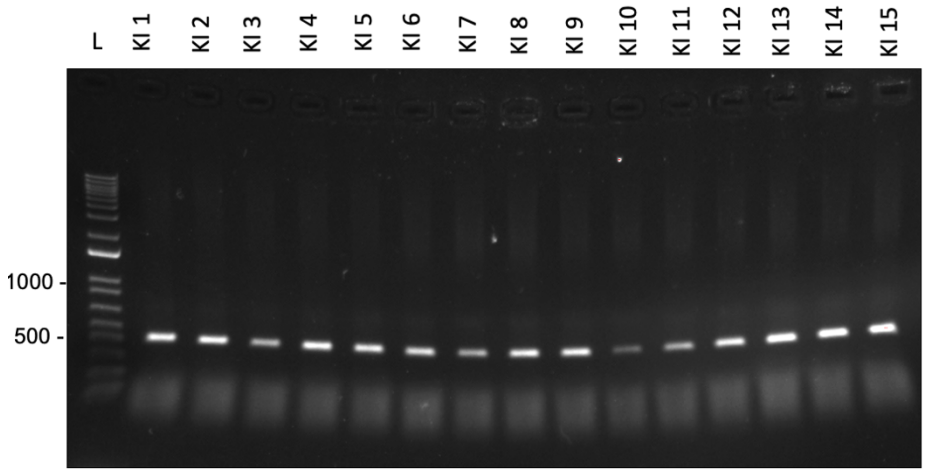

Figure 5.21 *Sac I*-digested HAP1 genomic fragments show unsuccessful integration of the patient mutation in attempted knockin HAP1 cell lines.

PCR products were amplified from genomic DNA purified from HAP1 knockin (KI) cell lines, transfected with pSpCas9(BB)-EGFP-sgRNA1 plasmid + a specific ssODN for integration of the patient mutant into the HAP1 genome. After Sac I digestion, fragments were separated by agarose gel electrophoresis, and run alongside a 1 kilobase (Kb) DNA ladder (L) (Invitrogen™, UK) for size comparison (as labelled). Gels were digitally visualized via UV transilluminator.

We concluded from this that another sgRNA sequence was necessary. As previously stated, we chose a spacer sequence that had did not have the highest quality score in order to enable both knockout and knockin generation at the same genetic. However, despite confirming sgRNA1/Cas9 cleavage on the desired genomic site *in vitro* (**Fig. 5.18**), it seems another sgRNA with higher sequence fidelity and access to a suitable PAM site is necessary. At the time of these results, work had begun with a *Tmco6*-knockout mouse strain (**Chapter 6**), and so attempted generation of a knockout HAP1 cellular model ceased in order to focus on this knockout animal model.

5.3 Conclusions

This work: 1) proved the subcellular localisation of TMCO6, 2) described CI deficiency and CI destabilisation in a cellular model of *TMCO6* gene silencing, 3) described the molecular and biochemical consequences of a TMCO6 overexpression model, 4) confirmed physical interaction between CI and TMCO6 via immunoprecipitation experiments, and 5) detailed the process for attempting to create a *TMCO6* knockout cellular model.

Firstly, confocal microscopy revealed that TMCO6 localises to the mitochondria, specifically the IMM. Secondly, shRNA-mediated *TMCO6* gene silencing led to reduced abundance of CI-containing supercomplex species, and an increase in TMCO6-containing CI intermediates, and a ~40 % reduction in CI specific enzymatic activity. Successful shRNA-knockdown cell lines displayed impaired cellular growth rate in glucose-rich media.

Inducible overexpression of *TMCO6.1* (NM_018502.5) and *TMCO6.2* (NM_001300980.1) transcript isoforms, either with wildtype or patient mutant (c.271C>T) sequences, led to a correlated increase in the steady-state level of endogenous TMCO6. Overexpression of FLAG-tagged TMCO6 isoforms, and wildtype/mutant variants of these, did not affect overall CI abundance or specific activity relative to total mitochondrial mass. Any differences in mitochondrial mass between TMCO6-overexpressing and non-induced or control cell lines were thought to be an effect of the DOX induction method.

Generation of *TMCO6* knockout and knockin cellular models were unsuccessful due to either incorrect target binding, PAM site recognition or Cas9-mediated cleavage at the correct genomic site. However, it is possible that TMCO6 protein ablation in these cells is non-viable. TMCO6 co-localises with CI by 2D-BNGE in HEK 293T cells, as had been found to be the case in skin fibroblasts.

Immunoprecipitation experiments using a native CI immunocapture kit reproducibly identified TMCO6 in the eluted protein fraction, confirming the physical interaction between TMCO6 and CI that was originally seen by 2D-BNGE using mitochondrial protein extracts from patient derived fibroblasts and HEK 293T cells. NDUFS6, which localises to the N-module/Q-module boundary of CI, is immuno-precipitated by HA-tagged TMCO6 *in vitro*.

The confirmation of the intracellular localisation of TMCO6 specifically to the IMM was crucial for allowing TMCO6 to be considered a contender as the causal protein for the severe CI deficiency detected in the human mitochondrial disease patient described in **Chapter 4**. Secondly, shRNA-mediated *TMCO6* gene expression knockdown further supported that TMCO6 affects CI stability and activity, producing a ~40 % reduction in its specific biochemical

activity by spectrophotometry and resulting in a loss of fully assembled CI and CI-containing supercomplexes, as shown by 1D-BNGE. The immunoprecipitation experiments that showed that endogenous TMCO6 physically interacts with the native CI holocomplex warrants further investigation to determine the specific CI subunit interactors, as discussed in **Chapter 8**. Although generation of a *TMCO6*-knockout cellular model was not achieved by CRISPR/Cas9, a transgenic *Tmco6*-knockout mouse model was used to study the effects of Tmco6 ablation on development, physiology, neuromuscular coordination and tissue-specific histopathology and mitochondrial metabolism (detailed in **Chapter 6**).

Chapter 6

Characterisation of a *Tmco6*-Knockout *In Vivo* Model

6.1 Introduction

As described in previous chapters, a novel mutation in *TMCO6* (NM_001300980.1:c.271C>T, p.Arg91Cys) was identified by WES in a paediatric male proband presenting with severe psychomotor delay, spasticity, dystonia, generalised hypotonia, epilepsy, and progressive demyelination of cortical and subcortical brain regions. A skeletal muscle biopsy revealed severe CI deficiency to a third of normal levels, although this same deficiency was not observed in patient-derived fibroblasts. TMCO6 was subsequently found to co-localise with the CI holocomplex by 2D-BNGE in these cells, and this result was corroborated by 2D-BNGE and immunoprecipitation experiments in HEK 293T cells, confirming physical interaction between TMCO6 and CI. Biochemically, shRNA-mediated gene silencing of human *TMCO6* in Flp-In™ HEK 293T cells caused a reduction in CI activity by 40 % relative to control values. Both the shRNA-knockdown cell lines and patient skin fibroblasts showed an increase in subassembly intermediates/degradation products, and a reduction in the levels of CI-containing supercomplexes by both 1D-BNGE and 2D-BNGE analyses, suggesting either destabilisation of the fully assembled holocomplex or stalled assembly at some stage prior to complete assembly. Despite these findings, the link between TMCO6 and CI biogenesis and function remained unclear. The work described in this chapter concerns the characterisation of a commercially available *Tmco6*-knockout murine model. Our first aim was to evaluate the physiological and behavioural phenotypes of Tmco6 ablation at the whole-organism level. Next, histological preparations and biochemical analyses were performed to discern differences in the structural architecture or in respiratory chain activities of post-mitotic tissues, respectively. Echocardiography and electrocardiography were performed to assess whether Tmco6 ablation resulted in cardiac dysfunction.

6.2 Results

6.2.1 Verifying Tmco6 Protein Ablation in a *Tmco6*-Knockout Murine Model

A transgenic *Tmco6*-knockout mouse model (B6N(Cg)-*Tmco6*$^{tm1.1(KOMP)Vlcg}$/J) was used in this work to study the effects of Tmco6 ablation on mitochondrial CI biogenesis and activity, and subsequently, development, physiology, neuromuscular coordination, and metabolism at the whole-organism and tissue-specific levels.

For generation of this strain, the ZEN-Ub1 Velocigene cassette, a *lacZ* reporter construct derived from *E. coli*, flanked by a neomycin resistance (*neo*^{R}) selection cassette, was inserted via homologous recombination between positions 36,894,829 and 36,901,908 of Chromosome 18 (Genome Build37) in mice embryonic stem cells of the C57BL/6NJ genetic background. Cre-mediated excision of the *neo*^{R} selection cassette was then achieved by selective crossing with a mouse line that constitutively expressed Cre recombinase. This multi-step process yielded a 7,080 bp deletion within *Tmco6*, disrupting all coding exons and intervening genomic sequences (see **Fig. 2.1**).

Firstly, for verification of gene disruption at the genomic level, and for all genotyping of progeny, we used two sets of primers to amplify either exons 3 and 4 of the *Tmco6* gene, yielding a 384 bp product (**Fig. 6.1 A.**), or part of the ZEN Ub1 reporter cassette and the downstream remainder of *Tmco6* exon 12/3' UTR (**Fig. 6.1 B.**). This strategy confirmed the absence of essential coding exons and verified the presence of the transgenic reporter construct in knockout animals, as well as clearly demonstrating WT and HET genotypes.

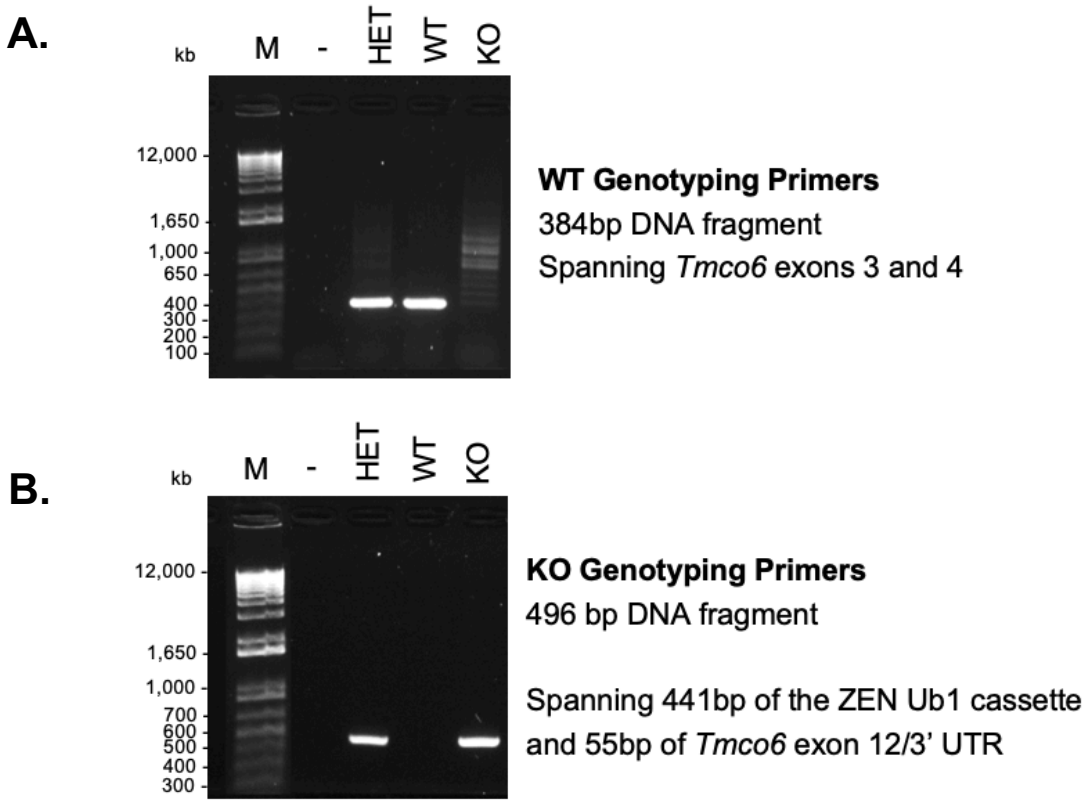

Fig. 6.1 PCR verifies absence of two essential *Tmco6* exons.

Figure shows the characteristic presentation of genotyping results for heterozygous (HET), homozygous wildtype (WT) or homozygous knockout (KO) mice. PCR was performed as per **section 2.5.1** using genomic DNA extracted from ear biopsies of mice, taken on the day of weaning, and a negative control reaction (-). Two different pairs of primers were used (sequences specified in **Table 2.23**) for PCR amplification of (**A.**) 384 bp spanning *Tmco6* exons 3 and 4 and the intervening intronic sequence, or (**B.**) 496 bp covering a proportion of the ZEN Ub1 gene cassette, the latter part of *Tmco6* exon 12 and a part of the 3' untranslated region (UTR). Fragments were separated by size via agarose gel electrophoresis, and samples were run alongside a 1 kb DNA marker (M) (Invitrogen™, UK) for fragment size comparison (as labelled). Gels were visualized by a UV transilluminator.

We then sought to confirm the loss of *Tmco6* gene expression by RT-qPCR using cDNA retrotranscribed from total RNA from liver (**Fig. 6.2**). Specific TaqMan gene expression assays for *Tmco6* and a housekeeping gene, *Myh10* were used; the amplicon sequences for each are detailed in **Table 2.10**. This strategy showed no gene expression of *Tmco6* in knockout mice (n = 3), but revealed ample expression in both wildtype (n = 2) and heterozygous (n = 1) mice for three technical replicates per animal. This result suggested that the knockout mice do in fact completely lack the Tmco6 protein given the total lack of any recognisable *Tmco6*-encoding mRNA transcripts.

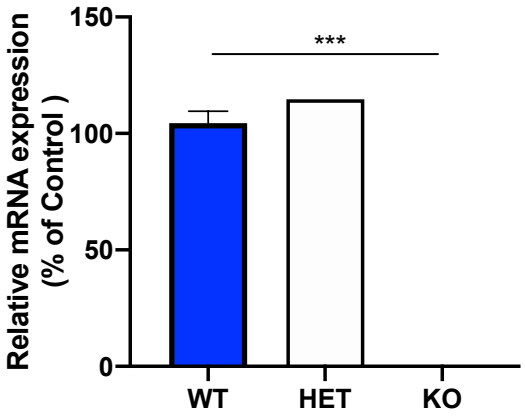

Fig. 6.2 *Tmco6* mRNA transcripts are absent in knockout animals.

RT-qPCR was performed as per **section 2.2.12** and revealed total loss of *Tmco6* mRNA in liver from 3-month-old homozygous knockout (KO) animals (*n* = 3), normalised to the expression of *Myh10,* and expressed as percentage, compared to homozygous WT mice (*n* = 2) and heterozygous mice (*n* = 1). Data are presented as mean ± range. Measurements were performed in technical triplicates per animal. *** $p < 0.0005$, calculated by one-way ANOVA with Tukey's multiple comparisons *post hoc* test applied.

Lastly, we attempted to confirm the absence of endogenous Tmco6 steady-state level in KO mouse tissues by Western blotting and immunodetection using two commercial antibodies raised against the human TMCO6 protein. Both antibodies were advertised by their respective manufacturer to recognise the murine orthologue. The first (Catalogue Number: 20117-1-AP, Proteintech®) is a rabbit polyclonal antibody raised against the last 87 residues at the C-terminus of the human TMCO6 primary sequence: NVAEKGPAYCQRLWPGPLLPALLHTLA FSDTEVVGQSLELLHLLFLYQPEAVQVFLQQSGLQALERHQEEAQLQDRVYALQQTALQG. This peptide shared 76 % sequence identity with the murine primary sequence. The second (Catalogue Number: NBP1-57660, Novus Biologicals), also a rabbit polyclonal antibody, was raised against 50 residues towards the N-terminus of the human TMCO6 primary sequence: LRQAQRGTEEKEREGALVSLRRGLQHPETQQTFIRLEGSMRTLVGLLTSN, and shared 90 % sequence identity with the murine protein sequence. The estimated molecular weight of mouse Tmco6 is 54.9 kDa, and both manufacturers alleged the antibodies to recognise a single band of this size. As shown in **Fig. 6.3 A.** and **B.**, no specific bands corresponding to the predicted size were observed in brain or skeletal muscle tissue homogenates using either primary antibody. Instead, a large number of unspecific bands were present at a similar intensity in the heterozygous, wildtype and knockout samples for both tissues. We concluded from this that these commercially available endogenous antibodies raised against the human primary sequence did not recognise the native protein in mice.

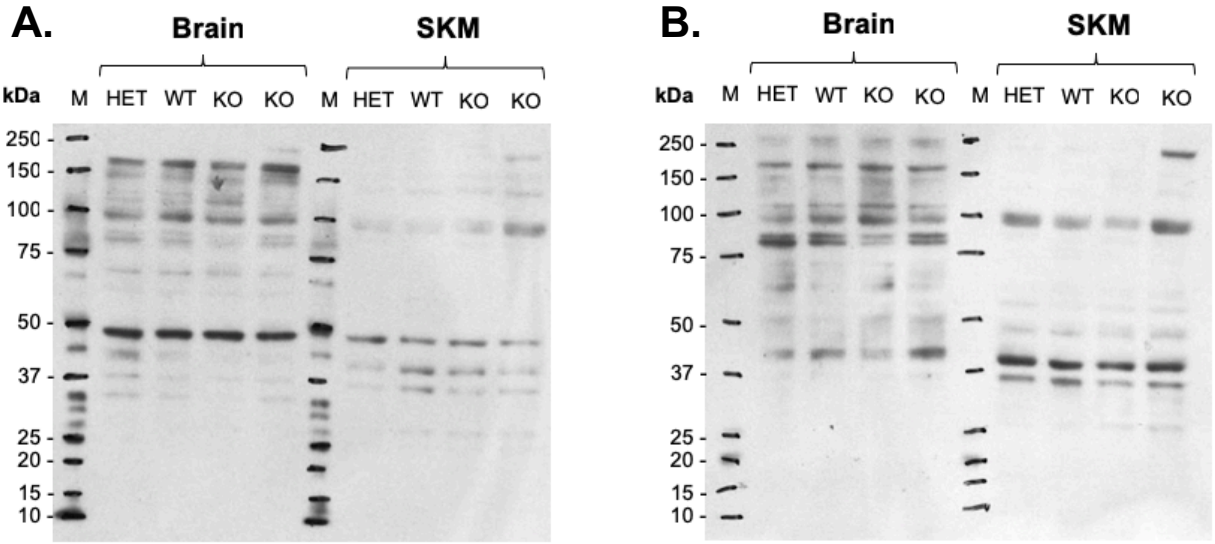

Fig. 6.3. Tmco6 Immunodetection Trials in brain and skeletal muscle tissues.

SDS-PAGE (4-12 % NuPAGE Bis-Tris, Thermo Fisher Scientific), Western blot analysis and immunodetection of 30 µg of protein lysates from heterozygous (HET), homozygous wildtype (WT) or homozygous knockout (KO) brain and skeletal muscle tissues. (**A.**) Immunodetection was carried out using an anti-TMCO6 primary antibody from Proteintech® (Catalogue Number: 20117-1-AP). (**B.**) Immunodetection was carried out using an anti-TMCO6 primary antibody from Novus Biologicals (Catalogue Number: NBP1-57660).

6.2.2 Phenotypic Characterisation of *Tmco6*-KO Mice

6.2.2.1 Skewed Mendelian Segregation of *Tmco6*-KO Mice

Mating of heterozygous mice and genotyping of offspring from 35 litters (n = 250) revealed a non-Mendelian distribution with statistically significant lower representation of the knockout genotype, as determined by Chi-squared analysis (χ^2 = 6.664 with 2 df, p = 0.0357) (**Table 6.1**). This suggested that a proportion of knockout mice died during gestation or in the postnatal period prior to weaning, and thus genotyping. Males and females were observed within expected ratios, with 50.8 % males (n = 127) and 49.2 % females (n = 123) recorded; therefore, no sex bias was observed. Matings of homozygous knockout males (KO M) or females (KO F) with a heterozygous partner (HET M or HET F) also produced a skewed distribution from the expected 1:1 Mendelian ratio for HET:KO, showing again a lower percentage of the KO genotype than expected (**Table 6.2**). These results yielded statistically significant differences by Chi-squared analysis (χ^2 = 5.565 with 1 df, p = 0.0183 for KO M x HET F (n = 46), and χ^2 = 5.918 with 1 df, p = 0.0150 for KO F x HET M (n = 61)). Mating of homozygous knockout mice (KO M x KO F) resulted in small litters of between 3 and 6 pups, with total postnatal lethality in

the first few days of life. Genotyping of dead pups not cannibalised by parents revealed 100 % occurrence of the KO genotype, as expected.

Table 6.1. Distribution of *Tmco6* Genotypes from HET x HET Interbreeding

Genotype	Number Expected [%]		Number Observed [%]	
WT	62.5	[25 %]	66	[26 %]
HET	125	[50 %]	139	[56 %]
KO	62.5	[25 %]	45	[18 %]

Table 6.2. Distribution of *Tmco6* Genotypes from HET x KO Interbreeding

Cross	Genotype	Number Expected [%]		Number Observed [%]	
KO M x HET F	HET	23	[50 %]	31	[67 %]
	KO	23	[50 %]	12	[33 %]
KO F x HET M	HET	30.5	[50 %]	40	[66 %]
	KO	30.5	[50 %]	21	[34 %]

In order to investigate the possibility of embryonic lethality, embryos from matings of heterozygous mice were analysed. Mendelian ratios for embryos collected at E11.5 or E12.5 (n = 39) were as expected for heterozygous interbreeding (**Table 6.3)**, with the observed number of wild-type, heterozygous and knockout animals considered non-significant by Chi-squared analysis ($\chi^2 = 0.436$ with 2 df, $p = 0.8042$). This result suggests that the non-Mendelian ratios seen in adult offspring from HET x HET crosses (**Table 6.1**) resulted most likely from lethality in late-stage pregnancy after E12.5, or from fatalities in infancy.

Table 6.3. Distribution of *Tmco6* Genotypes from HET x KO Interbreeding

Genotype	Number Expected [%]		Number Observed [%]	
WT	9.75	[25 %]	8	[21 %]
HET	19.5	[50 %]	21	[54 %]
KO	9.75	[25 %]	10	[26 %]

6.2.2.2 *Tmco6*-KO Mice Display Reduced Body Weight and Hindlimb Feet Clasping

Body weights of knockout and control (heterozygous and wildtype) genotypic groups were measured weekly from the time of weaning to 10 months of age (40 weeks). Knockout mice consistently presented lower body weights than those of control littermates, with statistically significant differences from 12 weeks of age for males (**Fig 6.4 A.**) and 28 weeks of age for females (**Fig 6.4 B.**). As a consequence, **Fig 6.4 C.** shows the substantial difference in body sizes of two 8-month-old male littermates positioned side-by-side.

A phenotypic behaviour of *Tmco6* knockout animals was hindlimb clasping (**Fig 6.4 D.**), which became steadily more pronounced with age. Hindlimb clasping is commonly observed in murine models of neurodegenerative disease (Guyenet *et al.*, 2010), and can be used to mark neurological symptom progression with age. Moreover, approximately 15 % of all *Tmco6*-knockout mice (n = 7, consisting of 2 females and 5 males) developed epilepsy from 6 months of age onwards, characterised by recurrent and spontaneous myoclonic seizures, in which the mouse suffered sudden, full-body spasms frequently over the course of several minutes (videos available upon request). A timeline of physical and neurological phenotypic progression in this strain is depicted in **Fig. 6.4 E.**

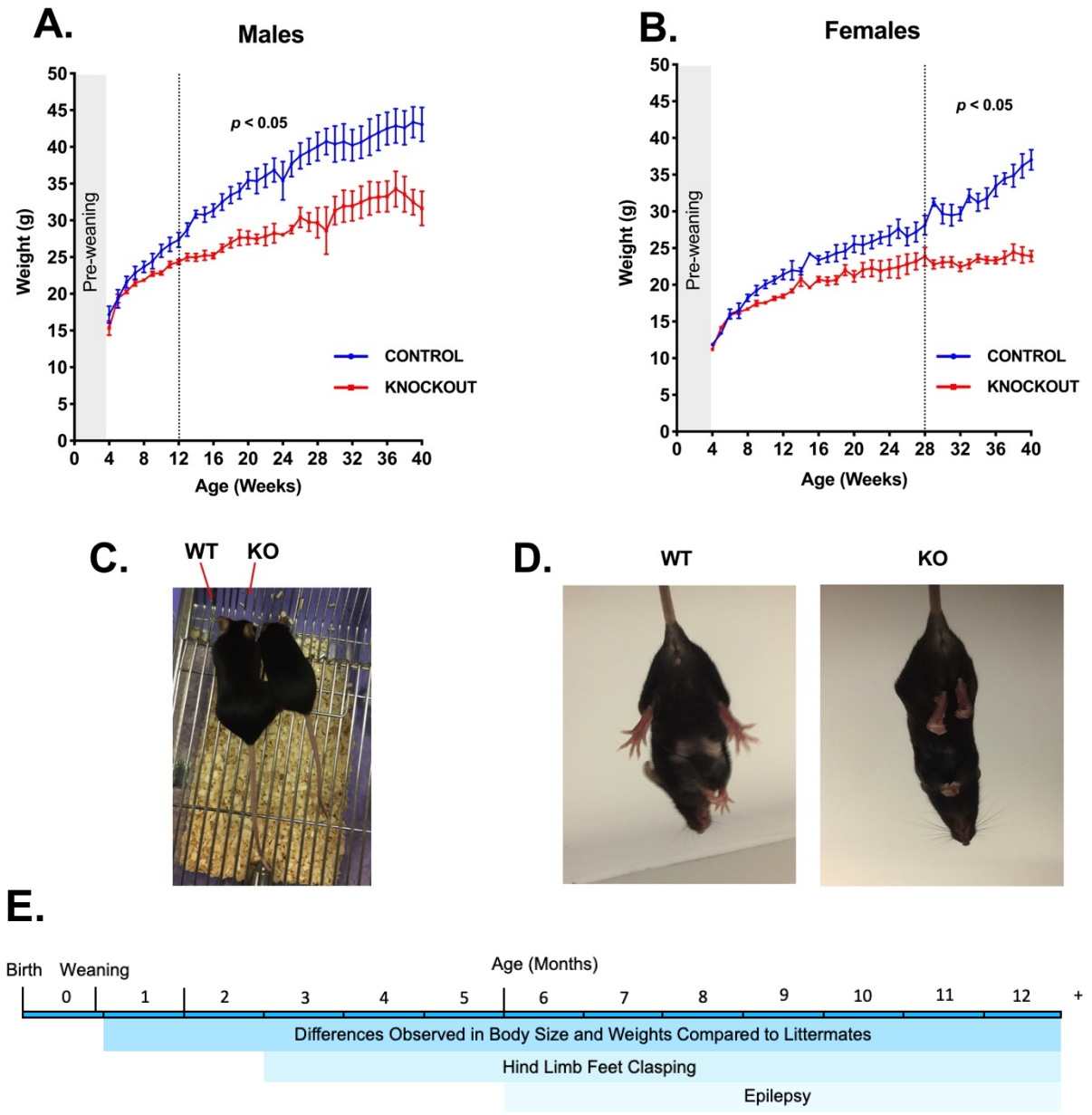

Fig. 6.4. Body composition and neurobehavioral phenotypes of *Tmco6*-knockout mice.

Body weight as a function of age was measured in wildtype and heterozygous mice, grouped together as 'controls', and Tmco6-knockout mice for (**A.**) males and (**B.**) females over 10 months on a weekly basis (n = 6 for each group). Student t- tests determined statistically different differences ($p < 0.5$) for males from 12 weeks of age, and for females from 28 weeks of age. (**C.**) Body sizes were noticeably different amongst litters for the knockout genotype compared to both heterozygous and wildtype counterparts, shown here by two 8-month old male littermates positioned side-by-side. (**D.**) Knockout animals displayed prominent hindlimb feet-clasping clearly observed from 3 months of age onwards, and which progressed in severity with age. (**E.**) A visual representation of the timeline of phenotypic onsets for the *Tmco6*-knockout strain.

6.2.2.3 *Tmco6*-KO Mice Show Impaired Exercise Tolerance and Motor Coordination

Leading on from these observations, we next sought to assess the motor capabilities and neuromuscular coordination of *Tmco6*-knockout mice relative to wildtype and heterozygous age-matched controls. Maximal exercise capability and endurance were evaluated by exhaustion trials, in which an automated treadmill and standardised program for increasing the belt speed by 0.3 m/min to a maximum speed of 75 m/min was used to run animals until they reached exhaustion, as defined in **section 2.5.4**. Both male and female *Tmco6*-knockout mice displayed significant exercise intolerance compared to heterozygous and wildtype littermates at 3 months of age to ~40 % of control levels (**Fig**. **6.5 A.**)**.** A statistically significant decrease for KO animals was also found at 12 months of age for female and male mice (**Fig. 6.5 B.**). Due to the large weights of the 12 month old males (> 52 g in most cases), and the natural loss of exercise capability with aging, the distance reached at exhaustion by WT and HET male controls at 12 months of age was less than for the young adult age group.

Neuromuscular coordination, balance and motor performance were next assessed using a Rotarod apparatus (Ingram and Reynolds, 1986). Mice were tasked with adapting to an increasing walking speed whilst maintaining balance on a cylindrical rod for a duration of 5 min. The latency to fall (s) was recorded manually per animal for three separate test trials, and these values were averaged per animal (as per **section 2.5.5**). As shown in **Fig. 6.5 C.**, *Tmco6*-knockout mice showed statistically significant decreases in latencies to fall at 3 months, 6 months and 12 months of age. This impaired balance and motility was progressive with age for both males and females, with 12-month-old knockout animals falling in approximately half of the time observed in knockout animals at 3 months of age for both genders. Males performed slightly worse than did females at all ages, potentially owing to their larger body sizes.

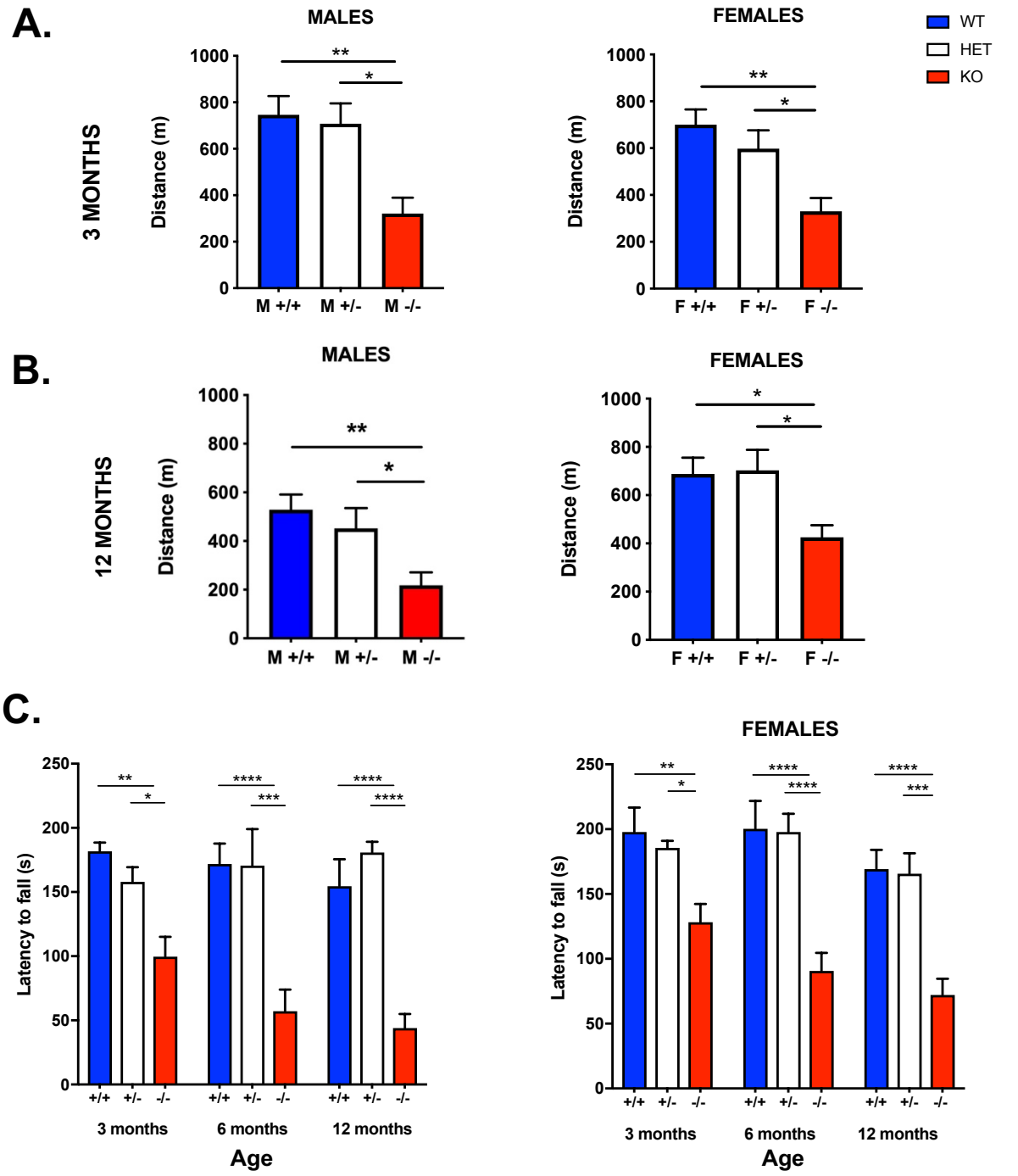

Fig. 6.5. *Tmco6*-knockout mice display impaired motor performance and coordination.

Motor performance and capability was assessed for male (M) and female (F) *Tmco6*-knockout (-/-), heterozygous (+/-) and homozygous wildtype (+/+) mice (n = 5 per group) at (**A.**) 3 months and (**B.**) 12 months of age by treadmill (as per **section 2.5.4**). Distance reached at exhaustion was recorded per animal. Data represent mean ± SEM. Statistical analysis: * $p < 0.05$, ** $p < 0.01$, calculated by one-way ANOVA with Tukey's multiple comparisons *post hoc* test applied. (**C.**) Latency to fall (s) was recorded in three separate trials, with values averaged per animal for male and female 3-month, 6-month and 12-month old *Tmco6*-knockout (-/-), heterozygous (+/-) and homozygous wildtype (+/+) mice run on a rotarod apparatus (n = 5 per group). Data represent mean ± SEM. Statistical analysis: * $p < 0.05$, ** $p < 0.01$, *** $p < 0.005$, **** $p < 0.001$, calculated by two-way ANOVA with Sidak's multiple comparisons *post hoc* test applied.

The pole test was then used to assess proprioception, which is the subconscious awareness of body orientation relative to the ground, and bradykinesia, the impaired ability to move the body or limbs in a coordinated way on command (Rial *et al.*, 2014). As shown in **Fig. 6.6**, male and female knockout showed increases in the time taken to turn 180^{o} and descend a 50 cm pole compared to both heterozygous and wildtype age-matched controls at all three ages tested, with statistically significant differences at 6 months and 12 months of age. It is worth noting that the knockout mice were often able to turn without difficulty in a comparable time to heterozygous and wildtype controls, suggesting no problem with proprioception, but could not descend the pole in a controlled manner engaging all four limbs, suggesting bradykinesia. Knockout animals often did not engage their hind limbs and instead wrapped them around the pole, using only their forelimbs to descend towards the home cage in sharp, jerky movements. Wildtype and heterozygous animals did not display this phenotype in any instance. In addition, approximately 30 % of knockout male and female mice in the 12 month age groups would not grasp the pole when performing the two adaptation trials, and if they did, some would fall immediately; these animals had to be discounted from performing the test.

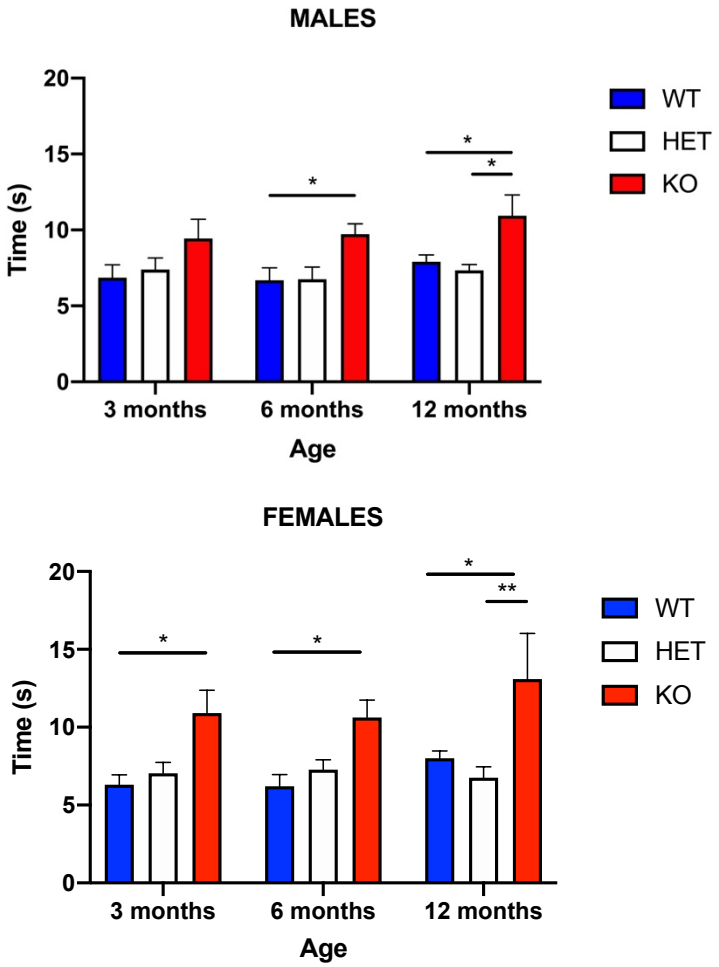

Fig. 6.6. *Tmco6*-knockout mice exhibit impaired coordination.

The pole test was performed as per **section 2.5.7** for male and female mice at 3 months, 6 months and 12 months of age to assess proprioception, the subconscious awareness of body orientation relative to the ground, and impaired coordination. The time (s) taken to turn 180^{o} and descend a 50 cm pole was recorded for 3 replicate trials per animal and these values averaged (n = 6 mice per genotypic group); data are presented as mean ± SEM. Statistical analysis: * $p < 0.05$, ** $p < 0.01$, calculated by two-way ANOVA with Sidak's multiple comparisons *post hoc* test applied.

6.2.2.4 *Tmco6*-KO Mice Have Decreased Motility and *In Vivo* Energy Metabolism

Given that *Tmco6*-knockout mice showed impaired exercise tolerance and neuromotor abnormalities in tests that assessed balance and motor coordination (**section 6.2.2.2**), we next sought to assess the impact of *Tmco6*-ablation on spontaneous motility, including locomotor and exploratory behaviours. The Oxymax Comprehensive Lab Animal Monitoring System (CLAMS) (Columbus Instruments, Ohio, USA) was used to monitor total movement, ambulatory movement, and rear movements in homeostatic conditions. This was achieved by infrared beam sensors in the *x*-, *y*- and *z*- planes surrounding each cage, with any beam breaks termed as 1 'count'. Total movement was defined as all infrared beam interruptions (total counts). When mice broke a series of infrared beams in sequence, meaning that they were moving deliberately, such as traversing the cage, counts were defined as ambulatory movements, and movements in the *y*-axis, i.e. when mice were standing upright on the hind-limbs in order to visually explore their environment, were counted as rear movements. Since male and female mice exhibited identical differences, only data from male mice are included here as representative. Night and day cycles were evaluated separately owing to the nocturnal nature of mice, and no significant differences were observed for measurements taken during the day. During the night, significant differences in rear movements were observed between wildtype (WT) and knockout (KO) male mice at 3 (**Fig. 6.7 A.**), 6 (**Fig. 6.7 B.**) and 12 months of age (**Fig. 6.7 C.**). In addition, total movement was decreased for KO mice at all ages, with statistically significant differences observed in 6 month and 12 month age groups. Although there was a trend in 3 month and 6 month knockout animals to explore less, as denoted by ambulatory movement, the only significant difference was observed in aged mice at 12 months of age. These results showed progressive deficiencies in locomotor and exploratory behaviours for KO animals with age, suggesting neuromuscular implications for ablation of the Tmco6 protein *in vivo*.

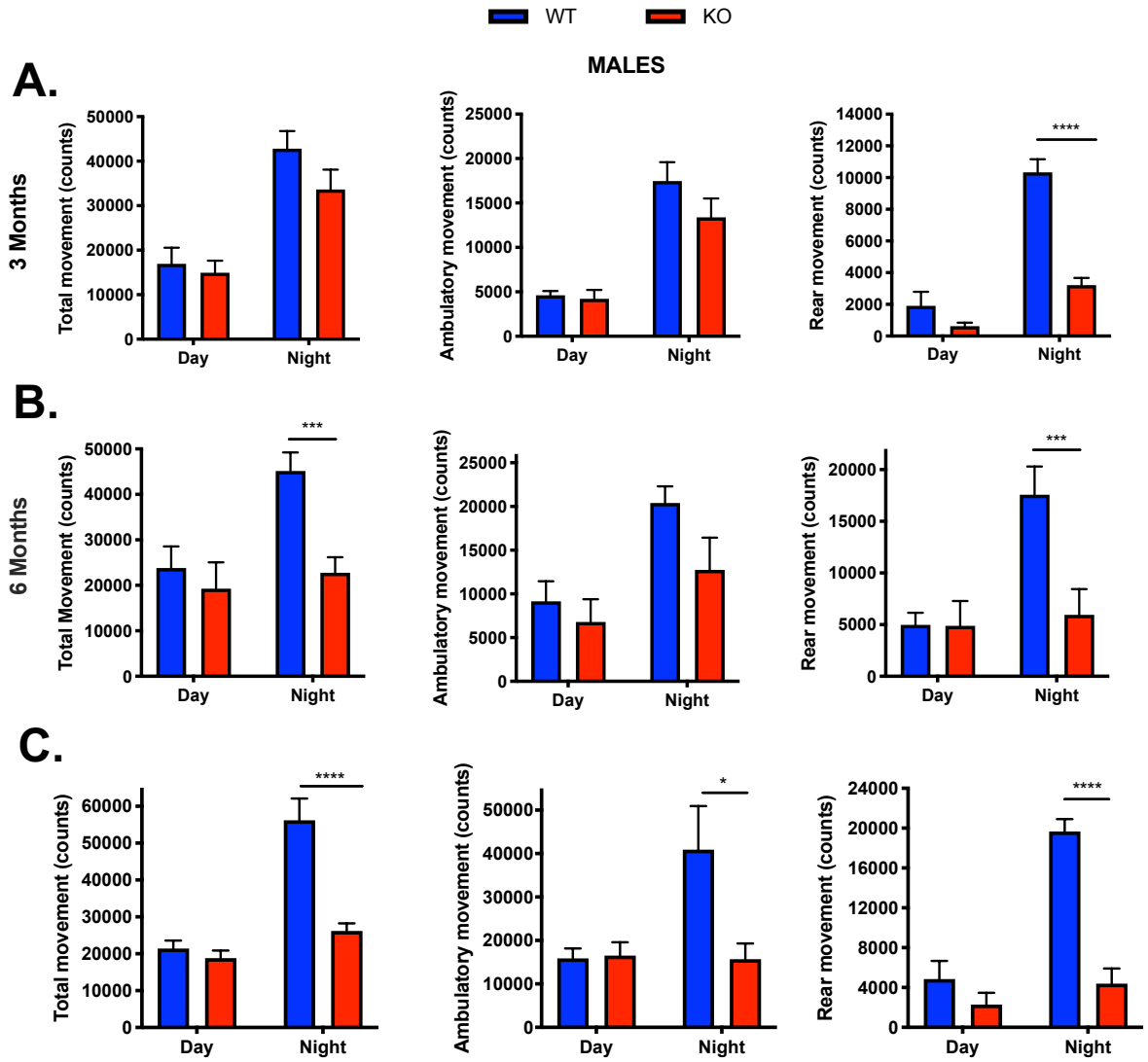

Fig. 6.7. Movement monitoring via CLAMS.

Total movement of male *Tmco6*-knockout (KO) or homozygous wildtype (WT) mice at (**A.**) 3, (**B.**) 6 and (**C.**) 12 months of age for 2 night and 1 day 12 h cycles via CLAMS, as per **section 2.5.3**. Total movement is defined as all infrared beam interruptions in the *x*-, *y*-, and *z*- axes (total counts). Ambulatory movement is defined as deliberate movement, i.e., traversing the cage, characterised by a sequence of infrared beam breaks in at least 2 planes. Rear movement is defined as infrared beam breaks in the *y*-axis, i.e. when mice were standing upright on the hind-limbs in order to visually assess their environment. Data are presented as mean ± SEM. 3 months: WT (n = 3), KO (n = 4), 6 months: WT (n = 3), KO (n = 3), 12 months: WT (n = 3), KO (n = 5). Statistical analysis: * $p < 0.05$, ** $p < 0.01$, *** $p < 0.005$, **** $p < 0.001$, calculated by two-way ANOVA with Sidak's multiple comparisons *post hoc* test applied.

The CLAMS was also used to measure nutritional intake, including food and water consumption, and several metabolic parameters, including O_2 consumption, CO_2 production, heat production and the respiratory exchange ratio (RER) for KO and WT control male mice at 3 months, 6 months and 12 months of age for 12 h day and night cycles (**Fig. 6.8**). All values were corrected for body mass per animal. There was a general trend that knockout animals consumed more food and water than did their age-matched wildtype controls, although these differences were not statistically significant. RER is a ratio between the amount of carbon dioxide produced and oxygen consumed by an aerobically respiring organism, with the resulting value indicating what type of substrate is being preferentially metabolised to produce energy, ie. sugars or fat. A RER of 0.7 indicates that the main fuel is fat, a RER of 0.85 means that both fat and carbohydrates are used, and a RER of 1.0 or above indicates that the main substrate used for energy is carbohydrate. Mice in both experimental groups at all ages showed normal RER values of around 0.85. Oxygen consumption and carbon dioxide production were used as variables by the CLAMS^{TM} software for indirect calorimetry to calculate heat production, which is directly related to energy expenditure, and was unchanged in knockout compared to wildtype mice at all ages. Significant increases in CO_2 production and O_2 consumption were observed at 12 months of age for KO animals, although the younger age groups showed a similar trend. *Tmco6*-KO mice are consuming more oxygen and producing more carbon dioxide than age-matched controls throughout the day and night (**Fig. 6.8**). This is unexpected given that male *Tmco6*-KO mice are moving less (**Fig 6.7**) than their wildtype littermates. Therefore, *Tmco6*-KO animals are undergoing higher than normal metabolic activity just to maintain basal survival. This finding could indicate that KO animals are requiring more energy that WT controls to regulate their body temperature, or to fulfil some other homeostatic metabolic process.

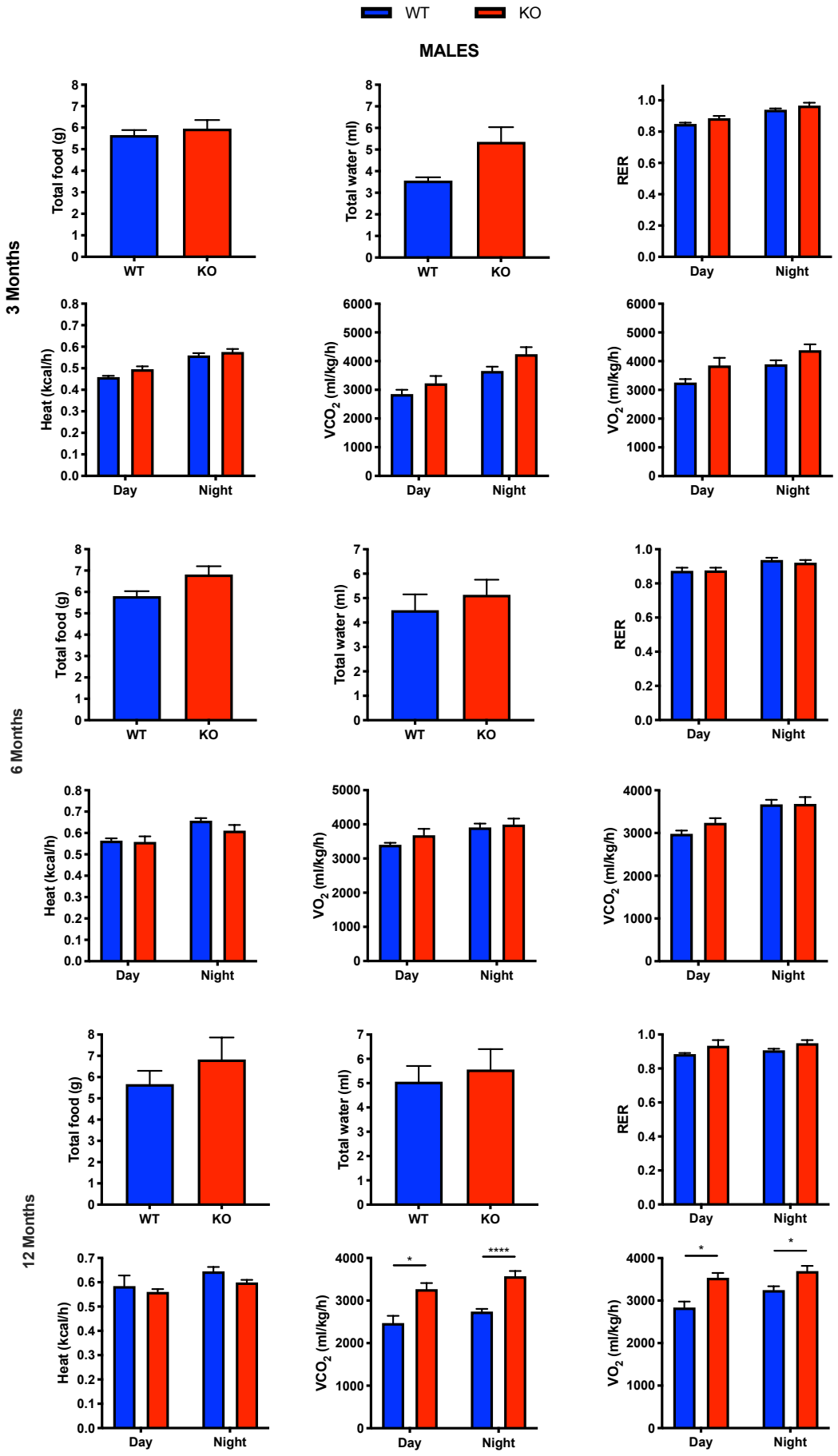
WT
KO
MALES
3 Months
6 Months
12 Months
Total food (g)
Total water (ml)
RER
Heat (kcal/h)
VCO2 (ml/kg/h)
VO2 (ml/kg/h)
WT
KO
Day
Night
*
****

Fig. 6.8. Energy metabolism monitoring via CLAMS.

Male Tmco6-knockout (KO) or homozygous wildtype (WT) mice were monitored at 3, 6 and 12 months of age for nutritional intake and various metabolic parameters for 2 night and 1 day 12 h cycles via CLAMS, as described in section 2.5.3. Total food (g) and water (ml) consumed was recorded per animal at the end of the experiment to assess overall consumption in the 36 h period. The sum of the volume of oxygen consumed (ml/kg/hr) and volume of carbon dioxide produced (ml/kg/hr) was recorded also. These were both used to calculate the respiratory exchange ratio (RER) and heat production (Kcal/hr) per animal, for day and night cycles in each case. Data are presented as mean ± SEM. 3 months: WT (n = 3), KO (n = 4), 6 months: WT (n = 3), KO (n = 3), and 12 months: WT (n = 3), KO (n = 5). Statistical analysis: * $p < 0.05$, ** $p < 0.01$, *** $p < 0.005$, **** $p < 0.001$, calculated by two-way ANOVA with Sidak's multiple comparisons post hoc test applied.

6.2.3 Histological Analyses of Tissues from *Tmco6*-KO Mice

6.2.3.1 Histopathological Alterations Observed in Brains of *Tmco6*-KO Mice

Murine tissues were subjected to histochemical and histological examination to assess whether *Tmco6*-ablation yielded structural or functional hallmarks of neurological disease. Both male and female tissues were analysed and showed identical phenotypes; therefore, as representative of both genders, only results showing male tissues are included herein.

Firstly, we assessed the presence of degenerating neurons in the brains of 3 and 12 month old male wildtype (WT) and knockout (KO) mice by means of the anionic fluorescent histofluorescent dye, PathoGreen™. As shown in **Fig. 6.9.**, PathoGreen™ staining highlighted degenerating neurons in sections from the striatum, thalamus and cerebral cortex in young adult (3 months) and aged (12 months) KO animals. WT animals show no PathoGreen™ signal in either age group, indicating that the neurodegeneration detected in KO animals is a result of *Tmco6*-abalation and not simply a by-product of regular aging.

In order to provide further support to this observation, astrogliosis was next evaluated by immunohistochemistry (IHC) with an anti-glial fibrillary acidic protein (GFAP) antibody (brown staining). Increased expression of GFAP in the brain is observed following neuronal cell death or damage to the central nervous system, and is a common marker of severe neuropathology. As shown in **Fig. 6.10**, *Tmco6*-KO animals display extensive accumulation of GFAP at both 3 and 12 months of age in PathoGreen™-positive regions of the brain. Far greater GFAP accumulation is observed in brains of the 12 month-old age group, ultimately indicating neurodegeneration that is progressive with age for KO animals.

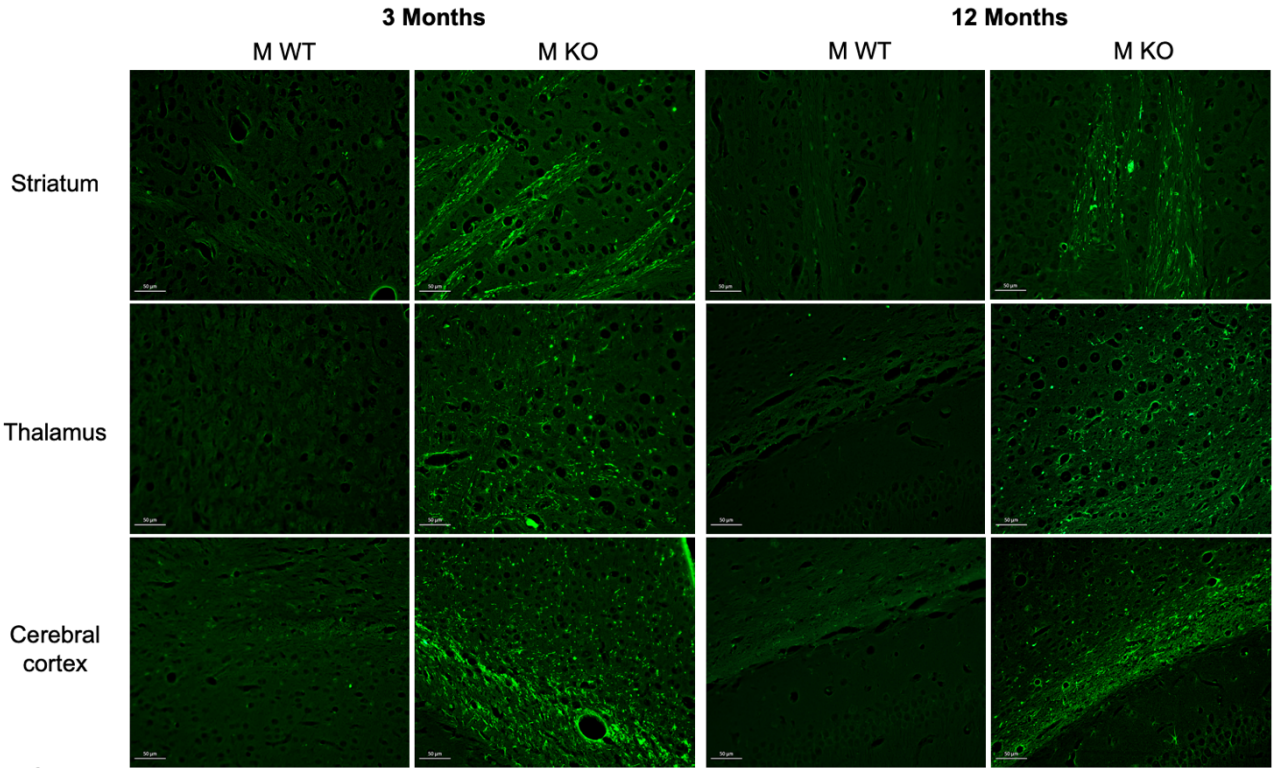

Fig. 6.9. Neurodegeneration observed throughout the brains of *Tmco6*-knockout mice.

Representative PathoGreen™ histofluorescent staining of the striatum, thalamus and cerebral cortex of 3 month and 12 month old male *Tmco6*-knockout (KO) or homozygous wildtype (WT) mice shows prominent neurodegeneration in these brain areas in KO animals. Scale bar = 50 µm, images taken at 20 X magnification. Sample preparation and imaging performed entirely by Raffaele Cerutti.

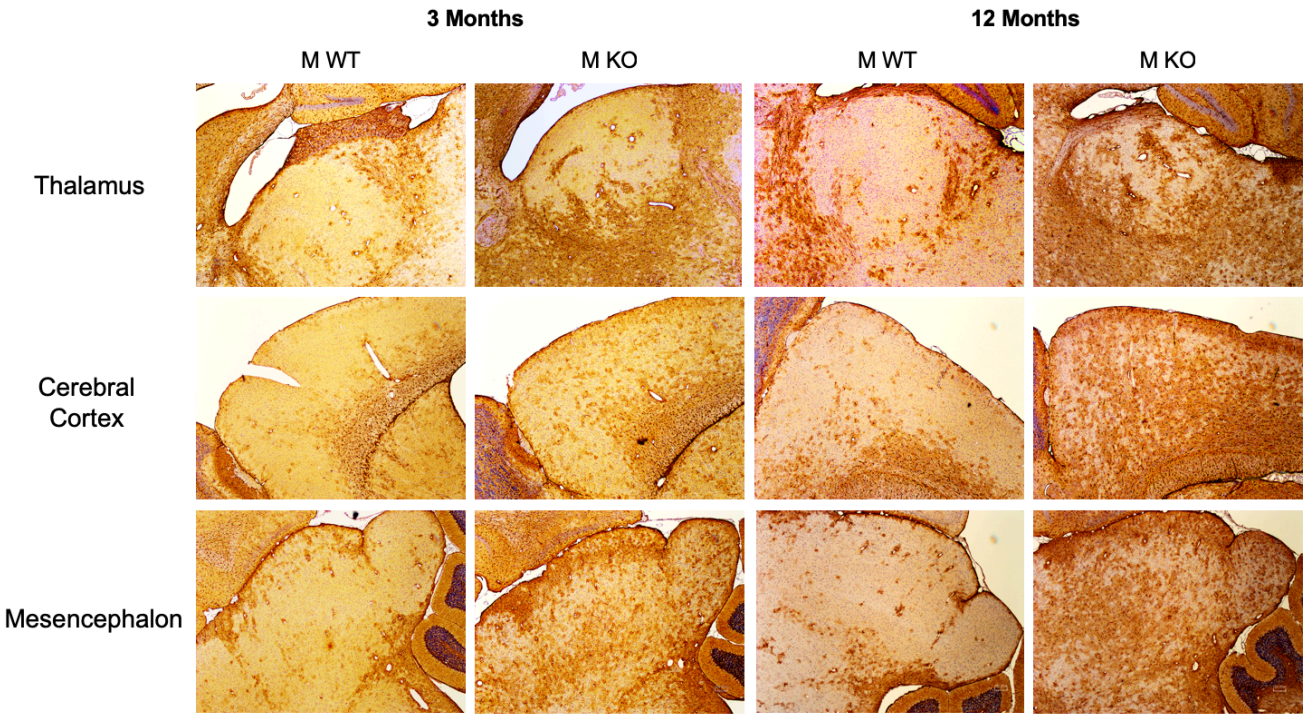

Fig. 6.10. Increased gliosis observed in brains of *Tmco6*-KO mice.

Representative GFAP immunohistochemistry of the thalamus, frontal cerebral cortex and mesencephalon of 3 month and 12 month old male *Tmco6*-knockout (KO) or homozygous wildtype (WT) mice shows increased astrogliosis in KO animals. Images taken at 4 X magnification. Sample preparation and imaging performed entirely by Raffaele Cerutti, as per **section 2.5.9**.

Protein aggregates (inclusions) containing ubiquitinylated proteins are sometimes found in neurons and other cell types in the central nervous system, indicative of neurological illness, as found in Alzheimer's disease, Parkinson's disease, polyglutamine disease, and rarer forms of neurodegenerative disease (Hegde and Upadhya, 2011). Ubiquitin accumulation was assessed by immunohistochemistry with an anti-ubiquitin antibody (brown staining) as shown in **Fig. 6.11** for 3 month and 12 month-old KO animals. Both age groups displayed focalised regions of ubiquitin signal accumulation, which was not seen in age-matched WT controls. There appears to be progression in ubiquitin accumulation from the 3 month- to 12 month-age groups for KO animals for thalamus, cerebral cortex and mesencephalon brain sections, in agreement with GFAP immunohistochemistry.

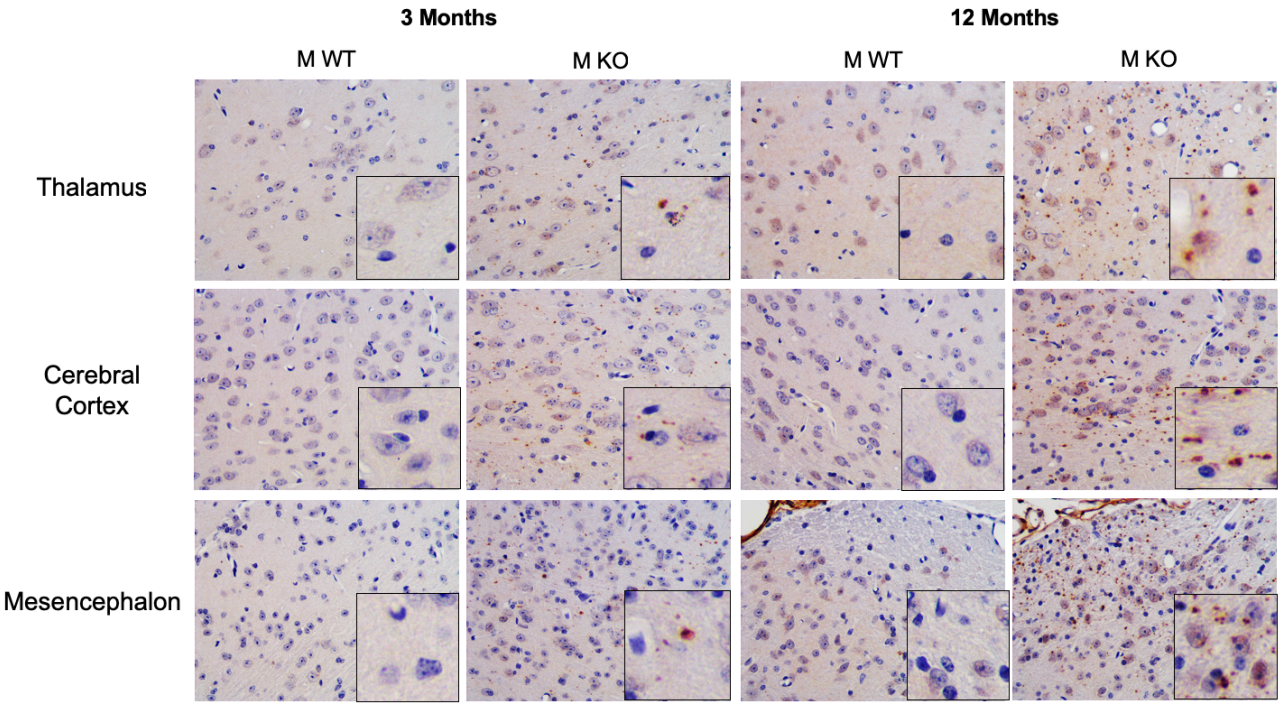

Fig. 6.11. Aggregation of ubiquitinated proteins observed in brains of *Tmco6*-KO mice.

Representative ubiquitin histofluorescent staining of the thalamus, cerebral cortex and mesencephalon of 3 month and 12 month old male *Tmco6*-knockout (KO) or homozygous wildtype (WT) mice shows increased aggregation of ubiquitinated proteins in KO animals, suggesting either dysfunction of the ubiquitin-proteasome system or proteolytic resistance of the protein aggregates. Images taken at 40 X magnification; insets show 80 X magnification. Sample preparation and imaging performed by Raffaele Cerutti, as per **section 2.5.9**.

Demyelination of axons impairs the conduction of nerve signals, and can lead to atrophy or degeneration of the affected neurons. Cyclic nucleotide 3'-phosphodiesterase (CNPase) is expressed only by myelin-forming cells and histofluorescent staining of CNPase can be used to detect myelinated axons in brain sections (brown staining). **Fig 6.12** shows representative sections of the neocortex from 3 month and 12 month old WT and KO mice, showing substantially less neuronal myelination in KO animals, especially in Layer I of the neocortical sections. Demyelination of neurons is one possible cause or contributing factor for the extensive neuronal degeneration seen by PathoGreen™ staining (**Fig. 6.9**), and corroborated by the increased astrogliosis detected by GFAP staining **(Fig. 6.10**) in 3 month- and 12 month-old KO mice.

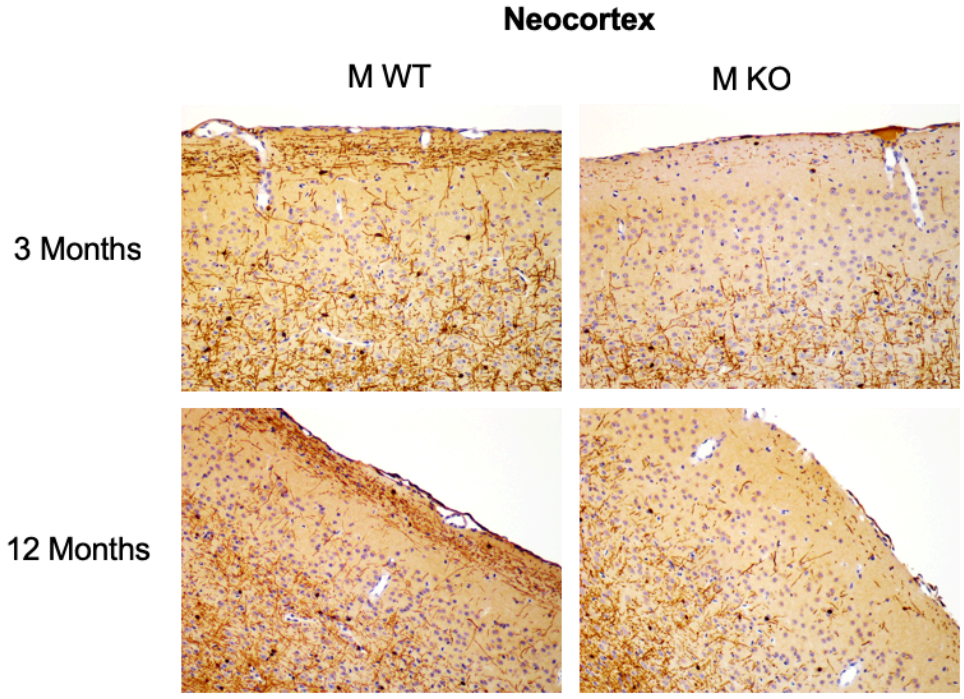

Fig. 6.12. Loss of myelinated neurons observed in brains of *Tmco6*-KO mice.

Representative CNPase histofluorescent staining of the neocortex of 3 month and 12 month old male *Tmco6*-knockout (KO) or homozygous wildtype (WT) mice shows decreased myelination of neurons in KO animals. Images taken at 20 X magnification. Sample preparation and imaging performed by Raffaele Cerutti, as per **section 2.5.9**.

Microglial cells are macrophagic cells that function in mediating immune responses in the central nervous system by targetting and removing dead or damaged neurons by phagocytosis. Thus, immunohistochemistry was used to identify the presence of CD68, expressed by activated microglial cells, in the brains of 3 month and 12 month old WT and KO mice. As shown in **Fig. 6.13**, KO brain sections show positive regions of CD68 signal (brown staining), indicating accumulation of activated microglial cells at these sites and an activated immune response. There seems to be similar abundances in CD68 expression in both 3 month and 12 month age groups, suggesting that at 3 months of age the maximum immune response has been achieved. If no further immune response is possible, this would result in neurological damage over time and a progession in the markers shown above (**Figs. 6.9 - 6.12**), as is the case here.

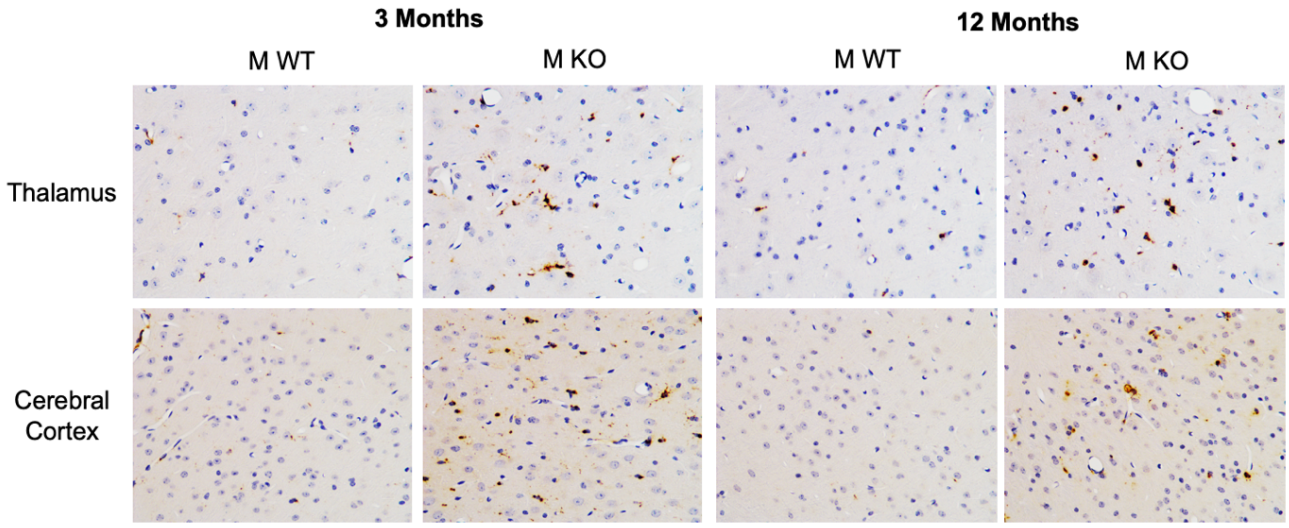

Fig. 6.13. CD68 IHC reveals increased amounts of microglia in brains of *Tmco6*-knockout mice.

Representative CD68 IHC of the thalamus and frontal cerebral cortex of 3 month and 12 month old male *Tmco6*-knockout (KO) or homozygous wildtype (WT) mice shows the presence of activated microglial cells in KO animals. Images taken at 40 X magnification. Sample preparation and imaging performed by Raffaele Cerutti, as per **section 2.5.9**.

6.2.3.2 Histochemical and Histological Analyses of Other Tissues of *Tmco6*-KO mice

Following on from investigation of the brain, we next sought to analyse other high-energy tissues from 3 month-old KO animals. We had previously observed impaired motor endurance via treadmill and test for *Tmco6*-KO mice (**Fig. 6.5**), and hypothesised that skeletal and cardiac muscles of these animals may be affected. Hematoxylin and eosin (H&E) histological staining of skeletal muscle sections showed normal fibre morphologyin *Tmco6*-KO animals at 3 months of age (**Fig. 6.14 A.**), despite being slightly smaller in size, which was most likely due to the smaller overall body sizes of the KO animals. No centralized nuclei, which would be suggestive of a myopathy (Folker and Baylies, 2013), were found. Histochemical evaluation of NADH (**Fig. 6.14 B.**), SDH (**Fig. 6.14 C.**) and COX (**Fig. 6.14 D.**) revealed no observable differences in intensity of the three between WT and KO animals. For cardiac sections, H&E staining again revealed no apparent differences in overall morphology, presence of altered fibre structure or cellular architecture (**Fig. 6.15**). Picrosirius red staining was used to reveal the presence of fibrosis in the cardiac tissue. Muscle fibres (yellow) and collagen (red) showed no difference between WT or KO hearts, as shown in **Fig. 6.15**.

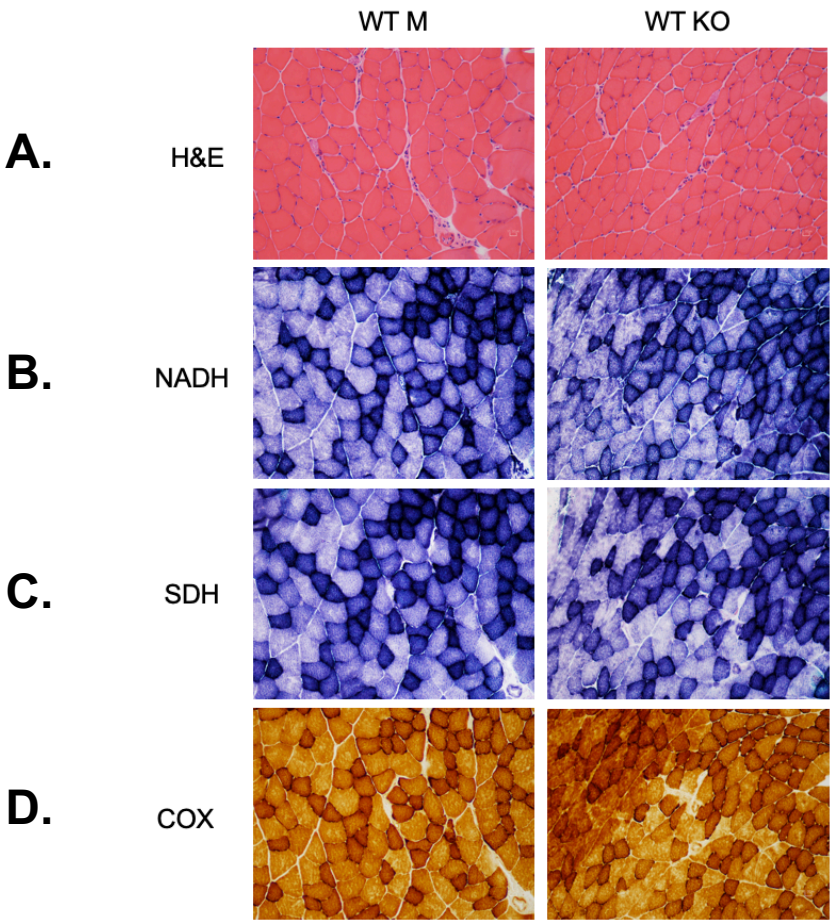

Fig. 6.14. Skeletal muscle showed no histochemical changes in *Tmco6*-KO mice.

Representative (**A.**) H&E histofluorescent staining, (**B.**) NADH, (**C.**) SDH and (**D**.) COX histochemical reactions of skeletal muscle sections from 3 month-old male *Tmco6*-knockout (KO) or homozygous wildtype (WT) mice. Images taken at 20 X magnification. Sample preparation and imaging performed entirely by Raffaele Cerutti, as per **section 2.5.9**.

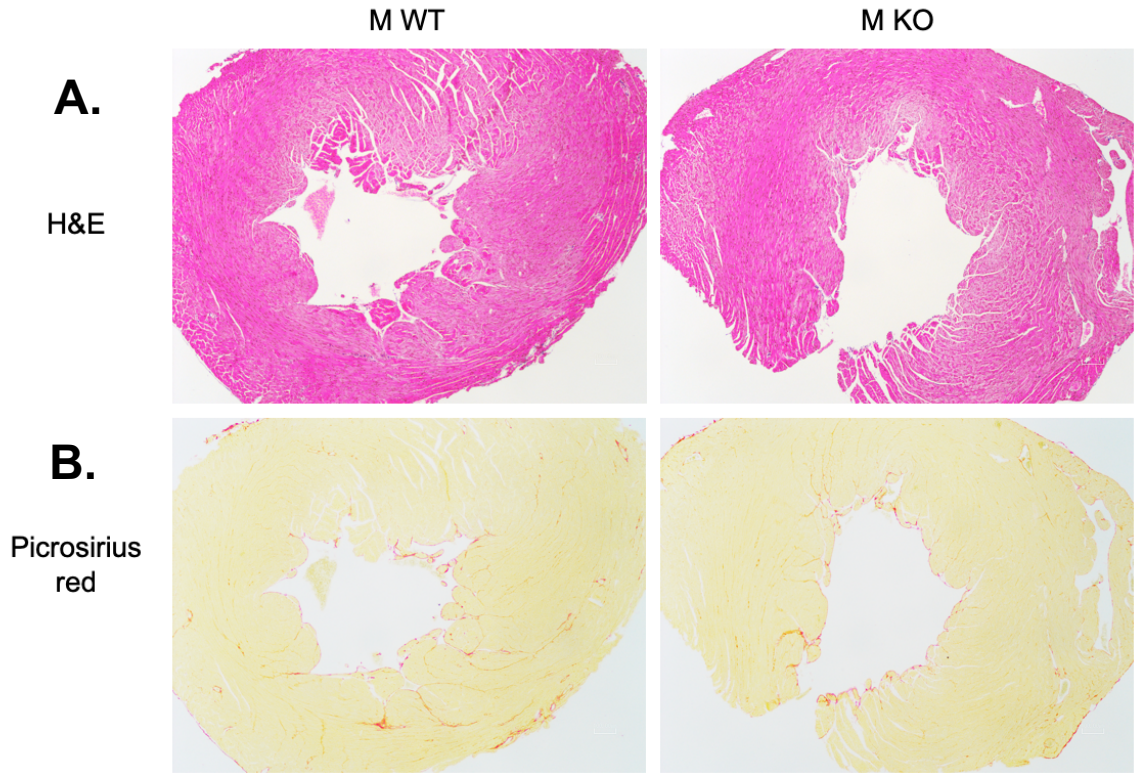

Fig. 6.15. Hearts showed no histological alterations in *Tmco6*-KO mice.

Representative (**A.**) H&E and (**B.**) Picrosirius red staining of heart sections from 3 month-old male *Tmco6*-knockout (KO) or homozygous wildtype (WT) mice. Images were taken at 4 X magnification. Sample preparation and imaging performed by Raffaele Cerutti, as per **section 2.5.9**.

Kidney and liver tissues were also analysed by H&E staining (**Fig. 6.16**), revealing no structural or cellular abnormalities. Kidneys were also analysed by periodic acid-Schiff staining to detect abnormal glomeruli and by cleaved caspase-3 IHC, which detects presence of apoptotic cells, and both revealed no differences (data not shown). Liver was also analysed by cleaved caspase-3 and Ki-67 IHC, the latter of which marks proliferating cells after liver damage. Again, no differences for KO mice compared to counterpart WT animals at 3 months of age were observed (data not shown).

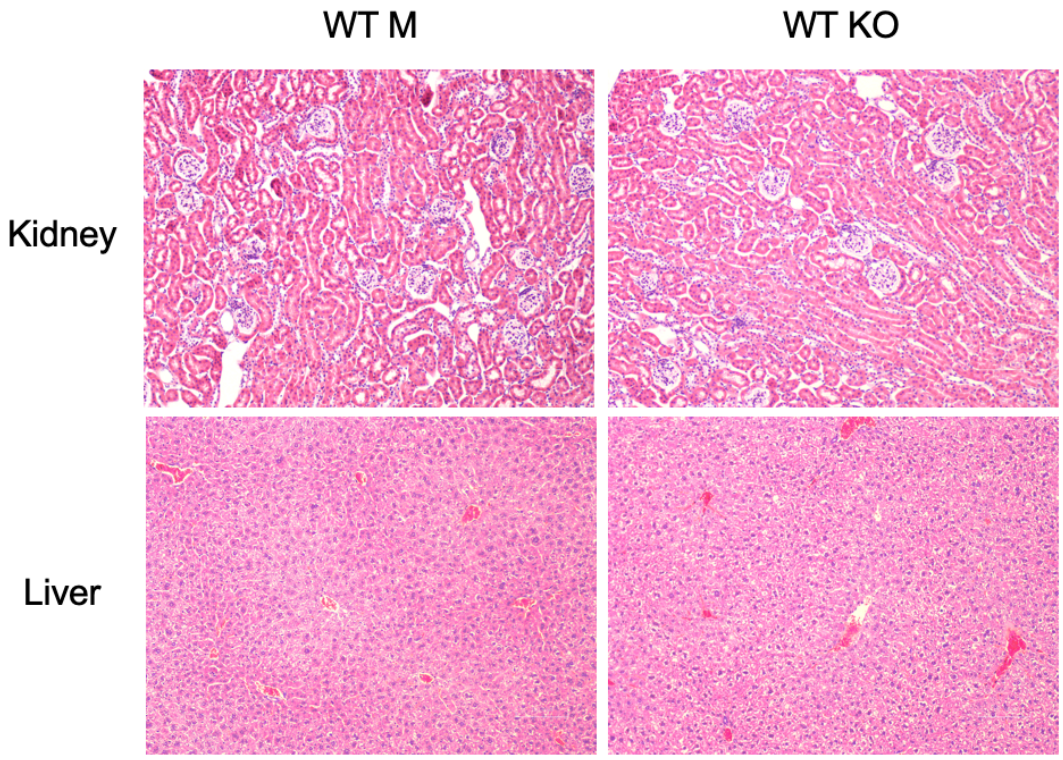

Fig. 6.16. Kidney and liver also showed no histological alterations in *Tmco6*-KO mice.

Representative H&E staining of kidney and liver sections from 3 month-old male *Tmco6*-knockout (KO) or homozygous wildtype (WT) mice. Images were taken at 10 X magnification. Sample preparation and imaging performed by Raffaele Cerutti, as per **section 2.5.9**.

In summary, *Tmco6*-knockout brains showed neurodegeneration, associated with increased astrogliosis, accumulation of ubiquitinated protein aggregates, recruitment of inflammatory microglial cells and demyelination of axons, in 3 month- and 12 month-old animals. Skeletal muscles of 3 month-old KO mice showed small fibres, but no centralised nuclei by H&E staining and no qualitative differences detected by NADH, SDH or COX histochemistry. Hearts of KO mice displayed no structural abnormalities or fibrosis. Kidneys and liver also revealed no apparent abnormalities by H&E staining, supported by additional histological staining.

6.2.4 Biochemical Investigation of *Tmco6*-KO Cells and Tissues

6.2.4.1 Investigating Mitochondrial Respiratory Chain Activities in *Tmco6*-KO MEFs

Patient fibroblasts with a homozygous recessive mutation in human *TMCO6* demonstrated no mitochondrial respiratory chain enzymatic deficiencies by spectrophotometric analysis (**Fig. 4.14**). To assess whether murine fibroblasts showed any alteration to normal respiratory chain complex activities, biochemical measurements were carried out for *Tmco6*-KO MEFs, derived from E11.5 and E12.5 embryos as per **section 2.5.2**. No enzymatic deficiencies were observed for CI, CII, SDH, CIII or CIV, with specific activities of each normalised to CS activity (**Fig. 6.17**); a non-significant downwards trend was observed for all complexes for KO cells (*n* = 3) compared to WT controls (*n* = 3).

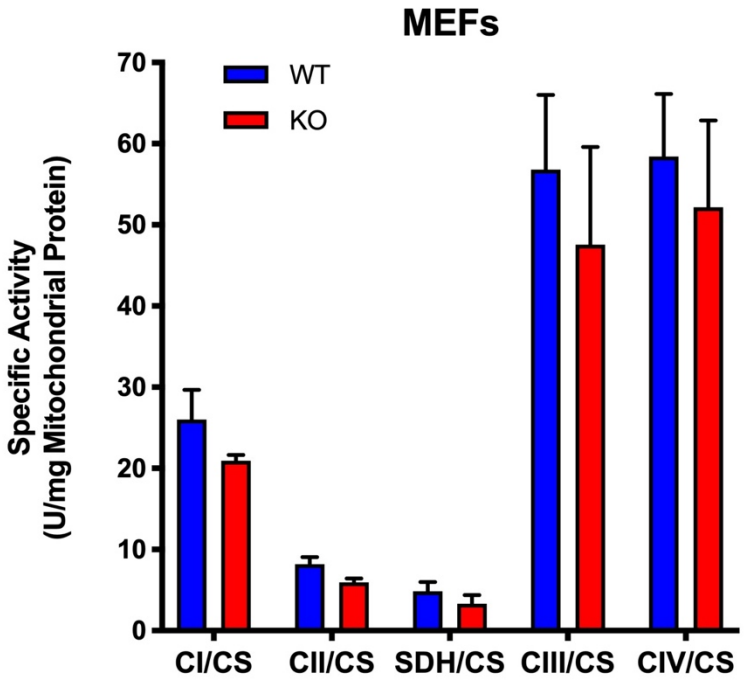

Fig. 6.17. Biochemical analysis of the mitochondrial respiratory chain in MEFs.

Complex I (CI), succinate dehydrogenase (SDH), Complex II (CII), Complex III (CIII) and Complex IV (CIV) enzymatic activities were performed as per **section 2.7.1**, with resulting values normalised to the activity of citrate synthase (CS) for wildtype and knockout MEFs (*n* = 3 for either genotype). Data are presented as mean ± SEM. Two-way ANOVA with Sidak's multiple comparisons test revealed no statistically significant differences.

6.2.4.2 Investigating Mitochondrial Respiratory Chain Activities in *Tmco6*-KO Tissues

To quantify any alteration in the functioning of the mitochondrial respiratory chain in *Tmco6*-knockout mice, kinetic measurements of CI, SDH, CII, CIII, and CIV specific enzymatic activities were performed spectrophotometrically with tissue homogenates from brain (**Fig. 6.18 A.**), heart (**Fig. 6.18 B.**), liver (**Fig. 6.18 C.**) and skeletal muscle (**Fig. 6.18 D.**) from 3 month old animals. Surprisingly, despite the various neurobehavioral and histopathological differences we had observed (**sections 6.2.2** and **6.2.3**), no differences in CI activity, nor the activities of any of the other mitochondrial respiratory complexes, were detected in brain homogenates of 3 month old KO mice (n = 3), compared to HET and WT age-matched controls (n = 2 per group) (**Fig. 6.18 A.**). Also, despite having showed no obvious abnormalities by histological analyses, heart (**Fig. 6.18 B.**) and skeletal muscle (**Fig. 6.18 D.**) homogenates both revealed isolated CI deficiency. The more severe CI deficiency was observed in heart, with ~70-85 % reduction for KO mice compared to WT and HET controls. For skeletal muscle, there was a ~40 % reduction in CI activity for KO animals. These results are highly significant since they recapitulate the initial observation made in the muscle biopsy from the patient of an isolated CI deficiency, and provide further support to the hypothesis that *TMCO6* is the causative gene of that defect.

Given that brains of KO animals had clear histopathological abnormalities, we sought to separate the different regions of the brain to assess whether a localised mitochondrial enzymatic deficiency in one portion of the brain was present, but was being masked by using whole brain homogenates. Brains of control (WT and HET) and KO 3 month old mice (n = 4 for both genotypic groups) were dissected into crude forebrain, midbrain and hindbrain sections. Again, we observed no enzymatic deficiencies for CI, SDH, CII, CIII or CIV for forebrain (**Fig. 6.19 A.**), midbrain (**Fig. 6.19 B.**) or hindbrain (**Fig. 6.19 C.**) regions, suggesting that the neurodegeneration and associated phenotypes observed ubiquitously throughout the brain by histology could be due to some cause of *Tmco6*-ablation not related to respiratory chain deficiency. However, values from KO samples tend to be lower than controls, at least in fore- and midbrain regions.

Since we had observed reduction of CI supercomplexes by BNGE in patient and shRNA-knockdown HEK 293T cell lines, we wanted to assess CI activity in relation to the other respiratory chain complexes, and not just in isolation. Aerobic respiration, measured by the rate of O_2 consumption, was determined by Oroboros for brains of 3 month old control (WT and HET, n = 3) and knockout (KO, n = 3) mice. **Fig. 6.20** shows significant reduction in CI-linked aerobic respiration for KO animals, calculated as respiration requiring ADP as a

substrate minus the residual O_2 flux after addition of the CI inhibitor, rotenone. This showed that despite there being no specific CI enzymatic deficiency in knockout brains, electron flow through the electron transport chain was inhibited at the CI point of entry.

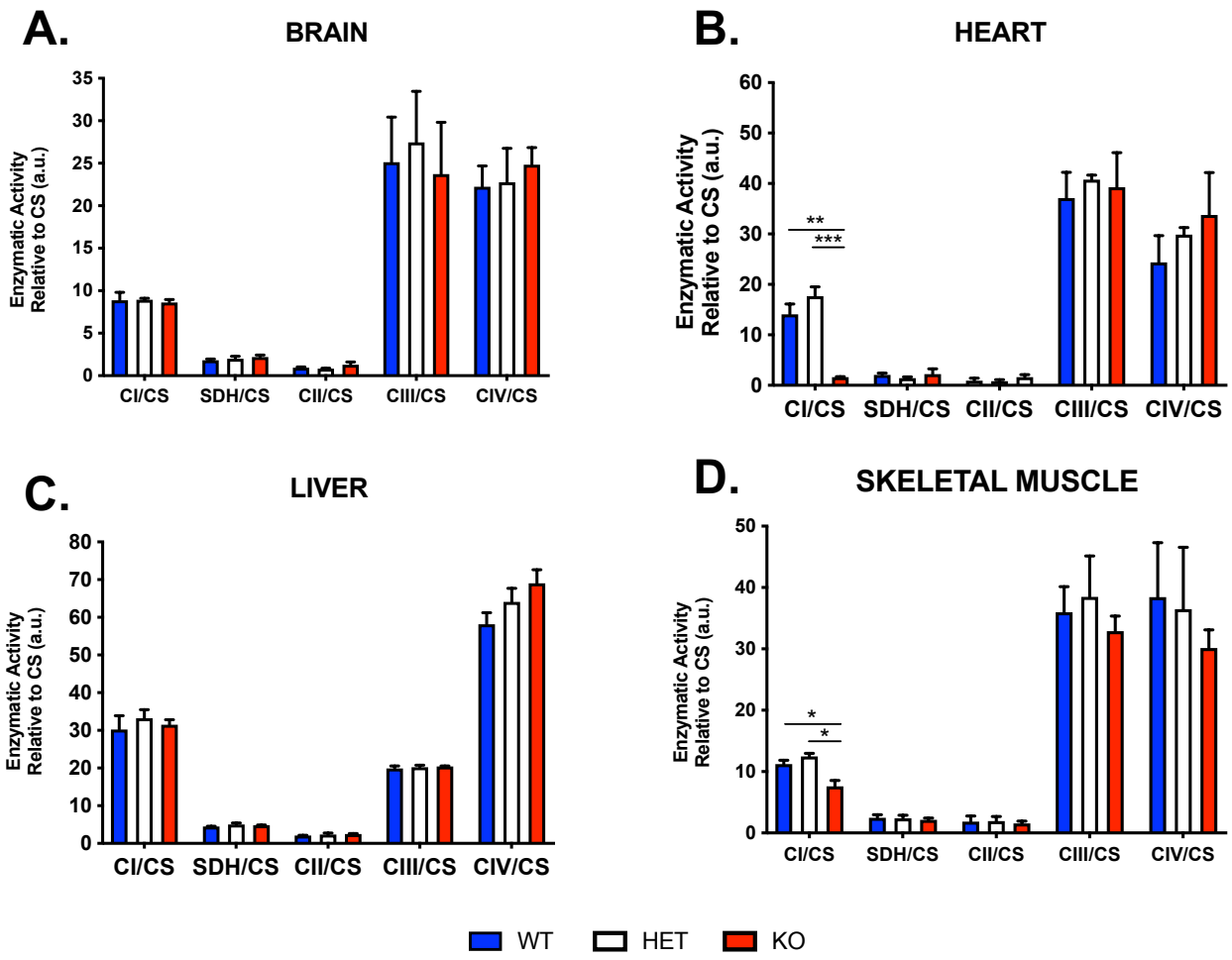

Fig. 6.18. Biochemical analyses of brain, heart, liver and skeletal muscle homogenates from *Tmco6*-KO mice show tissue-specific metabolic differences.

Complex I (CI), succinate dehydrogenase (SDH), Complex II (CII), Complex III (CIII) and Complex IV (CIV)enzymatic activities were performed as per **section 2.7.1**, with resulting values normalised to the activity of citrate synthase (CS) for 3 month old wildtype (WT) (n = 2), heterozygous (HET) (n = 2) and knockout (KO) (n = 3) (**A.)** brain, (**B.**) heart, (**C.**) liver and (**D.**) skeletal muscle protein homogenates. Data are presented as mean ± range. Statistical analysis: * $p < 0.05$, ** $p < 0.01$, *** $p < 0.005$, calculated by two-way ANOVA with Sidak's multiple comparisons *post hoc* test applied.

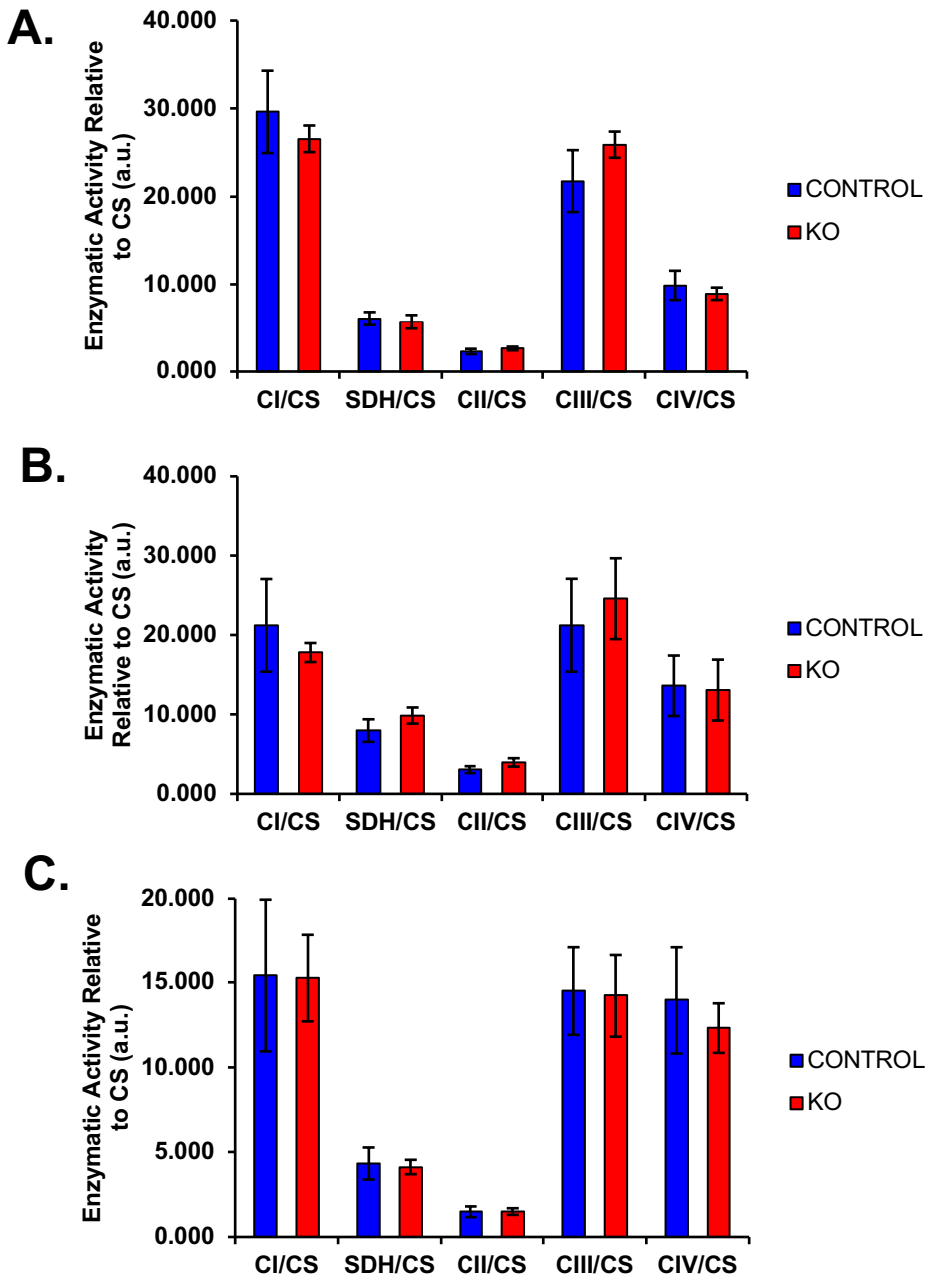

Fig. 6.19. Biochemical analyses of forebrains, midbrains and hindbrains of 3 month old *Tmco6*-KO mice show no differences in respiratory chain enzymatic activities.

Complex I (CI), succinate dehydrogenase (SDH), Complex II (CII), Complex III (CIII) and Complex IV (CIV) enzymatic activities were performed as per **section 2.7.1**, with resulting values normalised to the activity of citrate synthase (CS) for 3 month old control, consisting of wildtype and heterozygous animals (*n* = 4), and knockout (KO) (*n* = 4) (**A.**) forebrains, (**B.**) midbrains and (**C.**) hindbrains. Data are presented as mean ± SD. Statistical analysis by two-way ANOVA with Sidak's multiple comparisons *post hoc* test applied revealed no significant differences.

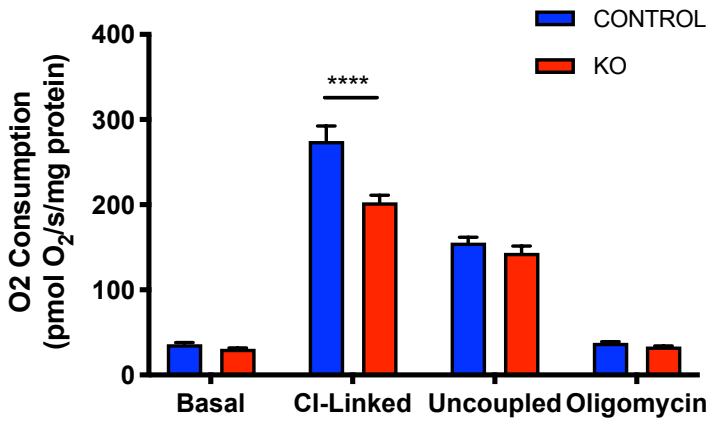

Fig. 6.20. CI-linked aerobic respiration is significantly decreased in *Tmco6*-KO brains.

Mitochondrial O_2 consumption rate was measured in brains from 3 month old control (WT and HET, *n* = 3) and knockout (KO, *n* = 3) genotypic groups in technical duplicates using an Oxygraph-2k respirometer (Oroboros Instruments, Innsbruck, Austria) as per **section 2.7.3**. Basal = mitochondrial O_2 consumption rate at 37 °C, CI-linked = ADP-dependent O_2 consumption minus residual OXPHOS-independent respiration after addition of rotenone, Maximal = maximal respiration following uncoupling of the respiratory chain by CCCP (C2759, Sigma-Aldrich®), Oligomycin = halting of aerobic respiration following addition of the CV inhibitor, oligomycin (O4876, Sigma-Aldrich®). Data are presented as mean ± SEM (*n* = 3). Statistical analysis: **** $p < 0.001$, calculated by two-way ANOVA with Sidak's multiple comparisons test applied. No differences in basal, maximal or oligomycin-inhibited respiration were detected for the knockout relative to the control group, but CI-linked respiration was significantly lower in knockout brains.

Since heart and skeletal muscle homogenates showed significant deficiencies in CI enzymatic activity for 3 month old *Tmco6*-knockout animals compared to both wildtype and heterozygous controls (**Fig. 6.18**), we repeated biochemical measurements for 12 month old WT, HET and KO mice to observe if this phenotype was also present in older animals. We also wanted to observe whether the severity of the CI deficiency was progressive with age. As shown in **Fig. 6.21 A.**, the isolated CI deficiency in cardiac muscle was comparable to that observed for 3 month old animals. The same trend was also seen in skeletal muscle (**Fig. 6.21 B.**), with equivalent differences to the 3 month old age group. Interestingly, skeletal muscle of 12 month old KO mice also exhibited COX deficiency of approximately 25 % compared to both WT and HET controls.

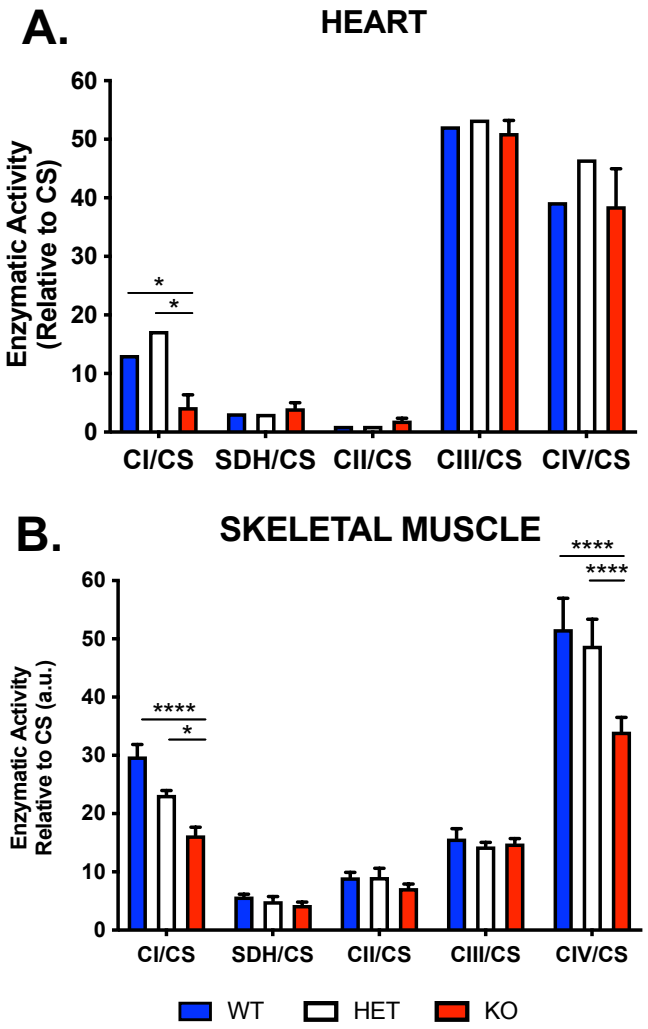

Fig. 6.21. 12 month old heart and skeletal muscles homogenates show conserved CI deficiency for *Tmco6*-KO mice.

Complex I (CI), succinate dehydrogenase (SDH), Complex II (CII), Complex III (CIII) and Complex IV (CIV) enzymatic activities were performed as per **section 2.7.1**, with resulting values normalised to the activity of citrate synthase (CS) for 12month old wildtype (WT), heterozygous (HET) and knockout (KO) mice for (**A.**) heart and (**B.**) skeletal muscle tissue homogenates. Data are presented as mean ± SEM. Heart: WT (n = 1), HET (n = 1) and KO (n = 3), Skeletal muscle: WT (n = 3), HET (n = 3) and KO (n = 4). Statistical analysis: * p < 0.05, **** p < 0.001, calculated by two-way ANOVA with Sidak's multiple comparisons *post hoc* test applied.

6.2.5 Molecular Investigation of *Tmco6*-KO Tissues

SDS-PAGE, 1D-BNGE and CI in-gel activity were performed for brain, heart, skeletal muscle and liver tissues to assess differences in the steady-state levels of CI subunits, assembly factors, CI holocomplex abundance and abundances of any subcomplex or supercomplex CI-containing species, and to visually asses any CI activity differences in these tissues. The analysis was used in part to try to narrow down where in the CI biogenesis pathway TMCO6 may be involved.

Firstly, we analysed total protein homogenates from brains of 3 month old WT, (*n* = 2), HET (*n* = 2) and KO (*n* = 3) mice, and immunoblotted various CI subunits localising to each of the CI modules, as well as several subunits of the other respiratory complexes. As shown in **Fig. 6.22**, no differences in abundances of any OXPHOS subunits were found. 1D-BNGE, Western blot analysis showed no difference in CI holocomplex abundance or in the amount of any other respiratory chain complex (**Fig. 6.23 B.**). In addition, 3 month old KO mouse brains again did not show differences in CI activity, this time shown qualitatively by in-gel activity (**Fig. 6.23 A**.).

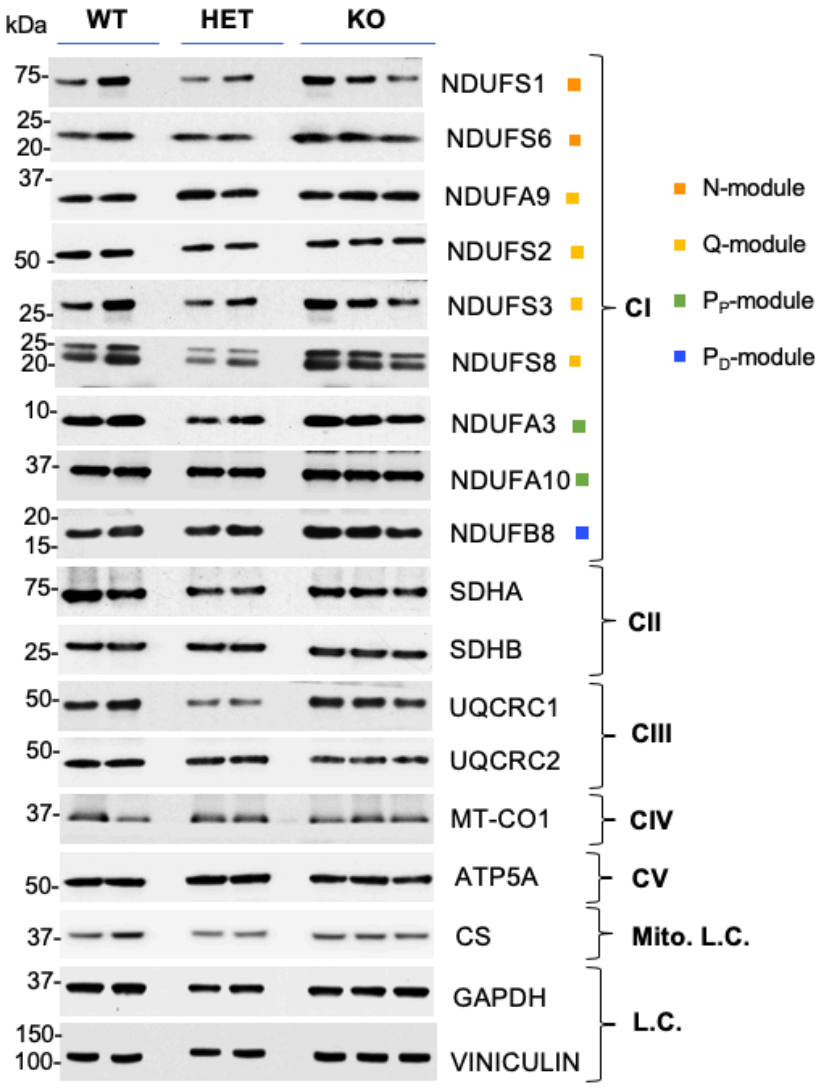

Fig. 6.22. 3 month old brains of *Tmco6*-knockout mice show no differences in OXPHOS subunit abundance by SDS-PAGE and Western blot analysis.

SDS-PAGE was performed as per **section 2.6.2** with 20 µg of protein from whole tissue homogenates obtained from 3 month old WT (*n* = 2), HET (*n* = 2) and KO (*n* = 3) mice. WB analysis followed for immunodetection of CI subunits NDUFS1, NDUFS6, NDUFA9, NDUFS2, NDUFS3, NDUFS8, NDUFA3, NDUFA10, and NDUFB8, CII subunits SDHA and SDHB, CIII subunits UQCRC1 and UQCRC2, CIV subunit MT-CO1, CV subunit ATP5A, mitochondrial loading control CS, and cytosolic loading controls GAPDH and VINCULIN using the primary antibodies and concentrations detailed in **Table 2.29**.

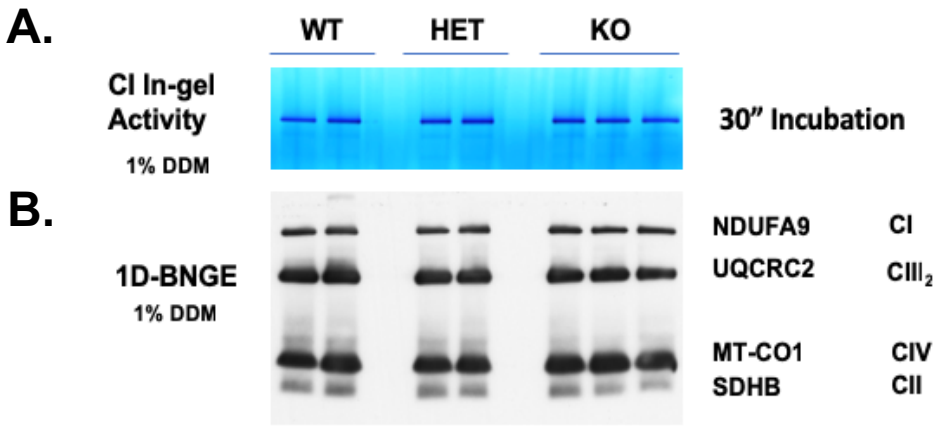

Fig. 6.23. 3 month old brains of *Tmco6*-knockout mice show no differences in CI in-gel activity or OXPHOS complex abundances by 1D-BNGE and Western blot analysis.

(**A.**) CI in-gel activity for 120 µg mitochondrial protein treated with 1 % DDM from 3 month old WT, (*n* = 2), HET (*n* = 2) and KO (*n* = 3) hearts was performed by NADH/NBT staining (see **section 2.7.2**). No difference in activity was observed by this qualitative method. (**B.**) 1D-BNGE was performed with 120 µg mitochondrial protein treated with 1 % DDM from 3 month old WT, (*n* = 2), HET (*n* = 2) and KO (*n* = 3) mice, resolved using 3 – 12 % gradient Novex® NativePAGE gels as per **section 2.6.3**. Immunodetection of native CI, CII, $CIII_2$, and CIV was performed by WB analysis by successive incubations with primary antibodies against NDUFA9, SDHB, UQCRC2, and MT-CO1, respectively (for antibody manufacturer details and concentrations used for each, see **Table 2.29**).

We next analysed total protein homogenates from hearts of 3 month and 12 month old WT, HET and KO mice (*n* = 3 for each group), by SDS-PAGE and WB blotting analysis. As shown in **Fig. 6.24**, differences in abundances of CI subunits in 3 month old animals were not found; however 12 month old animals showed a significant difference in the abundance of NDUFS1 (N-module). The steady-state levels of all other OXPHOS subunits tested for the KO genotype were in line with control values. Fresh samples were prepared to verify the difference in NDUFS1, again by SDS-PAGE and WB analysis. In addition to NDUFS1, NDUFS6 was also immunodetected since it had been found to be pulled down by HA-tagged TMCO6 in immunoprecipitation experiments in HEK 293T cells (**Fig. 5.21**). As shown in **Fig. 6.25 A.** and **B.**, statistically significant differences in NDUFS1 and NDUFS6 abundance were shown relative to the loading control, GAPDH. It is significant that both subunits are part of the N-module, suggesting TMCO6 may be involved, at least in part, in late-stage CI modular assembly.

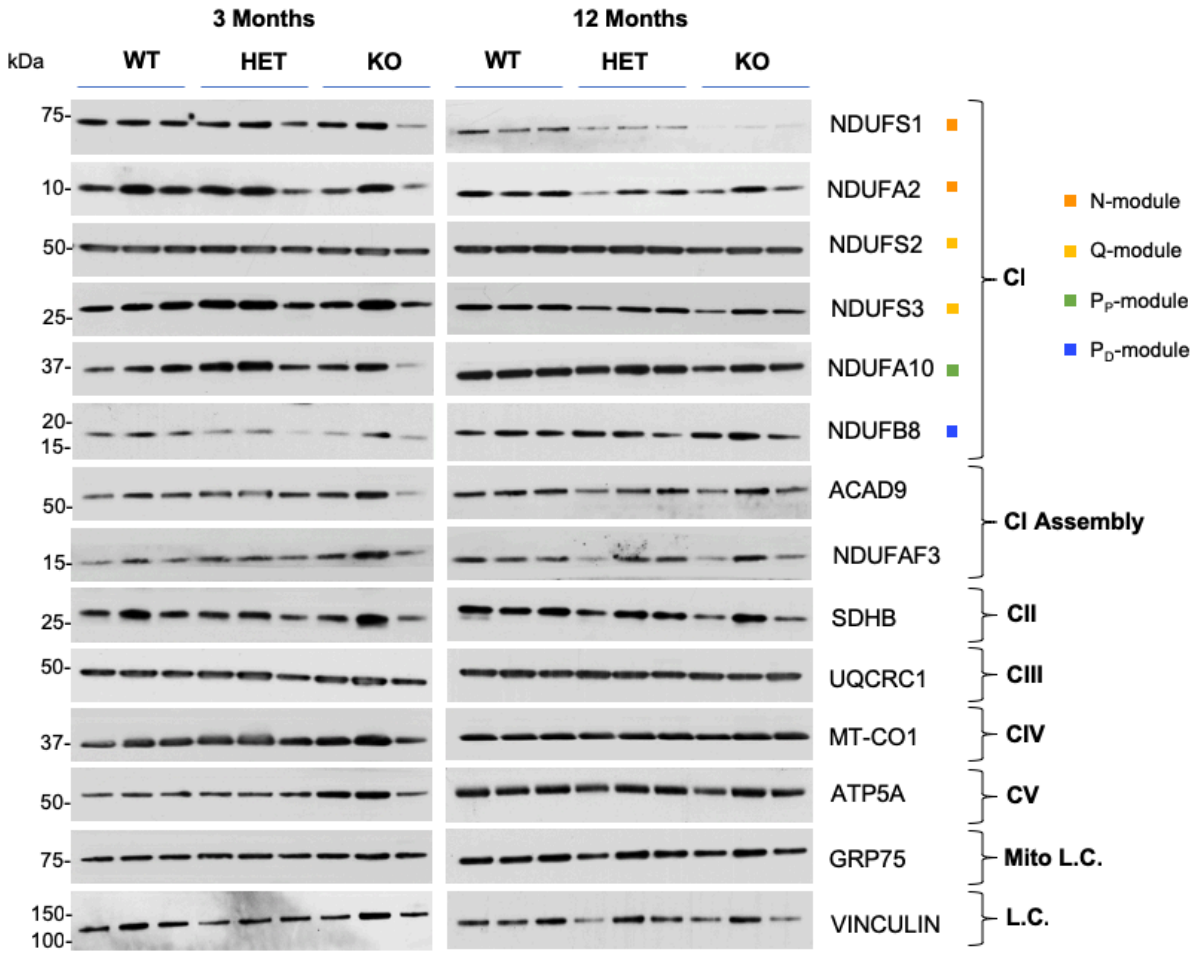

Fig. 6.24. Hearts from 3 month and 12 month old Tmc*co6*-knockout mice show no significant difference in steady-state levels except for NDUFS1.

SDS-PAGE was performed as per **section 2.6.2** with 20 µg of protein from whole tissue homogenates obtained from 3 and 12 month old WT, HET and KO mice (*n* = 3 per group). WB analysis followed for immunodetection of CI subunits NDUFS1, NDUFA2, NDUFS2, NDUFS3, NDUFA10, and NDUFB8, CI assembly factors ACAD9 and NDUFAF3, CII subunit SDHB, CIII subunit UQCRC1, CIV subunit MT-CO1, CV subunit ATP5A, mitochondrial loading control (L.C.) GRP75, and cytosolic loading control VINCULIN, using the primary antibodies and concentrations detailed in **Table 2.29**.

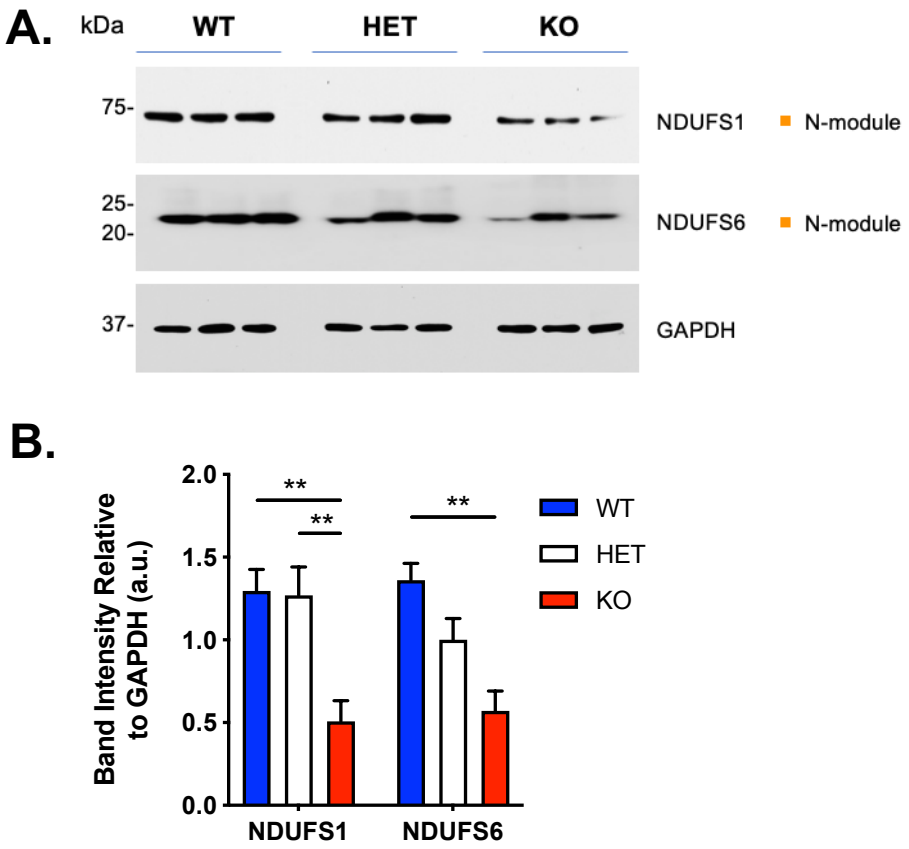

Fig. 6.25. 3 month old hearts of *Tmco6*-knockout mice show significant differences in the quantity of CI subunits NDUFS1 and NDUFS6

(**A.**) SDS-PAGE was performed as per **section 2.6.2** with 20 µg of protein from whole tissue homogenates obtained from 12 month old WT, HET and KO murine hearts (*n* = 3 for each genotypic group). WB analysis followed for immunodetection of CI subunits NDUFA2, NDUFS1, and NDUFB8, CII subunit SDHA, CIII subunit UQCRC2, CV subunit ATP5A, mitochondrial loading control GRP75, and cytosolic loading controls GAPDH and VINCULIN using the primary antibodies and concentrations detailed in **Table 2.29**. (**B.**) Densitometric analysis was performed by ImageJ Fiji Gel Analysis software for relative band intensities of NDUFS1 and NDUFS6, normalised to the signal for GAPDH per sample. Data are presented as mean ± SEM. Statistical analysis: ** $p < 0.01$, calculated by two-way ANOVA with Sidak's multiple comparisons *post hoc* test.

1D-BNGE was used to analyse respiratory chain complex abundances in hearts of WT (*n* = 2), HET (*n* = 2) and KO (*n* = 3) 3 month-old mice. Immunodetection of NDUFA9 (N- module/Q-module boundary) by Western blotting showed no discernible differences in CI holocomplex abundance (**Fig. 6.26 B.**), but there was a statistically significant ~ 40 % difference in CI in-gel activity signal by densitometric quantification (**Fig. 6.26 A.** and **C.**). CII (as immunodetected by SDHB), $CIII_2$ (UQCRC2) and CIV (MT-CO1) levels were comparable between KO, HET and WT mice.

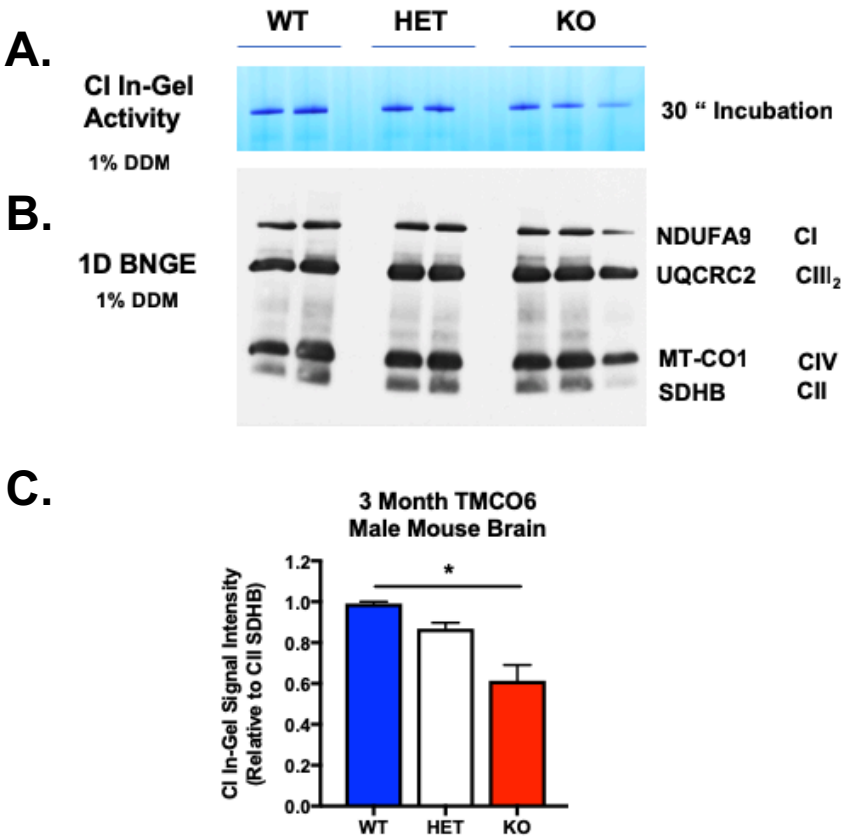

Fig. 6.26. 3 month old hearts of *Tmco6*-knockout mice show a difference in CI in-gel activity but little difference in OXPHOS complex abundances by 1D-BNGE.

(**A.**) CI in-gel activity for 120 µg mitochondrial protein treated with 1 % DDM from 3 month old WT (*n* = 2), HET (*n* = 2) and KO (*n* = 3) hearts was performed by NADH/NBT staining (see **section 2.7.2**), showing statistically significant differences in staining intensities for KO compared to WT samples (see **C.**). (**B.**) 1D-BNGE was performed as above using 3 – 12 % gradient Novex® NativePAGE gels, as per **section 2.6.3**. Immunodetection of native CI, CII, $CIII_2$, and CIV was performed by WB analysis by successive incubations with primary antibodies against NDUFA9, SDHB, UQCRC2, and MT-CO1, respectively (for antibody details, see **Table 2.29**). (**C.**) Densitometric quantification of CI in-gel band staining relative to CII signals revealed statistically significant CI activity reduction by ~ 40 % for KO animals compared to WT and HET controls. Data are presented as mean ± range. Statistical analysis: * $p < 0.01$, one-way ANOVA with Tukey's multiple comparisons *post hoc* test applied.

Skeletal muscles were next analysed as described above for brain and heart, by SDS-PAGE and WB blotting analysis to assess differences in OXPHOS subunit quantities, and by 1D-BNGE and CI in-gel activity to determine any alterations in abundance of the CI holocomplex or its biochemical activity. As shown in **Fig. 6.27 A.**, the only protein whose steady-state level was altered consistently in KO mice was NDUFB8 (P_D-module). However, densitometric analysis (**Fig. 6.27 B**.) found no statistically significant reduction in the abundance of NDUFB8 for KO mice.

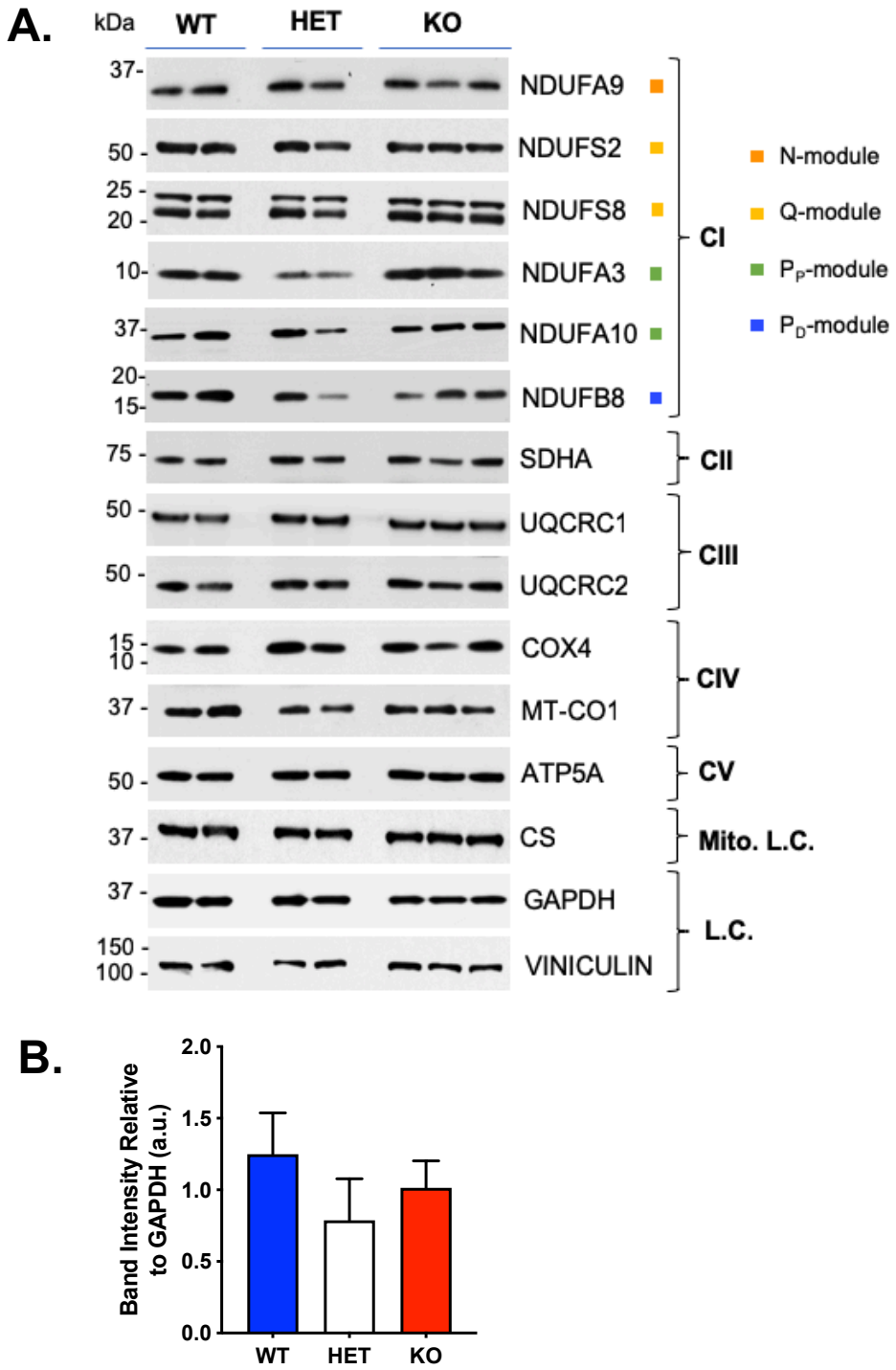

Fig. 6.27. No differences in OXPHOS subunit levels were observed in skeletal muscle.

(**A.**) SDS-PAGE was performed as per **section 2.6.2** with 20 µg of protein from 3 month old WT (*n* = 2), HET (*n* = 2) and KO (*n* = 3) skeletal muscle homogenates. Immunodetection of CI subunits NDUFA9, NDUFS2, NDUFS8, NDUFA3, NDUFA10 and NDUFB8, CII subunit SDHA, CIII subunits UQCRC1 and UQCRC2, CIV subunit MT-CO1, CV subunit ATP5A, mitochondrial L.C. CS, and cytosolic L.C.s GAPDH and VINCULIN followed (see **Table 2.29**). (**B.**) Densitometric quantification was performed for NDUFB8, relative to GAPDH. Data are presented as mean ± range. No significant differences were found by one-way ANOVA with Tukey's multiple comparisons *post hoc* test.

1D-BNGE was used to analyse respiratory chain complex abundances in skeletal muscles of 3 month old mice (*n* = 2 for WT, HET and KO genotypes). Immunodetection of NDUFA9 by Western blotting showed no discernible differences in steady-state levels of the CI holocomplex (**Fig. 6.28 B.**), and there were no qualitative differences in CI in-gel activity signal (F**ig. 6.28 A.** and **C.**) for KO compared to control WT and HET animals. The difference observed by spectrophotometry (**Fig. 6.18**) if still present, it is under the sensitivity limit in this method. CII (as immunodetected by SDHB), $CIII_2$ (UQCRC2) and CIV (MT-CO1) levels were comparable between WT, HET and KO mice.

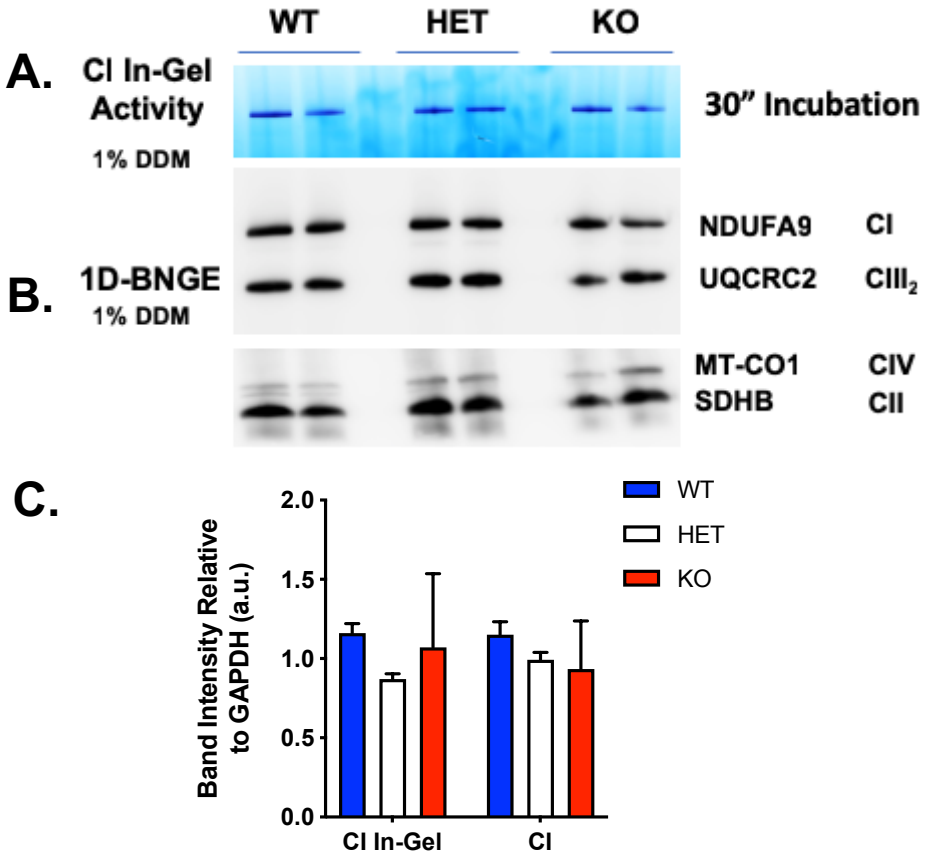

Fig. 6.28. Mitochondrial protein complex levels are unaffected in KO skeletal muscle.

(**A.**) CI in-gel activity for 120 µg mitochondrial protein treated with 1 % DDM from 3 month old WT, HET and KO (all *n* = 2) skeletal muscle was performed by NADH/NBT staining (see **section 2.7.2**). No difference in activity was observed by this qualitative method. (**B.**) 1D-BNGE was performed as per **section 2.6.3**. Immunodetection of native CI, CII, $CIII_2$, and CIV was performed by WB analysis by successive incubations with primary antibodies against NDUFA9, SDHB, UQCRC2, and MT-CO1, respectively (for antibody manufacturer details and concentrations used for each, see **Table 2.29**. (**C.**) Data are presented as mean ± range. Densitometric quantification of CI in-gel band intensities the CI holocomplex, both relative to CII, revealed no differences by statistical analysis: two-way ANOVA with Sidak's multiple comparisons test applied.

Finally, we analysed the livers of 3 month KO, HET and WT mice. As shown in **Fig. 6.29 A.**, no differences in the abundances of OXPHOS subunits, including those of CI, were found for KO mice compared to control groups by SDS-PAGE and WB analysis. Densitometric analysis of NDUFS1 (**Fig. 6.29 B.**) showed a non-significant difference for the KO samples compared to controls. For analysis of mature mitochondrial protein complexes by 1D-BNGE, mitochondrial protein extracts from liver were solubilised with either 1 % DIG (**Fig. 6.30 A.**), or 1 % DDM (**Fig. 6.30 B.**). DIG-solubilisation was used here to allow for the visualisation of supercomplex species to assess any differences resulting from absence of the Tmco6 protein. There were no differences observed in the steady-state levels of any of the respiratory chain complexes, or in CI activity of the mature CI homocomplex or any CI-containing supercomplex species, evaluated qualitatively by in-gel activity.

In summary of the results of the molecular investigation into *Tmco6*-knockout murine tissues, the steady-state levels of N-module subunits NDUFS1 and NDUFS6 were reduced to ~ 40 % of control levels in hearts of aged mice. SDS-PAGE and WB analysis did not reveal any other significant alterations for subunits of CI, or any subunits of the other respiratory chain complexes, for hearts or for all other tissues examined, i.e. brains, skeletal muscles, and liver ay 3 or 12 months of age. 1D-BNGE showed no changes in CI abundance, or in the abundances of the other mature protein complexes, but coupled with in-gel activity, it only revealed a significant decrease in CI activity for KO hearts.

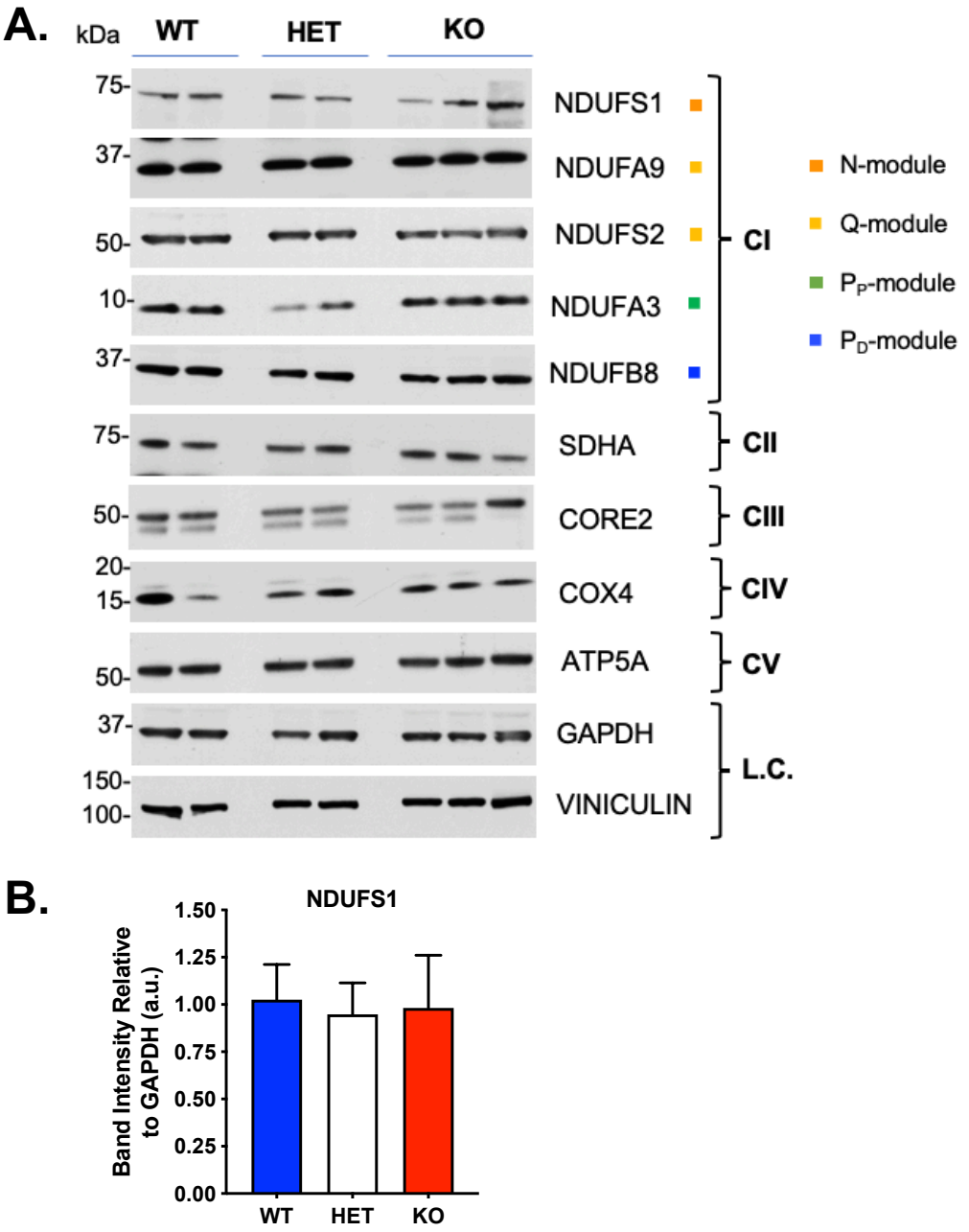

Fig. 6.29. No differences in OXPHOS subunit levels were observed in liver.

(**A.**) SDS-PAGE was performed as per **section 2.6.2** with 20 µg of protein from 3 month old WT, HET and KO (*n* = 3) liver homogenates. Immunodetection of CI subunits NDUFS1, NDUFA9, NDUFS2, NDUFA3, and NDUFB8, CII subunit SDHA, CIII subunit UQCRC2 (Core 2), CIV subunit COX4, CV subunit ATP5A, and cytosolic loading controls (L.C.) GAPDH and VINCULIN followed (see **Table 2.29**). (**B.**) Densitometric quantification was performed for NDUFS1, relative to GAPDH, and no significant differences were found by one-way ANOVA with Tukey's multiple comparisons *post hoc* test. Data are presented as mean ± SEM.

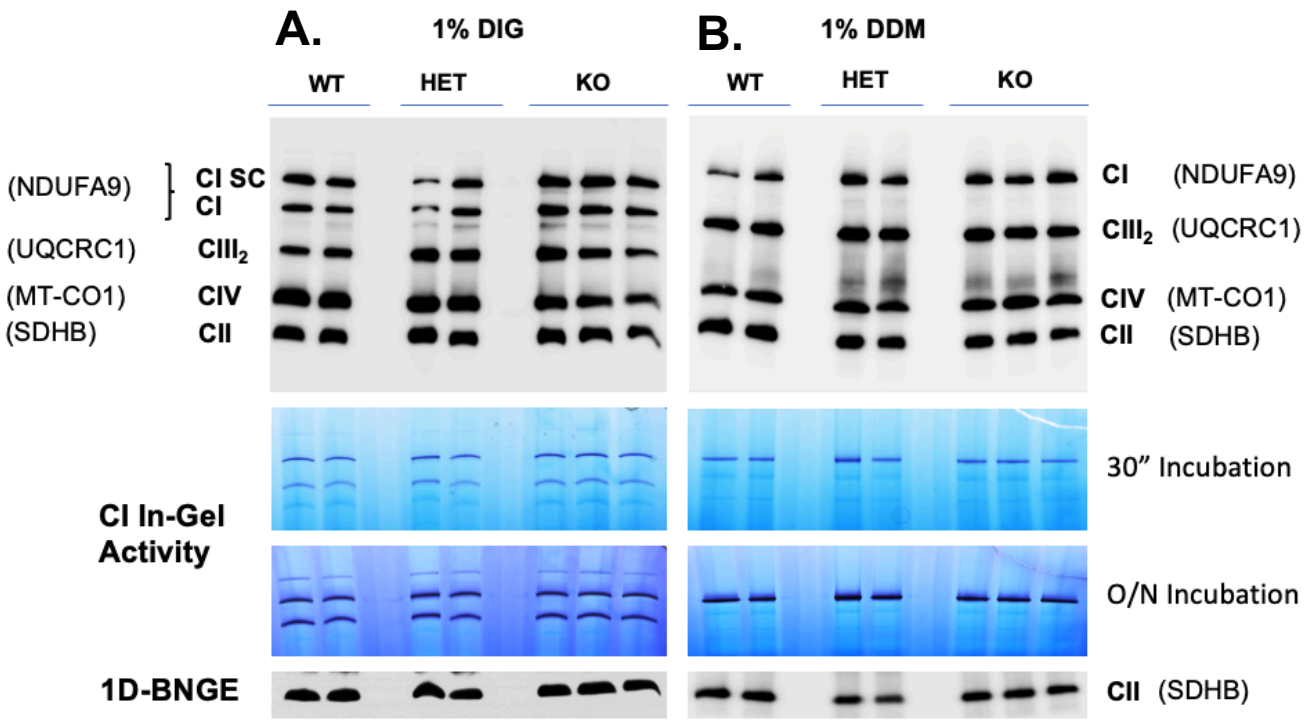

Fig. 6.30. Mitochondrial protein complex levels are unaffected in KO liver.

TOP: 1D-BNGE was performed with 120 µg mitochondrial protein treated with (**A.**) 1 % DIG or (**B.**) 1 % DDM from 3 month old WT, HET and KO (all *n* = 2) livers as per **section 2.6.3**. Immunodetection of native CI, CII, $CIII_2$, and CIV was performed by WB analysis by successive incubations with primary antibodies against NDUFA9, SDHB, UQCRC2, and MT-CO1, respectively (for antibody manufacturer details and concentrations used for each, see **Table 2.29**. BOTTOM: CI in-gel activity was performed by NADH/NBT staining (see **section 2.7.2**). No difference in activity was observed by this qualitative method relative to the signals of CII, immunodetected by SDHB.

6.2.6 Analysis of Cardiac Function and Respiratory Rate in *Tmco6*-KO Mice

Following on from the observation that *Tmco6*-ablation results in severe CI deficiency in hearts of 3M and 12M KO animals, cardiovascular function and physiology were evaluated by echocardiography and electrocardiography using the Vevo 770® High Resolution Imaging System (VisualSonics, Inc., Toronto, Canada) for the age group that showed the worse phenotype (12 onths old). Imaging was performed by Stephen Moore at the Phenomics Laboratory (West Forvie Site, Cambridge, UK).

Aged (12 month old) wildtype (WT) and knockout (KO) mice were sedated with isoflurane gas and systematically imaged in parasternal short axis (**Fig 2.9 A.**), long axis (**Fig 2.9 B.)** and apical four-chamber (**Fig 2.9 C.**) views in the pulsed-wave (PW) doppler or motion (M) modes, as previously described (Gao *et al.*, 2011). These acquired images were used to calculate a large number of functional parameters. The ones of interest to us were those that assessed cardiac function for different areas of the heart. These were: aortic ejection time (AET), left ventricle (LV) myocardial performance index (MPI), mitral valve (MV) atrial (A) and early (E) peak wave flows (mm/s), MV E/A peak ratio, right ventricular outflow tract mean velocity time integral (RVOT VTI) (mm/s), cardiac output (CO) (ml/min), ejection fraction (EF) (%), fraction shortening (FS) (%), HR (bpm), stroke volume (SV) (µl), and volumes expelled in diastole and systole (V;d, V;s) (µl), all calculated by the Vevo LAB and Auto LV Analysis software packages (VisualSonics).

No obvious morphological defects were observed in KO hearts by echocardiography. As shown in **Table 6.4,** the only statistically significant difference in echocardiographic parameters detected between KO and WT 12 month old cohorts was for RVOT VTI, which is used to assess right ventricular systolic function. Decreased RVOT VTI is associated with hypotension and decreased flow of deoxygenated blood to the lungs. Importantly, reduction of right ventricular systolic function has been found in humans to correlate with impaired exercise tolerance (Ojji *et al.*, 2016), as seen in *Tmco6*-KO 3 and 12 month old mice by exhaustion trials (**Fig. 6.5 A.** and **B.**). Despite not yielding a significant difference by statistical analyses, the CO, EF, SV, FS, V;d and V;s values were all decreased to varying extents for the KO mice, all normalised to body weights per animal. These values together suggest impaired ability of KO hearts to efficiency pump blood around the body, and can result from a range of underlying causes. One of which is contractility. Indeed, KO animals showed far less contractility in parasternal short axis views compared to controls (video available upon request). In addition, we observed a decrease in the HR of KO animals compared to age-matched WT controls. This result was explored further by ECG, as described below.

Table 6.4. Echocardiography Results for 12-Month Old Male *Tmco6*-KO Mice

For WT and KO, n = 4. Data are presented as mean ± SEM. Statistical analysis: two-way ANOVA with Sidak's multiple comparisons *post hoc* test applied. n.s. = non-significant.

Parameter	Unit	WT	KO	Significant?
Aortic Ejection Time (AET)	ms	41.7 ± 2.2	49.3 ± 5.5	n.s.
Left Ventricle Myocardial Performance Index (LV MPI)	-	0.8 ± 0.1	0.8 ± 0.2	n.s.
Mitral Valve E/A Peak Ratio (M/V E/A)	-	1.7 ± 0.4	1.6 ± 0.1	n.s.
Right Ventricular Outflow Tract Mean Velocity Time Integral (RVOT VTI)	mm/s	-511.7 ± 22.9	-428.4 ± 39.9	p = 0.003
Cardiac Output (CO)	ml/min	24.4 ± 3.7	19.0 ± 4.4	n.s.
Ejection Fraction (EF)	%	57.5 ± 6.9	52.3 ± 3.2	n.s.
Fraction Shortening (FS)	%	30.3 ± 4.6	26.7 ± 1.8	n.s.
Heart Rate (HR)	bpm	467 ± 58.2	427.5 ± 60.1	n.s.
Stroke Volume (SV)	µl	52.4 ± 5.6	42.2 ± 7.9	n.s.
Volume Expelled In Diastole (V;d)	µl	92.3 ± 13.8	82.4 ± 19.0	n.s.
Volume Expelled In Systole (V;s)	µl	39.9 ± 11.4	35.1 ± 11.3	n.s.

Electrocardiogram (ECG) traces of KO and WT mice (n = 4 per group) determined signs of perturbed electrophysiology in 12 month-old *Tmco6*-KO hearts. Firstly, WT (**Fig. 6.31 A.**) animals were always found to have faster heart rates than for KO (**Fig. 6.31 B.**) littermates, with approximately 3 beats for the KO for every 4 of the WT. This trend was true for all 4 knockouts. Secondly, KO animals displayed 4:1 with occasional 3:1 atrial flutter (both as labelled in **Fig. 6.31 B.**), in which instead of a single P-wave, denoting atrial depolarisation at the beginning of a heartbeat, there are instead three or four separate waves. Typical atrial flutter results from a re-entrant circuit around the tricuspid valve (Masè, Disertori and Ravelli, 2009). **Fig. 6.32** shows two representative KO and two representative WT traces, where this pattern is clearly shown in KOs, but is completely absence for WTs. It is worth noting that the amplitudes of WT and KO QRS peaks are comparable. It is only the x-axis (time) values that differ.

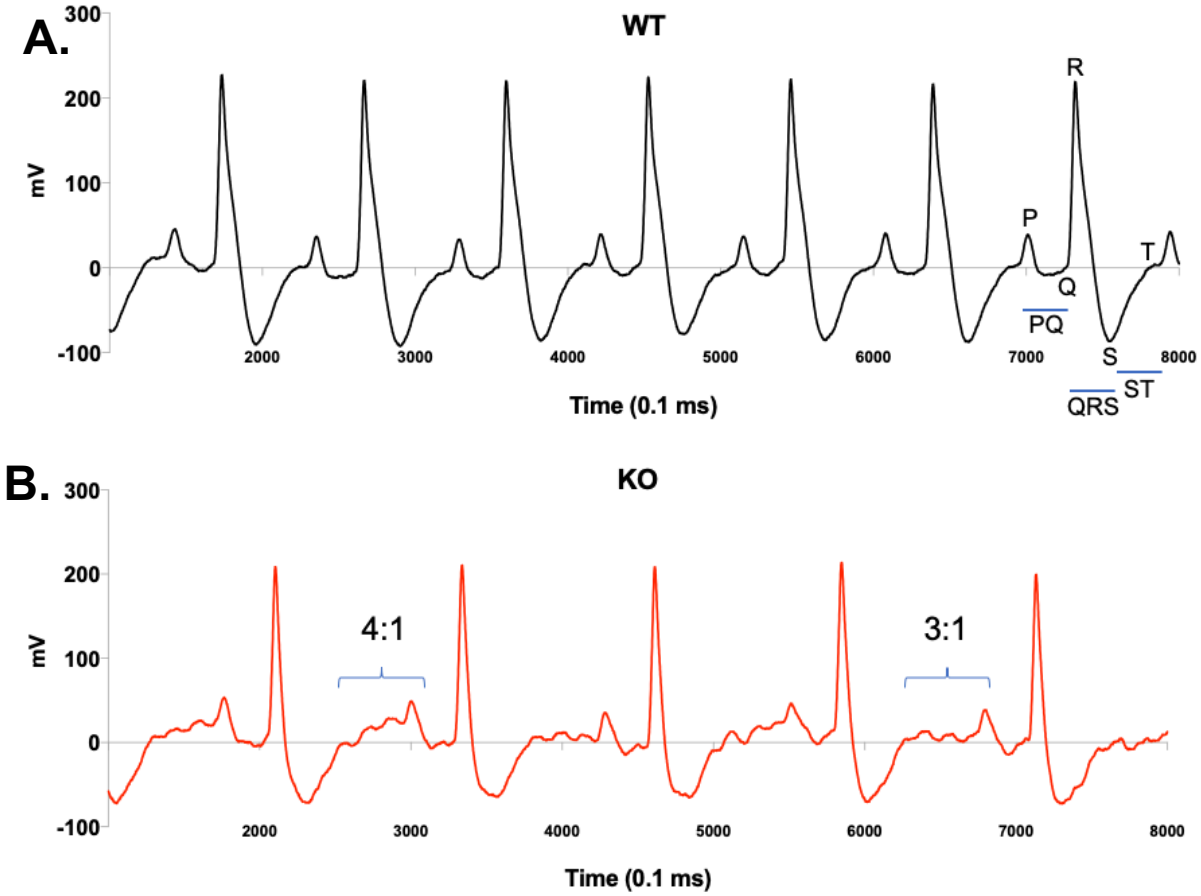

Fig. 6.31. 12 month old KO mice have 3 heart beats for every 4 of WT controls.

Cardiovascular function and physiology were evaluated by echocardiography for 12 month old male (**A.**) wildtype (WT) and (**B.**) knockout (KO) mice (*n* = 4 per group) using the Vevo 770® High Resolution Imaging System (VisualSonics, Inc., Toronto, Canada). Electrocardiogram (ECG) traces for representative WT (black) and KO (red) mice shows a pattern of 4 heart beats for the WT for every 3 of the KO. For an overview of the components of a murine ECG waveform, see **Fig. 2.9 D.** 3:1 or 4:1 atrial flutter is labelled for 2 indicative sections in the KO.

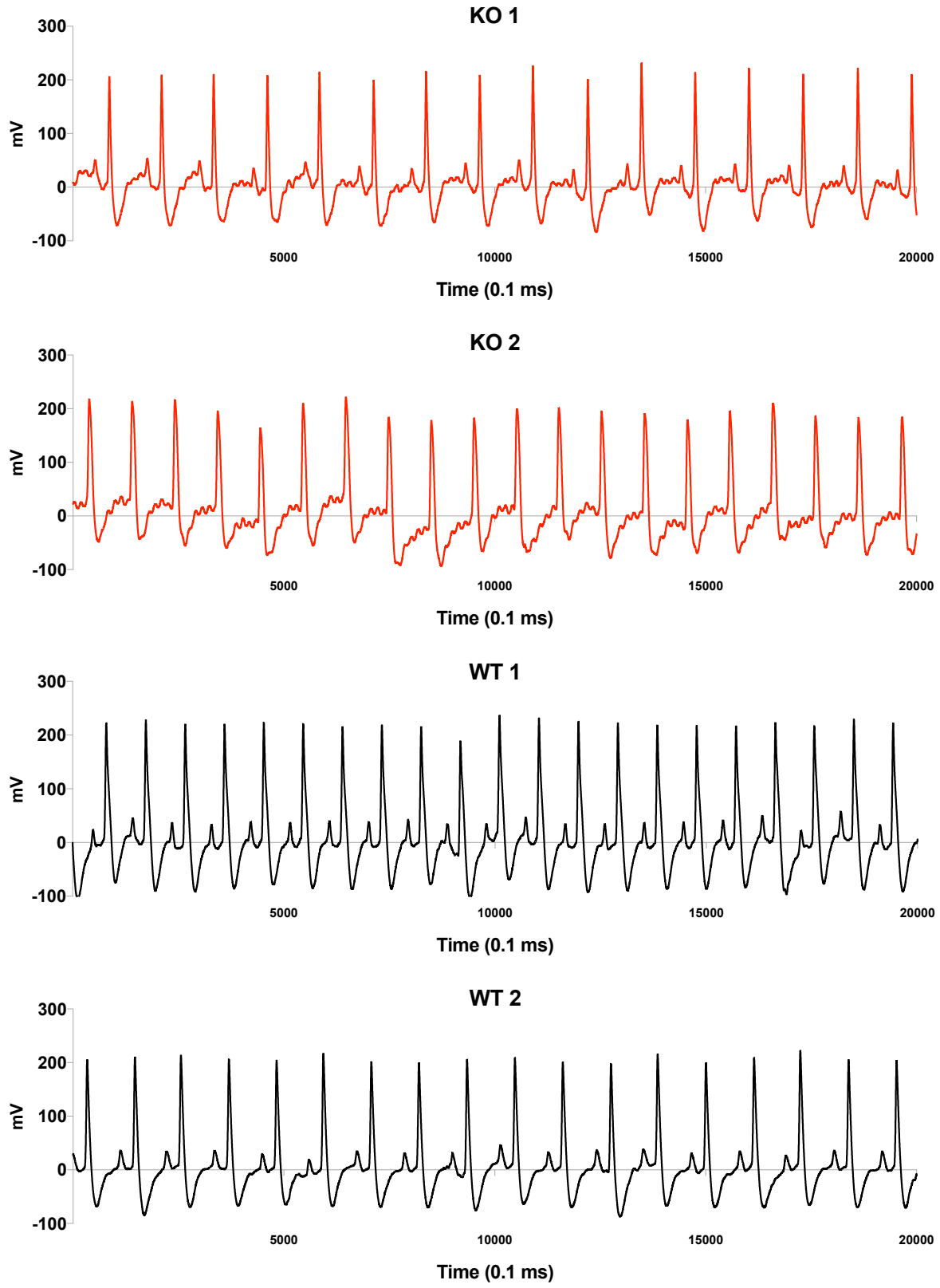

Fig. 6.32. KO 12 month old animals display 3:1 or 4:1 atrial flutter.

Representative electrocardiogram traces for two wildtype (WT) and two knockout (KO) 12 M mice are shown, displaying 3:1 or 4:1 atrial flutter in the KO. Traces were generated by the Vevo 770® High Resolution Imaging System (VisualSonics, Inc., Toronto, Canada).

To quantify these differences, PQ, QRS and ST intervals (see **Fig. 6.31 A.** for the respective span of each) were calculated per animal by averaging the durations per interval for three separate heart beats (**Table 6.5**). These results (*n* = 4 biological replicates for WT and KO genotypic groups) suggest that the decreased HR seen in KO animals is most likely caused by the atrial flutter, since there is only statistically significant increase in the PQ interval, which is almost doubled compared to that of age-matched WT controls. The QRS interval is comparable between WT and KO animals, suggesting no problem with the ventricular depolarisation. The ST interval is shorter in KO animals versus WT animals, but not considered to be statistically significant. The ST interval marks the time taken for ventricular repolarization, and has been found to be shortened following myocardial infarction and ischaemia (Hurst, 1997). The decreased ST interval could also be related to decreased right ventricular function, as observed by reduction in RVOT VTI in KO animals by echocardiography (**Table 6.4**).

Table 6.5. Electrocardiography Results for 12-Month Old Male *Tmco6*-Knockout Mice

For WT and KO, *n* = 4. Data are presented as mean ± SEM. Statistical analysis: two-way ANOVA with Sidak's multiple comparisons *post hoc* test applied. n.s. = non-significant.

Interval	Unit	WT	KO	Significant?
PQ	ms	38.5 ± 6.7	58.4 ± 7.6	$p = 0.0286$
QRS	ms	29.6 ± 4.1	30.4 ± 0.9	n.s.
ST	ms	37.4 ± 3.3	23.9 ± 3.1	n.s.

Additionally, respiration rate per animal was monitored throughout cardiac imaging, and interestingly, striking differences were observed between WT and KO genotypic groups (*n* = 4 each). **Fig. 6.33** shows overlap of representative KO and WT respiration curves, showing a three-fold average increase in respiration rate for KO animals compared to WT counterparts. **Fig. 6.34** shows full traces of 2 representative WT and 2 representative KO 12 month old mice over 3 seconds. The quantification of this data is shown in **Table 6.6**. KO animals breathed similarly whilst under anaesthetic than when conscious. It is possible that if the blood of KO animals is not being oxygenated quickly enough to sustain homeostatic function due to decreased right ventricular function (**Table 6.4**), then these mice are forced to breath in air more rapidly to compensate for the amount of oxygen needed to meet the body's various aerobic demands. This also explains the result observed by CLAMS of higher O_2 consumption and CO_2 production in 12 M KO male mice (**Fig. 6.8**), despite significantly less overall

movement (**Fig. 6.7**). Lastly, increased respiration rate is also commonly found in human patients that suffer from atrial flutter (Masè, Disertori and Ravelli, 2009).

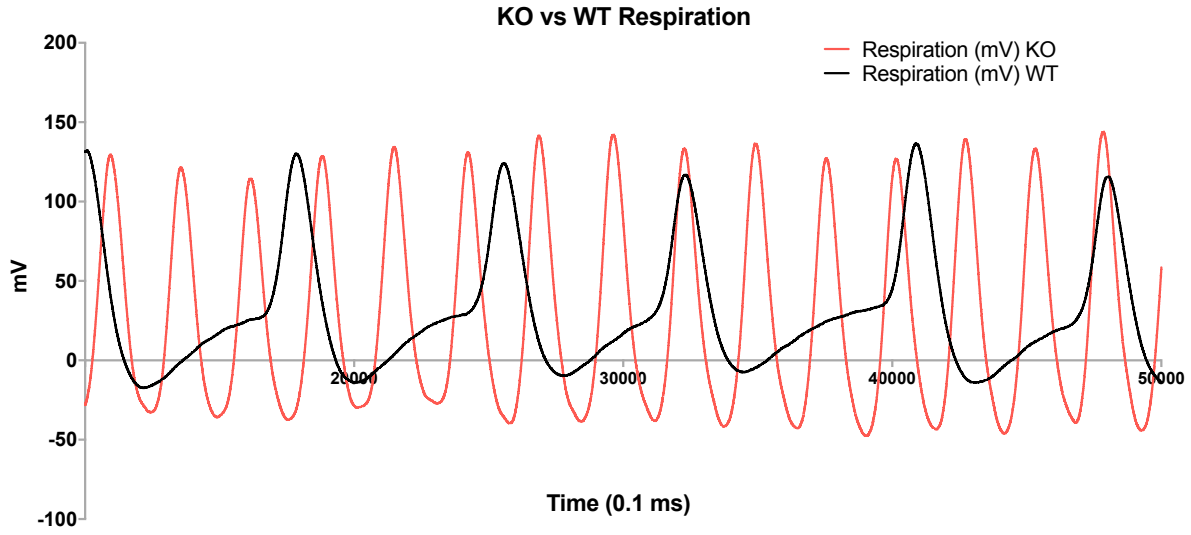

Fig. 6.33. 12 month old KO mice have a three-fold faster breathing rate than WT controls.

Respiration was recorded by electro-contact pads on the VEVO mouse handling platform positioned underneath wildtype (WT) and knockout (KO) male mice at 12 months of age during electrocardiographic monitoring (n = *4* per genotypic group), and as shown by two representative traces above, KO animals had a three-fold faster breathing rate than did WT animals.

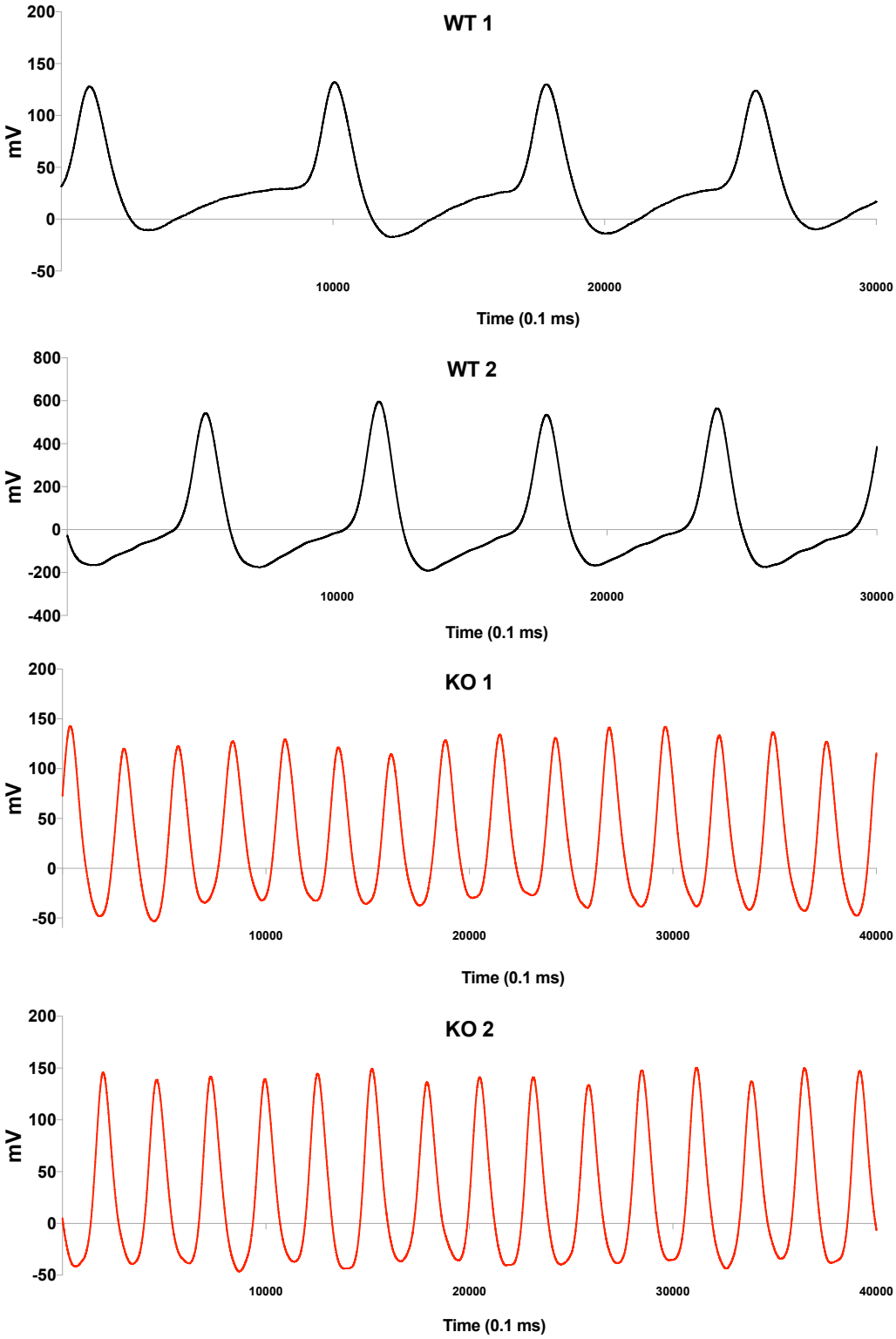

Fig. 6.33. 12 month old KO mice have a three-fold faster breathing rate than WT controls.

Respiration for 2 wildtype (WT) and 2 knockout (KO) male mice at 12 months of age, recorded during electrocardiographic monitoring; KO animals had a three-fold faster breathing rate than did WT animals.

Table 6.6. Respiratory Rates of 12-Month Old Male *Tmco6*-Knockout Mice

For WT and KO, $n = 4$. Data are presented as mean ± SEM. Statistical analysis: two-tailed Student's *t*-test. n.s. = non-significant.

	Unit	WT	KO	Significant?
Respiratory Rate	Breaths/sec	2.25 ± 0.25	3.5 ± 0.0	$p = 0.0170$

In summary, *Tmco6*-KO mice exhibit decreased right ventricular function by echocardiographic analysis, and perturbations to electrophysiology, suggesting atrial flutter. No other abnormalities in cardiac function or physiology were detected. Furthermore, *Tmco6*-KO animals have a threefold increase in respiration rate.

6.3 Conclusions

The work of this chapter: 1) characterises neurological, behavioural and motor phenotypes of a *Tmco6*-knockout murine model, 2) investigates histopathological abnormalities of different tissue types, 3) assesses the molecular and metabolic consequences of *Tmco6*-ablation in a tissue-specific manner and 4) evaluates cardiac function and electrophysiology following detection of severe CI deficiency in KO hearts.

A transgenic *Tmco6*-KO mouse model, B6N(Cg)-*Tmco6*$^{tm1.1(KOMP)Vlcg}$/J, was used in order to characterise the effects of Tmco6-ablation on mammalian development, physiology, neuromuscular coordination and metabolism. PCR-based genotyping of *Tmco6*-KO, HET and WT genomic DNA indicated absence of two essential coding exons, and RT-qPCR confirmed total loss of all coding *Tmco6* mRNA transcripts. Native murine Tmco6 protein could not be accurately detected by Western blotting and immunodetection using two commercial antibodies raised against different regions of the human orthologue.

Heterozygous matings (n = 250) revealed a non-Mendelian distribution of the KO genotype. Phenotypic characterisation of this mouse line revealed that body weights of KO animals are significantly lower than for HET and WT control animals, from 12 weeks of age for males and 28 weeks of age for females. KO mice also exhibit atypical neurobehaviors such as progressive hind-limb clasping, and epilepsy, characterised by a series of full-body myoclonic seizures in quick succession. KO 3 month-old mice exhibited impaired exercise tolerance by treadmill exhaustion tests, and both 3 month and 12 month old animals display a progressive impairment of motor coordination and balance at 3, 6 and 12 months of age by rotarod evaluation. Additionally, KO animals display bradykinesia at all ages, as determined by the pole test. CLAMS evaluation found a significant lack of exploratory and locomotor behaviours in KO animals at 3, 6 and 12 months of age. Curiously, KO animals also consumed more oxygen and expelled more carbon dioxide than age-matched controls, suggesting that they must undergo higher than normal metabolic activity in order to maintain basal survival.

Histopathological investigation of *Tmco6*-KO brains showed neurodegeneration, increased astrogliosis, accumulation of ubiquitin-rich inclusion bodies, recruitment of inflammatory microglial cells, and hypomyelination of axons in 3 month and 12 month age groups.

Cultured MEFs did not harbor any mitochondrial respiratory complex deficiencies, similarly to what was observed for human patient-derived fibroblasts (**Fig. 4.14**). Biochemical measurement of respiratory chain complex activities (CI-CV) in the brains of 3 month-old KO animals showed no appreciable differences compared to controls; however, CI-linked O_2

consumption was significantly reduced as measured by Oroboros using fresh brain tissue. Skeletal muscle and heart showed isolated CI deficiencies at 3 and 12 months of age, whereas the liver showed no biochemical abnormalities.

CI N-module subunits NDUFS1 and NDUFS6 were found significantly decreased in 12 month old *Tmco6*-KO hearts by SDS-PAGE and Western blot analyses. Furthermore, in-gel activity measurement revealed isolated CI deficiency by qualitative means. Echocardiography detected a statistically significant reduction in right ventricle systolic function in 12 month-old *Tmco6*-KO mice. These animals were also found to exhibit atrial flutter by electrocardiography. We observed increased respiration rates and slower heart rates in these animals compared with age-matched WT controls.

The study of this murine model was crucial in beginning to understand where and how TMCO6 functions in humans. *Tmco6*-KO mice developed epilepsy and presented with poor motor endurance and coordination, similarly to the human patient described in **Chapter 4**, suggesting both neurological and muscular impairment. Indeed, histopathological analyses indicated neurodegeneration throughout the brain, as well as an activated immune response. No CI deficiency, nor any other mitochondrial respiratory chain complex functional deficiencies, were observed in KO brains, which was at first surprising, but they did reveal statistically significant reduction in CI-dependent O_2 consumption. Perhaps lack of the Tmco6 protein is indirectly causing these phenotypes, or the protein has another functional role that does not concern its physical interaction with CI. Further experimentation is needed to investigate this. We also observed tissue-specific metabolic and molecular effects of Tmco6-ablation. Liver appeared metabolically functional in KO animals, whereas the heart displayed a range of molecular and biochemical abnormalities, including a significant, isolated CI deficiency. Given these results, we next endeavoured to assess whether it would be possible to rescue the CI deficiency observed in KO hearts by AAV-mediated functional complementation with the wildtype human gene, *TMCO6*. Administration of the patient mutant variant was performed concurrently to determine whether the patient mutant TMCO6 variant exacerbates or does not alter any of the observed cardiac or neuromotor phenotypes, potentially providing proof of pathogenicity.

Chapter 7

Investigating the Effects of AAV-Mediated Gene Delivery of Human Wildtype or Patient Mutant *TMCO6* to *Tmco6*-KO Mice

7.1 Introduction

As described in **Chapter 6**, we observed severe, isolated CI deficiency in hearts of young adult (3 months old) and aged (12 months old) *Tmco6*-knockout (KO) mice. We hypothesised that gene delivery of wildtype (WT) human *TMCO6* may functionally complement and thereby rescue the cardiac phenotype of this strain. In addition, delivery of the human patient mutant *TMCO6* genomic variant (c.271C>T, as described in **Chapter 4**) was also performed in order to confirm or deny the pathogenicity of this mutation. In particular, we sought to determine whether stable expression of the patient mutant variant (termed here as 'MUT') is capable of rescuing the CI deficiency in KO hearts, or whether it would instead exacerbate the observed neuromotor, cardiac and biochemical phenotypes, and/or lead to pathogenic phenotypes not originally observed in 3 month-old *Tmco6*-KO mice. Hence, young adult KO and WT animals underwent adeno-associated virus (AAV)-mediated systemic delivery of human WT or MUT *TMCO6* cDNA by tail-vein intravenous injections, using cardiotropic serotype AAV9 particles. When mice were nearing 3 months of age, we evaluated neuromotor behaviours by treadmill, rotarod, pole tests and CLAMS, and cardiac function and physiology by echocardiography and electrocardiography. Upon collection of tissues at 3 months of age, histological analyses were used to discern differences in the structural architecture and histopathological presentation of hearts in these animals. Cardiac CI activity was measured following stable expression of WT human *TMCO6* or the MUT variant in both WT and KO genotypic groups. This gene delivery method was not intended as a gene therapy approach, but rather as a means of confirming whether the patient *TMCO6* mutation is pathogenic *in vivo*. That said, the information gained could be potentially useful for future therapeutic applications.

7.2 Results

7.2.1 AAV-mediated Gene Delivery of Human WT and Patient MUT *TMCO6*

In the previous chapter, a *Tmco6*-knockout mouse model, B6N(Cg)-*Tmco6*$^{tm1.1(KOMP)Vlcg}$/J, was studied to understand where and how the uncharacterised protein, Tmco6, functions *in vivo*. *Tmco6*-KO mice displayed hindlimb clasping and a proportion of these mice developed myoclonic epilepsy from 6 months of age (**Fig. 6.4**). Both male and female KO animals were generally smaller in mass and size compared to age-matched controls (**Fig. 6.4**), and presented with poor motor endurance and coordination (**Fig. 6.5**). These findings were similar to those found for a human mitochondrial disease patient with a homozygous recessive mutation in *TMCO6* (c.271C>T), as described in detail in **Chapter 4**. Spectrophotometry and Oroboros techniques revealed tissue-specific mitochondrial enzymatic deficiencies in *Tmco6*-KO mice brains, skeletal muscles and hearts. Despite there being no specific CI enzymatic deficiency (**Fig. 6.18 A.**) in brains of KO mice at 3 months of age, electron flow through the electron transport chain was impaired at the CI point of entry (**Fig. 6.20**)**.** Hearts and skeletal muscle of 3 month and 12 month old KO males both showed isolated CI deficiency. The more severe CI deficiency was observed in KO hearts, with molecular abnormalities discovered as well, including a significant reduction in steady-state levels of N-module subunits NDUFS1 and NDUFS6 by SDS-PAGE and Western blot analysis. Echocardiography showed decreased right ventricular function and electrocardiography determined atrial flutter in KO mice hearts. No other abnormalities in cardiac function or physiology were detected at this time.

These results led us to question whether we could use the hearts of this *Tmco6*-KO model in order to 1) perform functional rescue experiments, and 2) to assess the pathogenicity of the human patient mutation (p.Arg91Cys) in causing mitochondrial disease. We devised an AAV9-mediated gene delivery strategy to administer either the WT cDNA sequence of human *TMCO6* (CCDS4233.2, CCDS Database), or its patient mutant c.271C>T counterpart (termed in this work as 'MUT', for 'mutant'), both labelled with C-terminal HA tags, to KO or WT young adult mice. It has been shown that in animal models, AAV-mediated viral genomes persist, in an episomal state, for essentially the entire life-span of the lab animal, most reliably in post-mitotic or slowly-dividing tissues (Gammage *et al.,* 2016). A titre of 4.5 x 10^{11} AAV particles carrying either WT, AAV2-HSA-TMCO6-cDNA-HA (**Fig. 2.10**), or MUT, AAV2-HSA-TMCO6_MUT-cDNA-HA, cardiotropic AAV9 vectors were administered by tail-vein intravenous injection into 5 – 8 week old, weaned KO and WT mice (**Fig. 7.1 A.**). This process led to the creation of 4 distinct transgenic groups: *Tmco6*$^{+/+\ (AAV\ WT)}$, *Tmco6*$^{+/+\ (AAV\ MUT)}$, *Tmco6*$^{-/-\ (AAV\ WT)}$, and *Tmco6*$^{-/-\ (AAV\ MUT)}$. The *Tmco6*$^{+/+\ (AAV\ WT)}$ group acted as an experimental control.

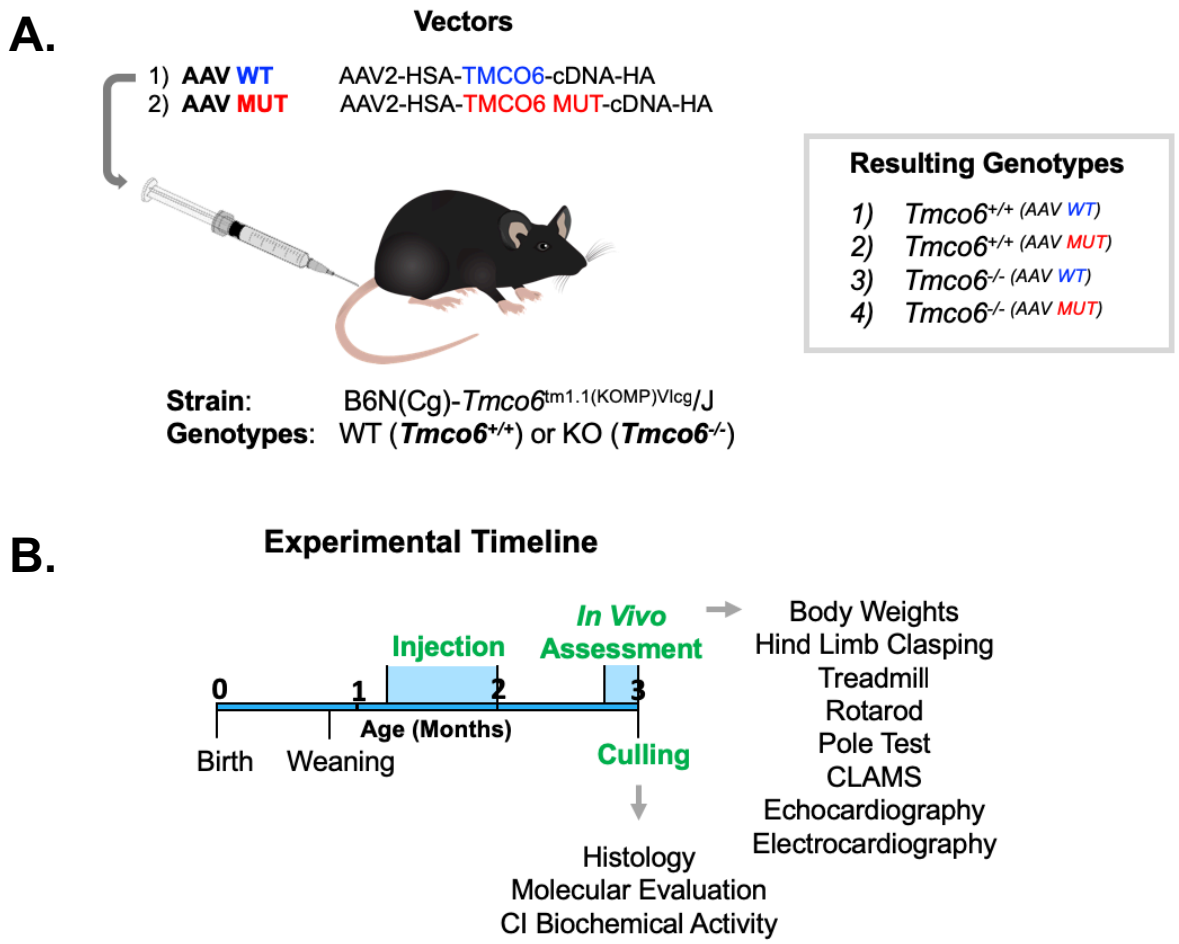

Figure 7.1. Gene delivery of human WT or patient MUT *TMCO6* cDNA to a *Tmco6*-knockout transgenic mouse line, and experimental timeline.

(**A.**) Transgenic *Tmco6*-knockout (KO, *Tmco6*$^{-/-}$) mice (B6N(Cg)-*Tmco6*$^{tm1.1(KOMP)Vlcg}$/J, The Jackson Laboratory) and counterpart wildtype (WT, *Tmco6*$^{+/+}$) mice of this strain were administered a titre of 4.5 x 10^{11} AAV particles carrying either AAV2-HSA-TMCO6-cDNA-HA or AAV2-HSA-TMCO6_MUT-cDNA-HA AAV9 vectors (derived from the AAV2 serotype, hence the vector name) by tail-vein intravenous injections at 5-8 weeks of age, as shown. Injections were performed by Dr. Carlo Viscomi (Senior Investigator Scientist, Mitochondrial Medicine Laboratory, MRC MBU, University of Cambridge, UK). The resulting four genotypes of this process are included in the grey box. (**B.**) Experimental timeline for procedures (highlighted in green), including injection of serotype AAV9 vectors at 5-8 weeks of age, *in vivo* assessment as listed, and culling at 3 months of age. At this time, various tissues were collected as described in **section 2.5.9** and subjected to the methods labelled beneath, as detailed in-text.

7.2.2 Physical and Neuromotor Behaviours of AAV9-Transduced Mice

In vivo assessment of the four transgenic groups was performed using the methods listed in **Fig. 7.1 B**. Firstly, body weights were recorded weekly from the day of injection until three months of age separately for males (*Tmco6*$^{+/+\ (AAV\ WT)}$, *n* = 4, *Tmco6*$^{+/+\ (AAV\ MUT)}$, *n* = 4, *Tmco6*$^{-/-\ (AAV\ WT)}$, *n* = 3, and *Tmco6*$^{-/-\ (AAV\ MUT)}$, *n* = 3) (**Fig. 7.2 A**.) and females (*Tmco6*$^{+/+\ (AAV\ WT)}$, *n* = 4, *Tmco6*$^{+/+\ (AAV\ MUT)}$, *n* = 4, *Tmco6*$^{-/-\ (AAV\ WT)}$, *n* = 4, and *Tmco6*$^{-/-\ (AAV\ MUT)}$, *n* = 5) (**Fig. 7.2 B**.). Statistically significant differences were shown by two-way ANOVA with Sidak's multiple comparisons test in males at 4 weeks post-injection, and for females from 2 weeks post-injection for the *Tmco6*$^{-/-\ (AAV\ MUT)}$ mice compared to the experimental control group, Tmco6$^{+/+\ (AAV\ WT)}$, for both sexes. *Tmco6*$^{-/-\ (AAV\ MUT)}$ females showed a complete "plateau" in weight gain after a month, whereas counterpart male mice started to gain weight from one week after injection. Interestingly, wildtype male and female Tmco6$^{+/+}$ animals that were injected with the mutant *TMCO6* vector (*Tmco6*$^{+/+\ (AAV\ MUT)}$) also showed a plateau in weight gain for two or three weeks following injection, unlike the Tmco6$^{+/+\ (AAV\ WT)}$ controls. Conversely, knockout *Tmco6*$^{-/-}$ animals expressing the wildtype *TMCO6* cDNA sequence (*Tmco6*$^{-/-\ (AAV\ WT)}$) showed consistent weight gains, considered to be non-significant compared to the control group for both sexes. This indicates that whilst stable expression of WT *TMCO6* led to normal weight gain in *Tmco6*$^{+/+}$ and *Tmco6*$^{-/-}$ animals, MUT *TMCO6* did not.

Next, the atypical neurobehavior of hindlimb clasping was assessed (see **section 2.5.6**), and was found only in Tmco6$^{-/-}$ strains, as before, despite expression of WT or MUT versions of *TMCO6* (**Fig 7.3**). The phenotype was less severe for *Tmco6*$^{-/-\ (AAV\ WT)}$ animals, with no obvious twisting of the body and intervals of normal extended limb posture, as opposed to *Tmco6*$^{-/-\ (AAV\ MUT)}$ mice, who had pronounced hindlimb clasping, often with a twisted body, and no extension of hindlimbs away from the abdomen at any time during the 10 s test duration. *Tmco6*$^{+/+\ (AAV\ MUT)}$ animals did not show hindlimb clasping per se, but would kick their hindlimbs quickly in bursts, a phenotype not observed in control *Tmco6*$^{+/+\ (AAV\ WT)}$ animals. In summary, this test showed no rescue in the hindlimb clasping phenotype of knockout animals as a result of WT *TMCO6* overexpression. However, there was relative worsening of this neurobehavior in MUT *TMCO6*-expressing animals (*Tmco6*$^{+/+\ (AAV\ MUT)}$ and *Tmco6*$^{-/-\ (AAV\ MUT)}$) compared to WT *TMCO6*-expressing groups (*Tmco6*$^{+/+\ (AAV\ WT)}$ and *Tmco6*$^{-/-\ (AAV\ WT)}$).

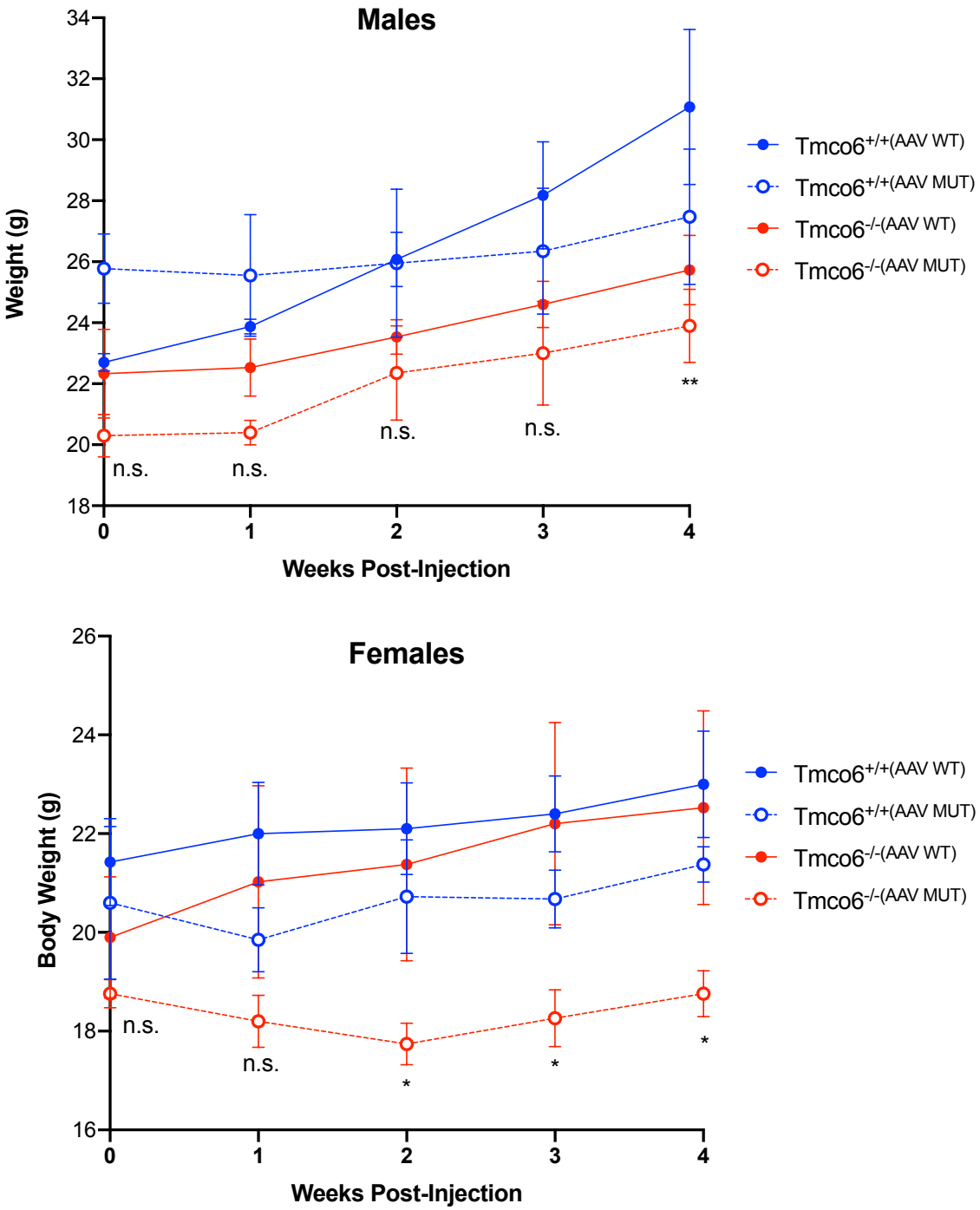

Figure 7.2. Body weights of *Tmco6*$^{+/+}$ and *Tmco6*$^{-/-}$ mice stably expressing WT or MUT *TMCO6* over 1 month following AAV9-mediated gene delivery by tail-vein injection.

Body weight as a function of age was measured for (**A.**) male (Tmco6$^{+/+\ (AAV\ WT)}$, n = 4, Tmco6$^{+/+\ (AAV\ MUT)}$, n = 4, Tmco6$^{-/-\ (AAV\ WT)}$, n = 3, and Tmco6$^{-/-\ (AAV\ MUT)}$, n = 3) and female (Tmco6$^{+/+\ (AAV\ WT)}$, n = 4, Tmco6$^{+/+\ (AAV\ MUT)}$, n = 4, Tmco6$^{-/-\ (AAV\ WT)}$, n = 4, and Tmco6$^{-/-\ (AAV\ MUT)}$, n = 5) mice over 1 month on a weekly basis from the day of AAV9 injection. Data are presented as mean ± SEM. Statistical analysis: n.s. = non-significant, * $p < 0.05$, ** $p < 0.01$, calculated by two-way ANOVA with Sidak's multiple comparisons post hoc test.

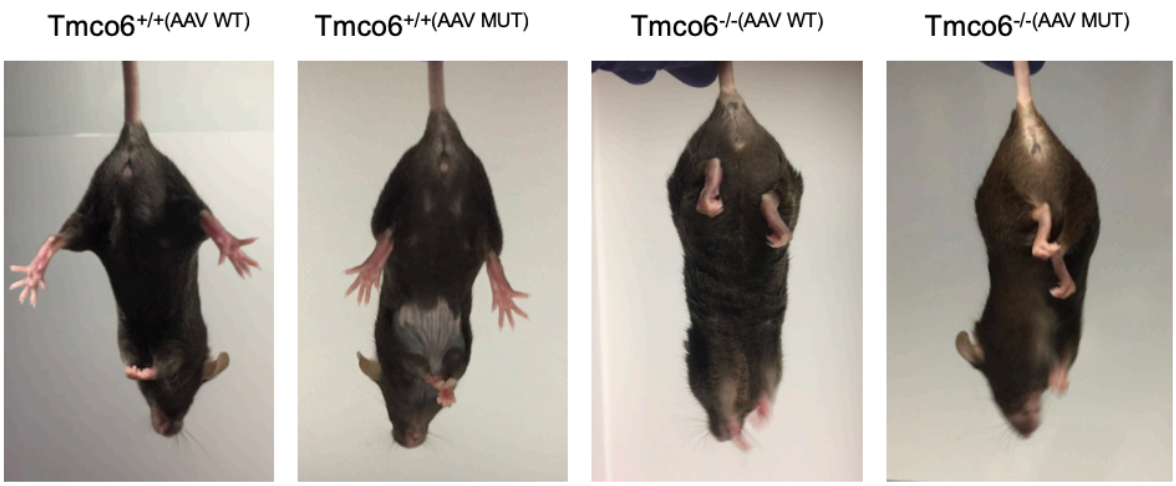

Figure 7.3. Hindlimb clasping of *Tmco6*$^{+/+}$ and *Tmco6*$^{-/-}$ mice stably expressing WT or MUT *TMCO6* at 3 months of age.

Hindlimb clasping was assessed for *Tmco6*$^{+/+\ (AAV\ WT)}$ (*n* = 7), *Tmco6*$^{+/+\ (AAV\ MUT)}$ (*n* = 7), *Tmco6*$^{-/-\ (AAV\ WT)}$ (*n* = 8), and *Tmco6*$^{-/-\ (AAV\ MUT)}$ (*n* = 7) mice; one representative animal for each genotypic group is shown.

No epilepsy was observed in any of the mice for *Tmco6*$^{+/+\ (AAV\ WT)}$ (*n* = 7), *Tmco6*$^{+/+\ (AAV\ MUT)}$ (*n* = 7), *Tmco6*$^{-/-\ (AAV\ WT)}$ (*n* = 8), or *Tmco6*$^{-/-\ (AAV\ MUT)}$ (*n* = 7) groups. This was expected given that *Tmco6*$^{-/-}$ (also termed KO) animals did not display onset of epilepsy until 6 months of age at the earliest (**Fig. 6.4 E.**). Perhaps observing these mice for longer would reveal changes in the proportion of animals that developed epilepsy, or perhaps the average age of onset; however, it was not possible to deduce this information from the 3 month animals studied here.

We next sought to assess the motor capabilities and neuromuscular coordination of *Tmco6*-knockout or wildtype mice stably expressing human WT or patient MUT *TMCO6*. Maximal exercise tolerance and motor endurance was evaluated by exhaustion trials using an accelerating treadmill (see **section 2.5.4**). As shown in **Fig. 7.4 A.**, the *Tmco6*$^{-/-\ (AAV\ WT)}$ group ran significantly further than the *Tmco6*$^{-/-\ (AAV\ MUT)}$ group (*n* = 7) for both, in line with the *Tmco6*$^{+/+\ (AAV\ WT)}$ control group. This indicates that the MUT human TMCO6 protein variant is not capable of recovering the exercise intolerance we had observed in these animals (**Fig. 6.5 A.**), perhaps owing to impaired protein function, whereas the WT TMCO6 protein can. Indeed, there is a statistically significant difference between the distance run for the experimental control group *Tmco6*$^{+/+\ (AAV\ WT)}$ (*n* = 7) and the *Tmco6*-knockout MUT group, *Tmco6*$^{-/-\ (AAV\ MUT)}$, in line with what was observed for *Tmco6*$^{-/-}$ and *Tmco6*$^{+/+}$ mice (**Fig. 6.5 A.**). Although there was not a significant

difference between the *Tmco6*$^{+/+\ (AAV\ WT)}$ and *Tmco6*$^{+/+\ (AAV\ MUT)}$ groups, there was a downwards trend for animals expressing the MUT protein variant (NP_001287909.1:p.Arg91Cys).

Next, rotarod tests were performed for the four genotypic groups (**Fig. 7.4 B.**) in order to assess neuromuscular coordination and balance; a statistically significant difference was observed only between *Tmco6*$^{-/-\ (AAV\ MUT)}$ mice and the experimental control group, *Tmco6*$^{+/+\ (AAV\ WT)}$ (*n* = 7 for both), with the former losing grip and falling within approximately half of the time of the latter. This observation was in line with the difference that had been observed previously between *Tmco6*$^{-/-}$ and *Tmco6*$^{+/+}$ mice (**Fig. 6.5 C.**), and suggests that MUT *TMCO6* expression does not exacerbate or alter the abnormal neuromotor phenotype observed in 3 month old Tmco6$^{-/-}$ mice. Also, the WT-complemented *Tmco6*$^{-/-\ (AAV\ WT)}$ group (*n* = 8) displayed only a slight increase in the latency to fall compared to *Tmco6*$^{-/-\ (AAV\ MUT)}$ animals, and the mean value was not similar to that of either *Tmco6*$^{+/+\ (AAV\ WT)}$ or *Tmco6*$^{+/+\ (AAV\ MUT)}$ (n = 7) groups. This suggests that WT *TMCO6* expression does not rescue neuromuscular coordination and balance to a significant extent in *Tmco6*$^{-/-}$ animals.

The pole test was then used to assess proprioception and neuromotor coordination. As shown in **Fig. 7.4 C.**, *Tmco6*$^{+/+\ (AAV\ MUT)}$ and *Tmco6*$^{-/-\ (AAV\ MUT)}$ mice showed increases in the time taken to turn 180º and descend a 50 cm pole compared to age-matched control *Tmco6*$^{+/+\ (AAV\ WT)}$ and *Tmco6*$^{-/-\ (AAV\ WT)}$ groups, although no statistically significant differences were identified. The time taken to descend the pole for *Tmco6*$^{-/-\ (AAV\ MUT)}$ mice mirrors that of 3 month old Tmco6$^{-/-}$ male and female mice (**Fig. 6.6**). Qualitatively, *Tmco6*$^{-/-\ (AAV\ MUT)}$ mice had difficulty engaging all four limbs to descend the pole, and instead wrapped their hindlimbs around the pole and slid, or descended by only independently moving the forelimbs. *Tmco6*$^{-/-\ (AAV\ WT)}$ mice displayed instead controlled descents, engaging all four limbs the majority of the time. *Tmco6*$^{+/+\ (AAV\ MUT)}$ mice also showed a small increase in time taken to descend the pole compared to the experimental control group *Tmco6*$^{+/+\ (AAV\ WT)}$, suggesting some impaired muscle control for MUT *TMCO6*-expressing animals.

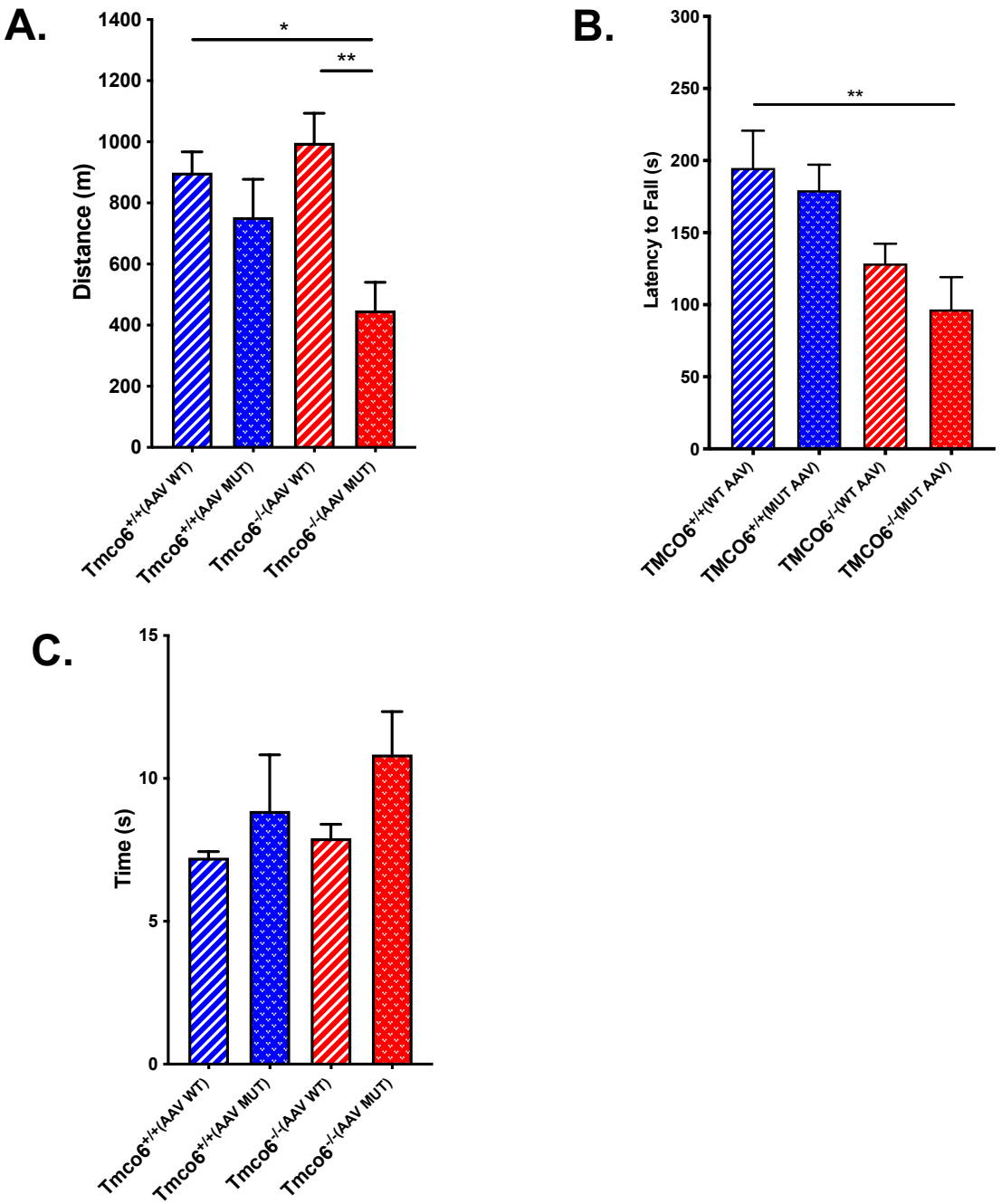

Fig. 7.4. Complementation of WT *TMCO6* in *Tmco6*$^{-/-}$ mice rescues exercise capability but does not completely rescue neuromotor coordination and balance.

(**A.**) Motor performance and capability was assessed for *Tmco6*$^{+/+\ (AAV\ WT)}$ (n = 7), *Tmco6*$^{+/+\ (AAV\ MUT)}$ (n = 7), *Tmco6*$^{-/-\ (AAV\ WT)}$ (n = 8), and *Tmco6*$^{-/-\ (AAV\ MUT)}$ (n = 7) mice at 3 months of age by treadmill (as per **section 2.5.4**). Distance reached at exhaustion was recorded per animal. (**B.**) Latency to fall (s) was recorded in three separate trials for the four genotypic groups mentioned in **A.**, with values averaged per animal. (**C.**) The pole test was performed as per **section 2.5.7** to assess proprioception and bradykinesia. The time (s) taken to turn 180^{o} and descend a 50 cm pole was recorded for 3 replicate trials per animal and these values averaged. Data represent mean ± SEM. Statistical analysis: * $p < 0.05$, ** $p < 0.01$, calculated by one-way ANOVA with Tukey's multiple comparisons *post hoc* test applied in all cases.

7.2.3 MUT *TMCO6* Expression Causes Impaired Locomotor Behaviours *In Vivo*

Given that *Tmco6*$^{-/-\ (AAV\ MUT)}$ mice showed impaired exercise tolerance compared to *Tmco6*$^{-/-\ (AAV\ WT)}$ mice and the experimental control group, *Tmco6*$^{+/+\ (AAV\ WT)}$ (**section 7.2.2**), we next sought to assess if spontaneous motility, including locomotor and exploratory behaviours, was impacted as a result of MUT *TMCO6* expression. For this, CLAMS monitoring was performed for non-transduced *Tmco6*$^{+/+}$ (n = 3) and *Tmco6*$^{-/-}$ (n = 4) mice, and the four transduced *Tmco6*$^{+/+\ (AAV\ WT)}$ (n = 3), *Tmco6*$^{+/+\ (AAV\ MUT)}$ (n = 3), *Tmco6*$^{-/-\ (AAV\ WT)}$ (n = 4), and *Tmco6*$^{-/-\ (AAV\ MUT)}$ (n = 4) groups. Despite no statistically significant differences determined for total (**Fig. 7.5 A.**), and ambulatory (**Fig. 7.5 B.**) movements, *Tmco6*$^{-/-\ (AAV\ WT)}$ mice displayed values closer to *Tmco6*$^{+/+}$ than to *Tmco6*$^{-/-}$ animals. As shown previously for 3 month old *Tmco6*$^{-+/+}$ and *Tmco6*$^{--/-}$ mice, nocturnal rearing movements (**Fig. 7.5 C.**) were found to be significantly reduced in *Tmco6*$^{-/-\ (AAV\ MUT)}$ animals, to the same extent as *Tmco6*$^{-/-}$ animals. Rearing movements require muscle tone and maintained posture for mice to sit up and visually explore their environment. *Tmco6*$^{-/-\ (AAV\ WT)}$ mice displayed more of these rearing movements than did the *Tmco6*$^{-/-\ (AAV\ MUT)}$ group, suggesting improvement of muscle tone and posture in the former. In terms of ambulatory movement (**Fig. 7.5 B.**), *Tmco6*$^{-/-\ (AAV\ WT)}$ mice behaved as both *Tmco6*$^{+/+}$ non-transduced and *Tmco6*$^{+/+\ (AAV\ WT)}$ experimental control groups. Whereas, *Tmco6*$^{-/-\ (AAV\ MUT)}$ mice traversed the cage less during both day and night cycles than any of the other genotypic groups, including *Tmco6*$^{-/-}$ mice. The amount of total movements (**Fig. 7.5 A.**) of the different groups was variable, but notably, *Tmco6*$^{-/-\ (AAV\ WT)}$ mice moved more than did counterpart *Tmco6*$^{-/-}$ non-transduced and *Tmco6*$^{-/-\ (AAV\ MUT)}$ mice. These results indicate that WT *TMCO6* expression improves spontaneous locomotor and exploratory behaviours of *Tmco6*-knockout animals, particularly rearing movements, and MUT *TMCO6* expression reproducible did not. No similar trends were observed for the transduced *Tmco6*$^{+/+}$ groups *Tmco6*$^{+/+\ (AAV\ WT)}$ and *Tmco6*$^{+/+\ (AAV\ MUT)}$.

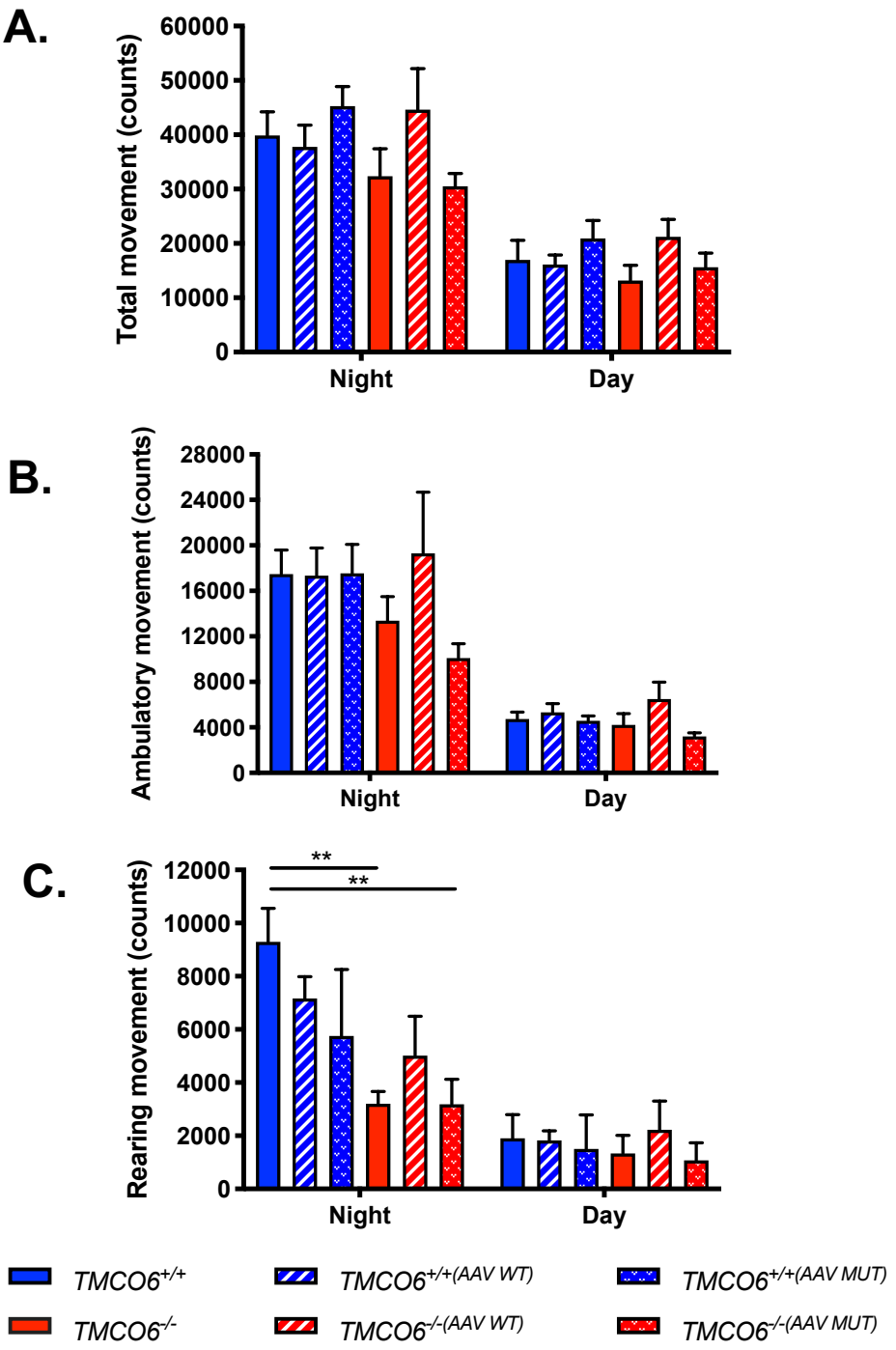

Fig. 7.5. Complementation of WT *TMCO6* in *Tmco6*$^{-/-}$ mice improves locomotor and exploratory behaviours.

(**A.**) Total, (**B.**) ambulatory and **C.**) rearing movements of *Tmco6*$^{+/+}$ (n = 3), *Tmco6*$^{+/+\ (AAV\ WT)}$ (n = 3), *Tmco6*$^{+/+\ (AAV\ MUT)}$ (n = 3), *Tmco6*$^{-/-}$ (n = 4), *Tmco6*$^{-/-\ (AAV\ WT)}$ (n = 4), and *Tmco6*$^{-/-\ (AAV\ MUT)}$ (n = 4) mice at 3 months of age was recorded by CLAMS for 2 night and 1 day cycles (see **section 2.5.3**). Data are presented as mean ± SEM. Statistical analysis: ** p < 0.01, calculated by two-way ANOVA with Sidak's multiple comparisons *post hoc* test applied.

7.2.4 *In Vivo* Metabolic Evaluation of AAV-Transduced Mice via CLAMS

The CLAMS was additionally used for metabolic evaluation to measure O_2 consumption (**Fig. 7.6 A.**) and CO_2 production (**Fig. 7.6 B.**), which in turn were used to calculate heat production (**Fig. 7.6 C.**), and the respiratory exchange ratio (RER) (**Fig. 7.6 D.**) for non-transduced *Tmco6*$^{+/+}$ (*n* = 3) and *Tmco6*$^{-/-}$ (*n* = 4) mice, and the four transduced *Tmco6*$^{+/+\ (AAV\ WT)}$ (*n* = 3), *Tmco6*$^{+/+\ (AAV\ MUT)}$ (*n* = 3), *Tmco6*$^{-/-\ (AAV\ WT)}$ (*n* = 4), and *Tmco6*$^{-/-\ (AAV\ MUT)}$ (*n* = 4) mouse lines. Expression of either WT or MUT *TMCO6* in *Tmco6*$^{+/+}$ mice led to non-significant changes in O_2 consumption (**Fig. 7.6 A.**) and CO_2 production (**Fig. 7.6 B.**) compared to untreated *Tmco6*$^{+/+}$ mice. *Tmco6*$^{-/-\ (AAV\ MUT)}$ mice still consumed more oxygen than *Tmco6*$^{+/+}$, *Tmco6*$^{+/+\ (AAV\ WT)}$ and *Tmco6*$^{+/+\ (AAV\ MUT)}$ groups. In the case of *Tmco6*$^{-/-}$ mice, expression of WT or MUT *TMCO6* did not change O_2 consumption. However, both *Tmco6*$^{-/-\ (AAV\ WT)}$ and *Tmco6*$^{-/-\ (AAV\ MUT)}$ mice showed significant reductions in CO_2 production compared to counterpart *Tmco6*$^{-/-}$ mice.

RER values indicate which substrate is preferentially metabolised to produce energy in an aerobically respiring organism. **Fig. 7.6 C.** shows a significant reduction in RER to approximately 0.7 for *Tmco6*$^{-/-\ (AAV\ WT)}$ and *Tmco6*$^{-/-\ (AAV\ MUT)}$ mouse lines, indicating that almost all the energy in these animals is being produced from fat as a substrate, and not through the catabolism of sugars. This result suggests that both WT and MUT TMCO6 protein variants prompt a change in metabolic state in these mice in which fats are preferentially used over carbohydrates, perhaps to avoid mitochondrial OXPHOS. This result was true for both night and day cycles revealing that this is a constant feature of these animals.

Lastly, heat production had not been found to be significantly altered between *Tmco6*$^{+/+}$ and *Tmco6*$^{-/-}$ groups previously (**Fig. 6.8**). This result was shown again (**Fig. 7.6 D.**); however, both WT and MUT *TMCO6* expression in either *Tmco6*$^{+/+}$ or *Tmco6*$^{-/-}$ mice produced statistically significant reductions in overall heat production, indicating impaired thermogenesis in these animals. It appears that AAV-mediated gene delivery of either WT or MUT human *TMCO6* leads to a reduction in overall heat production, suggesting less respiration in these animals. We cannot discount that this finding is a by-product of the AAV gene delivery approach used, since all transduced mouse lines show reductions in heat production compared to non-transduced *Tmco6*$^{+/+}$ and *Tmco6*$^{-/-}$ mice.

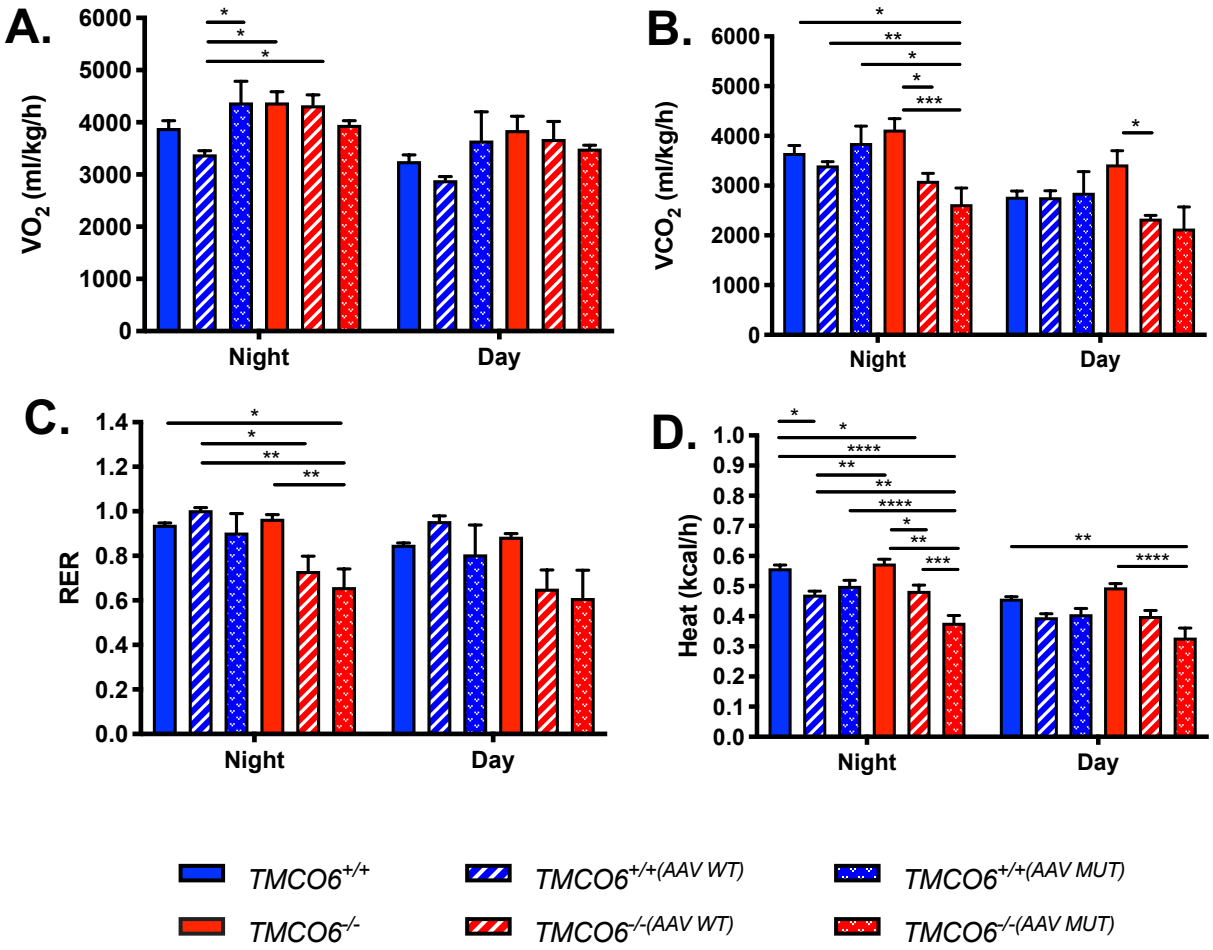

Fig. 7.6. Metabolic monitoring via CLAMS.

Non-transduced *Tmco6*$^{+/+}$ (*n* = 3) and *Tmco6*$^{-/-}$ (*n* = 4) mice and transduced *Tmco6*$^{+/+\ (AAV\ WT)}$ (*n* = 3), *Tmco6*$^{+/+\ (AAV\ MUT)}$ (*n* = 3), *Tmco6*$^{-/-\ (AAV\ WT)}$ (*n* = 4), and *Tmco6*$^{-/-\ (AAV\ MUT)}$ (*n* = 4) mouse lines were monitored at 3 months of age for various metabolic parameters for 2 night and 1 day 12 h cycles via CLAMS, as described in **section 2.5.3**. The sum of the volumes of (**A.**) oxygen consumed (ml/kg/hr) and (**B.**) volume of carbon dioxide produced (ml/kg/hr) was recorded. These were used to calculate the (**C.**) respiratory exchange ratio (RER) and (**D.**) heat production (Kcal/hr) per animal, for day and night cycles in each case. Data are presented as mean ± SEM. Statistical analysis: * $p < 0.05$, ** $p < 0.01$, *** $p < 0.005$, **** $p < 0.001$, calculated by two-way ANOVA with Sidak's multiple comparisons *post hoc* test applied.

7.2.5 Echocardiography and Electrocardiography of AAV9-Transduced Mice

Cardiovascular function and physiology were measured by echocardiography and electrocardiography using the Vevo 770® High Resolution Imaging System (VisualSonics, Inc., Toronto, Canada) for the *Tmco6*$^{+/+\ (AAV\ WT)}$ (*n* = 5), *Tmco6*$^{+/+\ (AAV\ MUT)}$ (*n* = 3), *Tmco6*$^{-/-\ (AAV\ WT)}$ (*n* = 7), and *Tmco6*$^{-/-\ (AAV\ MUT)}$ (*n* = 7) mouse lines, with all measurements performed by Stephen Moore at the Phenomics Laboratory (West Forvie Site, Cambridge, UK). Our aim was to assess whether WT *TMCO6* expression could improve or entirely rescue the right ventricular systolic functional defect observed in *Tmco6*$^{-/-}$ mice (**Table 6.4**), and secondly, whether MUT TMCO6 expression would rescue or exacerbate this defect, or potentially cause others. Mice were sedated with isoflurane gas and systematically imaged in parasternal short axis (**Fig 2.9 A.**), long axis (**Fig 2.9 B.)** and apical four-chamber (**Fig 2.9 C.**) views in the pulsed-wave (PW) doppler or motion (M) modes, as previously described (Gao *et al.*, 2011). Again, these acquired images were used to calculate aortic ejection time (AET), left ventricle (LV) myocardial performance index (MPI), mitral valve (MV) atrial (A) and early (E) peak wave flows (mm/s), MV E/A peak ratio, right ventricular outflow tract mean velocity time integral (RVOT VTI) (mm/s), cardiac output (CO) (ml/min), ejection fraction (EF) (%), fraction shortening (FS) (%), HR (bpm), stroke volume (SV) (µl), and volumes expelled in diastole and systole (V;d, V;s) (µl) with the associated Vevo LAB and Auto LV Analysis software packages (VisualSonics).

No obvious morphological abnormalities were observed for any of the *Tmco6*$^{+/+\ (AAV\ WT)}$, *Tmco6*$^{+/+\ (AAV\ MUT)}$, *Tmco6*$^{-/-\ (AAV\ WT)}$, or *Tmco6*$^{-/-\ (AAV\ MUT)}$ mouse lines by echocardiography. As shown in **Table 7.1,** the only statistically significant difference in echocardiographic parameters between *Tmco6*$^{-/-\ (AAV\ MUT)}$ mice and the experimental control, *Tmco6*$^{+/+\ (AAV\ WT)}$, was RVOT VTI. Notably, the difference between the WT *TMCO6*-complemented knockout line, *Tmco6*$^{-/-\ (AAV\ WT)}$, and *Tmco6*$^{-/-\ (AAV\ MUT)}$ mouse lines was considered to be highly significant by two-way ANOVA with Sidak's multiple comparisons test. Recovery of right heart systolic function was found as a result of WT *TMCO6* expression in adult *Tmco6*$^{-/-}$ animals, as shown by the rescued RVOT VTI value. However, expression of the human patient mutant variant did not result in any phenotypic rescue for *Tmco6*$^{-/-\ (AAV\ MUT)}$ mice. Despite no significant differences determined by statistical analyses for CO, EF, SV, FS, V;d and V;s for any of the mouse lines, these values were all decreased to similar extents for both the *Tmco6*$^{-/-\ (AAV\ MUT)}$ and *Tmco6*$^{-/-\ (AAV\ WT)}$ groups, suggesting that cardiac function may still be impaired to some extent in WT *TMCO6*-expressing *Tmco6*$^{-/-}$ animals. Heart rates of *Tmco6*$^{-/-\ (AAV\ MUT)}$ and *Tmco6*$^{-/-\ (AAV\ WT)}$ groups were similarly lower compared to the age-matched *Tmco6*$^{+/+\ (AAV\ WT)}$ and *Tmco6*$^{+/+\ (AAV\ MUT)}$ control groups. We next sought to assess this difference in HR further by electrocardiographic analyses.

Table 7.1. Echocardiography Results for AAV9-Transduced Mice Reveal Recovery of RVOT VTI by WT *TMCO6* Expression

Tmco6$^{+/+\ (AAV\ WT)}$, *n* = 5, *Tmco6*$^{+/+\ (AAV\ MUT)}$, *n* = 3, *Tmco6*$^{-/-\ (AAV\ WT)}$, *n* = 7, and *Tmco6*$^{-/-\ (AAV\ MUT)}$, *n* = 7. Data are presented as mean ± SEM. Statistical analysis: two-way ANOVA with Sidak's multiple comparisons *post hoc* test applied. n.s. = non-significant.

PARAMETER	UNIT	*TMCO6*$^{+/+}$ *(AAV WT)*	*TMCO6*$^{+/+}$ *(AAV MUT)*	*TMCO6*$^{-/-}$ *(AAV WT)*	*TMCO6*$^{-/-}$ *(AAV MUT)*	SIGNIFICANT?
AET	ms	46.5 ± 5.0	53.0 ± 2.1	47.1 ± 2.3	50.8 ± 3.6	n.s.
LV MPI	-	0.87 ± 0.17	0.78 ± 0.07	0.77 ± 0.05	0.73 ± 0.08	n.s.
M/V E/A	-	1.64 ± 0.08	1.67 ± 0.06	1.65 ± 0.08	1.80 ± 0.11	n.s.
RVOT VTI	mm/s	-518.8 ± 21.7 ****	-436.2 ± 2.8	-461.4 ± 39.6 ****	-358.6 ± 43.5 **** ****	****p = <0.001 ****p = <0.001
CO	ml/min	22.1 ± 1.3	21.7 ± 2.0	17.6 ± 1.3	16.3 ± 1.0	n.s.
EF	%	61.7 ± 2.7	63.3 ± 2.9	62.1 ± 3.2	59.4 ± 2.5	n.s.
FS	%	33.1 ± 1.9	34.1 ± 2.0	33.3 ± 2.3	31.2 ± 1.8	n.s.
HR	bpm	431 ± 19.3	421.8 ± 29.0	415.1 ± 23.8	415.2 ± 22.1	n.s.
SV	µl	52.5 ± 3.9	51.4 ± 2.5	42.4 ± 2.2	39.7 ± 2.3	n.s.
V;D	µl	85.3 ± 6.3	81.8 ± 7.0	68.8 ± 3.4	67.1 ± 3.9	n.s.
V;S	µl	32.8 ± 3.9	30.4 ± 5.0	26.4 ± 3.0	27.4 ± 2.6	n.s.

Representative ECG traces for *Tmco6*$^{+/+\ (AAV\ WT)}$ (*n* = 5) (**Fig. 7.7 A.**), *Tmco6*$^{+/+\ (AAV\ MUT)}$ (*n* = 3) (**Fig. 7.7 B.**), *Tmco6*$^{-/-\ (AAV\ WT)}$ (*n* = 7) (**Fig. 7.7 C.**), and *Tmco6*$^{-/-\ (AAV\ MUT)}$ (*n* = 7) (**Fig. 7.7 D.**) mouse lines show signs of perturbed electrophysiology for *Tmco6*$^{+/+\ (AAV\ MUT)}$, *Tmco6*$^{-/-\ (AAV\ WT)}$ and *Tmco6*$^{-/-\ (AAV\ MUT)}$ hearts. *Tmco6*$^{-/-\ (AAV\ MUT)}$ animals were found to display 4:1 atrial flutter (**Fig 7.7 D.**) in which instead of a single P-wave, denoting atrial depolarisation at the beginning of a heartbeat, there were instead four separate waves resulting from re-entrant circuits around the tricuspid valve. This was observed previously, along with 3:1 atrial flutter, in the non-transduced *Tmco6*$^{-/-}$ mouse line (**Fig. 6.31 A.**). The mice of the *Tmco6*$^{+/+\ (AAV\ WT)}$ experimental control group showed comparable waveforms to the non-transduced *Tmco6*$^{+/+}$ mouse line (**Fig. 6.31 A.**), with no obvious electrophysiological abnormalities. However, the *Tmco6*$^{+/+\ (AAV\ MUT)}$ and *Tmco6*$^{-/-\ (AAV\ WT)}$ genotypic groups both presented with J waves (also termed Osborn waves), which are abnormal positive deflections occurring at the junction between the QRS

complex and the ST segment (highlighted by the blue arrowheads in **Fig. 7.7 B** and **C.**). J waves are found in ventricular fibrillation, denoting early repolarisation of the ventricles, brain injury, hypothermia, myocardial infarction, and several types of cardiac myopathies (Thiene *et al.*, 1988). The J waves of *Tmco6*$^{+/+\ (AAV\ MUT)}$ mice are more prominent than those shown by the *Tmco6*$^{-/-\ (AAV\ WT)}$ group. Additionally, these two groups show less overall QRS peak amplitude than the *Tmco6*$^{+/+\ (AAV\ WT)}$ experimental control mice, suggesting weaker pumping of the hearts of these animals.

In summary, *Tmco6*$^{-/-\ (AAV\ WT)}$ mice showed a rescue of the atrial flutter but also revealed lower amplitudes, denoting weaker pumping, and clear presence of J waves, which are hallmarks of ventricular dysfunction. *Tmco6*$^{+/+\ (AAV\ MUT)}$ mice also displayed J-waves, with greater severity than shown in *Tmco6*$^{-/-\ (AAV\ WT)}$ mice. It is not possible to discern from these ECG traces alone what is the underlying cause of this altered electrophysiology, although ventricular dysfunction is a potential cause. Together these data strongly suggest that perturbations to the steady-state levels of MUT or WT TMCO6 can have adverse effects on cardiac function, including both atrial and ventricular functions.

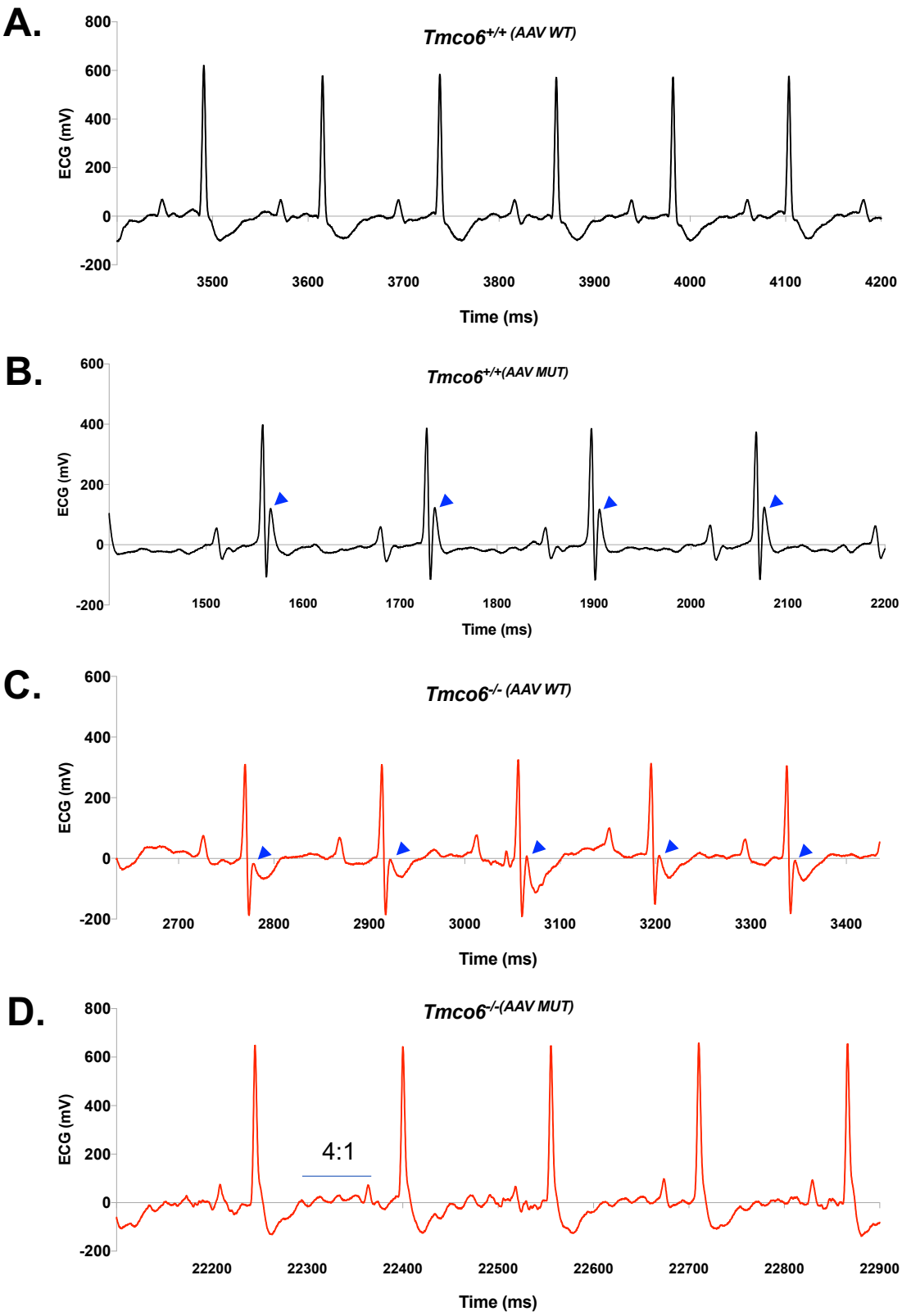

Fig. 7.7. ECG reveals pathological electrophysiology in AAV9-transduced mice.

Cardiovascular function was evaluated by electrocardiography with representative ECG traces over 800 ms are shown for 3 month old (**A.**) *Tmco6*$^{+/+\ (AAV\ WT)}$ (*n* = 5), (**B.**) *Tmco6*$^{+/+\ (AAV\ MUT)}$ (*n* = 3), (**C.**) *Tmco6*$^{-/-\ (AAV\ WT)}$ (*n* = 7), and (**D.**) *Tmco6*$^{-/-\ (AAV\ MUT)}$ (*n* = 7) mouse lines. For an overview of the components of a murine ECG waveform, see **Fig. 2.9 D.** Blue arrowheads = J waves.

Next, respiration rate was assessed for *Tmco6*$^{+/+\ (AAV\ WT)}$ (*n* = 5) (**Fig. 7.8 A.**), *Tmco6*$^{+/+\ (AAV\ MUT)}$ (*n* = 3) (**Fig. 7.8 B.**), *Tmco6*$^{-/-\ (AAV\ WT)}$ (*n* = 7) (**Fig. 7.8 C.**), and *Tmco6*$^{-/-\ (AAV\ MUT)}$ (*n* = 7) (**Fig. 7.8 D.**) mouse lines. We had observed a statistically significant three-fold increase in respiratory rate for non-transduced *Tmco6*$^{-/-}$ mice (**Table 6.6**), and therefore sought to determine if this phenotype were worsened or rescued following expression of human WT or MUT *TMCO6*. As shown in **Fig. 7.8 C.**, *Tmco6*$^{-/-\ (AAV\ WT)}$ mice showed normal respirator in line with the experimental control group, *Tmco6*$^{+/+\ (AAV\ WT)}$. In addition, this result was quantified for all biological replicates (**Table 7.2**), and showed a statistically significant reduction in breathing rate for *Tmco6*$^{-/-\ (AAV\ WT)}$ animals relative to *Tmco6*$^{-/-\ (AAV\ MUT)}$ mice. Interestingly, *Tmco6*$^{+/+\ (AAV\ MUT)}$ mice showed a mild, but not statistically significant, increase in respiratory rate compared to the *Tmco6*$^{+/+\ (AAV\ WT)}$ experimental control group, and *Tmco6*$^{-/-\ (AAV\ WT)}$ mice showed a mild recovery in the observed respiratory rate. *Tmco6*$^{-/-(AAV\ MUT)}$ animals also breathed far more shallowly than did mice of the other three genotypic groups. Together this suggests that either directly or indirectly, TMCO6 significantly affects respiration i*n vivo*.

Table 7.2. Respiratory Rates of AAV9-Transduced Mice

Tmco6$^{+/+\ (AAV\ WT)}$, *n* = 5, *Tmco6*$^{+/+\ (AAV\ MUT)}$, *n* = 3, *Tmco6*$^{-/-\ (AAV\ WT)}$, *n* = 5, and *Tmco6*$^{-/-\ (AAV\ MUT)}$, *n* = 5. Data are presented as mean ± SEM. Statistical analysis: two-way ANOVA with Sidak's multiple comparisons *post hoc* test applied. n.s. = non-significant.

Group	Unit	Respiration Rate (Breaths per 3 s)	Significant?
***Tmco6*$^{+/+\ (AAV\ WT)}$**	Breaths/sec	2.4 ± 0.25*	n.s.
***Tmco6*$^{+/+\ (AAV\ MUT)}$**	Breaths/sec	3.0 ± 0.00	n.s.
***Tmco6*$^{-/-\ (AAV\ WT)}$**	Breaths/sec	3.2 ± 0.20	n.s.
***Tmco6*$^{-/-\ (AAV\ MUT}$**	Breaths/sec	4.84 ± 0.45*	**p* = 0.0209

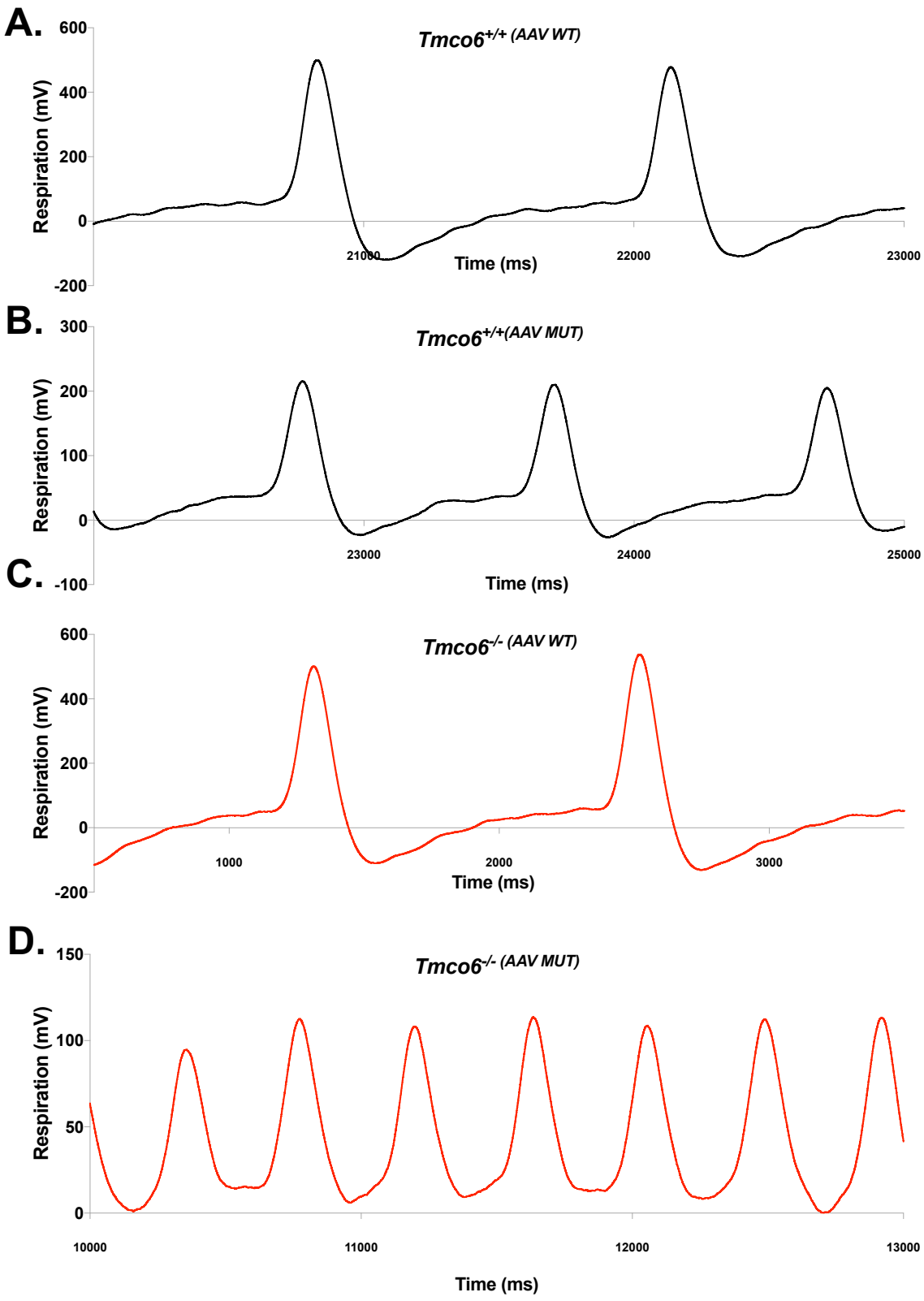

Fig. 7.8. WT TMCO6-expression in *Tmco6*$^{-/-}$ mice rescues breathing rate to normal levels.

Representative respiratory curves for (**A.**) *Tmco6*$^{+/+\ (AAV\ WT)}$ (*n* = 5), (**B.**) *Tmco6*$^{+/+\ (AAV\ MUT)}$ (*n* = 3), (**C.**) *Tmco6*$^{-/-\ (AAV\ WT)}$ (*n* = 7), and (**D.**) *Tmco6*$^{-/-\ (AAV\ MUT)}$ (*n* = 7) mouse lines over a period of 3 seconds.

7.2.6 Hearts of *Tmco6*$^{-/-\ (AAV\ MUT)}$ Mice Show Severe Cardiac Fibrosis

Hematoxylin and eosin (H&E) staining of cardiac sections was performed for *Tmco6*$^{+/+\ (AAV\ WT)}$, *Tmco6*$^{+/+\ (AAV\ MUT)}$, *Tmco6*$^{-/-\ (AAV\ WT)}$, and *Tmco6*$^{-/-\ (AAV\ MUT)}$ mice. Picrosirius red staining was performed on serial sections to stain muscle fibres (yellow) and collagen (red), with presence of the latter used as an indicator of cardiac fibrosis. As shown by the representative images in **Fig. 7.9 A.** – **D.**, all of the four transduced mouse lines displayed some degree of fibrosis (red staining). It is likely that the small amounts of fibrosis detected for *Tmco6*$^{+/+\ (AAV\ WT)}$ (**Fig. 7.9 A.**), *Tmco6*$^{+/+\ (AAV\ MUT)}$ (**Fig. 7.9 B.**), and *Tmco6*$^{-/-\ (AAV\ WT)}$ (**Fig. 7.9 C.**) groups is a consequence of the AAV9-mediated gene delivery strategy. A very different pattern was observed for *Tmco6*$^{-/-\ (AAV\ MUT)}$ mice (**Fig. 7.9 D.**, one representative image shown of 4) where extensive collagen staining throughout the cardiac muscle was detected, indicating severe cardiac fibrosis. This result was not ever observed in 3 month old or 12 month old *Tmco6*$^{-/-}$ hearts (**Fig. 6.15**), and seems to be a unique pathological effect of the MUT *TMCO6* protein. Cardiac fibrosis is characterised by cardiomyocyte death and proliferation of cardiac fibroblasts that result in thickening of the ventricle walls, and subsequently reduced contractility of the heart (Lexow *et al.*, 2013). This is often found to lead to impaired systolic function, as we observed to be significantly decreased for these *Tmco6*$^{-/-\ (AAV\ MUT)}$ mice compared to the WT *TMCO6*-expressing *Tmco6*$^{-/-\ (AAV\ WT)}$ mouse line (see “RVOT VTI” parameter values in **Table 7.1**).

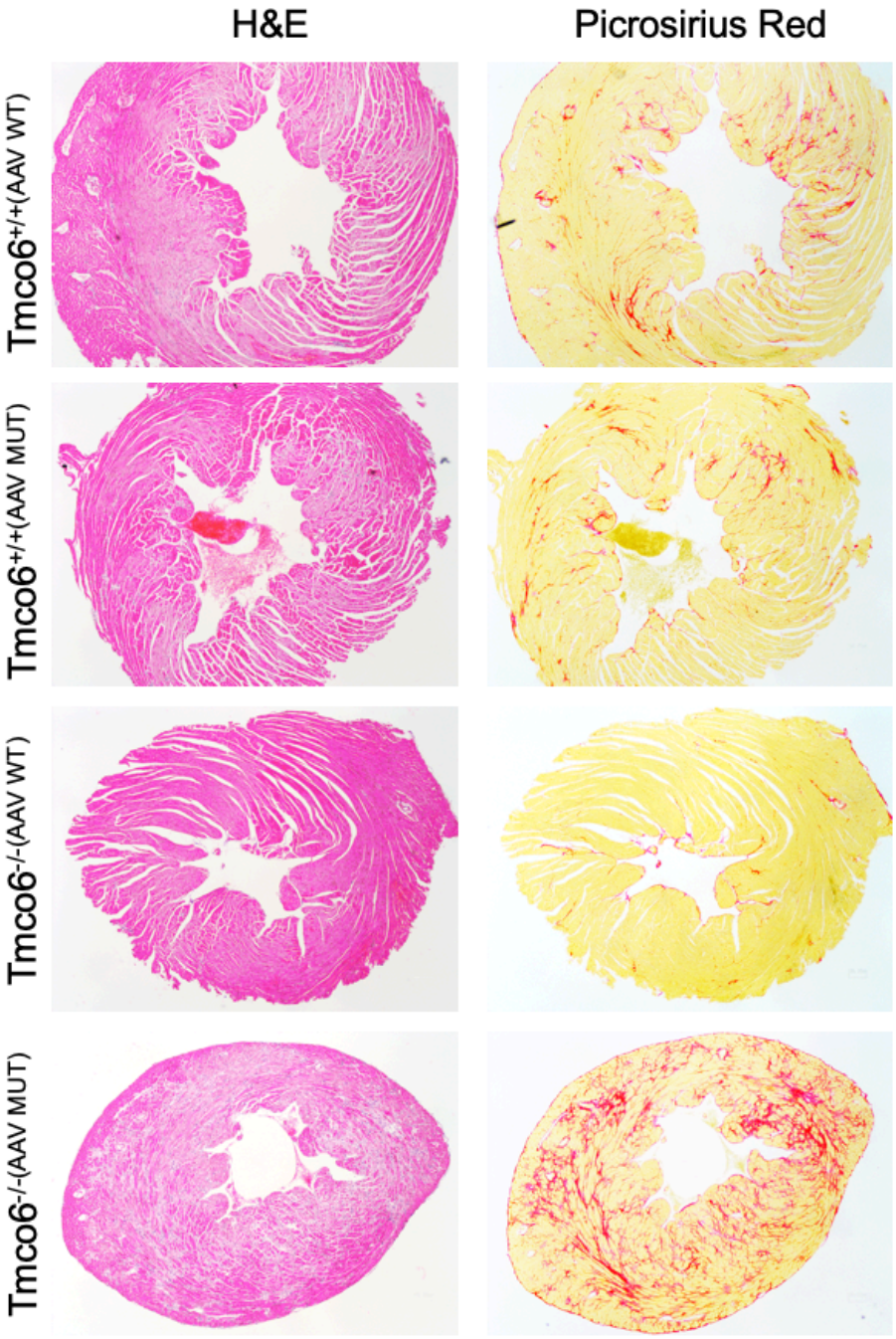

Fig. 7.9. MUT *TMCO6*-expression in *Tmco6*$^{-/-}$ mice causes severe cardiac fibrosis.

Representative H&E and Picrosirius red staining of heart sections from 3 month-old (**A.**) *Tmco6*$^{+/+\ (AAV\ WT)}$, (**B.**) *Tmco6*$^{+/+\ (AAV\ MUT)}$, (**C.**) *Tmco6*$^{-/-\ (AAV\ WT)}$, and (**D.**) *Tmco6*$^{-/-\ (AAV\ MUT)}$ mice. Images were taken at 4 X magnification. Sample preparation performed and image compiled by Raffaele Cerutti, as per **section 2.5.9**.

7.2.7 WT *TMCO6* Expression Rescues CI Deficiency in *Tmco6*$^{-/-}$ Hearts Whilst MUT *TMCO6* Expression Does Not

Using snap-frozen hearts from non-transduced *Tmco6*$^{+/+}$ (*n* = 5) and *Tmco6*$^{-/-}$ (*n* = 6) mice, and the four transduced *Tmco6*$^{+/+\ (AAV\ WT)}$ (*n* = 3), *Tmco6*$^{+/+\ (AAV\ MUT)}$ (*n* = 3), *Tmco6*$^{-/-\ (AAV\ WT)}$ (*n* = 3), and *Tmco6*$^{-/-\ (AAV\ MUT)}$ (*n* = 4) mouse lines, specific biochemical activity for CI was determined by spectrophotometric measurement (see **section 2.7.1**), with CS activity used to normalise all values. As shown clearly in **Fig. 7.10** and evidenced by statistical analysis (one-way ANOVA with Tukey's multiple comparisons test applied), the *Tmco6*$^{-/-\ (AAV\ WT)}$ group shows complete rescue of CI activity to normal levels, relative to the non-transduced *Tmco6*$^{+/+}$ group, and both transduced groups, *Tmco6*$^{+/+\ (AAV\ WT)}$ and *Tmco6*$^{+/+\ (AAV\ MUT)}$. This indicates that human WT TMCO6 is able to complement the CI activity of young adult *Tmco6*$^{-/-}$ mice. What is critical to observe is that the patient mutant variant, as shown by the *Tmco6*$^{-/-\ (AAV\ MUT)}$ group, is only slightly increase compared to the original 3 month old cohort (*Tmco6*$^{-/-}$), but still significantly lower than the *Tmco6*$^{-/-\ (AAV\ WT)}$ group. Therefore, the patient mutant variant (MUT *TMCO6*) is most likely non-functional or inherently pathogenic. Our *in vivo* assessment of the *Tmco6*-knockout mouse model determined similar pathogenic phenotypes compared to the human patient described in **Chapter 4**, namely development of epilepsy, poor locomotor ability and reduced spontaneous movement, atypical neurobehaviors, histopathological findings in the brain including hypomyelination and neurodegeneration, and ultimately, the isolated CI deficiencies found in certain highly aerobic tissue types. In combination with this result, the inability of MUT *TMCO6* to restore CI/CS activity to homeostatic levels in *Tmco6*-ablated mice indicates that this mutation is very likely responsible for his mitochondrial disease.

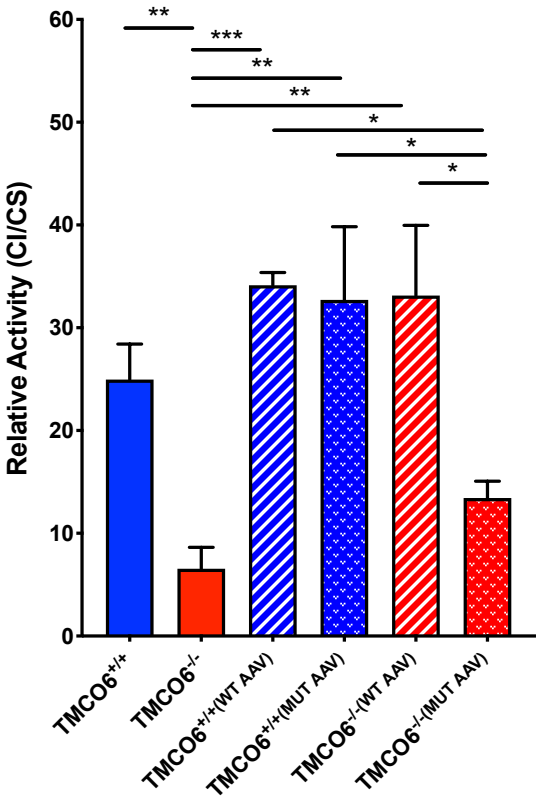

Fig. 7.10. MUT *TMCO6*-expression in *Tmco6*$^{-/-}$ mice hearts does not rescue CI enzymatic activity to normal levels whilst WT *TMCO6*-expression does.

Complex I (CI) enzymatic activity was measured as per **section 2.7.1**, with resulting values normalised to the activity of citrate synthase (CS) for 3 month-old wildtype non-transduced *Tmco6*$^{+/+}$ (n = 5) and *Tmco6*$^{-/-}$ (n = 6) mice, and the four transduced *Tmco6*$^{+/+\ (AAV\ WT)}$ (n = 3), *Tmco6*$^{+/+\ (AAV\ MUT)}$ (n = 3), *Tmco6*$^{-/-\ (AAV\ WT)}$ (n = 3), and *Tmco6*$^{-/-\ (AAV\ MUT)}$ (n = 4) mouse lines. Data are presented as mean ± SEM. Statistical analysis: * $p < 0.05$, ** $p < 0.01$, ** $p < 0.005$ calculated by two-way ANOVA with Sidak's multiple comparisons *post hoc* test applied.

7.2.8 Molecular Investigation of Hearts from AA9-Transduced Mice

SDS-PAGE was performed for murine hearts from non-transduced *Tmco6*$^{+/+}$ (*n* = 3) and *Tmco6*$^{-/-}$ (*n* = 3) mice, and the four transduced *Tmco6*$^{+/+\ (AAV\ WT)}$ (*n* = 3), *Tmco6*$^{+/+\ (AAV\ MUT)}$ (*n* = 3), *Tmco6*$^{-/-\ (AAV\ WT)}$ (*n* = 4), and *Tmco6*$^{-/-\ (AAV\ MUT)}$ (*n* = 4) mouse lines (**Fig. 7.11 A.**). Subsequent Western blotting and immunodetection with an anti-HA antibody showed the relative expression of the WT or MUT TMCO6 protein in transduced mice, normalised to the signal of the cytosolic loading control, GAPDH. Densitometric quantification of the HA signal, corresponding to the TMCO6.1-HA protein, relative to GAPDH signal intensity per animal (**Fig. 7.11 B.**) showed great variation in the relative levels of transgene expression. This is likely due to the systemic delivery approach, where in some animals a large viral load made its way to the heart and in others this delivery would be less efficient and/or specific. Indeed, we observed basal levels of *TMCO6* transgene expression in other tissues, including the liver, diaphragm, kidneys and skeletal muscle of transduced animals (data not shown). Direct injection into the heart, as previously described (Prasad *et al.*, 2011), could minimise systemic exposure of the viral vectors and concentrates delivery directly to the heart in future.

Secondly, NDUFS1, which had been found to be reduced to a third of normal levels in hearts of aged (12 month old) *Tmco6*$^{-/-}$ mice (**Fig. 6.25**) showed no overall reduction in abundance for *Tmco6*$^{-/-\ (AAV\ MUT)}$ or *Tmco6*$^{-/-\ (AAV\ WT)}$ mice. NDUFS3 (Q-module) and NDUFA10 (P_P- module) also showed no variations in relative abundance following transduction of WT or MUT human *TMCO6* of either *Tmco6*$^{+/+}$ or *Tmco6*$^{-/-}$ mice, normalised to the loading control GAPDH. This is somewhat expected given that no molecular differences were observed in 3 month-old animals in the non-transduced cohorts (**Fig. 6.24**), and differences seemed to only become visible with age.

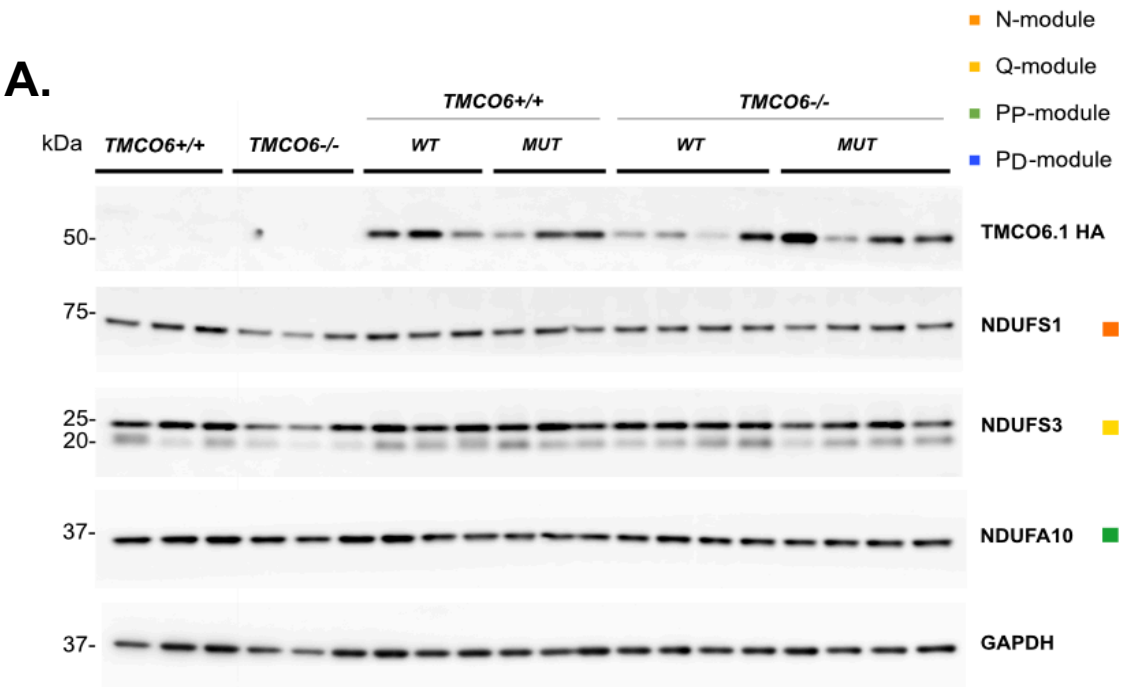

B. Densitometry of TMCO6.1-HA protein expressed in heart tissue per animal

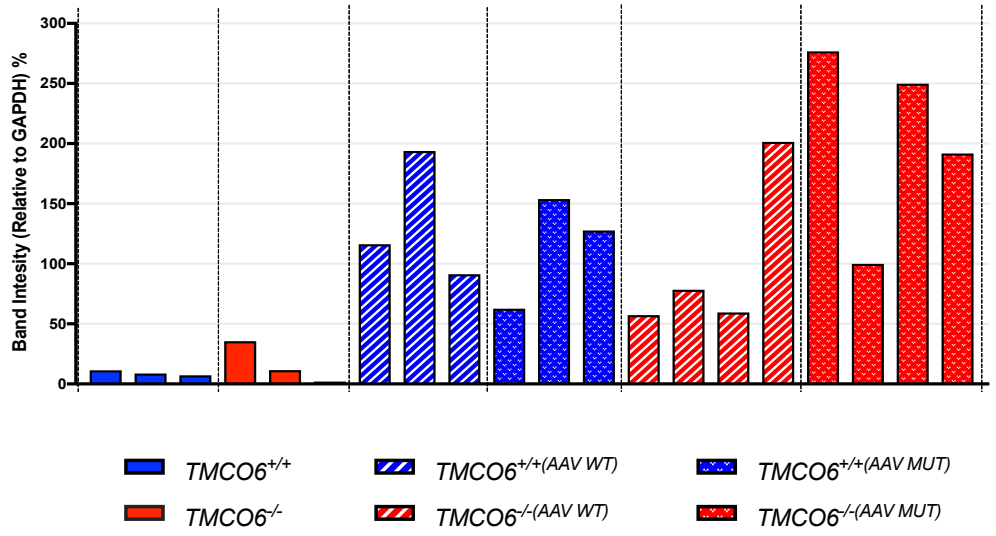

Fig. 6.24. Relative TMCO6.1-HA, NDUFS1, NDUS3 and NDUFA10 steady-state levels in AAV9-transduced mice.

(**A.**) SDS-PAGE was performed as per **section 2.6.2** with 20 µg of protein from whole tissue homogenates from *Tmco6*$^{+/+}$ (*n* = 3) , *Tmco6*$^{-/-}$ (*n* = 3), *Tmco6*$^{+/+\ (AAV\ WT)}$ (*n* = 3), *Tmco6*$^{+/+\ (AAV\ MUT)}$ (*n* = 3), *Tmco6*$^{-/-\ (AAV\ WT)}$ (*n* = 4), and *Tmco6*$^{-/-\ (AAV\ MUT)}$ (*n* = 4) mice. WB analysis followed for immunodetection of CI subunits NDUFS1, NDUFS3, and NDUFA10, and cytosolic loading control GAPDH, using the primary antibodies and concentrations detailed in **Table 2.29**. (B.) Densitometric quantification was performed using Fiji Image J Gel Analysis software. Data are presented per mouse line.

7.3 Conclusions

The work of this chapter: 1) details an AAV-mediated gene delivery strategy for stably expressing WT or MUT human *TMCO6* in hearts of *Tmco6*-knockout or WT mice, 2) investigates physical, behavioural and neuromotor phenotypes of these transduced mice, 3) assesses the function consequences of expressing WT or MUT *TMCO6* in *Tmco6*-ablated mice hearts by echocardiography and electrocardiography, 4) shows cardiac fibrosis specifically resulting from MUT *TMCO6*-expression by histological staining and 4) confirms the pathogenicity of the human patient protein variant, NM_018502: c.271C>T.

In summary of the results of this chapter, intravenous administration of cardiotropic serotype AA9 vectors encoding WT or MUT TMCO6 cDNA sequences, each with C-terminal HA-tags, was used to create four distinct transgenic groups*: Tmco6*$^{+/+\ (AAV\ WT)}$*, Tmco6*$^{+/+\ (AAV\ MUT)}$*, Tmco6*$^{-/-\ (AAV\ WT)}$*,* and *Tmco6*$^{-/-\ (AAV\ MUT)}$*.* Mice transduced with MUT *TMCO6* displayed a plateau in weight gain for one or more weeks following injection. Conversely, animals transduced with WT *TMCO6* showed consistent weight gains form the day of injection. The hindlimb clasping phenotype originally observed in *Tmco6*$^{-/-}$ mice was not rescued by WT *TMCO6* expression, but was alleviated.

Expression of the MUT *TMCO6* transgene did not rescue motor capability and exercise tolerance of *Tmco6*$^{-/-}$ mice, as shown by treadmill experiments. Conversely, animals transduced with WT *TMCO6* showed significant recovery in motor performance. Motor coordination and balance for these mice was assessed by rotarod, and motor coordination evaluated by pole tests. Both showed a mild improvement in *Tmco6*$^{-/-\ (AAV\ WT)}$ compared to *Tmco6*$^{-/-\ (AAV\ MUT)}$ animals, and an inverse trend observed for *Tmco6*$^{+/+\ (AAV\ MUT)}$ mice compared to the experimental control group, *Tmco6*$^{+/+\ (AAV\ WT)}$.CLAMS revealed statistically significant improvements in locomotor and exploratory behaviours in *Tmco6*$^{-/-}$ mice expressing WT *TMCO6* versus the MUT variant. Interestingly, CLAMS also showed a hypothermia-like phenotype for both transduced *Tmco6*$^{-/-}$ mice groups (*Tmco6*$^{-/-\ (AAV\ WT)}$ and *Tmco6*$^{-/-\ (AAV\ MUT)}$) compared to non-transduced *Tmco6*$^{+/+}$ and *Tmco6*$^{-/-}$ mice, with decreases in overall heat production and RER.

In terms of cardiac function, echocardiography showed a significant recovery of right heart systolic function (as indicated by RVOT VTI values) for *Tmco6*$^{-/-\ (AAV\ WT)}$ animals compared to the *Tmco6*$^{-/-\ (AAV\ MUT)}$ group. Expression of the human patient mutant variant, *TMCO6* MUT, did not result in any phenotypic rescue. Electrocardiography revealed that whilst *Tmco6*$^{-/-\ (AAV\ MUT)}$ mice still displayed atrial flutter, both *Tmco6*$^{+/+\ (AAV\ MUT)}$ and *Tmco6*$^{-/-\ (AAV\ WT)}$ mouse lines showed a novel pathogenic ECG feature, a J wave, which denotes early repolarisation of the ventricles

and is characteristic of hypothermia and several cardiomyopathies. Respiration rates were improved in *Tmco6*$^{-/-\ (AAV\ WT)}$ animals compared to the *Tmco6*$^{-/-\ (AAV\ MUT)}$ group. MUT *TMCO6* expression in wildtype *Tmco6*$^{+/+}$ mice also seemed to increase the respiratory rate in these animals compared to the *Tmco6*$^{+/+\ (AAV\ WT)}$ control group. Histopathological staining of hearts from the *Tmco6*$^{-/-\ (AAV\ MUT)}$ group displayed extensive cardiac fibrosis, not seen for any of the other transduced or non-transduced mouse lines. Cardiac fibrosis is often found to lead to impaired systolic function and cardiac failure.

Biochemical measurement by spectrophotometry revealed total recovery of the isolated CI deficiency in *Tmco6*$^{-/-\ (AAV\ WT)}$ hearts, and no such rescue in *Tmco6*$^{-/-\ (AAV\ MUT)}$ mice, indicating that the human patient TMCO6 protein variant (NP_060972.3: p.Arg91Cys) is most likely non-functional. Lastly, SDS-PAGE and Western blot analysis showed variable expression of TMCO6.1 HA in the different genotypic groups, and no differences in the abundances of CI subunits NDUFS1 (N-module), NDUFS3 (Q-module) or NDUFA10 (P_P-module).

This gene delivery strategy was crucial in assessing the pathogenicity of the human TMCO6 mutant protein (NP_001287909.1:p.Arg91Cys). In additional to no recovery of any of the phenotypes observed for age-matched *Tmco6*$^{-/-}$ mice, *Tmco6*$^{-/-\ (AAV\ MUT)}$ animals displayed additional pathogenic phenotypes including extensive cardiac fibrosis. Critically, *Tmco6*$^{-/-\ (AAV\ MUT)}$ mice hearts revealed no functional complementation of CI activity, as was shown for *Tmco6*$^{-/-\ (AAV\ WT)}$ animals. All other phenotypes were similar to those described for the human patient described in **Chapter 4**. Given these results, we are confident that the novel mutation in *TMCO6* described in this work is responsible for the phenotype of the human patient, including the isolated CI deficiency. Additional experiments are necessary to pinpoint the exact mitochondrial role(s) of TMCO6, and to further elucidate its role in CI biogenesis and stability. The implications and future directions of this work will be discussed in **Chapter 8.**

Chapter 8

Discussion and Future Aims

8.1 Discussion

8.1.1 The Revolution of Mitochondrial Disease Gene Discovery by WES

Mitochondrial diseases present a diagnostic challenge for both clinicians and scientists due to their phenotypic and genetic heterogeneity. The molecular diagnosis of mitochondrial disease is complicated by the dual genomic regulation of mitochondria, with a pathogenic gene variant potentially being found in either mitochondrial or nuclear genomes (Gorman *et al.*, 2016). In addition to causal genes often being subunits or assembly factors directly involved in OXPHOS (Ghezzi and Zeviani, 2012), mitochondrial diseases have also been found to result from alterations to the cofactors of the OXPHOS complexes (Stenton and Prokisch, 2018), proteins responsible for mitochondrial dynamics (Suárez-Rivero *et al.*, 2016), namely the fission and fusion processes, and from those necessary for the maintenance and regulation of the mtDNA (Viscomi and Zeviani, 2017). In fact, the advent of whole exome sequencing (WES) and bioinformatic analyses have allowed for the detection of mitochondrial disease genes not previously known to have mitochondrial functions. The stalwart techniques of homozygosity mapping (Seelow *et al.*, 2009), used for identifying recessive traits in consanguineous families, and Sanger sequencing of single genes or panels of suspected candidate genes (Wortmann *et al.*, 2017), are both effective strategies still used today, but they are comparatively laborious and time-consuming methods that rely on a narrowing down of potential genetic candidates, either from selecting genes based on a characteristic clinical phenotype or from knowing the aetiology of a disease within a family. In contrast, WES allows for the unbiased sequencing of all exonic regions of the human genome, in which ~85 % of known monogenic disease-causing mutations are found (Botstein and Risch, 2003), and has been crucial to the rapid rate of discovery of new mitochondrial disease genes in recent years, even by investigating single patients, as in this study.

Along with the many advantages of WES comes the challenge of interpreting the significance of the results. Particularly in the case of mitochondrial diseases, variant filtering must be applied in order to prioritise proteins with known or suspected mitochondrial localisation, and those already found to be associated with the particular respiratory chain defect(s) observed in a patient (Choi *et al.*, 2009). This is because, by querying exome-wide, WES enables the identification of pathogenic variants in non-mitochondrial genes that are presenting clinically as mitochondriopathy (Panneman, Smeitink and Rodenburg, 2018). Increasingly, interrogation of transcriptomic, proteomic and metabolic data is complementing genomic molecular diagnostics (Stenton and Prokisch, 2018), and the growing number of large-scale patient cohort studies (Theunissen *et al.*, 2018) is aiding our collective understanding of genotype-phenotype correlations in mitochondrial disease. However, individual patient case

reports owing to genetic diagnosis by WES remain a powerful tool of identifying new and unstudied mitochondrial disease genes.

To date, more than 300 individual human genes have been identified in causing mitochondrial diseases (Stenton and Prokisch, 2018), including more recently, animal-specific factors, such as APOPT1 (more recently renamed COA8) (Signes *et al.*, 2019), LRPPRC (Cui *et al.*, 2019), and TMEM126B (Alston *et al.*, 2016), only present in Metazoan species. Much of what is currently known regarding human OXPHOS protein complex assembly has been possible due to genetic manipulation and study of orthologues in lower order model organisms, such as baker's yeast, *Saccharomyces cerevisiae* (Stoldt *et al.*, 2018), and the fruit fly, *Drosophila melanogaster* (Garcia *et al.*, 2017). However, in order to identify and characterise higher order OXPHOS assembly factors and associated proteins requires the study of cultured cell lines, principally from humans, and *in vivo* mammalian models. The existence of these animal-specific factors could relate to the fact that OXPHOS assembly and regulation is more complex in higher organisms, owing to the tissue-specific demands for energy, and the relatively higher overall dependency on aerobic respiration for survival of these organisms. Ultimately, the list of OXPHOS assembly factors and associated regulatory proteins found only in higher organisms is most likely incomplete, and requires further elucidation.

In this work, two patients that had been diagnosed with mitochondrial diseases by means of clinical, biochemical and histopathological findings were selected from enrolment in the present study, since initial mtDNA sequencing and Sanger sequencing of a panel of pre-selected OXPHOS-related genes had failed to yield any potential genetic candidates. Therefore, WES was undertaken to examine the entire exome of these individuals, and found mutant variants in two proteins that are only present in vertebrates, and were relatively unstudied at the time of their identification. These variants were compound heterozygous mutations in *COA7* (c NM_023077.3:c.410A>G;c.287+1G>T) and a homozygous recessive mutation in *TMCO6* (NM_018502.5: c.271C>T). Both of these genes were selected for experimental investigation given that *COA7* mutations had never before been implicated in mitochondrial disease, despite its putative designation as a COX assembly factor (Kozjak-Pavlovic *et al.*, 2014), and *TMCO6* had never before been linked to mitochondrial function in general, or in fact, any intracellular role or the pathology of human disease of any kind. We therefore sought to assess whether these genomic variants were 1) responsible for the observed clinical and biochemical phenotypes relating to COX or CI deficiency, respectively, and 2) whether or not these proteins were indeed new mitochondrial disease genes.

8.1.2 Implications of Confirming Pathogenicity and Subcellular Localisation of COA7

Patient-derived skin fibroblasts served as the molecular basis of our investigation into COA7, Extraction of total RNA from primary patient skin fibroblasts, and retrotranscription to cDNA, revealed that each of the two compound heterozygous *COA7* mutations were very likely pathogenic; the former owing to disruption of a highly conserved tyrosine residue and a drastic substitution to cysteine (**Fig. 3.6**), and the latter due to skipping of the entirety of the second of three coding exons during transcription, leading to an in-frame 47 amino acid deletion in the gene product (NP_075565.2: p.Tyr137Cys; p.Cys37_Gly84del) (**Fig. 3.5**). Indeed, we observed complete loss of detectable COA7 protein by SDS-PAGE and Western blot analysis (**Fig. 3.7**). Biochemical measurements determined COX deficiency to a third of control levels (**Fig. 3.10**), to an identical extent as had been shown for shRNA-mediated *COA7* gene silencing in HeLa cells (Kozjak-Pavlovic *et al.*, 2014). We also observed an equivalent reduction in mature COX steady-state level (**Fig. 3.8**), with significant decreases found in the quantities of the COX subunits MT-CO2 and COX5B (**Fig. 3.7**). A "global" reduction was found by 2D-BNGE and Western blot analysis for the abundance of COX intermediates, the COX holocomplex and COX-containing supercomplexes (**Fig. 3.9**), suggesting impaired COX assembly and stability in these cells. This time using patient-derived fibroblasts that had undergone immortalisation, we performed functional complementation by lentiviral transduction of the wildtype *COA7* cDNA sequence. This process rescued both COX activity (**Fig. 3.15**) and assembly, shown by the recovered levels of COX subunits (**Fig. 3.11**), the fully assembled COX holocomplex (**Fig. 3.12**), and COX intermediates and supercomplexes (**Fig. 3.13** and **3.14**), to normal levels, providing further support to the pathogenicity of the mutations.

In addition to proving the pathogenicity of these two novel *COA7* variants, this investigation highlighted in which part of COX biogenesis COA7 most likely participates. Human COX assembly is mediated by more than 30 known assembly factors, with roles including the control of mtRNA stability and translation, insertion of mtDNA encoded subunits into the IMM, biosynthesis of copper and heme prosthetic groups, and the stabilisation of the three separate COX modules, which include one of each of the three mtDNA-encoded subunits (MT-CO1, MT-CO2 and MT-CO3) (Timón-Gómez *et al.*, 2017). In our experiments, MT-CO1 abundance was only slightly reduced, and not to a statistically significant extent, in primary patient skin fibroblasts by SDS-PAGE, Western blotting and subsequent densitometric quantification (**Fig. 3.7 B.**), and its abundance was completely unaffected following lentiviral transduction of the wildtype *COA7* cDNA sequence (**Fig. 3.11**). In addition, COX5A abundance was unaffected in the latter (**Fig. 3.11**). Together, these results signified no disruption to early-stage COX

assembly involving the MT-CO1/MITRAC module (Signes and Fernandez-Vizarra 2018) as a result of the loss-of-function mutations in *COA7*. In contrast, MT-CO2 and COX5B abundance were significantly reduced in primary patient fibroblasts (**Fig. 3.7 A.** and **B.**), and specifically, MT-CO2 steady-state level was found to be completely restored to control levels following complementation of immortalised cells with the wildtype *COA7* cDNA sequence (**Fig. 3.11**). Initial reduction, and then complementation, of MT-CO2 levels following complementation suggests involvement of COA7 in facilitating correct MT-CO2 module assembly, before incorporation of MT-CO3 module. In support of this, COA7 protein levels were found very recently to be increased following CRISPR/Cas9-mediated knockout of hypoxia induced gene 1 domain family members HIGD2A and HIGD2A, human orthologues of yeast Rcf1 and Rcf2 (named for respiratory complex factors), by quantitative mass-spectrometry (Hock *et al.*, 2019). COX assembly factors COA4, COA6, CMC2 and COX11 were also found to be increased following ablation of HIGD2A, in particular. All of these assembly factors are involved in steps of COX biogenesis before MT-CO3 module integration, and in fact, HIGD2A was concluded to act as the first protein to mediate MT-CO3 module integration into COX (Hock *et al.*, 2019). Therefore, COA7 is most likely to be involved only in MT-CO2 module assembly, but the exact role of this protein in this stage of COX biogenesis remains unknown. The principal aim of any future directions of this work would be to determine and detail the role of COA7 in COX assembly, as will be discussed below.

As a second aim of this research, we endeavoured to confirm the submitochondrial localisation of COA7. The only seminal work regarding this protein had experimentally determined COA7 to be both soluble and mitochondrial, and had specifically designated its submitochondrial localisation to be the IMS by subcellular fractionation, SDS-PAGE and Western blot analysis (Kozjak-Pavlovic *et al.*, 2014). However, the experimental control in this case were mitoplasts from HeLa cells solubilised first with 1 % Triton and then incubated with 50 µg/ml of proteinase K, which should have eliminated all presence of the COA7-specific band detectable by SDS-PAGE and Western blotting. However, presence of a band at a slightly smaller size was found in this sample at a similar intensity as for untreated samples. Therefore, we sought to verify, and if necessary, correct, the submitochondrial localisation of this protein. As described in **Chapter 3**, our initial results were misleading owing to the relative protease insensitivity of the COA7 protein, which led to the presence of a COA7-specifc signal at the correct size by SDS-PAGE and Western blot analysis despite subjection to protease treatment, this time in the form of two different concentrations of trypsin (25 and 50 µg/ml). However, recent evidence that COA7 is an interactor of CHCHD4/MIA40, the principal component of the disulphide-relay system responsible for the import and targeting of IMS proteins (Mohanraj, *et al.* 2019), led us to reconsider this finding and attempt to resolve this apparent contradiction. We opted for two

biochemical approaches, one employing protease digestion and the other only using OMM solubilisation by digitonin. In addition, we used super-resolution microscopy of HA-tagged COA7 in a COA7-HA overexpressing HeLa cell line to determine COA7 localisation relative to markers for each of the mitochondrial compartments. For the first of the biochemical experiments, a range of digitonin (DIG) concentrations were used to gradually open the OMM of isolated mitochondria from HEK 293T cells, and both supernatant and pelleted samples were collected following ultracentrifugation (**Fig. 3.16 A**.). COA7 is detectable in supernatant fractions from 150 µg/ml digitonin onwards, with associated decrease in the pelleted fractions. This is similar to the behaviour of OMM protein TOMM20 and IMS proteins AIF and CYT *C*, and contrasted to the pattern shown for IMM protein COX4, and MM protein SOD2, both of which did not appear in the supernatant fractions with any concentration of digitonin. Secondly, when the same procedure was followed but with the subsequent addition of 150 µg/ml trypsin to each fraction (**Fig. 3.16 B**.), COA7 was degraded from 150 µg/ml DIG onwards, similarly to AIF and CYT *C*, COX4, and SOD2, and unlike TOMM20, which was degraded immediately following addition of protease. Taken together, these two biochemical experiments strongly indicated that COA7 is an IMS protein. Super-resolution fluorescence microscopy was employed to visually determine the submitochondrial localisation of HA-tagged COA7 in HeLa cells overexpressing the wildtype *COA7* cDNA sequence. The resulting HA signal overlapped significantly with that of the IMS marker SMAC (**Fig. 3.17**). This multi-part method supplied conclusive evidence that COA7 is a mitochondrial protein localising to the IMS.

Upon publication of these first pathogenic mutations in *COA7* (Martinez Lyons *et al.* 2016), investigations were conducted by other research groups into 1) the mitochondrial import pathway of the COA7 protein into the IMS though interaction with MIA40, part of the MIA pathway, and the application of proteasome inhibition as a novel therapeutic strategy (Mohanraj *et al.*, 2019), and 2) into the diagnoses of additional mitochondrial disease patients whose conditions arose from pathogenic *COA7* mutations (Higuchi *et al.*, 2018).

For the former, Mohanraj *et al.* investigated our patient cells and generated additional cellular models with equivalent mutant variants as a means of studying impaired mitochondrial protein import in mitochondrial disease (Mohanraj *et al.*, 2019). Both pathogenic mutant variants were found to be imported into the mitochondria more slowly than the wildtype COA7 protein, and in addition, the majority of the intracellular steady-state levels of both were found to mis-localise to the cytosol and become degraded by the action of the UPS. The phenomenon of retro-translocation to the cytosol and subsequent protease degradation of improperly folded IMS proteins has been described previously (Bragoszewski *et al.*, 2015). Protease inhibition experiments partially rescued COX activity in patient cells, suggesting a conceptually novel

therapeutic approach for mitochondrial diseases. Separately from these findings, this research characterised COA7 as a non-canonical substrate of MIA40, establishing interaction between the two through disulphide bonding, and confirming that COA7 is imported into the IMS by the MIA pathway (Stojanovski, Bragoszewski and Chacinska, 2012). Also, of the 13 known COA7 cysteine residues, the authors determined that 10 were found to be crucial to its intrinsic tertiary structure by forming 5 separate disulphide bonds, and the three cysteine residues were present in a reduced, unbound state through a combination of *in silico* modelling and thiol trapping experiments. Furthermore, these methods indicated that the 5 predicted SEL-1 domain repeats in COA7 (**Fig. 1.7 B.**) are stabilised by these disulphide bridges, with each domain characterised by a specific arrangement of cysteine residues. Lastly, homology modelling and molecular dynamics simulations demonstrated that the patient's paternally inherited mutant protein variant (NP_075565.2: p.Tyr137Cys), by adding another cysteine residue, most likely affects the disulphide bonds naturally occurring between residues C100 and C111, causing misfolding and destabilisation of the native COA7 protein. This research not only suggested a role for protease inhibition as a means of therapeutic treatment for mitochondrial diseases arising from protein degradation, but also characterised the intramolecular stability of COA7 in terms of its SEL-1 like repeat motifs and disulphide bridge composition, in turn allowing for better understanding of why the human patient mutant variants are pathogenic *in vivo*.

Secondly, this research stemmed diagnoses of additional mitochondrial disease patients whose conditions arose from pathogenic *COA7* mutations. Higuchi *et al.* identified four unrelated Japanese patients from a case series of patients with Charcot-Marie-Tooth (CMT) disease or other suspected inherited peripheral neuropathies, each found to harbour pathogenic mutations in *COA7* by WES (Higuchi *et al.*, 2018). The mutant variants were different from the two we had described in all cases; these were NM_023077:c.17A>G,p.Asp6Gly for patient 1, NM_023077:c.115C>T,p.Arg39Trp in patient 2, NM_023077:c.17A>G;446G>T,p.Asp6Gly;p.Ser149Ile in patient 3, and NM_023077:c.17A>G;430delG,p. Asp6Gly;Gly144fs in patient 4. COX deficiency is notoriously heterogeneous in its clinical presentation (Rak *et al.*, 2016); however, it is worth noting that our proband displayed some classical hallmarks of syndromes linked to COX deficiency. For example, the mode of inheritance was autosomal recessive, with infantile onset of symptoms characteristic of encephalomyopathy, including developmental delay, ataxia, dysarthria, cognitive impairment, hyporeflexia and muscle wasting, white matter degeneration (leukodystrophy), and demyelinating sensory peripheral neuropathy. The additional four patients shared a characteristic set of neurological features, including sensory peripheral neuropathy, ataxia with cerebellar atrophy, and some patients showed progressive

leukodystrophy and spinal cord atrophy by MRI. The authors have suggested naming this unique clinical presentation as spino-cerebellar ataxia with axonal neuropathy type 3. COX deficiency was the predominant mitochondrial respiratory chain defect found in biochemical measurement of fibroblasts from patients 1-3, although CI deficiency was detected in fibroblasts of patient 1. However, this CI deficiency was not found in measurement of a muscle biopsy from the same patient, in which only isolated COX deficiency was found, indicating that perhaps the former was an anomalous result. Notably, the conditions of each of the four patients, and the proband described in this work, remained stable well into adulthood, which could be related to a partially dispensable role of COA7 in COX biogenesis. Indeed, the oldest of the patients described was 63 years of age at the time of diagnosis. In conclusion, this research has cemented *COA7* as a mitochondrial disease gene owing to COX deficiency, now associated with a characteristic clinical presentation.

8.1.3 Investigating TMCO6 as a Novel Mitochondrial Disease Protein

TMCO6, an entirely uncharacterised, nuclear-encoded protein found only in vertebrates, was identified by WES and subsequent bioinformatic filtering to be the most likely causal genetic candidate in a paediatric mitochondrial disease patient exhibiting CI deficiency (see **section 4.2.2**). CI deficiency is the most frequently occurring isolated mitochondrial respiratory chain defect associated with mitochondrial disease (Rodenburg, 2016), and although genotype-phenotype correlations are notoriously difficult to deduce, the majority of CI deficient patients present with neurodegeneration, leukoencephalopathy and associated neuromotor symptoms (Distelmaier *et al.*, 2009). However, additional tissue-specific consequences of this condition beyond perturbations to the brains are being increasingly studied, including the emerging role of CI deficiency in causing cardiovascular diseases (Forte *et al.*, 2019).

The clinical presentation of the proband described in this work aligns well with characteristic neuromuscular phenotypes of nuclear-encoded CI deficiency (Distelmaier *et al.*, 2009), with disease onset in the first year of life including psychomotor delay, muscular hypotonia, nystagmus, no acquisition of motor or language milestones and epilepsy. MRI scans performed at 16 months and 7 years of age discovered cortical and subcortical hypomyelination, and progressive cerebral and cerebellar atrophy, with sparing of the spinal cord (**Fig. 4.3**). Cerebellar atrophy is not a common phenotype of nuclear-encoded CI deficiency, nor is an absence of lesions of the brainstem; however, the extensive leukodystrophy is typical and cerebellar atrophy has been well-documented in mtDNA-encoded variants that cause CI deficiency (Lebre *et al.*, 2011). The proband also displayed an increase in intraventricular lactate (22 mg/dl, n.v. 9-19 mg/dl) and a reduction of N-acetyl

aspartate (NAA) (**Fig. 4.4**), the most prominent MRS signal abnormalities observed in mitochondrial disorders (Lunsing *et al.*, 2017), and indicative of lactic acidosis, which is very commonly found in paediatric mitochondrial disease cases (Loeffen *et al.*, 2000). Additionally, the autosomal recessive mode of inheritance of a rare mutant variant (NM_018502.5: c.271C>T) owing to consanguineous parents (**Fig. 4.5**) is fitting of this group of disorders (Kirby and Thorburn, 2008). Overall, the proband in this work presents with typical clinical hallmarks of mitochondrial disease owing to CI deficiency.

Cell-based strategies were used to determine TMCO6 subcellular localisation, and following on from this, immunoprecipitation experiments independently concluded physical interaction between TMCO6 and CI. Cellular models were then generated to probe the role of TMCO6 in CI biogenesis, stability and/or function. ICC was used to determine for the first time the subcellular localisation of endogenous TMCO6 in HeLa and 143B cells relative to the mitochondrial network, as stained by MitoTracker^{TM} Red CMXRos and nuclei, as stained by DAPI (**Fig. 5.1**). Despite prediction of an IBB domain (**Fig 4.2**), found only in nuclear proteins, TMCO6 was found to be totally absent in the nucleus of these cells and instead localised entirely to the mitochondria (**Fig. 5.1**), suggesting misleading annotation or alternative function of this domain feature, or possibly some sort of protein shuttling role for TMCO6 between the nucleus and CI within mitochondria. It is worth noting TMCO6 is not predicted by the MitoCarta 2.0 database to localise to mitochondria. Subcellular fractionation and molecular analyses independently determined TMCO6 to be a mitochondrial protein (**Fig. 5.2**). Hypotonic swelling and protease digestion experiments found TMCO6 to be protected in all conditions, suggesting localisation to the IMM or MM (**Fig. 5.3**). Lastly, TMCO6 was found to be present in membrane fractions of sonicated mitochondria in isotonic conditions, and only upon increased salt concentration would it become dissociated from the membrane (**Fig. 5.4**). We concluded IMM localisation of TMCO6, in a membrane-tethered fashion as opposed to total embedment, given its susceptibility to dissociation. Following this, immunoprecipitation experiments confirmed physical interaction between native CI and TMCO6 (**Fig. 5.14**). This result was reproducible no matter the method of elution used. In reverse, pulldown experiments using the endogenous TMCO6 antibody were inconclusive, likely due to the fact that the natural abundance of the endogenous protein is very low. Instead, we used a cellular model of inducible HA-tagged *TMCO6* (isoform 1) (NM_001300980.1) expression to perform immunoprecipitation experiments, with subsequent SDS-PAGE and Western blot analyses (**Figs. 5.14** and **5.15**). This method showed presence of NDUFS6 in eluate fractions eluted by two different methods (**Fig. 5.15**). This supports a role for TMCO6 in N-module assembly or modulation, of which NDUFS6 is a part. It is possible that longer exposures of these

membranes could have revealed other potential interactors; however, more rigorous proteomic strategies would be preferable for deducing protein interactors of TMCO6 *in vivo*.

In the same vein as described above for *COA7*, we first sought to verify the pathogenicity of the homozygous recessive mutant variant in *TMCO6* (NM_018502.5:c.271C>T) and determine its molecular and biochemical impact using patient-derived skin fibroblasts in both cases. Initial *in silico* assessment had predicted strong likelihood of pathogenicity of the mutant *TMCO6* variant (**Fig. 4.6**). However, this process proved not to be straightforward early on given that the endogenous TMCO6 protein was still detectable in protein lysates from patient-derived primary and immortalised skin fibroblasts by SDS-PAGE and Western blot analysis (**Fig. 4.8** and **4.9**). No reduction in steady-state level of fully assembled CI was consistently found (**Fig. 4.10**), although a slight reduction of holocomplex abundance was detected following immunodetection of NDUFS1 (**Fig. 4.11**). Most importantly, the severe CI deficiency originally detected in patient skeletal muscle was not found to be present in these cultured fibroblasts (**Fig. 4.15**). It is worth noting that lack of CI deficiency in fibroblasts, but presence in skeletal muscle, has been well documented in CI deficient mitochondrial disease patients (Ruitenbeek *et al.*, 1996; Swalwell *et al.*, 2011), and is perhaps due to a tissue-specific effect of a mutant variant, or only detrimental effects occurring in tissues that have higher demands in aerobic metabolism than fibroblasts. The lack of any observable CI deficiency in these cells made them unsuitable for functional complementation experiments, and necessitated the generation and study of additional cellular models (**Chapter 5**). However, the two results that came out of this initial investigation that pointed strongly in the direction of a role for TMCO6 in CI function, biogenesis and/or regulation were 1) specific co-migration of endogenous TMCO6 with fully-assembled CI by 2D-BNGE (**Fig 4.13**), and 2) significant reduction in the abundances of CI-containing supercomplex species (**Fig. 4.12**).

The obvious question this raises is why has TMCO6 not been identified in mass spectrometry-based complexomics screens highlighting factors involved in assembly and structure of CI (Lopez-Fabuel *et al.*, 2016; Stroud *et al.*, 2016; Guerrero-Castillo *et al.*, 2017), nor in any of the completed mammalian CI structures (Zhu, Vinothkumar and Hirst, 2016; Agip *et al.*, 2018; Fiedorczuk and Sazanov, 2018)? For the former, this absence from complexomics results could be due to a fleeting association of TMCO6 with CI during its biogenesis, or to fragile interaction between the two, so that no significant accumulation of TMCO6 would ever be found to occur with CI subassembly intermediates. This same result has been shown in the case of assembly factors NUBPL, NDUFAF5, NDUFAF6, and NDUFAF7, all of whom could not be found in association with the CI holocomplex or any CI subassemblies by complexomics (Stroud *et al.*, 2016). This same reasoning could apply to its absence from mammalian

structures of CI. Principally, these structures are compiled by using purified mature CI holocomplexes, lacking all assembly factors, so the absence of TMCO6 in these structures is largely expected. Additionally, if TMCO6 is indeed somehow involved in the interaction of CI with other respiratory chain complexes to form supercomplexes, as seemed to be the case from 1D-BNGE and Western blot results in patient fibroblasts (**Fig. 4.12**) and following shRNA-knockdown in HEK 293T cells (**Fig. 5.8 A.**), its physical association with CI could be even more difficult to establish. This difficulty has been shown for COX7A2L, which acts as a checkpoint of assembly in the integration of $CIII_2$ into supercomplex configurations (Lobo-Jarne *et al.*, 2018), but was not found in any holocomplex structures or complexomics data for any of the individual respiratory chain complexes previously (Lapuente-Brun *et al.*, 2013; Hock *et al.*, 2019). Even a structural subunit of CI, NDUFV3 (N-module), was found to be consistently missing in models of CI's interaction with $CIII_2$ and CIV (Wu *et al.*, 2016), so it is plausible that TMCO6 may not be detectable by such approaches either, despite interaction with CI of CI-containing supercomplexes *in vivo*.

Immortalised patient skin fibroblasts showed the greatest decrease in the steady-state levels of N- and Q-module CI subunits (**Fig. 4.9**), suggesting perturbation to assembly of these modules, and less or no effect on the assembly of the P_P and P_D modules. One patient of a study of four with pathogenic mutations in *NDUFA6*, which encodes a Q-module structural subunit, demonstrated no CI holocomplex reduction or CI enzymatic deficiency in patient skin fibroblasts despite clear perturbation to CI assembly and reduction in abundance of N- and Q-module subunits by complexomics analysis (Alston *et al.*, 2018). This similar presentation to that of our proband suggests that the CI assembly defect in our proband's fibroblasts is still a true pathological defect leading to mitochondrial disease, despite no associated CI deficiency (**Fig. 4.15**) in this cell type. Sometimes, subassembly species containing N- or Q-module subunits are found to be accumulated in abundance as a result of deleterious mutations to genes encoding CI assembly factors, as is the case for null mutations in *NDUFAF2* (McKenzie and Ryan, 2010). Patients were found to have accumulated intermediates containing the Q-module subunits NDUFS2 and NDUFS3 (Hoefs *et al.*, 2009). Looking into the modular assembly of CI further suggests that the accumulation of a ~ 680 kDa NDUFB8-containing subcomplex in patient cells (**Fig. 4.10 A.**) is in fact portion of the P_P and P_D modules waiting for incorporation with the Q-module (Guerrero-Castillo *et al.*, 2017), perhaps stalled at this point of assembly. In addition, immunodetection of 1D-BNGE gels with NDUFS3 and NDUFB8 showed lack of a ~900 kDa subunit, most likely to be CI lacking the N-module with associated assembly factors still attached (McKenzie and Ryan, 2010). It is possible that TMCO6 is involved in some part of Q-module stability/N-module assembly owing to these results.

However, further experiments are needed to validate or negate this hypothesis, as will be described below.

Lastly regarding these patient fibroblasts, we observed evidence of reduced mitochondrial mass in both primary (**Fig. 4.8**) and immortalised (**Fig. 4.9**) forms, evidenced through decreases in the steady-state levels of mitochondrial proteins from each of the respiratory chain complexes and of several mitochondrial mass markers not involved in OXPHOS (CS, HSP60 and TOMM20) by SDS-PAGE and Western blot analysis. Confocal microscopy experiments were conducted (data not included) to compare organisation and density of the mitochondrial network in primary patient fibroblasts compared to controls. The signal intensity of MitoTracker™ Red CMXRos staining in both cell lines did not reveal any obvious differences in overall mass; however, this approach did reveal some hyperfusion of the mitochondrial network, which can be indicative of cellular stress (Hoitzing, Johnston and Jones, 2015). This line of investigation requires more rigorous and high-resolution imaging strategies (see **section 8.2**).

Cellular models were next generated, including shRNA-mediated knockdown cell lines in HEK 293T cells, inducible overexpression models of both major wildtype *TMCO6* isoforms (termed here as *TMCO6.1* and *TMCO6.2*), and equivalent overexpressing cell lines expressing the patient mutant variants of both of these isoforms. Firstly, *TMCO6* gene silencing in HEK 293T cells was successful at the transcript level, shown by RT-qPCR (**Fig. 5.5**), and protein level, shown by SDS-PAGE and Western blotting (**Fig. 5.6**), with recovery in protein abundance observed soon after transduction. Gene silencing of *TMCO6* was also associated with statistically significant slower growth rate in glucose media (**Fig. 5.7**), and notably, isolated CI deficiency (**Fig. 5.8 B**.), as determined by spectrophotometric measurements and supported qualitatively by in-gel CI activity (**Fig. 5.8 A**.). TMCO6 was again found to co-localise with fully assembled CI in these cells by 2D-BNGE, and also in two discrete CI sub-assemblies, the ratios of which were skewed following TMCO6 gene silencing (**Fig. 5.9**). Our inducible overexpression cellular models showed that the TMCO6.1 protein isoform is more abundant than TMCO6.2 in these cells, and overexpression of the HA-tagged variants were associated with a knock-on increase in the abundance of the endogenous protein (**Fig. 5.11 A.** and **B.**). In these samples, NDUFA9 (N-module/Q-module boundary) followed the pattern shown by abundance of TMCO6 most faithfully; however, no significant differences in CI holocomplex abundance (**Fig. 5.12 B.** and **C.**) or specific CI activity (**Fig. 5.12 A.**) were found using this cellular model. Attempts to generate a TMCO6 knockout in HAP1 cells and also a knockin for the patient mutation using the same sgRNA (**Fig. 5.17**), were conducted but failed to introduce any detectable mutations or changes (detailed in **section 5.2.4**). This is possibly due to poor

target site fidelity or PAM motif recognition by this sgRNA. At the time of this research, work had begun to characterise a knockout murine model, so attempts at generation of a cellular *TMCO6*-knockout model ceased. In summary, the results gained from studying these cellular models supported *in vivo* interaction between TMCO6 and CI, and suggested that TMCO6 depletion or reduction impairs CI activity to a significant extent.

We then sought to characterise a commercially available *Tmco6*-knockout mouse model, B6N(Cg)-*Tmco6*$^{tm1.1(KOMP)Vlcg}$/J, in order to assess and investigate the role of Tmco6 in homeostatic development and function. *Tmco6*-KO mice displayed atypical neurobehaviors such as hindlimb clasping that progressed with age, and a proportion of KO animals developed myoclonic epilepsy from 6 months of age (**Fig. 6.4**). Both female and male KO animals were generally smaller in mass and size compared to age-matched controls (**Fig. 6.4**), and presented with poor motor endurance and coordination (**Fig. 6.5**). Spectrophotometry and Oroboros-based oxygraphic techniques revealed tissue-specific mitochondrial enzymatic deficiencies in *Tmco6*-KO mice brains, skeletal muscles and hearts, and no deficiency in murine fibroblasts. Despite there being no specific CI enzymatic deficiency in brains of KO mice at 3 months of age (**Fig. 6.18 A.**), which was a surprising finding given the extent of histopathological abnormalities (**section 6.2.3**), electron flow through the electron transport chain was impaired at the CI point of entry (**Fig. 6.20**)**.** Also, hearts and skeletal muscle of 3 month and 12 month old KO males showed isolated CI deficiency. The more severe CI deficiency of the two was observed in heart, with molecular abnormalities discovered as well, including a significant reduction in steady-state levels of N-module subunits NDUFS1 and NDUFS6 by SDS-PAGE and Western blot analysis, giving more weight to the involvement of Tmco6 in the assembly of this module. Lastly, echocardiography showed decreased right ventricular function and electrocardiography determined atrial flutter in KO mice hearts. No other abnormalities in cardiac function or physiology were detected at this time.

These findings were very similar to those found for the human mitochondrial disease patient with a homozygous recessive mutation in *TMCO6* (NM_018502.5: c.271C>T), as described in detail in **Chapter 4**. Firstly, MEFs did not show CI deficiency (**Fig. 6.17**), as had been the case for patient-derived fibroblast cells (**Fig. 4.15)**. Also, isolated CI deficiency was shown in murine *Tmco6*-KO skeletal muscle to a comparable extent to what had been shown in a skeletal muscle biopsy from the patient (~ 40 % reduction). Epilepsy was observed in both the human patient and the KO mice, along with impaired locomotor behaviours and neuromotor control. Very few spontaneous epilepsy models in mice exist (Gu and Dalton, 2017), and none describing myoclonic seizures in mice as a result of ablation of a mitochondrial protein have been previously published in the literature so this is a curious finding. The only striking

difference we identified between the patient and murine knockout model was cardiac dysfunction (**section 6.2.6**), and associated severe, isolated cardiac CI deficiency in *Tmco6*-KO hearts (**Fig. 6.18 B.**). The human proband had only ever had physical assessment of the heart carried out by means of a cardiac ultrasound, performed at 16 months of age, which had not been accompanied by echocardiography or electrocardiography. It is possible that an underlying, similar cardiac phenotype exists for the patient but is unknown at this time. Or equally, cardiomyopathy could be an idiosyncratic manifestation of murine *Tmco6*-ablation. However, cardiac dysfunction has been found in several cases of human CI deficiencies, including those associated with pathogenic mutations in NDUFS2 and NDUFA11 (Irwin, Parameshwaran and Pinkert, 2013), to name a couple. Furthermore, CI deficiency in murine models is being increasingly studied as the basis of cardiovascular dysfunction and disease (Forte *et al.*, 2019); deletion of *Ndufs6* has been found to result in specific cardiomyopathy and oxidative stress (Ke *et al.*, 2012) and heterozygous systemic *Ndufc2* deletion has been found to induce cardiovascular complications including ischemic stroke (Ohkubo *et al.*, 2002). The result for *Ndufs6* is particularly interesting since we have found the human NDUFS6 and TMCO6 proteins to interact by immunoprecipitation experiments in cultured HEK293T cells (**Fig. 5.16**), and both seemingly have associated cardiomyopathies in murine models. In addition to cardiac dysfunction, the phenotypic differences we observed such as decreased body weight and muscular weakness are similar to *Ndufs4*-knockout CI deficiency murine model mice that display ataxia and impaired growth (Kruse *et al.*, 2008). Lastly, rescuing CI deficiency in an idiopathic murine epilepsy model was found to result in anti-seizure effects (Simeone *et al.*, 2014), which if considered in reverse, could indicate a causal link between the epilepsy we have observed and the impaired CI-linked aerobic respiration in brains of these mice (**Fig. 6.20**). In summary, the physical and neurological findings, and biochemical phenotypes of this strain, indicate it to be a credible and useful *in vivo* model for studying the pathological effects of Tmco6-protein ablation in causing mitochondrial disease.

Comparing the results of this stable knockout *in vivo* model to the transient shRNA-mediated knockdown model in HEK293T cells, we observed some similarities and some differences. Firstly, CI deficiency was observed to approximately ~ 60 % of control levels for three separate, successful shRNA-knockdown cell lines (**Fig. 5.8 B.**), whereas the murine *Tmco6*-KO model showed great variability in the extent of CI deficiency in different tissues. Liver and brains, for example, displayed no specific CI deficiencies (**Fig. 6.18 A.** and **C.**), whereas skeletal muscle revealed an equivalent reduction to the cellular knockdown model of ~ 40 % reduction (**Fig. 6.18 D.**), and cardiac muscle showed a far greater reduction of approximately 80 % (**Fig. 6.18 B.**). Next, CI-containing supercomplexes were found significantly reduced as a result of gene silencing by 1D-BNGE and Western blot analysis (**Fig. 5.8 A.**), but livers of *Tmco6*-KO 3

month-old male mice showed no reduction in quantity of a single CI-containing supercomplex (**Fig. 6.30**). Perhaps repeating this experiment in CI deficient tissues such as skeletal muscle and hearts would show differently. These models demonstrate CI deficiency owing to depletion or reduction of TMCO6/Tmco6 steady-state levels, independently linking TMCO6 to CI function, assembly and/or stability.

Lastly, we questioned whether we could use the hearts of 3 month-old *Tmco6*-KO mice in order to 1) perform functional complementation rescue experiments with the human WT *TMCO6* cDNA sequence (NM_018502.5), and 2) to validate the pathogenicity of the human patient mutation (NP_060972.3: p.Arg91Cys) in causing mitochondrial disease. We devised an AAV9-mediated gene delivery strategy to administer either the WT or patient mutant human cDNA sequences to KO or WT young adult mice (**Fig. 7.1 A.**). This process led to the creation of 4 distinct transgenic groups: *Tmco6*$^{+/+\ (AAV\ WT)}$, *Tmco6*$^{+/+\ (AAV\ MUT)}$, *Tmco6*$^{-/-\ (AAV\ WT)}$, and *Tmco6*$^{-/-\ (AAV\ MUT)}$. In summary of the various results pertaining to the *Tmco6*$^{-/-\ (AAV\ MUT)}$ mice group, these animals were generally smaller than the complemented *Tmco6*$^{-/-\ (AAV\ WT)}$ group (**Fig. 7.2**)., exhibited more severe hindlimb clasping (**Fig. 7.3**), significantly worse performance by treadmill testing (**Fig. 7.4 A.**), somewhat worse performances for rotarod and pole tests (**Fig. 7.4 B.** and **C.**), displayed less overall locomotor exploratory and movement via CLAMS monitoring during the day and night (**Fig. 7.5**), exhibited significantly worst right ventricular function and presence of atrial flutter (**Table 7.1**), whereas *Tmco6*$^{-/-\ (AAV\ MUT)}$ mice did not, and they showed statistically faster respiratory rates (**Table 7.2**), severe cardiac fibrosis (**Fig. 7.9**), and finally, significantly reduced CI/CS activity (**Fig. 7.10**). Conversely, *Tmco6*$^{-/-\ (AAV\ WT)}$ mice showed rescued CI deficiency in cardiac tissue (**Fig. 7.10**) and no such cardiac fibrosis (**Fig. 7.9)**. These results were crucial in verifying pathogenicity of the human mutant variant and its inability to rescue CI deficiency due to *Tmco6*-ablation.

In summary we have shown that TMCO6 is a new human mitochondrial disease gene, leading to isolated, tissue-specific CI deficiency, epilepsy, neuropathy, and potentially cardiomyopathy. The patient mutant variant originally identified by WES (NM_018502.5: c.271C>T, NP_060972.3: p.Arg91Cys) is not capable of rescuing CI deficiency, nor any of its associated phenotypes, in a *Tmco6*-ablated murine model, and in fact, leads to novel onset of cardiac fibrosis. We do not yet know a mechanism of action for the human TMCO6 protein but suggest that it plays a role in Q-module stability and/or N-module assembly during CI biogenesis.

8.2 Future Aims

8.2.1 COA7 Project Future Aims

Any objectives of future work regarding COA7 would be to better define its role in COX biogenesis. This could be achieved in a number of ways; three are mentioned below.

Pulse-chase labelling of mitochondria-encoded peptides with [^{35}S]-methionine could be used to verify whether COA7 does in fact only affect downstream of MT-CO1 assembly during COX biogenesis. Cell pellets could be collected at specific time points following an original incubation with radiolabelled [^{35}S]-methionine for patient and control cells. 2D-BNGE and Western blotting could then be performed with subsequent immunodetection of various COX subunits to establish COX assembly kinetics of patient cells, control cells and patient cells complemented with *COA7*^{WT}. This technique has been used previously to determine impaired COX biogenesis in cultured skin fibroblasts from a human patient with a pathogenic mutant in *PET100* (Lim *et al.*, 2014).

As another means of investigation, immunoprecipitation experiments using primary antibodies raised against subunits of the MT-CO2 module, MT-CO2, COX5B, COX6C, COX7C, COX8A and, potentially, COX7B (Signes and Fernandez-Vizarra 2018), could be performed to observe whether COA7 co-interacts with any of these. This method could also be performed in reverse with anti-COA7 as the cross-linked bait antibody.

Generation of a *COA7*-knockout cellular model by CRISPR/Cas9, either in haploid or diploid human cells, could be useful to determine whether COA7 ablation is indeed viable in human cells, since this cannot be proven (but is not expected to be the case). Additionally, these cells could be assessed using the two methods described above to better study the exact step in COX biogenesis in which COA7 acts.

8.2.2 TMCO6 Project Future Aims

Much is still needed to elucidate the function of TMCO6 and to better understand its association with CI *in vivo*. In addition to main efforts being to determine the functional role of *TMCO6*, work should also be conducted to identify and characterise other mitochondrial disease patients whose syndromes are caused by *TMCO6* mutant variants, in order to better understand any variabilities in presentations of mitochondrial disease arising from *TMCO6* mutations, and also to investigate therapeutic options using the *Tmco6*-KO mice.

For the latter, searching through databases of patients with CI deficiencies that have undiagnosed molecular causes could yield other pathogenic *TMCO6* mutant variants. Detection of additional patients would also allow for phenotypic comparison with the proband described in this work, potentially leading to a defined set of characteristics for mitochondrial diseases resulting from pathogenicity of *TMCO6*.

For functional determination, CI complexomics combined with SILAC and quantitative mass spectrometry (Wang and Huang, 2008), could be used to determine perturbations to normal CI biogenesis as a result of changes to TMCO6 steady-state level. The aim of this work would be to investigate the role of TMCO6 in CI biogenesis by identifying whether it is found accumulated in certain CI subassemblies. For this, the inducible *TMCO6.1-HA* overexpressing HEK 293T cellular model could be used as the cellular basis of this experiment so that the TMCO6 steady-state level was higher than normal. Additionally, *Tmco6*-KO MEFs could be used since they are fast-growing and would showcase any CI assembly stalling or abnormalities due to total lack of Tmco6 protein, even if these cells do not have CI enzymatic deficiency.

2D-BNGE using samples prepared from transduced mice hearts (from the $Tmco6^{+/+\ (AAV\ WT)}$ group, for example) and immunodetection with an anti-HA antibody could be used to verify the result we found so far using the endogenous human anti-TMCO6 antibody that TMCO6 co-migrates partially with fully assembled CI. We have shown that HA-tagged TMCO6 localises to the mitochondria in immunoprecipitation experiments using the inducible overexpression HEK 293T cellular model, but have not shown the co-migration of HA-tagged TMCO6 and CI by 2D-BNGE in these cells. So far we have not proven this 2D-BNGE result by an independent means, and have only done so with the anti-TMCO6 endogenous antibody.

In order to better determine whether there was in fact a reduction in mitochondrial mass as a result of the human mutant variant of the TMCO6 protein, super resolution microscopy techniques could be used for patient fibroblasts and counterpart control cell lines. Staining of

the mitochondrial network using a mitochondrial marker, such as TOMM20, could reveal disruptions to the mitochondrial network and quantification methods could be used to quantify the signal intensity per cell area to reveal any significant differences in overall mitochondrial mass for patient cells versus controls.

The *Tmco6*-knockout murine model could be used for therapeutic treatment experiments to observe any ameliorative effects on the neurological, locomotor and physical presentation of this strain by using established or novel therapeutic treatments; either those that are already approved in the treatment of mitochondrial diseases, such as supplemental CoQ_{10} (Nightingale *et al.*, 2016), or novel therapeutic options for countering cardiomyopathy or CI deficiency could be explored if desired. This Tmco6-knockout model could also be used in the study of anti-epileptic drugs since it is a novel model of spontaneous epilepsy.

Mice electrocardiography could be additionally assessed by invasive electrode monitoring using classical ECG leads (Gao *et al.*, 2011). This would aid in generating consistent and strong electrophysiological data for comparison. We found that the non-invasive approach used here led to some differences in amplitudes and variable qualities of traces between mice of different sizes (smaller mice yielded higher quality traces than did larger/fatter mice), which proved difficult for monitoring 12 month old wildtype animals.

Repeating SDS-PAGE and blotting for various CI subunits should be performed for 12 month-old (aged) tissues to determine if the decreases in NDUFS1 and NDUFS6 N-module subunits seen in aged hearts are similarly changed in other tissue types. This method could also identify reductions or increases in other CI subunit levels or assembly factors in aged animal tissues, potentially.

References

Acín-Pérez, R. *et al.* (2008) 'Respiratory Active Mitochondrial Supercomplexes', *Molecular Cell*, 32(4), pp. 529–539. doi: 10.1016/j.molcel.2008.10.021.

Adzhubei, I. A. *et al.* (2010) 'A Method and Server for Predicting Damaging Missense Mutations', *Nature Methods*, 7(4), pp. 248–249. doi: 10.1038/nmeth0410-248.

Agip, A. N. A. *et al.* (2018) 'Cryo-EM Structures of Complex I from Mouse Heart Mitochondria in Two Biochemically Defined States', *Nature Structural and Molecular Biology*, 25(7), pp. 548–556. doi: 10.1038/s41594-018-0073-1.

Aich, A. *et al.* (2018) 'COX16 Promotes COX2 Metallation and Assembly During Respiratory Complex IV Biogenesis', *eLife*, 7, p. e32572. doi: 10.7554/eLife.32572.

Akram, M. (2014) 'Citric Acid Cycle and Role of Its Intermediates in Metabolism', *Cell Biochemistry and Biophysics*, 68(3), pp. 475–478. doi: 10.1007/s12013-013-9750-1.

Alston, C. L. *et al.* (2016) 'Biallelic Mutations in TMEM126B Cause Severe Complex I Deficiency with a Variable Clinical Phenotype', *American Journal of Human Genetics*, 99(1), pp. 217–227. doi: 10.1016/j.ajhg.2016.05.021.

Alston, C. L. *et al.* (2017) 'The Genetics and Pathology of Mitochondrial Disease', *Journal of Pathology*, 241(2), pp. 236–250. doi: 10.1002/path.4809.

Alston, C. L. *et al.* (2018) 'Biallelic Mutations in NDUFA6 Establish Its Role in Early-Onset Isolated Mitochondrial Complex I Deficiency', *American Journal of Human Genetics*, 103(4), pp. 592–601. doi: 10.1016/j.ajhg.2018.08.013.

Altmann, R. (1894) 'Die Elementarorganismen Und Ihre Beziehungen zu Den Zellen', *Die Elementarorganismen und ihre Beziehungen zu den Zellen*. Leipzig, p. 141. doi: 10.1109/PTC.2011.6019281.

Alvarez-Paggi, D. *et al.* (2017) 'Multifunctional Cytochrome c: Learning New Tricks from an Old Dog', *Chemical Reviews*, 117(21), pp. 13382–13460. doi: 10.1021/acs.chemrev.7b00257.

Amand, M. M., Hanover, J. and Shiloach, J. (2016) 'A Comparison of Strategies for Immortalizing Mouse Embryonic Fibroblasts', *Journal of Biological Methods*, 3(2), p. 41. doi: 10.14440/jbm.2016.110.

Amiott, E. A. and Jaehning, J. A. (2006) 'Mitochondrial Transcription Is Regulated via an ATP "Sensing" Mechanism that Couples RNA Abundance to Respiration', *Molecular Cell*, 22(3), pp. 329–338. doi: 10.1016/j.molcel.2006.03.031.

Amorim, A., Fernandes, T. and Taveira, N. (2019) 'Mitochondrial DNA in Human Identification: a Review', *PeerJ*, 7, p. e7314. doi: 10.7717/peerj.7314.

Andersson, S. G. E. *et al.* (1998) 'The Genome Sequence of Rickettsia prowazekii and the Origin of Mitochondria', *Nature*, 398(6707), pp. 133–140. doi: 10.1038/24094.

Andrews, B. *et al.* (2013) 'Assembly Factors for the Membrane Arm of Human Complex I', *Proceedings of the National Academy of Sciences of the United States of America*, 110(47), pp. 18934–18939. doi: 10.1073/pnas.1319247110.

Andrews, R. M. *et al.* (1999) 'Reanalysis and Revision of the Cambridge Reference Sequence for Human Mitochondrial DNA', *Nature Genetics*, 23(2), p. 147. doi: 10.1038/13779.

Antonicka, H., Leary, S. C., *et al.* (2003) 'Mutations in COX10 Result in a Defect in Mitochondrial Heme A Biosynthesis and Account for Multiple, Early-Onset Clinical Phenotypes Associated with Isolated COX Deficiency', *Human Molecular Genetics*, 12(20), pp. 2693–2702. doi: 10.1093/hmg/ddg284.

Antonicka, H., Mattman, A., *et al.* (2003) 'Mutations in COX15 Produce a Defect in the Mitochondrial Heme Biosynthetic Pathway, Causing Early-Onset Fatal Hypertrophic Cardiomyopathy', *American Journal of Human Genetics*, 72(1), pp. 101–114. doi: 10.1086/345489.

Baertling, F. *et al.* (2015) 'Mutations in COA6 Cause Cytochrome c Oxidase Deficiency and Neonatal Hypertrophic Cardiomyopathy', *Human Mutation*, 36(1), pp. 34–38. doi: 10.1002/humu.22715.

Baines, C. P. (2010) 'Role of the Mitochondrion in Programmed Necrosis', *Frontiers in Physiology*, 1, p. 156. doi: 10.3389/fphys.2010.00156.

Balsa, E. *et al.* (2012) 'NDUFA4 is a Subunit of Complex IV of the Mammalian Electron Transport Chain', *Cell Metabolism*, 16(3), pp. 378–386. doi: 10.1016/j.cmet.2012.07.015.

Banting, G. S. and Glerum, M. (2006) 'Mutational Analysis of the Saccharomyces cerevisiae Cytochrome c Oxidase Assembly Protein Cox11p', *Eukaryotic Cell*, 5(3), pp. 568–578. doi: 10.1128/EC.5.3.568-578.2006.

Barnhart, E. (2016) 'Mechanics of Mitochondrial Motility in Neurons', *Current Opinion in Cell Biology*, 38(1), pp. 90–99. doi: 10.1016/j.ceb.2016.02.022.

Benda, C. (1898) *Uber Die Spermatogenese Der Vertebraten und Hoeherer Everte- Braten. II. Die Histiogenese Der Spermien*, *Archiv Für Anatomie Und Physiologie*.

Bénit, P. *et al.* (2001) 'Large-Scale Deletion and Point Mutations of the Nuclear NDUFV1 and NDUFS1 Genes in Mitochondrial Complex I Deficiency', *American Journal of Human Genetics*, 68(6), pp. 1344–1352. doi: 10.1086/320603.

Benz, R. (1985) 'Porin from Bacterial and Mitochondrial Outer Membrane', *Critical Reviews in Biochemistry and Molecular Biology*, 19(2), pp. 145–190. doi: 10.3109/10409238509082542.

Benz, R. and McLaughlin, S. (1983) 'The Molecular Mechanism of Action of the Proton Ionophore FCCP (Carbonylcyanide p-Trifluoromethoxyphenylhydrazone)', *Biophysical Journal*, 41(3), pp. 381–398. doi: 10.1016/S0006-3495(83)84449-X.

Berrisford, J. M. and Sazanov, L. A. (2009) 'Structural Basis for the Mechanism of Respiratory Complex I', *Journal of Biological Chemistry*, 284(43), pp. 29773–29783. doi: 10.1074/jbc.M109.032144.

Bezawork-Geleta, A. *et al.* (2017) 'Mitochondrial Complex II: At the Crossroads', *Trends in Biochemical Sciences*, 42(4), pp. 312–325. doi: 10.1016/j.tibs.2017.01.003.

Blaza, J. N. *et al.* (2014) 'Kinetic Evidence against Partitioning of the Ubiquinone Pool and the Catalytic Relevance of Respiratory Chain Supercomplexes', *Proceedings of the National Academy of Sciences*, 111(44), pp. 15735–15740. doi: 10.1073/pnas.1413855111.

Bode, M. *et al.* (2015) 'Redox-Regulated Dynamic Interplay Between Cox19 and the Copper-Binding Protein Cox11 in the Intermembrane Space of Mitochondria Facilitates Biogenesis of Cytochrome c Oxidase', *Molecular Biology of the Cell*, 26(13), pp. 2385–2401. doi: 10.1091/mbc.E14-11-1526.

Bogenhagen, D. F. (2012) 'Mitochondrial DNA Nucleoid Structure', *BBA - Gene Regulatory Mechanisms*. Elsevier B.V., 1819(9–10), pp. 914–920. doi: 10.1016/j.bbagrm.2011.11.005.

Boland, T. and Ratner, B. D. (1995) 'Direct Measurement of Hydrogen Bonding in DNA Nucleotide Bases by Atomic Force Microscopy', *Proceedings of the National Academy of Sciences*, 69(5), pp. 2125–2130. doi: 10.1073/pnas.92.12.5297.

van Bon, B. W. M. *et al.* (2013) 'CEP89 is Required for Mitochondrial Metabolism and Neuronal Function in Man and Fly', *Human Molecular Genetics*, 22(15), pp. 3138–3151. doi: 10.1093/hmg/ddt170.

Bonora, M. *et al.* (2012) 'ATP Synthesis and Storage', *Purinergic Signalling*, 8(3), pp. 343–357. doi: 10.1007/s11302-012-9305-8.

Botstein, D. and Risch, N. (2003) 'Discovering Genotypes Underlying Human Phenotypes: Past Successes for Mendelian Disease, Future Approaches for Complex Disease', *Nature Genetics*, 33, pp. 228–237. doi: 10.1038/ng1090.

Bourens, M. *et al.* (2013) 'Redox and Reactive Oxygen Species Regulation of Mitochondrial Cytochrome C Oxidase Biogenesis', *Antioxidants and Redox Signaling*, 19(16), pp. 1940–1952. doi: 10.1089/ars.2012.4847.

Bourens, M. *et al.* (2014) 'Human COX20 Cooperates with SCO1 and SCO2 to Mature COX2 and Promote the Assembly of Cytochrome c Oxidase', *Human Molecular Genetics*, 23(11), pp. 2901–2913. doi: 10.1093/hmg/ddu003.

Bourens, M. and Barrientos, A. (2017a) 'A CMC 1-Knockout Reveals Translation-Independent Control of Human Mitochondrial Complex IV Biogenesis', *EMBO reports*, 18(3), pp. 477–494. doi: 10.15252/embr.201643103.

Bourens, M. and Barrientos, A. (2017b) 'Human Mitochondrial Cytochrome c Oxidase Assembly Factor COX18 Acts Transiently as a Membrane Insertase within the Subunit 2 Maturation Module', *Journal of Biological Chemistry*, 292(19), pp. 7774–7783. doi: 10.1074/jbc.M117.778514.

Bragoszewski, P. *et al.* (2015) 'Retro-Translocation of Mitochondrial Intermembrane Space Proteins', *Proceedings of the National Academy of Sciences*, 112(25), pp. 7713–7718. doi: 10.1073/pnas.1504615112.

Brandes, R. and Bers, D. M. (1997) 'Intracellular Ca2+ Increases the Mitochondrial NADH Concentration During Elevated Work in Intact Cardiac Muscle', *Circulation Research*, 80(1), pp. 82–87. doi: 10.1161/01.RES.80.1.82.

Calvaruso, M. A., Smeitink, J. and Nijtmans, L. (2008) 'Electrophoresis Techniques to Investigate Defects in Oxidative Phosphorylation', *Methods*, 46(4), pp. 281–287. doi: 10.1016/j.ymeth.2008.09.023.

Cannon, B. and Nedergaard, J. (2004) 'Brown Adipose Tissue: Function and Physiological Significance', *Physiological Reviews*, 84(1), pp. 277–359. doi: 10.1152/physrev.00015.2003.

Cannon, B. and Nedergaard, J. (2011) 'Nonshivering Thermogenesis and its Adequate Measurement in Metabolic Studies', *Journal of Experimental Biology*, 214(2), pp. 242–253. doi: 10.1242/jeb.050989.

Carafoli, E. and Lehninger, A. L. (1971) 'A Survey of the Interaction of Calcium Ions with Mitochondria from Different Tissues and Species', *The Biochemical Journal*, 122(5), pp. 681–690. doi: 10.1042/bj1220681.

Carroll, J. *et al.* (2006) 'Bovine Complex I is a Complex of 45 Different Subunits', *Journal of Biological Chemistry*, 281(43), pp. 32724–32727. doi: 10.1074/jbc.M607135200.

Castro, B. and Kuang, S. (2017) 'Evaluation of Muscle Performance in Mice by Treadmill Exhaustion Test and Whole-Limb Grip Strength Assay', *Bio-Protocol*, 7(8), p. e2237. doi: 10.21769/BioProtoc.2237.

Cavalier-Smith, T. (1987) 'Eukaryotes with No Mitochondria', *Nature*, 326, pp. 332–222. doi: 10.1038/326332a0.

Cavender, J. F. *et al.* (1995) 'Simian Virus 40 Large T Antigen Contains Two Independent Activities That Cooperate With a Ras Oncogene to Transform Rat Embryo Fibroblasts', *Journal of Virology*, 69(2), pp. 923–934.

Cerqua, C. *et al.* (2018) 'COX16 is Required for Assembly of Cytochrome c Oxidase in Human Cells and is Involved in Copper Delivery to COX2', *Biochimica et Biophysica Acta - Bioenergetics*. Elsevier, 1859(4), pp. 244–252. doi: 10.1016/j.bbabio.2018.01.004.

Challa, S. *et al.* (2004) 'Diagnosis of Mitochondrial Diseases: Clinical and Histological Study of Sixty Patients with Ragged Red Fibers', *Neurology India*, 52(3), pp. 353–358.

Chen, Y. C. *et al.* (2012) 'Identification of a Protein Mediating Respiratory Supercomplex Stability', *Cell Metabolism*, 15(3), pp. 348–360. doi: 10.1016/j.cmet.2012.02.006.

Chinnery, P. F. and Hudson, G. (2013) 'Mitochondrial Genetics', *British Medical Bulletin*, 106(1), pp. 135–159. doi: 10.1093/bmb/ldt017.

Choi, H. J. and Weis, W. I. (2005) 'Structure of the Armadillo Repeat Domain of Plakophilin 1', *Journal of Molecular Biology*, 346(1), pp. 367–376. doi: 10.1016/j.jmb.2004.11.048.

Choi, M. *et al.* (2009) 'Genetic Diagnosis by Whole Exome Capture and Massively Parallel DNA Sequencing', *Proceedings of the National Academy of Sciences of the United States of America*, 106(45), pp. 19096–190101. doi: 10.1073/pnas.0910672106.

Church, C. *et al.* (2005) 'A Role for Pet100p in the Assembly of Yeast Cytochrome c Oxidase: Interaction with a Subassembly that Accumulates in a Pet100 Mutant', *Journal of Biological Chemistry*, 280(3), pp. 1854–1863. doi: 10.1074/jbc.M410726200.

Čížková, A. *et al.* (2008) 'TMEM70 Mutations Cause Isolated ATP Synthase Deficiency and Neonatal Mitochondrial Encephalocardiomyopathy', *Nature Genetics*, 40(11), pp. 1288–1290. doi: 10.1038/ng.246.

Clay Montier, L. L., Deng, J. J. and Bai, Y. (2009) 'Number Matters: Control of Mammalian Mitochondrial DNA Copy Number', *Journal of Genetics and Genomics*, 36(3), pp. 125–131. doi: 10.1016/S1673-8527(08)60099-5.

Cost, G. J. and Cozzarelli, N. R. (2007) 'Directed Assembly of DNA Molecules via Simultaneous Ligation and Digestion', *Biotechniques*, 42(1), pp. 84–89. doi: 10.2144/000112283.

Cree, L. M., Samuels, D. C. and Chinnery, P. F. (2009) 'The Inheritance of Pathogenic Mitochondrial DNA Mutations', *Biochimica et Biophysica Acta - Molecular Basis of Disease*, 1792(12), pp. 1097–1102. doi: 10.1016/j.bbadis.2009.03.002.

Cui, J. *et al.* (2019) 'LRPPRC: A Multifunctional Protein Involved in Energy Metabolism and Human Disease', *Frontiers in Physiology*, 10, p. 595. doi: 10.3389/fphys.2019.00595.

Danial, N. N. and Korsmeyer, S. J. (2004) 'Cell Death: Critical Control Points', *Cell*, 116(2), pp. 205–219. doi: 10.1016/S0092-8674(04)00046-7.

Davies, K. M., Blum, T. B. and Kühlbrandt, W. (2018) 'Conserved In Situ Arrangement of Complex I and III2 in Mitochondrial Respiratory Chain Supercomplexes of Mammals, Yeast, and Plants', *Proceedings of the National Academy of Sciences of the United States of America*, 115(12), pp. 3024–3029. doi: 10.1073/pnas.1720702115.

Davis, C. W. *et al.* (2010) 'Nitration of the Mitochondrial Complex I Subunit NDUFB8 Elicits RIP1- and RIP3-Mediated Necrosis', *Free Radical Biology and Medicine*, 48(2), pp. 306–317. doi: 10.1016/j.freeradbiomed.2009.11.001.

Denko, N. *et al.* (2000) 'Epigenetic Regulation of Gene Expression in Cervical Cancer Cells by the Tumor Microenvironment', *Clinical Cancer Research*, 6(2), pp. 480–487.

Desler, C., Lykke, A. and Rasmussen, L. J. (2010) 'The Effect of Mitochondrial Dysfunction on Cytosolic Nucleotide Metabolism', *Journal of Nucleic Acids*. SAGE-Hindawi Access to Research, 2010, p. 701518. doi: 10.4061/2010/701518.

Ding, W. X. and Yin, X. M. (2012) 'Mitophagy: Mechanisms, Pathophysiological Roles, and Analysis', *Biological Chemistry*, 393(7), pp. 547–564. doi: 10.1515/hsz-2012-0119.

Distelmaier, F. *et al.* (2009) 'Mitochondrial Complex I Deficiency: From Organelle Dysfunction to Clinical Disease', *Brain*, 132(4), pp. 833–842. doi: 10.1093/brain/awp058.

Dizdaroglu, M. *et al.* (2002) 'Free Radical-Induced Damage to DNA: Mechanisms and Measurement', *Free Radical Biology and Medicine*, 32(11), pp. 1102–1115. doi: 10.1016/S0891-5849(02)00826-2.

Dröge, W. (2002) 'Free Radicals in the Physiological Control of Cell Function', *Physiological Reviews*, 82(1), pp. 47–95. doi: 10.1152/physrev.00018.2001.

Du, C. *et al.* (2000) 'SMAC, a Mitochondrial Protein that Promotes Cytochrome c-Dependent Caspase Activation by Eliminating IAP Inhibition', *Cell*, 102(1), pp. 33–42. doi: 10.1016/S0092-8674(00)00008-8.

Duchen, M. R. (2004) 'Roles of Mitochondria in Health and Disease', *Diabetes*, Suppl 1, pp. S96–S102. doi: 10.2337/diabetes.53.2007.s96.

Dudkina, N. V. *et al.* (2005) 'Structure of a Mitochondrial Supercomplex Formed by Respiratory Chain Complexes I and III', *Proceedings of the National Academy of Sciences of the United States of America*, 102(9), pp. 3225–3229. doi: 10.1073/pnas.0408870102.

Dzbek, J. and Korzeniewski, B. (2008) 'Control Over the Contribution of the Mitochondrial Membrane Potential (ΔΨ) and Proton Gradient (ΔpH) to the Protonmotive Force (Δp): In Silico Studies', *Journal of Biological Chemistry*, 283(48), pp. 33232–33239. doi: 10.1074/jbc.M802404200.

Elston, T., Wang, H. and Oster, G. (1998) 'Energy Transduction in ATP Synthase', *Nature*, 391(6666), pp. 510–513. doi: 10.1038/35185.

Embley, T. M. and Martin, W. (2006) 'Eukaryotic Evolution, Changes and Challenges', *Nature*, 440(7084), pp. 623–630. doi: 10.1038/nature04546.

Ernster, L. and Dallner, G. (1995) 'Biochemical, Physiological and Medical Aspects of Ubiquinone Function', *Biochimica et Biophysica Acta - Molecular Basis of Disease*, 1271(1), pp. 195–204. doi: 10.1016/0925-4439(95)00028-3.

Ernster, L. and Schatz, G. (1981) 'Mitochondria : A Historical Review', *Journal of Cell Biology*, 91(3), pp. 227s-255s.

Evans, D. R. and Guy, H. I. (2004) 'Mammalian Pyrimidine Biosynthesis: Fresh Insights into an Ancient Pathway', *Journal of Biological Chemistry*, 279(32), pp. 33035–33038. doi: 10.1074/jbc.R400007200.

Fassone, E. *et al.* (2010) 'FOXRED1, Encoding an FAD-Dependent Oxidoreductase Complex-I-Specific Molecular Chaperone, is Mutated in Infantile-Onset Mitochondrial Encephalopathy', *Human Molecular Genetics*, 19(24), pp. 4837–4847. doi: 10.1093/hmg/ddq414.

Fernández-Vizarra, E. *et al.* (2010) 'Isolation of Mitochondria for Biogenetical Studies: An Update', *Mitochondrion*, 10(3), pp. 253–262. doi: 10.1016/j.mito.2009.12.148.

Fernández-Vizarra, E., Tiranti, V. and Zeviani, M. (2009) 'Assembly of the Oxidative Phosphorylation System in Humans: What We have Learned by Studying its Defects', *Biochimica et Biophysica Acta - Molecular Cell Research*, 1793(1), pp. 200–211. doi: 10.1016/j.bbamcr.2008.05.028.

Fiedorczuk, K. and Sazanov, L. A. (2018) 'Mammalian Mitochondrial Complex I Structure and Disease-Causing Mutations', *Trends in Cell Biology*, 28(10), pp. 835–867. doi: 10.1016/j.tcb.2018.06.006.

Finsterer, J. and Zarrouk-Mahjoub, S. (2018) 'Biomarkers for Detecting Mitochondrial Disorders', *Journal of Clinical Medicine*, 7(2), p. 16. doi: 10.3390/jcm7020016.

Fischer, L. R. *et al.* (2011) 'SOD1 Targeted to the Mitochondrial Intermembrane Space Prevents Motor Neuropathy in the Sod1 Knockout Mouse', *Brain*, 134(1), pp. 196–209. doi: 10.1093/brain/awq314.

Fontanesi, F., Soto, I. C. and Barrientos, A. (2008) 'Cytochrome c Oxidase Biogenesis: New Levels of Regulation', *IUBMB Life*, 60(9), pp. 557–568. doi: 10.1002/iub.86.

Ford Doolittle, W. (1998) 'You are What You Eat: A Gene Transfer Ratchet Could Account for Bacterial Genes in Eukaryotic Nuclear Genomes', *Trends in Genetics*, 14(8), pp. 307–311. doi: 10.1016/S0168-9525(98)01494-2.

Fornuskova, D. *et al.* (2010) 'Novel Insights into the Assembly and Function of Human Nuclear-Encoded Cytochrome c Oxidase Subunits 4, 5a, 6a, 7a and 7b', *Biochemical Journal*, 428(3), pp. 363–374. doi: 10.1042/BJ20091714.

Forte, M. *et al.* (2019) 'Mitochondrial Complex I Deficiency and Cardiovascular Diseases: Current Evidence and Future Directions', *Journal of Molecular Medicine*, 97(5), pp. 579–591. doi: 10.1007/s00109-019-01771-3.

Gammage, P. A. *et al.* (2018) 'Genome Editing in Mitochondria Corrects a Pathogenic mtDNA Mutation In Vivo', *Nature Medicine*. Springer US, 24(11), pp. 1691–1695. doi: 10.1038/s41591-018-0165-9.

Gammage, P. A. and Frezza, C. (2019) 'Mitochondrial DNA: The Overlooked Oncogenome?', *BioMed Central Biology*, 17(53), pp. 1–10. doi: 10.1186/s12915-019-0668-y.

Gao, S. *et al.* (2011) 'Echocardiography in Mice', *Current protocols in mouse biology*, 1, pp. 71–83. doi: 10.1002/9780470942390.mo100130.

Garcia, C. J. *et al.* (2017) 'Regulation of Mitochondrial Complex I Biogenesis in Drosophila Flight Muscles', *Cell Reports*, 20(1), pp. 264–278. doi: 10.1016/j.celrep.2017.06.015.

Ghezzi, D. *et al.* (2008) 'FASTKD2 Nonsense Mutation in an Infantile Mitochondrial Encephalomyopathy Associated with Cytochrome C Oxidase Deficiency', *American Journal of Human Genetics*, 83(3), pp. 415–423. doi: 10.1016/j.ajhg.2008.08.009.

Ghezzi, D. *et al.* (2009) 'Paroxysmal Non-Kinesigenic Dyskinesia is Caused by Mutations of the MR-1 Mitochondrial Targeting Sequence', *Human Molecular Genetics*, 18(6), pp. 1058–1064. doi: 10.1093/hmg/ddn441.

Ghezzi, D. and Zeviani, M. (2012) 'Assembly Factors of Human Mitochondrial Respiratory Chain Complexes: Physiology and Pathophysiology', *Advances in Experimental Medicine and Biology*, 748, pp. 65–106. doi: 10.1007/978-1-4614-3573-0_4.

Ghezzi, D. and Zeviani, M. (2018) 'Human Diseases Associated with Defects in Assembly of OXPHOS Complexes', *Essays in Biochemistry*, 62(3), pp. 271–286. doi: 10.1042/EBC20170099.

Ghosh, A. *et al.* (2016) 'Mitochondrial Disease Genes COA6, COX6B and SCO2 have Overlapping Roles in COX2 Biogenesis', *Human Molecular Genetics*, 25(4), pp. 660–671. doi: 10.1093/hmg/ddv503.

Glerum, M. D., Shtanko, A. and Tzagoloff, A. (1996a) 'Characterization of COX17, a Yeast Gene Involved in Copper Metabolism and Assembly of Cytochrome Oxidase', *Journal of Biological Chemistry*, 271(24), pp. 14504–14509. doi: 10.1074/jbc.271.24.14504.

Glerum, M. D., Shtanko, A. and Tzagoloff, A. (1996b) 'Characterization of COX17, a Yeast Gene Involved in Copper Metabolism and Assembly of Cytochrome Oxidase', *Journal of Biological Chemistry*, 271(24), pp. 14504–14509. doi: 10.1074/jbc.271.24.14504.

Gorman, G. S. *et al.* (2015) 'Prevalence of Nuclear and Mitochondrial DNA Mutations Related to Adult Mitochondrial Disease', *Annals of Neurology*, 77(5), pp. 753–759. doi: 10.1002/ana.24362.

Gorman, G. S. *et al.* (2016) 'Mitochondrial Diseases', *Nature Reviews Disease Primers*. Macmillan Publishers Limited, 2(16080), pp. 1–23. doi: 10.1038/nrdp.2016.80.

Gossen, M. *et al.* (1995) 'Transcriptional Activation by Tetracyclines in Mammalian Cells', *Science*, 268(5218), pp. 1766–1769. doi: 10.1126/science.7792603.

Gu, B. and Dalton, K. A. (2017) 'Models and Detection of Spontaneous Recurrent Seizures in Laboratory Rodents', *Zoological Research*, 38(4), pp. 171–179. doi: 10.24272/j.issn.2095-8137.2017.042.

Guda, P., Guda, C. and Subramaniam, S. (2007) 'Reconstruction of Pathways Associated with Amino Acid Metabolism in Human Mitochondria', *Genomics, Proteomics and Bioinformatics*. Beijing Institute of Genomics, 5(3–4), pp. 166–176. doi: 10.1016/S1672-0229(08)60004-2.

Guerrero-Castillo, S. *et al.* (2017) 'The Assembly Pathway of Mitochondrial Respiratory Chain Complex I', *Cell Metabolism*. Elsevier Inc., 25(1), pp. 128–139. doi: 10.1016/j.cmet.2016.09.002.

Guo, R. *et al.* (2017) 'Architecture of Human Mitochondrial Respiratory Megacomplex I2III2IV2', *Cell*. Elsevier Inc., 170(6), pp. 1247-1257.e12. doi: 10.1016/j.cell.2017.07.050.

Guo, R. *et al.* (2018) 'Structure and Mechanism of Mitochondrial Electron Transport Chain', *Biomedical Journal*, 41(1), pp. 9–20. doi: 10.1016/j.bj.2017.12.001.

Guyenet, S. J. *et al.* (2010) 'A Simple Composite Phenotype Scoring System for Evaluating Mouse Models of Cerebellar Ataxia', *Journal of Visualized Experiments*. MyJove Corporation, 1(39), p. e1787. doi: 10.3791/1787.

Halliwell, B. and Cross, C. E. (1994) 'Oxygen-Derived Species: Their Relation to Human Disease and Environmental Stress', *Environmental Health Perspectives*, 102(10), pp. S5–S12. doi: 10.2307/3432205.

Hallmann, K. *et al.* (2016) 'Loss of the Smallest Subunit of Cytochrome c Oxidase, COX8A, Causes Leigh-Like Syndrome and Epilepsy', *Brain*, 139(2), pp. 338–345. doi: 10.1093/brain/awv357.

Hatefi, Y. (1985) 'The Mitochondrial Electron Transport and Oxidative Phosphorylation System', *Annual Review of Biochemistry*, 54, pp. 1015–1069. doi: 10.1146/annurev.biochem.54.1.1015.

Hayashi, T. *et al.* (2015) 'Higd1a is a Positive Regulator of Cytochrome c Oxidase', *Proceedings of the National Academy of Sciences of the United States of America*, 112(5), pp. 1553–1558. doi: 10.1073/pnas.1419767112.

Hayflick, L. and Moorhead, P. S. (1961) 'The Serial Cultivation of Human Diploid Cell Strains', *Experimental Cell Research*, 25(3), pp. 585–621. doi: 10.1016/0014-4827(61)90192-6.

Heath-Engel, H. M. and Shore, G. C. (2006) 'Mitochondrial Membrane Dynamics, Cristae Remodelling and Apoptosis', *Biochimica et Biophysica Acta - Molecular Cell Research*, 1763(5–6), pp. 549–560. doi: 10.1016/j.bbamcr.2006.02.006.

Hegde, A. N. and Upadhya, S. C. (2011) 'Role of Ubiquitin-Proteasome-Mediated Proteolysis in Nervous System Disease', *Biochimica et Biophysica Acta - Gene Regulatory Mechanisms*, 1809(2), pp. 128–140. doi: 10.1016/j.bbagrm.2010.07.006.

Heide, H. *et al.* (2012) 'Complexome Profiling Identifies TMEM126B as a Component of the Mitochondrial Complex I Assembly Complex', *Cell Metabolism*, 16(4), pp. 538–549. doi: 10.1016/j.cmet.2012.08.009.

Hempel, N. and Trebak, M. (2017) 'Crosstalk Between Calcium and Reactive Oxygen Species Signaling in Cancer', *Cell Calcium*, 63, pp. 70–96. doi: 10.1016/j.ceca.2017.01.007.

Herrero-Martín, M. D. *et al.* (2008) 'A New Pathologic Mitochondrial DNA Mutation in the Cytochrome Oxidase Subunit I (MT-CO1)', *Human Mutation*, 29(8), pp. 112–122. doi: 10.1002/humu.20800.

Higuchi, Y. *et al.* (2018) 'Mutations in COA7 Cause Spinocerebellar Ataxia with Axonal Neuropathy', *Brain*, 141(6), pp. 1622–1636. doi: 10.1093/brain/awy104.

Hirst, J. *et al.* (2003) 'The Nuclear Encoded Subunits of Complex I from Bovine Heart Mitochondria', *Biochimica et Biophysica Acta - Bioenergetics*, 1604(3), pp. 135–150. doi: 10.1016/S0005-2728(03)00059-8.

Hirst, J. (2010) 'Towards the Molecular Mechanism of Respiratory Complex I', *Biochemical Journal*, 425(2), pp. 327–339. doi: 10.1042/BJ20091382.

Hirst, J. (2011) 'Why Does Mitochondrial Complex I Have So Many Subunits?', *Biochemical Journal*, 437(2), pp. E1-3. doi: 10.1042/BJ20110918.

Hirst, J. (2013) 'Mitochondrial Complex I', *Annual Review of Biochemistry*, 82(1), pp. 551–575. doi: 10.1146/annurev-biochem-070511-103700.

Hirst, J. (2018) 'Open Questions: Respiratory Chain Supercomplexes- Why are They There and What Do They Do?', *BioMed Central Biology*, 16(1), p. 111. doi: 10.1186/s12915-018-0577-5.

Hiser, L. *et al.* (2000) 'Cox11p is Required for Stable Formation of the CuB and Magnesium Centers of Cytochrome c Oxidase', *Journal of Biological Chemistry*, 275(1), pp. 619–623. doi: 10.1074/jbc.275.1.619.

Hock, D. H. *et al.* (2019) 'HIGD2A is Required for Assembly of the COX3 Module of Human Mitochondrial Complex IV', *Molecular & Cellular Proteomics*, 2, p. RA120.002076. doi: 10.1101/787721.

Hoefs, S. J. G. *et al.* (2009) 'Baculovirus Complementation Restores a Novel NDUFAF2 Mutation Causing Complex I Deficiency', *Human Mutation*, 30(7), pp. E728-736. doi: 10.1002/humu.21037.

Hoitzing, H., Johnston, I. G. and Jones, N. S. (2015) 'What is the Function of Mitochondrial Networks? A Theoretical Assessment of Hypotheses and Proposal for Future Research', *BioEssays*, 37(6), pp. 687–700. doi: 10.1002/bies.201400188.

Horlbeck, M. A. *et al.* (2018) 'Mapping the Genetic Landscape of Human Cells', *Cell*, 174(4), pp. 953–967. doi: 10.1016/j.cell.2018.06.010.

Horn, D. *et al.* (2010) 'The Conserved Mitochondrial Twin Cx9C Protein Cmc2 is a Cmc1 Homologue Essential for Cytochrome c Oxidase Biogenesis', *Journal of Biological Chemistry*, 285(20), pp. 15088–15099. doi: 10.1074/jbc.M110.104786.

Horn, D., Al-Ali, H. and Barrientos, A. (2008) 'Cmc1p Is a Conserved Mitochondrial Twin CX9C Protein Involved in Cytochrome c Oxidase Biogenesis', *Molecular and Cellular Biology*, 28(13), pp. 4354–4364. doi: 10.1128/mcb.01920-07.

Horn, D. and Barrientos, A. (2008) 'Mitochondrial Copper Metabolism and Delivery to Cytochrome c Oxidase', *IUBMB Life*, 60(7), pp. 421–429. doi: 10.1002/iub.50.

Horvath, S. E. and Daum, G. (2013) 'Lipids of Mitochondria', *Progress in Lipid Research*, 52(4), pp. 590–614. doi: 10.1016/j.plipres.2013.07.002.

Howard, B. H. (1996) 'Replicative Senescence: Considerations Relating to the Stability of Heterochromatin Domains', *Experimental Gerontology*, 31(1–2), pp. 281–293. doi: 10.1016/0531-5565(95)00022-4.

Huber, A. H., Nelson, W. J. and Weis, W. I. (1997) 'Three-Dimensional Structure of the Armadillo Repeat Region of β-Catenin', *Cell*, 90(5), pp. 871–882. doi: 10.1016/S0092-8674(00)80352-9.

Hurst, W. J. (1997) 'Abnormalities of the S-T Segment - Part I', *Clinical Cardiology*, 20(6), pp. 511–520. doi: 10.1002/clc.4960200602.

Hüttemann, M. *et al.* (2011) 'The Multiple Functions of Cytochrome c and Their Regulation in Life and Death Decisions of the Mammalian Cell: From Respiration to Apoptosis', *Mitochondrion*, 11(3), pp. 369–381. doi: 10.1016/j.mito.2011.01.010.

Huynen, M. A. *et al.* (2016) 'Evolution and Structural Organization of the Mitochondrial Contact Site (MICOS) Complex and the Mitochondrial Intermembrane Space Bridging (MIB) Complex', *Biochimica et Biophysica Acta - Molecular Cell Research*, 1863(1), pp. 91–101. doi: 10.1016/j.bbamcr.2015.10.009.

Indrieri, A. *et al.* (2012) 'Mutations in COX7B Cause Microphthalmia with Linear Skin Lesions, an Unconventional Mitochondrial Disease', *American Journal of Human Genetics*. The American Society of Human Genetics, 91(5), pp. 942–949. doi: 10.1016/j.ajhg.2012.09.016.

Ingram, D. K. and Reynolds, M. A. (1986) 'Assessing the Predictive Validity of Psychomotor Tests as Measures of Biological Age in Mice', *Experimental Aging Research*. Routledge, 12(3), pp. 155–162. doi: 10.1080/03610738608259454.

Irwin, M. H., Parameshwaran, K. and Pinkert, C. A. (2013) 'Mouse Models of Mitochondrial Complex I Dysfunction', *International Journal of Biochemistry and Cell Biology*, 45(1), pp. 34–40. doi: 10.1016/j.biocel.2012.08.009.

Janssen, R. J. R. J. *et al.* (2006) 'Mitochondrial Complex I: Structure, Function and Pathology', *Journal of Inherited Metabolic Disease*, 29(4), pp. 499–515. doi: 10.1007/s10545-006-0362-4.

Jastroch, M. *et al.* (2010) 'Mitochondrial Proton and Electron Leaks', *Essays in Biochemistry*, 47, pp. 53–67. doi: 10.1042/BSE0470053.

Jinek, M. *et al.* (2012) 'A Programmable Dual RNA-Guided DNA Endonuclease in Adaptive Bacterial Immunity', *Science*, 337(6096), pp. 816–821. doi: 10.1126/science.1225829.

Jonckheere, A. I. *et al.* (2011) 'Restoration of Complex V Deficiency Caused by a Novel Deletion in the Human TMEM70 Gene Normalizes Mitochondrial Morphology', *Mitochondrion*, 11(6), pp. 954–963. doi: 10.1016/j.mito.2011.08.012.

Jones, D. T. (1999) 'Protein Secondary Structure Prediction Based on Position-Specific Scoring Matrices', *Journal of Molecular Biology*, 292(2), pp. 195–202. doi: 10.1006/jmbi.1999.3091.

Junqueira, L. C. U., Bignolas, G. and Brentani, R. R. (1979) 'Picrosirius Staining Plus Polarization Microscopy, a Specific Method for Collagen Detection in Tissue Sections', *The Histochemical Journal*, 11(4), pp. 447–455. doi: 10.1007/BF01002772.

Kadenbach, B. (2017) 'Regulation of Mammalian 13-Subunit Cytochrome c Oxidase and Binding of Other Proteins: Role of NDUFA4', *Trends in Endocrinology and Metabolism*. Elsevier Ltd, 28(11), pp. 761–770. doi: 10.1016/j.tem.2017.09.003.

Kanduc, D. *et al.* (2002) 'Cell Death: Apoptosis Versus Necrosis', *International Journal of Oncology*, 21(1), pp. 165–170. doi: 10.3892/ijo.21.1.165.

Kawai, H. *et al.* (2007) 'Caspase Cascade Proceeds Rapidly After Cytochrome c Release from Mitochondria in Tumor Necrosis Factor-α-Induced Cell Death', *Journal of Pharmacological Sciences*, 103(2), pp. 159–167. doi: 10.1254/jphs.FP0060877.

Ke, B. X. *et al.* (2012) 'Tissue-Specific Splicing of an Ndufs6 Gene-Trap Insertion Generates a Mitochondrial Complex I Deficiency-Specific Cardiomyopathy', *Proceedings of the National Academy of Sciences of the United States of America*, 109(16), pp. 6165–6170. doi: 10.1073/pnas.1113987109.

Kelley, D. E. *et al.* (2002) 'Dysfunction of Mitochondria in Human Skeletal Muscle in Type 2 Diabetes', *Diabetes*, 51(10), pp. 2944–2950. doi: 10.2337/diabetes.51.10.2944.

Kim, D. W. (2001) 'Real Time Quantitative PCR', *Experimental & molecular medicine*, 331(1), pp. S101–S109.

Kim, H. J. *et al.* (2012) 'Structure, Function, and Assembly of Heme Centers in Mitochondrial Respiratory Complexes', *Biochimica et Biophysica Acta - Molecular Cell Research*, 1823(9), pp. 1604–1616. doi: 10.1016/j.bbamcr.2012.04.008.

Kim, J. S., He, L. and Lemasters, J. J. (2003) 'Mitochondrial Permeability Transition: A Common Pathway to Necrosis and Apoptosis', *Biochemical and Biophysical Research Communications*, 304(3), pp. 463–470. doi: 10.1016/S0006-291X(03)00618-1.

Kingsbury, B. F. (1912) 'Cytoplasmic Fixation', *The Anatomical Record*, 6(2), pp. 39–52. doi: 10.1002/ar.1090060202.

Kirby, D. M. and Thorburn, D. R. (2008) 'Approaches to Finding the Molecular Basis of Mitochondrial Oxidative Phosphorylation Disorders', *Twin Research and Human Genetics*, 11(4), pp. 395–411. doi: 10.1375/twin.11.4.395.

Koonin, E. V. (2010) 'The Origin and Early Evolution of Eukaryotes in the Light of Phylogenomics', *Genome Biology*, 11, p. 209. doi: 10.1186/gb-2010-11-5-209.

Koscielny, G. *et al.* (2014) 'The International Mouse Phenotyping Consortium Web Portal, a Unified Point of Access for Knockout Mice and Related Phenotyping Data', *Nucleic Acids Research*. 2013/11/03. Oxford University Press, 42(1), pp. 802–809. doi: 10.1093/nar/gkt977.

Koshiba, T. *et al.* (2004) 'Structural Basis of Mitochondrial Tethering by Mitofusin Complexes', *Science*, 305(5685), pp. 858–862. doi: 10.1126/science.1099793.

Kotecki, M., Reddy, P. S. and Cochran, B. H. (1999) 'Isolation and Characterization of a Near-Haploid Human Cell Line', *Experimental Cell Research*, 252(2), pp. 273–280. doi: 10.1006/excr.1999.4656.

Kozjak-Pavlovic, V. *et al.* (2014) 'C1orf163/RESA1 is a Novel Mitochondrial Intermembrane Space Protein Connected to Respiratory Chain Assembly', *Journal of Molecular Biology*, 426(4), pp. 908–920. doi: 10.1016/j.jmb.2013.12.001.

Kozjak-Pavlovic, V. (2017) 'The MICOS complex of Human Mitochondria', *Cell and Tissue Research*, 367(1), pp. 83–93. doi: 10.1007/s00441-016-2433-7.

Kruse, S. E. *et al.* (2008) 'Mice with Mitochondrial Complex I Deficiency Develop a Fatal Encephalomyopathy', *Cell Metabolism*, 7(4), pp. 312–320. doi: 10.1016/j.cmet.2008.02.004.

Ku, C. *et al.* (2015) 'Endosymbiotic Origin and Differential Loss of Eukaryotic Genes', *Nature*, 524(7566), pp. 427–432. doi: 10.1038/nature14963.

Kühlbrandt, W. (2015) 'Structure and Function of Mitochondrial Membrane Protein Complexes', *BioMed Central Biology Biology*, 13, p. 89. doi: 10.1186/s12915-015-0201-x.

Kunji, E. R. S. (2004) 'The Role and Structure of Mitochondrial Carriers', *FEBS Letters*, 564(3), pp. 239–244. doi: 10.1016/S0014-5793(04)00242-X.

Kunji, E. R. S. *et al.* (2016) 'The Transport Mechanism of the Mitochondrial ADP/ATP Carrier', *Biochimica et Biophysica Acta - Molecular Cell Research*, 1863(10), pp. 2379–2393. doi: 10.1016/j.bbamcr.2016.03.015.

Kuznetsov, A. V. and Margreiter, R. (2009) 'Heterogeneity of Mitochondria and Mitochondrial Function Within Cells as Another Level of Mitochondrial Complexity', *International Journal of Molecular Sciences*, 10(4), pp. 1911–1929. doi: 10.3390/ijms10041911.

Kytövuori, L. *et al.* (2017) 'Case Report: A Novel Frameshift Mutation in the Mitochondrial Cytochrome c Oxidase II Gene Causing Mitochondrial Disorder', *BioMed Central Neurology*, 17(1), p. 96. doi: 10.1186/s12883-017-0883-5.

Labun, K. *et al.* (2019) 'CHOPCHOP v3: Expanding the CRISPR Web Toolbox Beyond Genome Editing', *Nucleic Acids Research*, 47(1), pp. 171–174. doi: 10.1093/nar/gkz365.

Lane, N. and Martin, W. (2010) 'The Energetics of Genome Complexity', *Nature*, 467, pp. 929–934. doi: 10.1038/nature09486.

Lang, F. B., Gray, M. W. and Burger, G. (1999) 'Mitochondrial Genome Evolution and the Origin of Eukaryotes', *Annual Review of Genetics*, 33, pp. 351–397. doi: 10.1146/annurev.genet.33.1.351.

Lapuente-Brun, E. *et al.* (2013) 'Supercomplex Assembly Determines Electron Flux in the Mitochondrial Electron Transport Chain', *Science*, 340(6140), pp. 1567–1570. doi: 10.1126/science.1230381.

Lazarou, M. *et al.* (2007) 'Analysis of the Assembly Profiles for Mitochondrial- and Nuclear-DNA-Encoded Subunits into Complex I', *Molecular and Cellular Biology*, 27(12), pp. 4228–4237. doi: 10.1128/mcb.00074-07.

Leary, S. C. *et al.* (2004) 'Human SCO1 and SCO2 have Independent, Cooperative Functions in Copper Delivery to Cytochrome c Oxidase', *Human Molecular Genetics*, 13(17), pp. 1839–1848. doi: 10.1093/hmg/ddh197.

Lebre, A. S. *et al.* (2011) 'A Common Pattern of Brain MRI Imaging in Mitochondrial Diseases with Complex I Deficiency', *Journal of Medical Genetics*, 48(1), pp. 16–23. doi: 10.1136/jmg.2010.079624.

Legati, A. *et al.* (2016) 'New Genes and Pathomechanisms in Mitochondrial Disorders Unraveled by NGS Technologies', *Biochimica et Biophysica Acta - Bioenergetics*, 1857(8), pp. 1326–1335. doi: 10.1016/j.bbabio.2016.02.022.

Letts, J. A. and Sazanov, L. A. (2017) 'Clarifying the Supercomplex: the Higher-Order Organization of the Mitochondrial Electron Transport Chain', *Nature Structural and Molecular Biology*, 24(10), pp. 800–808. doi: 10.1038/nsmb.3460.

Lexow, J. *et al.* (2013) 'Cardiac Fibrosis in Mice Expressing an Inducible Myocardial-Specific Cre Driver', *Disease Models and Mechanisms*, 6(6), pp. 1470–1476. doi: 10.1242/dmm.010470.

Lill, R. *et al.* (2012) 'The Role of Mitochondria in Cellular Iron-Sulfur Protein Biogenesis and Iron Metabolism', *Biochimica et Biophysica Acta - Molecular Cell Research*, 1823(9), pp. 1491–1508. doi: 10.1016/j.bbamcr.2012.05.009.

Lim, S. C. *et al.* (2014) 'A Founder Mutation in PET100 Causes Isolated Complex IV Deficiency in Lebanese Individuals with Leigh Syndrome', *American Journal of Human Genetics*, 94(2), pp. 209–222. doi: 10.1016/j.ajhg.2013.12.015.

Lindmark, D. G. and Müller, M. (1973) 'Hydrogenosome, a Cytoplasmic Organelle of the Anaerobic Flagellate Tritrichomonas Foetus, and its Role in Pyruvate Metabolism', *Journal of Biological Chemistry*, 248, pp. 7724–7728.

Liu, X. *et al.* (1996) 'Induction of Apoptotic Program in Cell-Free Extracts: Requirement for dATP and Cytochrome c', *Cell*, 86(1), pp. 147–157. doi: 10.1016/S0092-8674(00)80085-9.

Liu, Y. *et al.* (2018) 'TIMMDC1 Knockdown Inhibits Growth and Metastasis of Gastric Cancer Cells Through Metabolic Inhibition and AKT/GSK3β/β-Catenin Signaling Pathway', *International Journal of Biological Sciences*, 14(10), pp. 1256–1267. doi: 10.7150/ijbs.27100.

Livak, K. J. and Schmittgen, T. D. (2001) 'Analysis of Relative Gene Expression Data Using Real-Time Quantitative PCR and the 2-ΔΔCT Method', *Methods*, 25(4), pp. 402–408. doi: 10.1006/meth.2001.1262.

Lobo-Jarne, T. *et al.* (2018) 'Human COX7A2L Regulates Complex III Biogenesis and Promotes Supercomplex Organization Remodeling without Affecting Mitochondrial Bioenergetics', *Cell Reports*, 25(7), pp. 1786–1799. doi: 10.1016/j.celrep.2018.10.058.

Loeffen, J. *et al.* (2000) 'Isolated Complex I Deficiency in Children: Clinical, Biochemical and Genetic Aspects', *Human Mutation*, 15(2), pp. 123–134. doi: 10.1002/(SICI)1098-1004(200002)15:2<123::AID-HUMU1>3.0.CO;2-P.

Lopez-Fabuel, I. *et al.* (2016) 'Complex I Assembly into Supercomplexes Determines Differential Mitochondrial ROS Production in Neurons and Astrocytes', *Proceedings of the National Academy of Sciences of the United States of America*, 113(46), pp. 13063–13068. doi: 10.1073/pnas.1613701113.

Lorenzi, I. *et al.* (2018) 'The Mitochondrial TMEM177 Associates with COX20 During COX2 Biogenesis', *Biochimica et Biophysica Acta - Molecular Cell Research*, 1865(2), pp. 323–333. doi: 10.1016/j.bbamcr.2017.11.010.

Lott, K. and Cingolani, G. (2011) 'The Importin β Binding Domain as a Master Regulator of Nucleocytoplasmic Transport', *Biochimica et Biophysica Acta - Molecular Cell Research*, 1813(9), pp. 1578–1592. doi: 10.1016/j.bbamcr.2010.10.012.

Luger, A. L. *et al.* (2018) 'Doxycycline Impairs Mitochondrial Function and Protects Human Glioma Cells from Hypoxia-Induced Cell Death: Implications of Using Tet-Inducible Systems', *International Journal of Molecular Sciences*, 19(5), p. E1504. doi: 10.3390/ijms19051504.

Lundin, C. R. *et al.* (2016) 'Regulatory Role of the Respiratory Supercomplex Factors in Saccharomyces cerevisiae', *Proceedings of the National Academy of Sciences of the United States of America*, 113(31), pp. E4476–E4485. doi: 10.1073/pnas.1601196113.

Lunsing, R. J. *et al.* (2017) 'Diagnostic Value of MRS-Quantified Brain Tissue Lactate Level in Identifying Children with Mitochondrial Disorders', *European Radiology*, 27(3), pp. 976–984. doi: 10.1007/s00330-016-4454-8.

Manfredim, G. and Beal, M. F. (2006) 'The Role of Mitochondria in the Pathogenesis of Neurodegenerative Diseases', *Brain Pathology*, 10(3), pp. 462–472. doi: 10.1111/j.1750-3639.2000.tb00278.x.

Manjo, G. and Joris, I. (1995) 'Apoptosis, Oncosis, and Necrosis', *American Journal of Pathology*, 146(1), pp. 3–15.

Mannella, C. A. (2006) 'Structure and Dynamics of the Mitochondrial Inner Membrane Cristae', *Biochimica et Biophysica Acta - Molecular Cell Research*, 1763(5–6), pp. 542–548. doi: 10.1016/j.bbamcr.2006.04.006.

Mans, B. J. *et al.* (2004) 'Comparative Genomics, Evolution and Origins of the Nuclear Envelope and Nuclear Pore Complex', *Cell Cycle*, 3(12), pp. 1612–1618.

Maranzana, E. *et al.* (2013) 'Mitochondrial Respiratory Supercomplex Association Limits Production of Reactive Oxygen Species from Complex I', *Antioxidants and Redox Signaling*, 19(13), pp. 1469–1480. doi: 10.1089/ars.2012.4845.

Marchi, S., Patergnani, S. and Pinton, P. (2014) 'The Endoplasmic Reticulum-Mitochondria Connection: One Touch, Multiple Functions', *Biochimica et Biophysica Acta - Bioenergetics*, 1837(4), pp. 461–469. doi: 10.1016/j.bbabio.2013.10.015.

Marmocchi, F. *et al.* (1975) 'The Effect of the Presence of the Metal Prosthetic Groups on the Subunit Structure of Bovine Superoxide Dismutase in Sodium Dodecyl Sulfate', *Physiological Chemistry and Physics*, 7(5), pp. 465–471.

Martin, W. F. *et al.* (2016) 'Energy for Two: New Archaeal Lineages and the Origin of Mitochondria', *Bioessays*, 38(9), pp. 850–856. doi: 10.1002/bies.201600089.

Martin, W. F. and Mentel, M. (2010) 'The Origin of Mitochondria', *Nature Education*, 3(9), p. 58. doi: 10.1038/nature04546.

Martin, W. and Müller, M. (1998) 'The Hydrogen Hypothesis for the First Eukaryote', *Nature*, 392(6671), pp. 37–41. doi: 10.1038/32096.

Martínez-Cayuela, M. (1995) 'Oxygen Free Radicals and Human Disease', *Biochimie*, 77(3), pp. 147–161. doi: 10.1016/0300-9084(96)88119-3.

Martínez-Reyes, I. *et al.* (2016) 'TCA Cycle and Mitochondrial Membrane Potential Are Necessary for Diverse Biological Functions', *Molecular Cell*, 61(2), pp. 199–209. doi: 10.1016/j.molcel.2015.12.002.TCA.

Martinez Lyons, A. *et al.* (2016) 'COA7 (C1orf163/RESA1) Mutations Associated with Mitochondrial Leukoencephalopathy and Cytochrome c Oxidase Deficiency', *Journal of Medical Genetics*, 53(12), pp. 846–849. doi: 10.1136/jmedgenet-2016-104194.

Masè, M., Disertori, M. and Ravelli, F. (2009) 'Cardiorespiratory Interactions in Patients with Atrial Flutter', *Journal of Applied Physiology*, 106(1), pp. 29–39. doi: 10.1152/japplphysiol.91191.2008.

Massa, V. *et al.* (2008a) 'Severe Infantile Encephalomyopathy Caused by a Mutation in COX6B1, a Nucleus-Encoded Subunit of Cytochrome C Oxidase', *American Journal of Human Genetics*, 82(6), pp. 1281–1289. doi: 10.1016/j.ajhg.2008.05.002.

Massa, V. *et al.* (2008b) 'Severe Infantile Encephalomyopathy Caused by a Mutation in COX6B1, a Nucleus-Encoded Subunit of Cytochrome C Oxidase', *American Journal of Human Genetics*, 82(6), pp. 1281–1289. doi: 10.1016/j.ajhg.2008.05.002.

McCarron, J. G. *et al.* (2013) 'From Structure to Function: Mitochondrial Morphology, Motion and Shaping in Vascular Smooth Muscle', *Journal of Vascular Research*, 50(5), pp. 357–371. doi: 10.1159/000353883.

McEwen, J. E. *et al.* (1993) 'Sequence and Chromosomal Localization of Two PET Genes Required for Cytochrome c Oxidase Assembly in Saccharomyces cerevisiae', *Current Genetics*, 23(1), pp. 9–14. doi: 10.1007/BF00336742.

McFarland, R., Taylor, R. W. and Turnbull, D. M. (2010) 'A Neurological Perspective on Mitochondrial Disease', *The Lancet Neurology*, 9(8), pp. 829–840. doi: 10.1016/S1474-4422(10)70116-2.

McKenzie, M. and Ryan, M. T. (2010) 'Assembly Factors of Human Mitochondrial Complex I and Their Defects in Disease', *IUBMB Life*, 62(7), pp. 497–502. doi: 10.1002/iub.335.

Mentel, M. and Martin, W. (2008) 'Energy Metabolism Among Eukaryotic Anaerobes in Light of Proterozoic Ocean Chemistry', *Philosophical Transactions of the Royal Society of London - Series B, Biological Sciences*, 363(1504), pp. 2717–2729. doi: 10.1098/rstb.2008.0031.

Michel, H. (1998) 'The Mechanism of Proton Pumping by Cytochrome c Oxidase', *Proceedings of the National Academy of Sciences of the United States of America*, 95(22), pp. 12819–12824. doi: 10.1073/pnas.95.22.12819.

Mick, D. U. *et al.* (2010) 'Coa3 and Cox14 are Essential for Negative Feedback Regulation of COX1 Translation in Mitochondria', *Journal of Cell Biology*, 191(1), pp. 141–154. doi: 10.1083/jcb.201007026.

Mick, D. U. *et al.* (2012) 'MITRAC Links Mitochondrial Protein Translocation to Respiratory Chain Assembly and Translational Regulation', *Cell*. Elsevier Inc., 151(7), pp. 1528–1541. doi: 10.1016/j.cell.2012.11.053.

Milenkovic, D. *et al.* (2017) 'The Enigma of the Respiratory Chain Supercomplex', *Cell Metabolism*, 25(4), pp. 765–776. doi: 10.1016/j.cmet.2017.03.009.

Miller, W. L. (2013) 'Steroid Hormone Synthesis in Mitochondria', *Molecular and Cellular Endocrinology*. Elsevier Ireland Ltd, 379(1–2), pp. 62–73. doi: 10.1016/j.mce.2013.04.014.

Mitchell, P. (1961) 'Coupling of Phosphorylation to Electron and Hydrogen Transfer by a Chemiosmotic Type of Mechanism', *Nature*, 191(4784), pp. 144–148. doi: 10.1038/191144a0.

Mitchell, P. and Moyle, J. (1969) 'Estimation of Membrane Potential and pH Difference across the Cristae Membrane of Rat Liver Mitochondria', *European Journal of Biochemistry*, 7(4), pp. 471–484. doi: 10.1111/j.1432-1033.1969.tb19633.x.

Mkaouar-Rebai, E. *et al.* (2011) 'Molecular-Clinical Correlation in a Family with a Novel Heteroplasmic Leigh Syndrome Missense Mutation in the Mitochondrial Cytochrome c Oxidase III Gene', *Journal of Child Neurology*, 26(1), pp. 12–20. doi: 10.1177/0883073810371227.

Mohanraj, K. *et al.* (2019) 'Inhibition of Proteasome Rescues a Pathogenic Variant of Respiratory Chain Assembly Factor COA7', *EMBO Molecular Medicine*, 11(5), p. E9561. doi: 10.15252/emmm.201809561.

Montague, T. G. *et al.* (2014) 'CHOPCHOP: A CRISPR/Cas9 and TALEN Web Tool for Genome Editing', *Nucleic Acids Research*, 42(1), pp. 401–407. doi: 10.1093/nar/gku410.

Moore, C. B. *et al.* (2010) 'Short Hairpin RNA (shRNA): Design, Delivery, and Assessment of Gene Knockdown', *Methods in molecular biology (Clifton, N.J.)*, 629, pp. 141–158. doi: 10.1007/978-1-60761-657-3_10.

Mootha, V. K. *et al.* (2003) 'Integrated Analysis of Protein Composition, Tissue Diversity, and Gene Regulation in Mouse Mitochondria', *Cell*, 115(5), pp. 629–640. doi: 10.1016/S0092-8674(03)00926-7.

Moreno-Lastres, D. *et al.* (2012) 'Mitochondrial Complex I Plays an Essential Role in Human Respirasome Assembly', *Cell Metabolism*, 15(3), pp. 324–325. doi: 10.1016/j.cmet.2012.01.015.

Mourier, A. *et al.* (2014) 'The Respiratory Chain Supercomplex Organization is Independent of COX7A2L Isoforms', *Cell Metabolism*, 20(6), pp. 1069–1075. doi: 10.1016/j.cmet.2014.11.005.

Muller, F. (2000) 'The Nature and Mechanism of Superoxide Production by the Electron Transport Chain: Its Relevance to Aging', *Journal of the American Aging Association*, 23(4), pp. 227–253. doi: 10.1007/s11357-000-0022-9.

Murphy, M. P. (2009) 'How Mitochondria Produce Reactive Oxygen Species', *Biochemical Journal*, 417(1), pp. 1–13. doi: 10.1042/BJ20081386.

Nedergaard, J. *et al.* (2001) 'UCP1: The Only Protein Able to Mediate Adaptive Non-Shivering Thermogenesis and Metabolic Inefficiancy', *Biochimica et Biophysica Acta - Bioenergetics*, 1504(1), pp. 82–106. doi: 10.1016/S0005-2728(00)00247-4.

Nicholls, D. G. (1974) 'The Influence of Respiration and ATP Hydrolysis on the Proton-Electrochemical Gradient across the Inner Membrane of Rat-Liver Mitochondria as Determined by Ion Distribution', *European Journal of Biochemistry*, 50(1), pp. 305–315. doi: 10.1111/j.1432-1033.1974.tb03899.x.

Nightingale, H. *et al.* (2016) 'Emerging Therapies for Mitochondrial Disorders', *Brain*, 139(6), pp. 1633–1648. doi: 10.1093/brain/aww081.

Nijtmans, L. G. J. *et al.* (1998) 'Assembly of Cytochrome c Oxidase in Cultured Human Cells', *European Journal of Biochemistry*, 254(2), pp. 389–394. doi: 10.1046/j.1432-1327.1998.2540389.x.

Nijtmans, L. G. J., Henderson, N. S. and Holt, I. J. (2002) 'Blue Native Electrophoresis to Study Mitochondrial and Other Protein Complexes', *Methods*, 26(4), pp. 327–334. doi: 10.1016/S1046-2023(02)00038-5.

Nolan, T., Hands, R. E. and Bustin, S. A. (2006) 'Quantification of mRNA Using Real-Time RT-PCR', *Nature Protocols*, 1, pp. 1559–1582. doi: 10.1038/nprot.2006.236.

Nouws, J. *et al.* (2012) 'Assembly Factors as a New Class of Disease Genes for Mitochondrial Complex I Deficiency: Cause, Pathology and Treatment Options', *Brain*, 135(1), pp. 12–22. doi: 10.1093/brain/awr261.

O'Gorman, S., Fox, D. T. and Wahl, G. M. (1991) 'Recombinase-Mediated Gene Activation and Site-Specific Integration in Mammalian Cells', *Science*, 251(4999), pp. 1351–1355. doi: 10.1126/science.1900642.

Ogilvie, I., Kennaway, N. G. and Shoubridge, E. A. (2005) 'A Molecular Chaperone for Mitochondrial Complex I Assembly is Mutated in a Progressive Encephalopathy', *Journal of Clinical Investigation*, 115(10), pp. 2784–2792. doi: 10.1172/JCI26020.

Ohkubo, R. *et al.* (2002) 'Cerebrovascular Disorders and Genetic Polymorphisms: Mitochondrial DNA5178C is Predominant in Cerebrovascular Disorders', *Journal of the Neurological Sciences*, 198(1–2), pp. 31–35. doi: 10.1016/S0022-510X(02)00055-2.

Ojji, D. B. *et al.* (2016) 'Right Ventricular Systolic Dysfunction Is Common in Hypertensive Heart Failure: A Prospective Study in Sub-Saharan Africa', *PLoS ONE*, 11(4), p. E0153479. doi: 10.1371/journal.pone.0153479.

Oláhová, M. *et al.* (2015) 'A Truncating PET100 Variant Causing Fatal Infantile Lactic Acidosis and Isolated Cytochrome c Oxidase Deficiency', *European Journal of Human Genetics*, 23(7), pp. 935–939. doi: 10.1038/ejhg.2014.214.

Omasits, U. *et al.* (2014) 'Protter: Interactive Protein Feature Visualization and Integration with Experimental Proteomic Data', *Bioinformatics*, 30(6), pp. 884–886. doi: 10.1093/bioinformatics/btt607.

Ota, T. *et al.* (2004) 'Complete Sequencing and Characterization of 21,243 Full-Length Human cDNAs', *Nature Genetics*, 36(1), pp. 40–45. doi: 10.1038/ng1285.

Pacheu-Grau, D. *et al.* (2015) 'Cooperation Between COA6 and SCO2 in COX2 Maturation During Cytochrome c Oxidase Assembly Links Two Mitochondrial Cardiomyopathies', *Cell Metabolism*, 21(6), pp. 823–833. doi: 10.1016/j.cmet.2015.04.012.

Pagliarini, D. J. *et al.* (2008) 'A Mitochondrial Protein Compendium Elucidates Complex I Disease Biology', *Cell*, 134(1), pp. 112–123. doi: 10.1016/j.cell.2008.06.016.

Pagliarini, D. J. and Rutter, J. (2013) 'Hallmarks of a New Era in Mitochondrial Biochemistry', *Genes and Development*, 27(24), pp. 2615–2627. doi: 10.1101/gad.229724.113.

Palade, G. E. (1953) 'An Electron Microscope Study of the Mitochondrial Structure', *Journal of Histochemistry & Cytochemistry*, 1(4), pp. 188–211. doi: 10.1177/1.4.188.

Panneman, D. M., Smeitink, J. A. and Rodenburg, R. J. (2018) 'Mining for Mitochondrial Mechanisms: Linking Known Syndromes to Mitochondrial Function', *Clinical Genetics*, 93(5), pp. 943–951. doi: 10.1111/cge.13094.

Paradies, G. *et al.* (2014) 'Functional Role of Cardiolipin in Mitochondrial Bioenergetics', *Biochimica et Biophysica Acta - Bioenergetics*. Elsevier B.V., 1837(4), pp. 408–417. doi: 10.1016/j.bbabio.2013.10.006.

Parsons, D. F. and Yano, Y. (1967) 'The Cholesterol Content of the Outer and Inner Membranes of Guinea-Pig Liver Mitochondria', *BBA - Biomembranes*, 135(2), pp. 362–364. doi: 10.1016/0005-2736(67)90132-0.

Paul, B. T. *et al.* (2017) 'Mitochondria and Iron: Current Questions', *Expert Review of Hematology*, 10(1), pp. 65–79. doi: 10.1080/17474086.2016.1268047.

Perkins, G. *et al.* (1997) 'Electron Tomography of Neuronal Mitochondria: Three-Dimensional Structure and Organization of Cristae and Membrane Contacts', *Journal of Structural Biology*, 119(3), pp. 260–272. doi: 10.1006/jsbi.1997.3885.

Pernas, L. and Scorrano, L. (2016) 'Mito-Morphosis: Mitochondrial Fusion, Fission, and Cristae Remodeling as Key Mediators of Cellular Function', *Annual Review of Physiology*, 78, pp. 505–531. doi: 10.1146/annurev-physiol-021115-105011.

Pickles, S., Vigié, P. and Youle, R. J. (2018) 'Mitophagy and Quality Control Mechanisms in Mitochondrial Maintenance', *Current Biology*, 28(4), pp. 170–185. doi: 10.1016/j.cub.2018.01.004.

Pierrel, F. *et al.* (2007) 'Coa1 Links the Mss51 Post-Translational Function to Cox1 Cofactor Insertion in Cytochrome c Oxidase Assembly', *EMBO Journal*, 26(20), pp. 4335–4346. doi: 10.1038/sj.emboj.7601861.

Pitceathly, R. D. S. *et al.* (2013) 'NDUFA4 Mutations Underlie Dysfunction of a Cytochrome c Oxidase Subunit Linked to Human Neurological Disease', *Cell Reports*. The Authors, 3(6), pp. 1795–1805. doi: 10.1016/j.celrep.2013.05.005.

Pitceathly, R. D. S. and Taanman, J. W. (2018) 'NDUFA4 (Renamed COXFA4) Is a Cytochrome c Oxidase Subunit', *Trends in Endocrinology and Metabolism*. Elsevier Ltd, 29(7), pp. 452–454. doi: 10.1016/j.tem.2018.03.009.

Plitzko, B. and Loesgen, S. (2018) 'Measurement of Oxygen Consumption Rate (OCR) and Extracellular Acidification Rate (ECAR) in Culture Cells for Assessment of the Energy Metabolism', *Bio-Protocol*, 8(10), p. e2850. doi: 10.21769/bioprotoc.2850.

Porcelli, A. M. *et al.* (2005) 'pH Difference Across the Outer Mitochondrial Membrane Measured with a Green Fluorescent Protein Mutant', *Biochemical and Biophysical Research Communications*, 326(4), pp. 799–804. doi: 10.1016/j.bbrc.2004.11.105.

Prasad, K. M. R. *et al.* (2011) 'A Single Direct Injection into the Left Ventricular Wall of an Adeno-Associated Virus 9 (AAV9) Vector Expressing Extracellular Superoxide Dismutase from the Cardiac Troponin-T Promoter Protects Mice Against Myocardial Infarction', *Journal of Gene Medicine*, 13(6), pp. 333–341. doi: 10.1002/jgm.1576.

Prudent, J. and McBride, H. M. (2017) 'The Mitochondria–Endoplasmic Reticulum Contact Sites: a Signalling Platform for Cell Death', *Current Opinion in Cell Biology*, 47, pp. 52–63. doi: 10.1016/j.ceb.2017.03.007.

Rak, M. *et al.* (2016) 'Mitochondrial Cytochrome c Oxidase Deficiency', *Clinical Science*, 130(6), pp. 393–407. doi: 10.1042/CS20150707.Mitochondrial.

Ran, A. F. *et al.* (2013) 'Genome Engineering Using the CRISPR-Cas9 System HHS Public Access', *Nature Protocols*, 8(11), pp. 2281–2308. doi: 10.1038/nprot.2013.143.

Ren, X. *et al.* (2017) 'Redox Signaling Mediated by Thioredoxin and Glutathione Systems in the Central Nervous System', *Antioxidants and Redox Signaling*, 27(13), pp. 989–1010. doi: 10.1089/ars.2016.6925.

Renkema, G. H. *et al.* (2017) 'Mutated PET117 Causes Complex IV Deficiency and is Associated with Neurodevelopmental Regression and Medulla Oblongata Lesions', *Human Genetics*. Springer Berlin Heidelberg, 136(6), pp. 759–769. doi: 10.1007/s00439-017-1794-7.

Rhee, H. W. *et al.* (2013) 'Proteomic Mapping of Mitochondria in Living Cells via Spatially Restricted Enzymatic Tagging', *Science*, 339(6125), pp. 1328–1331. doi: 10.1126/science.1230593.

Rhein, V. F. *et al.* (2013) 'NDUFAF7 Methylates Arginine 85 in the NDUFS2 Subunit of Human Complex I', *Journal of Biological Chemistry*, 288(46), pp. 33016–33026. doi: 10.1074/jbc.M113.518803.

Rhein, V. F. *et al.* (2016) 'NDUFAF5 Hydroxylates NDUFS7 at an Early Stage in the Assembly of Human Complex I', *Journal of Biological Chemistry*, 291(28), pp. 14851–14860. doi: 10.1074/jbc.M116.734970.

Rial, D. *et al.* (2014) 'Behavioral Phenotyping of Parkin-Deficient Mice: Looking for Early Preclinical Features of Parkinson's Disease', *PLoS ONE*. Public Library of Science, 9(12), p. e114216. Available at: https://doi.org/10.1371/journal.pone.0114216.

Richman, T. R. *et al.* (2016) 'Loss of the RNA-Binding Protein TACO1 Causes Late-Onset Mitochondrial Dysfunction in Mice', *Nature Communications*, 7(11884), pp. 1–14. doi: 10.1038/ncomms11884.

Richter-Dennerlein, R. *et al.* (2016) 'Mitochondrial Protein Synthesis Adapts to Influx of Nuclear-Encoded Protein', *Cell*, 167(2), pp. 471–483. doi: 10.1016/j.cell.2016.09.003.

Rodenburg, R. J. (2016) 'Mitochondrial Complex I-Linked Disease', *Biochimica et Biophysica Acta - Bioenergetics*, 1857(7), pp. 938–945. doi: 10.1016/j.bbabio.2016.02.012.

Rodenburg, R. J. T. (2011) 'Biochemical Diagnosis of Mitochondrial Disorders', *Journal of Inherited Metabolic Disease*, 34(2), pp. 283–292. doi: 10.1007/s10545-010-9081-y.

Ruitenbeek, W. *et al.* (1996) 'Genetic Counselling and Prenatal Diagnosis in Disorders of the Mitochondrial Energy Metabolism', *Journal of Inherited Metabolic Disease*, 19(4), pp. 581–587. doi: 10.1007/BF01799118.

Ruzzenente, B. *et al.* (2012) 'LRPPRC is Necessary for Polyadenylation and Coordination of Translation of Mitochondrial mRNAs', *EMBO Journal*, 31(2), pp. 443–456. doi: 10.1038/emboj.2011.392.

Saada, A. *et al.* (2009) 'Mutations in NDUFAF3 (C3ORF60), Encoding an NDUFAF4 (C6ORF66)-Interacting Complex I Assembly Protein, Cause Fatal Neonatal Mitochondrial Disease', *American Journal of Human Genetics*, 84(6), pp. 718–727. doi: 10.1016/j.ajhg.2009.04.020.

Sagan, L. (1967) 'On the Origin of Mitosing Cells', *Journal of Theoretical Biology*, 14(3), pp. 225–274.

Saiki, R. K. *et al.* (1985) 'Enzymatic Amplification of β-Globin Genomic Sequences and Restriction Site Analysis for Diagnosis of Sickle Cell Anemia', *Science*, 230(4732), pp. 1350–1354. doi: 10.1126/science.2999980.

Salmon, P. *et al.* (2000) 'Reversible Immortalization of Human Primary Cells by Lentivector-Mediated Transfer of Specific Genes', *Molecular Therapy*, 2(4), pp. 404–414. doi: 10.1006/mthe.2000.0141.

Saneto, R. P., Friedman, S. D. and Shaw, D. W. (2008) 'Neuroimaging of Mitochondrial Disease', *Mitochondrion*, 8(5–6), pp. 396–413. doi: 10.1016/j.mito.2008.05.003.

Sanger, F., Nicklen, S. and Coulson, A. R. (1977) 'DNA Sequencing with Chain-Terminating Inhibitors', *Proceedings of the National Academy of Sciences of the United States of America*, 74(12), pp. 5463–5467. doi: 10.1073/pnas.74.12.5463.

Sazanov, L. A. (2015) 'A Giant Molecular Proton Pump: Structure and Mechanism of Respiratory Complex I', *Nature Reviews Molecular Cell Biology*, 16, pp. 375–388. doi: 10.1038/nrm3997.

Schägger, H. (2002) 'Respiratory Chain Supercomplexes of Mitochondria and Bacteria', *Biochimica et Biophysica Acta - Bioenergetics*, 1555(1–3), pp. 154–159. doi: 10.1016/S0005-2728(02)00271-2.

Schägger, H. and von Jagow, G. (1991) 'Blue Native Electrophoresis for Isolation of Membrane Protein Complexes in Enzymatically Active Form', *Analytical Biochemistry*, 199(2), pp. 223–231. doi: 10.1016/0003-2697(91)90094-A.

Schieber, M. and Chandel, N. S. (2014) 'ROS Function in Redox Signaling and Oxidative Stress', *Current Biology*. Elsevier, 24(10), pp. 453–462. doi: 10.1016/j.cub.2014.03.034.

Schindelin, J. *et al.* (2012) 'Fiji: An Open-Source Platform for Biological-Image Analysis', *Nature Methods*, 9, pp. 676–682. doi: 10.1038/nmeth.2019.

Schlame, M. (2008) 'Cardiolipin Synthesis for the Assembly of Bacterial and Mitochondrial Membranes', *Journal of Lipid Research*, 49(8), pp. 1607–1620. doi: 10.1194/jlr.R700018-JLR200.

Schmued, L. C. and Hopkins, K. J. (2000) 'Fluoro-Jade: Novel Fluorochromes for Detecting Toxicant-Induced Neuronal Degeneration', *Toxicologic Pathology*, 28(1), pp. 91–99. doi: 10.1177/019262330002800111.

Schultz, B. E. and Chan, S. I. (2001) 'Structures and Proton-Pumping Strategies of Mitochondrial Respiratory Enzymes', *Annual Review of Biophysics and Biomolecular Structure*, 30(1), pp. 23–65. doi: 10.1146/annurev.biophys.30.1.23.

Seelow, D. *et al.* (2009) 'Homozygosity Mapper - An Interactive Approach to Homozygosity Mapping', *Nucleic Acids Research*, 37(2), pp. 593–599. doi: 10.1093/nar/gkp369.

Sharma, H. *et al.* (2005) 'Mutations in the Mitochondrial DNA D-loop Region are Frequent in Cervical Cancer', *Cancer Cell International*, 5, p. 34. doi: 10.1186/1475-2867-5-34.

Sharma, L., Lu, J. and Bai, Y. (2009) 'Mitochondrial Respiratory Complex I: Structure, Function and Implication in Human Diseases', *Current Medicinal Chemistry*, 16(10), pp. 1266–1277. doi: 10.2174/092986709787846578.

Sharma, V. *et al.* (2017) 'Insights into Functions of the H Channel of Cytochrome c Oxidase from Atomistic Molecular Dynamics Simulations', *Proceedings of the National Academy of Sciences of the United States of America*, 114(48), pp. E10339–E10348. doi: 10.1073/pnas.1708628114.

Sheftel, A. D. *et al.* (2009) 'Human Ind1, an Iron-Sulfur Cluster Assembly Factor for Respiratory Complex I', *Molecular and Cellular Biology*, 29(22), pp. 6059–6073. doi: 10.1128/mcb.00817-09.

Shihab, H. A. *et al.* (2015) 'An Integrative Approach to Predicting the Functional Effects of Non-Coding and Coding Sequence Variation', *Bioinformatics*, 31(10), pp. 1536–1543. doi: 10.1093/bioinformatics/btv009.

Shoshan-Barmatz, V. *et al.* (2010) 'VDAC, a Multi-Functional Mitochondrial Protein Regulating Cell Life and Death', *Molecular Aspects of Medicine*, 31(3), pp. 227–285. doi: 10.1016/j.mam.2010.03.002.

Shteyer, E. *et al.* (2009) 'Exocrine Pancreatic Insufficiency, Dyserythropoeitic Anemia, and Calvarial Hyperostosis Are Caused by a Mutation in the COX4I2 Gene', *American Journal of Human Genetics*, 84(3), pp. 412–417. doi: 10.1016/j.ajhg.2009.02.006.

Sicheritz-Pontén, T., Kurland, C. G. and Andersson, S. G. E. (1998) 'A Phylogenetic Analysis of the Cytochrome b and Cytochrome c Oxidase I Genes Supports an Origin of Mitochondria From Within the Rickettsiaceae', *Biochimica et Biophysica Acta - Bioenergetics*, 1365(3), pp. 545–551. doi: 10.1016/S0005-2728(98)00099-1.

Signes, A. *et al.* (2019) 'APOPT1/ COA8 Assists COX Assembly and is Oppositely Regulated by UPS and ROS', *EMBO Molecular Medicine*, 11(1), p. e9582. doi: 10.15252/emmm.201809582.

Signes, A. and Fernandez-Vizarra, E. (2018) 'Assembly of Mammalian Oxidative Phosphorylation Complexes I–V and Supercomplexes', *Essays in Biochemistry*, 62(3), pp. 255–270. doi: 10.1042/EBC20170098.

Siletsky, S. A. and Konstantinov, A. A. (2012) 'Cytochrome c Oxidase: Charge Translocation Coupled to Single-Electron Partial Steps of the Catalytic Cycle', *Biochimica et Biophysica Acta - Bioenergetics*, 1817(4), pp. 476–488. doi: 10.1016/j.bbabio.2011.08.003.

Simeone, K. A. *et al.* (2014) 'Targeting Deficiencies in Mitochondrial Respiratory Complex I and Functional Uncoupling Exerts Anti-Seizure Effects in a Genetic Model of Temporal Lobe Epilepsy and in a Model of Acute Temporal Lobe Seizures', *Experimental Neurology*, 251, pp. 84–90. doi: 10.1016/j.expneurol.2013.11.005.

Sinha, R. A. *et al.* (2010) 'Evidence of a Bigenomic Regulation of Mitochondrial Gene Expression by Thyroid Hormone During Rat Brain Development', *Biochemical and Biophysical Research Communications*, 397(3), pp. 548–552. doi: 10.1016/j.bbrc.2010.05.154.

Sjöstrand, F. S. (1953) 'Electron Microscopy of Mitochondria and Cytoplasmic Double Membranes', *Nature*, 171, pp. 30–31. doi: 10.1038/171030a0.

Sompayrac, L. and Danna, K. J. (1991) 'The Amino-Terminal 147 Amino Acids of SV40 large T Antigen Transform Secondary Rat Embryo Fibroblasts', *Virology*, 181(1), pp. 412–415. doi: 10.1016/0042-6822(91)90516-E.

Soto, I. C. *et al.* (2012) 'Biogenesis and Assembly of Eukaryotic Cytochrome c Oxidase Catalytic Core', *Biochimica et Biophysica Acta - Bioenergetics*. Elsevier B.V., 1817(6), pp. 883–897. doi: 10.1016/j.bbabio.2011.09.005.

Sousa, J. S. *et al.* (2016) 'Functional Asymmetry and Electron Flow in the Bovine Respirasome', *eLife*, 5, p. E21290. doi: 10.7554/eLife.21290.

Starkov, A. A. (2008) 'The Role of Mitochondria in Reactive Oxygen Species Metabolism and Signaling', *Annals of the New York Academy of Sciences*, 1147(1), pp. 37–52. doi: 10.1196/annals.1427.015.

Stefani, D. De *et al.* (2014) 'A 40 kDa Protein of the Inner Membrane is the Mitochondrial Calcium Uniporter', *Nature*, 476(7360), pp. 336–340. doi: 10.1038/nature10230.A.

Stefely, J. A. and Pagliarini, D. J. (2017) 'Biochemistry of Mitochondrial Coenzyme Q Biosynthesis', *Trends in Biochemical Sciences*, 42(10), pp. 824–843. doi: 10.1016/j.tibs.2017.06.008.

Stehling, O. and Lill, R. (2013) 'The Role of Mitochondria in Cellular Iron-Sulfur Protein Biogenesis: Mechanisms, Connected Processes, and Diseases', *Cold Spring Harbor Perspectives in Medicine*, 5(8), p. E11312. doi: 10.1101/cshperspect.a011312.

Stenton, S. L. and Prokisch, H. (2018) 'Advancing Genomic Approaches to the Molecular Diagnosis of Mitochondrial Disease', *Essays in Biochemistry*, 62(3), pp. 399–408. doi: 10.1042/EBC20170110.

Stewart, J. B. *et al.* (2008) 'Purifying Selection of mtDNA and Its Implications for Understanding Evolution and Mitochondrial Disease', *Nature Reviews Genetics*, 9(9), pp. 657–662. doi: 10.1038/nrg2396.

Stewart, J. B. and Chinnery, P. F. (2015) 'The Dynamics of Mitochondrial DNA Heteroplasmy: Implications for Human Health and Disease', *Nature Reviews Genetics*. Nature Publishing Group, 16(9), pp. 530–542. doi: 10.1038/nrg3966.

Stojanovski, D., Bragoszewski, P. and Chacinska, A. (2012) 'The MIA Pathway: A Tight Bond Between Protein Transport and Oxidative Folding in Mitochondria', *Biochimica et Biophysica Acta - Molecular Cell Research*, 1823(7), pp. 1142–1150. doi: 10.1016/j.bbamcr.2012.04.014.

Stoldt, S. *et al.* (2018) 'Spatial Orchestration of Mitochondrial Translation and OXPHOS Complex Assembly', *Nature Cell Biology*, 20, pp. 528–534. doi: 10.1038/s41556-018-0090-7.

Strausberg, R. L. *et al.* (2002) 'Generation and Initial Analysis of More Than 15,000 Full-Length Human and Mouse cDNA Sequences', *Proceedings of the National Academy of Sciences of the United States of America*, 99(26), pp. 16899–16903. doi: 10.1073/pnas.242603899.

Strogolova, V. *et al.* (2012) 'Rcf1 and Rcf2, Members of the Hypoxia-Induced Gene 1 Protein Family, Are Critical Components of the Mitochondrial Cytochrome bc1-Cytochrome c Oxidase Supercomplex', *Molecular and Cellular Biology*, 32(8), pp. 1363–1373. doi: 10.1128/MCB.06369-11.

Stroud, D. A. *et al.* (2015) 'COA6 is a Mitochondrial Complex IV Assembly Factor Critical for Biogenesis of mtDNA-Encoded COX2', *Human Molecular Genetics*, 24(19), pp. 5404–5415. doi: 10.1093/hmg/ddv265.

Stroud, D. A. *et al.* (2016) 'Accessory Subunits are Integral for Assembly and Function of Human Mitochondrial Complex I', *Nature*. Nature Publishing Group, 538(7623), pp. 123–126. doi: 10.1038/nature19754.

Suárez-Rivero, J. *et al.* (2016) 'Mitochondrial Dynamics in Mitochondrial Diseases', *Diseases*, 5(1), p. 1. doi: 10.3390/diseases5010001.

Swalwell, H. *et al.* (2011) 'Respiratory Chain Complex I Deficiency Caused by Mitochondrial DNA Mutations', *European Journal of Human Genetics*, 19(7), pp. 769–775. doi: 10.1038/ejhg.2011.18.

Tamiy, G. *et al.* (2014) 'A Mutation of COX6A1 Causes a Recessive Axonal or Mixed Form of Charcot-Marie-Tooth Disease', *American Journal of Human Genetics*. The American Society of Human Genetics, 95(3), pp. 294–300. doi: 10.1016/j.ajhg.2014.07.013.

Tarasov, A. I., Griffiths, E. J. and Rutter, G. A. (2012) 'Regulation of ATP Production by Mitochondrial Ca2+', *Cell Calcium*, 52(1), pp. 28–35. doi: 10.1016/j.ceca.2012.03.003.

Taylor, N. G. *et al.* (2017) 'The Assembly Factor Pet117 Couples Heme A Synthase Activity to Cytochrome Oxidase Assembly', *Journal of Biological Chemistry*, 292(5), pp. 1815–1825. doi: 10.1074/jbc.M116.766980.

Temperley, R. *et al.* (2010) 'Hungry Codons Promote Frameshifting in Human Mitochondrial Ribosomes', *Science*, 327(5963), p. 301. doi: 10.1126/science.1180674.

Theunissen, T. E. J. *et al.* (2018) 'Whole Exome Sequencing is the Preferred Strategy to Identify the Genetic Defect in Patients with a Probable or Possible Mitochondrial Cause', *Frontiers in Genetics*, 9, p. 400. doi: 10.3389/fgene.2018.00400.

Thiene, G. *et al.* (1988) 'Right Ventricular Cardiomyopathy and Sudden Death in Young People', *New England Journal of Medicine*, 318(3), pp. 129–133. doi: 10.1056/NEJM198801213180301.

Thompson, K. *et al.* (2018) 'OXA1L Mutations Cause Mitochondrial Encephalopathy and a Combined Oxidative Phosphorylation Defect', *EMBO Molecular Medicine*, 10(11), p. E9060. doi: 10.15252/emmm.201809060.

Thorburn, D. R. *et al.* (2004) 'Biochemical and Molecular Diagnosis of Mitochondrial Respiratory Chain Disorders', *Biochimica et Biophysica Acta - Bioenergetics*, 1659(2–3), pp. 121–128. doi: 10.1016/j.bbabio.2004.08.006.

Timón-Gómez, A. *et al.* (2017) 'Mitochondrial Cytochrome c Oxidase Biogenesis: Recent Developments', *Seminars in Cell & Developmental Biology*, 76, pp. 163–178. doi: 10.1016/j.semcdb.2017.08.055.

Tocilescu, M. A. *et al.* (2007) 'Exploring the Ubiquinone Binding Cavity of Respiratory Complex', *Journal of Biological Chemistry*, 282(40), pp. 29514–29520. doi: 10.1074/jbc.M704519200.

Traaseth, N. *et al.* (2004) 'Role of Calcium Signaling in the Activation of Mitochondrial Nitric Oxide Synthase and Citric Acid Cycle', *Biochimica et Biophysica Acta - Bioenergetics*, 1658(1–2), pp. 64–71. doi: 10.1016/j.bbabio.2004.04.015.

Tsujimoto, Y. and Shimizu, S. (2007) 'Role of the Mitochondrial Membrane Permeability Transition in Cell Death', *Apoptosis*, 12(5), pp. 835–840. doi: 10.1007/s10495-006-0525-7.

Tsukihara, T. *et al.* (1996) 'The Whole Structure of the 13-subunit Oxidized Cytochrome c Oxidase at 2.8 A', *Science*, 272(5265), pp. 1136–1144.

Turunen, M., Olsson, J. and Dallner, G. (2004) 'Metabolism and Function of Coenzyme Q', *Biochimica et Biophysica Acta - Biomembranes*, 1660(1–2), pp. 171–199. doi: 10.1016/j.bbamem.2003.11.012.

Tzagoloff, A. and Dieckmann, C. L. (1990) 'PET Genes of Saccharomyces cerevisiae', *Microbiological Reviews*, 54(9), pp. 211–225. doi: 10.1001/archderm.140.9.1127.

Ugalde, C. *et al.* (2004) 'Human Mitochondrial Complex I Assembles Through the Combination of Evolutionary Conserved Modules: A Framework to Interpret Complex I Deficiencies', *Human Molecular Genetics*, 13(20), pp. 2461–2472. doi: 10.1093/hmg/ddh262.

Vendelin, M. *et al.* (2005) 'Mitochondrial Regular Arrangement in Muscle Cells: A "Crystal-Like" Pattern', *American Journal of Physiology - Cell Physiology*, 288(3), pp. 757–767. doi: 10.1152/ajpcell.00281.2004.

Verma, A. *et al.* (2016) 'Magnetic Resonance Spectroscopy - Revisiting the Biochemical and Molecular Milieu of Brain Tumors', *Biochimica et Biophysica Acta - Clinical*, 5, pp. 170–178. doi: 10.1016/j.bbacli.2016.04.002.

Vidoni, S. *et al.* (2017) 'MR-1S Interacts with PET100 and PET117 in Module-Based Assembly of Human Cytochrome c Oxidase', *Cell Reports*. ElsevierCompany., 18(7), pp. 1727–1738. doi: 10.1016/j.celrep.2017.01.044.

Vinothkumar, K. R., Zhu, J. and Hirst, J. (2014) 'Architecture of Mammalian Respiratory Complex I', *Nature*. Nature Publishing Group, 515(7525), pp. 80–84. doi: 10.1038/nature13686.

Viscomi, C. and Zeviani, M. (2017) 'MtDNA-maintenance defects: syndromes and genes', *Journal of Inherited Metabolic Disease*. Journal of Inherited Metabolic Disease, 40(4), pp. 587–599. doi: 10.1007/s10545-017-0027-5.

Vukotic, M. *et al.* (2012) 'Rcf1 Mediates Cytochrome Oxidase Assembly and Respirasome Formation, Revealing Heterogeneity of the Enzyme Complex', *Cell Metabolism*, 15(3), pp. 336–347. doi: 10.1016/j.cmet.2012.01.016.

Walker, J. E. (2013) 'The ATP Synthase: The Understood, the Uncertain and the Unknown', *Biochemical Society Transactions*, 41(1), pp. 1–16. doi: 10.1042/BST20110773.

Wang, L. (2016) 'Mitochondrial Purine and Pyrimidine Metabolism and Beyond and Beyond', *Nucleosides, Nucleotides & Nucleic Acids*. Taylor & Francis, 35(10–12), pp. 578–594. doi: 10.1080/15257770.2015.1125001.

Wang, X. *et al.* (2014) 'Oxidative Stress and Mitochondrial Dysfunction in Alzheimer's Disease', *Biochimica et Biophysica Acta - Molecular Basis of Disease*, 1842(8), pp. 1240–1247. doi: 10.1016/j.bbadis.2013.10.015.

Wang, X. and Huang, L. (2008) 'Identifying Dynamic Interactors of Protein Complexes by Quantitative Mass Spectrometry', *Molecular and Cellular Proteomics*, 7(1), pp. 46–57. doi: 10.1074/mcp.M700261-MCP200.

West, A. P., Shadel, G. S. and Ghosh, S. (2011) 'Mitochondria in Innate Immune Responses', *Nature Reviews Immunology*, 11(6), pp. 389–402. doi: 10.1038/nri2975.

Wiedemann, N. *et al.* (2003) 'Machinery for Protein Sorting and Assembly in the Mitochondrial Outer Membrane', *Nature*, 424(6948), pp. 565–571. doi: 10.1038/nature01753.

Wiedemann, N., Frazier, A. E. and Pfanner, N. (2004) 'The Protein Import Machinery of Mitochondria', *Journal of Biological Chemistry*, 19(3), pp. 357–372. doi: 10.1074/jbc.R400003200.

Wikström, M., Krab, K. and Sharma, V. (2018) 'Oxygen Activation and Energy Conservation by Cytochrome c Oxidase', *Chemical Reviews*, 118(5), pp. 2469–2490. doi: 10.1021/acs.chemrev.7b00664.

Wirth, C. *et al.* (2016) 'Structure and Function of Mitochondrial Complex I', *Biochimica et Biophysica Acta - Bioenergetics*, 1857(7), pp. 902–914. doi: 10.1016/j.bbabio.2016.02.013.

Wittig, I., Braun, H. P. and Schägger, H. (2006) 'Blue Native PAGE', *Nature Protocols*, 1, pp. 418–428. doi: 10.1038/nprot.2006.62.

Wittig, I. and Schägger, H. (2008) 'Features and Applications of Blue-Native and Clear-Native Electrophoresis', *Proteomics*, 8(19), pp. 3974–3990. doi: 10.1002/pmic.200800017.

Wortmann, S. B. *et al.* (2017) 'A Guideline for the Diagnosis of Pediatric Mitochondrial Disease: The Value of Muscle and Skin Biopsies in the Genetics Era', *Neuropediatrics*, 48(4), pp. 309–314. doi: 10.1055/s-0037-1603776.

Wu, M. *et al.* (2016) 'Structure of Mammalian Respiratory Supercomplex I1III2IV1', *Cell*. Elsevier, 167(6), pp. 1598-1609.e10. doi: 10.1016/j.cell.2016.11.012.

Xu, F. *et al.* (2004) 'The Role of the LRPPRC (Leucine-Rich Pentatricopeptide Repeal Cassette) Gene in Cytochrome Oxidase Assembly: Mutation Causes Lowered Levels of COX (Cytochrome c Oxidase) I and COX III mRNA', *Biochemical Journal*, 382(1), pp. 331–336. doi: 10.1042/BJ20040469.

Yamada, E. W. and Huzel, N. J. (1988) 'The Calcium-Binding ATPase Inhibitor Protein from Bovine Heart Mitochondria. Purification and properties', *Journal of Biological Chemistry*, 263(23), pp. 11498–11503.

Yang, D. *et al.* (1985) 'Mitochondrial Origins', *Proceedings of the National Academy of Sciences*, 82(13), pp. 4443–4447. doi: 10.1073/pnas.82.13.4443.

Ye, H. and Rouault, T. A. (2010) 'Human Iron-Sulfur Cluster Assembly, Cellular Iron Homeostasis, and Disease', *Biochemistry*, 49(24), pp. 4945–4956. doi: 10.1021/bi1004798.

Yoshikawa, S., Shinzawa-Itoh, K. and Tsukihara, T. (1998) 'Crystal Structure of Bovine Heart Cytochrome c Oxidase at 2.8 A Resolution', *Journal of Bioenergetics and Biomembranes*, 30(1), pp. 7–14. doi: https://doi.org/10.1023/A:1020595108560.

Zerbetto, E., Vergani, L. and Dabbeni-Sala, F. (1997) 'Quantification of Muscle Mitochondrial Oxidative Phosphorylation Enzymes via Histochemical Staining of Blue Native Polyacrylamide Gels', *Electrophoresis*, 18(11), pp. 2059–2064. doi: 10.1002/elps.1150181131.

Zeviani, M. and Di Donato, S. (2004) 'Mitochondrial Disorders', *Brain*, 127(10), pp. 2153–2172. doi: 10.1093/brain/awh259.

Zeviani, M., Spinazzola, A. and Carelli, V. (2003) 'Nuclear Genes in Mitochondrial Disorders', *Current Opinion in Genetics and Development*, 13(3), pp. 262–270. doi: 10.1016/S0959-437X(03)00052-2.

Zhu, J., Vinothkumar, K. R. and Hirst, J. (2016) 'Structure of Mammalian Respiratory Complex I', *Nature*. Nature Publishing Group, 536(7616), pp. 354–358. doi: 10.1038/nature19095.

Zhu, Z. *et al.* (1998) 'SURF1, Encoding a Factor Involved in the Biogenesis of Cytochrome c Oxidase, is Mutated in Leigh Syndrome', *Nature Genetics*, 20(4), pp. 337–343. doi: 10.1038/3804.

Zong, S. *et al.* (2018) 'Structure of the Intact 14-Subunit Human Cytochrome c Oxidase', *Cell Research*, 28(10), pp. 1026–1034. doi: 10.1038/s41422-018-0071-1.

Zurita Rendón, O. *et al.* (2014) 'The Arginine Methyltransferase NDUFAF7 is Essential for Complex I Assembly and Early Vertebrate Embryogenesis', *Human Molecular Genetics*, 23(19), pp. 5159–5170. doi: 10.1093/hmg/ddu239.